Technical Report Documentation Page

1. Report No.	2. Government Accession No.	3. Recipient's Catalog No.
FHWA/TX-14/0-6009-2		

4. Title and Subtitle	5. Report Date
EVALUATION OF BINDER AGING AND ITS INFLUENCE IN AGING OF HOT MIX ASPHALT CONCRETE: TECHNICAL REPORT	Published: January 2014
	6. Performing Organization Code

7. Author(s)	8. Performing Organization Report No.
Charles J. Glover, Rongbin Han, Xin Jin, Nikornpon Prapaitrakul Yuanchen Cui, Avery Rose, James J. Lawrence, Meghana Padigala, Edith Arambula, Eun Sug Park and Amy Epps Martin	Report 0-6009-2

9. Performing Organization Name and Address	10. Work Unit No. (TRAIS)
Texas A&M Transportation Institute College Station, Texas 77843-3135	11. Contract or Grant No. Project 0-6009

12. Sponsoring Agency Name and Address	13. Type of Report and Period Covered
Texas Department of Transportation Research and Technology Implementation Office 125 E. 11th Street Austin, Texas 78701-2483	Technical Report: October 2007–August 2012
	14. Sponsoring Agency Code

15. Supplementary Notes

Project performed in cooperation with the Texas Department of Transportation and the Federal Highway Administration.
Project Title: Evaluation of Binder Aging and its Influence in Aging of Hot Mix Asphalt Concrete
URL: http://tti.tamu.edu/documents/0-6009-2.pdf

16. Abstract

TxDOT Project 0-6009 was a comprehensive interdisciplinary research effort that has developed the ability to predict asphalt oxidative hardening over time and pavement depth, and the impact of this hardening on mixture durability. The many interrelated research and development accomplishments form three major elements: 1) *Pavement Binder Oxidation Model Development* (improved pavement temperature model, binder oxidation kinetics parameters, binder diffusion coefficients, model for predicting binder oxidation in pavements); 2) *Mixture Test Development and Measurements* (method for testing prismatic specimens cut from pavement cores, measurements of binder oxidation in pavements, measurements of binder oxidation in laboratory mixtures, evaluation of seal coat effectiveness); and 3) an *HMA Mixture Design Approach That Includes Binder Oxidation* (accelerated binder aging test, mixture design and analysis system, software user interface). Suggestions for implementation and future work include: 1) Introduce the software user interface to TxDOT engineers, 2) Adopt the accelerated aging test, 3) Implement a strategy for evaluating existing pavements by testing recovered binders for their oxidation and hardening kinetics, 4) Incorporate the pavement transport and thermal oxidation model into a new pavement design guide, 5) Further evaluate the effectiveness of maintenance treatments, 6) Further validate the pavement oxidation and hardening model, 7) Improve our fundamental understanding of oxidation kinetics chemistry and reaction kinetics, 8) Improve our fundamental understanding of the correlation between PAV and POV reaction kinetics parameters.

17. Key Words	18. Distribution Statement
Asphalt Oxidation Kinetics, Asphalt Oxidative Hardening, Accelerated Binder Aging Test, Asphalt Activation Energy, Asphalt Aging Analysis using Air Void Distribution, Chip Seal, Mixture Stiffness, DSR Function, Carbonyl Area, Pressure Aging Vessel.	No restrictions. This document is available to the public through NTIS: National Technical Information Service Alexandria, Virginia http://www.ntis.gov

19. Security Classif.(of this report)	20. Security Classif.(of this page)	21. No. of Pages	22. Price
Unclassified	Unclassified	526	

Form DOT F 1700.7 (8-72) Reproduction of completed page authorized

EVALUATION OF BINDER AGING AND ITS INFLUENCE IN AGING OF HOT MIX ASPHALT CONCRETE: TECHNICAL REPORT

by
Charles J. Glover, PhD, P.E.
Professor/Research Engineer
Artie McFerrin Department of Chemical Engineering/Texas A&M Transportation Institute

Rongbin Han, Xin Jin, Nikornpon Prapaitrakul
Former Graduate Research Assistants
Artie McFerrin Department of Chemical Engineering/Texas A&M Transportation Institute

Yuanchen Cui, Avery Rose
Graduate Research Assistants
Artie McFerrin Department of Chemical Engineering/Texas A&M Transportation Institute

James J. Lawrence, Meghana Padigala
Former Graduate Research Assistants, Texas A&M Transportation Institute

Edith Arambula
Associate Research Engineer, Texas A&M Transportation Institute

Eun Sug Park
Research Scientist, Texas A&M Transportation Institute

and

Amy Epps Martin, PhD, P.E.
Research Engineer, Texas A&M Transportation Institute

Report 0-6009-2
Project 0-6009
Project Title: Evaluation of Binder Aging and its Influence in Aging of Hot Mix Asphalt Concrete

Performed in cooperation with the
Texas Department of Transportation
and the
Federal Highway Administration

Published: January 2014

TEXAS A&M TRANSPORTATION INSTITUTE
College Station, Texas 77843-3135

DISCLAIMER

This research was performed in cooperation with the Texas Department of Transportation (TxDOT) and the Federal Highway Administration (FHWA). The contents of this report reflect the views of the authors, who are responsible for the facts and the accuracy of the data presented herein. The contents do not necessarily reflect the official view or policies of the FHWA or TxDOT. This report does not constitute a standard, specification, or regulation.

This report is not intended for construction, bidding, or permit purposes. The engineer in charge of the project was Charles J. Glover, P.E. #48732, TX. The United States Government and the State of Texas do not endorse products or manufacturers. Trade or manufacturers' names appear herein solely because they are considered essential to the object of this report.

ACKNOWLEDGMENTS

This project was conducted in cooperation with TxDOT and FHWA and the authors are indebted to them for their support and funding of this research project. The authors also offer thanks to Mr. Gerald Peterson, for providing valuable leadership, support and technical assistance as the TxDOT project director, Mr. Robert Lee and Ms. K.C. Evans for serving as members of the project monitoring committee, and special thanks to Dr. German Claros for his belief in the value of this research and support of this project in his role as TxDOT Pavements and Materials Research Engineer throughout the project. We also thank Arif Chowdhury, Rick Canatella, and David Zeig, of the Texas A&M Transportation Institute for their laboratory and field contributions and Dr. Robert L. Lytton for his very helpful discussions of instrument design and data analysis. Finally, the authors also thank the various TxDOT district offices that provided assistance in material and pavement core procurement.

TABLE OF CONTENTS

Page

List of Figures ..... **xiii**

List of Tables ..... **xviii**

CHAPTER 1. INTRODUCTION **1**
BACKGROUND PERSPECTIVE FOR THIS PROJECT 2
Binder Oxidation and Hardening *2*
The Importance of Oxidative Hardening to Mixture Performance *8*
Oxidation in Pavements *9*
Maintenance Treatments to Retard Oxidation *20*
Pavement Service Life Design *21*
MAINTENANCE TREATMENT SURVEYS 22
User Survey – TxDOT Project 0-1787 (Texas Tech) *22*
User Survey – TxDOT Project 0-6009 ..... *25*
SUMMARY 26

CHAPTER 2. PROJECT DESIGN AND FINAL REPORT OVERVIEW **29**
FIELD SECTIONS 31
EDE 1. BINDER OXIDATION AND HARDENING 35
EDE 1-1. Database of Binder Oxidation and Hardening Kinetics Parameters *36*
EDE 1-2. Database of Pavement Temperatures across Texas *38*
EDE 1-3. Pavement Oxidation and Hardening Rates (Thermal Transport Model) *39*
EDE 1-4. Improved Model of Pavement Oxidation and Hardening Rates *39*
EDE 1-5. Pavement Oxidation and Hardening Rates (Thermal and Oxygen Transport Model) *40*
EDE 1-6. Field Binder Aging Rates for Calibration of the Transport Model *40*
EDE 1-7. Laboratory Binder Aging Test *41*
EDE 2. MAINTENANCE TREATMENT EFFECTIVENESS IN REDUCING AGING 41
EDE 3. DECLINE OF MIXTURE FATIGUE RESISTANCE DUE TO AGING 42
SUMMARY 44

CHAPTER 3. OXIDATION KINETICS AND HARDENING PARAMETERS FOR 24 BINDERS COMMONLY USED BY TXDOT **47**
ABSTRACT 47
INTRODUCTION 47
Asphalt Materials *47*
Asphalt Characterization *48*
Asphalt Aging Kinetics – Constant-Rate Period *48*
Asphalt Aging Kinetics – Fast-Rate Period *48*
Objectives *49*
MATERIALS AND METHODOLOGY 49
Materials *49*
Aging Procedure *50*
Materials Characterization *51*
RESULTS AND DISCUSSION 51
Task Progress *51*
Analysis of Carbonyl Area Data *51*
Summary of Oxidation Kinetics Data *55*

Correlation between Fast-Rate and Constant-Rate Kinetics *55*
Correlation between Activation Energy and Frequency Factor *56*
Analysis of Rheological Data *58*
Viscosity and DSR Function Hardening Susceptibility *59*
SUMMARY 60

CHAPTER 4. OXYGEN DIFFUSIVITY IN ASPHALTS AND MASTICS 63
ABSTRACT 63
INTRODUCTION 63
MATERIALS AND METHODOLOGY 64
Overview of the Experimental Design *64*
Materials *65*
Methodology *66*
RESULTS AND DISCUSSION 71
Oxidation Rates at ES And SI of Asphalt Film *71*
Estimation of P_{si} and Calculation of Oxygen Diffusivity *72*
Correlation of Oxygen Diffusivity with Binder Viscosity *72*
Prediction of Carbonyl Growth in an Asphalt Film Using the Diffusivity Correlation *75*
Effect of Mastic Fines on Oxygen Diffusivity in Asphalts *77*
Calculation of Pavement Oxidation *78*
SUMMARY 79

CHAPTER 5. COMPARISONS OF THE IMPACT OF SEVERAL AIR TEMPERATURE MODELS ON CALCULATIONS OF PAVEMENT TEMPERATURE AND ASPHALT OXIDATION 81
ABSTRACT 81
INTRODUCTION 81
OBJECTIVES 82
PRELIMINARIES 82
Pavement Temperature Models and Pavement Thermo-Physical Properties *82*
Oxidation Model *82*
SINGLE SITE IMPACT OF AIR TEMPERATURE ON PAVEMENT TEMPERATURE 83
Sensitivity of Pavement Temperature to Annual Mean Air Temperature *84*
Sensitivity of Pavement Temperature to Hourly Air Temperature Variations *85*
MULTI-SITE COMPARISONS OF FIVE COMMON AIR TEMPERATURE MODELS (PHASE ONE) 86
Methodology *86*
Results and Discussion *88*
MULTI-SITE EVALUATION OF A STATISTICAL PATTERN AIR TEMPERATURE MODEL (PHASE TWO) 89
Materials and Methods *89*
Methodology of the Pattern Model *90*
CASE STUDY OF THE PATTERN MODEL 92
Results and Discussions *94*
SUMMARY 100

CHAPTER 6. MODELING PAVEMENT TEMPERATURE FOR USE IN BINDER OXIDATION MODELS AND PAVEMENT PERFORMANCE PREDICTION 103
ABSTRACT 103
INTRODUCTION 103
MODEL CONCEPTS AND DEVELOPMENT 105
Heat Transfer in Pavement *105*

The Surface Boundary Condition *106*
Bottom Boundary Condition *107*
Numerical Solution of the Model *108*
OBTAINING MODEL INPUT DATA AND PARAMETERS 108
Climate Databases and Hourly Air Temperature Analysis *108*
Interpolating Site-Specific Pavement Parameters *109*
MODEL VALIDATION AND APPLICATION 116
Lamar, Texas, Pavement Site 48-1068 ..... *116*
Otter Tail Minnesota, Pavement Site 27-1028 ..... *118*
SUMMARY 119

CHAPTER 7. A TRANSPORT MODEL OF ASPHALT BINDER OXIDATION IN PAVEMENTS 121
ABSTRACT 121
INTRODUCTION 121
Asphalt Aging in Pavements *121*
Pavement Temperature Model *122*
OBJECTIVES 123
METHODOLOGY 124
Analyzing Air Void Structure in the Pavement *124*
Binder Oxidation Model Development *124*
RESULTS AND DISCUSSION 127
Outputs from the Binder Oxidation Model *127*
Model Parameter Estimation *128*
Binder Oxidation Model Calculation Using Temperature Profile from Pavement Temperature Prediction Model *131*
SUMMARY 133

CHAPTER 8. IMPROVED PAVEMENT OXIDATION MODEL: DEVELOPMENT AND VALIDATION 135
ABSTRACT 135
INTRODUCTION 135
MATERIALS AND METHODOLOGY 136
Overview of the Experimental Design *136*
Materials and Pavement Sites *137*
Methodology *138*
MATHEMATIC MODEL OF PAVEMENT OXIDATION 142
Vertical Transport of Oxygen through an Air Void Channel *142*
Horizontal Oxygen Diffusion and Reaction from an Air Void Channel *145*
Pavement Air Void Characterization: Extending Model Calculation to Entire Pavement Layers *147*
RESULTS AND DISCUSSION 152
Model Calculation of Oxidation Rates for One Air Void Channel *152*
Model Calculation of Layer-by-Layer Bulk Oxidation Rates for a Pavement *154*
Model Validation *160*
SUMMARY 169

CHAPTER 9. MODELING ASPHALT OXIDATION IN PAVEMENT WITH FIELD VALIDATION 171
ABSTRACT 171
INTRODUCTION 171
MODEL DEVELOPMENT 172

Model Components *172*
Accessible Air Void and Mixture Design *173*
Asphalt Oxidation Kinetics *173*
Oxygen Transport-Reaction Model and Oxygen Diffusivity *174*
FIELD CALIBRATION AND VALIDATION OF PAVEMENT OXIDATION MODEL 175
Materials *175*
Methodology *175*
Results and Discussion *176*
SUMMARY 178

CHAPTER 10. AN OXIDATIVE AGING STUDY OF SEAL COAT TREATED PAVEMENT 179
ABSTRACT 179
INTRODUCTION 179
OBJECTIVES 180
EXPERIMENTAL METHODOLOGY 180
Materials *180*
Binder Extraction and Recovery *181*
Recovered Binder Aging in the Pressure Oxidation Vessel (POV) *182*
Fourier Transform Infrared Spectrometer (FTIR) *182*
Dynamic Shear Rheometer *182*
RESULTS AND DISCUSSION 183
Oxidation Evaluation *183*
Recovered Binder Pressure Oxidation Vessel Testing *188*
SUMMARY 194

CHAPTER 11. DIRECT TENSION TESTING OF HOT MIX ASPHALT FIELD SAMPLES 195
DIRECT TENSION TESTING OF FIELD SAMPLES 195
Field Sample Selection *195*
Sample Configuration and Preparation *196*
Machine Modifications *198*
Test Modifications *199*
Analysis Modifications *200*
RESULTS 200
SUMMARY 203

CHAPTER 12. INVESTIGATION OF AGING EFFECTS AT A SINGLE FIELD SITE USING DIRECT TENSION TESTING 205
MATERIALS 205
TESTING METHODOLOGY 206
Sample Preparation *206*
LMLC Samples *206*
Field Samples *208*
Binder Extraction *209*
HMA Mixture Testing *210*
VEC TEST *210*
RDT TEST* *211*
Binder Testing *211*
TEST RESULTS 211
Extracted Binder Test Results *212*
Field Sample Test Results *215*

LMLC Sample Test Results *217*
COMPARISON OF TEST RESULTS 219
LMLC vs. Field Samples *219*
LMLC Samples vs. Extracted Binder *220*
Field Samples vs. Extracted Binders *222*

CHAPTER 13. COMPARISON OF AGING IN THE FIELD WITH ACCELERATED LABORATORY AGING 225
MATERIALS AND TESTING 225
Site Selection *225*
X-Ray CT Analysis *226*
US 277 Laredo District *228*
US 83 Childress District *230*
SH 24 Paris District *232*
Discussion *233*
LMLC Sample Preparation *234*
Field Sample Preparation *235*
Testing Procedures *236*
LMLC SAMPLE TEST RESULTS 237
FIELD SAMPLE TEST RESULTS 239
COMPARISON OF FIELD AND LMLC SAMPLE RESULTS 243
SUMMARY 245

CHAPTER 14. AN ACCELERATED METHOD FOR COMPARING BINDERS FOR PAVEMENT DURABILITY (AN ACCELERATED BINDER AGING TEST) 247
ABSTRACT 247
INTRODUCTION 247
EXPERIMENTAL METHODS 248
*Pressure Aging Vessel** *248*
Pressure Oxidation Vessel *249*
Fourier Transform Infrared Spectrometer *249*
Dynamic Shear Rheometer *249*
RESULTS AND DISCUSSION 249
Reaction Rate *249*
Rheological Properties *254*
Activation Energy Comparison *257*
Kinetics Parameters Correlation *260*
AN ACCELERATED BINDER AGING TEST 260
SUMMARY 264

CHAPTER 15. TOWARD A FRAMEWORK FOR INCORPORATING AGING IN MIXTURE DESIGN 265
MATERIAL SELECTION 265
FIELD SAMPLE TEST RESULTS 266
BINDER VS. MIXTURE RESULTS 271
RECOMMENDATIONS FOR MIXTURE DESIGN SYSTEM 276

CHAPTER 16. PAVEMENT AGING MODEL GRAPHICAL USER INTERFACE AND SUPPORTING SOFTWARE 279
INTRODUCTION TO THE AGING MODEL GRAPHICAL USER INTERFACE AND SUPPORTING SOFTWARE 279
Overview of Software *279*
Software Packages Supplied *280*

USING THE AGING MODEL GRAPHICAL USER INTERFACE (AMG) 282
Introduction *282*
Inputs *283*
Outputs *289*
USING THE REACTION KINETICS PARAMETERS GRAPHICAL USER INTERFACE 292
Introduction *292*
Reaction Kinetics Parameters from Full POV Lab Testing *293*
Constant Rate Activation Energy from PAV Lab Test Results *300*
USING THE TEMPERATURE PROFILE GRAPHICAL USER INTERFACE (TPG) 301
Introduction *301*
Part 1: Using the TPG (Inputs Already Determined) *302*
Part 2: Suggested Methods of: Determining Input Parameters, Determining the Summer and Winter Period, and Formatting Inputs *306*
SUMMARY 313

CHAPTER 17. SUMMARY AND RECOMMENDATIONS 315
SUMMARY 315
Development of a Pavement Oxidation Model *316*
Mixture Test Development and Measurements *318*
An HMA Mixture Design Approach That Includes Binder Oxidation *321*
RECOMMENDATIONS 322

REFERENCES 325

APPENDIX A CARBONYL CONTENT AT ES AND SI: EXPERIMENTAL MEASUREMENT VERSUS MODEL CALCULATION 335

APPENDIX B PAVEMENT TEMPERATURE 341

APPENDIX C AIR VOID CHARACTERIZATION 363

APPENDIX D CALCULATED FIELD OXIDATION RATES OF FIELD VALIDATION SITES 379

APPENDIX E TABLES OF REHEOLOGICAL PROPERTIES, CARBONYL AREA, AND DSR FUNCTION HARDENING WITH PAVEMENT SERVICE TIME DATA 393

APPENDIX F TABLES OF BULK S.G., AIR VOID, AND BINDER CONTENT DATA 459

APPENDIX G TABLES OF HMAC LMLC MIXTURE PROPERTY DATA 491

APPENDIX H TABLES OF HMAC FIELD SAMPLE MIXTURE PROPERTY DATA 497

LIST OF FIGURES

Page

Figure 1. Typical Hardening Response of an Unmodified Asphalt Binder to Oxidation. 5
Figure 2. DSR Function Growth of Recovered Binders from Texas and Minnesota, Aged in Environmental Room (60°C) (Data from Woo et al., 2007). 7
Figure 3. Impact of Binder Oxidative Hardening on Mixture Fatigue Resistance. 8
Figure 4. Calculated versus Measured DSR Function Growth. 11
Figure 5. DSR Function Hardening with Pavement Service Time in Texas and MnROAD Pavements. 13
Figure 6. Binder Hardening Related to Local Pavement Accessible Air Voids. 15
Figure 7. Schematic Representation of Pavement Heat Transfer. 16
Figure 8. Sample Calculation of Pavement Temperatures Using the EICM Method at 48-1068, TX (Mar-03-1994 to Mar-09-1994), Compared with Field Measurements. 17
Figure 9. Sample Calculations of Pavement Temperature Using Enhanced Numerical Model Principle at 48-1068, TX (Mar-03-1994 to Mar-09-1994), Compared with Field Measurement. 18
Figure 10. Schematic Outline of the Research Plan and Experimental Design Elements. 30
Figure 11. Field Section Locations and Texas Environmental Zones. 32
Figure 12. Typical Test Section and Coring Layout. 35
Figure 13. Daily Pavement Temperature Variation, July 1994, Refugio, Texas. 38
Figure 14. Testing of Prismatic Specimens in Direct Tension for CMSE. 42
Figure 15. Testing Protocol for Pavement Cores. 44
Figure 16. CA Growth of ALON PG64-22 at Five Temperatures. 51
Figure 17. Temperature Dependency of k_c Values for ALON PG64-22. 53
Figure 18. Comparison of Model Prediction (Dashed Lines) of CA to Experimental Data (Symbols) for ALON PG 64-22. 54
Figure 19. Empirical Linear Correlation between the Fast-Rate and Constant-Rate Activation Energies. 56
Figure 20. Isokinetic Temperature 359.4 K of Constant-Rate Reaction Obtained from Various Data Sources. 57
Figure 21. The Correlation between Fast-Rate Kinetics Parameters. 58
Figure 22. HS of Limiting Viscosity of ALON PG64-22. 58
Figure 23. HS of DSR Function of ALON PG64-22. 59
Figure 24. Schematic of Thin Film Model Configuration. 67
Figure 25. Sample Comparison of Oxidation Rates at ES and SI (SEM 64-22). 71
Figure 26. Correlation of D/T with Limiting Viscosity (η_o^*) 75
Figure 27. Sample Calculation of Carbonyl Growth at ES and SI of an Asphalt Film of SEM 64-22: Model Calculation vs. Experimental Measurement. 76
Figure 28. Sensitivities of Calculated Oxygen Diffusivity to Variations in c and α. 77
Figure 29. Effect of Volume Fraction of Aggregate Fines on Oxygen Diffusivity. 78
Figure 30. Calculation of Pavement Oxidation with Different Oxygen Diffusivity. 79
Figure 31. The Effects of Various Inputs on Pavement Temperature. 84
Figure 32. The Effect of Different Annual Mean Air Temperatures on Pavement Temperatures. 85

Figure 33. The Effect on Pavement Temperatures of Using a Single Daily Average Air Temperature Compared to Using Measured Hourly Temperatures. 86
Figure 34. Seasonal-Trend Decomposition of Hourly Air Temperature Data Shown for 30 Days. 93
Figure 35. The Pattern Component of Figure 4 Shown for Five Days. 93
Figure 36. Comparison of Air Temperature Calculations before and after Linear Transformation with Measured Data. 94
Figure 37. Yearly Temperature Patterns for Six Locations. 97
Figure 38. Schematic Representation of Heat Transfer Model of Pavement. 105
Figure 39. Model Parameters Sensitivity Analysis: Effect of Changing Model Parameters in Their Practical Ranges to Average of Absolute Error of Model Prediction. 110
Figure 40. Distribution Map of 29 SMP Pavement Sites Studied 111
Figure 41. Distribution of Optimized Albedo Values: (a) Summer; (b) Winter (U.S. Maps Courtesy of Tom Patterson). 113
Figure 42. Distribution of Optimized Values of the Algebraic Difference between Emissivity and Absorption Coefficient: (a) Summer, (b) Winter (U.S. Maps Courtesy of Tom Patterson). 115
Figure 43. Distribution of Optimized Values of Absorption Coefficient (U.S. Map Courtesy of Tom Patterson). 116
Figure 44. Comparison of Model Predicted Annual Hourly Pavement Temperature and Field Measurement at 25 mm below the Surface: (a) Pavement 48-1068 (Lamar, Texas); (b) Pavement 27-1028 (Otter Tail, Minnesota). 118
Figure 45. Modeling Concept of Asphalt Binder Oxidation in Pavements. 125
Figure 46. Results from Transport Model of Binder Oxidation in Pavements for Binder Thickness of 1mm at 333.3 K. 128
Figure 47. Carbonyl Area Growth of Asphalt Mixture in Environmental Room Aging. 129
Figure 48. Air Void Radius Distribution and Air Void Coordinate. 129
Figure 49. Oxidation Model vs. ER Aging Rate before and after Parameter Optimization Process: Case 1. 130
Figure 50. Oxidation Model vs. ER Aging Rate before and after Parameters Optimization Process: Case 2. 131
Figure 51. Pavement Temperature Profile for SH 21 in Bryan, TX, during July 1994. 132
Figure 52. Calculated Carbonyl Area from Binder Oxidation Model at Various Depths. 133
Figure 53. Schematic of X-Ray CT System and Gray Scale Images Obtained. 139
Figure 54. X-ray CT Image Analysis: (a) Original Grayscale Image; (b) Black-and-White Image after Threshold; and (c) Black-and-White Image of Interconnected Air Void. 140
Figure 55. Schematic of Two Steps Involved in Oxygen Transport and Reaction in Pavements. 143
Figure 56. Sample Calculation of Oxygen Concentration Profile in an Air Void Channel at Two Limit Conditions. 145
Figure 57. Sample Statistical Distribution of Air Void Size in a Pavement Layer of US82. 148
Figure 58. Air Void Distribution at Different Layers of Pavement US82. 148
Figure 59. Example of Air Void Probability Plot for an Asphalt Pavement Specimen, Log-Normal Distribution and Weibull Distribution. 150
Figure 60. Sample Calculation of Air Void Distribution with a Log-normal Distribution Function. 151

Figure 61. Effect of Air Void Radius on Calculated Yearly Carbonyl Growth. 152
Figure 62. Effect of Shell Distance on Calculated Yearly Carbonyl Growth. 153
Figure 63. Sample Calculation of Carbonyl Growth for an Air Void Channel as a Function of Depth of Pavement Layers. 154
Figure 64. Schematic Layout of the Model Structure to Calculate Oxidation Rate for a Pavement Layer. 155
Figure 65. Pavement Temperature of US82 at Different Depths in Pavements in a Summer Period. 156
Figure 66. Bulk Carbonyl Growth Rates (Oxidation Rates) of US82 for One-Year Period at Different Pavement Layers. 159
Figure 67. Measured Oxidation Rates of Asphalt Binders in Various Pavements. 161
Figure 68. Temperature Profiles of Top Layer of Validation Pavement Core at (a): Winter from January 15 to January 30, 1994, and (b): Summer from July 1 to July 15, 1994. 163
Figure 69. Collection of Representative Images of Total Air Void for Each Field Cores. 164
Figure 70. Comparison of Measured and Modeled Field Oxidation Rates. 168
Figure 71. Comparison of Field Data and Model Estimates of CA for US 277 Shoulder. 177
Figure 72. Comparison of CA Calculations using Different Models for US 277 Shoulder. 178
Figure 73. Sample Core with Seal Coat Treatment from US 82 Shoulder Section Collected in 2009. 181
Figure 74. Carbonyl Area Distributions in Wheel Path Cores for Years 1 and 2. 183
Figure 75. Carbonyl Area Distributions in Wheel Path Cores for Years 1 and 3. 184
Figure 76. Carbonyl Area Distributions in Shoulder Cores for Years 1 and 2. 184
Figure 77. Carbonyl Area Distributions in Shoulder Cores for Years 1 and 3. 185
Figure 78. Average Carbonyl Areas for Field Cores. 186
Figure 79. Average DSR Function for Field Cores. 186
Figure 80. DSR Function Hardening Susceptibility for Each Layer in Field Cores. 188
Figure 81. Carbonyl Area Growth for Pavement Binder in POV. 189
Figure 82. Carbonyl Area Growth for 1st Layer (Mixed) Binder in POV. 189
Figure 83. Carbonyl Area Growth for Seal Coat Layer Binder in POV. 190
Figure 84. Activation Energies for Field-recovered (a) Original Binder, (b) 1st Layer Binder, and (c) Seal Coat Layer Binder. 191
Figure 85. DSR Function Hardening Susceptibilities. 192
Figure 86. DSR Function Hardening Susceptibility for Recovered Binder and Recovered Binder after POV. 193
Figure 87. DSR Function Hardening Susceptibility for the Seal Coat Binder. 194
Figure 88. Sample Trimming Procedures with Ends (a) Untrimmed and (b) Trimmed. 197
Figure 89. (a) Vertical Gluing Jig and (b) Horizontal Magnetic Gluing Vice with Three Inch Wide Sample. 198
Figure 90. Three-Inch Wide Sample Attached to Ball and Socket Joint Shown with Movable Base Plate. 199
Figure 91. Vertical Gluing Jig (a) and Test Setup (b) for LMLC Samples. 208
Figure 92. Field Sample Testing Configuration. 208
Figure 93. Magnetic Gluing Vice for Field Samples. 209
Figure 94. Field Sample Test Setup with Ball and Socket Joint at Base. 210
Figure 95. CA of LMLC Samples at Optimum Binder Content. 212
Figure 96. CA of LMLC Samples at Medium AV. 213

Figure 97. CA Value with Depth and Years for US 277 Shoulder. 213
Figure 98. CA Value with Depth and Years for US 277 Wheel Path. 214
Figure 99. Average Combined CA for All Sections of US 277. 215
Figure 100. Eve for US 277 Field Samples. 216
Figure 101. N_f for US 277 Field Samples. 217
Figure 102. E_{ve} for LMLC Samples at Differing AV. 218
Figure 103. E_{ve} for LMLC Samples at Differing Binder Contents. 218
Figure 104. Number of Loads to Fatigue Failure for LMLC Samples with Medium AV and Optimum Binder Content. 219
Figure 105. Laboratory to Field E_{ve} Comparison. 220
Figure 106. E_{ve} vs. CA for LMLC Samples with Different AV and Increasing Age. 221
Figure 107. E_{ve} vs. CA for LMLC Samples with Different Binder Contents and Increasing Age. 221
Figure 108. E_{ve} vs. CA of Field Samples for US 277 between 2008 and 2011. 222
Figure 109. X-ray CT Equipment. 226
Figure 110. Sample of X-ray CT Image. 227
Figure 111. Total and Interconnected AV Yearly Results for US 277. 228
Figure 112. Total and Interconnected AV Results for Untreated and Treated Sections on US 277. 229
Figure 113. Total and Interconnected AV Yearly Results for US 83. 230
Figure 114. Total and Interconnected AV Results for Untreated and Treated Sections on US 83. 231
Figure 115. Total and Interconnected AV Yearly Results for SH 24. 232
Figure 116. Total and Interconnected AV Results for Untreated Sections on SH 24. 233
Figure 117. Test Setup for (a) LMLC and (b) Field Samples. 236
Figure 118. E_{ve} Trends for Artificially Laboratory-Aged LMLC Samples. 238
Figure 119. N_f Trends for Artificially Laboratory-Aged LMLC Samples. 239
Figure 120. E_{ve} for Field Samples Taken from the Wheel Path. 240
Figure 121. E_{ve} for Field Samples Taken from the Shoulder. 241
Figure 122. N_f for Field Samples Taken from the Wheel Path. 242
Figure 123. N_f for Field Samples Taken from the Shoulder. 243
Figure 124. LMLC and Field Sample Combined E_{ve} Results. 244
Figure 125. LMLC and Field Sample Combined N_f Results. 244
Figure 126. Carbonyl Area Increases with Hours of PAV Aging. 250
Figure 127. Carbonyl Area Increases with Days of POV Aging. 250
Figure 128. CA Rate vs. 1/RT, Activation Energy for Martin PG70-22 is 86.25 kJ/mol. 252
Figure 129. Comparison of 90°C Reaction Rates Determined from PAV and POV Methods. 252
Figure 130. Comparison of 100°C Reaction Rates Determined from PAV and POV Methods. 253
Figure 131. Limiting Viscosity HS of Martin PG 70-22 from PAV. 255
Figure 132. Low Shear Rate Limiting Viscosity HS of Martin PG 70-22 from POV. 256
Figure 133. DSR Function HS of Martin PG 70-22 from PAV. 256
Figure 134. DSR Function HS of Martin PG 70-22 from POV. 257
Figure 135. E_{AC} (4 atm and 20 atm, abs O_2) vs. E_{AC} (1 atm abs air). 258
Figure 136. PAV (20.7 atm Air Gauge) vs. POV (1 atm Air abs) Activation Energy. 259

Figure 137. AP^{α} vs. E_{AC} from PAV Data..... 260
Figure 138. E_{ve} for Shoulders of All Field Sites. 267
Figure 139. N_f for Shoulders of All Field Sites..... 268
Figure 140. E_{ve} for Wheelpaths of All Field Sites. 269
Figure 141. N_f for Wheelpaths of All Field Sites..... 270
Figure 142. Example Plot of E_{ve} vs. DSR_f to Examine AV Effect (US 277). 272
Figure 143. Example Plot of E_{ve} vs. DSR_f to Examine Binder Content Effect (US 277). 272
Figure 144. Example Plot of N_f vs. DSR_f to Examine AV Effect (US 277). 273
Figure 145. Example Plot of N_f vs. DSR_f to Examine Binder Content Effect (US 277)..... 273
Figure 146. Average Log-Log Slope of N_f vs. DSR_f versus Average FT_e. 275
Figure 147. Flow Chart of Recommended Mixture Design System with Aging..... 277
Figure 148. Image of Aging Model Graphical User Interface (AMG)..... 283
Figure 149. Image of CA vs. Time Pop up Window Graphical Result. 290
Figure 150. Image of DSR Fn vs. Time Pop up Window Graphical Result..... 291
Figure 151. Reactions Kinetics Parameters Graphical User Interface..... 293
Figure 152. Results from Aging Experiment Window. 295
Figure 153. Window for Visual Determination of Which Data Should Be Considered in the Optimization and the Apparent Beginning of the Constant Rate Period. 296
Figure 154. Original Data and Optimized Model Shown Together Window..... 298
Figure 155. Results from Aging Experiment, with Constant Rate Regression Lines..... 299
Figure 156. Temperature Profile Graphical User Interface. 301
Figure 157. Site Specific Hourly Inputs Formatted as Required by the TPG..... 304
Figure 158. Annual Mean Total Snowfall Map Taken from the NCDC Website (http://cdo.ncdc.noaa.gov/cgi-bin/climaps/climaps.pl)..... 309
Figure 159. Distribution of Optimized Albedo Values. Taken from Chapter 6 (Han et al., 2011a). 310
Figure 160. Distribution of Optimized Values of ADBAE. Taken from Chapter 6 (Han et al., 2011a)..... 311
Figure 161. Annual Mean Relative Humidity Map. Taken from the NCDC Website (http://cdo.ncdc.noaa.gov/cgi-bin/climaps/climaps.pl)..... 312
Figure 162. Distribution of Optimized Values of Absorption Coefficient. Taken from Chapter 6 (from Han et al., 2011a). 312

LIST OF TABLES

Page

Table 1. Field Sections for the Aging Experiment (EDE 3). 33
Table 2. Field Sections for Maintenance Treatment Experiment (EDE 2). 34
Table 3. Binders Selected for TxDOT Project 0-6009. 37
Table 4. Binder Oxidation Nominal Sampling Schedule. 37
Table 5. Relation of the Report Chapters to the Test Plan, Figure 10. 45
Table 6. Binders Selected for Oxidation Kinetics Study 50
Table 7. Binder Oxidation Sampling Schedule. 50
Table 8. Optimized Model Parameters for 15 Asphalts. 54
Table 9. Summary of Oxidation Kinetics Parameters. 55
Table 10. Viscosity and DSR Function Hardening Susceptibility. 60
Table 11. List of Materials and Material Parameters. 65
Table 12. Summary of P_{SI} and D_{O2} for Studied Asphalt Binders. 73
Table 13. Summary of D_{O2} for Studied Asphalt Mastics at Different Volume Fraction of Aggregate Fines. 77
Table 14. Information for the Pavement Sites Studied. 87
Table 15. RMSE and BIAS for Modeled Hourly Air Temperatures for One Year. 88
Table 16. Statistical Comparisons of Modeled Versus Measured Hourly Pavement Temperatures for One Year for Five Air Temperature Input Models. 88
Table 17. Percent Difference in One-Year Asphalt Oxidation Rates Calculated from Modeled versus Measured Hourly Pavement Temperatures for Five Air Temperature Input Models. 89
Table 18. Pavement Sites Selected for Study of the Performance of Hourly Air Temperature Models. 90
Table 19. RMSE and MAE of Estimated Hourly Air Temperatures of One Year. 95
Table 20. RMSE and MAE of Estimated Hourly Pavement Surface Temperatures for One Year. 95
Table 21. Absolute Error Statistics of Asphalt Oxidation and Hardening Rates at Calculated Pavement Surface Temperature and Atmospheric Pressure. 96
Table 22. RMSEs (°C) of Hourly Air Temperature Using Onsite Pattern, Offsite Pattern and Sine-Sine Model. 97
Table 23. Comparison of Hourly Air Temperature Estimates Using Seasonal Patterns and Yearly Pattern for Nine States in the U.S. 98
Table 24. Comparison of Summer and Winter Patterns. 98
Table 25. Errors in Predicting Summer Asphalt Oxidation Rates. 99
Table 26. Absolute Error Statistics of Oxidation Rates (CA/year) Using Daily Maximum and Minimum Air Temperatures Obtained from Hourly Data. 100
Table 27. Optimized Model Parameters of 29 Pavement Sites across the Country. 112
Table 28. Carbonyl Area of the Recovered Binder (Exxon AC-20) from SH 21, TX. 133
Table 29. List of Field Sites Studied. 138
Table 30. Oxidation and Hardening Kinetic Parameters of Binders from Field Sites. 142

Table 31. Average Air Void Radius Calculated for Each Air Void Range at Different Pavement Layers of US82. 157
Table 32. Number of Air Voids Calculated for Each Air Void Range at Different Pavement Layers of US82. 157
Table 33. Shell Distance Calculated for Each Air Void Range at Different Pavement Layers of US82. 157
Table 34. P_{av} Calculated for Each Air Void Range at Different Pavement Layers of US82..... 158
Table 35. Oxidation Rates Calculated for Each Air Void Range at Different Pavement Layers of US82. 159
Table 36. Summary of Air Void Parameters at the Top Layer of Pavement Cores. 165
Table 37. Summary of Maximum and Minimum Oxidation Rates Calculated for Each Pavement Core Layers. 167
Table 38. Comparison of Measured and Modeled Field Oxidation Rates. 168
Table 39. Data of Field Cores, Binders, and Loose Mix.* 175
Table 40. Layer-by-Layer Diffusion Depth (mm) and CA of US 277 and US 82 Field Cores. 176
Table 41. Pavement Construction and Coring Information. 181
Table 42. DSR Function Parameter Estimates for the Different Binder Data Sets. 193
Table 43. Field Sample Characteristics. 196
Table 44. Field Sample VEC and RDT* Test Results. 201
Table 45. D-Optimal Statistical Design for LMLC Samples. 207
Table 46. Binder Content and Air Voids for US 277 Samples. 207
Table 47. Asphalts Used in the Study. 248
Table 48. Constant-Rate Reaction Rates for Eight Binders. 251
Table 49. Summary of Constant-Rate Kinetics Parameters at POV and PAV Conditions. 254
Table 50. Hardening Susceptibility for Eight Binders. 255
Table 51. Measured and Calculated Kinetics Parameters Based on PAV Activation Energies and Fast-Rate-Constant-Rate Correlations. 263
Table 52. Field Sample Collection Sites. 266
Table 53. Slopes of E_{ve} vs. DSR_f and N_f vs. DSR_f for LMLC Samples (Log-Log). 274
Table 54. Predicted vs. Measured Log-Log Field Slopes of N_f vs. DSR_f. 276

CHAPTER 1. INTRODUCTION

In spite of mounting evidence in recent years that asphalt binders oxidize in pavements and that this oxidation is harmful to pavement durability, implementation of this evidence to design practice has been slow. Three likely hypothetical arguments for the lack of implementation are: that below the immediate surface, temperatures are moderated enough so as to greatly reduce oxidation, that oxygen transport into the pavement below the surface is insignificant, and that binder hardening is self limiting due to accompanying decreases in oxygen diffusivity with oxidation and/or because of depletion of reactive components.

In fact, all three of these hypotheses have been incorporated into the mechanistic-empirical design guide (MEPDG) resulting in the assumptions that: 1) binders do not oxidize below about the top inch of pavement, and 2) binder hardening in that top inch advances only to a maximum, limiting viscosity (AASHTO, 2004). Furthermore, concerning the impact of binder oxidation on mixture (pavement) performance, the design guide assumes that binder oxidation does not fundamentally affect the fatigue decline of mixtures as a function of loading cycles.

However, it has indeed become clear that the assumptions of the design guide are incorrect. The next section of this chapter details recent literature findings that support the notion that binder oxidation occurs in pavements and significantly below just the top inch. Reports that this oxidation has a negative impact on mixture and thus pavement fatigue also are cited. Furthermore, the notion of a limiting viscosity has not been born out, either by laboratory studies of binder oxidation or by aged binders recovered from aged pavements. In short, all of the assumptions of the design guide with respect to binder oxidation and hardening in pavements and its impact on pavement performance, appear to be incorrect.

With an improved appreciation of the extent of binder oxidation in pavements and its importance to pavement durability, a better quantitative understanding of this phenomenon is considered essential to cost-effective pavement design and maintenance planning. This improved understanding includes a better knowledge of the progression of binder oxidation in pavements through pavement milestones such as: hot mix plant processing, placement, the early (fast-rate) period oxidation, and the later (constant-rate) period oxidation. Fast-rate and constant-rate period oxidation periods refer to binder oxidation kinetics at constant temperature and not to what actually occurs in pavements at non-constant temperature. The next section of this chapter provides more background detail on the reaction kinetics. Also needed is an ability to predict how each binder it will respond to pavement service as it moves through these milestones. To achieve this understanding, further development of binder tests, coupled with calibration with field binder aging data, were essential.

For example, while the rolling thin-film oven test does a good job of quantifying the extent of binder oxidation and hardening that takes place in the hot-mix process, tests that go beyond this point are problematic. The pressure aging vessel procedure oxidizes binders to a significantly more extended level over a 20-hour period; however, how this level corresponds to in-service aging time has been unknown and variable, depending on climate and binder kinetics, plus mixture parameters such as air voids. In addition, how binder hardening in service affects performance has not been adequately quantified. Some mixtures show less decline of mixture

fatigue resistance in response to binder oxidative hardening than others, and there is little understanding about why. Binders can easily be aged to a particular level in the laboratory. The questions have always been "How does such aging correspond to in-service aging?" and "What is its relevance to pavement performance?" Thus, calibration of laboratory aging to field aging has been essential.

The effectiveness of maintenance treatments is another issue that has not been well understood, and as such, the optimal time of placement has been unknown. A prime question to be addressed was how well treatment binders prevent oxidation by sealing the surface of the pavement. Actually, this is a two-part question. First, do treatments seal the surface, and second, if they do, is this surface sealing sufficient to prevent oxidation. It may well be that oxygen can still find a way to reach the binder from below the surface.

This chapter provides further background perspective on the issues introduced above: binder oxidation kinetics and hardening in both controlled laboratory conditions and in pavements; the effect of binder hardening on mixture fatigue resistance; and maintenance treatments. Also, two surveys of Texas Department of Transportation (TxDOT) districts regarding their use of maintenance treatments are summarized.

BACKGROUND PERSPECTIVE FOR THIS PROJECT

As outlined above, although evidence that binder oxidation in pavements occurs, that it occurs beyond the near-surface of the pavement, that it is ongoing throughout the life of the pavement, and that it has a very profound effect on pavement durability is mounting and gaining acceptance, important implementation questions remain. Understanding how best to design mixtures in a way that takes binder oxidation into account to achieve maximum pavement durability is a very complex but important issue. A second, related issue is the use of maintenance treatments to impede or reduce binder oxidation in pavements.

This TxDOT project (Project 0-6009) was designed to provide information on these issues so as to achieve significant improvements to pavement durability at significant life-cycle cost savings to TxDOT. The discussion that follows presents a background and literature survey of key issues that impact the major concern of this project, which is long-term pavement performance. Of specific interest are binder oxidation and hardening in pavements, their impact on pavement design and performance, and maintenance treatments.

Binder Oxidation and Hardening

Important questions concerning binder oxidation and hardening have been studied over the years:

- What are the reactions involved in binder oxidation?
- How fast does binder oxidation occur in controlled laboratory conditions and in pavements?
- What is the impact of oxidation on binder physical properties?
- What is the mixture response in terms of fatigue resistance to binder oxidation?

Recent work on the first three questions prior to this project is considered further in this section, and the last question is addressed in the next section.

Oxidation Chemistry

Perhaps the most fundamental issue impacting binder hardening in pavements is the basic binder oxidation chemistry. This issue has been explored rather extensively in significant reports by Lee and Huang (1973), Lau et al. (1992), Petersen et al. (1993) and others. A general observation of these reports is that carbonyl compounds form as a result of oxidation and that, while the exact nature of the carbonyl compounds and the formation rates as a function of temperature and oxygen partial pressure may vary from asphalt to asphalt, the common factor is that for each asphalt the carbonyl content can be used as a surrogate for total oxidative changes. Qualitatively the carbonyl growth varies linearly with total oxygen increase, even though the quantitative dependence varies from asphalt to asphalt (Liu et al., 1998b).

Oxidation Kinetics – the Constant-Rate Period

A second aspect of binder oxidation is the oxidation kinetics, studied and reported by Petersen et al. (1993), Liu et al. (1996), and others. The basic carbonyl reaction rate can generally be described using an Arrhenius expression (Eq. 1-1) for temperature variation and pressure dependence:

$$\frac{d\mathrm{CA}}{dt} = r_{\mathrm{CA}} = AP^{\alpha}e^{-E/RT} \tag{1-1}$$

where A is the frequency (pre-exponential) factor, P is the pressure, α is the reaction order with respect to oxygen pressure, E is the activation energy, R is the gas constant, and T is the absolute temperature. Values of A, E, and α are very asphalt dependent, though A and E are generally correlated (Liu et al., 1996). Recent studies by Domke et al. (2000) show that the activation energy, E, is also pressure dependent for many asphalts, and this dependence is a function of asphaltenes.

Lau et al. (1992) reported results for 10 asphalts in which they determined values for E, α, and A. In general, the reaction rates of asphalt binders undergo an initial rapid rate period that declines over time until a constant rate period is reached and the reaction rate given in the equation above describes this constant rate period. The early time, faster rate period has been variously described as the "initial jump" by Lau et al. (1992) or the "initial spurt" by Petersen et al. (1993). The point is that while the parameters of the oxidation rates vary from one asphalt to another, the basic form of the reaction rates are essentially the same. Kinetic parameters have been determined for a number of different asphalts including the SHRP core asphalts and others. Glover et al. (2005) report many of these results.

Oxidative Hardening

A third facet of binder oxidation is the impact that the oxidation has on the binder's physical properties. Fundamentally, the oxidation of the binder creates carbonyl compounds, primarily by oxidizing aromatic compounds in the naphthene aromatic, polar aromatic, and asphaltene fractions. These more polar carbonyl groups result in stronger associations between asphalt components, which increase the asphaltene fraction, and in turn lead to a stiffening of the binder in both its elastic modulus and its viscosity. Results have been reported in terms of the low shear rate limiting viscosity, and it has been observed that this viscosity increases in direct proportion to the carbonyl band infrared carbonyl growth (Martin et al., 1990). The proportionality factor has been termed the hardening susceptibility (Lau et al., 1992; Domke et al., 1999).

More recently, a DSR function (G′/(η′/G′) measured at 44.7°C, 10 rad/s and time-temperature shifted to 15°C 0.005 rad/s) has been defined that includes both elastic and viscous properties and at more mid-range test conditions (frequency and/or temperature) than are represented by the low shear rate limiting viscosity (which, by definition, is at very low frequency or, equivalently, at high temperatures). This DSR function also increases linearly with carbonyl content, and the slope of this relationship is termed the DSR function hardening susceptibility. Glover et al. (2005) report the DSR function hardening susceptibility for a number of asphalts.

For either of these hardening functions, one can develop kinetics equations, just as can be done for carbonyl formation kinetics in that the hardening rate can be expressed in an Arrhenius rate form, thereby bypassing the carbonyl kinetics. Equivalently, the hardening susceptibility can be multiplied by the oxidation reaction rate to obtain the hardening rate, again, after the initial jump period has been passed, with the reaction rate constant at a fixed temperature.

Oxidation Kinetics – a Broader View

The oxidation kinetics discussion above was restricted to the constant-rate period of binder oxidation. Binder oxidation is somewhat more complicated, involving a fast but declining rate period leading up to the constant-rate period. Eq. 1-2 includes the various mechanisms by which hardening occurs, in the absence of oxygen diffusion resistance:

$$\ln\eta_t = \ln\eta_o + \Delta(\ln\eta_{ot}) + \Delta(\ln\eta_j) + r_\eta \cdot t \tag{1-2}$$

where η_o is the original viscosity, η_t is the viscosity at time t, $\Delta(\ln \eta_{ot})$ is the hardening in the hot mix plant simulated by an oven test, $\Delta(\ln \eta_j)$ is the hardening that occurs in an early rapid "initial jump" stage, and r_η is the subsequent constant rate of hardening. Figure 1 shows this sequence in which η_{ot} is the viscosity after the oven test and η_j is the viscosity after the initial jump defined by the intercept of the constant-rate line. Region A will be defined as the time for the initial jump, and region B is a constant-rate region. Eq. 1-2 is valid for time long enough to carry the process past region A. If there is diffusion resistance, this rate will decline as the asphalt hardens. Eq. 1-2 and Figure 1 are expressed in terms of zero-shear viscosity η_o* but hardening in terms of

other properties (such as the dynamic shear rheometer, [DSR] function G′/(η′/G′), discussed above and in the next section, follow the same hardening kinetics.

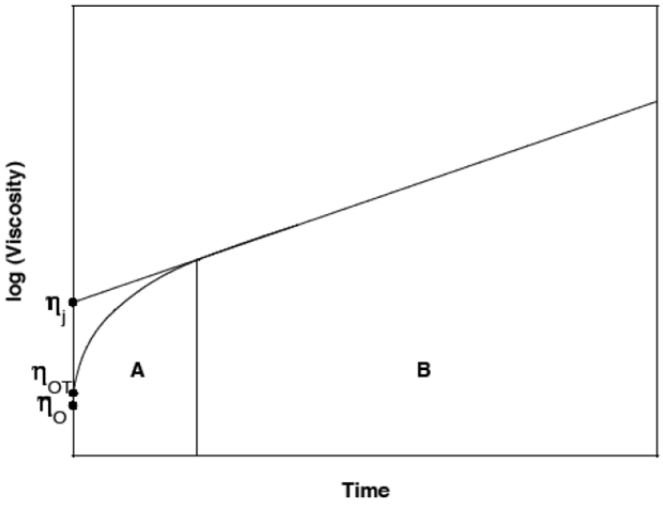


Figure 1. Typical Hardening Response of an Unmodified Asphalt Binder to Oxidation.

Asphalt oxidative hardening is almost entirely caused by asphaltene formation (Lin, 1995; Lin et al., 1995, 1996, 1998), and the rate can be expressed as follows:

$$r_\eta = \frac{\partial \ln \eta}{\partial t} = \frac{\partial \ln \eta}{\partial \mathrm{AS}} \cdot \frac{\partial \mathrm{AS}}{\partial \mathrm{CA}} \cdot \frac{\partial \mathrm{CA}}{\partial t} \tag{1-3}$$

where $\partial \ln \eta / \partial \mathrm{AS}$ is the impact of asphaltene (AS) increase on increasing viscosity and is affected by asphaltene size, which in turn is affected by maltene solvent power; $\partial \mathrm{AS}/\partial \mathrm{CA}$ is the extent to which increases in carbonyl area (CA) produce asphaltenes; and $\partial\ \mathrm{CA}/\partial t$ is the rate of CA formation. The increase of CA correlates linearly with oxidation (Liu et al., 1998b). Eq. 1-4 can be simplified as:

$$r_\eta = \mathrm{HS} \cdot r_{\mathrm{CA}} \tag{1-4}$$

where HS is the combination of the first two terms in Eq. 1-3. This combination is remarkably constant as oxidation proceeds and is independent of oxidation temperature below about 100–110°C. It has a characteristic value for each asphalt except that it is pressure dependent. This term is called the hardening susceptibility (Lau et al. 1992; Domke, 1999). The rate of carbonyl formation is given above as Eq. 1-1 (Lin et al., 1996; Lin et al., 1998; Liu et al., 1997).

The following equation summarizes these results where [P] or [T,P] or [P] indicates that the property is a function of temperature or temperature and pressure, or just pressure:

$$\ln \eta_t = \ln \eta_{ot} + \Delta(\ln \eta_j)[P] + r_{\mathrm{CA}}[T,P] \cdot \mathrm{HS}[P] \cdot t \tag{1-5}$$

Because only one term is multiplied by time, the relative rankings of asphalts from any accelerated aging procedure will change with the length of the test as well as with the temperature and pressure. Note that particularly relevant hardening rate parameters are the initial jump (η_j), the hardening susceptibility (HS), and the oxidation rate, r_{CA}.

The Fast-Rate Reaction Period

Figure 1 showed binder reaction kinetics, in terms of binder rheology, separated into an initial fast-rate (initial jump) period and a second constant-rate period. Accurately representing binder oxidation in pavements requires understanding the relative amount of time spent by the binder in each of these different periods during the course of a pavement's life. The following discussion addresses literature reports of these two reaction periods and the fast-rate period reaction kinetics.

The Fast-Rate Period in Pavements. While the reaction kinetics of binder oxidation during the constant-rate period (described above) have been studied extensively, the early-time, fast-rate period reaction kinetics has been studied much less, providing a source of error in comparisons of field and laboratory binder oxidative hardening. Though in the laboratory we can assure that the fast-rate period of oxidation has been passed, it is more difficult to tell when it ends in the field due to the lower field temperatures and the cyclical nature of temperatures in pavements. Using constant-rate period kinetics to assess field aging without knowing if the fast-rate period has been passed may contribute considerable error and uncertainty to the results and conclusions. Thus, an improved understanding of oxidation kinetics during the fast-rate period is important.

Recovered binders from field cores from Texas and Minnesota (MnROAD) were measured for rheological properties and then aged further in a 60°C environmental room for up to eight months (Woo et al., 2007). Figure 2 shows the stiffness (in the form of the DSR function) of each of the extracted and recovered binders (zero months ER aging) plus increases that occur with further ER aging (2, 4, 6, and 8-month ER aging). If the binder, as recovered from the core, together with its subsequently-aged samples all form a single straight line, then they are all past the fast-rate (initial jump) period. However, if the binder, as recovered from the core, lies below a straight line formed by its subsequently-aged samples, then the core sample was not past the initial jump. From the figure, it seems clear that the binder recovered from the Texas pavements had passed the fast-rate period after two to three years aging in the pavement, whereas the MnROAD AC 120/150 binder was still within this period, even after 12 years of field aging. From these data, it seems that the fast-rate period of aging is not as important for Texas pavements, relative to long term pavement aging, as it is for Minnesota.

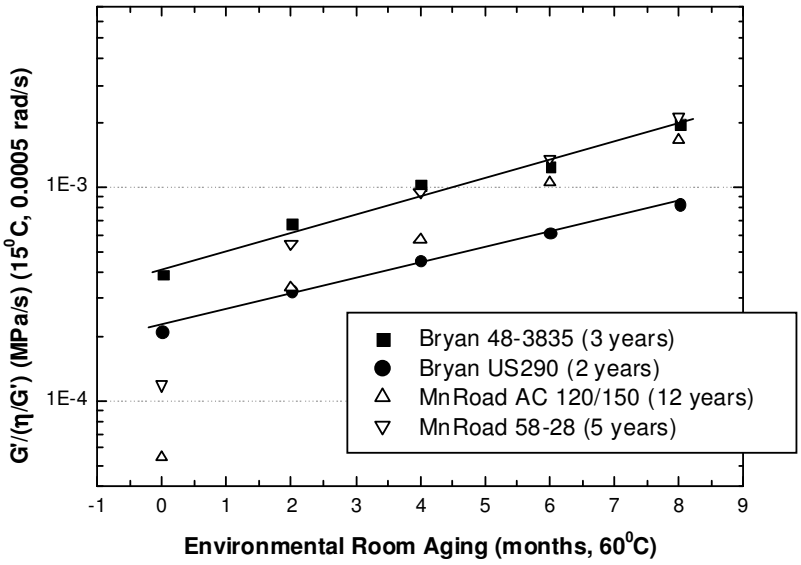


Figure 2. DSR Function Growth of Recovered Binders from Texas and Minnesota, Aged in Environmental Room (60°C) (Data from Woo et al., 2007).

Fast-Rate Period Reaction Kinetics. Dickinson and Nicholas (1949) investigated oxygen absorption by tar oils. Two parallel reactions were suggested, one a first order reaction with respect to phenol and the other a zero order reaction with respect to aromatics. The combined effect of these two reactions produced an early time fast (but declining) rate period of oxygen absorption, followed by a later-time constant-rate period after the first reaction terminated due to depletion of phenol, the limiting reactant. The reaction kinetics model they proposed for tar oil was:

$$M = k \cdot t + M_2 \cdot [1 - \exp(k_2 \cdot t)] \tag{1-6}$$

where M is total amount of oxygen absorbed by the tar oil and k and k_2 are reaction constants for the constant-rate and fast-rate reactions, respectively. The constant-rate reaction constant k is temperature and oxygen pressure dependent according to $k = A \cdot P^{\alpha} \cdot \exp(-E_a / RT)$, and k_2 is independent of temperature and pressure for tar oil. M_2 is the maximum oxygen absorption due to the first reaction, which depends linearly on oxygen pressure, $M_2 \propto P$.

A similar model was observed for oxygen absorption by asphalt. Van Oort (1956) measured oxygen absorption by seven-micron thin films of asphalt at 22°C and atmospheric pressure. Seven different asphalts were aged for 50 weeks. From the oxygen absorption versus time relation, a fast increase of oxygen absorption was observed during the first 10 weeks; however, the rate of absorption decreased until a constant rate was reached after about 30 to 40 weeks.

Viscosity changes with time showed a trend similar to oxygen absorption but had the apparent advantage of being able to be determined more precisely. This observation suggests that viscosity change rather than oxygen absorption might be a better indicator of the beginning of constant rate period, as viscosity is closely related to binder performance. In addition, viscosity change is mainly due to oxidation which leads to carbonyl area growth, while oxygen absorption not only leads to the formation of CA but also leads to products that have no apparent effect on viscosity. Thus, the study of CA and viscosity would seem to be the better variables for the understanding of fast-rate aging period.

Despite the obvious similarity of kinetics between asphalt and tar oil, three possible differences should be explored. First, it is quite possible that k_2 for asphalts is temperature and pressure dependent. Second, M_2 may be a non-linear function of oxygen pressure. Finally, neat binders have a finite (non-zero) initial viscosity or carbonyl area.

The Importance of Oxidative Hardening to Mixture Performance

Impact of Binder Oxidation on Mixture Fatigue

The above discussion has addressed the issue of binder oxidation reaction and kinetics and the resulting binder hardening. A fourth issue regarding binder oxidation is "So what?" Assuming binders oxidize in pavements, what is the importance of this oxidation to pavement performance? For example, to what extent is the fatigue life of a pavement impacted by binder oxidation? Walubita et al. (2005a, 2005b, 2006a and 2006b, 2006c) recently addressed this question. The results indicate that binder oxidation in pavements can have a very significant negative impact on pavement fatigue life (fatigue resistance). While the mechanism of this fatigue life decline with oxidation is not yet well understood, early data indicate that it is a very important phenomenon and that there can be significant differences between different mixture designs as shown in Figure 3. The reasons for these differences need to be understood.

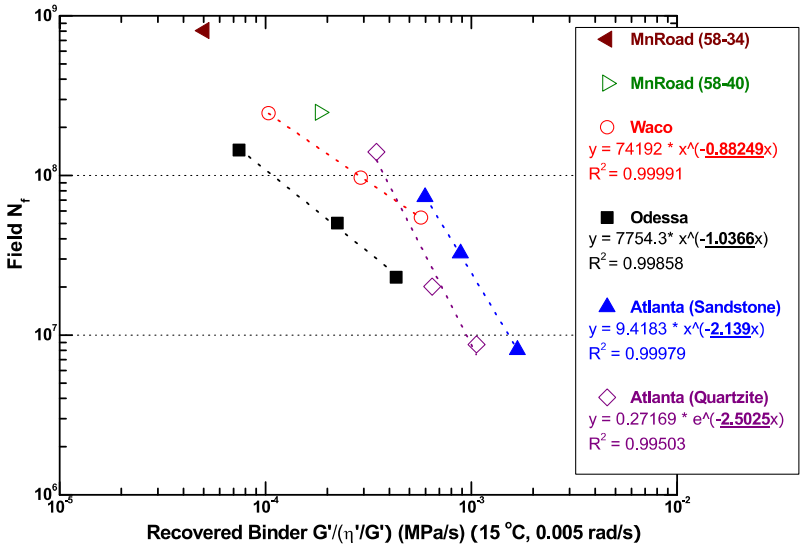


Figure 3. Impact of Binder Oxidative Hardening on Mixture Fatigue Resistance.

Specific results from this recent multi-year research project that directly impact the experimental plan presented later in this project report in Chapter 2 include:

- Fatigue life decreases significantly primarily as a result of aging due to binder oxidation and its subsequent effect on mixture properties.
- The decrease in fatigue life is a function of more than just the binder stiffening due to oxidative aging. Thus mixture parameters that may be controlled during the mix design process are important to ensure adequate fatigue resistance.
- Different mixtures show unique declines in fatigue life due to aging.
- The CMSE approach is valid for understanding the different mixture responses to aging.
- Two different methods show promise in capturing the effects of aging on fatigue life. One method is more empirical but practical, and the second facilitates greater understanding of the aging mechanism.

So, the decline of mixture fatigue resistance under controlled-strain conditions is an important phenomenon that varies from mixture to mixture. Unknown, however, are the quantitative contributions of each of the various mixture parameters (air voids, binder content, binder composition, aggregate type, and aggregate gradation) to the differences in decline of mixture fatigue life with binder oxidation. Quantitative assessment of these differences is essential. Also, assessing pavement durability as it is influenced by binder oxidation and traffic loading, and in light of laboratory conclusions on the effect of binder aging on mixture fatigue resistance, will require monitoring pavement fatigue resistance over time.

Oxidation in Pavements

The final issue of binder oxidation in pavements is the question of whether binders oxidize in pavements at all in the face of presumed reduced temperatures and restricted oxygen transport to the binder below the surface. The work discussed above showed that binders harden as a result of oxidation and that the kinetics of oxidation and the hardening that results from oxidation are quite well known (or can be measured) and can be described quantitatively in terms of oxidation temperature and pressure. The work discussed above also indicates that if binders oxidize in pavements, the impact on pavement fatigue performance can be profound. All of these factors, however, are moot if binder oxidization does not occur in pavements, and the question of whether this oxidation occurs has no clear answer in the literature. In fact, a very well cited and accepted literature report concludes that binder oxidation occurs only in the top inch of the pavement and that below the top inch the binder is left virtually unaffected by years of use and years of environmental exposure (Coons and Wright, 1968). Their conclusion is formalized in a recently developed mechanistic empirical pavement design guide (AASHTO, 2004) that assumes in its calculation that binders oxidize only in the top inch. Parenthetically, calculations performed using the MEPDG under TxDOT Project 0-4468 suggest that binder oxidation and the consequent increase in pavement stiffness (and the presumed decrease in deformation under load as a result of this stiffness) actually have a *positive, beneficial* impact on pavement fatigue life.

Contradicting the work of Coons and Wright and the assumptions of the pavement design guide are the extensive data reported in Glover et al. (2005) in which a large number of Texas pavements were cored, the binder extracted and recovered, and then the sample tested to

determine binder stiffness as a function of age in the pavement. The results of this work indicate rather strongly that in fact binders can age in pavements well below the surface and that the hardening of binder in the pavement is virtually unabated over time. These data also are reported in a recent paper by Al-Azri et al. (2006).

A Simple Model of Binder Oxidation in Pavements

More recent work provided significant new results on binder hardening in pavements that relate both to modeling binder oxidation and to calibration with binders recovered from pavements (Woo et al., 2007). The discussion of this model is presented in some detail below because this simple model provides the basic concepts and results of more detailed models that will be explored in this project.

The model considers the pavement to behave as a semi-infinite slab with an imposed periodic temperature at the pavement surface. The periodicity occurs daily because of daytime and nighttime temperatures swings, and yearly due to seasonal variations of temperature. Such a model is used extensively in geology to estimate the temperature of the earth's crust as a function of time and depth, and it is now considered whether such a model is applicable for hot mix asphalt (HMA) pavements (U.S. Geological Survey, 2006). Such a model of temperature in the pavement as a function of time and depth below the surface follows the well-known thermal diffusion model given by Eq. 1-7 in which $Q(x,t) = (T(x,t) - T_{avg})$ is the temperature deviation from (oscillation about) an average temperature, t is time, and x is depth below the surface into the pavement.

$$\frac{\partial \Theta}{\partial t} = \kappa \frac{\partial^2 \Theta}{\partial x^2} \tag{1-7}$$

In this equation, κ is the thermal diffusivity, which is equal to $k/(\rho C)$, where k is the thermal conductivity, ρ is density, and C is the heat capacity of the solid material. This model assumes no temperature variation parallel to a pavement's surface, so it is an unsteady-state, one-dimensional model.

It is assumed the pavement is initially at uniform temperature (T_{avg}) and that at the surface there is imposed a temperature oscillation (of amplitude A, frequency ω and phase shift ε). These conditions provide initial and boundary conditions according to Eqs. 1-8.

$$\begin{aligned} &\text{I.C.:} \Theta(x,0) = 0 \\ &\text{B.C.: for } x=0 \text{ and } t > 0,\ \Theta(0,t) = A\cos(\omega t - \varepsilon) \end{aligned} \tag{1-8}$$

The asymptotic, periodic solution to this problem is given by Eq. 1-9 (Carslaw and Jaeger, 1959).

$$\Theta = Ae^{-x(\omega/2\kappa)^{1/2}} \cos\left[\omega t - x\left(\frac{\omega}{2\kappa}\right)^{1/2} - \varepsilon\right] \tag{1-9}$$

Thus, according to this model, the temperature, after a sufficiently long period of time persists as a periodic temperature profile that is attenuated in amplitude according to the depth below the surface and also shifted in phase according to the depth below the surface.

Measured temperature profiles are available from SHRP program long-term pavement performance (LTPP) site measurements and allow estimates of the thermal diffusivity independently from both the amplitude attenuation and from the phase shift. As an example, temperature amplitude data from Refugio, Texas (LTPP site 48-1060), provided an estimate of thermal diffusivity of 0.010 cm^2/s and the phase shift data provide an estimate of 0.0092 cm^2/s. The agreement between these two estimates is very good. Note also that the model says that the temperatures at various depths should oscillate about the same average temperature.

Comparisons to Field Aging. Using this model for pavement temperature as a function of time and depth, and using known asphalt binder oxidation kinetics parameters while also assuming that the transport rate of oxygen to the binder does not limit the oxidation rate, estimates of binder oxidation in Texas SH 21 were calculated. By neglecting the effect of oxygen diffusion resistance we obtain an upper limit estimate of the binder oxidation rate.

The same procedure was followed for a pavement that was part of the MnROAD controlled study. Original binder was not available, so binder oxidation kinetic parameters were determined experimentally by aging binder that was recovered from a core in the laboratory in 1-mm thick films and at 60°C, 75°C, and 95°C.

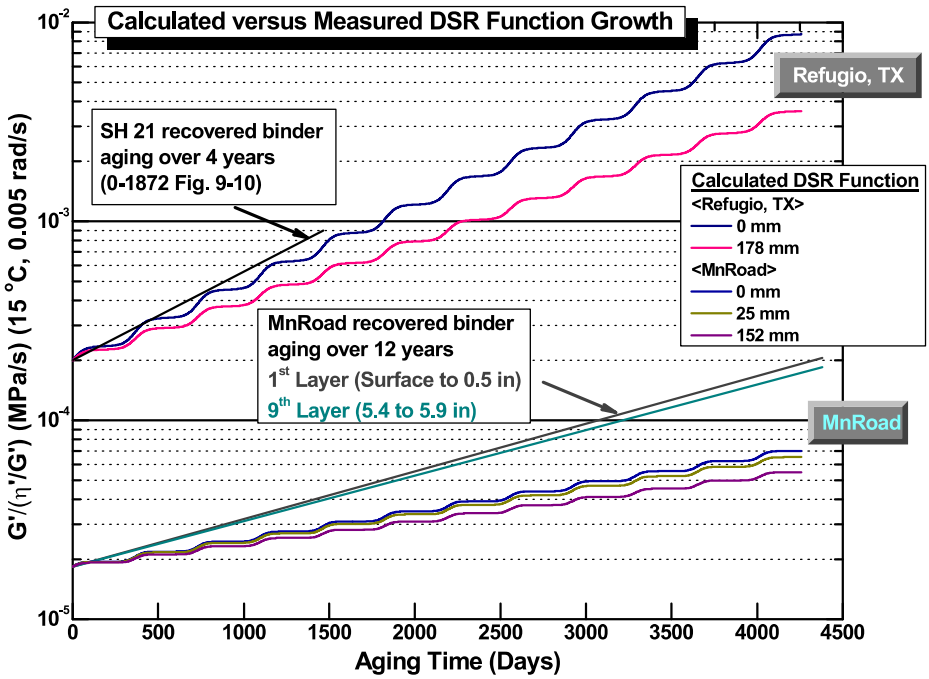


Figure 4. Calculated versus Measured DSR Function Growth.

Figure 4 shows the binder hardening over time expressed in terms of the DSR function for both the SH 21 and MnROAD pavements. Note that calculations are made for the surface and 178 mm (7 inches) below the surface. According to the model, while greater depths provide different rates, they do not provide grossly different rates compared to zero.

Figure 4 also shows lines that represent the actual measured hardening rate of the binder in both the SH 21 and MnROAD pavements. The agreement between the actual pavement hardening rates and the corresponding calculated hardening rates based upon the temperature model and the binder oxidation kinetics is quite good and suggests that for these pavements, the assumption of good oxygen availability to the binder is acceptable. In the calculated carbonyl and DSR function oxidation curves, the near-zero hardening rates during the winter months versus the much higher hardening rate during the summer months is evident in the stair-step calculations.

Note that in Figure 4, the measured hardening of binder in the pavement in Minnesota occurs at a significantly lower rate than the hardening rate of binder in Texas Highway 21. The MnROAD values are approximate average hardening rates for the MnROAD pavement, based on the 1st and 9th layers of the Cell 1 core. The 1st and 9th layers both appear to have ample access to oxygen (accessible air voids of from 3 to 5 percent) and aged at essentially the same rate. Thus, it is those rates that are depicted by the slopes of the two lines together with the stair-step calculations.

Note also that for the binder recovered from the MnROAD cell, the binder hardening rates are higher than for the stair-step model calculations. A couple of reasons seem possible. First, an initial pavement value was not measured, and an error in estimating this value would affect the rate. Second, binder aging over most of the service life of the pavement may well have occurred during the initial jump portion of binder aging kinetics and therefore at a higher aging rate than would be calculated from the measured constant-rate period kinetic parameters. This probably is the more likely explanation, based on recovered binder initial jump measurements.

Accelerated Binder Oxidation Test. As a final observation using binder oxidation model calculations, the issue of whether measurements of laboratory aging rates at a single elevated temperature, albeit near pavement aging temperatures, can provide accurate relative rankings of binder aging in pavements is reviewed. Because pavement aging occurs over a range of temperatures whereas the ER aging occurs at a single temperature, the nonlinear effect of temperature on reaction rates through the Arrhenius equation, in principle, can result in reversals in the order of the rankings. Calculations of (model) pavement binder aging rates were reported for seven SHRP asphalts, plus two others, and compared to calculated 60°C hardening rates (Woo et al., 2007). Some reversals were seen in these calculations. Specifically, AAB-1 ranked with the second highest rate in the ER at 60°C but was tied for sixth highest by the pavement calculation. Also, ABM-1 was fourth at 60°C but second in the "pavement."

The reported conclusion stated that the only correct method for estimating (annual average) reaction rates in pavements is to measure rates at several temperatures, from these measurements calculate reaction parameters, and then use an appropriate model to calculate expected pavement hardening rates based on these parameters (Woo et al., 2007). On the other

hand it was noted that the range of the ratio of laboratory (60°C) hardening rates to field (pavement, near the surface, annual average) hardening rates is only from 13 to 19, perhaps not so large a range for an engineering estimate. Stated differently, for all of these various binders, one month of aging in the laboratory at 60°C was equivalent to from 13 to 19 months in the pavement at the location considered by their model.

Of course, the issue always comes down to accuracy of the measurement versus time to make the measurement. The calculations of the nine binders described above provided 60°C to "pavement" hardening rate ratios that varied by up to 46 percent. Similar calculations for single-temperature laboratory rate measurements of 40, 80, and 100°C gave high ratio (lab to field) values that exceeded low ratio values by 35, 72, and 109 percent. The tradeoff in time was that a one-day test at 100°C would correspond (roughly) to five days at 80°C, one month at 60°C, and six months at 40°C.

The conclusion is that developing an accelerated binder aging test that ranks asphalts the same as pavement aging is challenging at best and fundamentally impossible at worst because of the different effects of time, temperature, and pressure on different materials.

Measurements of Binder Aging in Pavements

Woo et al. (2007) reported the hardening of various binders in pavements in the form of the DSR function . Figure 5 summarizes the results. This figure shows DSR function values for binders recovered from pavements versus the corresponding pavement service age. Both Texas pavements and the MnROAD pavements are summarized. Both unmodified and modified binders appear in the figure. The bulk of the binders reported were modified.

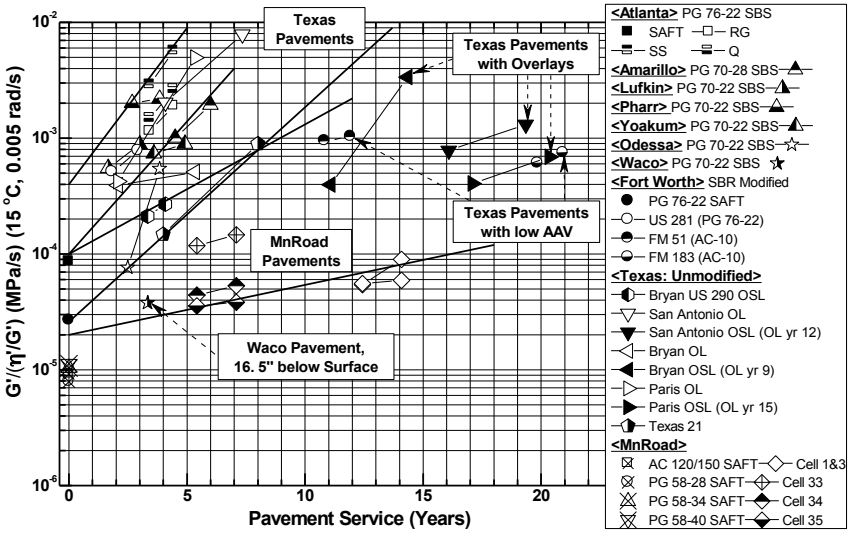


Figure 5. DSR Function Hardening with Pavement Service Time in Texas and MnROAD Pavements.

Based upon the above data a number of conclusions were reported concerning modified and unmodified binder aging in pavements in Texas.

- Texas pavements constructed from both modified and unmodified binders age and harden at comparable rates given sufficiently high accessible air voids. The rate is largely determined by the temperature as a function of time and position (depth) in the pavement provided the accessible air voids are sufficiently high (four percent or greater). This temperature function is established solely by the climate conditions.
- This dominant impact of temperature notwithstanding, there is considerable evidence that when the accessible air voids in pavements are sufficiently low (2 percent or less) the hardening rate of binders in Texas pavements can be significantly reduced, thereby prolonging the service life of the pavements to 15 or 20 years or more.
- Some of the Texas pavements appear to be under aged relative to the other binders, perhaps due to the application of a chip seal and/or overlay one to three years before coring the pavement. This phenomenon has been observed before and these data may be an indication again that the right kind of treatment during a pavement's service might well soften the binder and rehabilitate it, thus providing an extended pavement life.
- If a binder with an inherently low hardening rate (slow oxidation kinetics and minimal physical response to the oxidation) is used in a pavement, and if a low enough level of accessible air voids can be achieved (in the range of 2 percent or less), then the pavement has a real chance of providing service over a very extended period of time.
- Binder DSR function hardening rates in Texas are about twice the rate for the corresponding binder in Minnesota at comparable air void conditions.
- In order to estimate pavement binder hardening rates, values of the binder reaction kinetics parameters are required. Approximating the rate with measurements at 60°C may give a rate from which a rough estimate can be calculated, but the nonlinear activation energy effect can cause significant error (discussed just before "Measurements of Binder Aging in Pavements").
- Calculations from the pavement oxidation model and known binder reaction kinetics parameters indicate that 60°C hardening rates range from 13 to 19 times the calculated pavement binder aging rates as discussed previously.

The Importance of Accessible Air Voids

As noted above, low levels of accessible air voids appear to relate to binder oxidation. Figure 6 shows data for four pavements, where low accessible air voids appear to affect binder aging rates. Each dashed line connects data for successively deeper 0.5-inch slices of a single core, starting at the pavement surface ("1st"). In Figure 6, the binder DSR function is shown layer-by-layer versus the accessible air voids of that layer. Cell 1 is particularly instructive as a strong DSR function versus accessible air voids correlation is seen both near the surface (slices 1 and 2) and also in the deepest part of the core (slices 6 through 9). While these specific data are from the MnROAD sites (used because of the 6 inch core thicknesses), the results appear to reflect aging in Texas pavements also (Figure 5, Fort Worth FM 51 and SH 183).

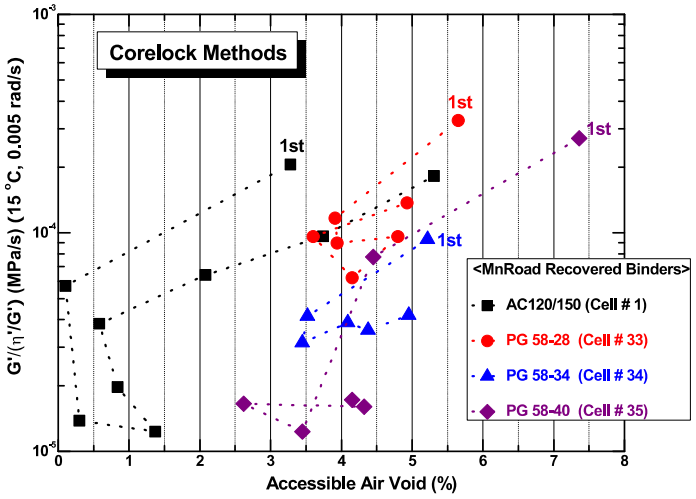


Figure 6. Binder Hardening Related to Local Pavement Accessible Air Voids.

More Realistic Models of Thermal and Oxygen Transport in Pavements

From the discussion above, it is clear that while a simplified model of binder oxidation in pavements may perform reasonably well in some cases, improved temperature calculations and estimates of oxygen transport that account for restricted air voids are needed in many others. Improved methods for estimating pavement temperatures are reported in the literature; by contrast, improved methods for estimating oxygen transport are embryonic. Both of these topics are discussed further, below.

Improved Models for Calculating Temperature in Pavements. Accurate calculations of binder oxidation in pavements require accurate pavement temperatures, over both time (daily and seasonally) and position (depth) and as a function of climate (site location). In recent years, considerable research has been conducted to establish suitable methods of modeling and calculating pavement temperatures. While this work primarily has been used to estimate changes in pavement properties with temperature as well as for the purpose of materials selection, it also provides a foundation for calculating binder oxidation in pavements and subsequent changes in binder properties that result from this oxidation.

In early development of pavement temperature calculation methods, interactions between climatic conditions and pavement temperatures were correlated using either empirical equations or simple mathematic models (Barber, 1957; Rumney and Jimenez, 1969). Following these initial efforts, Solaimanian and Kennedy (1993). developed an advanced analytical approach to calculating maximum pavement temperatures. Their method employed heat and energy transfer fundamentals but used the problematic assumption of a steady-state thermal energy balance over the entire pavement slab, from the pavement surface to a specific (but not stated in the article) subgrade depth. Most recently, Diefenderfer et al. (2006) proposed an empirical equation derived from linear regression techniques to predict pavement maximum and minimum temperatures from known maximum and minimum ambient air temperatures, pavement location, and depth below the pavement surface. This method, though providing good results at the pavement

surface, failed to predict pavement temperatures accurately below the surface because they also inaccurately assumed that pavement temperature is a linear function of depth.

In general all of these methods, developed using either empirical equations or analytical approaches, have focused primarily on determining the yearly maximum and minimum pavement temperatures for the purpose of binder selection. As such they are unable to provide accurate calculations of temperature as a function of both time and depth, due to model shortcomings in capturing fundamental aspects of heat transfer processes in the pavement.

Fundamental thermal energy balance models for pavements have been discussed by a number of authors (Dempsey, 1970; Solaimanian and Kennedy, 1993). Figure 7 depicts the heat transfer process. The most significant heat source at the pavement surface is shortwave solar radiation directly from the sun. Both the pavement surface and air act like blackbodies to emit long-wave radiation to each other as up-welling and down-welling long-wave radiation. Additionally, heat transfer occurs at the pavement surface by convection. The net heat flux received by the pavement surface by those four mechanisms then propagates into and through the pavement by conduction.

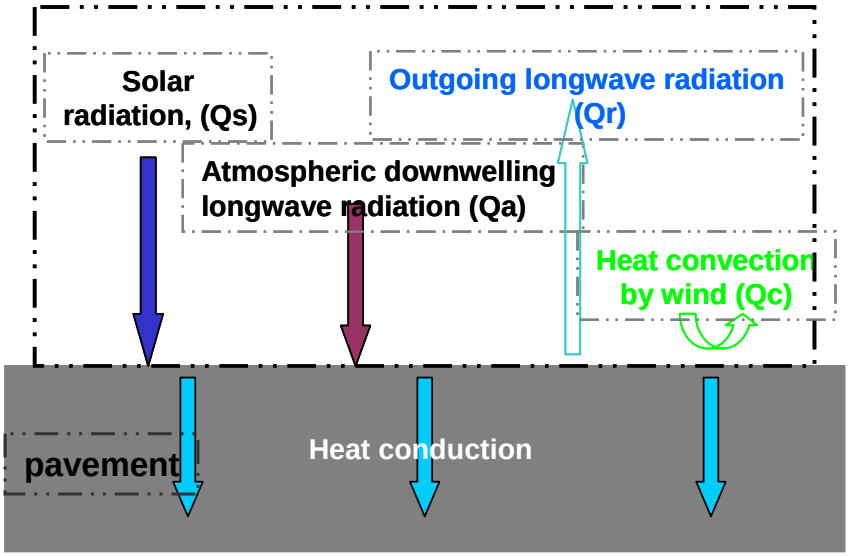


Figure 7. Schematic Representation of Pavement Heat Transfer.

Incorporating these fundamental processes, a one-dimensional heat simulation model called the climatic material structure model (CMS) was proposed to calculate continuous pavement temperature profiles numerically (Dempsey, 1970). The model was later integrated into the enhanced integrated climate model (EICM) (Lytton et al., 1989) and was further incorporated in the current prevailing pavement design guide (MEPDG). This model divides the pavement into different layers and applies a finite difference approximation method to numerically calculate pavement temperatures at each layer as a function of time and depth. This model also assumes a steady-state thermal energy balance over the entire pavement/subgrade from the surface to a depth ranging from 9 to 18 m (depending on location), where a constant temperature (equal to the water table temperature) was used as a boundary condition. Within the pavement, the heat conduction process was modeled with the Fourier's law thermal diffusivity

equation. With known required climatic input data including solar radiation, ambient temperature, and wind speed in hourly format and with assumed constant model parameters including albedo, emissivity, and thermal diffusivity, the model can be solved numerically to obtain the temperature in each pavement layer.

Although this EICM model can be used to predict continuous real-time pavement temperature profiles for the needs of general pavement design, rather inaccurate results have been reported (Ahmed et al. 2005), when compared to measured pavement temperatures, especially at pavement layers close to the surface (Figure 8). Those differences are most likely caused primarily by the assumption of a steady-state thermal energy balance over a finite layer of pavement and subgrade. This assumption must be questioned because there is no fundamental reason that the energy flux at the pavement surface should equal that due to conduction at some depth below the surface. Other possible sources of error are the inaccuracy of climatic input data (especially hourly solar radiation), the assumption of a constant temperature bottom boundary condition, and the assumption that model parameters are constant and universal. In fact, model parameters such as albedo, emissivity, and absorption coefficient are site-specific, and their values are highly sensitive to environmental conditions.

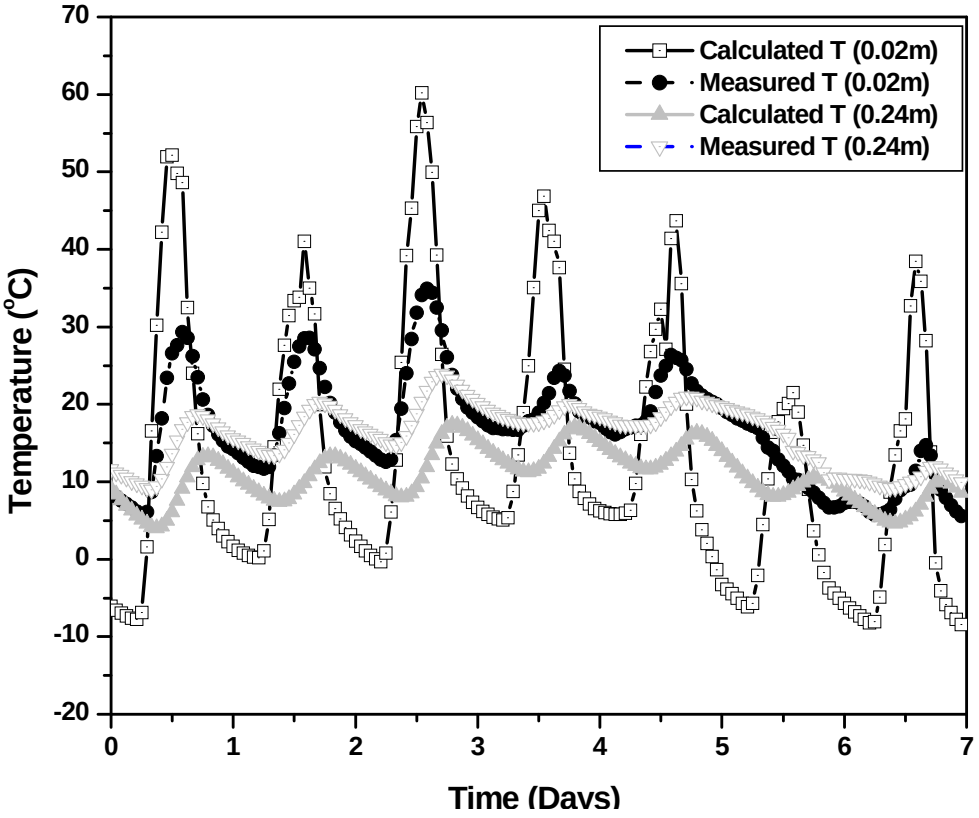


Figure 8. Sample Calculation of Pavement Temperatures Using the EICM Method at 48-1068, TX (Mar-03-1994 to Mar-09-1994), Compared with Field Measurements.

Several authors have recently reported models having significant improvements in temperature prediction accuracy and consistency (Hermasson et al., 2000, 2004; Gui et al., 2007). These models, compared to the EICM model, employ an unsteady-state thermal energy balance at the pavement surface, thereby avoiding the steady-state assumption over a finite thickness of the pavement. Measurements of hourly climatic input data and site-specific model parameters, estimated from field pavement temperature measurements were used as input to the model. Hermansson (2000) used a fixed temperature (an approximation of the annual mean temperature) as the bottom boundary condition at 5 m; Gui et al. used a fixed temperature of 33.5°C at a depth of 3 m. Figure 9 shows a comparison of model calculations to field measurements.Clearly, great improvement has been achieved with this unsteady-state balance at the pavement surface.

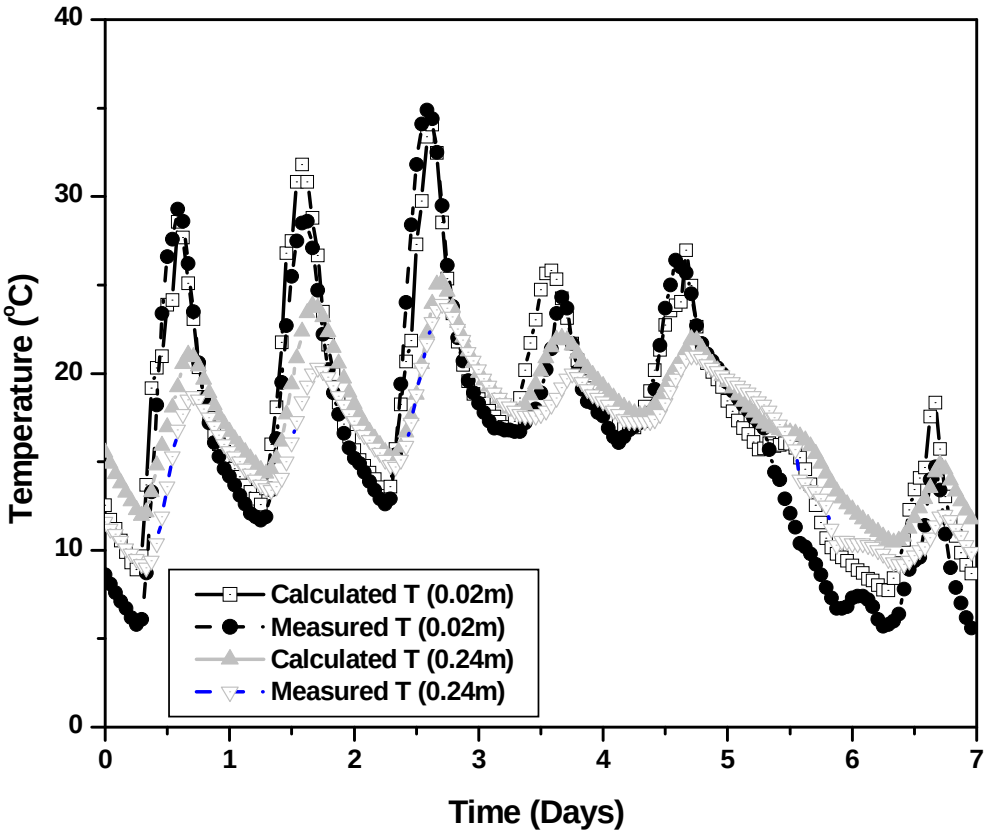


Figure 9. Sample Calculations of Pavement Temperature Using Enhanced Numerical Model Principle at 48-1068, TX (Mar-03-1994 to Mar-09-1994), Compared with Field Measurement.

Despite their success with model accuracy and consistency, applications of these enhanced models were limited to a relatively short time scale and specific pavement sites and are highly dependent on the availability of hourly climatic input data and of site-specific model

parameters. How to obtain accurate hourly climatic data and site-specific model parameters at any given pavement site have become key issues to be addressed.

Modeling Oxygen Transport in Pavements. Efforts to include the effect of oxygen transport into pavements and through binders are practically non-existent. Lunsford (1994) developed a one-dimensional, flat, thin-film model and performed calculations for approximate cyclical pavement temperature variations to estimate the effect of diffusion on oxidation. As binder oxidized, he estimated changes to the binder viscosity, based on approximate experimental data, and the resulting change to binder diffusivity. Thus the model accounted for the effect of oxygen diffusion on binder oxidation and vice versa. However, the model was very approximate in that the geometry was for flat films, and the calculations were done for film thicknesses of the order of 1 mm, which probably were not representative of actual field conditions. Trial calculations were made for various film thicknesses and compared to binder oxidation in a small number of pavements.

The air void characteristics of each pavement depend on several factors including the degree of compaction, method of compaction, aggregate gradation and shape, and binder content (Consuegra et al., 1989; Sousa et al., 1991). It is important to understand how these variables impact the internal structure of asphalt concrete. By using imaging processes and non-destructive techniques, researchers are able to characterize the materials based on their distribution in the asphalt core samples (Danison et al., 1997; Masad et al., 1999a, b).

The x-ray computed tomography (CT) and image analysis methods have been used to study the air void distribution in asphalt specimens. Typically, it is found that a higher amount of air voids exists at the top and the bottom portions of a pavement lift while there is a smaller amount of voids in the middle (Masad et al., 2002). A study of the internal structure of the pavement core suggests that there is a connectivity of void channels vertically within the core (Al-Omari et al., 2002). X-ray CT scanning with a resolution of 0.1 mm per pixel was used in these studies (Masad et al., 2005). In addition, recent X-ray CT analysis shows that with 0.1 mm per pixel resolution, typical permeable friction course samples having a total air void 15 to 20 percent have an average void radius of 2–3 mm, whereas dense-graded mixtures having total air voids less than 10 percent have an average void radius of 1 mm. There is a possibility that higher resolution X-ray CT imaging may reveal additional smaller air voids in pavement core samples which would provide a more accurate interpore spacing that for a pavement oxidation transport model discussed in the next section.

Oxygen transport limitations are important to establishing binder hardening rates in pavements. If the interconnected (or accessible) air voids are sufficiently low, then delivery of oxygen to the binder is hindered. Therefore, an improved model of binder oxidation in pavements that includes oxygen transport needs to be developed.

An improved pavement oxidation transport model should be based on three interlinked processes:

- Diffusion of oxygen into the asphalt binder mastic in the pavement.
- Heat transfer into the pavement that results in temperature variations with depth and time.

- The rate of asphalt binder oxidation, which is a function of oxygen concentration, temperature in the binder, and oxidation kinetics parameters specific to each binder.

A fourth issue affecting oxygen transport is air voids distribution in the mixture through its affect on the availability of oxygen to the binder. The diffusion process is coupled to both temperature and oxidation because both of these factors affect oxygen diffusivity.

The concept of approximating the binder film in the pavement as a thin film is probably reasonable for high air voids content where there are a large number of pores passing through the pavement so that the distance from any pore to the binder, even to the farthest binder away, is not very far. According to results from X-ray CT analysis, a more realistic model for a reduced number of air voids might be a cylindrical model that assumes that the oxygen diffuses from the pore in a radial direction into a cylindrical shell of binder. In this case, the relevant parameter would be the thickness of this cylindrical shell, relative to the diameter of the pore containing the air. The smaller the air voids, the greater the ratio of this binder shell to the pore diameter and thus the more time required for oxygen to diffuse through the binder. A similar approach was also used in the study of oxygen diffusion in engineered cardiac tissue (Radisic et al., 2005).

To obtain oxygen partial pressure profiles in the pavement oxidation models, the governing partial differential equation (PDE) system will be solved for the oxygen partial pressure as a function of time and distance away the from air void-binder interface in a cylindrical coordinate system. In principle the oxygen partial pressure profile can be used to calculate CA and viscosity profiles and histories in the pavement, which then can be combined with an appropriate performance model to estimate pavement durability and performance, taking into account binder oxidative hardening.

Maintenance Treatments to Retard Oxidation

Maintenance treatments applied to the surface of a pavement, typically as a chip seal treatment, may conceivably penetrate into the pores of a pavement to reduce binder oxidation or to be absorbed by the in situ binder, resulting in a softening of a hardened pavement. Whether such penetration and absorption occurs has not been well documented, if at all, and it remains a very real question as to whether maintenance treatments can play such a role in improving the durability and longevity of pavements.

In the case of hot asphalt cement treatments, some indirect evidence suggests that maintenance binders are able to penetrate into the pavement. In Project 0-1872 cores obtained from Texas SH 21 showed that recovered binder properties became progressively harder and harder over years of sampling, with the exception of cores taken in 2002 after a chip seal and overlay were placed in 2000. Cores were sliced into three 2-inch thick layers and either retrograde stiffening with aging time (i.e., softening) or virtually no stiffening, of the recovered binder from the 1996 cores to the 2002 cores occurred in all three layers, suggesting that sealant penetration may have occurred through the pavement, well beyond its topmost portions. In the more recent Project 0-4688 several pavements were cored that had overlays and probably seal coats or tack coats with the overlay. In these cases too, there appears to be an unusually soft binder in that part of the core underneath the overlay compared to other pavement binders of that

age. However, these data are even more problematic because there is no documentation of a seal coat, and these results do not constitute controlled data.

The effectiveness of fog seal emulsions in either rejuvenating or slowing the oxidation of the in situ binder was studied rather extensively in the recently completed Project 0-5091. Pavement cores with and without fog seal treatments were cut into nominally quarter inch slices and each slice was analyzed for binder properties and the presence of the fog seal treatment. In virtually all cases there was no evidence found of softening of the binder or even of the emulsion asphalt material. The results suggested that the emulsions may pass through the pavement. Only the top inch of the pavement was studied so it is entirely possible that the emulsion material flowed through this part of the pavement and away from the surface. These emulsions contain the asphalt material as asphalt droplets of the order of 10 microns diameter that may be able to be carried by the emulsifying solvent (typically water) through the pavement pores, which are typically an order of magnitude bigger in diameter, without being absorbed by the in situ binder. At any rate, no evidence of rejuvenation by these emulsions was found, nor was there any evidence that the emulsions retarded binder oxidation in the pavements. The single exception to these conclusions is that EB44 coal tar material was detected in the top 6 mm (1/4 inch) of the pavement, and this treatment actually resulted in a harder recovered binder.

There appears to be very inconclusive evidence that hot asphalt maintenance treatments may penetrate the pavement and remain behind with the in situ binder to affect its oxidative hardening. Furthermore, rather careful data point to an ineffectiveness of fog seal treatments. However, this research team found no case of documentation showing that maintenance treatments may actually soften the in situ pavement binder and therefore rejuvenate the binder from the perspective of fatigue or other cracking. The issue is two-fold: 1) whether the maintenance treatments penetrate into the pavement (and how deep); and 2) whether once the binder penetrates into the pavement it then can reduce the aging of binders. Extracting and recovering the binder may give an indication as to this latter effect. An alternative method is to actually test the mixture properties.

Ultimately, the effectiveness of an asphalt maintenance treatment will depend upon its ability to penetrate into the pavement. It will also depend upon the nature of the maintenance treatment as to composition of the binder (asphaltene free) and viscosity. If the hot asphalt is too high a viscosity, then it will not flow effectively into the pores of the pavement. Transport of the binder through the pavement will also depend upon the temperature of the pavement versus the temperature of the binder and how much the binder cools as it penetrates the pavement. Of course, another factor is the structure of the pavement itself as both the air voids content and the pore size distribution will affect the flow of the maintenance treatment into the pavement.

Pavement Service Life Design

Pavement service life depends upon a large number of variables:

- Overall pavement system strength.
- Pavement integrity in the face of climate (moisture damage).

- Pavement resistance to permanent deformation.
- Embrittlement of the pavement binder due to oxidation.

The mechanistic empirical pavement design guide has been developed in recent years to take all of these factors into account in optimizing the design of a pavement. Unfortunately, from a binder oxidation and hardening perspective, most of what it does is wrong because it is based upon old literature. To be specific, the MEPDG assumes that pavement binders do not oxidize below the top 25 mm (1 inch) of the pavement. It assumes that hardening of the binder stops after a certain period of time and does not take into account the deterioration of mixture fatigue resistance with binder oxidative hardening. The net effect of these difficulties is that in the controlled stress environment that the design guide calculates in most cases, binder oxidative hardening actually improves fatigue resistance for about the first ten years of the pavement and thereafter ceases to have a positive effect because at about that point it assumes no more binder hardening. These calculations were made in TxDOT Project 0-4468 and likely result from the design guide calculating that in a controlled stress environment a stiffer pavement (due to binder oxidation) results in less pavement deformation under load and therefore a reduced negative impact on fatigue life. Thus the design guide almost certainly is in serious need of correction in the area of binder oxidation and its impact on pavement durability.

MAINTENANCE TREATMENT SURVEYS

In order to evaluate the effectiveness of maintenance treatments in reducing aging, a better understanding of the design and construction practices associated with these is necessary. Data from current and previous surveys were collected and summarized with respect to Texas seal coats, more commonly called chip seals and officially termed surface treatments by TxDOT. These surveys included information related to material selection processes, design, and construction practices. The review was also conducted in order to discover what practices, if any, are being used to address oxidation and aging in HMA pavements.

User Survey – TxDOT Project 0-1787 (Texas Tech)

While performing a study for the development of the current TxDOT Seal Coat Manual, Texas Tech researchers conducted structured face-to-face interviews with TxDOT employees from each of the 25 districts. Those interviewed included district employees who were familiar with the seal coat process, including contract administrators, designers, inspectors, maintenance workers, and materials personnel (Senadheera et al., 2000). The Texas Tech interviewers examined the current construction practices for seal coats including planning methods and design, materials used, quality control, equipment, and construction methods.

Much of the information gleaned from the interviews for the TxDOT Seal Coat Manual study was similar to the information to be acquired through surveys for this project. Questions in the following specific categories were asked with respect to seal coats:

- General information.
- Design.
- Contract.

- Materials.
- Equipment.
- Construction.
- Quality control.
- Performance.
- Continuous improvement.

For the purposes of this report, information was reviewed and summarized from the general information, design, materials, construction, and performance categories.

General Information

From the general information category of questions, Texas Tech researchers discovered that the TxDOT districts with more rural roads had significantly more lane miles with seal coat than those districts in urban areas. Among all districts, 76 percent of the districts had 50 percent or more of their roads seal coated. Only one district was using seal coats strictly as a preventive maintenance measure. Thirteen of the other districts attempted to follow a preventive maintenance schedule. However, lack of maintenance funding prevented them from strictly adhering to the schedule. The remaining twelve districts applied seal coats on an as needed basis.

Design

In the *Statewide Seal Coat Constructability Review* report, the design section covered questions that ranged from project selection to bid or contract letting. For this study, relevant items addressed in the interview include the project selection process and design procedures. Roads selected for seal coats were those that exhibited cracking, flushing, lack of skid resistance, and oxidation. Generally, seal coats are not applied to roads that have significant structural failures or deficiencies. However, in cases where funding for full or partial depth repair is not available, seal coats may be applied to seal the pavement until funding does become available.

Two methods of design were used: the Modified Kearby method and an experience-based method. The Modified Kearby method is based on aggregate embedment for a determined binder application rate. The binder application rate is determined from existing conditions on the roadway receiving the treatment. The experience-based method depends upon the experience of an individual to determine the application rates of the materials. Most districts determined their application rates based on past experience. Many districts believed that because of the many field adjustments that are made in seal coat applications, relying on a specific design method was not practical. However, at the time that the *Statewide Seal Coat Constructability Review* was published, the Modified Kearby method was gaining approval. This method determines a starting application rate and then adjusts that rate depending on existing field conditions at the time of application. TxDOT personnel stated that this method is a good method for training inexperienced personnel.

Materials

The materials section of the interviews addressed selection of material type and grade, availability, and cost. For the purposes of this report, responses with respect to material type and grade are summarized.

Material selection was based on either maximization of seal coat performance or maximization of lane miles sealed for the amount of funding available. The majority of the districts used two main aggregate gradations. These were Grade 3 and Grade 4. Grade 4 was used most frequently due to its smoother finish, which is believed to reduce windshield damage from loose aggregate and requires less binder. Grade 4 also seems to provide a smoother ride surface than Grade 3, thus resulting in fewer complaints by the public. The users of Grade 3 aggregate claim that it is much more forgiving of variation in the binder application rate. The larger aggregate size exhibits less flushing and bleeding problems. Some districts used modified Grade 3 and 4 aggregates. These aggregates were more uniformly graded. However, some believe that the additional cost for minimal benefit does not warrant its use.

Regardless of the aggregate type used, aggregates are generally pre-coated in order to control the dust particles on the aggregate surfaces. Softer asphalts are typically used, such as AC-3 and AC-5, for pre-coating. The pre-coated aggregate method seems to be effective only when asphalt cement is used as the binder for the seal coat.

Selection of binder type varies from district to district. Some districts use one binder while others use up to six different binders for various jobs. Most of the districts used three different binders in their seal coat projects. The binder used can be based on several factors. Some districts select binders based on average daily traffic (ADT), with higher ADT roads getting the higher quality binders. Other districts may select binders based on local prices or allow the contractor to select the most economical binder available to them. The most commonly used asphalt cement binder types include the following:

- AC-10-latex.
- AC-5-latex.
- AC-10.
- AC-5.
- AC-15-5TR.
- AC-15P.

Of these binders, the AC-15-5TR binder is used by the majority of the districts. This tire rubber modified asphalt seemed to produce satisfactory results. The AC-15P and AC-5 are also frequently used. However, districts that used the AC-5 binder seemed to have significant problems with bleeding. Asphalt cement binders were typically used in the hotter and drier months of the year.

Of the emulsified asphalt binders used, the most common were:

- CRS-2H.
- HFRS-2P.
- HFRS.
- CRS-2.
- CRS-2P.

Significantly more districts chose CRS-2P over the other emulsified asphalt binders. The emulsified asphalt binders were typically used in cooler months or when there was a higher probability of rain.

Construction

Seal coat season, surface preparation, traffic control, material application, rolling, and brooming were addressed during the construction portion of the interviews. For the purpose of this project, seal coat season and surface preparation are summarized.

The districts all generally agreed that the summer months were the best for applying seal coats. This period of time varied depending on latitude. Those districts located in the south had a longer seal coat season than those in the north. Districts also preferred to finish seal coating in a reasonable time before the first cold spell. This allowed for better adhesion between aggregate and binder. Start dates run from April 1 to June 1, while finish dates were distributed between August 31 and October 31.

Surface preparation typically involves crack sealing and patching. Crack sealing prevents binder from being lost in the cracks, and patching levels the pavement surface.

Performance

In the performance section of the interviews, the districts were asked which distress types were observed and which were the most predominant. The common distresses observed included flushing, shelling, cracking, streaking, and oxidation. Of these, flushing and shelling were the most predominant distresses observed.

While these interviews provided a wealth of information with respect to the past practices associated with seal coats in Texas, very little was mentioned concerning oxidation and aging. In some instances seal coats were used to address oxidation but were usually a secondary concern. If seal coat applications are found to significantly reduce aging in HMA pavements, the practices summarized above may be helpful identify some of the mechanisms that contribute to this effect.

User Survey – TxDOT Project 0-6009

As part of this project, a short answer survey was created in order to assess the use of seal coats to reduce aging on Texas roadways. A limited number of TxDOT personnel from the Fort Worth, Brownwood, and Atlanta Districts, who have been with the department for several years

and are involved with district laboratory and pavement design, were selected for the survey. These generally included district laboratory and pavement engineers as well as district laboratory supervisors. The questions were designed to assess the current practices and uses associated with seal coats, how the pavements are selected for treatment, and whether or not they are specifically used to reduce aging.

Responses indicate that seal coat treatment sections are most often selected based on routine maintenance/pavement management plans. These plans provide a timeframe during which pavements are sealed on a regularly scheduled basis. Sealing typically is performed on a five to seven-year schedule, with some districts treating surfaces on a six to eight-year schedule.

As a particular pavement section approaches this age range, it is submitted for approval and funding. If funding is approved, the section is sealed, typically during the summer months. Existing pavements are prepared by sweeping and crack sealing. In some cases, small localized repairs of the HMA and subbase are made prior to sealing. If the section to be treated is located in an area without curb and gutter, maintenance crews blade vegetation off the edge of the existing HMA.

Once the surface is prepared, asphalt binder is applied at a rate of 0.40 to 0.45 gallons per square yard. The rate of application varies based on the type of binder used and existing surface conditions. The rate is determined by evaluating field conditions, by visual inspections, by calculations using agency-recommended equations from the TxDOT Seal Coat and Surface Treatment Manual, and by past experience. Aggregate application rates range from one cubic yard of aggregate per 90 square yards of pavement to one cubic yard of aggregate per 125 square yards of pavement. These application rates also are determined according to aggregate type, calculation using agency recommended equations from the TxDOT Seal Coat and Surface Treatment Manual, inspection, and past experience. Experienced field personnel are a critical part of a successful application.

Seal coats are not used in areas with high turning movements, high traffic volumes, or on road sections where significant vehicle acceleration or deceleration occurs. One respondent also indicated that seal coat use is avoided on sections where the structural repairs needed are beyond the scope of a seal coat application. Problems encountered in seal coat applications included flushing and loss of aggregate.

While respondents indicated that seal coats extend the life of the pavement, aging did not appear to be a primary reason for applying the treatment. Seal coats were typically applied to improve skid resistance and to serve as a moisture barrier. It appears that seal coats are most often applied based on a typical timeframe for application.

SUMMARY

Binder oxidation in pavements and its impact on pavement performance has been addressed by numerous laboratory studies of binder oxidation chemistry, reaction kinetics, and hardening and its impact on mixture fatigue. Studies also have included some work on binder oxidation and hardening in pavements and the effectiveness of maintenance treatments. Yet more

such studies are needed to better understand the fundamentals of pavement performance as a function of climate and pavement parameters. TxDOT Project 0-6009 was conducted to address these important and interrelated issues.

CHAPTER 2. PROJECT DESIGN AND FINAL REPORT OVERVIEW

The objective of the experimental design (ED) was to select representative HMA mixtures, corresponding field sections, and laboratory tests and conditions for the project experimental plan. This plan addresses the three objectives and four products of this project, as outlined in the Background Summary.

The three objectives are:

- Development and calibration of a laboratory test to assess binder aging during the production process and during the field service of the pavement.
- Incorporation of aging for use in a HMA mix design system to produce mixtures that provide adequate resistance to fatigue cracking, including guidelines to optimize resistance of HMA to aging.
- Evaluation of the use of maintenance treatments to reduce the aging of asphalt pavements starting at early ages.

The four products are:

- A new test procedure to characterize binder aging and predict service life for different applications (Chapter 14).
- An HMA mix design component that incorporates aging and its effect on resistance to fatigue cracking (Chapter 16).
- Guidelines for optimizing HMA mixture resistance to aging (Chapter 15).
- Guidelines for the best maintenance treatments to reduce the aging of binders (Chapter 10).

In order to fulfill these objectives and develop these products, the following three experimental design elements (EDE) were conceived:

- EDE 1: a selection of field sections from previous and newly constructed projects for calibration and validation of the binder oxidation and hardening model.
- EDE 2: a subset of newly constructed field sections exposed to different maintenance treatments (including corresponding control sections) for monitoring with respect to effectiveness in reducing aging in the maintenance treatment experiment.
- EDE 3: the same larger collection of field sections from EDE 1 and a corresponding subset of laboratory mixed-laboratory compacted (LMLC) specimens for calibration and validation of the mixture aging model contained in the fatigue analysis system and identification and assessment of mixture factors that affect the decline of mixture fatigue resistance due to aging in the aging experiment.

These design elements are outlined schematically in Figure 10. Experimental measurements were conducted on binders, laboratory mixtures, and pavement cores. These measurements were used to better understand binder oxidation processes in pavements and their resulting impact on mixture and pavement fatigue processes. These results were used to address the three objectives of the project and to develop the four products.

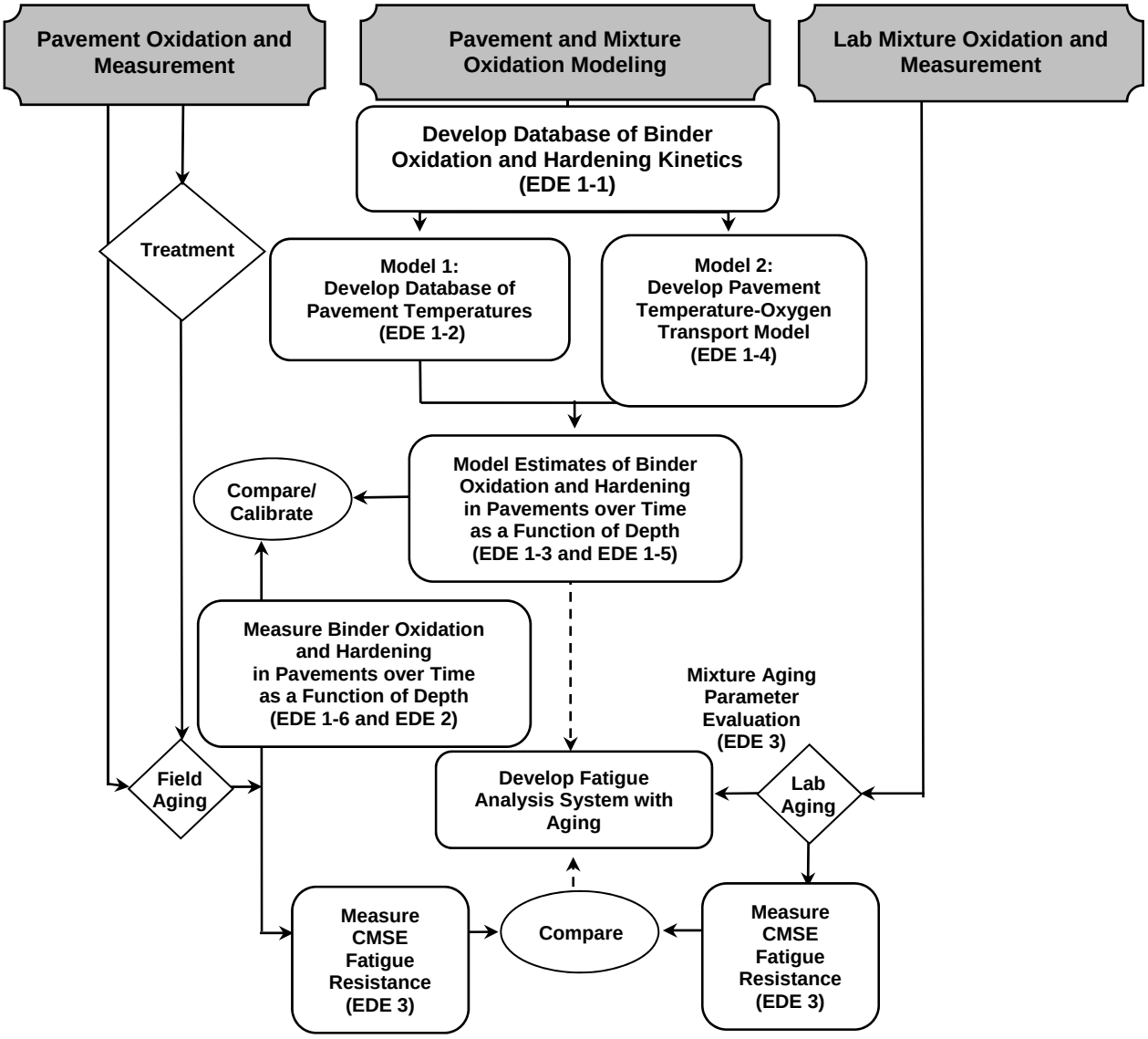


Figure 10. Schematic Outline of the Research Plan and Experimental Design Elements.

Figure 10 shows three paths of experimental research. Binder oxidative reaction and hardening properties and pavement temperatures were used in pavement oxidation models and compared to measurements of pavement oxidation (EDE 1). Measurements of pavement oxidation and hardening also were made on treated pavements (EDE 2). Laboratory mixture measurements were used to evaluate mixture parameters such as mixture type, air voids, binder content, aggregate type and gradation as to their impact on the decline of fatigue resistance, thereby providing a better fundamental understanding of fatigue resistance in mixtures (EDE 3). Such an understanding is essential to achieving the objectives of developing a laboratory procedure that includes estimating fatigue resistance and predicting service life. Also as part of EDE 3, these mixture measurements were compared to measurements of fatigue in aged pavements.

The role of model-based estimates of binder oxidation rates in pavements is unique and deserves further comment. The model (initially developed in TxDOT Project 0-4688 and to be further developed in this project) used fundamental input data: binder oxidation kinetics and hardening susceptibility parameters, pavement temperature cycles (both daily and annual) as a function of time and depth, and oxygen transport in pavements, including diffusion in binder and mastic films. Estimates of binder oxidation and hardening over time and as a function of pavement depth, in principle, can then be used to estimate pavement performance, specifically changes to fatigue resistance. This work evaluated and calibrated such an analysis process by conducting parallel measurements of binder oxidative aging and fatigue resistance, obtained from field cores over the five-year term of the project, and comparing them to the model estimates. Laboratory measurements of the effect of binder oxidation on fatigue resistance provide essential information to the modeling process on the importance of various mixture fatigue parameters.

One point bears further emphasis. The combination of 1) developing a transport model of binder oxidation in permeable pavements; and 2) comparing model-calculated oxidation to measured oxidation in pavements is designed to obtain the maximum effect from limited field data. With a sound physical model that is based on fundamental physical laws and laboratory measurements of binder and mixture properties and then further calibrated with actual field data, much more accurate calibrations of laboratory aging to that in the field can be obtained than from a much larger set of field data used to statistically calibrate field aging to laboratory tests. Basically, a model based in the fundamentals of thermal and oxygen transport is required in order to account for pavement aging that occurs over a range of temperature and with possibly limited oxygen supply. The value of using such a physical model should not be overlooked or underestimated, both from the perspective of obtaining accuracy from a laboratory test and from the perspective of obtaining the most information from the field cores. Such a fundamentals-based approach also provides a better mix design procedure that includes fatigue resistance of HMA.

This chapter presents the selected field sections and corresponding materials, coring schedule, and specimen fabrication first. Next the three individual EDEs are described in further detail. The chapter concludes with a brief outline of how the data gathered through the EDEs were used to achieve the three objectives and develop the four products and an outline of the chapters where these elements are discussed in this report.

FIELD SECTIONS

Nineteen mixtures from eighteen field sections have been identified to span the five different environmental zones in Texas (Table 1, Table 2, and Figure 11), and an additional section was identified at MnROAD. These field sections are all dense-graded HMA, and all but six of them are surface mixtures. The Amarillo (AMR) and Atlanta (ATL) sites are now covered with a seal coat and a microseal, respectively. Waco (WAC), Laredo (LRD) 01, and LRD 02 are underlying layers in perpetual pavement sections. Bryan (BRY) is now covered by a course matrix-high binder (CMHB) layer. A range of commonly used TxDOT binders and aggregates are represented (Table 1 and Table 2). Twelve of the field sections are from previous TxDOT projects, and seven of them were constructed in Texas in the 2008 construction season. Nine new

or recently constructed (within the past two years) Texas field sections and the MnROAD test section were used in both the aging and maintenance treatment experiments as shown in Figure 11 (for the Texas sections) and Table 1 and Table 2. A total of twelve field sections have original binder available for development of the laboratory aging test, and three of the new Texas field sections (highlighted in italics in Table 1) were used in the laboratory evaluation of mixture parameters (including binder and AV content) and their effect on decline in mixture fatigue resistance.

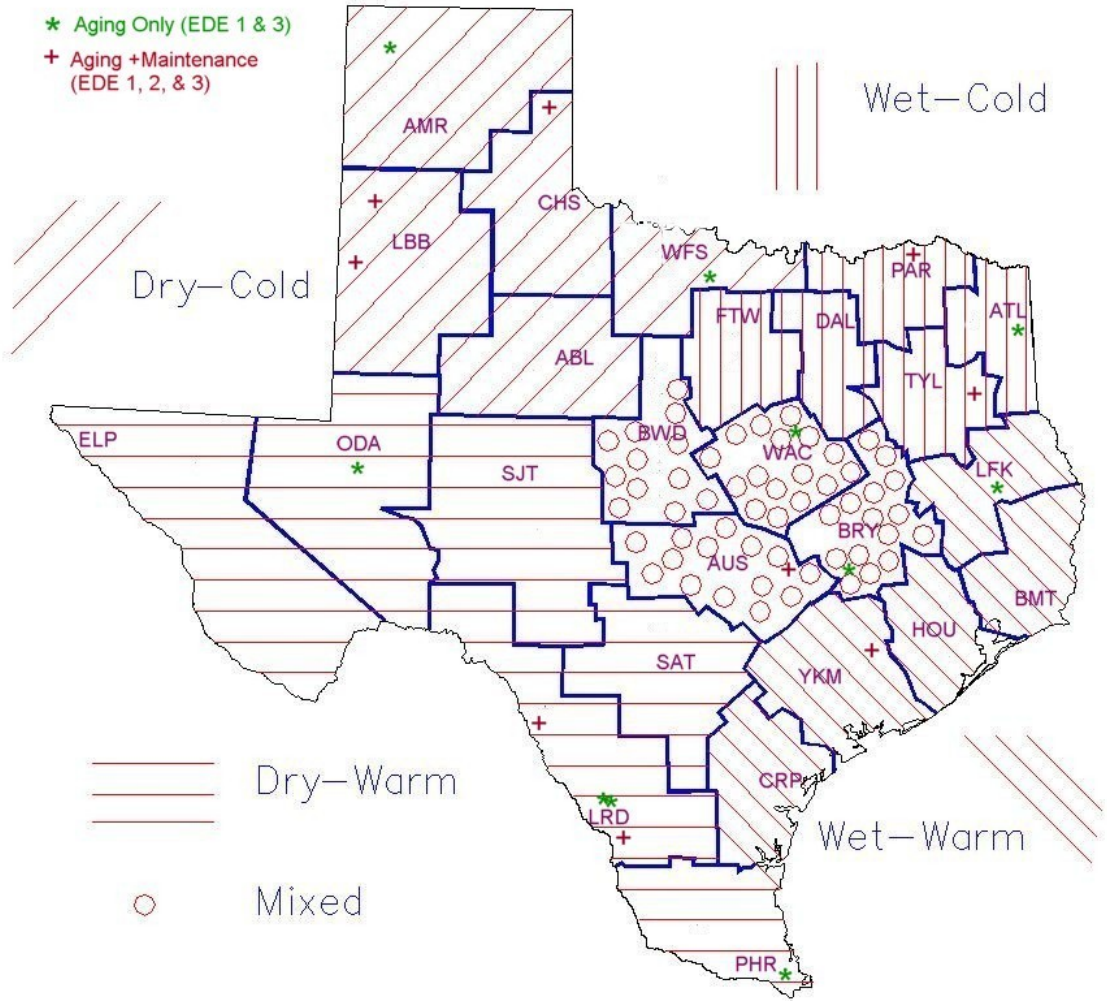


Figure 11. Field Section Locations and Texas Environmental Zones.

Table 1. Field Sections for the Aging Experiment (EDE 3).

Section ID/ District	Loca-tion	Environ-mental Zone	Binder Type (*=original binder)	Aggregate Type	Mix Type (Thickness)	Construction Date
BRY	US 290	WW	PG 64-22	Limestone	Type C (2")	2002
ATL	IH 20	WC	PG 76-22 (SBS)	Sandstone	12.5mm Superpave (2.5")	2001
WAC	IH 35 Layer #5	M	PG 70-22 (SBS)	Igneous/ Limestone	19mm Superpave (3.5")	2003
WFS	SH 59	DC	PG 70-22	Limestone	Type D (2")	2007
LRD01	IH 35 Layer #3	DW	*PG 76-22 (SBS)	Traprock/ Gravel	25mm SFHMA (6")	2007
LRD02	IH 35 Layer #5	DW	*PG 70-22 (SBS)	Gravel	12.5mm Superpave (2")	2007
LFK	US 69	WW	PG 70-22	Gravel	Type C (2")	2003
LRD03	FM 649	DW	*PG 76-22	Limestone (absorptive)	Type C (2")	2006
LRD04	*US 277*	*DW*	**PG 70-22*	*Limestone*	*Type C (3")*	*2008*
TYL	US 259	WC	*PG 70-22	Sandstone/ Limestone	Type C (2")	2007
AUS	SH 21	WW	*PG 70-22	Limestone	Type C (2”)	2007
LBB01	US 82	DC	*PG 70-28	Limestone	CMHB-F (3")	2008
LBB02	US 84	DC	*PG 70-28	Gravel/ Limestone	CMHB-C (2")	2008
CHS	*US 83*	*DC*	**PG 70-28*	*Granite*	*Type D (2")*	*2008*
YKM	SH 36	WW	*PG 64-22	Limestone (absorptive)	Type D (2")	2006
ODA	FM 1936	DW	PG 70-22 (SBS)	Rhyolite	CMHB-F (3")	2002

Table 1. Field Sections for the Aging Experiment (EDE 3). (Continued)

Section ID/ District	Loca-tion	Environ-mental Zone	Binder Type (*=original binder)	Aggregate Type	Mix Type (Thickness)	Construction Date
PHR	FM 2994	DW	PG 70-22 (SBS)	River Gravel	Type D (3")	2002
AMR	US 54	DC	PG 70-28	River Gravel	(2")	1998
PAR	*SH 24*	*WC*	**PG 64-22*	*Sandstone*	*Type D (2")*	*2008*
MN	MnRD	NA	*TBD	TBD	TBD	2008

Table 2. Field Sections for Maintenance Treatment Experiment (EDE 2).

Section ID/ District	Location	Environmental Zone	Seal Coat Binder Type	Seal Coat Aggregate Type
LRD03	FM 649	DW	PASS	Gr. 4 Precoated LRA
LRD04	US 277	DW	AC 15-P	Gr. 4 Precoated LRA
TYL	US 259	WC	AC-20-5TR	TBD
AUS	SH 21	WW	TBD	TBD
LBB01	US 82	DC	AC-15-P or AC 15-5TR	Gr. 4 Precoated Limestone
LBB02	US 84	DC	AC-15-P or AC 15-5TR	Gr. 4 Precoated Limestone
CHS	US 83	DC	AC-15-5P	TBD
YKM	SH 36	WW	CRS-2P	Pre-coated Limestone
PAR	SH 24	WC	AC 20-XP	Gr. 4 Precoated Sandstone
MN	MnRD	NA	TBD	TBD

Five coring dates for new field sections and three coring dates for previous field sections are planned. For the new field sections constructed in the FY08 construction season, cores were procured at the time of construction or soon after construction and in the next four fall (or fall/winter) seasons after each summer of aging. Additional cores for these new field sections were only taken at three coring dates for mixture testing (summer 2008, fall 2009, and fall 2011).

For previously placed field sections, cores were procured at these same three coring dates (summer 2008, fall 2009, and fall 2011). For this project, at each coring date cores were taken both on the shoulder, where only aging would have affected the HMA mixture, and in the wheelpath, where the simultaneous effects of traffic and aging would have affected the HMA mixture properties. Figure 12 shows a typical coring layout. Presumably there would be a difference in air voids between specimens obtained from shoulder and wheelpath. Thus to validate the binder oxidation and hardening model, binders were extracted from cores of field sections every year for new field sections and every other year for previously placed field sections. To calibrate and validate the mixture aging model contained in the fatigue analysis system, mixture tests of cores from field sections were conducted every other year for both new field sections and previous sections. This coring schedule provided a significant amount of data to calibrate and validate both the binder oxidation and hardening model and the mixture aging model within the fatigue analysis system. As previously discussed, this project capitalized on the reduced data required for calibration and validation of theoretical models instead of using statistically-based empirical models with limited application.

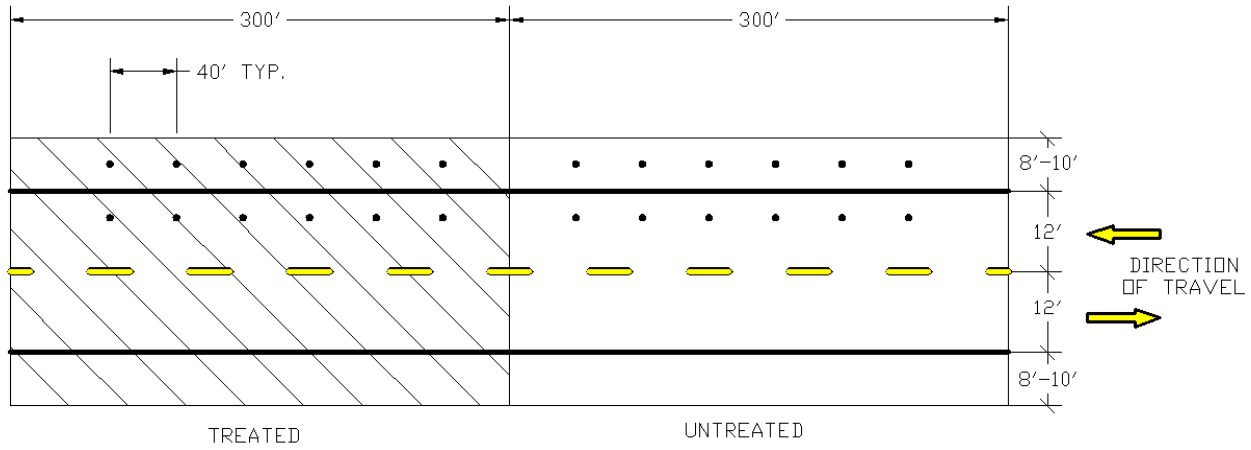


Figure 12. Typical Test Section and Coring Layout.

EDE 1. BINDER OXIDATION AND HARDENING

As noted previously, early work supports several observations and conclusions concerning binder aging in pavements and the development of binder aging tests.

- First, an aging test conducted at a single temperature, is not sufficient to rank binder oxidative aging rates in pavements. Based upon the simple, but surprisingly accurate, temperature pavement oxidation model, it was seen for a variety of binders that their rankings of hardening rate at 60°C in an environmental room (ER) do not necessarily match the rankings that are expected to occur in pavements.
- Second, knowing only binder aging rates in pavements is not sufficient for predicting pavement performance and durability. There are many other factors that are important to pavement performance besides binder oxidation and hardening, including the overall pavement structure (stiffness), loading level and frequency, and loading mode (controlled

strain versus controlled stress, e.g., established largely by asphalt concrete layer stiffness relative to the overall pavement system stiffness).

- Third, there is significant support for the conclusion that if air voids (and interconnected air voids in particular) are high, then binder oxidation rates in pavements are largely determined by pavement temperatures and their variation over time (daily and annual thermal cycles).
- Fourth, if air voids (and especially interconnected air voids) are sufficiently low (probably less than about 2 percent interconnected air voids), then oxidation rates are slowed significantly by oxygen transport in the pavement.

These conclusions support the notion that measuring laboratory oxidation and hardening rates and converting these measurements directly to field hardening rates through a simple calibration is a highly problematic concept. To address these difficulties, several binder aging sub-elements, EDE 1-1 through EDE 1-6, are described below. EDE 1-1 through EDE 1-6, taken together, focus on developing an improved model of binder oxidation and hardening in pavements that would then be used to estimate hardening rates. Such an approach ultimately was less costly and much more reliable than pavement rate predictions based upon "calibrations" of laboratory measurements for the reasons cited previously. Collectively, these EDEs include but go well beyond those suggested by the project statement.

Then, in spite of the difficulties mentioned above with a simple binder test and in addition to the planned model-based approach, an alternate method for assessing binder aging rates in the laboratory is described in EDE 1-7 (not shown in Figure 10).

EDE 1-1. Database of Binder Oxidation and Hardening Kinetics Parameters

Understanding basic binder oxidation reaction kinetics is key to developing a pavement binder oxidation rate model. Different binders have different activation energies and different initial jump characteristics. As a result, different binders exposed to the same oxidation conditions (temperature and oxygen pressure) were oxidize at different rates. But even more relevant to pavement oxidation, binders that react at different rates at one temperature (60°C, for example) may well experience relative rate reversals in service in the pavement due to the range of temperatures that the binders experience over time and the binders' differences in activation energies.

Developing a database of binders typically used by TxDOT on a region or district basis and then adding over time to this database will allow TxDOT engineers to be able to make reasonable estimates of binder durability in pavements, provided that a good model of oxidation can be developed. Table 3 lists 24 binders for study, binders that are those most used by TxDOT, plus ones that are used in the planned field studies (EDE 3). The list also includes a mix of unmodified base binders plus modified grades.

Table 3. Binders Selected for TxDOT Project 0-6009.

Manufacturers	Binder Types
Alon	PG 64-22 PG 70-22S PG 76-22S
Lion	PG 64-22 PG 70-22S PG 76-22S
Valero-Ardmore	PG 64-22 PG 70-22S PG 76-22S
Valero-CC	PG 64-22 PG 70-22S PG 76-22S
Valero-Houston	PG 64-22 PG 70-22S PG 76-22S
SEM (Koch)	PG 64-22 PG 70-22S PG 76-22S PG 70-28S
Martin	PG 64-22 PG 70-22S
Eagle	PG 64-22 PG 70-22S
Wright	PG 76-22S

Oxidation (carbonyl area) and rheology (low shear rate viscosity and DSR function) of both unaged binders and binders aged at different levels at 0.2 atm oxygen pressure were tested to measure binder oxidation and hardening kinetics. These data included both fast-rate and constant-rate period measurements for each binder. Because using more temperatures increased confidence in the measured reaction activation energies, reaction rates were measured at five temperatures (140, 160, 180, 200, and 210°F). At each temperature, oxidation rates were determined with measurements for at least nine time points—four earlier time points in the fast reaction rate period and at least five time points in the constant-rate period. Approximate times, based on previous binder aging data, are given in the following table.

Table 4. Binder Oxidation Nominal Sampling Schedule.

Aging Temperature	Fast Rate Period Aging Time (days)	Constant Rate Period Aging Time (days)
200 and 210°F	1, 2, 4, 6	10, 15, 20, 25, 30
160 and 180°F	1, 3, 5, 7	10, 20, 30, 40, 50, 60
140°F	1, 5, 10, 15	20, 30, 45, 60, 75, 90

Five pressure oxidation vessels with controllable oxygen pressure and temperature were used to age binders in thin films. Both modified and unmodified binder oxidation and hardening

kinetics in both the fast-rate and constant-rate periods were determined, and the effect of polymer modification on binder oxidation kinetics were evaluated.

EDE 1-2. Database of Pavement Temperatures across Texas

Pavement temperatures vary with time (by day, by weather, and by season) and with depth (distance away from the boundary condition established by these temporal variations). Accurate model calculations of binder oxidation required accurate representations of pavement temperatures. Generally, as noted in Chapter 2, these variations are reasonably well represented by a daily sinusoidal function superimposed on an annual seasonal sinusoidal function. Because climate varies across Texas due to cloud cover, moisture, and latitude, these temperature variations were different in the different climate zones of Texas. This EDE gathered available recorded temperature histories in several pavements and versus depth (from the LTPP program) throughout Texas and from them established the temperature model parameters (Eqs. 1-8 and 1-9) for representative locations in Texas. These parameters include the mean pavement temperature including its seasonal variation, the amplitude of the daily and annual temperature variations, and pavement thermal diffusivity. As an example, from TxDOT Project 0-4688 the amplitude at Refugio, Texas, during the summer was 22°C, and in Minneapolis, Minnesota, the summertime amplitude was 20°C(Figure 13).

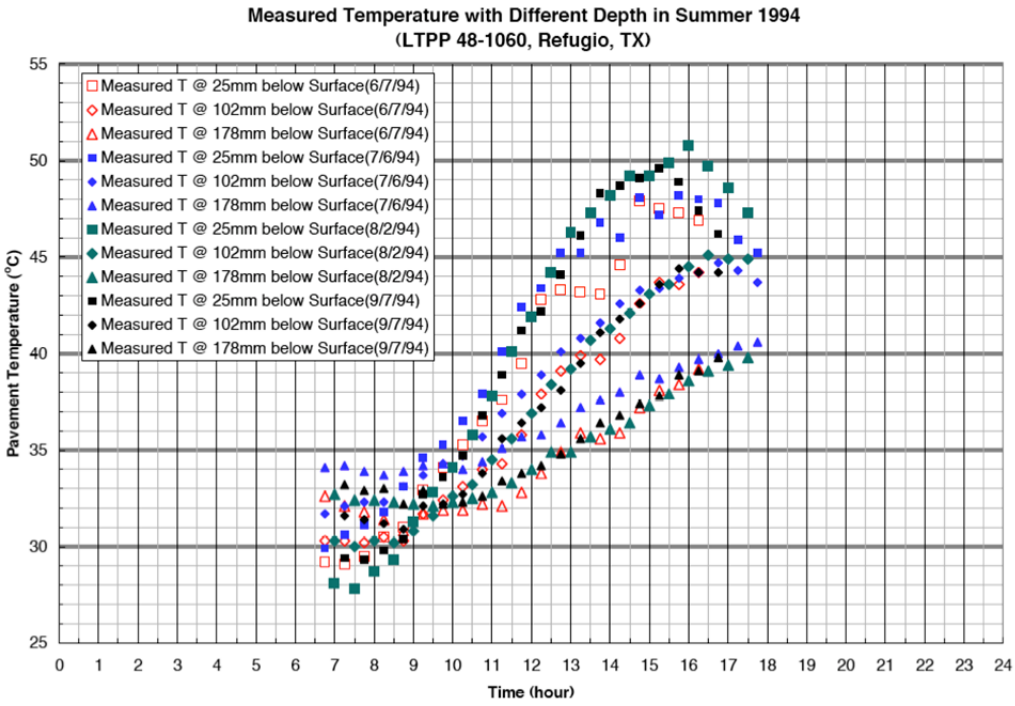


Figure 13. Daily Pavement Temperature Variation, July 1994, Refugio, Texas.

As an alternative to pavement temperature data, improved models were used to calculate temperatures. As noted in Chapter 1, the EICM model of the MEPDG was not satisfactory, so the models of Hermansson (2000, 2004) and Gui et al. (2007), with further improvements developed in this research, were used. The calculated profiles were compared to the archived

LTPP profiles to assess the model's ability to provide adequate temperature histories as a function of depth.

EDE 1-3. Pavement Oxidation and Hardening Rates (Thermal Transport Model)

This EDE sub-element used the results of EDE 1-1 and EDE 1-2 to estimate typical binder hardening rates in a variety of climates across Texas and for a variety of binders. Early in the project, before more detailed pavement temperature models were developed, these model-based estimates served to provide project researchers limiting-case calculations to estimate pavement oxidative hardening over time in specific regions and climates of Texas. These estimates assumed that oxygen transport to the binder is plentiful so that only temperature and binder properties determine the binder hardening rates in the pavement. (Extensive pavement and laboratory mixture data from TxDOT Projects 0-1872, 0-4468, and 0-4688 provide no indication that aggregates affect either the fundamental oxidation chemistry or the reaction kinetics of binders in pavements. Therefore, aggregates were neglected as a factor in this model.) Even as improved temperature modeling capability was developed, the "no oxygen diffusion resistance" limiting case was used throughout the project as a simplified method of calculating pavement oxidation rates and a reality check of the more complex models. This simplified diffusion model remains as an option in the final software user interface presented in Chapter 16.

EDE 1-4. Improved Model of Pavement Oxidation and Hardening Rates

It is clear from pavement binder oxidation data of TxDOT Projects 0-4688 and 0-5091 that oxygen transport limitations sometimes are important in establishing binder hardening rates in pavements. If the interconnected (or accessible) air voids are sufficiently low, then delivery of oxygen to the binder is hindered. In this EDE sub-element, an improved model of binder oxidation in pavements that includes oxygen transport was developed.

Model development began with the model proposed by Lunsford (1996). He approximated the diffusion from an oxygen source (air in the pores in the pavement) through a flat film of binder. A parameter of the model was the binder film thickness and the greater this thickness, the greater the effect of the diffusion limitation. Lunsford also made very approximate measurements of the diffusivity of oxygen in binders with ad hoc experiments that were designed primarily for measuring oxidation kinetics. The statistical error in the diffusivity measurements was appreciable, however. Lunsford concluded that film thickness can have a major impact on binder oxidation rates. His model was further explored in this EDE sub-element.

The concept of approximating the binder film in the pavement as a thin film is probably reasonable for high air voids content where there are a large number of pores passing through the pavement so that the distance from any pore to the binder, even to the farthest binder away, is not very great. A more realistic model for a reduced number of air voids might be a cylindrical model that assumes that the oxygen diffuses from the pore in a radial direction into a cylindrical shell of binder. In this case, the relevant parameter would be the thickness of this cylindrical shell relative to the diameter of the pore containing the air. The smaller the air voids, the greater the ratio of this binder shell to the pore diameter and thus the more time required for oxygen to diffuse through the binder.

For either model, improved values for the diffusivity of oxygen in the binders were needed as a function of binder stiffness, which means they had to be measured as a function of binder temperature and state of oxidation.

A further hindrance of oxygen diffusion into the binder would be the presence of mineral fines that are impervious to diffusion. Such fines would impede the diffusion of oxygen into the binder and would require that oxygen molecules take a more tortuous path through the binder, thus lengthening the diffusion path and thereby effectively reducing the oxygen diffusivity. Measurements of the diffusivity of oxygen in mastics was needed in order to quantify this effect.

Therefore, diffusivities in both neat binders and mastics were measured following the procedure of Lunsford. Films of defined binder (or mastic) thickness were placed onto aluminum trays and oxidized in a controlled temperature and oxygen environment. The carbonyl growth rate that occurs at the surface exposed to oxygen was compared to the rate at the interface of the binder (or mastic) film with the tray. The only way oxygen reaches that interface is by diffusion through the film. Thus the carbonyl growth rate at that interface, relative to the growth rate at the air surface, allowed the diffusivity to be measured by matching the growth rate to a reaction and diffusion transport model.

With values of the diffusivities of oxygen in binders and mastics, measured binder oxidation rates in pavements may then be used to measure effective film thicknesses according to either the flat film diffusion model or the cylindrical diffusion model and thereby calibrating the diffusion model.

EDE 1-5. Pavement Oxidation and Hardening Rates (Thermal and Oxygen Transport Model)

This EDE sub-element used the results of EDE 1-1 and EDE 1-2 and the thermal and oxygen transport model of EDE 1-4 to estimate typical binder hardening rates in a variety of climates across Texas and for a variety of binders and different levels of air voids (total and interconnected) and mixture/pavement types. These model-based estimates then served as a look-up catalog for pavement designers to estimate pavement oxidative hardening over time in specific regions and climates of Texas. Alternatively, a spreadsheet or other computational approach may be used to calculate results for a specific situation, given appropriate model parameters and material and pavement properties.

EDE 1-6. Field Binder Aging Rates for Calibration of the Transport Model

This project offers a unique opportunity to monitor a significant number of pavements over enough time to accurately determine binder hardening rates in pavements and to evaluate the effect of air voids and depth in the pavement on these rates. As described in the EDE sub-elements above, the best approach to including the impact of the large number of variables that affect binder pavement aging is with fundamentals-based models, and that is the approach taken in this experimental plan.

However, fundamental principles are not sufficient, and key to calibration and verification of the pavement aging models discussed in EDE 1-3 and EDE 1-4 were measurements of binder aging in the field. Cores obtained from field sections (Figure 11) during the course of this project were analyzed for air voids [either by the CoreLok® or the saturated surface dry methods (SSD)], interconnected air voids (by X-ray CT), or accessible air voids (by CoreLok and SSD); and then the binder extracted and recovered using methodologies developed by the researchers (Burr et al., 1990; Burr et al., 1991; Cipione et al., 1991; Burr et al., 1993; Burr et al., 1994). The recovered binder was then analyzed for oxidation by infrared spectroscopy and for physical properties by dynamic shear rheometry (DSR) to provide the key data: binder aging and hardening rates in pavements.

EDE 1-7. Laboratory Binder Aging Test

EDE 1-1 through EDE 1-6 address a fundamental, model-based effort to calculate binder aging rates in pavements. Such a procedure requires a detailed binder reaction kinetics database that is time consuming to update on a routine basis. As an alternative approach, a more rapid method of modeling binder pavement oxidation has been developed, based upon determining binder oxidation kinetics parameters at a combination of higher temperature and pressure. The results are then converted to atmospheric air conditions through a correlation developed from the work of this project. The approach is reported in Chapter 14.

EDE 2. MAINTENANCE TREATMENT EFFECTIVENESS IN REDUCING AGING

The essential objective of this EDE is to assess the effectiveness of maintenance treatments in reducing aging. Figure 11 and Table 2 describe the location and materials in the selected field sections for the maintenance treatment experiment. Based on the results of this experiment, recommendations on the optimal treatment and associated HMA mixture parameters and environmental conditions will be produced in a set of guidelines.

Two questions arise with respect to the effectiveness of maintenance treatments in reducing aging:

- How well do the treatments penetrate into the pavement?
- How well do they retard the in situ binder's aging?

Extraction and recovery of binder and measurement of its properties (DSR, Fourier transform infrared spectroscopy, size exclusion chromatography) may be able to address the first question (and such analyses will be conducted), especially if pavement cores are sawn into a number of slices and the recovered binder analyzed. Also, x-ray computed tomography (CT) may be able to detect penetration of the maintenance treatment binder into the underlying pavement layer. These analyses were performed also.

However, neither extraction and recovery nor X-ray CT alone can address the effect of the treatment on *mixture* properties. Thus, this EDE required using mixture physical property tests in addition to binder tests to evaluate whether the maintenance treatments affect the rate at which oxidative aging changes the mixture properties. Therefore, a modified version of the

fundamental calibrated mechanistic with surface energy (CMSE) mixture fatigue analysis approach was used as the primary method to measure the mixture properties of treated and corresponding untreated pavement sections. Modifications include the following:

- Testing of prismatic specimens cut parallel to the road surface from pavement cores and tested on end (Figure 13).
- Separation of the different mechanisms of energy dissipation during fatigue cracking, including the effects of apparent stiffness and phase angle changes and plastic deformation.
- Measurement of Poisson's ratio during the relaxation modulus (RM) test.
- Expansion of the healing assessment during the repeated direct tension (RDT) test.
- Expansion of the aging assessment beyond an aging shift factor.

Work on these modifications continues beyond the scope of the work reported in this research report.

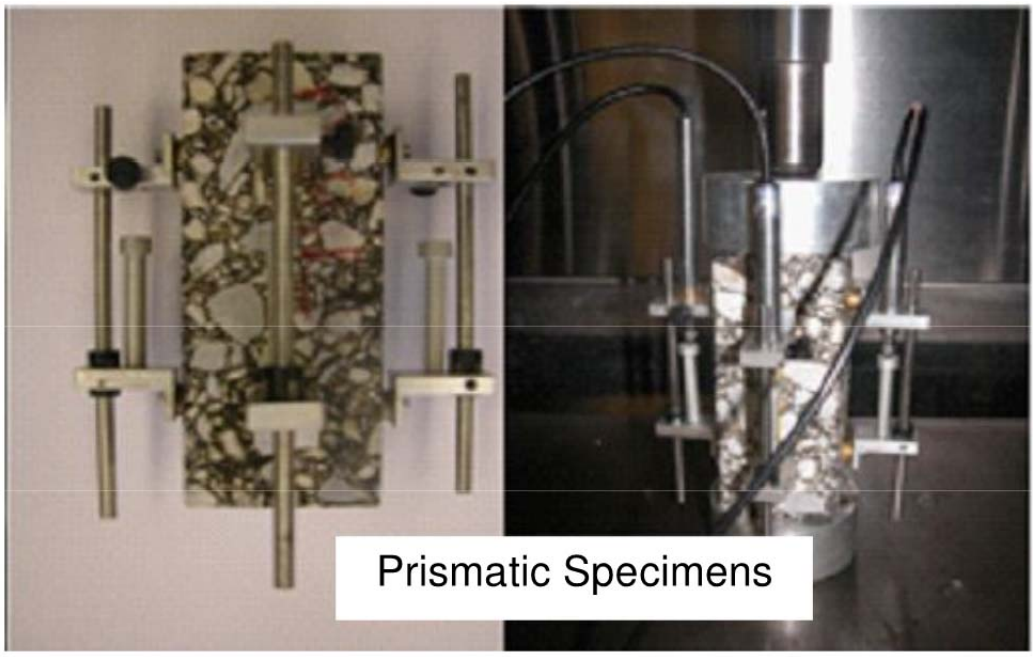


Figure 14. Testing of Prismatic Specimens in Direct Tension for CMSE.

EDE 3. DECLINE OF MIXTURE FATIGUE RESISTANCE DUE TO AGING

Figure 11 and Table 1 describe the location and materials in the selected field sections for the aging experiment that includes mixture testing of field cores taken at construction and after both two and four years. Figure 14 summarizes the testing of field cores from the selected field sections including extraction, recovery, and testing of the binder for EDE 1.

X-ray CT and image analysis techniques also were used in the aging experiment to examine the internal microstructure of HMA mixtures, including air void (AV) distribution and

interconnectivity and binder content and distribution in terms of film thickness. These factors are some of the HMA mixture parameters to be identified in terms of the role they play in the aging mechanism. CoreLok was used to determine total air voids as a necessary calibration for the X-ray CT method. Accessible AV and interconnected AV as determined using CoreLok and X-ray CT, respectively, also were determined as an important parameter related to aging.

The mixture testing again used a modified version of the fundamental CMSE fatigue analysis approach to further understand aging and its effect on mixture fatigue resistance. Results from this analysis facilitated quantitative incorporation of aging effects in a practical mix design system that includes the simultaneous effects of traffic, aging, environment, and pavement structure.

An additional experiment using LMLC specimens, from a subset of the selected field sections for the aging experiment (Figure 11 and Table 1), was conducted to identify and assess mixture parameters that affect the decline of mixture fatigue resistance due to aging. A modified version of the CMSE fatigue analysis approach again was used to evaluate the effect of these factors by testing the LMLC specimens. Recommendations on the optimal combinations of the levels of the identified factors or parameters to control aging were produced in a set of guidelines based on the results of the extensive experiment.

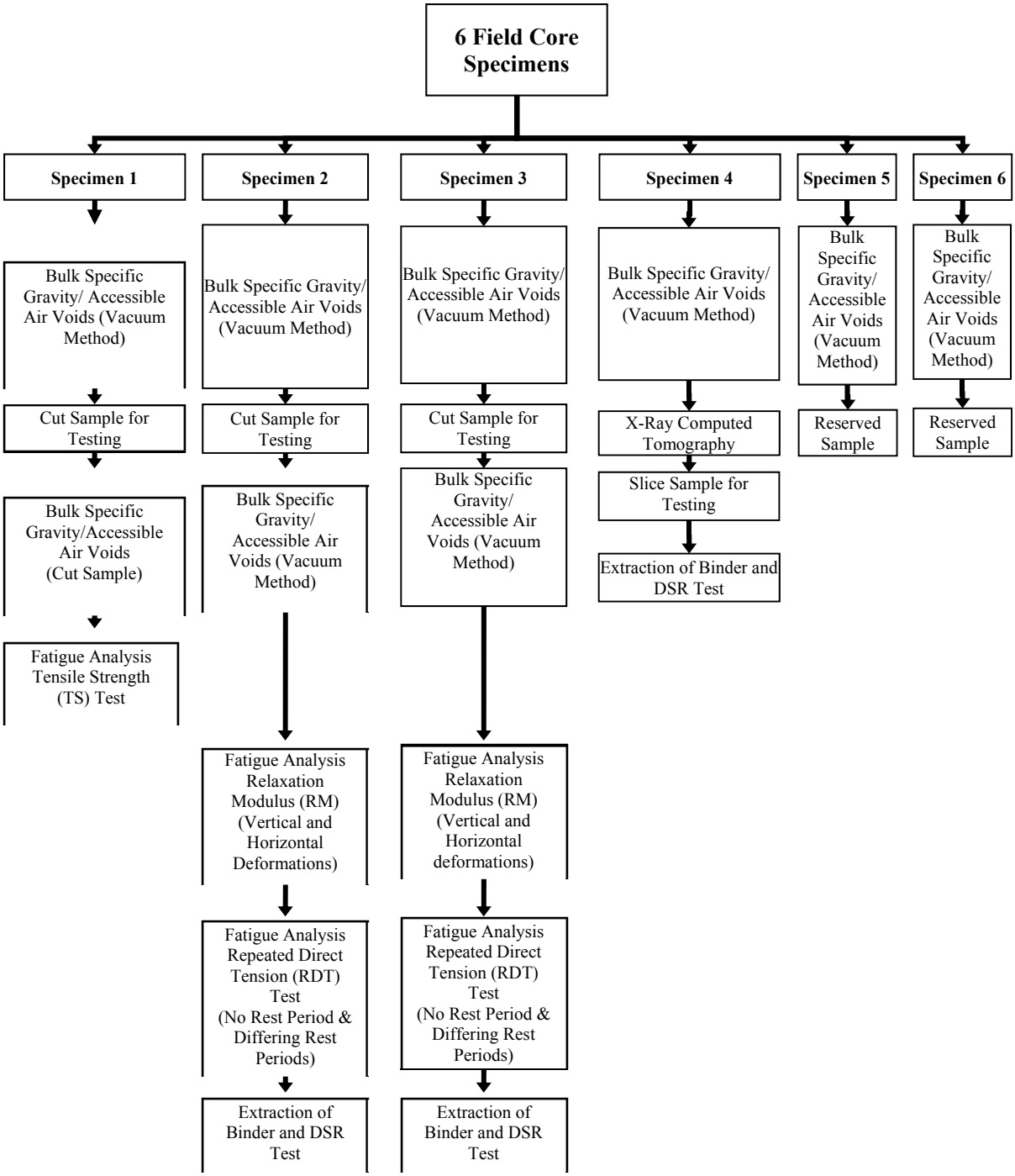


Figure 15. Testing Protocol for Pavement Cores.

SUMMARY

This has been a very complex project with interrelated climate, binder, and mixture contributions. To address this complexity, the members of this research team have investigated the several effects separately and from a fundamentals-based perspective. The separate fundamental characteristics thus determined are used to assemble a basis for rationally and

quantitatively understanding the effects of binder oxidation in pavements, as a function of depth and over time, to improve pavement performance prediction and thereby improving pavement design.

The data gathered through the three EDEs described in this chapter were utilized to achieve the three objectives and develop four products in this project and to move closer to being able to use fundamental binder, mixture, and pavement characteristics to predict pavement performance. From an age-related cracking perspective, this would mean being able to predict fatigue cracking and the impact of binder oxidation from a binder oxidation model developed from EDE 1-4 data and appropriate pavement and mixture parameters and traffic loading. One essential mixture parameter is its fatigue life decline (as defined by CMSE analysis) with binder hardening, evaluated from data like that collected in EDE 3. Then the simplest model would be a controlled strain, cumulative damage analysis similar to that performed in TxDOT Project 0-4688. A more complex model would be a controlled stress analysis. The model results of mixture fatigue resistance change over time as the result of binder oxidative hardening were compared to measurements of field cores for validation.

As a guide to this report, the results of the various elements of the test plan described above are presented in Chapters 3 through 16. Each chapter's relation to the test plan outlined schematically in Figure 10 is given in Table 5.

Table 5. Relation of the Report Chapters to the Test Plan, Figure 10.

Chapter	Short Title	EDE and/or Product*
3	Oxidation Kinetics Model	1-1
4	Oxygen Diffusivity	1-4
5	Air Temperature Model	1-2
6	Pavement Temperature Model	1-2
7	Pavement Oxidation Model 1	1-4
8	Pavement Oxidation Model 2	1-4
9	Pavement Oxidation Model 3	1-4
10	Seal Coat Study	2/Prod 4
11	Testing of HMA Field Samples	3
12	A Field Site Study of Mixture Aging	3
13	Field versus Laboratory Mixture Aging	3
14	An Accelerated Binder Aging Test	FAS/Prod 1
15	Mix Design and Analysis System	FAS/Prod 2
16	Software User Interface	FAS/Prod 3

* Product 1: A new test procedure to characterize binder aging, and predict service life for different applications.
* Product 2: HMA mix design component that incorporates aging and its effect on resistance to fatigue cracking
* Product 3: Guidelines for optimizing HMA mixture resistance to aging
* Product 4: Guidelines for best maintenance treatments to reduce aging of binders.

CHAPTER 3. OXIDATION KINETICS AND HARDENING PARAMETERS FOR 24 BINDERS COMMONLY USED BY TXDOT

[Pages 47 through 61 reprinted, in large part and with permission, from Jin, X., R. Han, Y. Cui, and C.J. Glover. (2011) Fast-Rate-Constant-Rate Oxidation Kinetics Model for Asphalt Binders. *Industrial & Engineering Chemistry Research*, Vol. 50 (23), pp. 13373–13379. Copyright 2011 American Chemical Society.]

ABSTRACT

This chapter summarizes work conducted on the task to enlarge the database of asphalt oxidation and hardening kinetics parameters. The database covers 24 asphalts, nine of which are currently used in Texas pavements. Information in the database includes parameters for both fast-rate and constant-rate kinetics and both low shear rate limiting viscosity and DSR function hardening susceptibilities. With the input from this database, the pavement oxidation model that is being developed in TxDOT Project 0-6009 will be able to predict asphalt oxidation and hardening in pavements as a function of time, depth, and environmental conditions.

At controlled temperature and pressure, initial asphalt oxidization occurs at a fast but decreasing rate as it transitions to a slower constant-rate period. The importance of fast-rate kinetics has been proved by both laboratory and field data. Therefore, both fast-rate and constant-rate kinetics are obtained in this study.

So far, all 24 binders have been aged in the laboratory at three to five elevated temperatures and atmospheric air pressure. Kinetics parameters and hardening susceptibility data have been obtained and presented in this report. An isokinetic temperature of 86.2°C was observed at which all of the measured asphalts oxidize at a rate of 0.0266 CA/day. This universal rate may be useful in developing a fast aging test because it readily provides a data point at a given temperature before conducting an aging test.

INTRODUCTION

Asphalt Materials

The significant impact of binder oxidation on pavement performance is well recognized and many research projects have been conducted to address important issues. Changes to asphalt composition and rheological properties with oxidative aging are among the most important topics. Modern asphalt binder, as a bottom product from the crude oil refinery industry, consists of millions of chemical species. Some components react with oxygen, while others (e.g., saturates) show almost no reactivity. In practice, instead of examining individual chemical species, researchers study asphalt material in terms of functional groups. From functional group analysis, Petersen (2009) summarized that the naturally present asphalt components are aromatics, carboxylic acids, 2-quinolone types, sulfide, pyrrolic types, and phenolic types. He also summarized that the major products of oxidation are ketones, anhydride, carboxylic acid,

and sulfoxides. Among those products, the most important oxidative products are the carbonyl functional groups, which is the major contributor to binder hardening.

Asphalt Characterization

The formation of carbonyl functional groups (C=O) can be measured using Fourier transform infrared spectroscopy (FT-IR) and was defined quantitatively as the integral area of carbonyl region from 1,650 to 1,820 cm^{-1} of FTIR spectrum. This area is named carbonyl area and measured in arbitrary units.

Several researchers have studied binder chemical-physical property relationships (Martin et al., 1990; Lau et al., 1992; Domke et al., 1999). By aging binders at different conditions, they found that log (low shear rate limiting viscosity) increases linearly with carbonyl area. They termed the slope of this relationship the viscosity hardening susceptibility. Experimental data show that viscosity HS is binder source dependent and oxygen pressure dependent, but not temperature dependent.

In addition to the log viscosity versus CA correlation, the logarithm of dynamic shear rheometer (DSR) function, log [G′/(η′/G′)] relates linearly to log (binder ductility) for ductility values less than 10 cm, and it increases linearly with carbonyl formation (Glover et al., 2005). This DSR function is measured at 44.7°C, 10 rad/s, and time-temperature shifted to 15°C, 0.005 rad/s. This test condition corresponds to a mid region of the master curves and thus reflects the importance of both the elastic modulus and viscous flow on stress building in viscoelastic materials under deformation.

Asphalt Aging Kinetics – Constant-Rate Period

Binders typically oxidize in two stages, a fast-rate period and a constant-rate period. Most previous work (Liu et al., 1996; Domke et al., 1999; Glover et al., 2005) focused on constant-rate kinetics of binder oxidation because the duration of the fast-rate period was assumed to be short and with a smaller impact long-term performance, especially in the laboratory under elevated temperature and oxygen pressure. The carbonyl formation rate during the constant-rate period is:

$$r = A \cdot P^{\alpha} \cdot e^{(-E_a / RT)} \tag{3-1}$$

where A is the frequency factor, P is oxygen pressure, α is the reaction order with respect to oxygen pressure, E_a is the activation energy, R is the gas constant, and T is the absolute temperature (K). The rate of carbonyl formation, or equivalently, the rate of oxidation, is dependent on oxygen pressure, temperature, and activation energy. Binders from different sources have different activation energies and reaction order and thus different aging rates at the same temperature.

Asphalt Aging Kinetics – Fast-Rate Period

Early fast-rate oxidation of binder has been long observed in laboratory aging experiments. Van Oort (1956) studied the oxygen absorption and viscosity change with time of

several binders aging at room temperature and atmospheric pressure. Both oxygen absorption and viscosity changes showed a fast increase at early times, and then the rates of change decreased to slower, constant rates at later times.

Herrington (1998) aged several types of binders at constant temperatures (50, 60, and 70°C) and 300 psi (about 20 atm) air pressure. Viscosities at 60°C were measured at different aging times. Herrington proposed a two-reaction model in logarithmic viscosity:

$$P = M(1 - e^{-k_2 t}) + kt \tag{3-2}$$

where P is the change of logarithmic viscosity, k and k_2 are reaction constants for the zero order reaction and first order reaction, respectively, M is the maximum or long-term change in log viscosity due to the first reaction.

Kinetics parameters k and k_2 were obtained for two types of binders, S180 and I180. The fact that the temperature dependence of these two parameters obeys the Arrhenius equation very well further confirmed the applicability of this model. Because the change of logarithmic viscosity shows a linear relationship with carbonyl area growth, it seems the same model should also fit carbonyl area data.

Some studies on binder aging characterize the fast-rate period with an initial jump, which is the intercept of constant-rate reaction line of carbonyl area formation (Liu et al., 1996; Domke et al., 1999; Glover et al., 2005). The difference between the initial jump (the constant-rate period zero-time intercept) and the initial (unaged) carbonyl area is thus the limiting formation of carbonyl area due to the first order reaction in the two-reaction model. Liu et al. (1996), based on a study of 15 asphalts, concluded that while the initial jump is not a function of temperature, it is a function of oxygen pressure.

Objectives

The objectives of this study were 1) to add to the current database on asphalt binder oxidation kinetics, including the fast-rate oxidation period and 2) to investigate possible reaction models for both the fast-rate and constant-rate periods. Of particular interest are possible correlations between the two periods for the asphalts, either separately or collectively.

MATERIALS AND METHODOLOGY

Materials

Asphalt binders widely in use in Texas pavements were selected for the oxidation kinetics study, including a number of base binders and their polymer-modified derivatives. The purpose of selecting such a great number of binders is to build a kinetics database for use with mixture performance evaluations that are related to binder oxidation. Table 6 shows information on the selected binders.

Table 6. Binders Selected for Oxidation Kinetics Study and Rheology Characterization.

Manufacturers	Binder Types	Corresponding Field Section
ALON	PG 64-22	NA
	PG 70-22	LBB (US 84) (2009-6)
	PG 76-22	NA
LION	PG 64-22	SH24
	PG 70-22	TYL (US259) (2007-2)
	PG 76-22	ATL (US259) (2005)
Valero-O	PG 64-22	NA
	PG 70-22	NA
	PG 76-22	NA
Valero-C	PG 64-22	NA
	PG 70-22	LRD04 (IH35 #5) (2007 Fall)
	PG 76-22	LRD04 (IH35 #3) (2007 Fall)
	PG 76-22*	LRD (FM649) (2006-3)
	PG 76-22**	LRD (SH44)
Valero-H	PG 64-22	NA
	PG 70-22	NA
	PG 76-22	NA
SEM	PG 64-22	NA
	PG 70-22	WFS (SH59) (2007-7)
	PG 70-28*	LBB (US82) (2008-7)
	PG 70-28	CHS (US83) (2008-6)
	PG 76-22	NA
MARTIN	PG 64-22	YKM (SH36) (2006-7)
	PG 70-22	NA

Aging Procedure

Asphalt binders are prepared as 1mm films in asphalt trays, and then aged in pressure oxidation vessels (POV) at three to five elevated temperatures (140, 158, 176, 192, 208°F; 60, 70, 80, 89, 98°C) and atmospheric air pressure. As binders age, two to three replicate samples are collected at each time point according to the schedule in Table 7.

Table 7. Binder Oxidation Sampling Schedule.

Aging Temperature (°F)	Aging Time (Days)
140	2, 5, 10, 15, 20, 30, 45, 60, 75, 90
158 and 176	1, 3, 5, 7, 10, 20, 30, 40, 50, 60
192 and 208	1, 2, 4, 6, 10, 15, 20, 25, 30

Materials Characterization

Two analytical techniques were used to characterize the unaged and aged binders. Infrared spectroscopy was used to measure the carbonyl area as discussed in the literature review and a Carri-Med CSL 500 controlled stress rheometer was used to measure both the low shear rate limiting viscosity and the DSR function. The low shear rate limiting viscosity is obtained from a frequency sweep at 60°C from 0.1 rad/s to 100 rad/s. The DSR function is measured at 44.7°C and 10 rad/s then time-temperature shifted to 15°C, 0.005 rad/s (Ruan et al., 2003).

RESULTS AND DISCUSSION

Task Progress

To date, all 24 binders have been aged and characterized. Results obtained include fast-rate and constant-rate kinetics parameters, viscosity hardening susceptibility, and DSR function hardening susceptibility. Fast-rate data were collected for 15 binders. For the remaining 9 binders, fast-rate kinetics can be deduced from constant-rate kinetics based on empirical correlations, as discussed later.

Analysis of Carbonyl Area Data

Carbonyl area, low shear rate limiting viscosity and DSR function were measured. Figure 16 shows the CA growth with time at five aging temperatures for a representative binder, ALON PG64-22.

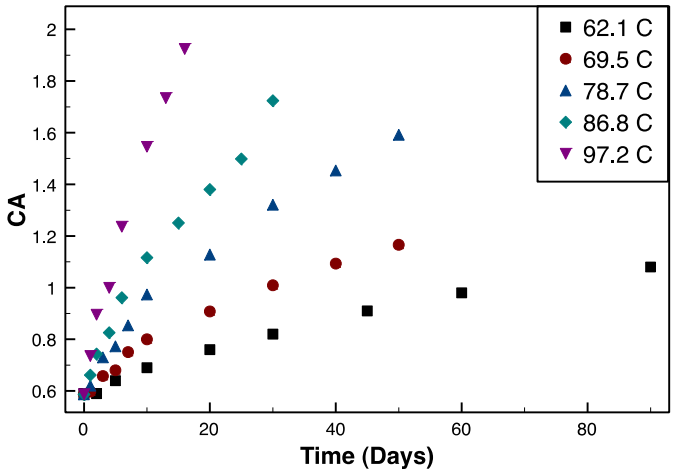


Figure 16. CA Growth of ALON PG64-22 at Five Temperatures.

The carbonyl area formation with time at each temperature is modeled according to the following equations:

$$CA = CA_{\text{tank}} + M(1 - \exp(-k_f t)) + k_c t \tag{3-3}$$

$$k_f = A_f \exp(-E_{af} / RT) \tag{3-4}$$

$$k_c = A_c \exp(-E_{ac} / RT) \tag{3-5}$$

where $M = (CA_0 - CA_{\text{tank}})$, CA_{tank} is the carbonyl area of the unaged tank asphalt, CA_0 is the intercept of the constant-rate line, k_f and k_c are two reaction constants that are temperature dependent according to the Arrhenius Eqs. 3 and 4.

Note that M is not temperature dependent but is asphalt source dependent and oxygen partial pressure dependent (Liu et al., 1996; Domke et al., 2000). Domke et al. (2000) found that M values (at the same oxygen partial pressure) for different asphalts can be related to its compositional parameter, heptane asphaltenes, and pentane asphaltenes ratio (C7/C5), with M values decreasing with increasing C7/C5 ratio. This suggests a method for obtaining M value from compositional analysis without time-consuming aging experiments.

The three terms in Eq. 2 incorporate the three elements important to the aging process. The first term is the initial carbonyl area for the unaged tank asphalt, the aging starting point. The second term characterizes the fast-rate aging process that follows a first-order reaction that terminates on the depletion of reactants. Three model parameters M (or equivalently $CA_0 - CA_{\text{tank}}$), A_f, and E_{af} are associated with this first-order reaction. These parameters also determine the transition from fast-rate period to constant-rate period, which is theoretically infinite. However, practically, the first-order reaction might be considered as terminated when its rate is within a certain percent of the rate of constant-rate reaction. The third term characterizes the on-going constant-rate reaction, with two model parameters A_c and E_{ac}. Although the first-order and constant-rate reactions are not tied to specific or identified reaction mechanisms but rather are empirical descriptors of the overall reaction kinetics for which the many reactants participating in these reactions are unknown, the model fits the data quite well, as shown later.

In this model, six model parameters were identified: CA_{tank}, M, A_f, E_{af}, A_c, and E_{ac}. While CA_{tank} can be measured directly on tank asphalt, the other five are to be determined from analysis of kinetics data.

Using linear regression on the constant-rate data, k_c values were obtained as the slope of the constant-rate line at each aging temperature. The temperature dependency of k_c is shown in Figure 17, indicating a strong Arrhenius correlation. The activation energy of ALON PG64-22 is 83.2 KJ/mol, and the frequency factor is 3.68×10^{10} CA/day.

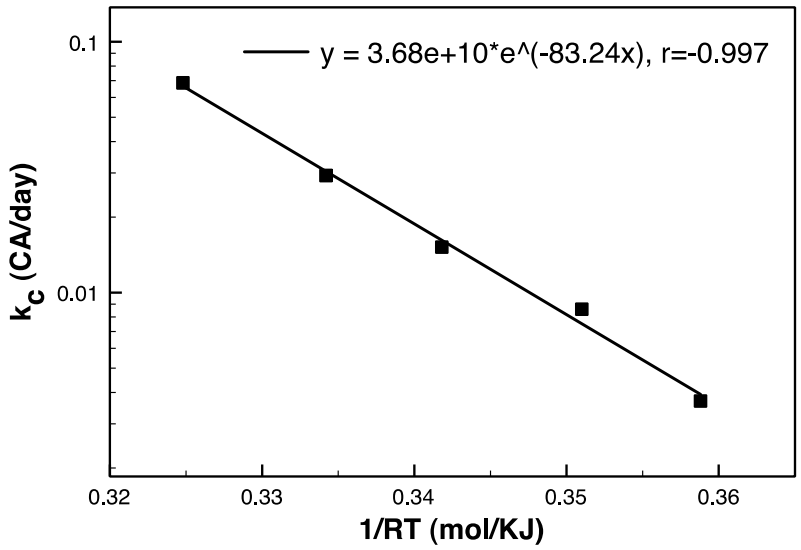


Figure 17. Temperature Dependency of k_c Values for ALON PG64-22.

Next, the constant-rate reaction kinetics parameters (activation energy and frequency factor) obtained from constant-rate data and the average value of M ($CA_0 - CA_{tank}$, where CA_0 is the intercept of each constant-rate line) at five temperatures were used as initial values for optimization of all five model parameters. The objective of the optimization was to minimize the mean square error of model estimates of CA at all aging temperatures and times. The optimization is done using the *optim* function implemented in statistical software R (R Development Core Team, 2011).

This global optimization approach of the five model parameters worked well for 15 binders shown in Table 8. For each binder, this globally-optimal E_{ac} is within 0.12 KJ/mol of the locally-optimal E_{ac}, determined from the constant-rate data only. These globally optimized parameters are listed in Table 8.

Table 8. Optimized Model Parameters for 15 Asphalts.

	CA_0	A_f (1/Day)	E_{af} (KJ/mol)	A_c (CA/Day)	E_{ac} (KJ/mol)
Alon PG 64-22	0.761	9.13×10^{7}	58.4	4.12×10^{10}	83.4
Alon PG 70-22	0.690	3.50×10^{8}	60.8	6.46×10^{9}	78.3
Alon PG 76-22	0.750	2.21×10^{7}	52.6	4.71×10^{9}	77.0
Lion PG 64-22	0.874	2.71×10^{9}	68.5	4.05×10^{11}	90.6
Martin PG 64-22	0.723	7.37×10^{6}	51.9	8.81×10^{8}	72.5
Martin PG 70-22	0.690	2.64×10^{8}	60.9	1.98×10^{11}	88.0
SEM PG 64-22	0.768	3.09×10^{6}	47.6	2.33×10^{8}	68.8
SEM PG 70-22	0.700	3.83×10^{7}	54.4	1.09×10^{10}	79.9
SEM PG 70-28	0.594	3.34×10^{7}	49.1	1.03×10^{9}	72.5
SEM PG 76-22	0.671	1.80×10^{6}	45.2	8.07×10^{7}	64.9
Valero-C PG 64-22	0.548	8.04×10^{9}	67.2	1.56×10^{11}	87.4
Valero-C PG 70-22	0.826	3.27×10^{10}	75.4	3.26×10^{13}	103.8
Valero-C PG 76-22	0.889	2.57×10^{6}	47.2	1.65×10^{8}	68.1
Valero-H PG 76-22	0.711	5.65×10^{9}	68.6	1.10×10^{11}	86.9
Valero-O PG 64-22	0.727	5.78×10^{7}	57.3	2.20×10^{10}	81.3

Using these five optimal model parameters for each asphalt, the proposed model provides calculations of carbonyl formation over time at each temperature that agree well with experimental measurements. This agreement validates the applicability of the empirical model for use in sophisticated pavement oxidation models to predict binder oxidation in pavements. The comparison for Alon PG 64-22 (dashed lines) is shown in Figure 18.

.

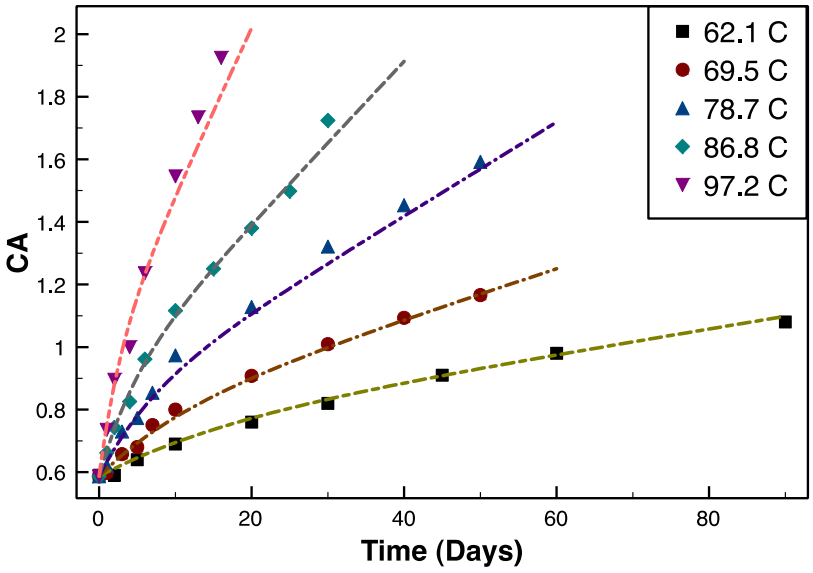


Figure 18. Comparison of Model Prediction (Dashed Lines) of CA to Experimental Data (Symbols) for ALON PG 64-22.

Summary of Oxidation Kinetics Data

Table 9 summarizes the kinetics parameters for all 24 binders studied. For nine binders, the fast-rate kinetics parameters shown in italics were obtained from constant-rate kinetics based on correlations shown later.

Table 9. Summary of Oxidation Kinetics Parameters.

	Constant-Rate Kinetics		Fast-Rate Kinetics	
Binder	**A_c (CA/day)**	**E_{ac} (KJ/mol)**	**A_f (1/day)**	**E_{af} (KJ/mol)**
ALON PG 64-22	4.12E+10	83.4	9.13E+07	58.4
ALON PG 70-22	6.46E+09	78.3	3.50E+08	60.8
ALON PG 76-22	4.71E+09	77.0	2.21E+07	52.6
LION PG 64-22	4.05E+11	90.6	2.71E+09	68.5
LION PG 70-22	4.77E+08	70.1	*6.68E+06*	*49.2*
LION PG 76-22	6.09E+10	84.7	*4.15E+08*	*61.6*
Valero-O PG 64-22	2.20E+10	81.3	5.78E+07	57.3
Valero-O PG 70-22	2.53E+09	75.2	*2.83E+07*	*53.5*
Valero-O PG 76-22	4.73E+07	64.0	*1.19E+06*	*44.0*
Valero-C PG 64-22	1.56E+11	87.4	8.04E+09	67.2
Valero-C PG 70-22	3.26E+13	103.8	3.27E+10	75.4
Valero-C PG 76-22	1.65E+08	68.1	2.57E+06	47.2
Valero-C PG 76-22*	2.87E+10	82.9	*2.50E+08*	*60.1*
Valero-C PG 76-22**	5.25E+12	97.8	*1.69E+10*	*72.7*
Valero-H PG 64-22	7.91E+07	65.5	*1.82E+06*	*45.3*
Valero-H PG 70-22	3.38E+07	62.7	*8.24E+05*	*42.9*
Valero-H PG 76-22	1.10E+11	86.9	5.65E+09	68.6
SEM PG 64-22	2.33E+08	68.8	3.09E+06	47.6
SEM PG 70-22	1.09E+10	79.9	3.83E+07	54.4
SEM PG 70-28*	8.61E+09	79.0	*8.28E+07*	*56.8*
SEM PG 70-28	1.03E+09	72.5	3.34E+07	49.1
SEM PG 76-22	8.07E+07	64.9	1.80E+06	45.2
MARTIN PG 64-22	8.81E+08	72.5	7.37E+06	51.9
MARTIN PG 70-22	1.98E+11	88.0	2.64E+08	60.9

Correlation between Fast-Rate and Constant-Rate Kinetics

Remarkably, the two activation energies, E_{af} and E_{ac} for all 15 asphalts plotted against each other in Figure 19, reveal a good linearity:

$$E_{af} = 0.85E_{ac} - 10.4 \tag{3-6}$$

The maximum error between E_{af} values calculated from E_{ac} values and the linear equation and E_{af} values obtained from optimization was 5.4 KJ/mol for the 15 binders, well within the ± 10

(KJ/mol) mentioned in the previous section. Therefore, it is suggested that this correlation can be used to estimate E_{af} from E_{ac}. Although it is an empirical correlation with no apparent fundamental basis, it is of significant practical value.

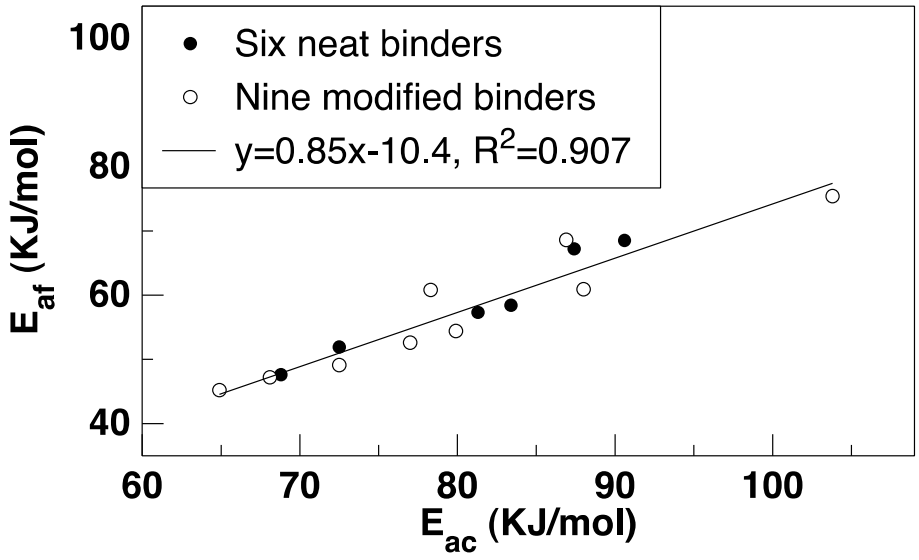


Figure 19. Empirical Linear Correlation between the Fast-Rate and Constant-Rate Activation Energies.

Correlation between Activation Energy and Frequency Factor

Domke et al. (2000) reported an isokinetic temperature of 378.2 K for constant-rate kinetics. At this temperature and 0.2 atmospheric oxygen partial pressure, all binders of different types showed the same aging rate during the constant-rate period. A similar temperature was obtained in this work. However, the activation energies in this work covered a broader range from 64.9 to 103.8 KJ/mol, while the range from Domke et al. (2000) was 82 to 90 KJ/mol. Furthermore, binders studied herein include SBS-modified binders and thus extend the concept of isokinetic temperature to polymer-modified binders.

Figure 20 shows the constant-rate activation energies and frequency factors on a semi-log scale for all 24 binders studied in this work, plus data of binders aged at 0.2 atmospheric oxygen partial pressure from Liu et al. (1996) and Domke et al. (2000). The correlation equation is:

$$A_c = 0.0266 \exp(0.3347 E_{ac}) \tag{3-7}$$

The slope of the line is $1/RT_{iso}$ (mol/KJ) and the intercept ($E_{ac} = 0$) is the aging rate at T_{iso}. The isokinetic temperature T_{iso} is 359.4 K (86.2°C) with an isokinetic aging rate of 0.0266 CA/day. This rate at the isokinetic temperature is useful in two respects. First, it provides a universal aging rate for asphalts that is independent of its source and type, thus reducing the number of different temperatures by one at which experiments need to be conducted in order to make reasonable estimates of constant-rate kinetics parameters. Second, it provides the basis for ranking the pavement oxidation rates of asphalts by aging at only one elevated temperature,

because the ranking at temperatures higher than T_{iso} will invert at temperatures lower than T_{iso}. However, it should be emphasized that oxidation rates alone cannot assess the superiority of binders, because different binders may show different hardening susceptibilities and thus different hardening rates.

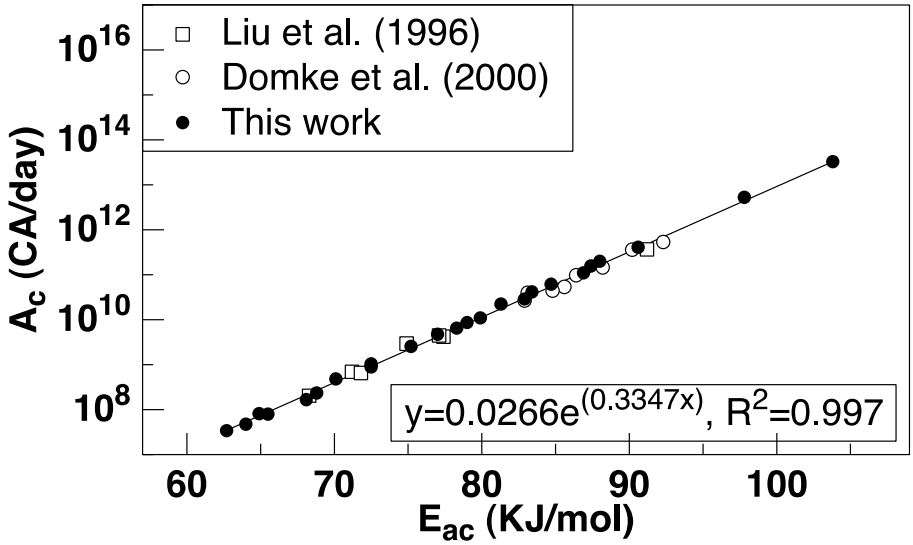


Figure 20. Isokinetic Temperature 359.4 K of Constant-Rate Reaction Obtained from Various Data Sources.

Interestingly, the fast-rate activation energies and logarithmic frequency factors for the 15 binders in Table 8 also show a linear correlation (Figure 21):

$$A_f = 0.520 \exp(0.3328 E_{af}) \tag{3-8}$$

Note, however, that the concept of an isokinetic temperature does not apply for a first order reaction.

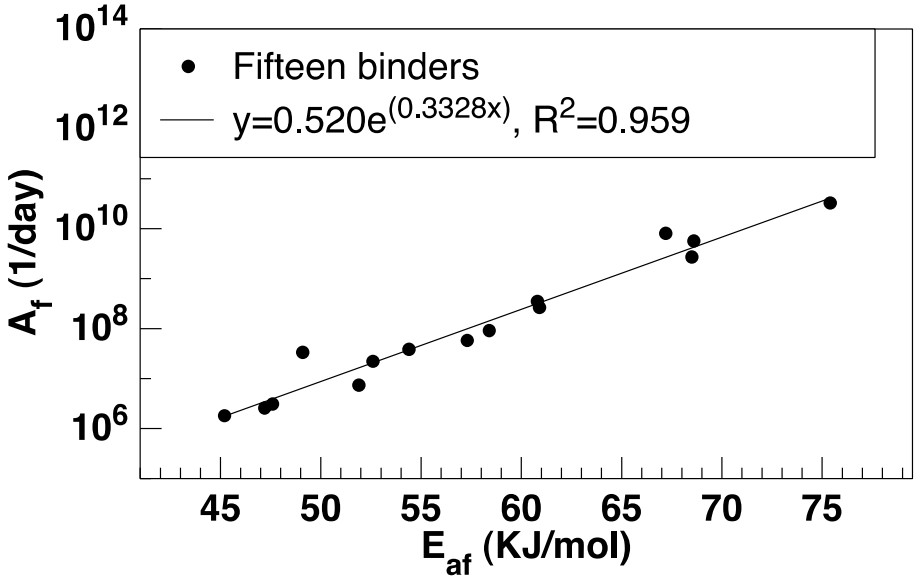


Figure 21. The Correlation between Fast-Rate Kinetics Parameters.

Analysis of Rheological Data

Hardening susceptibilities (HS) of low shear rate limiting viscosity and DSR function for ALON PG64-22 are shown in Figure 22 and Figure 23 in semi-log scale.

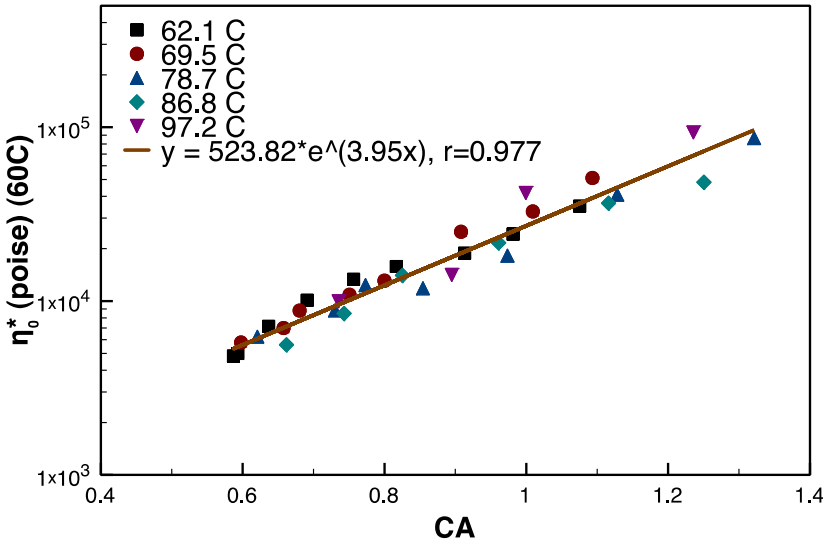


Figure 22. HS of Limiting Viscosity of ALON PG64-22.

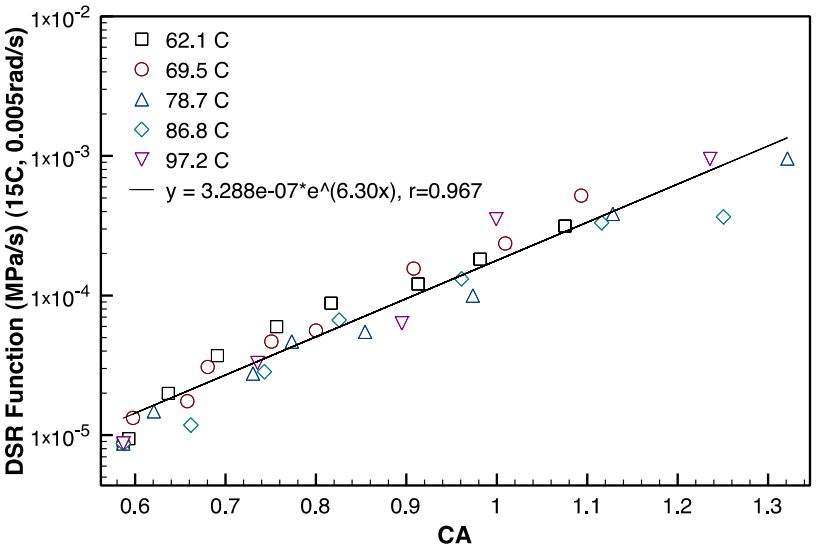


Figure 23. HS of DSR Function of ALON PG64-22.

Viscosity and DSR Function Hardening Susceptibility

HS and DSR function data are tabulated in Table 10. Generally, polymer modified binder is expected to have lower viscosity hardening susceptibility than its base binder (Glover et al., 2005). However, in this study, some binders (ALON, VAL-H, and LION) do not follow such a trend. This is probably because those binders are obtained from the field or manufacturer, and it is not guaranteed that the base binder of the polymer-modified binder is the same as the unmodified binder. For most of the binders, a higher viscosity HS corresponds to a higher DSR Function HS, with the exception of the ALON binders.

Table 10. Viscosity and DSR Function Hardening Susceptibility.

Binder	Viscosity HS (1/CA)	DSR Function HS (1/CA)
ALON PG 64-22	3.95	6.30
ALON PG 70-22	3.04	5.95
ALON PG 76-22	5.03	5.45
LION PG 64-22	2.33	4.23
LION PG 70-22	2.46	3.48
LION PG 76-22	3.10	3.98
Valero-O PG 64-22	5.22	6.54
Valero-O PG 70-22	5.40	6.14
Valero-O PG 76-22	5.68	5.36
Valero-C PG 64-22	3.34	5.12
Valero-C PG 70-22	3.97	3.68
Valero-C PG 76-22	4.65	4.80
Valero-C PG 76-22*	3.56	3.74
Valero-C PG 76-22**	4.34	4.41
Valero-H PG 64-22	3.72	3.84
Valero-H PG 70-22	4.10	4.15
Valero-H PG 76-22	3.15	3.48
SEM PG 64-22	4.86	6.52
SEM PG 70-22	4.51	6.11
SEM PG 70-28*	3.22	4.38
SEM PG 70-28	4.53	5.50
SEM PG 76-22	3.73	5.58
MARTIN PG 64-22	5.12	5.52
MARTIN PG 70-22	5.02	4.02

SUMMARY

Twenty-four binders have been aged in POV apparatuses from which kinetics data were obtained. The proposed "fast-rate, constant-rate" oxidation kinetics model described the experimental kinetics data quite well for 15 asphalt binders, both neat and modified binders. Model parameters were obtained from global optimization. Sensitivity analysis showed that the M value is a more sensitive parameter than the fast-rate period rate constant.

Empirical correlations were found between model parameters. These correlations allow estimating fast-rate kinetics parameters from constant-rate kinetics parameters, reducing the number of model parameters from six to three: CA_{tank} (the carbonyl area of tank asphalt), M, and E_{ac} (the constant-rate activation energy). This reduction of parameters not only simplifies the kinetics model but also saves the time and effort required to obtain the fast-rate oxidation kinetics data.

Rheological data confirmed previous reports that hardening susceptibilities of each binder were independent of aging temperature and aging period. With oxidative reaction kinetics parameters and hardening susceptibility, the proposed model was capable of predicting binder oxidation and hardening as a function of time and temperature. Such a capability is fundamentally important to pavement oxidation models, to improving pavement design, and to predicting pavement performance.

Future work is suggested to further extend the application of the kinetics model. The oxygen partial pressure dependence of the fast-rate kinetics should be explored. The pressure dependence of M suggests that the frequency factor of the fast-rate reaction probably is also a function of oxygen partial pressure. It will be also very interesting to develop a more direct method of measuring M than calculating from the intercept of constant-rate data, as suggested by Domke et al. (1999).

CHAPTER 4. OXYGEN DIFFUSIVITY IN ASPHALTS AND MASTICS

[Pages 63 through 79 reprinted from Han, R., Jin, X., and Glover, C.J. (2013) Oxygen Diffusivity in Asphalts and Mastics. *Petroleum Sci. and Technol*., Volume 31, Issue 15, pp. 1563–1573. Copyright 2013. Reproduced by permission of Taylor & Francis Group, LLC. (http://www.tandfonline.com).]

ABSTRACT

Oxidation of binders in pavements is recognized as an important contributor to pavement deterioration. Recent research efforts have developed a transport model for the purpose of estimating binder oxidation in pavements as a function of time and depth below the pavement surface, with predictions of pavement durability as the ultimate objective. The model relies on binder oxidation kinetics and oxygen diffusivity values in asphalt binders and mastics. Previous research has provided oxidation kinetics parameters for a number of binders, but accurate diffusivity values are rare. This topical report summarizes work conducted on the task to determine oxygen diffusivity in asphalt binders and mastics.

Determination of oxygen diffusivity in binders was made based on laboratory oxidation experiments in binder films of known reaction kinetics by comparing the oxidation rates at the binder surface and at a solid-binder interface at the film depth.

For neat asphalts, oxygen diffusivities ($\mathcal{D}_{O_2}$) ranged from 10^{-10} to 10^{-11} m^2/s, with $\log(\mathcal{D}_{O_2}/T)$ varying linearly with $\log(\eta_o^*)$ for both base asphalts and polymer-modified binders (PMB). For asphalt mastics, oxygen diffusivity was observed to decrease as filler volume fraction increased. Quantitatively, this effect follows a theoretical estimate of the effect of a dilute suspension of spherical inclusions on diffusivity.

INTRODUCTION

Asphalt oxidation has been studied for many years with respect to reaction kinetics and the resulting chemical and physical changes. An important part of the oxidation process is the formation of carbonyl (– C=O) groups that increase the associations between polar species (Petersen, 1986; Liu et al., 1996). The increased associations that arise because of the carbonyl formation produce a dramatic stiffening of the asphalt rheology, characterized most notably by an increase in its low shear rate viscosity (Lau et al., 1992; Lin et al., 1995). This low shear rate limiting viscosity relates exponentially to these carbonyl increases.

Given an adequate supply of oxygen, asphalt binders in pavements will harden and become brittle (Al-Azri et al., 2006). Over time, as pavement ductility decreases, pavement cracking increases (*Transportation Research Record*, 1958; Doyle, 1958; Halstead, 1963; Kandhal, 1977; Kandhal and Koehler, 1984; Kandhal and Wenger, 1975; Woo et al., 2007). A key question is how quickly oxygen can be supplied to the binder to feed the reaction. The answer to this question relies in part on the permeability of the pavement to air through connected air void, and in part on oxygen diffusivity in binders.

The literature is rather limited on oxygen diffusion in asphalt materials and on values of oxygen diffusivity and its relation to other asphalt properties. Part of the difficulty with measuring diffusivity is separating transport behavior from reaction. Lunsford made an early and important proof of principle attempt to measure oxygen diffusivity and its dependence on asphalt viscosity using fundamental transport and reaction theory on 1 mm asphalt films (Lunsford, 1994). Although conceptually sound, the 1 mm asphalt films that he used were too thin to establish the strong diffusion dependence needed for accurate diffusivity measurements, the result of the films being designed for reaction kinetics measurements instead of diffusivity. Nevertheless, the work stands as an important demonstration of the method for making these measurements.

A further hindrance to oxygen diffusion in pavements is the presence of aggregates that are impervious to diffusion. Such aggregates require that oxygen molecules take a longer, more tortuous, path through the binder, thus reducing the effective oxygen diffusivity. Measurements of this effect in asphalt mastics have not been reported.

The primary objective of this work was to measure oxygen diffusivity in both unmodified and modified binders using laboratory oxidation of binder films of known reaction kinetics and to relate these diffusivity measurements to temperature and binder rheology. A second objective was to quantify the effect of aggregate fines on oxygen diffusivity in mastics.

MATERIALS AND METHODOLOGY

Overview of the Experimental Design

Asphalt or mastic samples were deposited into a pre-molded aluminum tray to form a thin asphalt/mastic film (Figure 24). Two surfaces were created: the exposed surface (ES) with direct interfacial contact between the binder material and atmospheric oxygen, and the substrate interface (SI) between the asphalt film and the aluminum support tray that is impermeable to oxygen. This configuration allows oxygen from the atmosphere above the ES to be absorbed by the film and then to diffuse and react throughout it, while blocking oxygen absorption at the SI. Reaction throughout the film results in an oxygen concentration gradient that is a function of time and depth inside the film and thus a difference in oxidation rates at the ES and SI. By comparing oxidation rates at the ES and the SI using an oxygen diffusion and reaction model, oxygen diffusivity throughout the film can be estimated first by a method that assumes oxygen diffusivity is constant during the oxidation period and uniform throughout the film, at an appropriate average value.

This approximate method was then verified with detailed calculations of the diffusion and reaction transport model. Using this method, oxygen diffusivities for a number of asphalts and polymer-modified asphalts of different rheology were determined at several temperatures. In addition, oxygen diffusivities for asphalt mastics with different volume fractions of fines were measured at several temperatures to study the effect of impermeable aggregate fines on oxygen diffusivity.

Materials

Eight asphalt binders (five base binders and three polymer-modified binders) were used in this study to measure oxygen diffusivity in neat binders. Three asphalt mastics with three different volume fractions of aggregates fines (0, 10, and 25 percent) were prepared to evaluate the effect of fines on oxygen diffusivity. Due to experimental design limitations on the film thickness, aggregate fines (sandstone) sized between sieve #100 (150 μm) and sieve #200 (75 μm) were used to prepare the mastics. Table 11 summarizes the binder materials used in this study, along with their oxidation and hardening properties.

All asphalts used in this study were pre-oxidized to move them past the fast-rate reaction period into the constant-rate reaction region. Table 11 provides the constant-rate oxidation kinetics parameters (AP^{α} and E) for these binders, which are required for the oxygen diffusivity calculations. The rate of oxidation in the constant-rate reaction region (indicated by carbonyl content production) can generally be described using an Arrhenius expression for temperature variation and pressure dependence, as given in Eq. 4-1 (Liu et al., 1996).

$$r_{CA} = \frac{\partial CA}{\partial t} = AP^{\alpha} e^{-E/RT} \tag{4-1}$$

where, AP^{α} is the frequency (pre-exponential) factor, P is the pressure, α is the reaction order with respect to oxygen pressure, E is the activation energy, R is the gas constant, and T is the absolute temperature.

Values of AP^{α}, and E vary with the asphalt binder, and were measured experimentally by oxidizing asphalts at different temperatures.

Table 11. List of Materials and Material Parameters.

Asphalt	Oxidation and Hardening Parameters				Mastics Prepared with
	$\ln(AP^{\alpha})$ ln (CA/day)	E (kJ/Mol)	HS (1/CA)	m ln (poise)	
Alon 64-22	21.905	76.256	3.527	6.633	√
Alon 76-22	22.642	78.769	3.388	8.310	
SEM 64-22	21.611	75.228	4.935	5.551	√
SEM 70-22	22.051	76.468	4.028	7.047	√
Lion 64-22	23.013	79.002	3.739	5.535	
Lion 70-22	18.391	65.334	3.154	8.204	
Valero-H 64-22	18.769	67.649	4.427	6.248	
Martin 64-22	19.974	70.047	5.095	6.005	

Methodology

Asphalt/Mastic Film Preparation

Asphalt mastics were prepared by stirring asphalt with fines at 163°C, 1000 rpm for half an hour under a nitrogen blanket (to prevent oxidation). Thin asphalt or mastic films were fabricated by depositing the appropriate amount of asphalt or mastic in a pre-molded aluminum tray. The optimized film thicknesses of asphalt binder at each test temperature were 1.5 mm at 60°C, 2 mm at 75°C, and 2.5 mm at 90°C. The film thicknesses were designed to be thick enough to establish diffusion as a significant factor within the film, yet not be too thick as to give too long a test time.

Carbonyl Measurement

Oxidation of asphalt is characterized by the formation of carbon and oxygen double bonds, C=O. A Nicolet 6700 Fourier Transform Infrared Spectroscopy (FT-IR) spectrometer was used to analyze the carbonyl content. Growth in the area under the FTIR spectrum from 1650 to 1820 cm^{-1} in arbitrary units, the carbonyl area, is used to represent this oxidation.

Measurement of Oxidation Rates at the ES and SI

Asphalt/mastic films were oxidized in pressure oxidation vessels at three different temperatures and at 1 atm air pressure. Samples were retrieved at different time points. Small amounts of asphalt were scratched using a spatula from the top surface of the film and used to measure carbonyl content at ES. Then asphalt was gently removed from an aluminum tray, and the remaining asphalt residue at asphalt and aluminum support interface were collected to measure carbonyl content at SI. At each temperature, a constant-rate model was fit to the carbonyl content measurements to obtain the oxidation rate at both the ES and SI.

Limiting Zero Shear Complex Viscosity (η_o) Measurement*

The rheological properties of the asphalts were measured on a CarriMed 500 controlled stress dynamic shear rheometer, with 2.5 cm diameter parallel-plate geometry and 500 micrometer gap. Viscosity master curves were constructed with viscosity measurement at the 60°C and 80°C in frequency range from 0.1 rad/s to 100 rad/s. The specific rheological property used in this study that relates well to oxygen diffusivity is the low-shear rate limiting complex viscosity η_o*. This property is read from a viscosity master curve at low frequency end where viscosity approaches a plateau. This property is independent of frequency or shear rate for unmodified binders.

Estimation of Base Binder η_o for Polymer-Modified Binders*

The viscosity of each of the polymer-modified binders was determined as above, but an estimate of the hypothetical base binder viscosity in the PMB also was made. This determination was made from the measured viscosity of the PMB, coupled with hardening susceptibility relations for both the PMB and the base binder, as described below. This viscosity versus

carbonyl relationship for both the base asphalt and the PMB are well represented by Eq. 4- 2 (Martin et al., 1990; Lau et al., 1992),

$$\ln \eta_0^* = HS \cdot CA + m \tag{4-2}$$

where *HS* is termed the hardening susceptibility, the change in log-viscosity with respect to the change in carbonyl content, measured as FTIR carbonyl area, and *m* is the log-viscosity intercept. *HS* and *m* are asphalt dependent and are affected by polymer modification; their values for the studied asphalts (for both base binders and their corresponding polymer-modified binders) are summarized in Table 11.

Oxidation of the PMB increases the CA of the asphalt component of the PMB, but the polymer makes no contribution. Accordingly, η_o* for the PMB together with the *HS* relation for the PMB was used to calculate the corresponding CA for the PMB; then this CA was used to calculate η_o* for the base asphalt using its own specific *HS* relation.

Thin Film Model for Oxygen Diffusivity Calculation

Thin asphalt films are fabricated by depositing an appropriate amount of asphalt or mastic into a pre-molded aluminum tray to form a finite thickness as depicted in Figure 24. There are two surfaces in this thin film model: the exposed surface that is in direct contact with oxygen, and the substrate interface between the asphalt and aluminum tray support. The oxygen concentration in the asphalt at the ES is in equilibrium with the ambient atmosphere, 1 atm for these experiments. At the SI, due to the impermeable nature of aluminum, the oxygen concentration gradient is zero. Inside the film, asphalt oxidation (and thus oxygen consumption) results in asphalt hardening over time plus an oxygen concentration gradient that is a function a time and depth inside the film.

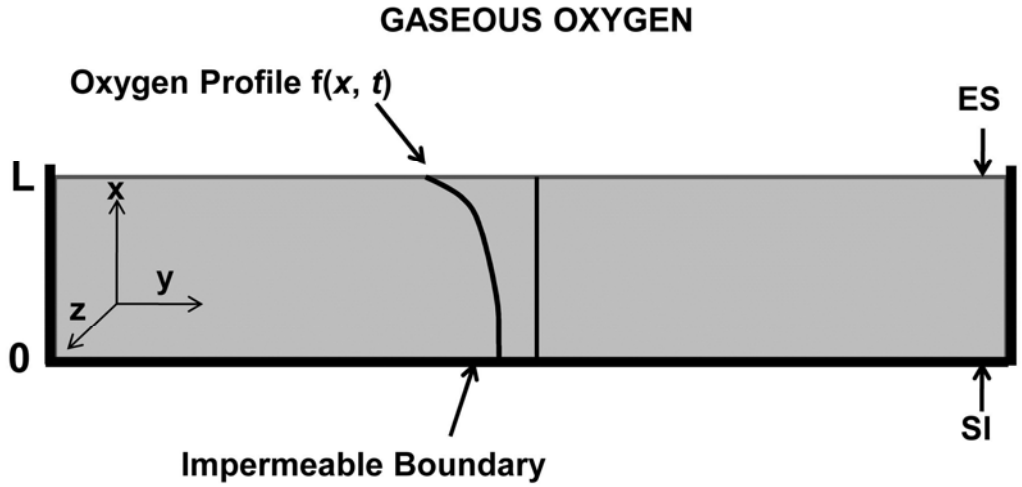


Figure 24. Schematic of Thin Film Model Configuration.

A mathematical model accounting for oxygen diffusion and reaction in a differential volume of the asphalt film is given by:

$$\left(\frac{\partial C_{O_2}}{\partial t}\right) = -\nabla \cdot N_{O_2} - r_{O_2} \tag{4-3}$$

where, C_{O_2} is the oxygen concentration and r_{O_2} is the rate of oxygen consumption.

The molar flux of oxygen, N_{O_2} , can be expressed by Fick's first law of diffusion:

$$N_{O_2} = -\mathcal{D}_{O_2} \nabla C_{O_2} \tag{4-4}$$

where, $\mathcal{D}_{O_2}$ is the oxygen diffusivity in the asphalt binder.

Oxygen transport in the asphalt film is assumed to occur in only one direction, based on the experiment configuration. Eq. 4-1 is further developed as:

$$\left(\frac{\partial C_{O_2}}{\partial t}\right) = \left(\frac{\partial \mathcal{D}_{O_2}}{\partial x}\right)\left(\frac{\partial C_{O_2}}{\partial x}\right) + \mathcal{D}_{O_2}\left(\frac{\partial^2 C_{O_2}}{\partial x}\right) - r_{O_2} \tag{4-5}$$

where, *x* is the depth into the film and diffusivity varies with depth due to different levels of oxidation (binder hardening) in the film.

Because the experiments are designed at low oxygen pressure, the ideal gas law converts oxygen gas phase partial pressure P_{O_2} to asphalt phase concentration C_{O_2} using *T* and the dimensionless Henry's Law constant *h*:

$$C_{O_2} = h\left(\frac{P_{O2}}{RT}\right) \tag{4-6}$$

For asphalt materials, a dimensionless value of 0.0076 at 30°C has been estimated based on literature report (Dickinson 1984). It is a function of temperature according to Eq. 4-7:

$$h = h_0\left[1 + 0.00215\left(T - T_r\right)\right] \tag{4-7}$$

where h_0 is the dimensionless Henry's law constant at reference temperature T_r, and the unit for the constant is in reciprocal of degree Celsius.

It has been found that the oxygen reaction rate is directly proportional to carbonyl growth rate for asphalts:

$$r_{O_2} = cr_{CA} \tag{4-8}$$

where, c is dependent of asphalt, ranging from 2.75×10^{-4} gmol O_2 / mL CA to 4.59×10^{-4} gmol O_2 / mL CA for c obtained for ten asphalts (Liu et al., 1998a). In this study, an average value of 3.71 is used for asphalts studied.

Combining Eqs. 4-4, 4-5, and 4-7, the governing equation for this diffusion and reaction process is given in terms of P, h, and CA kinetics as:

$$\left(\frac{\partial P}{\partial t}\right) = \left(\frac{\partial \mathcal{D}_{O_2}}{\partial x}\right)\left(\frac{\partial P}{\partial x}\right) + \mathcal{D}_{O_2}\left(\frac{\partial^2 P}{\partial x}\right) - \left(\frac{cRT}{h}\right) r_{CA} \tag{4-9}$$

In this equation, P throughout the film is the gas phase oxygen partial pressure that would be in equilibrium with the asphalt phase oxygen concentration at that point in the film. The equation is cast in terms of P rather than C_{O_2} because the reaction kinetics is cast as a function of P, avoiding measurements of C_{O_2}.

For the final form, the boundary conditions and the initial condition are:

$P_{ES} = P$ (gas)	at $x = 0$	[Exposed Surface]
$\frac{\partial P}{\partial x} = 0$	at $x = \mathrm{L}$	[Substrate Interface]
$P = 0$	at $t = 0$	[Initial Condition]

With oxygen diffusivity (or diffusivity as a function of the level of oxidative aging, CA) specified, the above model can be solved numerically to obtain the oxygen partial pressure in the film as a function of time, temperature and depth below the film surface. However, this model as stated is not sufficient to allow determining values for diffusivity and the model must be viewed differently.

In this work, the oxygen partial pressure at the substrate interface at a specified time was inferred from measured reaction rates at both the ES and SI and used as additional information. Applying Eq. 4-1 to both surfaces, oxidation rates at the exposed surface and the substrate interface relate to partial pressures according to:

$$r_{ES} = A P_{ES}^{\ \alpha} e^{-E/RT} \tag{4-10}$$

$$r_{SI} = A P_{SI}^{\ \alpha} e^{-E/RT} \tag{4-11}$$

For a given asphalt, A, E are constant and the film temperature is uniform, so combining Eq. 4-10 and 4-11 gives:

$$P_{SI} = P_{ES}\left(\frac{r_{SI}}{r_{ES}}\right)^{1/\alpha} \tag{4-12}$$

From Eq. 4-12, we can calculate a value for the oxygen pressure at the substrate interface by comparing measured oxidation rates at the exposed surface and the substrate interface. Reaction order α for a number of asphalts has been measured and varies from about 0.23 to 0.3 (Liu et al., 1996); an average value of 0.27 was used for these calculations.

The estimated value of the oxygen pressure at the SI is based on the average oxidation rate for the entire test period, while the exact time to achieve this particular oxygen pressure at the SI is unknown. However, a linear decrease of pressure at the SI (P_{SI}) over time is indicated by model simulation. With this observation, $P_{SI(i)}$ at given time t can be shown as:

$$P_{SI(i)} = P_{SI(0)} + \frac{\left(P_{SI(0)} - P_{SI(1)}\right)}{\left(t_0 - t_1\right)}\left(t_i - t_0\right) \tag{4-13}$$

Here, $P_{SI(0)}$ is P_{SI} at the start of the experiment, time (t_0); and $P_{SI(1)}$ is P_{SI} at the end of the experiment, at time (t_1).

The average oxidation rate at the SI for the entire testing period will be a function of $P_{SI(i)}$, according to:

$$r_{SI} = \frac{\int_{t_0}^{t_1} k{P_{SI(i)}}^{\alpha} dt}{\left(t_0 - t_1\right)} e^{-E/RT} \tag{4-14}$$

Substituting $P_{SI(i)}$, Eq. 4-13, into Eq. 4-14 and then inserting Eq. 4-14 into Eq. 4-12, and followed by several mathematical steps, we see that P_{SI} can be estimated based upon oxidation rate at both SI and ES for the entire testing period as follows:

$$P_{SI} = \left[\frac{\left({P_{SI(0)}}^{1+\alpha} - {P_{SI(1)}}^{1+\alpha}\right)}{\left(P_{SI(0)} - P_{SI(1)}\right)\left(1+\alpha\right)}\right]^{1/\alpha} \tag{4-15}$$

$P_{SI(0)}$ ranges from 0.15 to 0.2 atm and $P_{SI(1)}$ ranges from 0 to 0.1 atm in experiments. In their practical ranges, the value of P_{SI} obtained is always close to the mean value of $P_{SI(0)}$ and $P_{SI(1)}$, suggesting that the time to obtain this measured value of P_{SI} at SI is close to the mean time for the experiment.

Then with an estimated value of oxygen pressure at the SI at a given time and depth in the asphalt film and asphalt reaction kinetics parameters known, a trial-and-error numerical solution of the model was used to obtain optimal estimates of diffusivity by comparing oxygen pressure at the substrate interface (inferred from the measured oxidation rate) to these model calculations according to Eq. 4-9. To start with, an assumption of constant oxygen diffusivity during the relatively short testing period is made.

An oxygen concentration gradient in an asphalt film exists whereby oxygen transport is limited by diffusion, which will further induce gradients of asphalt oxidation rate, asphalt oxidation level, and asphalt rheology with time. Oxygen diffusivity, as a property that might be influenced by asphalt physical properties, should also be a function of time and depth in the film. Because of that, Eq. 4-9 states that oxygen diffusivity is a variable, changing with time and depth in the film as oxidation level changes. However, it is not clear how oxygen diffusivity changes with oxidation level. In this study, an assumption of constant oxygen diffusivity during the short testing period (independent of oxidation level and depths in the film) was made, and diffusivities for studied asphalts were calculated in this way. These calculated diffusivity values will then be used to correlate with asphalt binder rheology to establish the relationship between oxygen diffusivity with asphalt rheology. By comparing calculated carbonyl growth at both ES and SI (using Eq. 4-9 with established correlation) with measured value, the initial assumption of constant oxygen diffusivity during the short testing period was examined.

RESULTS AND DISCUSSION

Oxidation Rates at ES And SI of Asphalt Film

Carbonyl growth at both the ES and SI were measured as a function of oxidation time and temperatures, as shown in Figure 25. For a given oxidation temperature, the oxidation rate at the SI is less than the oxidation rate at the ES, verifying the existence of an oxygen gradient in the film, which is essential for diffusivity measurement. At each temperature, measurements of CA at both the ES and SI over an appropriate test period were used to obtain estimates of constant oxidation rates. Complete data on measured CA at ES and SI for eight studied asphalt binders were reported in the Appendix A.

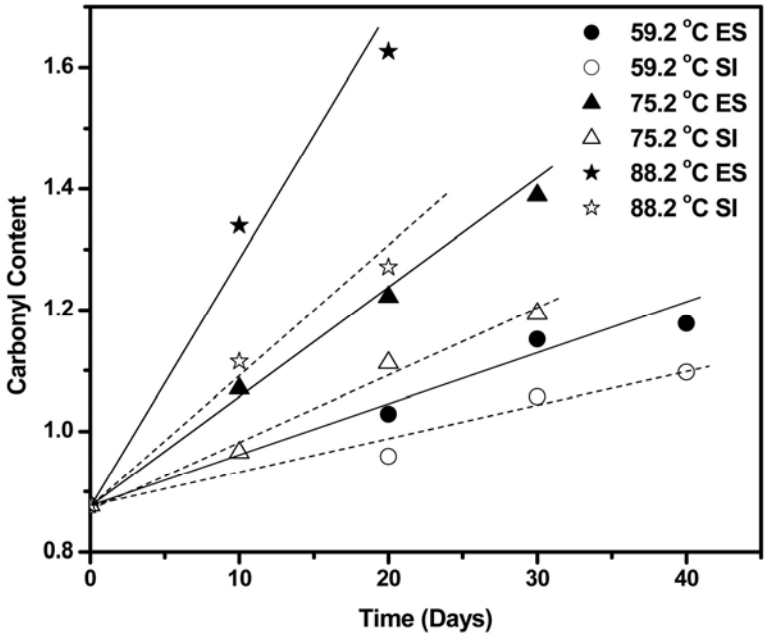


Figure 25. Sample Comparison of Oxidation Rates at ES and SI (SEM 64-22).

Estimation of P_{si} and Calculation of Oxygen Diffusivity

Oxygen pressure at the substrate interface was then calculated by comparing oxidation rates at the ES and SI with Eq. 4-12. Then with SI oxygen pressures, their corresponding times determined as described above, asphalt film thickness, and asphalt reaction kinetics parameters known, oxygen diffusivity for each binder and temperature were estimated numerically based on the model described above. For each experiment, Table 12 shows the P_{SI} corresponding to the measured oxidation rate at the SI, the approximate time when this P_{SI} value is reached, and the diffusivity estimate. Diffusivities were of the order of 10^{-10} to 10^{-11} m^2/s over temperatures from 60° to 90°C.

Correlation of Oxygen Diffusivity with Binder Viscosity

Further analysis was conducted to establish correlations between asphalt material properties, test conditions, and oxygen diffusivity. Diffusivity of a single solute molecule A through a stationary medium B is given by (Bird et al., 2001):

$$\mathcal{D}_{AB} = \mathrm{K}T\left(\frac{u_A}{F_A}\right) \tag{4-16}$$

where T is temperature, K is Boltzmann's constant, (u_A/F_A) is the "mobility" of a molecule A (the steady-state average velocity attained by the molecule under the action of a unit force). For asphalt materials, this property might be highly associated with asphalt viscosity and the extent of molecular interaction for different asphalt components.

Table 12. Summary of P_{SI} and D_{O2} for Studied Asphalt Binders.

Asphalt	Temperature (^{o}C)	Time[a] (days)	P_{SI} (atm)	D_{O2}[b] (m^2/s)
Alon 64-22	59.3	25	0.0332	1.20×10^{-11}
	75.2	15	0.0088	4.42×10^{-11}
	88.2	10	0.0604	2.64×10^{-10}
Alon 76-22	63.4	15	0.1172	2.90×10^{-11}
	76.2	15	0.0984	1.00×10^{-10}
	87.3	5	0.0896	3.05×10^{-10}
SEM 64-22	59.2	20	0.0597	1.42×10^{-11}
	75.2	15	0.0408	6.55×10^{-11}
	88.2	10	0.0184	1.75×10^{-10}
SEM 70-22	59.2	20	0.0795	1.68×10^{-11}
	75.2	15	0.0311	5.35×10^{-11}
	88.2	15	0.0187	2.48×10^{-10}
Lion 64-22	55.8	25	0.0517	1.05×10^{-11}
	74.6	20	0.0551	7.60×10^{-11}
	89.2	10	0.0686	3.58×10^{-10}
Lion 70-22	63.4	20	0.1237	5.40×10^{-11}
	76.2	15	0.1096	1.62×10^{-10}
	87.3	5	0.0926	4.10×10^{-10}
Valero-H 64-22	55.8	25	0.0154	8.60×10^{-12}
	74.6	20	0.0731	6.61×10^{-11}
	89.2	10	0.0465	1.80×10^{-10}
Martin 64-22	63.4	15	0.0224	1.58×10^{-11}
	76.2	15	0.0388	7.70×10^{-11}
	87.3	5	0.0637	2.60×10^{-10}

[a]The time at which oxygen pressure in the film at the SI reaches P_{SI} (near the mid-time).
[b]The (uniform) diffusivity throughout the film at the reported time.

To this effort, oxygen diffusivity divided by absolute temperature ($\mathcal{D}_{O_2}/T$) is plotted against the asphalt's low shear rate limiting viscosity (η_o*) at 60°C, each on a log scale, in Figure 26. For polymer-modified binders, the viscosity of the base asphalt correlated much better with diffusivity than the viscosity of the modified asphalt. This correlation suggests that from the perspective of diffusing oxygen molecules, the relevant diffusion medium is the base asphalt, not the polymer modified network.

As shown in Figure 26, a clear decrease of $\mathcal{D}_{O_2}/T$ with increases in η_o* was observed for each binder, and the data as a whole show a clear power law dependence that is consistent with Eq. 4-17:

$$\frac{\mathcal{D}_{O_2}}{T} = 5.21\times 10^{-12}\left(\eta_0^{\,*}\right)^{-0.55} \tag{4-17}$$

Interestingly, Eq. 4-17 can also be partially validated with fundamental laws, with the assumption that asphalt is a colloidal system with a discrete asphaltene hard core suspended in a maltene continuous phase. An effective oxygen diffusivity, in this scenario, will be a function of volume fraction of asphaltene (which is impermeable to oxygen), as shown below:

$$\frac{\mathcal{D}}{\mathcal{D}_0} = 1 - \frac{3\phi}{2+\phi} \tag{4-18}$$

where $\mathcal{D}$ is effective diffusivity, $\mathcal{D}_0$ is diffusivity in maltene phase, and ϕ is volume fraction of asphaltene.

Meanwhile, using the viscosity mean-field theory (Lin, 1995), the viscosity of a solvent is increased by solid spherical particles in relation to their volume fraction according to

$$\eta = \eta_0 e^{2.5\phi} \tag{4-19}$$

Assuming there is a correlation of the form of Eq. 4-17, with a pre-exponential unknown value of A and unknown power factor of B, substituting Eqs. 4-18 and 4-19 into Eq. 4-17 leads to:

$$B \approx \frac{-3\phi}{5\phi + 2.5\phi^2} \tag{4-20}$$

The typical asphaltene content in asphalt is from 5 to 30 percent, which gives a range of B from −0.52 to −0.59. The value of B obtained from the data falls within this theoretical range, consistent with the empirical correlation of Eq. 4-14. With this correlation, one can obtain a value of oxygen diffusivity by measuring the low shear rate limiting viscosity of asphalt, an easily measurable property.

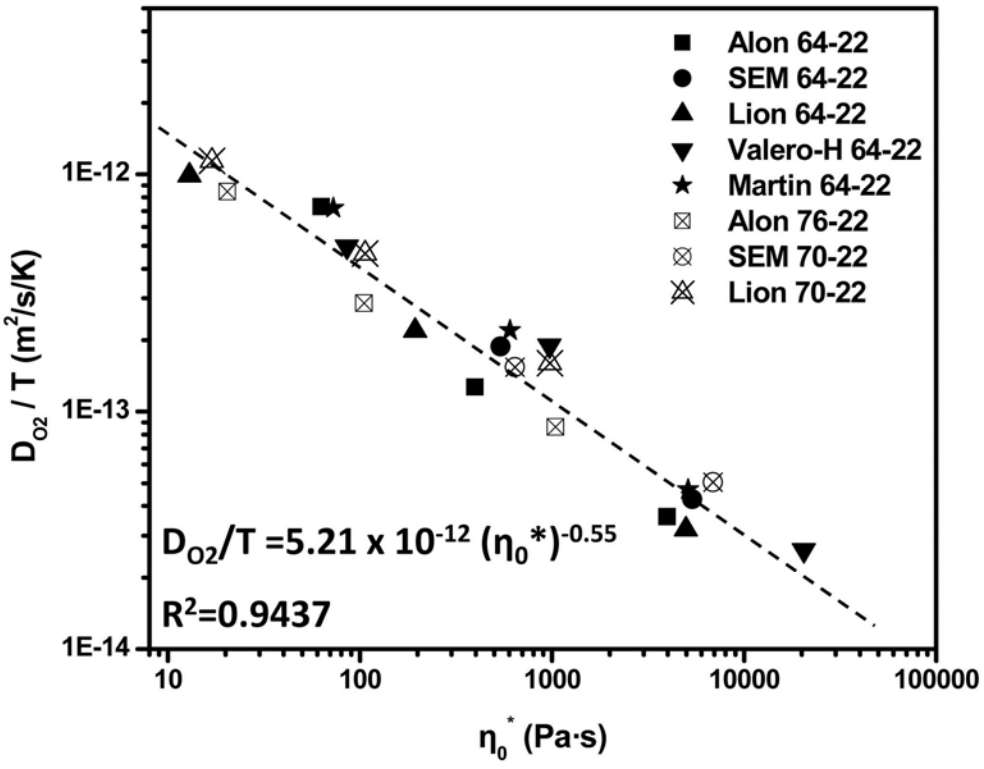


Figure 26. Correlation of D/T with Limiting Viscosity *(η_o*)*

Prediction of Carbonyl Growth in an Asphalt Film Using the Diffusivity Correlation

The above correlation between ($\mathcal{D}_{O_2}/T$) and (η_o*) is based on diffusivity values that were calculated using a pseudo-steady-state assumption of constant oxygen diffusivity during the oxidation period, in spite of the fact that as oxidation proceeded, $\mathcal{D}_{O_2}$ decreased throughout the film and in a way that varied with depth in the film. To evaluate this assumption, carbonyl growth over time at the ES and SI for the various experiments was calculated using Eq. 4-9 while allowing oxygen diffusivity to change with oxidation according to Eqs. 4-2 and 4-17. These CA values were then compared to the experimental measurements. Figure 27 shows a sample comparison of CA versus oxidation time for an asphalt film of SEM 64-22. Appendix A contains complete data on modeled CA at ES and SI for eight studied asphalt binders. There is a good match between model calculations and experimental measurement of carbonyl growth, suggesting that the ($\mathcal{D}_{O_2}/T$) versus (η_o*) correlation describes the experimental data well, and that the diffusivity values determined by using the pseudo-steady-state assumption over the test period are accurate to within the limitations of the data.

As a further assessment of the accuracy of the diffusivity values reported above, the effects of varying the pressure power α in kinetics Eq. 4-1 and the factor relating the reactive incorporation of oxygen into asphalt molecules to FTIR CA measurements, c in Eq. 4-8, were determined. These parameters vary between asphalts, and averages of the values that have been measured to date were used in the diffusivity calculations. Measured values of α range from

about 0.23 to 0.30 with an average of 0.27 used in the calculations, while c varies from about 2.75×10^{-4} to 4.59×10^{-4} gmol O_2 / mL CA with an average value of 3.71×10^{-4} gmol O_2 / mL CA used in the calculation. So, the question was how much impact the variations within these ranges would have on the calculated values of diffusivity.

The sensitivity of estimated oxygen diffusivity values to variations in α and c is demonstrated in Figure 28 for asphalt binder SEM 64-22. Varying α over the range of values results in diffusivity variations of about 25 percent. Similarly, variations in c result in diffusivity variations of about 60 percent. A more complete assessment of diffusivity confidence intervals has not yet been made.

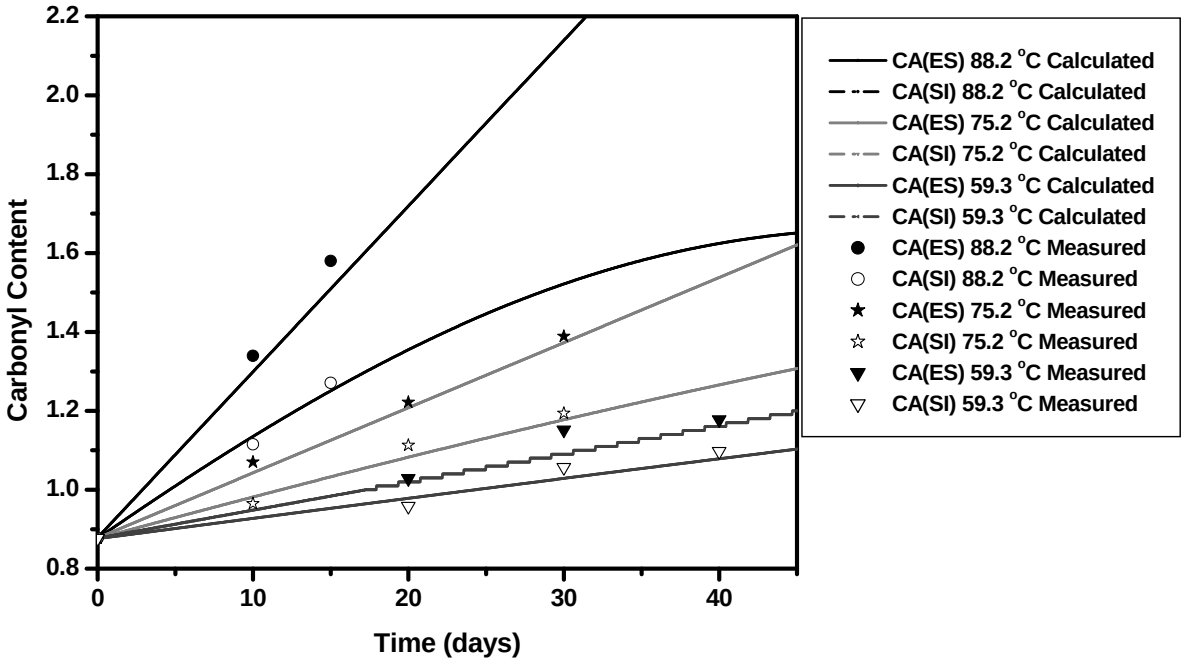


Figure 27. Sample Calculation of Carbonyl Growth at ES and SI of an Asphalt Film of SEM 64-22: Model Calculation vs. Experimental Measurement.

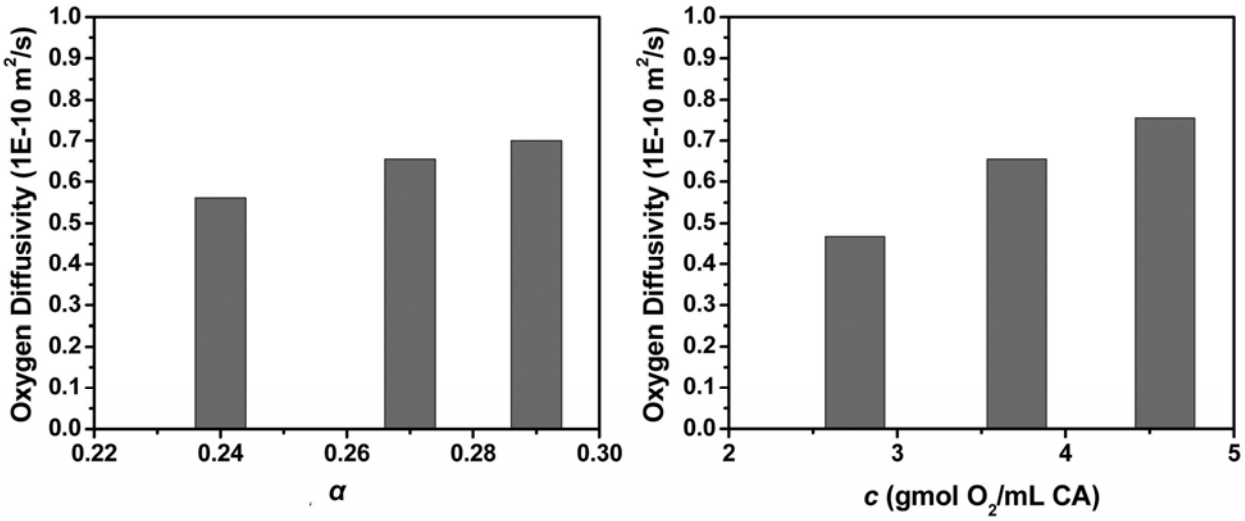


Figure 28. Sensitivities of Calculated Oxygen Diffusivity to Variations in *c* and *α*.

Effect of Mastic Fines on Oxygen Diffusivity in Asphalts

A further hindrance to oxygen diffusion through binders in pavements is the presence of aggregate fines that are impervious to diffusion. To quantify this effect, oxygen diffusivities for three asphalt mastics with three different volume fractions of aggregate fines (0, 10, and 25 percent) were measured; Table 13 summarizes the data.

Table 13. Summary of D_{O2} for Studied Asphalt Mastics at Different Volume Fraction of Aggregate Fines.

Mastics	Temperature	D_{O2} (m^2/s)		
		ϕ=0%	ϕ =10%	ϕ =25%
Alon 64-22	58.3	1.20×10^{-11}	8.60×10^{-12}	5.95×10^{-12}
	75.0	4.42×10^{-11}	3.90×10^{-11}	3.60×10^{-11}
	87.8	2.64×10^{-10}	2.16×10^{-10}	1.65×10^{-10}
SEM 64-22	62.9	1.42×10^{-11}	1.10×10^{-11}	9.63×10^{-12}
	75.8	6.55×10^{-11}	6.32×10^{-11}	3.48×10^{-11}
	88.4	1.75×10^{-10}	1.40×10^{-10}	1.00×10^{-10}
SEM 70-22	58.3	1.68×10^{-11}	1.38×10^{-11}	9.65×10^{-12}
	75.0	5.35×10^{-11}	4.70×10^{-11}	3.80×10^{-11}
	87.8	2.48×10^{-10}	2.30×10^{-10}	1.63×10^{-10}

A universal trend, decreasing oxygen diffusivity with an increase in the volume fraction of fines, was observed for each binder at each test temperature. Other than volume fraction of filler, oxygen diffusivity in mastics does not show any clear dependence on either test temperatures or binder types beyond that shown in Figure 29.

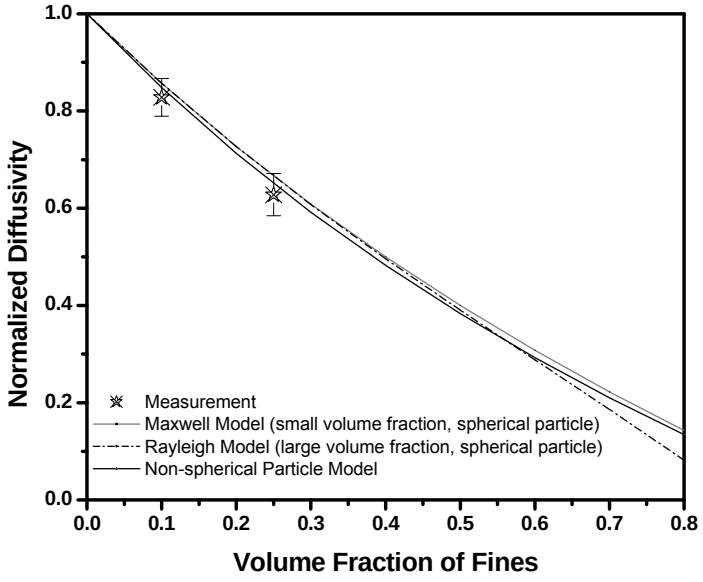


Figure 29. **Effect of Volume Fraction of Aggregate Fines on Oxygen Diffusivity.**

The effect of volume fraction of inclusions on transport behavior in heterogeneous materials has been well understood for many years. Theoretically, with a known volume fraction of fines for a given mixture design, oxygen diffusivity in mastics can be estimated from those conventional prediction models to a very reasonable degree of accuracy. Figure 29 shows the comparison of measured average diffusivity dependency over volume fraction of fines with what is predicted by conventional models (Maxwell, Rayleigh, or non-spherical complex models). A very good fit between those averages and the predictions of the conventional models is evident. Note also that over the volume fraction range from 0 to 60 percent; these three model predictions agree well with each other.

Calculation of Pavement Oxidation

To demonstrate the importance of oxygen diffusivity in pavement oxidation estimation, sample calculations were made with an oxidation model (Prapaitrakul et al., 2009). The model elements include simplified air void characterization, a pavement temperature profile model (Han *et al.*, 2010), asphalt binder oxidation kinetics, and oxygen diffusivity. Holding all model input parameters (temperature, air void properties, binder kinetics parameters) constant, the oxidation rate at 0.02m below the pavement surface was calculated using oxygen diffusivity established by the correlation (Eq. 4-17) and compared with calculation based on a single oxygen diffusivity, as shown in Figure 30.

Diffusivity values for the field conditions of these calculations ranged from 10^{-13} to 10^{-11} m^2/s (varying with field temperature and asphalt viscosity). A decrease in the average yearly oxidation rate (from 0.064 CA/year in the first year to 0.052 CA/year in the seventh year) was observed due to oxidative hardening of the asphalt and a consequent decrease in diffusivity at a

fixed temperature, in accordance with Eq. 4-17. Models that use a constant diffusivity at each temperature fail to capture this hardening effect on oxidation rates.

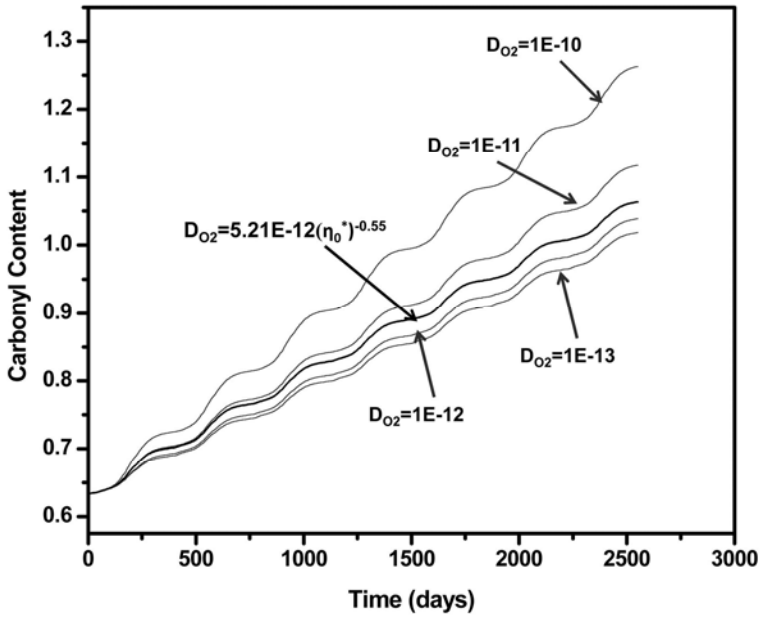


Figure 30. **Calculation of Pavement Oxidation with Different Oxygen Diffusivity.**

SUMMARY

In this work, estimates of oxygen diffusivity in binders were made based on laboratory oxidation experiments in binder films of known reaction kinetics. Comparing the oxidation rates at the binder surface and at a solid-binder interface at the film depth allowed determination of oxygen diffusivity.

For neat asphalts, oxygen diffusivities (D) ranged from10^{-10} to 10^{-11} m^2/s, varying with temperature (T) and asphalt low shear rate limiting viscosity (η_o*); log(D/T) varied linearly with log(η_o*) for both base asphalts and polymer-modified binders according to Eq. 4-17. For asphalt mastics, oxygen diffusivity was observed to decrease as filler volume fraction increased. Quantitatively, this effect follows a theoretical estimate of the effect of a dilute suspension of spherical inclusions on diffusivity.

CHAPTER 5. COMPARISONS OF THE IMPACT OF SEVERAL AIR TEMPERATURE MODELS ON CALCULATIONS OF PAVEMENT TEMPERATURE AND ASPHALT OXIDATION

ABSTRACT

Pavement temperature data are important to pavement design and performance. Hourly pavement temperatures as a function of depth can be calculated from hourly solar radiation, air temperature, and wind speed using a heat-transfer model. In Phase One of this work, five air temperature models were compared to hourly air temperature measurements for their impact on calculations of pavement temperature and asphalt binder oxidation. Annual mean and monthly mean air temperatures performed poorly. Daily mean air temperatures performed reasonably well for pavement temperature calculations but not as well for oxidation rate calculations. Single-sine and sine-sine models yielded the best results with the single-sine model being recommended because of its simplicity.

In Phase Two, a statistical pattern method of modeling air temperature was assessed for its ability to accurately match measured temperatures and as input for calculating pavement temperatures and oxidation. Statistical measures of accuracy demonstrate that while for air temperature and pavement temperature the three models (single sine, sine-sine, and pattern) are comparable, the pattern model clearly is more accurate and more precise for predicting asphalt oxidation and hardening rates, because of the more accurate treatment of high temperatures coupled with the non-linear Arrhenius oxidation kinetics.

INTRODUCTION

Pavement temperature as a function of time and depth affects pavement design, pavement permanent deformation and thermal cracking performance, and binder oxidation in pavements. While measured temperatures are available in the Long-Term Pavement Performance database for a limited number of pavements, modeling pavement temperatures is more practical and economical, so long as it is accurate enough for the purpose.

For pavement temperature calculations, measured hourly air temperatures are usually desired. However, measured hourly air temperatures are limited by availability. More practically, hourly air temperatures can be estimated from commonly available daily data, monthly averages, or even annual mean temperatures. Various air temperature models are presented in the climatic and agricultural literature. However, none has studied its effect on pavement temperature and pavement performance, and no guideline is available for selecting an air temperature model to meet specific application and accuracy requirements.

OBJECTIVES

The objectives of this work were:

- To study the influence and sensitivity of air temperature on pavement temperatures.
- To study the influence of five air temperature profile models on pavement temperature and asphalt oxidation near the pavement surface (Phase One).
- To study the effectiveness of a statistical pattern air temperature model at calculating pavement temperature and asphalt oxidation near the pavement surface (Phase Two).
- To provide a guideline for selecting an air temperature input method, for use in predicting pavement performance.

PRELIMINARIES

This section provides a review of pavement temperature models. It also briefly reviews the thin-film oxidation model, which was used to evaluate the effect of air temperature on asphalt oxidation in pavements.

Pavement Temperature Models and Pavement Thermo-Physical Properties

In general, two types of pavement temperature models have been presented in the literature. One type is a fundamental heat-transfer model (Hermansson, 2000; Minhoto et al., 2005; Han et al., 2011a) that uses inputs of hourly solar radiation, hourly air temperature and wind speed. The model outputs are hourly pavement temperature as a function of time and depth. The monthly mean absolute error was 2°C. Because the outputs are hourly, they can be used not only as environmental criteria in pavement design but also to predict pavement performance. A second type of model uses statistical regression to relate extremes (maximum and minimum) of pavement temperatures to extremes of air temperature (Bosscher et al., 1998; Diefenderfer et al., 2006) for binder performance grade (PG) selection. In this work, the heat-transfer model by Han et al. (2011a) was used for pavement temperature calculations.

The pavement heat-transfer model requires several pavement thermo-physical properties including thermal conductivity, volumetric heat capacity, emission and absorption coefficients, and the albedo of the pavement surface. Values of these parameters used in this paper were taken from the literature (Hermansson, 2004; Gui et al., 2007).

Oxidation Model

To evaluate the effect of different air temperature models on binder oxidation in pavements, a simplified thin-film asphalt transport and reaction model that neglects oxygen diffusion limitations was used (Prapaitrakul et al., 2009). Thin film oxidative aging was calculated at atmospheric pressure (0.2 atm oxygen partial pressure) and for pavement surface temperatures (as a function of time) calculated using each of the various air temperature model inputs as well as for actual measured hourly air temperatures. Carbonyl area growth directly reflects oxidation (Liu et al., 1998a), and the reaction follows an Arrhenius activation energy rate expression (Lau et al., 1992). Representative asphalt CA reaction rate kinetics parameters used in

this work were a pre-exponential factor of 3.68×10^{10} CA/day and an activation energy of 80 KJ/mol (Liu et al., 1996).

SINGLE SITE IMPACT OF AIR TEMPERATURE ON PAVEMENT TEMPERATURE

A pavement site in Lamar, Texas, (LTPP SHRP ID 1068) was selected arbitrarily as the subject. Measured hourly solar radiation data for 1994 were collected from the National Solar Radiation Database (NSRDB), hourly air temperature data for 1994 were collected from the LTPP Auto Weather Station (AWS), and daily average wind speed were collected from LTPP Virtual Weather Station (VWS). To evaluate the importance of various model simplifications, the effects of different model inputs (e.g., solar radiation, atmospheric radiation, convection) on pavement temperature were studied by deliberately turning off one or two inputs for the various example calculations. Although the effects might be coupled, this approach gave very reasonable first-order results.

Figure 31 shows measured pavement temperatures (cross) at a depth of 25 mm and the pavement temperatures (line) also at a depth of 25 mm calculated by using the model of Han et al. (2011a) from measured hourly inputs, i.e., solar radiation, air temperature, and wind speed. The data spanned four days in March 1994. When downwelling long-wave radiation from the air plus natural and forced convection between the atmosphere and the pavement surface were set to zero, the calculated pavement temperatures (dots) were shifted down significantly relative to calculated pavement temperatures (line) that included atmospheric radiation and convection. These calculations approximate a planet with no blanketing atmosphere, resulting in the large shift to colder temperatures. When solar radiation was set to zero (but in the presence of atmospheric radiation), the calculated pavement temperatures (squares) were shifted downward, and the maximum to minimum variations of pavement temperatures were greatly reduced. The small but not negligible variation was due to the cyclic hourly air temperatures caused by solar radiation on the atmosphere. For a final comparison, forced convection was turned off by setting wind speed to zero; natural convection remained in the convective heat transfer correlation. The calculated pavement temperatures (dashed line) were shifted higher, especially for daytime temperature peaks, than for the complete calculation, but the profile shape was largely the same.

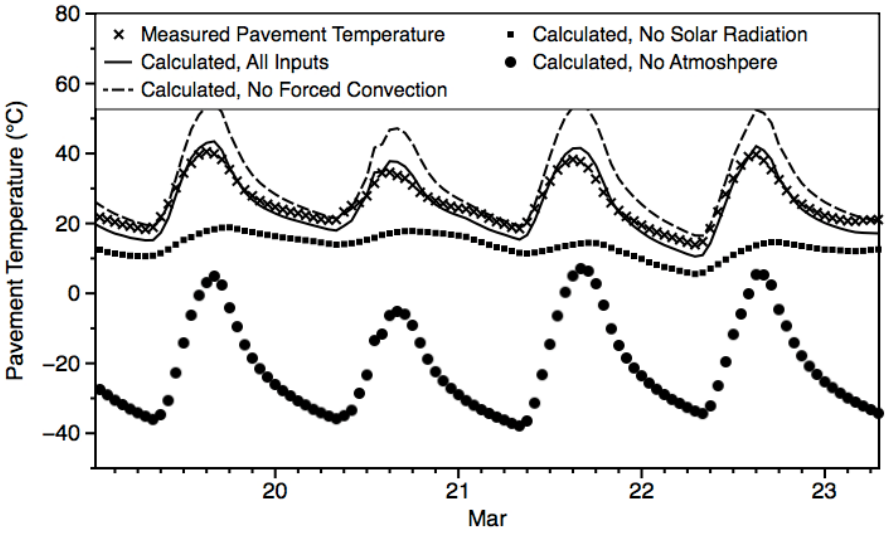


Figure 31. The Effects of Various Inputs on Pavement Temperature.

From the above discussion, we conclude:

- Air temperature and the presence of the atmosphere in general play an important role in moderating pavement temperatures and, to a lesser degree, influence the daily temperature variations. However, the effect of air temperature (both average and variations) on pavement temperature requires further analysis, which is presented in the next section.
- Solar radiation is mainly responsible for the large daily variations of pavement temperatures, although air temperature variations (an indirect effect of solar radiation) also play a role.
- Forced convective heat transfer induced by wind cools the pavement surface, especially during peak temperature hours.

Sensitivity of Pavement Temperature to Annual Mean Air Temperature

To study the effect of air temperature averages on pavement temperature, different yearly averages were used in the calculation, leaving everything else unchanged for the Lamar, Texas, site. The averages were selected to represent different annual means of daily average temperatures of the United States. The annual average at the southern parts of Texas and Florida can be above 70°F (21°C). In states having a latitude similar to that of Kansas, the annual mean is around 55°F (13°C), while in northern states it is below 40°F (4°C). Thus, as a simplified approach to assessing the effect of annual average air temperature on pavement near-surface temperatures, hourly air temperatures were assumed to be constant for the entire year at 40, 55, and 70°F (4, 13, and 21°C). The results are shown in Figure 32.

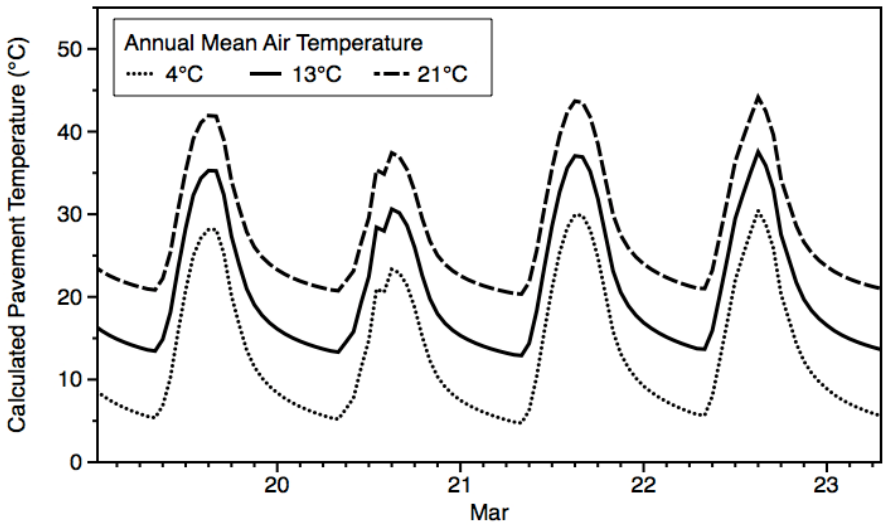


Figure 32. The Effect of Different Annual Mean Air Temperatures on Pavement Temperatures.

It is clear that the annual mean air temperature has a significant effect on pavement temperature, as would be expected, with pavement temperatures driven higher by the presence of warmer air. Furthermore, the annual mean temperature for the pavement is higher than that of the air because of the solar radiation. In this calculation, the annual mean pavement temperature in 4°C air was 13.8°C (standard deviation 8.6°C), in 13°C air it was 21.3°C (standard deviation 8.2°C), and in 21°C air it was 28.3°C (standard deviation 8.0°C). The standard deviations represent the fluctuation of pavement temperature around the annual mean through the entire year. The differences between annual mean calculated hourly pavement temperatures for different mean air temperatures were slightly smaller but close to the differences between the mean air temperatures. Specifically, the difference in mean hourly pavement temperatures for 4°C and 13°C air was 7.5°C (standard deviation 0.4°C), and the difference for 13°C and 21°C air was 7.0°C (standard deviation 0.3°C).

Sensitivity of Pavement Temperature to Hourly Air Temperature Variations

To study the effect of air temperature variation on pavement temperature, the use of daily averages versus hourly measurements of air temperature were compared. Results showed that the calculated annual mean pavement temperatures for these two scenarios were quite close, having a difference of 0.2°C. So, varying air temperature hourly through daily cycles as opposed to using a single constant temperature has a negligible effect on the calculated annual mean pavement temperature. By contrast, the calculated daily amplitudes of pavement temperature variation were smaller using daily average air temperatures in place of hourly values, as shown in Figure 33. The annual mean difference in daily amplitude was 3.8°C, which could have a significant effect on pavement oxidation.

From these analyses it is clear that having the correct mean air temperature is important for an accurate calculation of the mean pavement temperature. Furthermore, it is seen that daily variations of air temperature impact the daily variations of pavement temperature, although the

sensitivity to errors in magnitude is much less than one might expect. A separate question is how typical errors in air temperature might impact binder oxidation in the pavement. The following sections address this question.

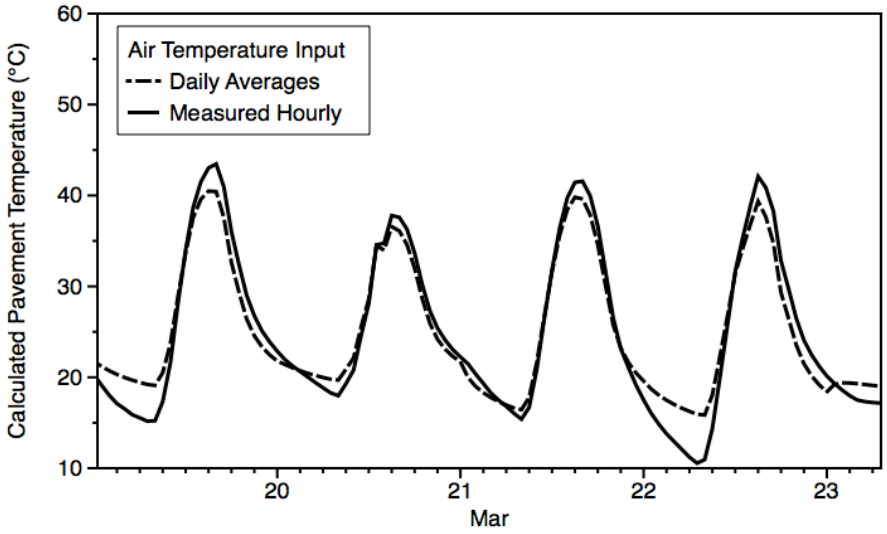


Figure 33. The Effect on Pavement Temperatures of Using a Single Daily Average Air Temperature Compared to Using Measured Hourly Temperatures.

MULTI-SITE COMPARISONS OF FIVE COMMON AIR TEMPERATURE MODELS (PHASE ONE)

Methodology

Three pavement sites in states having distinctly different climates were used in further comparisons of the impact of air temperature models on calculated pavement temperatures: Texas for high temperature, Montana for low temperature, and Kansas for median temperature. Detailed information for each site is listed in Table 14. Measured hourly air temperatures for the three sites were obtained from the LTPP Auto Weather Station database, and inputs of hourly solar radiation and wind speed data for the pavement temperature model were collected from the National Solar Radiation Data Base. Their USAF (United States Air Force) ID numbers are also shown in Table 14.

Air temperatures were provided to the pavement temperature model by three types of methods. One method (three models) provided mean temperatures (annual mean, AM; monthly mean, MM; and daily mean, DM), and a second method (two models, the single-sine, 1S model of Debele et al., 2007 and the sine-sine, 2S model of Baker et al., 1988) provided hourly estimates after their parameters were estimated using daily weather temperature data. The third method measured hourly data (from the LTPP database).

Table 14. Information for the Pavement Sites Studied.

Location	Killeen, TX	Greensburg, KS	Anaconda, MT
Elevation (m)	245	737	1221
Latitude	30.98°	37.61°	46.14°
Longitude	97.78°	99.28°	112.89°
LTTP AWS ID	48A807	200100	300800
NSRDB USAF ID	722575	724510	726785
Year of Data - C*	2002	2003	2003
Year of Data - O**	2003	2002	2002

*The year of data used for model comparison.

** The year of data used for model parameter optimization.

The definition for each mean is clear. The single-sine model provides air temperature values according to:

$$T(t) = T_{avg} + \frac{T_{\max} - T_{\min}}{2} \cos \frac{\pi (t - t_{\max})}{12} \tag{5-1}$$

where T(t) is the air temperature at time t (in hours), T_{avg}, T_{max} and T_{min} are the daily average, maximum and minimum temperatures, and t_{max} is the hour of the maximum temperature assumed to be the same for each day of the entire year and thus is an optimized constant parameter in the equation.

The sine-sine model is:

$$T(t) = T_{avg} - \frac{T_{\max} - T_{\min}}{2} \cos \frac{\pi (t - t_{\min})}{(t_{\max} - t_{\min})} \tag{5-2}$$

$$T(t) = T_{avg} + \frac{T_{\max} - T_{\min}}{2} \cos \frac{\pi (t - t_{\max})}{(t_{\max} - t_{\min})} \tag{5-3}$$

where Eq. 5-2 is for the period from minimum to maximum temperature; Eq. 5-3 is for the period from maximum to the next minimum; and t_{min} is the hour of minimum temperature, a single parameter for the entire year, optimized from measured hourly temperatures. The other variables are as previously defined.

These three methodologies provided five different hourly sets of air temperature versus time values, plus the measured hourly temperatures, to calculate six sets of hourly pavement temperatures at each of the three sites. Then each of these six sets of hourly pavement temperatures were used in the oxidation model to calculate yearly average binder oxidation rates (CA formed per year). Statistical comparisons of each of the five air temperature models to the hourly measured air temperature data included root mean square error (RMSE) based on hourly comparisons), bias (comparisons of annual mean temperature), and percent error in asphalt oxidation rate (difference between each air temperature model's generated value and the measured air temperature value).

Note that the purpose of this paper was to study the effect of different air temperature model inputs and not the performance of the pavement temperature model. Thus, pavement temperatures calculated from measured hourly air temperatures were used as the reference for comparison, and an air temperature model was considered to be better if it provided calculated pavement temperatures closer (by an appropriate statistical measure) to those calculated using the measured air temperatures.

Results and Discussion

In Table 15, the RMSE values (model versus measured temperature comparisons) became smaller from AM to MM to DM to 1S, while the difference between 1S and 2S is marginal. Note that the BIASs were exactly zero for AM, MM, DM, and 1S by definition. As one might expect, the 1S and 2S models were the most accurate. Furthermore, although the 2S model is more complex than the 1S, it did not improve the RMSE. This result is consistent with that reported in the climatic and agricultural literature (Baker et al., 1988).

Table 15. RMSE and BIAS for Modeled Hourly Air Temperatures for One Year.

Location	RMSE (BIAS)				
	AM	MM	DM	1S	2S
TX	9.5 (0)	6.0 (0)	4.5 (0)	2.6 (0)	2.6 (-0.2)
KS	11.7 (0)	6.5 (0)	4.5 (0)	2.5 (0)	2.4 (-0.4)
MT	11.2 (0)	6.5 (0)	4.4 (0)	2.7 (0)	2.6 (-0.1)
Mean	10.8 (0)	6.3 (0)	4.5 (0)	2.6 (0)	2.5 (-0.2)
Stdev	1.2 (0)	0.3 (0)	0.1 (0)	0.1 (0)	0.1 (0.1)

AM: Annual Mean; MM: Monthly Mean; DM: Daily Mean; 1S: Single-Sine; 2S: Sine-Sine

Table 16 shows statistical comparisons of the pavement temperatures calculated from the several air temperature models to those calculated using the hourly air temperature measurements. On average, for the three pavement locations the RMSE values for the pavement temperature calculations are 1.5 to 3 times smaller than those for the air temperatures (Table 15), while achieving no improvement in the standard deviations of the RMSE values at the three sites. Accuracy is improved by using a better air temperature model for input, but the amount of improvement is not as much as one might expect and there is a point of diminishing returns. For example, RMSE values for the 1S and 2S models are comparable, suggesting that the 1S model is the better choice for its simplicity.

Table 16. Statistical Comparisons of Modeled Versus Measured Hourly Pavement Temperatures for One Year for Five Air Temperature Input Models.

Location	RMSE (BIAS)				
	AM	MM	DM	1S	2S
TX	6.7 (-0.7)	3.4 (-0.6)	1.7 (0.1)	1.0 (-0.3)	1.1 (-0.5)
KS	8.7 (-0.2)	3.8 (-0.2)	1.9 (0.1)	0.9 (-0.2)	1.1 (-0.5)
MT	7.8 (0.4)	3.5 (0.5)	1.6 (0.6)	0.9 (-0.1)	1.0 (-0.2)
Mean	7.7 (-0.2)	3.6 (-0.1)	1.7 (0.3)	0.9 (-0.2)	1.1 (-0.4)
Stdev	1.0 (0.6)	0.2 (0.6)	0.2 (0.3)	0.0 (0.1)	0.0 (0.1)

While comparisons of pavement temperature calculations showed only marginal improvement in RMSE values for the 1S and 2S models over the DM model, comparison of percent error in oxidation rates (Table 17) showed a clear advantage of using 1S and SS. This is the consequence of the fact that oxidation rates follow a nonlinear Arrhenius function of temperature, and that the 1S and 2S models had better pavement temperature estimates at the high extremes of pavement temperatures. This observation is important to pavement performance prediction, for example for predicting fatigue resistance decline due to binder oxidation (Walubita et al., 2005a, 2005b; Woo et al., 2007).

Table 17. Percent Difference in One-Year Asphalt Oxidation Rates Calculated from Modeled versus Measured Hourly Pavement Temperatures for Five Air Temperature Input Models.

Location	Percent Differences in Oxidation Rate (CA/year)				
	AM	MM	DM	1S	2S
TX	-30	-8	-10	3	5
KS	-46	-13	-10	2	6
MT	-50	-18	-14	5	3
Mean	-42	-13	-11	3	5
Stdev	11	5	2	1	1

In summary, data in Table 15 through Table 17 showed consistent results. AM and MM models generally are not recommended for use in pavement temperature and oxidation rate calculations. And, while DM is better than AM and MM in predicting pavement temperatures, it still is not satisfactory for oxidation rate calculations because it does not adequately capture the effects of high pavement temperature extremes. The 1S and 2S models yield the best results and while their performances are comparable, 1S is recommended for use due to simplicity.

MULTI-SITE EVALUATION OF A STATISTICAL PATTERN AIR TEMPERATURE MODEL (PHASE TWO)

Materials and Methods

In Phase Two, six pavement sites in Table 18 were studied in addition to the three sites in Table 14. The hourly air temperature models were single-sine model, sine-sine model and the pattern model developed in this work. The pattern model will be described in detail later.

Similar to Phase One, measured hourly and daily air temperature data for an entire year were collected from the AWS module of the LTPP database. For the three models, two years of data were used: one for pattern analysis and parameter (t_{max} and/or t_{min}) optimization, another for comparison. Table 18 also lists the years of temperature for pattern analysis and comparison.

Table 18. Pavement Sites Selected for Study of the Performance of Hourly Air Temperature Models.

Location	Elevation (M)	Latitude	Longitude	AWS ID	USAF ID	Year of Data	
						C*	P**
Kingman, AZ	1122	35.41°	114.27°	040100	723700	2003	2004
Delhi, CA	36	37.42°	120.76°	060200	724815	2003	2002
Greensburg, KS	737	37.61°	99.28°	200100	724510	2003	2002
Anaconda, MT	1221	46.14°	112.89°	300800	726785	2003	2002
Battle Mt., NV	1417	40.72°	117.04°	320200	725825	2003	2002
Angelica, NY	79	42.35°	77.90°	360800	725157	2004	2003
Pollock, SD	569	45.93°	100.41°	460800	727640	2003	2004
Killeen, TX	245	30.98°	97.78°	48A807	722575	2002	2003
Kamas, UT	1977	40.56°	111.13°	490800	725720	2004	2003

*The year of data used for model comparison.

** The year of data used for model pattern analysis and parameter optimization.

For each location, hourly air temperature estimates using the three models were compared with measured data. Next, those estimates and measured data were used in a pavement temperature model (Han et al., 2011a) to predict hourly pavement temperature at the pavement surface for an entire year. Outputs from the pavement temperature model were compared with calculations using the actual measured air temperature. Furthermore, all four sets of pavement temperature data were used in an asphalt oxidation model to predict the average oxidation rate (carbonyl area formation per year) and hardening (viscosity increase per year).

Methodology of the Pattern Model

Qualitative comparisons of measured air temperature show that while hourly air temperature profiles undergo irregular variations throughout the day, they follow a general pattern, i.e. air temperature reaches a minimum at dawn, increases after sunrise, and reaches its maximum in the afternoon, then decreases after sunset. By using the pattern extracted from air temperature data for a specific site instead of one or more mathematical functions in an x-segment model, an improved air temperature calculation methodology was developed.

The following steps define the methodology of the new air temperature pattern model:

1. Collect daily average, maximum and minimum temperature data from a climate database, e.g., National Climate Data Center (NCDC) for the location of interest.

2. Collect an entire year of measured hourly air temperature data from a climate database, e.g., the LTPP database for that location. If the data for the exact location are not available, data from a nearby location can be used. This part of the procedure is discussed further in a later section of this paper.

3. Using the entire year of data obtained in Step 2, extract a single 24-hour pattern that is specific to the location of the data. The pattern is to be used to estimate hourly air temperature in subsequent years for which detailed data are not available. Determining

this pattern was done using a statistical approach, the seasonal-trend decomposition method of time series analysis (Brockwell and Davis 2002), as implemented in the function stl in the public domain software R (R Development Core Team 2010). According to this methodology, the hourly data of Step 2 is decomposed into three parts:

$$T = \text{trend} + \text{pattern} + \text{remainder} \tag{5-4}$$

where T is the hourly measured air temperatures, "trend" is the set of values of the daily average temperature for the entire year, "pattern" is a single periodic function repeating each day throughout the year, and "remainder" is the residual after the trend and pattern are extracted from the measured data. If the values of T are known (hourly for an entire year), then extracting these three components, and in particular the pattern, is straightforward.

Ultimately, however this is not the problem we wish to address. Of more interest is a procedure for estimating unknown hourly T given the pattern and routine weather data: daily maximum, minimum, and average values. The procedure, in this case, is to construct the trend from the daily average values plus an approximation to the remainder from the daily maximum and minimum values. This remainder does not exactly reproduce the hourly deviations from the pattern plus trend, but does provide a reasonable correction to provide estimates of the unknown T values. This is the analysis that is further described below.

4. Convert the daily average temperature data from Step 1 into hourly resolution by linear interpolation. The daily average temperatures are arbitrarily assumed to occur at noon. For every pair of daily average temperatures for two successive days, hourly temperatures are linearly interpolated from noon to noon. This step gives a first-order trend of the daily average temperature over an entire year.

5. Add the pattern from Step 3 to the hourly linear interpolation of the daily average temperature for the entire year.

6. Finally, linearly transform the result of Step 5 to match the maximum and minimum temperature of Step 1, according to Eq. 5-5:

$$T'_i = T'_{\min} + (T_i - T_{\min})\frac{(T'_{\max} - T'_{\min})}{(T_{\max} - T_{\min})} \tag{5-5}$$

where T_i and T'_i are the temperatures before and after linear transformation, i is time (in hour), T'_{max} and T'_{min} are the measured maximum and minimum temperatures from Step 1, T_{max} and T_{min} are the maximum and minimum temperatures before the linear transformation of Step 5. Eq. 5-5 is applied locally to estimate temperatures between the maximum and minimum temperatures for each pair of two successive days for the entire year. This adjustment to match the daily maximum and minimum temperatures is an alternative approximation to the remainder defined in Eq. 5-4.

CASE STUDY OF THE PATTERN MODEL

To demonstrate the methodology of this pattern model, a pavement site located in Brazos County, Texas, was selected. Measured daily average, maximum, and minimum air temperature data for an entire year were taken from the Automatic Weather Station module of the LTPP database. The AWS ID for this site is 48-0801.

Measured hourly air temperature data also were obtained from the same source. Using time series analysis, these hourly data were decomposed into the three components in Eq. 5-4, with the results shown for 30 days in Figure 34. The first row of Figure 34 shows the measured hourly air temperature. The second row is the repetitive 24-hour pattern, which is required for the new model. Figure 35 shows the pattern expanded over five days. The third row of Figure 34 is the trend component. It represents daily average temperature and follows the measured data closely through the year. The fourth row is the remainder. It embodies the irregular effects of rain, clouds, and other weather conditions on air temperature.

Of the three components provided by the time series analysis, the pattern component is the only one used directly in this new procedure. Figure 35 shows the pattern over five days. Comparing this pattern to a common 24-hour measured air temperature profile (see the measured data in Figure 36), two important similarities are observed. First, they are both a non-sinusoidal shape because the air temperature increases most quickly after sunrise but then decreases more slowly after sunset. Second, the time from the minimum to the maximum temperature is usually less than 12 hours, which also occurs because of the uneven effect of heating versus cooling.

Next, daily average air temperatures in hourly resolution are linearly interpolated between the successive daily average air temperatures of Step 1. The periodic pattern (also in hourly resolution) from the time series analysis obtained in Step 3 is then added hour by hour to these daily average temperatures over an entire year (Step 5).

Finally, the hourly numerical values are linearly transformed using Eq. 5-2 to force them to fit the daily maximum and minimum temperature data of Step 1. Figure 36 illustrates the temperature profile before and after linear transformation, along with the measured data. The advantage of linear transformation is clearly observed in preserving the shape of the temperature profile.

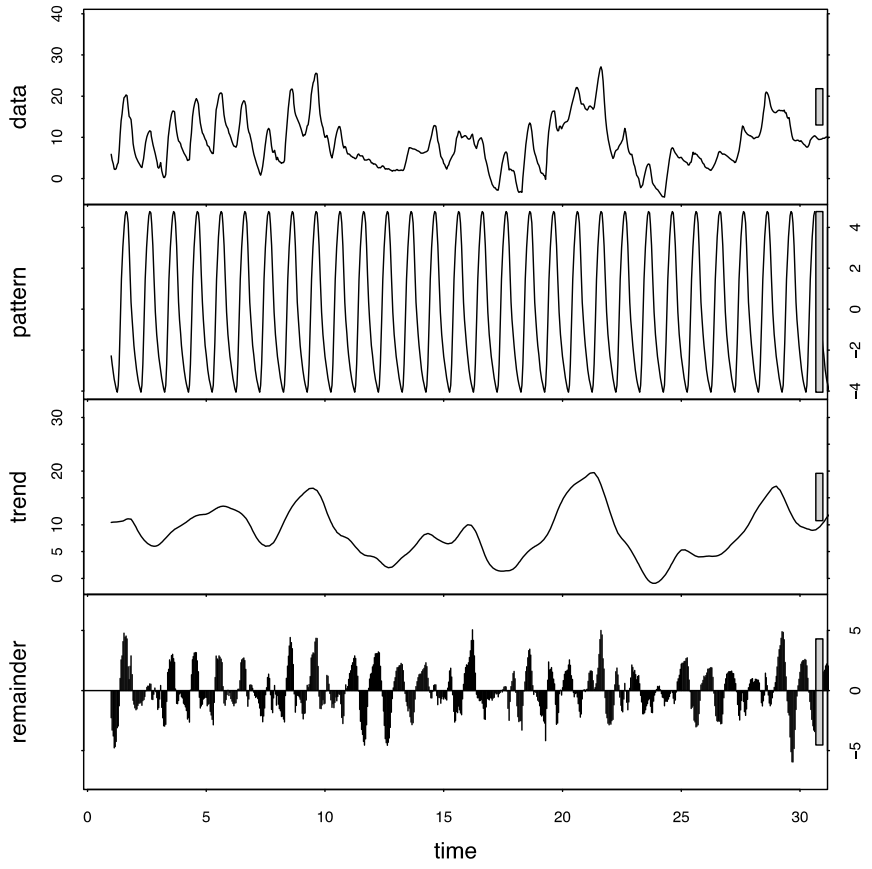


Figure 34. Seasonal-Trend Decomposition of Hourly Air Temperature Data Shown for 30 Days.

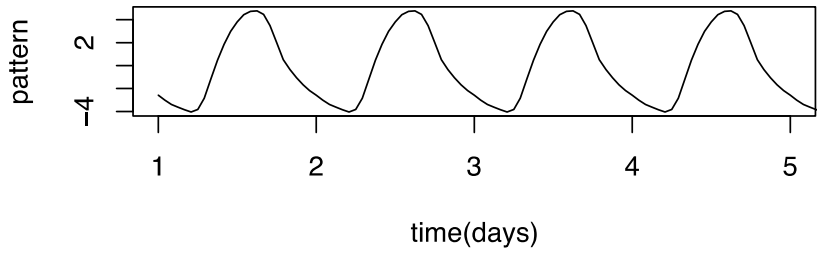


Figure 35. The Pattern Component of Figure 4 Shown for Five Days.

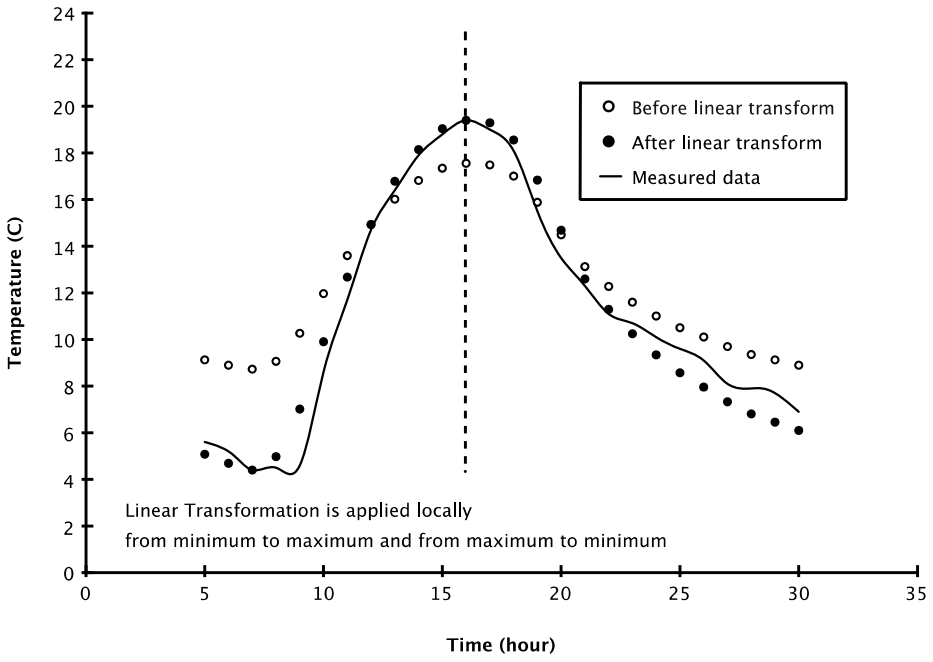


Figure 36. Comparison of Air Temperature Calculations before and after Linear Transformation with Measured Data.

Results and Discussions

Prediction of Hourly Air Temperature

Hourly temperatures for an entire year were estimated from daily average, maximum and minimum temperature data, using the pattern model, the single sinusoidal model, and the sine-sine model for locations listed in Table 18. RMSE and MAE (mean absolute error) statistics with respect to measured data are tabulated in Table 19.

From these statistics, the pattern model is consistently better than the single sinusoidal model and the sine-sine model. Surprisingly, the simple single sinusoidal model yields results comparable to the more complex sine-sine model.

Although the pattern model does produce better results, the improvement is not statistically significant in terms of hourly air temperature (on the order of one-tenth degree C per hour). However, the effect of air temperature on pavement performance is cumulative. A small amount of improvement might lead to much better results in prediction of pavement performance. Therefore, further evaluation is presented in the following sections.

Table 19. RMSE and MAE of Estimated Hourly Air Temperatures of One Year.

Location	RMSE (°C)			MAE (°C)		
	Pattern	1S	2S	Pattern	1S	2S
AZ	1.86	1.96	2.16	1.38	1.51	1.60
CA	1.53	1.65	1.73	1.15	1.28	1.32
KS	2.17	2.52	2.42	1.51	1.76	1.73
MT	2.52	2.68	2.64	1.85	2.02	1.94
NV	2.33	2.65	2.60	1.72	1.99	1.96
NY	2.66	2.67	2.77	1.84	1.89	1.92
SD	2.72	2.92	2.88	1.88	2.06	2.05
TX	2.31	2.61	2.56	1.51	1.82	1.71
UT	2.67	2.72	2.94	1.99	2.06	2.20
Mean	2.31	2.49	2.52	1.65	1.82	1.83
Stdev	0.40	0.41	0.38	0.28	0.27	0.26

Prediction of Pavement Surface Temperature

Pavement surface temperatures for an entire year for the nine locations in Table 18 were calculated using air temperatures from the previous section together with the pavement temperature model developed by Han et al. (2011a). Solar radiation and wind speed were obtained from NSRDB. For comparison purpose, the pavement structure and thermo-physical properties (albedo, emissivity, thermal diffusivity, etc.) were assumed to be the same for the nine locations.

The calculated pavement surface temperatures using modeled air temperatures were compared with those using measured air temperatures. The results are given in Table 20. Statistically, the three air temperature models do not show significant differences in their ability to produce accurate pavement temperature calculations. However, this result still leaves open the question of whether the models equally predict binder oxidation rates, the critical issue of interest to our work, as further discussed, below.

Table 20. RMSE and MAE of Estimated Hourly Pavement Surface Temperatures for One Year.

	RMSE (°C)			MAE (°C)		
Location	Pattern	1S	2S	Pattern	1S	2S
AZ	0.77	0.68	0.88	0.58	0.54	0.67
CA	0.62	0.62	0.75	0.48	0.50	0.59
KS	0.89	0.91	1.07	0.63	0.64	0.81
MT	0.79	0.92	1.02	0.73	0.70	0.76
NV	0.96	0.97	1.03	0.75	0.75	0.81
NY	1.03	0.96	1.13	0.76	0.73	0.87
SD	1.14	1.04	1.13	0.79	0.71	0.78
TX	0.96	0.97	1.12	0.65	0.70	0.83
UT	1.16	0.93	1.12	0.86	0.70	0.82
Mean	0.93	0.89	1.03	0.69	0.66	0.77
Stdev	0.18	0.14	0.13	0.12	0.09	0.09

Comparison of Asphalt Oxidation and Hardening Rates at Pavement Temperatures

An asphalt oxidation model that assumes no oxygen diffusion resistance was used as a third method for comparing the effectiveness of the air temperature models. Oxidative aging at atmospheric pressure (0.2 atm oxygen partial pressure) and pavement surface temperature (determined as described above) was calculated based upon Arrhenius reaction kinetics for carbonyl area formation using a pre-exponential factor of 3.68×10^{10} CA/day and an activation energy of 80 kJ/mol. The initial carbonyl area was taken as 0.589, the initial viscosity as 5365 poise, and the hardening susceptibility [d ln(viscosity)/d CA] as 3.95 1/CA.

Table 21 shows the yearly average oxidation and hardening rates and absolute errors (with respect to the yearly rates using measured air temperatures). Also shown are the averages and standard deviations of the absolute errors. The comparison in Table 21 reflects the cumulative effect of hourly air temperature on asphalt oxidation over an entire year. The results from the pattern model are not only more accurate (lower average error) but also more consistent from site to site (lower standard deviation) than the other two methods. A comparison of viscosity hardening shows similar results.

Table 21. Absolute Error Statistics of Asphalt Oxidation and Hardening Rates at Calculated Pavement Surface Temperature and Atmospheric Pressure.

Location	Oxidation Rate (CA/year)			Hardening Rate ([ln poise]/year)		
	Pattern	1S	2S	Pattern	1S	2S
AZ	0.00070	0.017	0.0041	4.22	7.47	6.1
CA	0.0049	0.013	0.015	5.82	6.82	6.98
KS	0.0012	0.0046	0.016	4.14	5.44	6.68
MT	0.00080	0.0057	0.0037	3.26	5.31	4.92
NV	0.00010	0.012	0.0017	1.97	6.5	4.12
NY	0.0055	0.0046	0.0066	5.13	4.97	5.28
SD	0.0025	0.00050	0.0055	4.48	3.34	5.19
TX	0.0040	0.0077	0.016	5.59	6.24	6.96
UT	0.0019	0.0035	0.00050	4.15	4.84	3.18
Mean	0.0020	0.0054	0.0062	4.79	6.23	6.09
Stdev	0.0024	0.0077	0.0076	4.73	6.31	6.05

This calculation, of course, includes the possibility of positive errors tending to cancel negative errors, because it uses neither absolute nor squared errors in temperature. However, it should also be noted that Arrhenius kinetics are non-linear in temperature; thus positive deviations in rates caused by positive errors in temperature at elevated temperatures do not cancel negative deviations in rates caused by equal negative deviations in temperature at lower temperatures. It is the effect of this non-linearity that is assessed by this calculation.

Offsite Pattern

An interesting question that dramatically affects the application of the pattern model is: can the same pattern obtained from one pavement site be applied to another one? If yes, what are the limitations?

To answer these questions, temperature patterns for three counties in Texas (Hidalgo County, Brazos County, and Bell County), and patterns for Battle Mountain, Nevada, and Angelica, New York, are plotted together in Figure 37. The three patterns of three counties in Texas are quite similar to each other, suggesting one pattern might be used for locations in the same state or same climate region. The differences between New York and Nevada patterns compared to the three Texas sites are significant. Thus for locations that are far apart, the use of offsite patterns is not recommended.

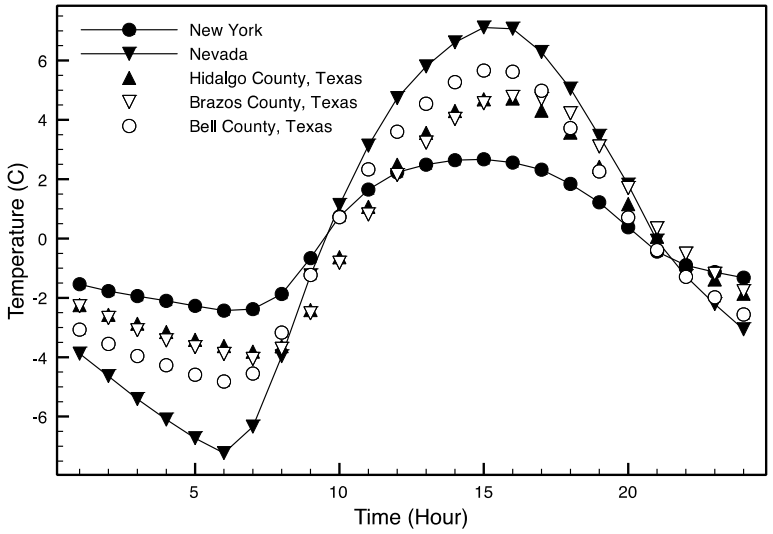


Figure 37. Yearly Temperature Patterns for Six Locations.

To demonstrate the possible applicability of offsite patterns, the pattern for Bell County, Texas (AWS ID 48A807), was used to estimate air temperatures for Brazos County and Hidalgo County, Texas. Table 22 compares hourly air temperatures obtained from onsite patterns to those obtained using offsite patterns. The offsite pattern estimates are not as good as onsite ones, but are still better than the Sine-Sine model.

Table 22. RMSEs (°C) of Hourly Air Temperature Using Onsite Pattern, Offsite Pattern and Sine-Sine Model.

Texas County	Onsite Pattern RMSE	Offsite Pattern RMSE	Sine-Sine RMSE
Bell	2.31	-	2.61
Brazos	1.97	2.10	2.33
Hidalgo	1.54	1.67	2.17

Seasonal Pattern

Patterns can be obtained by time series analysis of data for each specific season of interest. Generally, using seasonal patterns works better than a single yearly pattern, especially for estimating temperatures during the summer.

This section compares air temperature model calculations for summer using a summer pattern (June to August) and winter using a winter pattern (December to February) to calculations for those same periods using the single yearly pattern. The same data sets of the previous sections were used. The AWS ID and the year of data are listed above in Table 18. RMSE and MAE are presented in Table 23.

Table 23. Comparison of Hourly Air Temperature Estimates Using Seasonal Patterns and Yearly Pattern for Nine States in the U.S.

	RMSE				MAE			
Season	Summer		Winter		Summer		Winter	
Pattern	Seasonal	Yearly	Seasonal	Yearly	Seasonal	Yearly	Seasonal	Yearly
AZ	1.69	1.94	1.72	1.95	1.17	1.41	1.28	1.49
CA	1.14	1.36	1.62	1.60	0.89	1.08	1.13	1.13
KS	1.59	1.80	2.05	2.22	1.07	1.36	1.42	1.57
MT	1.98	2.22	3.01	3.04	1.45	1.75	2.21	2.24
NV	1.92	2.35	2.52	2.57	1.36	1.86	1.74	1.77
NY	1.92	1.95	3.16	3.29	1.42	1.46	2.13	2.22
SD	1.67	1.85	3.64	3.54	1.23	1.42	2.56	2.47
TX	1.49	1.50	3.08	2.97	0.97	1.03	2.09	2.03
UT	2.34	2.53	3.13	3.30	1.67	1.96	2.32	2.46
Mean	1.75	1.94	2.66	2.72	1.25	1.48	1.88	1.93
Stdev	0.34	0.38	0.71	0.67	0.25	0.32	0.50	0.47

Table 24. Comparison of Summer and Winter Patterns.

Location	Δt (hours)		ΔT (°C)	
	Summer	Winter	Summer	Winter
AZ	10	7	12.4	8.9
CA	10	8	16.8	8.9
KS	10	8	11.9	10.2
MT	10	7	12.7	5.4
NV	10	8	18.2	9.9
NY	11	6	7.1	3.4
SD	10	7	12.2	5.4
TX	9	9	9.4	8.6
UT	9	7	14.9	8.4

From Table 23, it is clear that using the two seasonal patterns generally yields smaller RMSE and MAE than using a single yearly pattern. This method accommodates the longer days and shorter nights of the summer and shorter days and longer nights of the winter better than using a single yearly 24-hour pattern. It also accommodates the larger amplitude of air temperature fluctuation during the summer versus the winter. These phenomena are shown quantitatively in Table 24.

The time (in hours) from the minimum to the maximum temperatures Δt is much longer for the summer pattern than for the winter pattern in northern climates (e.g., Montana), while the difference is much less in southern climates (e.g., Texas). Also, the amplitude ΔT (the difference

between the maximum and minimum temperatures) is greater for summer patterns than winter patterns.

In addition, the performance of summer patterns is generally better than winter patterns. This is probably due to the fact that during the summer, more days follow a diurnal pattern in which the low temperature occurs in the morning and the high temperature occurs in the afternoon. However, during winter, the diurnal variation has greater irregularities. This argument is supported by the study of distribution of "abnormal" days by Baker et al. (1988). Note that for Kansas and South Dakota, the yearly pattern works better than the winter pattern for the year's data that were evaluated, probably because of a large number of irregular days. Nonetheless, the majority of winter patterns show an advantage over yearly patterns.

Air temperatures calculated using seasonal patterns and yearly pattern were used to calculate pavement temperatures and asphalt oxidation rates during summer (June to August). The results were compared to calculations using measured hourly air temperatures. Results in Table 25 showed that summer patterns generally produce higher oxidation rates than the yearly pattern, and the summer pattern performance in predicting oxidation rates (as indicated by the mean error for the nine sites) was not as good as the yearly pattern (although still better than the other two models).

Table 25. Errors in Predicting Summer Asphalt Oxidation Rates.

	Oxidation Rate Difference[a] (CA/Summer[b])			
Location	Summer Pattern	1S	2S	Yearly Pattern
AZ	0.0066	0.0089	0.0012	-0.0009
CA	0.0008	0.0075	0.0085	0.0032
KS	0.0036	0.0029	0.0081	-0.0001
MT	0.0028	0.0039	0.0021	-0.0007
NV	0.0011	0.0078	-0.0022	-0.0014
NY	0.0029	0.0022	0.0031	0.0024
SD	-0.0002	0.0005	0.0029	-0.0019
TX	0.0054	0.0035	0.0077	0.0024
UT	0.0009	0.0023	-0.0008	-0.0016
Mean	0.0026	0.0044	0.0034	0.0002
Stdev	0.0022	0.0029	0.0039	0.0020

[a] $[(\text{Calculated Rate})_{\text{modeled air temp}} - (\text{Calculated Rate})_{\text{measured air temp}}]$

[b] Summer is June through August.

This result contradicted the expectation of better performance from seasonal patterns. This discrepancy likely arises from the fact that daily maximum air temperatures from AWS modules in the LTPP database are usually greater than those reported in the hourly data file, and that minimum temperatures in the daily data file are usually lower than those in the hourly data file. These kinds of inconsistency, also observed in the NCDC database, are due to the way daily and hourly data are measured and recorded. Daily data are daily extremes, while hourly data are temperatures averaged over each hour (Simpson et al., 2006, and North Dakota Agricultural

Weather Network, 2011). This suggests that in some sense, daily maximum and minimum temperatures are more accurate than values determined from hourly data when accurate high temperature values are critical to performance prediction. Seasonal patterns follow the hourly temperature profiles of summer and winter more precisely than the single yearly pattern, and thus are more sensitive to "error" in measured daily temperature when hourly air temperatures are considered as "true" values.

To verify this hypothesis, daily maximum, minimum, and average values were obtained from hourly data and then were used to reconstruct hourly air temperatures, pavement temperatures, and oxidation rates for an entire year using the same procedure for the seasonal pattern method, the yearly pattern method, the single sine model, and the sine-sine model. In Table 26, oxidation rates (CA/year) for the nine sites listed in Table 18 are compared in the form of averages and standard deviations of absolute errors. The expected better performance of seasonal patterns was clear.

Table 26. Absolute Error Statistics of Oxidation Rates (CA/year) Using Daily Maximum and Minimum Air Temperatures Obtained from Hourly Data.

	Seasonal Patterns	Yearly Pattern	1S	2S
Mean	0.0019	0.0026	0.0047	0.0030
SD	0.0007	0.0013	0.0036	0.0020

In practice, hourly air temperatures are usually constructed from measured daily data (daily average, daily maximum, and daily minimum) using the modeling methods discussed in previous sections, because measured hourly air temperature data are limited by availability. Also, it is important to reemphasize that temperature extremes from measured daily data are not consistent with temperature extremes from measured hourly data for the same weather station, and the temperature extremes likely are more reliable from the daily data than from the hourly data. These results suggest the possibility that using daily high, low, and average temperatures with the statistical pattern model or perhaps even the single-sine air temperature model is actually more accurate for predicting binder oxidation in pavements than using hourly measurements of temperature. To determine whether this is true will require further comparisons using more frequent temperature measurements than hourly to serve the purpose of providing correct air temperatures.

SUMMARY

Accurate hourly air temperature values are important for accurate hourly calculations of pavement temperature. Sensitivity analysis showed that the annual mean air temperature strongly affects the annual mean pavement temperature, and daily variations in air temperature affect daily variations in pavement temperatures, although to a much less extent than solar radiation.

Five air temperature models (annual mean, monthly means, daily means, single-sine, and sine-sine) were studied for their effect on pavement temperature and asphalt oxidation. Comparisons were made for three pavement sites. Annual mean and monthly mean air temperature models performed poorly in estimating pavement temperatures and oxidation rates. The daily mean temperature model performed better than annual mean and monthly mean

models in predicting pavement temperature but not well in oxidation rate calculations due to its poor calculation of the amplitude of pavement temperature variations. The single-sine and sine-sine air temperature models produced the most accurate results compared to those produced by using actual hourly measurements of air temperature. Because the results are comparable, the single-sine model is recommended for its simplicity.

The single-sine air temperature model, together with hourly solar radiation and wind data, used as input to the pavement temperature model of Han et al. (2011a) is recommended for further evaluation in making pavement temperature calculations for use in pavement design, performance prediction (including both thermal and fatigue cracking, and binder oxidation over time), and developing maintenance strategies.

To achieve even better results, a novel pattern model was developed to more accurately estimate hourly air temperatures from daily average, maximum, and minimum temperatures. The new model utilizes a non-sinusoidal pattern of air temperature fluctuation around the average temperature. The pattern is obtained from time series analysis over an entire year of measured hourly data and thus follows air temperature change closer than a presumed, even piecewise, function.

The pattern model was compared to a single sinusoidal model and a two-segment sine-sine model for nine locations in different states across the United States in terms of hourly air temperature, hourly pavement surface temperature, and thin-film asphalt oxidation rates and hardening. RMSE and MAE demonstrate that while for air temperature and pavement temperature the three models are comparable, the pattern model clearly is more accurate and more precise for predicting asphalt oxidation and hardening rates, because of the more accurate treatment of high temperatures coupled with the non-linear Arrhenius oxidation kinetics.

Application of an offsite pattern is also examined. Although the offsite pattern model can still predict reasonable results, use of an onsite pattern is recommended when available. Using seasonal 24-hour patterns specific for summer or winter also was examined; statistical analysis showed that this approach generally yielded better temperature calculations than using a single yearly pattern, especially during the summer.

In summary, model estimates provide the highest level of accuracy, while daily averages perform better than monthly and yearly averages. Use of a single-sine model together with measurements of daily high, low, and average temperatures is recommended for its simplicity. When more accurate estimates are required, the pattern model coupled with daily high, low, and average temperatures is an excellent method.

CHAPTER 6. MODELING PAVEMENT TEMPERATURE FOR USE IN BINDER OXIDATION MODELS AND PAVEMENT PERFORMANCE PREDICTION

[Pages 103 through 119 reprinted with permission from ASCE, from Han, Rongbin, Jin, Xin., and Glover, C. J. (2011) Modeling Pavement Temperature for Use in Binder Oxidation Models and Pavement Performance Prediction. *Journal of Materials in Civil Engineering*, Vol. 23(4), pp. 351–359.]

ABSTRACT

The ability to accurately predict pavement temperature variation with time and depth is critical to calculating binder oxidation in pavements and to understanding asphalt material behavior and predicting pavement performance. In this work, an improved one-dimensional model, coupled with methods to obtain model-required climate data from available databases and optimization of site-specific pavement parameters, was developed to calculate hourly pavement temperatures nationwide. Hourly solar radiation and daily average wind speed were obtained from existing databases. Hourly air temperatures were interpolated using a daily air temperature pattern developed from time series analysis and commonly recorded daily maximum and minimum air temperatures. Parameter estimation identified three critical site-specific pavement parameters: the albedo, the difference between the emissivity and absorption coefficient, and the absorption coefficient. Values of these parameters, optimized at 29 pavement sites nationwide based on the average hourly absolute error objective function, appear to correlate with climatic patterns, suggesting that these parameters be interpolated based on climate. The temperature model, proposed data sources and site-specific pavement parameters provided calculations that agreed well with experimental measurements.

INTRODUCTION

Accurate representation of pavement temperature as it varies with pavement site, time (day and season), and depth is extremely important in the calculation of asphalt physical properties and the prediction of pavement performance. For example, the accuracy of thermal cracking modeling relies highly on accurate representation of temperature changes.

Another example is binder oxidation, an ongoing process throughout a pavement's service life that may occur to a significant degree over the entire pavement's depth (Glover et al., 2005). This oxidation exhibits a profound impact on pavement durability as pavement fatigue life generally declines with increasing pavement oxidation level (Walubita et al., 2005a, 2005b; Walubita, 2006). Asphalt oxidation follows an Arrhenius relation; oxidation rates increase exponentially with decreasing inverse absolute temperature (Lin et al., 1996). Therefore, accurate representation of pavement temperature (as a function of time and depth) is essential to prediction of pavement oxidation and resulting performance.

Fundamental early models of heat transfer in pavements included shortwave solar radiation, down-welling and upwelling long-wave radiation, convective heat transfer at the pavement surface and heat conduction inside the pavement (Dempsey, 1970; Rumney and

Jimenez, 1969; Solaimanian and Kennedy, 1993). The enhanced integrated climate model, a one-dimensional coupled heat and moisture simulation model based on these fundamentals was developed and later integrated into the current mechanistic-empirical pavement design guide to couple pavement design with modeled pavement temperature (Lytton et al., 1989).

The EICM model uses a finite difference approximation for calculating heat conduction within the pavement and underlying layers, subject to heat fluxes at the surface (shortwave solar radiation, long-wave radiation, and convective heat transfer) and a constant-temperature boundary condition well below the pavement. Using required climatic input data including solar radiation, ambient temperature, and wind speed and constant model parameters such as pavement albedo, pavement emissivity and thermal diffusivity, the model is solved numerically for temperature over time and depth.

Although temperatures predicted with the EICM model satisfy pavement design needs in general, there have been some large errors when compared to measured pavement temperature. In one study of Ohio pavements, differences as high as 20°C were observed in the top 10 inches of pavement, and there was an average difference of 10°C 30 inches deep (Liang et al., 2006). Similar results are seen in the studies on New Jersey pavements (Ahmed et al., 2005), for which an average difference of 15°C over the top 20 inches was calculated from their reported data. These errors are most likely caused by several factors: the assumption that heat fluxes at the pavement surface are exactly balanced by conduction into the ground well below the surface, inaccuracy of input climatic data (especially calculated solar radiation) due to imperfect data interpolation schemes, the assumptions of the constant temperature boundary condition, and site-independent pavement-related model parameter values. As reported by other studies, model parameters such as pavement albedo are not constant but are region and season dependent (Hermansson, 2000; Hermansson, 2004). Due to those defects, a more precise pavement temperature model is needed in order to calculate accurate asphalt material and pavement properties, especially for properties that are highly sensitive to pavement temperature. Most importantly, in most pavement performance modeling efforts, years of pavement temperature data are required for models to monitor the progress of important pavement properties such as crack growth or asphalt oxidation. Any incorrect temperature data will not only give biased calculations but also accumulate error over time.

Recently, significant improvement in accuracy over the EICM model has been achieved by several groups using a similar one dimensional heat transfer model but with an unsteady-state surface heat flux boundary condition, measured model input data, and site-specific model parameters that were optimized based on measured pavement temperatures (Hermansson, 2000; Hermansson, 2004; Yavuzturk et al., 2005; Gui et al., 2007). Most of this work focused primarily on determining yearly maximum and minimum pavement temperatures for the purpose of binder selection. Recent efforts for more detailed modeling have been restricted to short time scales and to a specific pavement site, due to the general lack of accurate hourly climate input data and an understanding of how site specific pavement parameters vary with locations.

The objective of this work was to extend these previous efforts by developing a generally applicable method that is able to model pavement temperatures as a function of depth, more accurately over yearly time scales and for a large range of pavement sites. The model would be

useful for various applications, especially for calculations of binder oxidation in pavements, as it changes hour-by-hour and depth according to temperature.

MODEL CONCEPTS AND DEVELOPMENT

The one-dimensional model, similar to that of Gui et al. (2007), was developed based on radiation and conduction energy balance fundamentals. The heat transfer process is depicted schematically in Figure 38. There are multiple sources of heat transfer at the pavement surface: solar radiation and reflection of the solar radiation at the surface by a fraction $\tilde{\alpha}$, the albedo; absorption of atmospheric down-welling long-wave radiation by the pavement surface; emission by long-wave radiation to the atmosphere; and convective heat transfer between the pavement surface and the air close to the surface, which is enhanced by wind. Below the surface and within the pavement and ground beneath it, heat is transferred by conduction. Not included in this model is heat transfer enhancement by precipitation or the effect of moisture freeze and thaw in the pavement. Mathematical details of this model follow.

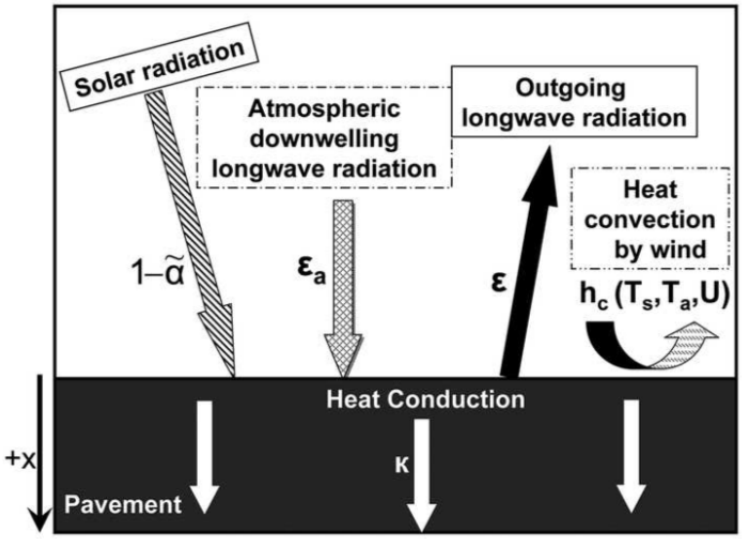


Figure 38. Schematic Representation of Heat Transfer Model of Pavement.

Heat Transfer in Pavement

Heat transfer in the pavement is governed by the classical thermal diffusion equation:

$$\frac{\partial T}{\partial t} = \kappa \frac{\partial^2 T}{\partial x^2} \tag{6-1}$$

where T is the pavement temperature as a function of time (t) and depth below the surface (x), and κ is the thermal diffusivity, $\kappa = k / \rho C$ where k is the thermal conductivity, ρ is the density, and C is the pavement heat capacity. Together with this equation, we consider a flux boundary condition at the pavement surface and a second flux condition at 3 m below the surface.

The Surface Boundary Condition

Considering a differential element of the pavement surface, its thermal energy (temperature) will change to the extent the fluxes from above and from below do not balance. The various fluxes shown in Figure 38 lead to the following surface condition:

$$\rho C \frac{\Delta x}{2} \frac{\partial T_s}{\partial t} = Q_s - \tilde{\alpha} \cdot Q_s + Q_a - Q_r - Q_c - Q_f \tag{6-2}$$

where

ρC is volumetric heat capacity of the pavement.

T_s is pavement surface temperature, K.

x is the depth below the pavement surface.

$\frac{\Delta x}{2}$ is the (differential) pavement thickness for the energy balance.

Q_s is heat flux due to solar radiation.

$\tilde{\alpha}$ is albedo of pavement surface, the fraction of reflected solar radiation.

Q_a is down-welling long-wave radiation heat flux from the atmosphere.

Q_r is outgoing long-wave radiation heat flux from the pavement surface.

Q_c is the convective heat flux between the surface and the air.

Q_f is the conduction from surface into the pavement.

The incoming and outgoing long-wave radiation are calculated by:

$$Q_a = \varepsilon_a \sigma T_a^4 \tag{6-3}$$

$$Q_r = \varepsilon \sigma T_s^4 \tag{6-4}$$

where

ε_a is absorption coefficient of pavement

ε is emission coefficient (emissivity) of pavement

T_s is pavement surface temperature, K

T_a is air temperature, K

$\sigma = 5.68 \times 10^{-8} W \cdot m^{-2} K^{-4}$ is Stefan-Boltzman constant

The convective heat flux is calculated as:

$$Q_c = h_c (T_s - T_a)$$

where h_c is heat transfer coefficient (W/m^{2}K) from the empirical equation (Lytton et al.1989):

$$h_c = 698.24 \cdot a \cdot [0.00144(\text{abs}(\frac{T_s + T_a}{2}))^{0.3} U^d + 0.00097(\text{abs}(T_s - T_a))^{0.3}] \tag{6-5}$$

where U is the hourly wind speed, m/s
a and d are two dimensionless empirical parameters

The heat flux within the pavement at the surface is expressed by Fourier's law:

$$Q_f = -k\left(\frac{\partial T}{\partial x}\right)\Big|_s$$

where $\left(\frac{\partial T}{\partial x}\right)\Big|_s$ is temperature gradient at the pavement surface
k is thermal conductivity of asphalt concrete

Combining these results, a thermal energy balance at the surface provides the surface boundary condition:

$$\rho C\frac{\Delta x}{2}\frac{\partial T_s}{\partial t} = Q_s - \tilde{\alpha}\cdot Q_s + \varepsilon_a \sigma T_a^4 - \varepsilon\sigma T_s^4 - h_c(T_s - T_a) + k\left(\frac{\partial T}{\partial x}\right)\Big|_s \quad (6\text{-}6)$$

Bottom Boundary Condition

Commonly, a constant-temperature boundary condition, some distance below the surface, is reported in the literature. For example, Hermansson (2000) used the annual mean temperature 5 m below the surface as a bottom boundary condition. Gui et al. (2007) used a measured temperature of 33.5°C at a depth of 3 m as the boundary condition. In the EICM model, temperatures were measured from water wells across the country at a depth of 10 to 18 m, from which an isothermal map was constructed. Such a constant-temperature boundary condition has the advantage of simplicity but the disadvantage that these temperatures are not accurately known.

For this work, an alternate approach was used. From measured data in the LTPP database, it was observed that temperatures at a depth beyond 2 m tend to vary approximately linearly with depth. Using this result, an alternate boundary condition was used at a depth of 3 m. That is:

$$\left(\frac{\partial T}{\partial x}\right)\Big|_{3m} = \text{independent of depth}$$

Such a boundary condition, which is based on field observation, has the advantage over the constant boundary condition in that it is location independent and does not require a specific value for the boundary condition. In addition, it is quite straightforward to implement this boundary condition in the finite difference calculation procedure. Of course, this condition is not strictly correct as extrapolating it to too great a depth will lead to significant error.

Numerical Solution of the Model

This model was solved numerically using a finite difference approximation method, together with required input data, including hourly solar radiation, air temperature, and wind speed, plus model parameter values. In the numerical solution, the pavement thickness was divided into cells, which are thinner near the surface and thicker at deeper levels. The number of cells was selected to satisfy the Courant-Friedrichs-Lewy (CFL) condition for stability and to produce good model accuracy (Gui et al., 2007). Each cell is given a temperature (equal to air temperature) at the start of the calculation as an initial condition. The model then calculates a new transient temperature for each cell at each time step.

OBTAINING MODEL INPUT DATA AND PARAMETERS

For any pavement site, model calculation requires accurate data including both site-specific hourly climatic data and pavement parameters. Climatic input data for the model includes hourly solar radiation, hourly air temperature, and daily average wind speed data in an hourly format. Pavement parameters include albedo, emissivity, absorption coefficient, thermal diffusivity, and heat transfer coefficient parameters.

Climate Databases and Hourly Air Temperature Analysis

Solar radiation imputed empirically based on extraterrestrial incident radiation has been commonly used in most pavement temperature modeling efforts including the EICM model. Recently, several more advanced models have been developed to produce more accurate solar radiation data based on satellite images which are available from the National Solar Radiation Database (NSRDB). In this work, hourly solar radiation data modeled using the SUNY model (Perez et al., 2002) or the METSTAT model (Maxwell, 1998) have been used. Those data are generally available and cover nearly all parts of the country from 1990 to 2005.

Daily average wind speed can be directly collected from the Virtual Weather Station program in the Long Term Pavement Performance database. Additionally, daily average wind speed can be obtained directly from the National Climatic Data Center or the meteorological network at each state. Although hourly wind speed is preferred, site-specific hourly wind speed data are difficult to obtain and highly dependent on unknown environmental conditions, making interpolation between locations problematic. Fortunately, the model is not overly sensitive to the wind speed and daily average values work quite well.

Hourly air temperature data are not commonly available in favor of daily maximum and minimum air temperatures, but reasonable estimates of hourly temperatures are needed for accurate temperature calculations. A conventional method to impute hourly air temperatures fits a sinusoidal function to the daily maximum and minimum air temperatures (EICM model, for example). However, the daily profile of air temperature is not exactly sinusoidal. Typically, the time for the air temperature to rise from the daily minimum temperature to the daily maximum temperature is about 9 hours, while 15 hours are taken for the air temperature to decrease from the daily maximum temperature to the daily minimum. In order to provide the model with accurate hourly air temperature data, a time-series analysis was employed (Brockwell and Davis

2002). Accordingly, an imputation method was developed to obtain a local hourly air temperature pattern from limited recorded hourly air temperature data. The pattern was then combined with commonly available recorded daily maximum, minimum, and average air temperatures to interpolate hourly air temperature data. Recorded daily maximum, minimum, and average air temperatures can be obtained easily from the Virtual Weather Station program in the LTPP database or NCDC.

Interpolating Site-Specific Pavement Parameters

In order to obtain good model estimates of pavement temperatures from accurate hourly climate input, numerical values of the pavement parameters need to be determined. Although some parameters are fairly well known (ρ, k, C, e.g.), others require a parameter estimation process. Site-specific model parameters are albedo, emissivity, absorption coefficient, thermal diffusivity, and the parameters a and d in the heat convection coefficient correlation.

The following discussion presents results of a parameter sensitivity analysis, optimization of the pavement parameters using 29 pavement sites widely distributed across the country, an analysis of the distribution of these parameters over a wide range of climatic regions, and interpolation strategies for each model parameter so that at any pavement site across the country reasonable values for the pavement parameters can be estimated. This analysis can be done with one to three months of continuous pavement temperatures, thereby providing a fairly large number of sites for analysis.

Study of Model Parameters' Sensitivities

To assess the sensitivity and importance of each parameter in the pavement temperature prediction model, parameters were varied independently of one another over a range of values based on typical literature values. The temperature average absolute error (model calculation versus reported data) was used as a statistical measure of the model accuracy. The results are presented in Figure 39 where the abscissa scale is different for each parameter with its values shown in the legend.

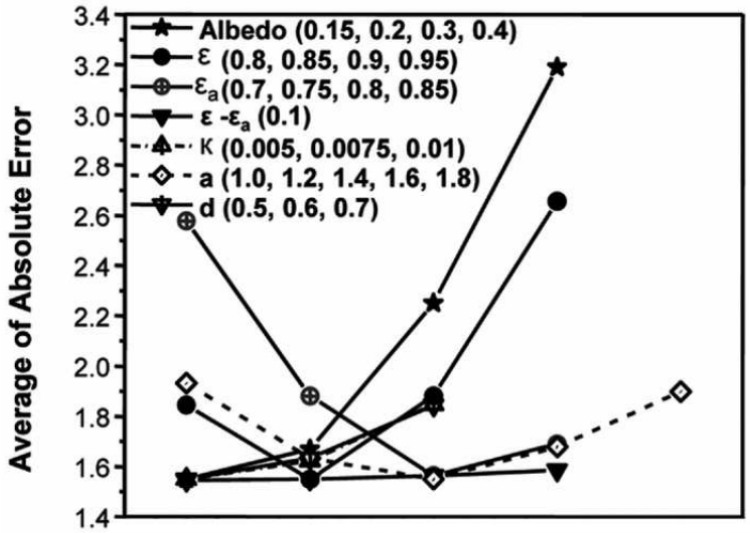


Figure 39. Model Parameters Sensitivity Analysis: Effect of Changing Model Parameters in Their Practical Ranges to Average of Absolute Error of Model Prediction.

As shown in Figure 39, when the albedo increased from 0.15 to 0.4, the average absolute error of the model prediction increased dramatically from about 1.5 to about 3.5 (°C), implying an important role of the albedo in temperature prediction. Similarly, changing the emissivity (from 0.8 to 0.95) or the absorption coefficient (from 0.7 to 0.85) alone induced a significant variation in the model prediction accuracy. Interestingly, although individual changes in the emissivity or the absorption coefficient can significantly affect model accuracy, if both parameters are changed together while keeping the difference between them constant, there is very little effect on the model prediction. We also observe from Figure 39 that the value of thermal diffusivity (κ), *a,* and *d* are relatively less important in terms of their effect on model accuracy. Thus, constant values of these three parameters are suggested. Studies have suggested that different aggregates have slightly different thermal diffusivity, from 0.002-0.01 m^2/s based on reported values on several aggregate types (Highter and Wall, 1984; Mrawire and Luca, 2006). Reported thermal diffusivity of asphalt concrete, made from different aggregate sources, has a range from 0.0035 to 0.015 m^2/s based different measurement techniques (Mrawire and Luca 2006; Luca and Mrawire, 2005). Based on optimization of thermal diffusivity of six pavement sites, a constant value of $0.005cm^2/s$ was selected as a reasonable value for the thermal diffusivity of the pavement. This value also agrees well with values recently reported by others (Luca and Mrawire, 2005). For *a* and *d*, values of 1.4 and 0.5 respectively were used.

Based on these results, it is clear that accurate values for the albedo and the difference between the emissivity and absorption coefficients are important for obtaining a good temperature prediction for each pavement site. Additionally, a value of either the emissivity or the absorption coefficient is required. In what follows, the researchers use the absorption coefficient, recognizing that having its exact value is not critical.

Optimization and Interpolation of Model Parameters

Although albedo, emissivity and the absorption coefficient are site specific, there is no clear understanding of how these parameters vary with climate and pavement properties. To

address this issue, parameter optimization has been conducted for these model parameters at 29 pavement sites across the country by comparing model estimates of pavement temperature to reported measurements. Previous studies (Hermansson, 2004) suggested that albedo and emissivity values in the winter are different from their values the rest of the year. Therefore, in this work, two separate sets of model parameters have been obtained, one set for the winter and one set for the other seasons (represented by summer). From further analysis of the distribution and seasonal variation of those model parameters, interpolation strategies have been developed for each model parameter and are presented below.

The algorithm to find values of the three parameters identified by sensitivity analysis (albedo, difference between emissivity and absorption coefficient, and the absorption coefficient) is straightforward. Each parameter was given a range of values and increments within the range based on literature reports. By examining the ability of each set of model parameters to give the best match between the measured and the calculated pavement temperatures, the optimum set was obtained. As a measure of the model's accuracy, the average hourly absolute difference between the measured and the calculated pavement temperatures was used. Using the average absolute error is preferred to the least-squares error, by which a section with unusual properties receives more weight than a section with more normal properties.

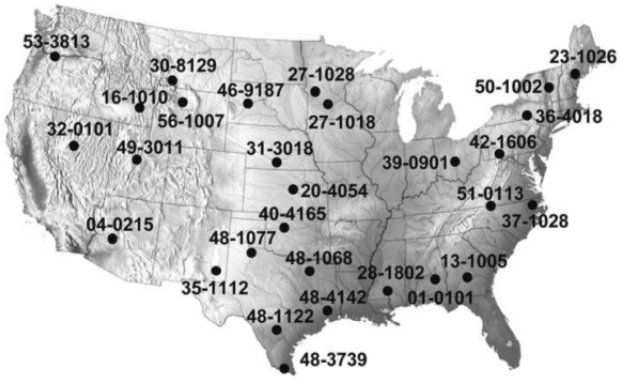


Figure 40. Distribution Map of 29 SMP Pavement Sites Studied (U.S. map courtesy of Tom Patterson).

Twenty-nine pavement sites were selected from the seasonal monitoring program of the long term pavement performance database (Figure 40). Those sites all have at least one month of continuous hourly temperatures measured in both the winter and summer. Model parameters were optimized by examining the ability of each set of model parameters to minimize the average absolute error in temperature in the middle depth of the asphalt layer. Optimized values of those parameters are summarized in Table 27; their distribution across the country is discussed below.

Table 27. Optimized Model Parameters of 29 Pavement Sites across the Country.

LTPP SECTION	STATE	SUMMER				WINTER			
		$\widetilde{\alpha}$	ε	ε_a	$\varepsilon - \varepsilon_a$	$\widetilde{\alpha}$	ε	ε_a	$\varepsilon - \varepsilon_a$
01-0101	Alabama	0.2	0.85	0.75	0.1	0.2	0.85	0.75	0.1
04-0215	Arizona	0.2	0.9	0.7	0.2	0.2	0.85	0.7	0.15
13-1005	Georgia	0.2	0.85	0.75	0.1	0.2	0.85	0.75	0.1
16-1010	Idaho	0.2	0.85	0.7	0.15	0.35	0.85	0.7	0.15
20-4054	Kansas	0.2	0.85	0.7	0.15	0.2	0.85	0.7	0.15
23-1026	Maine	0.2	0.8	0.75	0.05	0.3	0.8	0.75	0.05
27-1018	Minnesota	0.2	0.8	0.75	0.05	0.3	0.8	0.75	0.05
27-1028	Minnesota	0.2	0.8	0.75	0.05	0.3	0.8	0.75	0.05
28-1802	Mississippi	0.2	0.85	0.75	0.1	0.2	0.8	0.75	0.05
30-8129	Montana	0.2	0.9	0.7	0.2	0.35	0.85	0.7	0.15
31-3018	Nebraska	0.2	0.85	0.7	0.15	0.3	0.85	0.7	0.15
32-0101	Nevada	0.2	0.85	0.7	0.15	0.2	0.85	0.7	0.15
35-1112	New Mexico	0.2	0.85	0.7	0.15	0.2	0.85	0.7	0.15
36-4018	New York	0.2	0.9	0.75	0.15	0.35	0.85	0.75	0.1
37-1028	North Carolina	0.2	0.8	0.75	0.05	0.2	0.8	0.75	0.05
39-0901	Ohio	0.2	0.8	0.75	0.05	0.3	0.8	0.75	0.05
40-4165	Oklahoma	0.2	0.8	0.7	0.1	0.2	0.8	0.7	0.1
42-1606	Pennsylvania	0.2	0.9	0.75	0.15	0.3	0.85	0.75	0.1
46-9187	South Dakota	0.2	0.9	0.7	0.2	0.35	0.9	0.7	0.2
48-1068	Texas	0.15	0.85	0.7	0.15	0.15	0.85	0.7	0.15
48-1077	Texas	0.2	0.85	0.7	0.15	0.2	0.85	0.7	0.15
48-1122	Texas	0.15	0.85	0.75	0.1	0.15	0.85	0.75	0.1
48-3739	Texas	0.15	0.85	0.75	0.1	0.15	0.85	0.75	0.1
48-4142	Texas	0.15	0.85	0.75	0.1	0.15	0.85	0.75	0.1
49-3011	Utah	0.2	0.9	0.7	0.2	0.35	0.85	0.7	0.15
50-1002	Vermont	0.2	0.8	0.75	0.05	0.35	0.8	0.75	0.05
51-0113	Virginia	0.2	0.8	0.75	0.05	0.2	0.8	0.75	0.05
53-3813	Washington	0.2	0.85	0.75	0.1	0.35	0.85	0.75	0.1
56-1007	Wyoming	0.2	0.9	0.7	0.2	0.35	0.85	0.7	0.15

Albedo. Figure 41 shows the distribution of the optimized albedo values across the country at the 29 pavement sites for both summer and winter. As seen in Figure 41a, the summer optimized albedo values for most of the pavement sites are constant at 0.2, with a slight variation from 0.2 to 0.15 in several pavement sites in Texas. In the winter (Figure 41b), the optimal albedo values in the southern part of the country are the same as in the summer, while the albedo values in the north increased from 0.2 to from 0.3 to 0.35. Similar observations and conclusions have been reported in the literature (Hermansson, 2004; Kleinand and Julienne, 2002).

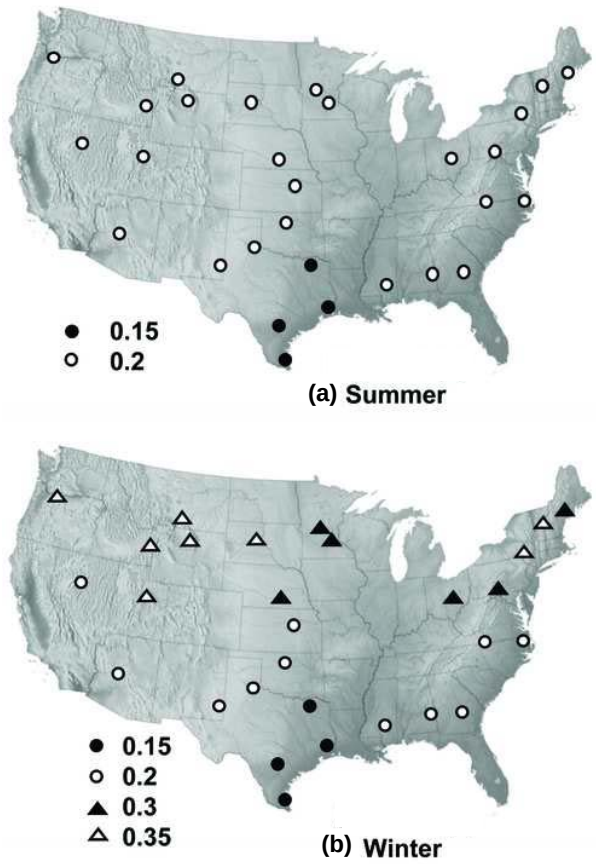


Figure 41. Distribution of Optimized Albedo Values: (a) Summer; (b) Winter (U.S. Maps Courtesy of Tom Patterson).

Although the exact reason for the albedo increase in the winter in the north is not clear, it seems that changes to the pavement surface, associated with the snow coverage and freeze state in the winter, likely is a key. This hypothesis is supported by comparing the optimized winter albedo values on a national snowfall or freeze state distribution map, published at NCDC online and based on the average of recorded data from 1961 to 1990 (NCDC, 2005). It seems that the seasonal albedo variation of pavement is more affected by the freeze state and snowfall, and less affected by other environmental factors and material properties of the pavement.

To interpolate albedo values at other pavement sites, a reasonable approach is to separate the northern and southern parts of the country according to the snowfall distribution map. As the albedo value in each region is quite stable in either the winter or summer, the value for the nearest pavement site in the same region, based on the 29 pavement sites studied in the work, can be adopted as the albedo value for the specific pavement site. Alternatively, the albedos for the nearest three pavement sites in the same regions can be averaged to obtain the albedo for the pavement of interest.

Because snowfall and freeze conditions vary with time, one question is how to determine winter versus non-winter periods. Ground albedo values have been recorded daily or monthly

during winter snow coverage and freeze than during other periods. Satellite recorded albedo values, although not specifically for pavements, have been collected in several databases that can be easily accessed (such as NCDC or NSRDB). For any specific pavement site and year of interest, recorded albedo data from these databases at the nearest location can be extracted. The winter period suggested by high albedo values in those databases may then be used to define the winter period for pavement calculations.

Algebraic Difference between Emissivity and Absorption Coefficient. The second important model parameter is the algebraic difference between the pavement emissivity and absorption coefficient. Figure 42 shows the optimized values of the parameter for the 29 national pavement sites on a national terrain map in both summer (Figure 42a) and winter (Figure 42b). Four different values were obtained, 0.05, 0.1, 0.15, and 0.2, and distribution patterns that follow climatic regions can be noted. Region A covers the northeast and east north central regions and generally experiences a humid climate with long winters. The optimized value for the algebraic difference in this region generally is 0.05. Region B, the southeast areas and part of the south is located in a mesothermal zone with humid sub-tropical climate. An optimized value of 0.1 is common for pavement sites in this region. In the absence of sufficient data to show otherwise, we also hypothesize that the west coast climates can be included in Region B and one data set supports this hypothesis; measured temperatures along this coast are sparse. Region D covers the western part of the country, especially mountain regions and a dry, cold climate is dominant. Here a value of 0.2 was generally obtained in the winter while in the summer a value of 0.15 was obtained. Region C is a transition zone between Regions B and D, and a value of 0.15 was commonly obtained, both winter and summer. Despite several slight deviations, the optimized value for the algebraic difference in most of the pavement sites followed these general trends reasonably well.

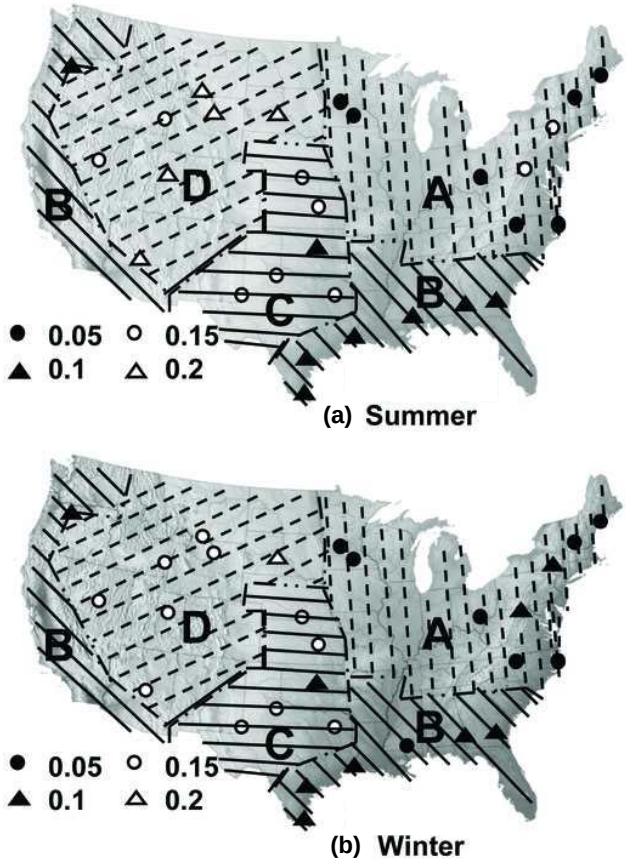


Figure 42. Distribution of Optimized Values of the Algebraic Difference between Emissivity and Absorption Coefficient: (a) Summer, (b) Winter (U.S. Maps Courtesy of Tom Patterson).

Previous studies have suggested that the absorption coefficient is mainly affected by the water partial pressure in the air. A linear relationship between absorption coefficients with partial pressure in a clear sky have been further developed using linear regression techniques (Viswanadham and Ramanadham, 1970). It also has been known that the long-wave emissivity of a pavement is mainly affected by the pavement surface property and environmental conditions (Kleinand and Julienne, 2002). From this perspective, it is not surprising to see that the optimized values of the algebraic difference between the emissivity and absorption coefficients varies from winter to summer at pavement sites in Region D, most likely due to climate effects. As emissivity also is affected by site-specific pavement surface properties, small deviations from the general trends of the climatic regions are reasonable.

With a known pavement location, values of the difference between the emissivity and absorption coefficient for any pavement site in each region can be approximated based on the above observed trends. Alternatively, to consider possible deviations from the general trends caused by different pavement material properties, parameter values obtained from the nearest three pavement sites (of the 29 sites studied in this work) and in the same climatic region, can be averaged to obtain a value for the specific pavement site.

Absorption Coefficient. The third important parameter is the absorption coefficient for down-welling long-wave 1radiation from the air. Figure 43 shows the estimated value of the absorption coefficients for the 29 pavement sections. Two values of the absorption coefficient, 0.75 in the east and south (and northwest) coastal regions and 0.7 in the drier Midwest to west regions were observed. As the absorption coefficient is mainly affected by the water partial pressure in the air, optimized values match quite well with national relative humidity distribution based on average recorded data from 1961 to 1990 (NCDC 2005). The optimized values in both winter and summer are the same, indicating the parameter is less affected by seasonal variation.

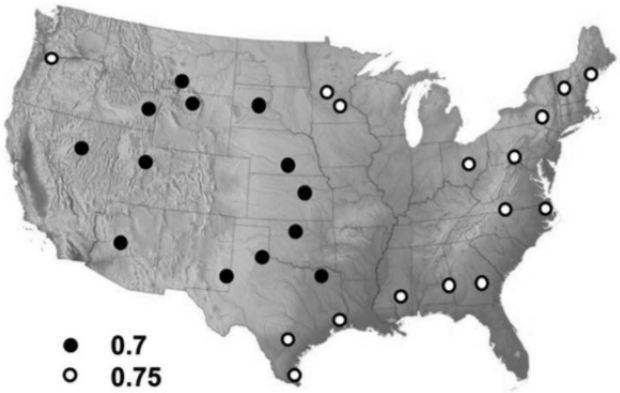


Figure 43. Distribution of Optimized Values of Absorption Coefficient (U.S. Map Courtesy of Tom Patterson).

Based on the 29 pavement sites studied in this work, values of the absorption coefficient at other pavement sites can be interpolated from their values at the nearest pavement sites in the same humidity region, obtained from the national humidity map.

MODEL VALIDATION AND APPLICATION

To demonstrate the process of obtaining hourly climatic data input and model parameters and to validate the accuracy of proposed pavement temperature models over an entire year, two distinct LTPP SMP sites were selected for inclusion in this study: pavement 48-1068 in Lamar, Texas, and pavement 27-1028 in Otter Tail, Minnesota. These sites are among the very few with hourly temperature data for an entire year, and as a function of depth, and they represent two very different climates. Pavement temperatures at those two pavement sites were calculated based on the above proposed procedures and then compared to field measured temperatures. The average absolute error between hourly predicted temperatures and measured temperatures was used to indicate the accuracy of model prediction.

Lamar, Texas, Pavement Site 48-1068

A complete record of measured hourly pavement temperatures was only available in 1994 in the LTPP database for pavement site 48-1068 and so pavement temperatures for that year were modeled and then compared to the measured data. The calculation started with collecting climatic data, including hourly solar radiation, ambient air temperature and wind speed. In the NSRDB, hourly solar radiation data were listed by state and site name. Although solar radiation

data for the Lamar site were not available, solar radiation data from a nearby site (Denison, 62 miles from Lamar) were available and were used instead. Daily maximum and minimum air temperatures recorded at the LTPP database were extracted and then combined with the daily air temperature pattern (developed using a time series analysis method based on limited recorded hourly air temperature data at the nearest weather station) to obtain required hourly air temperature data. Daily average wind speed data at the pavement site were obtained directly from the LTPP database (Virtual Weather Station).

Values of model parameters were then estimated from the parameter map with interpolation. For pavement site 48-1068, an albedo of 0.15 (the albedo value at the nearest pavement site 48-4142), a algebraic difference between emissivity and absorption coefficients of 0.1 (the value at the nearest pavement site in climate region C, 40-4165), and an absorption coefficient of 0.7 (the value at the nearest pavement site in the same humidity zone, 40-4165) were selected as constants throughout the year.

With estimates for these model parameters determined, pavement temperatures were calculated using the temperature model at three different depths of 25 mm, 128 mm and 232 mm below the surface. Figure 44(a) shows a sample visual, qualitative comparison of the calculations to the field measured temperatures over the one-year study period at 25 mm depth. An expanded comparison of the first two weeks in March was also provided. These comparisons, while falling short of a detailed quantitative comparison, demonstrate visually the ability of the model to capture daily and yearly pavement temperature fluctuations. Statistically, the average absolute error between the measured and predicted temperatures for the entire year is 2.4°C at 25 mm below the surface, 2.0°C at 128 mm below the surface, and 2.2°C at 232 mm below the surface.

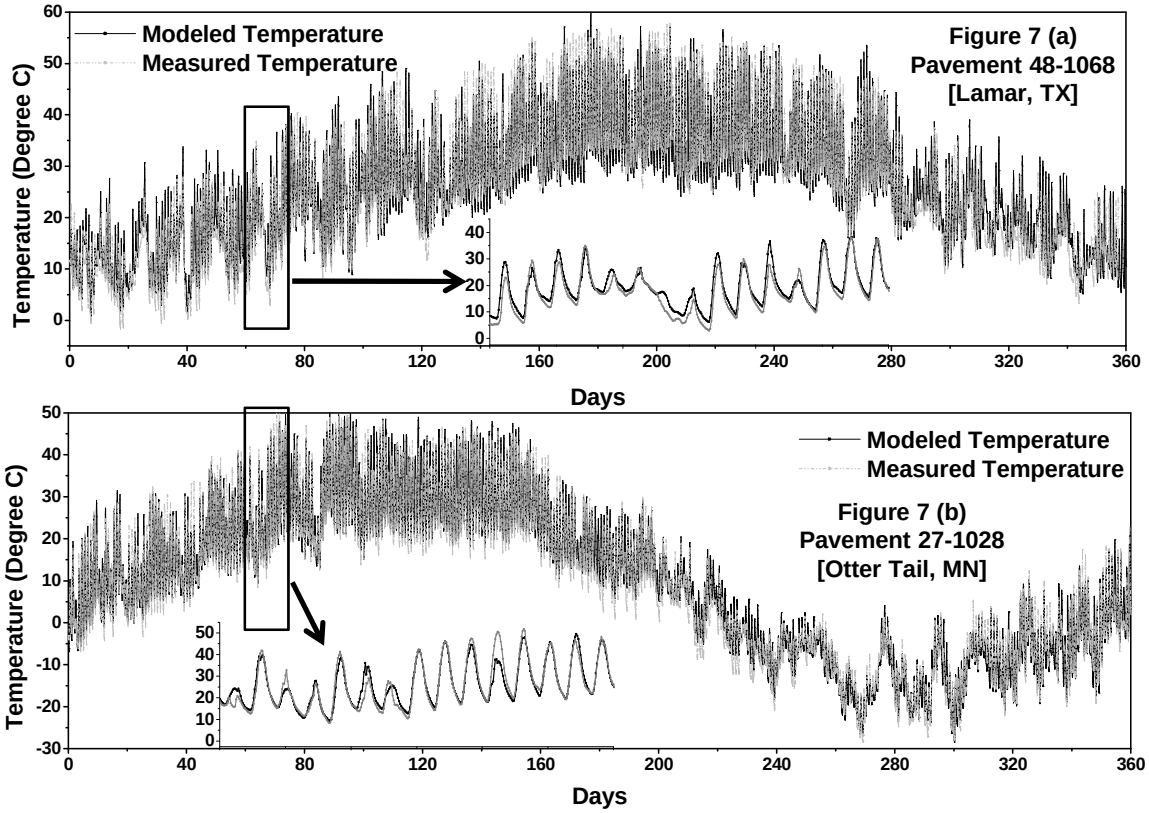


Figure 44. Comparison of Model Predicted Annual Hourly Pavement Temperature and Field Measurement at 25 mm below the Surface: (a) Pavement 48-1068 (Lamar, Texas); (b) Pavement 27-1028 (Otter Tail, Minnesota).

Otter Tail Minnesota, Pavement Site 27-1028

A complete record of measured hourly pavement temperatures was available in the LTPP database at this site only from April 1996 to March 1997, so pavement temperatures during that period were modeled and compared to measured data. The procedure to obtain hourly climatic data and model parameters for the Otter Tail, MN, pavement is quite similar to that for Lamar, TX, except that the procedure uses two sets of model parameters because model parameters in the winter differ from the values obtained for the summer. The parameter values, determined from the nearest pavement site 27-1018, were: albedo 0.3, algebraic difference between emissivity and absorption coefficients 0.05, and the absorption coefficient 0.75. In the summer, those parameters differ significantly from the winter values: albedo 0.2, difference between emissivity and absorption coefficients 0.05, absorption coefficient 0.75. The winter period, when the winter set of parameters needs to be used, was determined directly as the time when a high albedo value was recorded in NSRDB. At Fergus Falls (32 miles away from Otter Tail) from 1996 to 1997, a high albedo value was obtained only during January 1996 and January 1997. Therefore, for the one-year period April 1996 through March 1997, the winter set of parameter values were used only during January 1997.

With these estimates for the model parameters, pavement temperatures were calculated using the temperature model at three different depths of 25 mm, 115 mm, and 205 mm below the

surface. Figure 44(b) shows a sample comparison of the calculations to the field measured temperatures at pavement depths of 25 mm. An expanded comparison of the first two weeks in June was also provided. These comparisons, while falling short of a detailed quantitative comparison, demonstrate visually the ability of the model to capture daily and yearly pavement temperature fluctuations. Statistically, the average absolute error between the measured and predicted temperatures is 1.8°C at 25 mm below the surface, 2.0°C at 115 mm below the surface, and 1.9°C at 205 mm below the surface.

In general, while the model cannot exactly reproduce the measured pavement temperature profiles, it works quite well for those two sites. Statistically, only 1.3 percent of the calculations have an error as large as 10°C while 46 percent of the calculations have an error less than 2°C based on the yearly comparisons. Further improvements to the model should incorporate heat transfer enhancement by precipitation or the effect of moisture freeze and thaw in the pavement. Although yearly pavement profiles at depths below 25 mm are not shown in the figure, for these two sites, it is noted that the amplitude of the daily temperature fluctuations attenuates with depth, while the daily average temperature is about the same at different depths.

SUMMARY

An accurate model for pavement temperature prediction is critical in the study of asphalt material properties and pavement performance. This work provides a general tool to obtain accurate hourly pavement temperature as a function of depth at any desired pavement site for various applications, especially for calculations of pavement oxidation where fairly accurate results are required. To this purpose, an improved one-dimensional model was developed to predict pavement temperature nationwide based on heat transfer fundamentals. The model employs commonly recorded hourly solar radiation, daily average wind speed, and interpolated hourly air temperature as climate input data. Three key site-specific model parameters were identified and national distribution of their values correlates with climatic patterns, suggesting possible interpolation strategies based on climate. The temperature model, proposed data sources and interpolated model parameters provided calculations that agreed well with experimental measurements, suggesting a general approach to predict pavement temperature nationwide with acceptable accuracy. This model provides a powerful tool for engineers for pavement design, performance modeling, and pavement durability.

CHAPTER 7. A TRANSPORT MODEL OF ASPHALT BINDER OXIDATION IN PAVEMENTS

[Pages 121 through 134 reprinted with permission from Prapaitrakul N., Jin X., Han R., and Glover, C. J. (2009) A Transport Model of Asphalt Binder Oxidation in Pavements. *Road Materials and Pavement Design*, Vol 10 (Special Issue), pp. 95-113. Copyright 2009. Reproduced by permission of Taylor & Francis Group, LLC. (http://www.tandfonline.com).]

ABSTRACT

Field evidence is mounting that asphalt binder oxidization in pavements produces a binder that is more susceptible to thermal and fatigue cracking. While the fundamentals of this oxidation process are fairly well known, predicting quantitatively the rate of oxidation, and as a function of depth in the pavement, is not straightforward. A thermal and oxygen transport model, coupled with binder reaction kinetics, provides the basis for such calculations. A one-dimensional thermal transport model, coupled with site-specific model parameters and recent improvements in the availability of required input climate data, enables calculation of pavement temperatures throughout the year, which then is used in an asphalt binder oxidation and transport model to calculate binder properties in the pavement over time. Calculated binder property changes with depth and time are compared to measurements of binder oxidation in the field.

INTRODUCTION

Asphalt Aging in Pavements

Several studies have been conducted to explore basic binder oxidation chemistry (Lee and Huang, 1973; Lau et al., 1992; Petersen et al., 1993). From these reports, after an early, fast-rate period, the carbonyl compounds are formed at a rate that is a function of temperature and oxygen partial pressure. Liu et al. (1996) also found that the basic carbonyl reaction rate can generally be described using an Arrhenius expression for temperature variation and pressure dependence as given in Eq. 7-1:

$$\frac{dCA}{dt} = r_{CA} = AP^{\alpha} \exp\left(\frac{-E_a}{RT}\right) \tag{7-1}$$

where A is the frequency (pre-exponential) factor, P is the absolute oxygen pressure, α is the reaction order with respect to oxygen pressure, E_a is the activation energy, R is the gas constant, and T is the absolute temperature. Values of A, E_a, and α are very asphalt dependent, though A and E_a are generally correlated (Liu, et al., 1996; Domke et al., 2000).

Asphalt binder oxidation in pavements has been proven to be an ongoing process throughout a pavement's service life. Also, there is evidence that demonstrates that oxidation occurs through the depth of the pavement and has a significant effect on pavement performance (Glover et al., 2005; Al-Azri et al., 2006). Understanding the nature of the oxidation process and being able to predict the level of oxidation that occurs in pavements as a function of time and

depth are critical to pavement design improvement that will provide the greater pavement durability.

The most important consequence of asphalt binder oxidation in pavements is oxidative hardening. As non-asphaltene polar aromatic compounds in asphalt binders oxidize, they become asphaltenes, associated species that act like solid particles suspended in the asphalt, thereby producing an increase in asphalt elastic modulus and viscosity (Martin et al., 1990; Lau et al., 1992; Lin et al., 1995; Domke et al., 1999). Consequently, the performance of pavements is affected directly by asphalt binder oxidative hardening. Several studies by Walubita et al. (2005a, 2005b, 2006a, 2006b, and 2006c) indicate that oxidation of asphalt binder in pavements leads to a decline in pavement fatigue resistance. Woo et al. (2007) show that this decline in fatigue resistance leads to a dramatic decline in pavement service life.

Also, low levels of accessible air voids in pavements potentially relate to binder oxidation (Woo et al., 2007). As they report, when pavements have sufficiently high accessible air voids (great than 4 percent), the oxidation rate is largely determined by the temperature in the pavement. On the other hand, when the level of accessible air voids in the pavement is considerably lower (less than 2 percent), the hardening rate of binders in pavements is reduced significantly.

In order to understand the complex pavement asphalt oxidation process, researchers have analyzed asphalt samples and proposed empirical asphalt oxidation (aging) models (Brown et al., 1957; Lau, 1991; Lau et al., 1992). However, these proposed models do not include the effect of oxygen transport limitations (diffusion) into the asphalt binder. Lunsford (1994) proposed a preliminary oxidation model with the oxygen diffusion effect included. However, the study used approximate values for diffusivity and did not include the effect of fines and aggregate on diffusion. In addition, previous work has not implemented a pavement temperature model that provides temperature as a function of depth. Thus a thermal and oxygen transport model, necessary for accurate predictions of binder oxidation in pavements, has not yet been developed.

Pavement Temperature Model

One key environmental factor that influences asphalt pavement design and performance is pavement temperature, which varies with pavement site, time (day and seasonal) and depth. Accurate representation of pavement temperature is extremely important, particularly in predicting pavement performance such as thermal cracking and oxidative aging, issues that are highly sensitive to pavement temperature. The reaction kinetics of asphalt oxidation follow an Arrhenius activation energy relation; oxidation rates decrease exponentially with increasing inverse absolute temperature (Lin et al., 1996). Thermal stress induced by rapid low-temperature changes has been widely accepted as the main cause of thermal cracking of asphalt pavement.

Many measurements of pavement temperature variations over time and depth have been reported in the literature. Also, fundamental early models of heat transfer in pavements, involving shortwave solar radiation, down-welling and upwelling long-wave radiation, and convective heat transfer at pavement surfaces and heat conduction inside the pavement have been thoroughly discussed (Rumney and Jimenez, 1969; Dempsey, 1970; Solaimanian and

Kennedy, 1993). Following these endeavors, a one-dimensional coupled heat and moisture simulation model, the enhanced integrated climate model was developed and later integrated into the current mechanistic empirical pavement design guide to couple pavement design with modeled pavement temperature (Lytton, 1989).

The model uses a finite difference approximation for calculating heat conduction within the pavement and underlying layers, subject to heat fluxes at the surface (shortwave solar radiation, long-wave radiation, and convective heat transfer) and a constant-temperature boundary condition well below the pavement. Using required climatic input data including solar radiation, ambient temperature and wind speed, and constant model parameters such as albedo, emissivity, and thermal diffusivity, the model is solved numerically to obtain temperature as a function of time and depth.

Although temperatures predicted with the EICM model satisfy pavement design needs in general, there have been some large errors when compared to measured pavement temperature (Ahmed et al., 2005). These errors are most likely caused by several factors: the assumption that heat fluxes at the pavement surface are exactly balanced by conduction into the ground well below the surface, inaccuracy of climatic data (especially calculated solar radiation), plus the assumptions of the constant temperature boundary condition and site-independent model parameter values.

Recently, significant improvement over the EICM model has been achieved by several groups using a similar one dimensional heat transfer model but with an unsteady-state surface heat flux boundary condition, measured model input data, and site-specific model parameters that were optimized based on measured pavement temperatures (Gui et al., 2007; Hermansson, 2000; Hermansson, 2004).

OBJECTIVES

The objective of this study is to develop an improved model to predict the oxidation rate of binders in pavements with the input of binder kinetics data, temperature profile of the pavement, and mixture characteristics such as average distance between air void pores. The specific objectives of this study are:

- To analyze air void characteristics in pavements to categorize the mixture parameters used in this study.
- To improve the existing oxidation model based on the knowledge of oxidation kinetics, air void characteristics in pavement, oxygen diffusion into asphalt binders, and improved pavement temperature models.
- To estimate important parameters of the proposed oxidation model by using field oxidative aging data.
- To develop a protocol and procedures for the proposed oxidation model to estimate real pavement oxidation rates using binder kinetics, oxygen diffusivity, pavement temperature profiles, and air void characteristics of the pavements.

METHODOLOGY

Analyzing Air Void Structure in the Pavement

A crucial element of the binder oxidation model developed in this study is the influence of accessible air voids on the pavement oxidation process. Cores obtained from field sites were analyzed for air voids (either by the Corelok or the saturated surface dry methods-SSD), interconnected air voids (by X-ray CT) or accessible air voids (by Corelok or SSD). Corelok operating procedure can be found in the Operator's Guide (Instrotek Inc., 2001). Then the binder was extracted and recovered using methodologies developed by the researchers (Burr, et al., 1990; Burr et al., 1991; Cipione et al., 1991; Burr et al., 1993; Burr et al., 1994). The recovered binder was then analyzed for oxidation by infrared spectroscopy (FT-IR) and for physical properties by dynamic shear rheometry (DSR) to provide the binder aging and hardening rates corresponding to level of air voids in the pavements.

Another important component to verify the oxidation model is the air voids characteristic of pavement samples. X-ray computed tomography and image analysis techniques are used to examine the internal microstructure of HMAC mixtures, including air void distribution and interconnectivity and binder content and distribution in terms of film thickness. These factors are some of the HMAC mixture parameters to be identified in terms of the role they play in the aging mechanism. X-ray CT is a nondestructive technique used to visualize the interior characteristics of opaque objects. An X-ray source emits a beam of known intensity through the specimen, and a detector on the opposite side of the specimen measures the attenuated beam intensity. The specimen rotates 360° with respect to its center and moves at a specific fixed vertical interval to enable evaluation of the entire specimen volume. Then, a macro developed using the IPBasic capabilities of Image-Pro® Plus software can be used to process and analyze the X-ray CT images (Al-Omari et al., 2002) in terms of air void size, number, and average overall percent. Based on a user-input grayscale threshold, the macro transforms the original images into black-and-white compositions with black representing AV and white representing the solid materials (binder and aggregate). The appropriate threshold value is obtained by matching the measured average percent AV to that output by the macro.

CoreLok is used for determining total air voids of core specimens as a necessary calibration of gray scale for the X-ray CT method. As validation of the X-ray CT method, CoreLok has been used to determine accessible air voids (AAV) (those that water can penetrate when the CoreLok vacuum bag is opened underwater).

Binder Oxidation Model Development

The model proposed by Lunsford is a one-dimensional thin-film geometry in Cartesian coordinates. In addition, this model does not include the effect of air voids and mixture morphology on the oxidation rate determination.

In order to understand oxidation phenomena in pavements, an improved model to predict the oxidation rate with the input of binder kinetics data, temperature profile of the pavement, and mixture characteristics was developed in this study.

The oxygen transport limitations are also important in establishing binder hardening rates in pavements. If the interconnected (or accessible) air voids are sufficiently low, then delivery of oxygen to the binder is hindered.

An improved pavement oxidation transport model was based on three interlinked processes: 1) diffusion of oxygen into the asphalt binder mastic in the pavement, 2) heat transfer into the pavement that results in temperature variations with depth and time, and 3) asphalt binder oxidation, which is a function of oxygen concentration and temperature in the binder. A fourth issue that affects the oxygen transport and concentration is the air voids distribution in the mixture because it affects the availability of oxygen to the binder. The diffusion process is coupled to both temperature and the level of oxidation because both of these factors affect oxygen diffusivity.

The concept of approximating the binder film in the pavement as a thin film is probably reasonable for high air voids content where there are a large number of pores passing through the pavement so that the distance from any pore to the binder, even to the farthest binder away, is not very far. A more realistic model for a reduced number of air voids might be a cylindrical model that assumes that the oxygen diffuses from the pore in a radial direction into a cylindrical shell of binder (Figure 45). In this case, the relevant parameter would be the thickness of this cylindrical shell, relative to the diameter of the pore containing the air. The smaller the air voids, the greater the ratio of this binder shell to the pore diameter and thus the more time required for oxygen to diffuse through the binder.

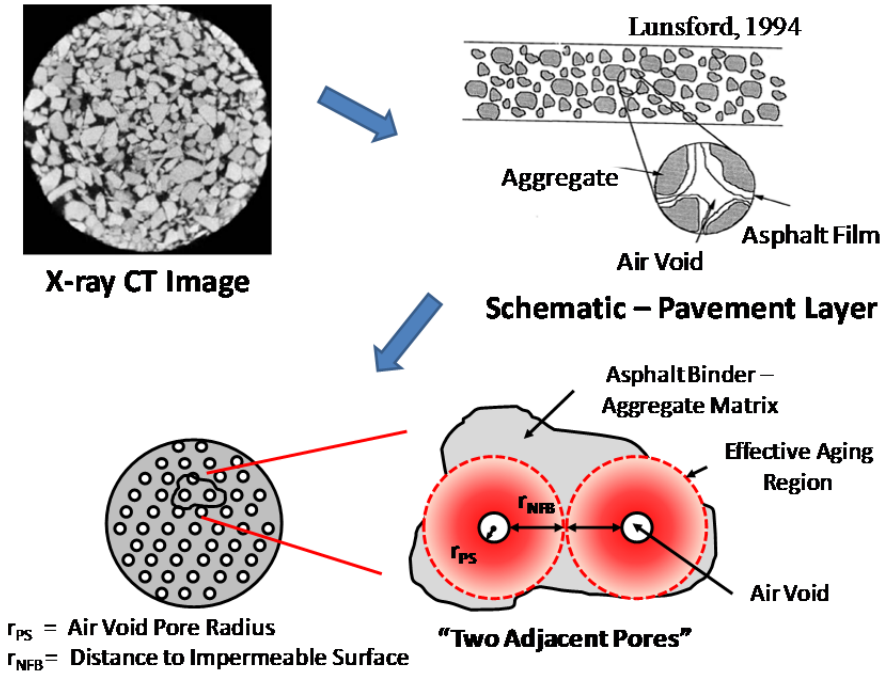


Figure 45. Modeling Concept of Asphalt Binder Oxidation in Pavements.

Eq. 7-2 expresses a mathematical equation accounting for oxygen diffusion and reaction in a differential volume (Bird et al., 2001):

$$\left(\frac{\partial C_{O_2}}{\partial t}\right) = -\nabla \cdot N_{O_2} - r_{O_2} \tag{7-2}$$

In asphalt, the molar flux of oxygen, N_{O_2}, can be expressed by Fick's first law of diffusion as given in Eq. 7-3:

$$N_{O_2} = -\mathcal{D}_{O_2} \nabla C_{O_2} \tag{7-3}$$

Lunsford (1994) combined the mathematical model of asphalt oxygen diffusion and reaction described above and Fick's law of diffusion to propose a one-dimensional diffusion and reaction model in a flat thin asphalt film. However, to obtain oxygen partial pressure profiles in the pavement oxidation model, the PDE system was solved for the oxygen partial pressure as a function of time and distance away the from air void-binder interface in a cylindrical coordinate system. In principle the oxygen partial pressure profile can be used to calculate CA and viscosity profiles and histories in the pavement, which then can be combined with an appropriate performance model to estimate pavement durability and performance, taking into account binder oxidative hardening. With this modeling concept, the PDE system and boundary conditions can be written as follow:

$$\left(\frac{\partial P}{\partial t}\right) = \frac{1}{r}\frac{\partial}{\partial r}\left(r\mathcal{D}_{O_2}\frac{\partial P}{\partial r}\right) - \left(\frac{cRT}{h}\right) r_{CA} \tag{7-4}$$

$\left(\frac{\partial P}{\partial r}\right) = 0$	at	$r = r_{NFB}$	No Flux Boundary
$P = P_{\text{gas}}$	at	$r = r_{PS}$	Air Void Surface
$P = 0$	at	$t = 0$	Initial Condition

where c is an experimental constant and h is the Henry's law constant.

In Eq. 7-4, $\mathcal{D}_{O_2}$ is an unknown and needs to be estimated. Reid et al. (1983) provides a model relating diffusivity to viscosity and temperature as given in Eq. 7-5:

$$\mathcal{D}_{O_2} = \mathcal{D}_0 \left(\eta_0^*\right)^B \tag{7-5}$$

In Lunsford's study, $\mathcal{D}_0$ and B were estimated and reported.

Lau et al. (1992) show that viscosity and carbonyl content are related by Eq. 7-6:

$$\eta_0^* = \exp\{HS \cdot CA + m\} \tag{7-6}$$

where *HS* is asphalt hardening susceptibility and *m* is an experimental parameter. *HS* and *m* are functions of temperature. Carbonyl content represents the level of oxidation of the binder and increases at rate r_{CA} so that the amount of oxidation can be represented by Eq. 7-7:

$$CA(t) = \int_0^t r_{CA}\, d\theta + CA_0 \tag{7-7}$$

where CA_0 is an integration constant and could be determined from experimental data.

Work has proceeded toward developing a combined heat and mass transport model for reaction of binders in compacted mixtures and pavements. Issues are the relative importance of diffusion and reaction rates in the binder as well as the accessibility of oxygen to the binder from the porous structures of the mixtures. The model that is being developed is conceived to provide oxygen to the binder radially from pores that pass through the mixture. The oxygen diffusivity in this model can be referred to as an effective diffusivity, D_e, which is described as a function of the actual oxygen diffusivity in the asphalt binder, the asphalt volume fraction (ε), and the tortuosity (τ). In this discussion, the asphalt volume fraction is the volume fraction occupied by asphalt binder in the mixture, and the tortuosity is the ratio of the oxygen diffusion path to the distance between two air voids. The presence of aggregate that forces a tortuous path for the oxygen, thereby producing a reduced effective diffusivity, complicates the model. The extent to which diffusion resistance slows the oxidation process relates directly to the ratio of the oxidation rate to the diffusion rate. The effective diffusivity can be expressed as follow (Basmadjian, 2004):

$$\mathcal{D}_e = \mathcal{D}_{O_2}\left(\frac{\varepsilon}{\tau}\right) \tag{7-8}$$

The model is essential to guiding the efficient and effective use of both laboratory and field mixture aging data for assessing the rate of binder hardening in pavements and its impact on pavement durability.

RESULTS AND DISCUSSION

Outputs from the Binder Oxidation Model

Figure 46 shows typical results from model calculations.The binder used for these calculations is an Ampet AC-20. The model cylindrical shell was 1 mm thick, spanning from a radius of 0.5 to 1.5 mm, and aging was simulated at a constant temperature of 333.3 K for 90 days to estimate the size of the effect of aging on viscosity ad diffusivity. The pore surface (PS) refers to the air void-binder interface, whereas, the no-flux boundary (NFB) refers to the surface of the radius at the half distance between two adjacent air voids.

Shown in the figure are carbonyl area and viscosity calculation, which were predicted to increase with aging time, and diffusivity, which is shown to decrease with aging time as the binder hardens.

Binder oxidation rates from field pavements in Texas (not shown) compare reasonably well to the calculated oxidation rates. However, additional field data and model calculation comparisons are required to adequately validate the oxidation model.

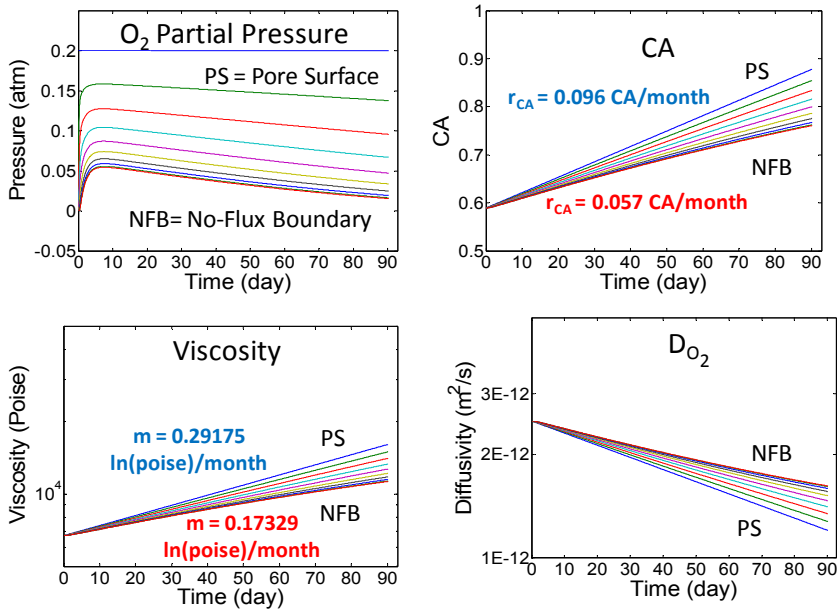


Figure 46. Results from Transport Model of Binder Oxidation in Pavements for Binder Thickness of 1mm at 333.3 K.

Model Parameter Estimation

This section discusses a parameter estimation process that may be used to determine unknown oxidation model parameters from known measured parameters together with measured environmental room mixture aging rates. However, due to the limited kinetics data and air void characteristics for the ER samples, ER aging rates were compared to mixture aging rates calculated using the oxidation kinetics parameters from previous research (and thus for a different binder) to demonstrate the model parameter estimation methodology and a potential important application of the model.

In the parameter estimation process, the results from oxidation model calculations were compared to asphalt mixture (PG 70-22) aging in the ER, at 60°C and 25 percent humidity. Three laboratory mixture replicates were aged in the ER for 9 months, and one core was sampled every 3 months. Then carbonyl area of asphalt binder of each core, which was extracted and recovered by the method previously mentioned, was measured, and the CA aging rate was calculated. The asphalt aging rate obtained from Environmental Room aging exhibits a linear relationship as shown in Figure 47.

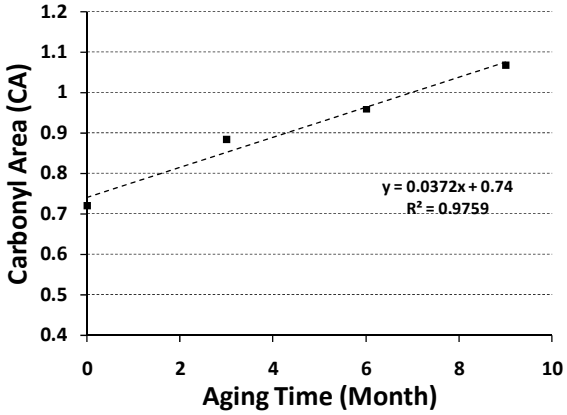


Figure 47. Carbonyl Area Growth of Asphalt Mixture in Environmental Room Aging.

The aging rate obtained was then used to compare to the model calculations, in a least squares optimization sense. In this study, parameter estimation is categorized into two cases.

Case 1: Known Mixture Air Void Characteristics, Unknown Asphalt Kinetic Parameters

Additional parameters needed for the optimization process are the air void characteristics of asphalt mixtures, which are the average air void radius, r_{PS}, and the average half-distance between two air voids (the average distance to the no-flux boundary), r_{NFB}. The difference between r_{NFB} and r_{PS} determines the maximum distance oxygen molecules travel in the asphalt film, which directly affects the oxygen diffusion. The air void spacing can be observed by X-ray CT scan, but the accuracy of the measurement depends on the scanning resolution of the equipment, which can be a time- and resource-consuming process for higher resolution. Figure 4 shows X-ray CT image analysis results of air void radius distribution with depth and the location of air voids at a single depth of the top layer of the core obtained from Highway US 59, Yoakum District, Texas. From the data, r_{PS} and r_{NFB} through the depth of the core were estimated to be approximately 0.87 mm and 1.27 mm, respectively.

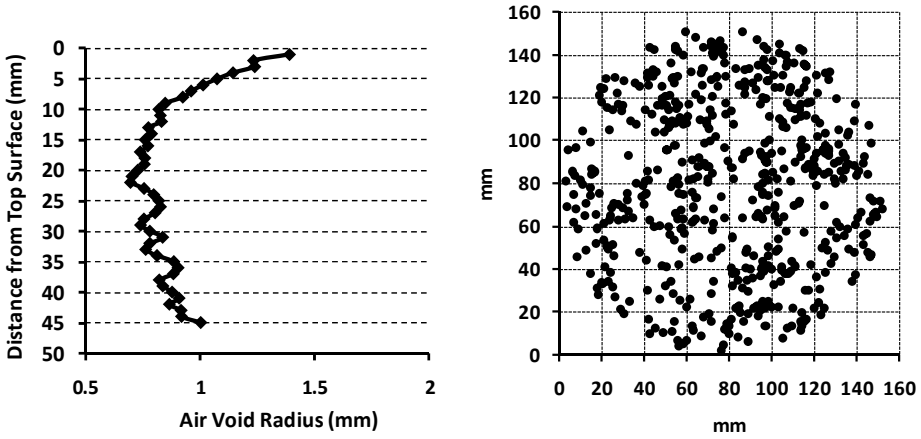


Figure 48. Air Void Radius Distribution and Air Void Coordinate.

From mixture design information, the asphalt volume fraction in the mixture of this study, which is the difference between voids in mineral aggregate (VMA) and air void content in the mixture, was reported to be 0.0735. In this case, the unknown parameters in PDE, equation (7-4), were the binder oxidation kinetics pre-exponential factor (A), activation energy (E_a), reaction order (α), and the mixture tortuosity (τ). The initial values used for parameter estimation were the Ampet AC-20 binder kinetics data reported by Lunsford (1994). After the least squares parameter estimation process, the results for A, E_a, α and τ were estimated to be 1.667×10^5 CA/sec atm^a, 81.1 kJ/mol, 0.285 and 2.33, respectively, as shown in Figure 49. With these estimated values, the least squares difference between the aging rate of model calculation and ER aging was 0.0057. In addition, these estimated kinetics parameters were within the range of kinetics data for asphalt binders reported by Lunsford (1994).

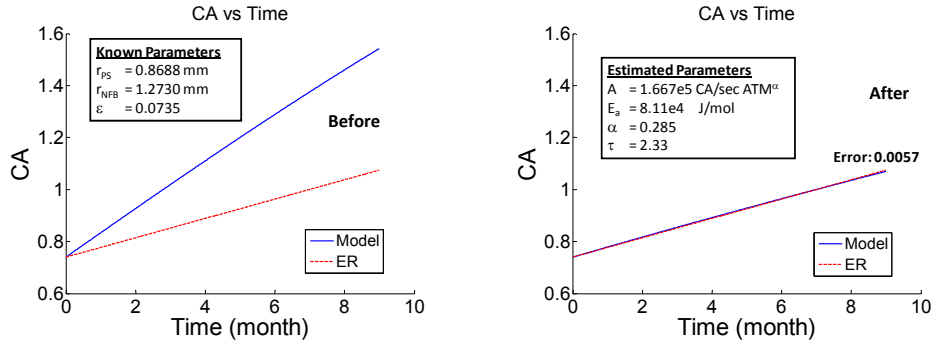


Figure 49. Oxidation Model vs. ER Aging Rate before and after Parameter Optimization Process: Case 1.

The initial values of A, E_a, α and τ used in this estimation were $3.105\text{x}10^4$ CA/sec atm^a, 74.8 kJ/mol, 0.285, and 1, respectively. In order to decrease the carbonyl growth rate of the model to match the ER aging rate, A, E_a, and τ were adjusted to higher values. However, α remained the same as the initial value.

As demonstrated in this estimation process, researchers can use this approach to estimate kinetic information for an asphalt binder when the mixture information and the ER aging rate are known. Then, these estimated kinetics data together with mixture characteristics can be used to calculate field aging rates using the pavement temperature profile.

Case 2: Known Asphalt Kinetic Parameters, Unknown Mixture Air Void Characteristics

In some cases, all asphalt kinetics data were known, but the mixture air void characteristics data were not available. Even though air void data can be determined with an X-ray CT scan, the machine might not be available for all laboratories or district locations. To be able to estimate the air void characteristics without of X-ray CT scanning will enable subsequent asphalt binder oxidation rate calculations in a pavement, when used with the actual real pavement temperature profile and ER aging of field cores.

Figure 50 shows the comparison between oxidation rate from model calculation and ER aging. The missing data, in this case, were mixture characteristic data: namely, r_{PS}, r_{NFB}, ε, and τ.

As for the binder kinetics data, Coastal AC-20 data reported from Lunsford (1994) were used in oxidation model calculation. After least squares estimation process, which had an error of 0.0017, the estimated values of r_{PS}, r_{NFB}, ε, and τ were 0.1375 mm, 3.875 mm, 0.1667, and 2.5, respectively.

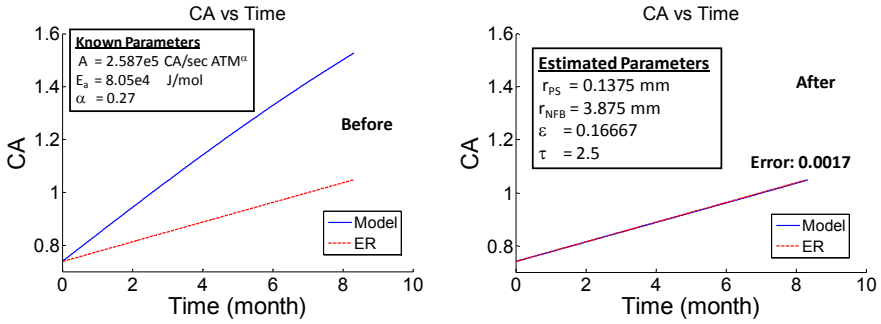


Figure 50. Oxidation Model vs. ER Aging Rate before and after Parameters Optimization Process: Case 2.

The kinetics data of Coastal AC-20 used in this calculation had values of A, E_a, and α as 2.587×10^5 CA/sec atm^a, 8.05 kJ/mol, and 0.266 (Lunsford, 1994). On the other hand, the initial values of mixture characteristic data used in the estimation process were the data for typical dense-graded mixtures obtained from the X-ray CT image analysis process. The set of initial values were 0.87 mm, 1.27 mm, 1, and 1 for r_{PS}, r_{NFB}, ε, and τ, respectively. From the estimation process, as τ and the difference between r_{NFB} and r_{PS} increased, indicating a thicker asphalt film and a longer path for oxygen to travel, the oxidation rate calculated from the model decreased. Also, as ε decreased, the oxidation rate decreased accordingly.

The parameter estimation process and results discussed in the previous section were important examples of how to use the oxidation model at constant temperature to estimate the unknown model parameters. Although the asphalt kinetics data, mixture air void characteristics, and the ER mixture sample were not perfectly matched, the above cases demonstrate the capabilities of parameter estimation coupled with the binder oxidation model. Further analysis using complete and corresponding binder and mixture data will be used to more accurately assess and improve the transport model.

Binder Oxidation Model Calculation Using Temperature Profile from Pavement Temperature Prediction Model

An accurate model for pavement temperature prediction is critical to the study of pavement material properties as well as their changes over time. For example, for the prediction of both binder oxidation and thermal cracking in pavements, pavement temperature as a function of time and depth is crucial. A one-dimensional numerical model has been developed to predict pavement temperature based on heat transfer fundamentals (Rumney and Jimenez, 1969; Demsey, 1970; Solaimanian and Kennedy, 1993). The model employs commonly available hourly solar radiation, daily average wind speed, and imputed hourly air temperature based on site-specific daily pattern derived using time series analysis as climate input data. Three key site-

specific model parameters were identified and the national distribution of their values correlate with climatic patterns, suggesting possible interpolation strategies based on climate. The temperature model, proposed data sources. and methods provided calculations that agreed well with experimental measurements, suggesting a general approach to predicting pavement temperatures nationwide with acceptable accuracy.

Figure 51 shows the hourly pavement temperature profiles generated by the pavement temperature prediction model for SH 21 located in Bryan, TX. Temperature histories for 3 depths, 20, 80, and 160 mm from the pavement surface, are shown for July 1994. Pavement temperatures were estimated for the entire one-year period of 1994 and used in the transport oxidation model to estimate binder oxidation throughout the year as a function of depth.

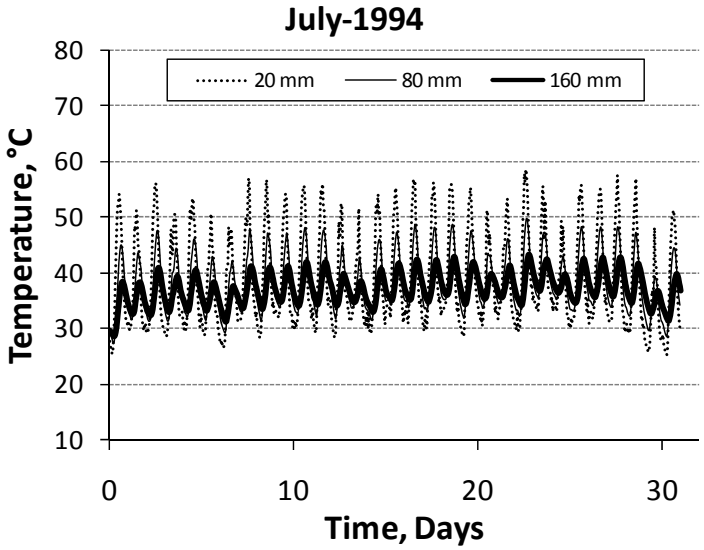


Figure 51. Pavement Temperature Profile for SH 21 in Bryan, TX, during July 1994.

Table 28 summarizes carbonyl area for each of the depths collected at various stations of SH 21 between Bryan and Caldwell from 1989 to 1996 (Glover, 2005). Aging rates of binder from each depth also are shown in the table. The overall aging rates of the top and bottom lifts for SH-21 can be estimated to be 0.05 CA/year. Glover (2005) also reported that asphalt binder used to construct SH 21 pavement was Exxon AC-20, whose binder kinetics data were reported by Domke (2000). However, the information for mixture air void characteristics was not available for this SH 21 pavement. The best available data for mixture air void characteristic at this time was the data from X-ray CT analysis of a comparable dense-graded mixture from US 59 pavement in Yoakum, TX.

Each temperature profile shown in Figure 51 was used in the binder oxidation model calculation, Eq. 7-4. The carbonyl area growth of Exxon AC-20 in the pavement for a one year period from January to December at various depths is shown in Figure 52. According to the oxidation model calculation, asphalt binder aging rates in the pavement were rather slow during spring and winter. On the other hand, the rate increased significantly during the summer due to higher pavement temperatures, as would be expected.

Table 28. Carbonyl Area of the Recovered Binder (Exxon AC-20) from SH 21, TX.

Station	Lifts	Depth Below Surface (in.)	Carbonyl Area			Aging rate (CA/Year)
			1989	1992	1996	
1277	Top	0 - 2	0.94	-	1.31	**0.053**
	Bottom	4 - 6	0.88	-	1.27	**0.056**
1394	Top	0 - 2	0.88	1.04	-	**0.053**
	Bottom	4 - 6	1.11	1.25	-	**0.047**

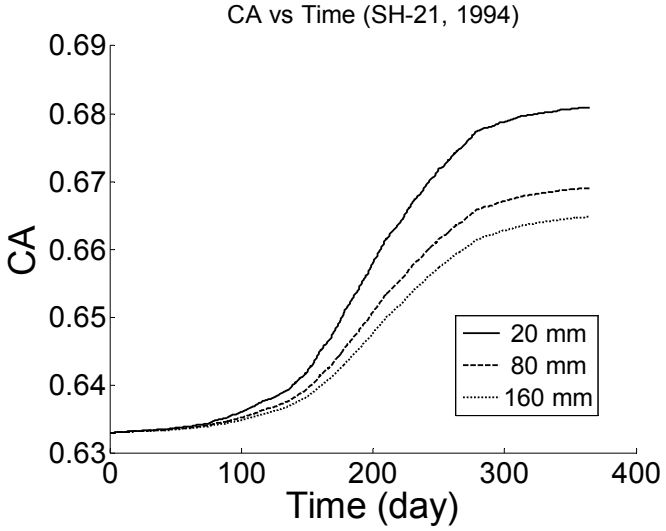


Figure 52. Calculated Carbonyl Area from Binder Oxidation Model at Various Depths.

Also from Figure 52, after one year, the carbonyl area of binder in each depth increased from the initial carbonyl area of 0.633 to 0.681, 0.669, and 0.665 for the depths of 20, 80, and 160 mm, respectively. Thus the aging rates of Exxon AC-20 are 0.048, 0.036, and 0.032 CA/year at the corresponding depths. By comparing these aging rates with the data reported in Table 28, the aging rate from top lifts agreed quite well with the model calculation, whereas the bottom lifts showed higher aging rates than values calculated by the model. The reason why the bottom lift calculation did not match the field measurement might come from the fact that mixture air void characteristic through the depth of pavement used in the model could be slightly different from actual SH 21 pavement structure. The X-ray CT analysis should be performed on the original SH 21 pavement core to obtain a better match of mixture air void characteristic. However, with limited availability of air void characteristic data, the substituted values were able to produce the reasonable aging rates to demonstrate the use of binder oxidation model together with pavement temperature prediction model to calculate the carbonyl area growth of asphalt binder in selected pavement. Further mixture data would certainly improve the accuracy of the binder oxidation model prediction.

SUMMARY

In this study, a binder oxidation model for pavements, which includes the effect of oxygen diffusion and pavement temperature as a function of time and depth, was developed in a

cylindrical coordinate system. Input components for the oxidation model are pavement temperature profile, binder oxidation kinetics and diffusion parameters and mixture air void characteristics. The one-dimensional thermal transport model, coupled with site-specific model parameters and recent improvements in the availability of required input climate data, enables calculation of pavement temperatures throughout the year to a surprisingly reliable extent. The asphalt binder kinetics data were gathered from existing literature, and the mixture air void characteristics were obtained using X-ray CT image analysis. However, when either binder kinetics or mixture parameters were missing, a least squares parameter estimation procedure at constant temperature can be applied to obtain reasonable parameter values. Despite the necessity of acquiring additional binder and mixture data, the binder oxidation model with available input data to date was able to calculate an average asphalt aging rate for a pavement reasonably close to the actual average oxidation rate observed in the field.

This study's essential significance introduces a mixture binder oxidation model as a cornerstone for subsequent research on asphalt oxidation in pavements and to demonstrate its applicability. Additional binder and mixture data are needed to assess the accuracy and validity of the model. Such a model is a critically important tool for pavement design and improvement and for maintenance scheduling.

CHAPTER 8. IMPROVED PAVEMENT OXIDATION MODEL: DEVELOPMENT AND VALIDATION

ABSTRACT

Quantitative assessment of asphalt binder oxidation for given pavements is critical to evaluate pavement performance deterioration as related to aging of asphalt binder and ultimately to improve pavement maintenance scheduling and pavement design protocols.

Efforts have been made in recent years to model binder oxidation in pavements. This work has progressed from a simple sinusoidal pavement temperature model coupled with assumed complete oxygen availability and constant-rate reaction kinetics to more complex pavement temperature calculations, coupled with oxygen diffusion from accessible pores (that were assumed to contain atmospheric air) to the surrounding asphalt throughout, and a single pore size and distance between pores. This prior work did not address a number of issues: 1) whether air freely permeates the pavement pores or is limited by diffusion, 2) improved knowledge of oxygen diffusion in binders and mastics, 3) the possibility of incorporating a distribution of pore sizes and inter-pore spacing, and 4) the effects of both fast-rate and constant-rate oxidation reactions.

In this work, a comprehensive computational model incorporating these additions was developed. This model requires independently measured physical properties and parameters that characterize pavement air voids, oxygen diffusivity, pavement temperature, and asphalt oxidation kinetics individually. With these inputs, oxygen transport through the air voids and oxygen transport and reaction within the asphalt-aggregate matrix were modeled to calculate asphalt oxidation rates in pavements as a function of time and depth.

Model calculations were validated with measured field asphalt oxidation rates for a number of interested pavements. There is a good match between model calculations with field measurement. Also, the measured oxidation rates for newly constructed pavements reflected the higher rates that resulted from fast-rate reaction kinetics whereas older pavements were observed to be oxidizing at rates that matched the slower constant-rate kinetics.

INTRODUCTION

While asphalt pavements are designed for optimum performance initially, over time as asphalt binders oxidize the properties of binder change and lead to a decrease in pavement durability (Al-Azri et al., 2006 and Woo et al., 2007). To design pavement mixtures with maximum pavement durability, binder oxidation must be taken into account. The ability to assess quantitatively how fast the oxidation occurs for a given pavement over time is an essential implementation issue.

Asphalt oxidation and hardening rates in pavements have been measured in several studies (Glover et al., 2005; Woo et al., 2007; Woo et al., 2008). These measurements normally involve collecting pavement cores over time, cutting core specimen into thin slices, extracting and recovering asphalt binders in each slice, and measuring recovered asphalt binder properties

including carbonyl content and viscosity. From these measurements, asphalt binder oxidation or hardening rates at different depths in a pavement is determined. Results from this study suggest that asphalt oxidation rates in pavements are largely determined by the temperature as a function of time and position (depth) in the pavement, provided the accessible air voids are sufficiently high (great than 4 percent), and that when the accessible air voids in pavements are sufficiently low (less than 2 percent) the hardening rate of binders is significantly reduced (Woo et al., 2007). While these field measurements provide insight on elements that influence asphalt binder oxidation, they were largely confined to specific pavements and locations; a quantitative deterministic model of binder oxidation in pavements is needed in order to predict and assess asphalt oxidation for any given pavements.

Recent studies have revealed that majority of air voids in pavements are interconnected air channels, existing from top to bottom of the specimen (Al-Omari et al., 2002 and Masad et al., 2007). This connectivity of air voids assures that ambient air can diffuse and/or flow into the air void channels and provides a path for access to and diffusion and reaction within the adjoining asphalt. From this perspective, oxygen transport and reaction in pavements is described as two interlinked steps: 1) Diffusion and/or flow of oxygen into interconnected air voids; and 2) Diffusion of oxygen in those air voids into nearby asphalt binder-aggregate matrix and reaction inside.

Prapaitrakul et al. (2009) made the first attempt recently to calculate asphalt binder oxidation in pavements with an oxygen transport and reaction model based on the concept that air void channels in pavements are positioned and connected from top to bottom (Prapaitrakul et al., 2009). However, this initial model was limited by: 1) assumption of a single air void channel size and an uniform air void distribution; 2) assumption of complete atmosphere air availability throughout all the air voids; and 3): arbitrary numbers of oxygen diffusivity in asphalt and mastics.

In this work, a comprehensive computational model based on oxygen transport and reaction fundamentals was developed with these limitations addressed. The resulting model contains only independently measured physical properties and parameters which characterizes pavement air voids, oxygen diffusivity, pavement temperature, and asphalt oxidation kinetics. Oxygen transport through the air voids and oxygen transport and reaction within the asphalt-aggregate matrix were modeled. From this model, asphalt oxidation rates in pavements as a function of time and depth were calculated. This model was validated by comparing measured field oxidation rates versus model calculations for a number of interested pavements in Texas and Minnesota.

MATERIALS AND METHODOLOGY

Overview of the Experimental Design

Mathematic model of vertical transport of oxygen through an air void channel and horizontal transport and reaction of oxygen within the asphalt-aggregate matrix layer associated with an air void channel were built based on mass transfer fundamentals. This model, along with independent measurement of pavement air voids, oxygen diffusivity, pavement temperature, and

asphalt oxidation kinetics, calculate layer-by-layer bulk asphalt oxidation rates for any given pavements.

Field oxidation rates for a number of pavements in Texas and Minnesota were measured and compared with model calculations to validate the model. In addition, this study investigated the effects of pavement temperature, air voids properties, and binder oxidation kinetics on field oxidation rates.

Materials and Pavement Sites

Table 29 summarized pavement sites selected in this study from Texas and Minnesota. The Texas sites range from Amarillo in the North to Laredo in the South and to the Lufkin in the East.

Field cores were taken from each site. Most of the field cores are taken from top surface layers of pavements, but some are from layers far below the surface, IH35 #5 at Waco and IH35 #4 at Laredo specifically. IH35 #5 at Waco is a 4-inch rich bottom layer (high asphalt binder content) sited on a 6-inch flex base at a depth of 16 inches below the pavement surface. IH35 #4 at Laredo is a 2-inch rich bottom layer (high asphalt binder content) rested on a 6-inch flex base at a depth of 14 inches below the pavement surface. Here the number after the name of the highway indicates the pavement layers studied. In Table 29, surface payment layers were used. The thicknesses of these various layers ranged up to four inches and down to as little as two inches. The Bryan District pavement (US290) contained unmodified binders, while other pavements are SBS polymer modified. Oxidation and hardening kinetics for all the binders are measured separately with either recovered binders from the field or same binders from manufacturer. Additionally, IH35 #4 at Laredo has the lowest accessible air void of 2.01 percent, while US290 at Bryan has accessible air void as high as 12.44 percentMost pavement layer has intermediate values from 5.86 percent to 7.91 percent. The ages of pavements range from new construction (US277) to six-year old (Amarillo US54) pavement for the first coring date. Coring at two times allowed a calculation of the actual field oxidation rates.

Table 29. List of Field Sites Studied.

District (State)	Highway	Thickness (inch)	PG (modifier)	Binder Supplier	AAV (%)	Cons.	1st Coring	2nd Coring
Laredo (TX)	US277	2.5	70-22 (SBS)	Valero-C	7.27	2008	07/2008	09/2009
Lufkin (TX)	US69	2	70-22 (SBS)	Marlin	7.91	2003	02/2005	06/2008
Bryan (TX)	US290	2.5	64-22 (Un)	Eagle	12.44	2002	10/2005	08/2008
Waco (TX)	IH35 #5	3	70-22 (SBS)	Alon	5.86	2003	10/2005	08/2008
Amarillo (TX)	US54	2.5	70-28 (SBS)	Alon	7.33	1998	12/2004	07/2008
Laredo (TX)	IH35 #4	2	70-22 (SBS)	Valero-C	2.01	2007	--	06/2008
Lubbock (TX)	US82	2						
Metro Area (MN)	I-94	4.5	AC-120(Un)	--	4.81	1993	11/2004	11/2008

Cores also included in the study were from Cell 1 of the MnRoad test site in Minnesota. The thickness of the core layer is 4.5 inches, taken from pavement surface. Oxidation reaction kinetic parameters were measured with recovered binders from the field sites. Accessible air void content for this pavement layer is 4.81 percent. Cell 1 was constructed in 1993, and cores were obtained from the MnRoad site in November 2004 and November 2008.

This collection of pavement cores covers a large variety of key elements that affect pavement oxidation, and provided data that could be used to assess the effects of pavement temperature (Texas versus Minnesota; surface layer versus bottom layer), air void properties (low accessible air void of 2.01 percent versus high accessible air void of 12.44 percent), and asphalt oxidation and hardening kinetics (a variety of asphalt binders used) on measured or modeled oxidation rates.

Methodology

Cores taken from field sites were analyzed for interconnected air voids (by X-ray CT) and total and accessible air voids (by CoreLok or SSD) first and then sliced into 0.5-inch layers for binder extraction and recovery of each layer. The recovered binders were analyzed for oxidation by infrared spectroscopy (FT-IR) and for physical properties by dynamic shear rheometry to provide data on asphalt binder oxidation and hardening rates in pavements. In addition, binders recovered from cores or similar asphalt binders from manufacturers (when core samples are not enough for kinetic measurement) were oxidized in pressure oxidation vessels (POVs) at controlled temperatures (3~5 temperatures) and pressure (1 atm air pressure) to measure oxidation and hardening kinetics of the asphalts.

X-ray CT Imaging Technique

X-ray CT imaging technique is used to investigate the air void characteristics and structure of pavement core specimens. It is ideal to study the interior of opaque solid objects in a non-destructive way. Two dimensional images most commonly known as "slices" can be obtained through this process. Each slice reveals the interior of the object on a plane. If stacked together, the slices build three dimensional image of the object. These slices are generally about 1 mm in thickness.

The X-ray system is composed of an X-ray source, a sample holder, and a detector, as demonstrated in schematic Figure 53 with gray scale image shown. To measure a specimen, an X-ray source emits a beam of known intensity through the specimen, and a detector on the opposite side of the specimen measures the attenuation of beam intensity. The specimen rotates 360° around its center, an image is produced from the different density measurements that are registered and represented by gray scale, and the specimen then moves at a specified incremental vertical interval. The whole procedure is repeated once again to produce the next image, until the whole solid is scanned.

X-ray CT Image Processing

The original gray scale images obtained from X-ray CT are converted to black and white by the assigned macro with a user-input threshold, where black areas represent the voids and white areas represent the aggregates and the mastic. The appropriate user-input threshold parameter was chosen between 0 and 56,000. By matching air void content obtained from X-ray CT with air void content obtained from experimental measurement (Corelok method), an appropriate threshold was obtained. The areas of the original images were converted to black (voids phase) if the gray intensity of the areas were less than the indicated threshold, and the areas were converted to white if the intensities were higher than the threshold (aggregate and mastic phase).

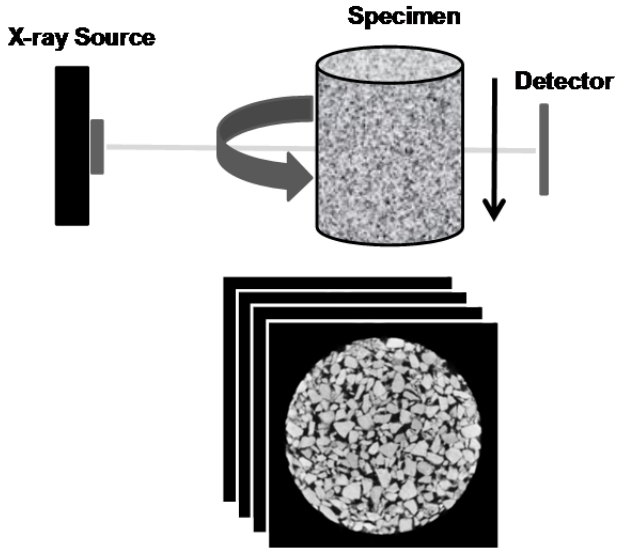


Figure 53. Schematic of X-Ray CT System and Gray Scale Images Obtained.

Interconnected air voids are the air void channels that connect the top to the bottom of specimens. To determine the interconnected air void content and distribution, stacks of images at different depth increments of the specimen will be collected, and these black-and-white images will be converted to binary bit files by macros (Masad, 2004). These binary files will be analyzed to determine the connected paths from the top to the bottom of the specimen by using a FORTRAN-built algorithm. From this, the interconnected air void content of these images will be calculated.

Figure 54 demonstrates the images obtained after each image analysis step. In sequence, they are the original gray image of a pavement specimen slice obtained with X-ray CT (a), black and white image of all the air voids in the slice after image processing (b), and black and white image of interconnected air voids in the slice after image processing (c).

Air void size and number of air voids for each black and white image could be statistically analyzed with image analysis software, Image J, using built-in function of analyze particles with proper calibration between actual image size and pixel of the image.

Air Void Measurement with CoreLok

Air void content of the specimens need to be measured as a necessary calibration of original gray scale images obtained from X-ray CT scanning. Here, the CoreLok method was used to determine total air void and accessible air voids (those that water can penetrate when the CoreLok vacuum bag is opened underwater) with bulk specific gravity and maximum specific gravity measured of the core specimen. The details of such measurements have been described in several reports (ASTM D2041 and ASTM D6752).

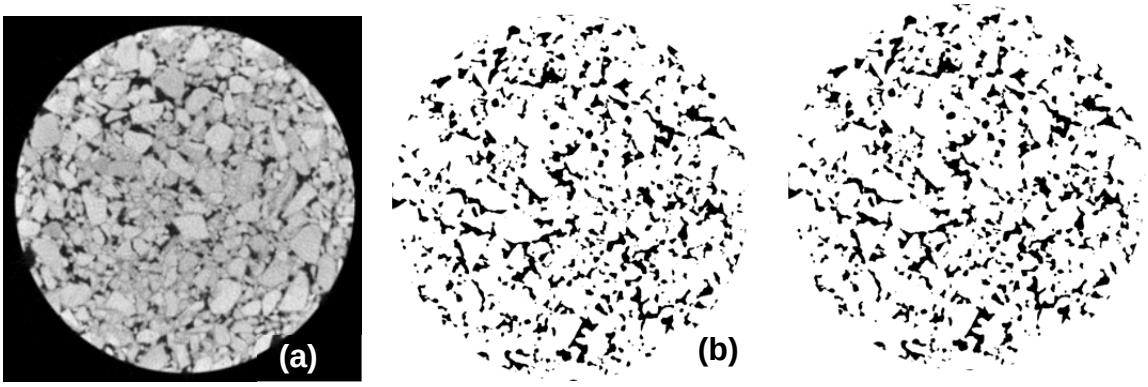


Figure 54. X-ray CT Image Analysis: (a) Original Grayscale Image; (b) Black-and-White Image after Threshold; and (c) Black-and-White Image of Interconnected Air Void.

Binder Extraction and Recovery

Extraction and recovery of the binder in the core specimens is conducted based on the procedures outlined by Burr et al. These procedures provide for a thorough wash and therefore extraction of the binder from the aggregate but with minimal hardening or softening of the binder in the solvent and with care taken to assure complete solvent removal during the recovery

process with a Rotovap device (Burr et al., 1991 and Burr et al., 1994). The extraction process uses washes in toluene followed by a 15 percent ethanol in toluene solvent mixture and size exclusion chromatography to assure removal of the solvent from the recovered binder.

Carbonyl Content Measurements with FTIR

FTIR measurement were conducted for recovered binders and also binders aged in POVs for kinetics studies. A Nicolet 6700 Fourier Transform Infrared Spectroscopy spectrometer was used to analyze the carbonyl content. Growth in the area under the FTIR spectrum from 1650 to 1820 cm^{-1} in arbitrary units, the carbonyl area, is used to monitor the progress of the asphalt oxidation.

Gel Permeation Chromatography (GPC)

After the binder was extracted and recovered, the GPC analyzed it to ensure complete solvent removal (Burr et al., 1993). Tests samples were prepared by dissolving 0.2 g of binder in 10 mL of Tetrahydrofuran (THF). The sample of interest was then sonicated to ensure complete dissolution. The sonicated sample was then filtered through a 0.45 μm PTFE syringe filter. Samples of 100 μL were injected into 1000, 500, and 50 Å columns in series with THF carrier solvent flowing at 1.0 mL per minute. Incomplete solvent removal results in a positive peak located at 38 minutes on the chromatogram.

Dynamic Shear Rheometer

The rheological properties of the binder were determined using a Carri-med CSL 500 controlled stress rheometer. The rheological properties of interest were the complex viscosity ηo* measured at 60°C and the storage modulus (G´) and the dynamic viscosity (η´), both at 44.7°C and 10 rad/s, in the time-sweep mode. A 2.5-cm composite parallel plate geometry was used with a 500 μm gap between the plates.

Asphalt Binder Oxidation and Hardening Kinetics Measurement

Knowing oxidation and hardening kinetic parameters of binders used in these field sites is essential for model calculations and evaluation of their impact to field oxidation rates. These parameters include activation energy, pre-exponential factor in the Arrenius equation of asphalt oxidation rate and viscosity hardening susceptibility, and m value in linear correlation between carbonyl content growth and increasing of log low shear limiting viscosity. Table 30 summarizes these oxidation and hardening kinetic parameters determined for each binders used in studied pavement sites.

Table 30. Oxidation and Hardening Kinetic Parameters of Binders from Field Sites.

Asphalt	Oxidation and Hardening Parameters			
	AP^{α} ln(CA/day)	E (kJ/Mol)	HS (1/CA)	m (poise)
Val-C 70-22 (US277)[a]	21.559	75.183	3.970	8.144
Marlin 70-22 (US69)[b]	24.783	84.841	6.890	3.940
Marlin 64-22 (US290)[a]	24.783	84.841	7.931	2.697
Alon 70-22 (IH35-Waco)[c]	22.399	77.512	4.490	6.758
Alon 70-28 (US54)[a]	21.686	54.947	4.950	7.409
Val-C 70-22 (IH35-LRD)[a]	23.044	72.970	7.550	4.970
AC-120 (I-94)[d]	22.289	77.411	3.290	5.513

a: Oxidation Kinetic parameters measured with recovered binders.
b: Oxidation kinetic parameters of base binder Marlin 64-22 is used, assuming polymer modification do not affect oxidation kinetics.
c: Oxidation kinetic parameters were interpolated with kinetic parameters of Alon 64-22 and Alon 76-22; Their AP^{α} and E of are21.905 and 76.256 for Alon 64-22 and 22.642 and 78.769 for Alon 76-22.
d: Average values of oxidation kinetic parameters from two separate measurements of oxidation kinetic parameters of recovered binders are used.

Binders recovered from cores or similar asphalt binders from manufacturers were oxidized in thin films in pressure oxidation vessels at controlled temperatures and pressure (1 atm air pressure). In the case where original binder and recovered are not available, interpolation strategies were used. Oxidation rates were measured at a minimum of three temperatures (60, 80, and 100°C) and a maximum of five temperatures (170, 180, 190, 200, and 210°F). Activation energy and pre-exponential factors are estimated from these data. Additionally, zero shear limiting viscosity of each recovered binder at different oxidation level (carbonyl content) will be measured and from which, viscosity hardening susceptibility and m value (intercept) is obtained.

MATHEMATIC MODEL OF PAVEMENT OXIDATION

Oxygen transport and reaction in pavement is described as two interlinked steps, as demonstrated in Figure 55: 1) diffusion and/or flow of oxygen from the atmosphere above the pavement into the interconnected air voids in the pavement; and 2) diffusion of oxygen from those air voids inside the adjoining asphalt-aggregate matrix where it reacts with the asphalt. Further details of elements of the model development are described below, including modeling transport through an air void channel, modeling transport and reaction within a finite asphalt-aggregate matrix layer associated with an air void channel, and extending calculations from one air void channel to all air void channels with characterization of pavement air void structures.

Vertical Transport of Oxygen through an Air Void Channel

In pavements, diffusion and/or convective flow of oxygen must occur in order to supply oxygen to the interconnected air channels. From these channels, oxygen diffuses into and reacts

within an asphalt-aggregate matrix. Accurately representing the oxygen concentration in those interconnected air channels is extremely important to modeling binder oxidation in pavements. This vertical oxygen transport process could occur by diffusion, when there is an oxygen concentration gradient between ambient air at the surface of the pavement and the oxygen concentration in the interconnected air voids, and/or by convective flow (for example, when air undergoes expansion or contraction with pavement temperature fluctuations); however, there are no direct measurements of such convective flow in pavements. In the case that oxygen transport is dominated by convective flow, it is fair to assume a constant 0.2 atm oxygen pressure in the interconnected air void channel, regardless of depth in the pavements, while in the case that primary oxygen transport is by diffusion, the oxygen concentration decreases with depth below the pavement surface in the air void channel.

In this work, both situations are considered, giving two distinct and extreme oxygen concentration profiles in the air voids. One profile assumes pure diffusion from the pavement surface down into the air void channel; the other assumes constant oxygen pressure in these interconnected air voids (0.2 atm oxygen) when convective flow dominates. These two conditions establish a range, instead of a single value, of asphalt binder oxidation rates in pavements. The assumption of constant oxygen pressure at 0.2 atm in interconnected air void gives the highest possible oxidation rate, while the assumption of vertical diffusion produces the lowest oxidation rate.

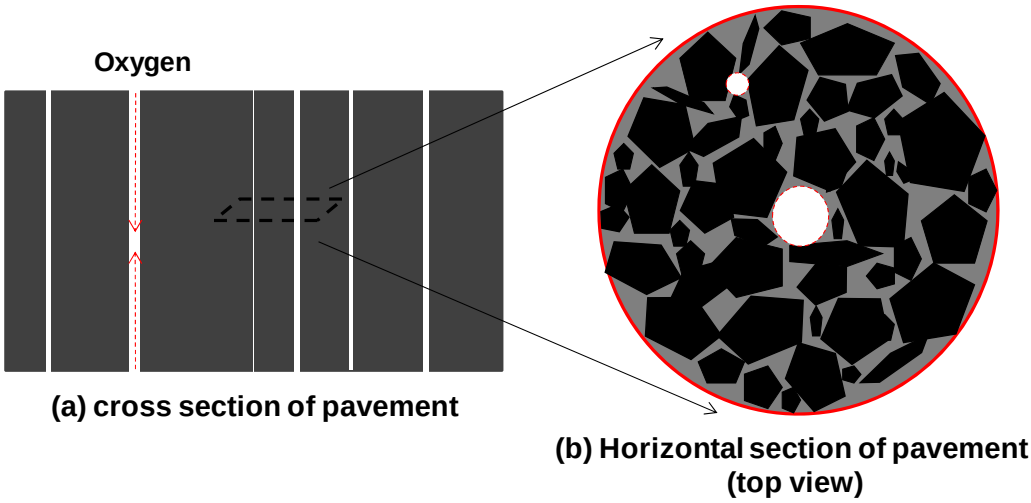


Figure 55. Schematic of Two Steps Involved in Oxygen Transport and Reaction in Pavements.

In the case of oxygen transport through the pores by diffusion only, the oxygen concentration through the voids needs to be determined. The oxygen concentration gradient is influenced by the air void size (diameter d), the distance oxygen must diffuse below the surface (z), the consumption rate of oxygen inside the adjoining asphalt-aggregate matrix (r_{O2}), and the oxygen diffusivity in air ($D_{O2\text{-Air}}$). Considering that the diameter of the air voids is much smaller than the diffusion distance below the pavement surface, the oxygen concentration gradient in the radial direction of the pore is neglected in this study. Therefore, the oxygen concentration in an air channel is a function of z only. With these assumptions, the oxygen partial pressure in an air

void channel as a function of time and distance from the surface in a cylindrical coordinate system is given in Eq. 8-1:

$$\left(\frac{\partial P}{\partial t}\right) = D_{O2-\text{Air}}\frac{\partial P}{\partial z} + A * r_{O2} \tag{8-1}$$

The boundary (BC) and initial (IC) condition are defined as:

$$\left(\frac{\partial P}{\partial z}\right) = 0 \text{ at } z = \text{half of the pavement depth} \tag{BC1}$$

$$P = 0.2 \text{ at } z = 0 \tag{BC2}$$

$$P = 0 \text{ at } t = 0 \tag{IC}$$

where $D_{O2\text{-Air}}$ is oxygen diffusivity in air; a constant value of 0.2 cm^2/s is used. A is the ratio of the area of the finite aggregate-asphalt matrix where oxidation occurs and the cross-sectional area of air the void channel. In this work, it was assumed that both the pavement top and bottom are exposed to ambient air so that a non-flux boundary condition is defined at half distance from pavement surface to pavement bottom. Ambient air at the bottom of the pavements is assumed because asphalt pavement base is rather porous and ambient air can easily get access to it from underground water table or from the sides of pavements.

The term r_{o2} in Eq. 8-1 is introduced because while oxygen diffuses throughout an air void channel, it is also continuously being consumed by the adjoining asphalt binder-aggregate matrix; this lumped-parameter model distributes that consumption evenly across the pore cross section rather than calculating it as transport from the pore at the pore surface. This oxygen consumption rate can be calculated with the horizontal diffusion and reaction model that is developed in the following section with known oxygen pressure in the air void and asphalt binder kinetics. A maximum oxygen consumption rate was used to calculate oxygen concentration gradient in an air void channel in this study. This maximum consumption rate was estimated by using asphalt binder oxidation kinetics parameters and the assumption of a constant oxygen pressure of 0.2 atm in an air void channel.

Figure 56 shows a sample calculation of oxygen concentration profile from the pavement surface to 0.25 m below the surface. This air void channel has a diameter of 0.5 mm, a shell thickness of 2 mm, and a length (depth) of 1 m. The asphalt binder used in the calculation is SEM 64-22. Two conditions (the one with oxygen transport by diffusion only in steady state and the one with ample convection through the pore) are established as a function of pavement depth, which can provide upper and lower limits for oxygen concentration in interconnected air void at a specified depth. The assumption of a rapic resupply of air by convective flow established the upper limits, a constant oxygen pressure at 0.2 atm throughout the air void channel that is independent of depth in pavement. The assumption that oxygen transport occurs by diffusion only provided the lower limit, a decreasing oxygen concentration from the surface of the pavement.

Upper and lower limits of oxygen concentrations for a pavement layer can then be easily read from the plot and used as inputs to calculate binder oxidation rates in the finite volume of

asphalt-aggregate matrix layer associated with this air void channel based on the horizontal diffusion and reaction model developed in the next section.

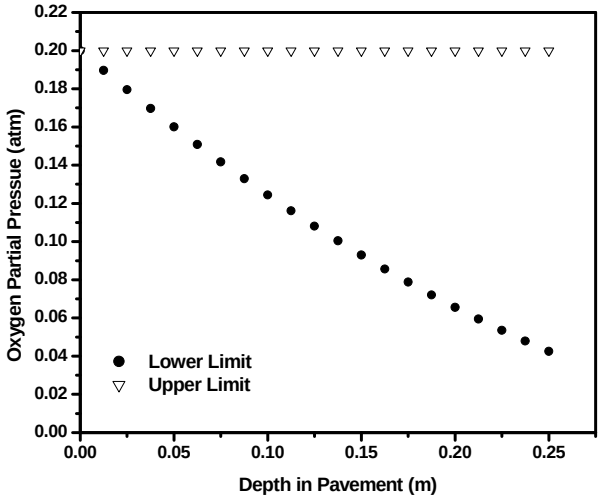


Figure 56. Sample Calculation of Oxygen Concentration Profile in an Air Void Channel at Two Limit Conditions.

Horizontal Oxygen Diffusion and Reaction from an Air Void Channel

From each air void channel, oxygen diffuses and reacts throughout the surrounding asphalt-aggregate matrix. The following equation accounts for the oxygen diffusion and reaction in a differential volume of the matrix:

$$\left(\frac{\partial C_{O_2}}{\partial t}\right) = -\nabla \cdot N_{O_2} - r_{O_2} \tag{8-2}$$

With Fick's first law of diffusion, a governing equation with boundary conditions could be used to estimate oxygen partial pressure throughout the matrix layer. The PDE system is solved for the oxygen partial pressure as a function of time and distance away the from the air void-matrix interface in a cylindrical coordinate system, including oxygen consumption by reaction and binder hardening (which decreases diffusivity) as a result of the oxidation. The resulting primary equation for the transport and reaction of oxygen in the asphalt-aggregate matrix is:

$$\left(\frac{\partial P}{\partial t}\right)=\frac{1}{r}\frac{\partial}{\partial r}\left(r\mathcal{D}_{O_2}\frac{\partial P}{\partial r}\right)-\left(\frac{cRT}{h}\right)r_{CA} \tag{8-3}$$

$$\left(\frac{\partial P}{\partial r}\right)=0 \quad \text{at} \quad r=r_{NFB} \quad \text{No Flux Boundary}$$

$$P=P_{\text{av}} \quad \text{at} \quad r=r_{PS} \quad \text{Air Void Surface}$$

$$P=0 \quad \text{at} \quad t=0 \quad \text{Initial Condition}$$

where h is the Henry's law constant; c (a conversion factor from oxygen partial pressure units to concentration units in the asphalt) is asphalt dependent, ranging from $2.75\text{x}10^{-4}$ gmol O_2/mL/CA to $4.59\text{x}10^{-4}$ gmol O_2/ mL/CA for ten asphalts reported by Liu et al. (1998a). In this study, an average value of $3.71\text{x}10^{-4}$ was used;. r_{NFB} is an average distance between air voids, and P_{av} is the oxygen partial pressure in the air voids that is a function of distance in the air void channel from the atmospheric end and is calculated using the diffusion or convection flow model in the first modeling step of vertical transport, as appropriate. r_{CA} is carbonyl growth rate, described using an Arrhenius expression for temperature variation and pressure dependence.

$\mathcal{D}_{O_2}$ can be expressed in terms of position (r), time (t), and pressure (P) with the following relations.

Oxygen diffusivity is a function of low shear limiting viscosity η_0^* (aging level) and temperature:

$$\frac{\mathcal{D}_{O_2}}{T}=5.21\times10^{-12}\left(\eta_0^*\right)^{-0.55} \tag{8-4}$$

Low shear limiting viscosity of asphalts is related to carbonyl content for asphalts according to (Lau et al., 1992):

$$\eta_0^*=\exp\{HS\cdot CA+m\} \tag{8-5}$$

where HS is asphalt hardening susceptibility and m is an experimental parameter. HS and m are functions of temperature and can be measured experimentally.

Carbonyl content can be represented by:

$$CA(t)=\int_0^t r_{CA}\,d\theta+CA_0 \tag{8-6}$$

where CA_0 is an integration constant determined from experimental data; and r_{CA} can be calculated for a asphalt with known reaction kinetic parameters. Combing Eq. 8-4, 8-5, and 8-6, $\mathcal{D}_{O_2}$ is expressed as a function of position, time, and oxygen pressure.

All the variables in Eq. 8-3 are functions of position (r), time (t), and pressure (P). With defined boundary condition and initial condition, oxygen pressure and oxidation rate are

numerically solved for a finite asphalt-aggregate matrix layer associated with an air void channel. Asphalt binder oxidation and hardening kinetic parameters required in this calculation are measured from separate experiments.

Pavement Air Void Characterization: Extending Model Calculation to Entire Pavement Layers

To extend model calculation from one air void channel to all the air void channels in a pavement layer, size and shell distance for each air voids need to be obtained. Air void characterization with X-ray CT and a series of image analysis techniques were utilized to obtain the required information.

Air Void in Pavements — Characterization with X-ray CT

Air void structure in pavements has been assessed with X-ray CT and image analysis techniques to examine the internal microstructure of asphalt mixtures, including air void distribution and interconnectivity. The detailed information and procedure has been described in the methodology. The final images after the imaging process are black and white images of total and interconnected air voids for each slice of the pavement core specimen.

A macro in image-J to analyze particle size and to count particle number is used to quantify the air void distribution from these final black and white images of X-ray CT. Information obtained from this analysis includes the number of air voids and size of each air void, from which radius and shell distance for each air void channel can be estimated. Figure 57 shows a sample air void size distribution obtained from this analysis for one image slice; air void size, in this particular slice, varies largely from 0.2 mm to 3 mm. The total number of air voids counted was 336.

Image slices at different depths of the pavement specimen provide air void size distribution and number of air voids as a function of depth. A pavement specimen of US82 EBS (east bound shoulder) was used as a demonstration. The 2-inch pavement core was divided into four half-inch layers starting at the pavement surface. The air void size distribution and number of air voids for each layer were analyzed and compared to the other layers. Figure 58 shows that the air void size distributions for the various layers are quite similar to each other. This conclusion holds with other pavement core specimens studied as well.

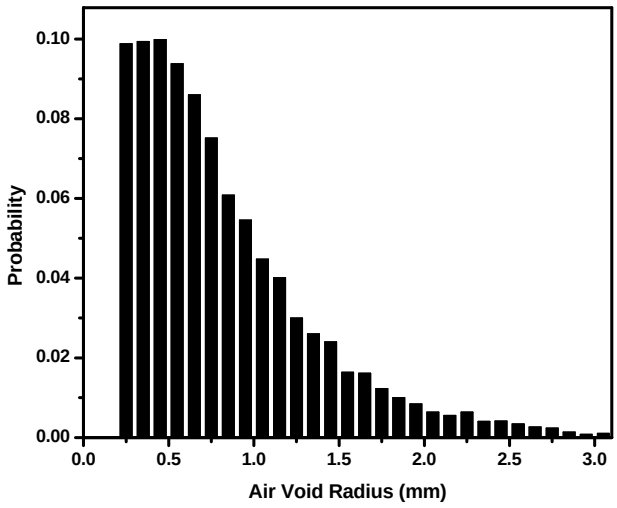


Figure 57. Sample Statistical Distribution of Air Void Size in a Pavement Layer of US82.

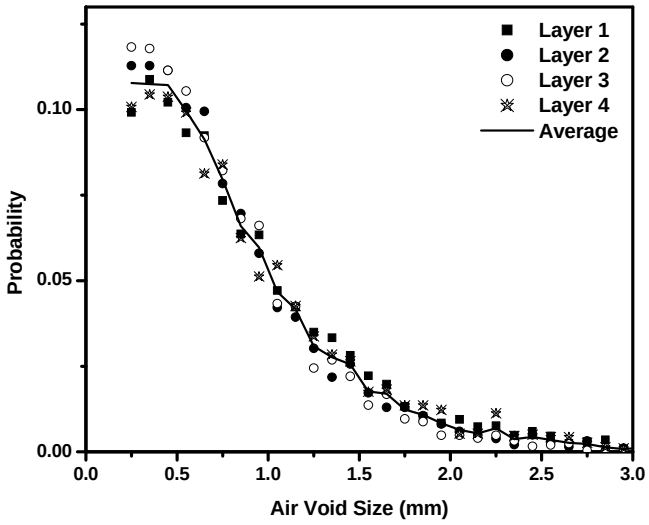


Figure 58. Air Void Distribution at Different Layers of Pavement US82.

However, some significant differences in the number of air voids exist in each layer. The numbers of air voids were 336, 259, 227, and 276 for layers 1 to 4. It has been observed that air void content varies with depth in pavements, resembling a "C" shape with higher air void content at the top and bottom portions of the specimen. Our observation of number of air voids in each layer agrees with this "C" shape distribution. This "C" shape distribution probably is due to the restriction imposed by the top and bottom surfaces during compaction.

X-ray CT Resolution Limit and Interpolation of Complete Air Void Distribution

One critical issue encountered when using X-ray CT for pavement air void analysis is undetected air voids with size smaller than 0.2 mm due to the resolution limit. The resolution of X-ray CT is affected by several factors such as the type and size of the X-ray source and detectors; the distance between the source, the solid, and the detector; and the method used for image reconstruction. The images of the pavement specimens were taken at a resolution in the range of 0.146 to 0.195 mm/pixel that is also the detection limit. Consequently, for the X-ray CT images, there is a clear cut-off size near 0.2 mm; below this size, no air voids are detected, and this phenomenon is seen in Figure 57. However, this apparent minimum air void size most likely is not correct in reality.

To obtain a complete profile of air void distribution that cannot be fully measured by X-ray CT, distribution functions (probability density functions) may be used to predict the complete air void size distribution with the available size distribution measured with X-ray CT as an input. The ideal probability density functions were determined by plotting the pore size cumulative probability versus the cumulative probability of a test distribution using statistical packages. If the distribution of the data matched the test distribution, the data points should cluster around the equality line. According to the probability plots, two distributions best fit the data — Lognormal and Weibull distributions. Figure 59 shows an example of the probability plots for a pavement specimen using the Weibull and log-normal distributions. Log-normal density functions were used thereafter for the analysis.

The probability density function of a log-normal distribution is:

$$f(x;\mu,\sigma) = \frac{1}{x\sigma\sqrt{2\pi}} e^{-\frac{(\ln x-\mu)^2}{2\sigma^2}}, x > 0 \quad (8\text{-}7)$$

where μ and σ are the mean and standard deviation of the variable's natural logarithm. By definition, the variable's logarithm is normally distributed. The location parameter μ can be any real number whereas the scale parameter σ can only be a positive real number. This type of distribution is commonly used to model continuous random data when the distribution is thought to be skewed. It has been shown that air void distribution in pavements might also follow such a distribution (Torres, 2004).

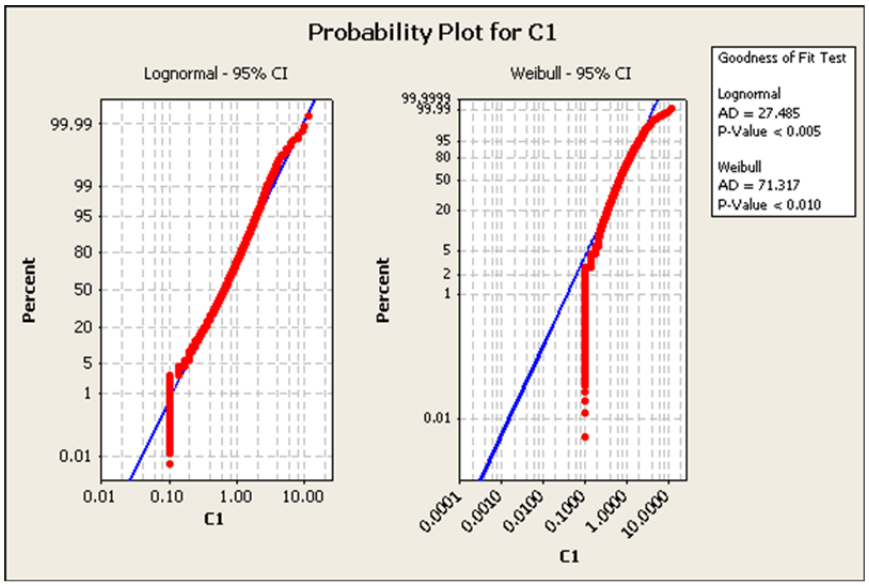


Figure 59. Example of Air Void Probability Plot for an Asphalt Pavement Specimen, Log-Normal Distribution and Weibull Distribution.

Measured size distributions of air voids, though incomplete, provide enough data to estimate lognormal distribution parameters, and then with those parameters, the entire distribution profile can be developed under the assumption that this distribution holds below the X-ray CT minimum resolution. Figure 60 provides a sample air void distribution obtained from a log-normal distribution with function parameters determined by analyzing the measured air void size distribution. Although the modeled air void distribution does not match exactly the measured air void distribution, overall it works pretty well. A complete air void size distribution and the actual total number of air voids are thus estimated by using this log-normal air void distribution.

As we can see from this complete profile of air void size distribution, the actual number of air voids in the range from 0 to 0.2 mm (area under the distribution curve from 0 to 0.2 mm as a fraction of the total area) is not that high, seven percent in this specific case. In practical use, in the absence of statistical packages, a reasonable approximation is to draw a straight line between point zero and the data point measured at 0.2 mm to use as a substitution of the air void distribution in that range.

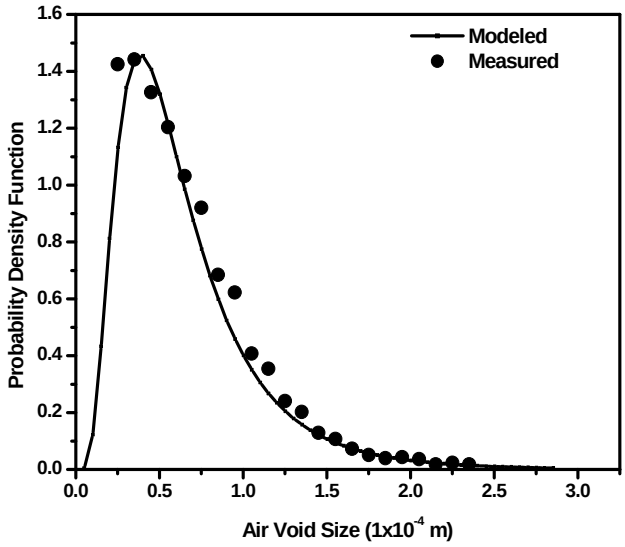


Figure 60. Sample Calculation of Air Void Distribution with a Log-normal Distribution Function.

The above developments using the X-ray CT technique and imaging analysis tools provide information on air voids size distribution and the number of air voids, for each pavement slice. From this information, air void parameters (air void radius and binder shell radius) for oxidation models can be estimated. The air void radius for each air void is directly obtained from image analysis, while with total number of air voids known, the average shell distance for each pavement is used as shell distance for each air void in the model calculations:

$$r_{NFB} = \frac{\text{Actual area of a pavement slice}}{\text{Number of air voids in this slice}} \tag{8-8}$$

Theoretically, with a known air void radius and shell distance for each air void channel in a pavement layer, the oxidation rate for every finite aggregate-asphalt matrix volume associated with an air void channel in the layer can be computed to obtain the bulk oxidation rate. However this calculation takes too much computational effort and time. For a pavement layer with 1000 distinguishable air voids, we would need to calculate 1000 times to get oxidation rates for every volume associated with each air void, which will take about 100 days to complete. To reduce the computational effort, air void sizes were divided into several ranges in this study, from 0 mm ~ 0.2 mm, 0.2 mm ~ 0.5 mm, 0.5 mm ~ 1 mm, 1 mm ~ 2 mm, and 2 mm ~ 3 mm. For each size range, the average air void radius (r_i) and the number of air voids (N_i) are determined, and the model then uses this information along with shell distance ($r_{NFB,i}$) to calculate representative oxidation rates for air voids in this size range. The bulk oxidation rate for a pavement layer will be the sum of oxidation rates per unit volume calculated for each size range:

$$r_{o2}(\text{total}) = \sum_{i=1}^{n} \frac{r_{o2}(i) * N_i}{N} \tag{8-9}$$

where N_i is number of air void in each size range, $r_{o2(i)}$ is oxidation rate calculated for this size range, N is the total number of air voids.

RESULTS AND DISCUSSION

Model Calculation of Oxidation Rates for One Air Void Channel

Sensitivity of Air Void Parameters in the Model

The above model calculation used one set of values for the air void size and shell distance model parameters, while the actual air voids in pavements exhibit a very large size distribution. The influence of air void size and shell distance on the final calculation was analyzed by changing their values over a practical range while keeping other input parameters constant.

As shown in Figure 61, with increases of air void radius from 0.1 mm to 3 mm while holding shell distance a constant, 5 mm, oxidation rates increase significantly from 0.041 to 0.057 CA/ year, suggesting that the air void radius is important in the model calculations.

For asphalt shell distance, while holding air void radius a constant of 0.5 mm, increases in the shell distance lead to a rapid decrease in oxidation rate, as shown in Figure 62. As the shell distance increases, the oxidation rates tend to approach a constant, most likely because oxygen, consumed by reaction, can no longer penetrate deeper into the matrix.

From these two figures, the model seems rather sensitive to air void radius and shell distance. Because air voids in the pavement have a wide size distribution, characterization of air voids and acquisition of representative air void parameters for use by the model is very important to accurate model estimates of asphalt binder oxidation in pavements.

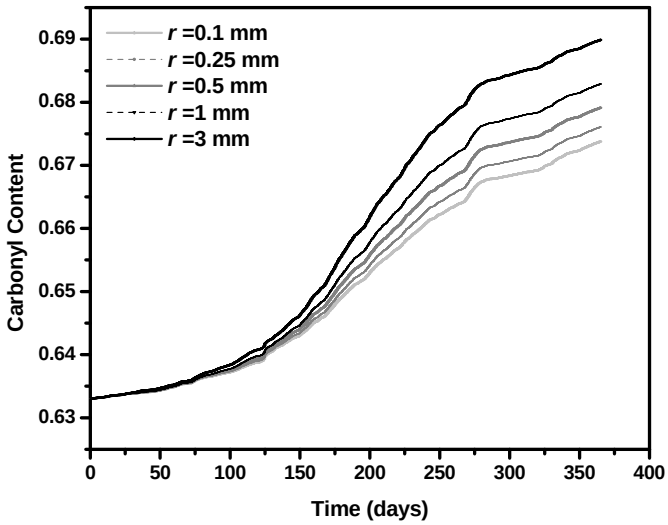


Figure 61. Effect of Air Void Radius on Calculated Yearly Carbonyl Growth.

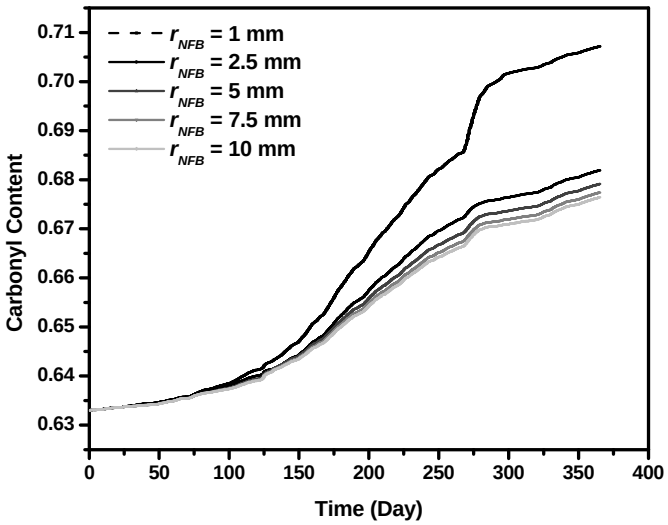


Figure 62. Effect of Shell Distance on Calculated Yearly Carbonyl Growth.

Layer-by-Layer Oxidation Rates for Matrix Associated with an Air Void Channel

With the above developed mathematical model, oxidation rates inside the finite aggregate-asphalt matrix associated with an air void channel at different depths in a pavement are calculated and shown in Figure 63. Here, pavement layers at 0.02 m, 0.08 m, and 0.16 m are selected. Input for this calculation includes kinetics parameters of asphalt SEM 64-22, a value of air void radius of 0.5 mm, a value of shell distance of 5 mm, pavement temperature profiles calculated at Lufkin, TX, for 1994, and calculated oxygen concentration profiles P_{av} (both upper and lower limits) in the air void channel as a function of depth. Output from the model calculation is the growth of carbonyl content in these three finite asphalt-aggregate matrix layers associated with the air void channel for the entire one-year period. At each depth, the model generates two carbonyl growth curves; one curve gives the highest oxidation rate, obtained from the upper limit of oxygen concentration in the air void channel (a constant 0.2 atm oxygen pressure), and the other provides the lowest carbonyl growth rate, calculated from the lower oxygen concentration limit in the air void channel.

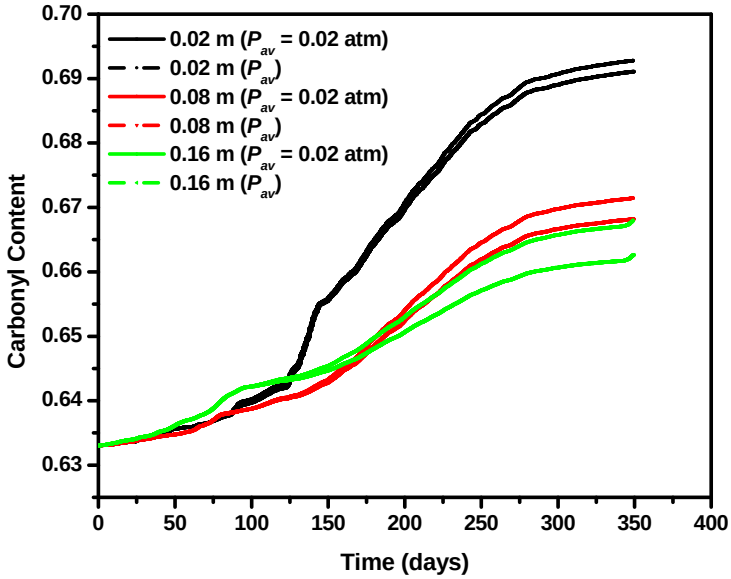


Figure 63. Sample Calculation of Carbonyl Growth for an Air Void Channel as a Function of Depth of Pavement Layers.

The effect of pavement temperature on oxidation is clearly shown by comparing either highest or lowest carbonyl growth rates at these three depths. Pavement temperature at the pavement surface has the largest daily temperature fluctuation and the highest average pavement temperatures. Therefore, it is not surprising to see that the yearly oxidation rate is highest at the surface. Then it decreases deeper into pavement because of decreasing daily temperature fluctuations that is coupled with the exponential reaction activation energy effect. In addition, the model results show that asphalt binder oxidation rates in the pavement were rather slow during spring and winter, and increased significantly during the summer due to higher pavement temperatures, as would be expected.

Also observed from model calculation is the effect of the oxygen pressure in the air void channel on oxidation rate. In general, the calculated oxidation rate is lower for the lower oxygen concentration values (due to the diffusion resistance) at each depth compared to the oxidation rate calculated at the higher oxygen pressure (0.2 atm oxygen throughout the air channel). At 0.02 m below the surface, there is a slightly reduced oxidation rate when the lower limit of oxygen concentration is used. This reduced rate is more evident at deeper pavement depths where oxygen pressure in the air channel is further reduced by diffusion resistance.

Model Calculation of Layer-by-Layer Bulk Oxidation Rates for a Pavement

Structural Layout of Model Calculation

Figure 64 shows a schematic layout of the model structure with essential elements for the calculation listed. For a payment layer at depth *d* in a given pavement, the pavement temperature at this depth [*T (t, d)*] is first calculated as a function of time based on the pavement temperature

model developed in Chapter 6. X-ray CT scanning of pavement core specimen is performed and processed X-ray CT images at depth *d* are obtained to analyze the air void size distribution and the number of air voids from which an average air void radius (r_i), number of air voids (N_i), and shell distance ($r_{NFB,i}$) for each size range.

An air void radius (r_i) and shell distance ($r_{NFB,i}$) pair exist for each air void size. The vertical transport model is applied to this air void radius (r_i) and shell distance ($r_{NFB,i}$) pair to generate the lower limit of P_{av} profile as a function of depth. Recalling from the vertical diffusion modeling section, we defined an upper limit profile and a lower limit profile of P_{av} depending on the oxygen transport behavior in interconnected air void (diffusion versus convection). From the profiles, lower limits of P_{av} values at depth *d* are determined.

Combining pavement temperature profiles at *d*, X-ray CT air void size and spacing characterization, upper and lower P_{av} values as a function of air void parameters, plus oxidation and hardening kinetics and diffusion parameters for the asphalt used in the pavements, the horizontal diffusion and reaction model was used to calculate a range of probable oxidation rates as a function of depth of *d* and air void parameters.

Thus, a bulk oxidation rate of this pavement layer was estimated with Eq. 9 based on calculated oxidation rates for each air void size range and number of air voids in this size range.

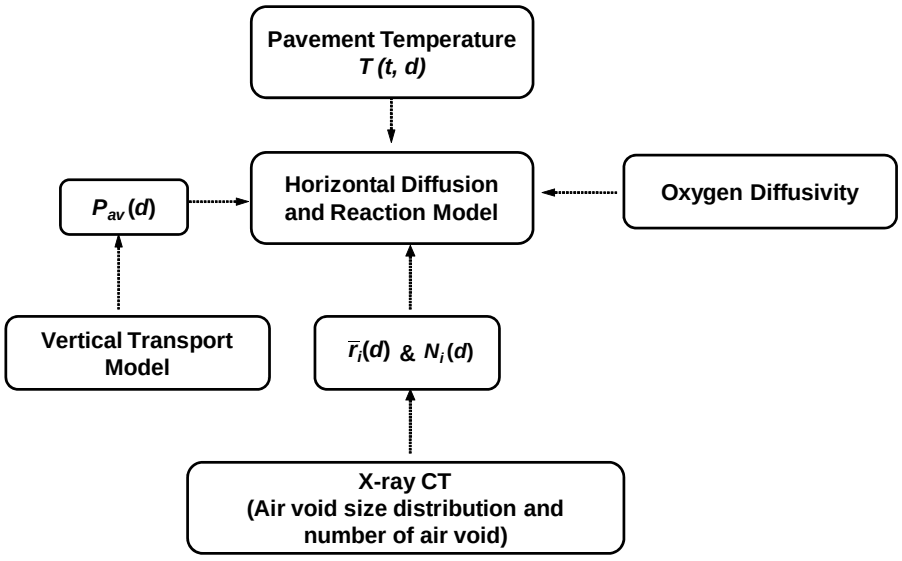


Figure 64. Schematic Layout of the Model Structure to Calculate Oxidation Rate for a Pavement Layer.

Sample Calculation of Oxidation Rates of Pavement US82 at Lubbock, TX

To demonstrate the calculation process further, yearly oxidation rates at different depths of pavement US82 at Lubbock, TX, were calculated. Four pavement layers at depth of 0.01 m, 0.02 m, 0.03 m, and 0.04 m were selected. The asphalt binder used for this pavement is Alon 76-22, oxidation and hardening kinetics of this binder is obtained from separate experiments and ready to use in this modeling work.

To start with, yearly climate data at Lubbock, TX, were collected and used as inputs of the pavement temperature model to calculate a yearly pavement profile at each studied pavement depths. Figure 65 shows a sample demonstration of a short summer period of pavement temperature calculated at each depth in the pavement. Here, daily temperature cycle of temperature for a period of 20 days is plotted. The amplitude of each cycle decreases with depths, with about 10°C difference between the first layer at 0.01 m below the surface and the fourth layer at 0.04 m below the surface. Coupled with the exponential reaction activation energy effect, it will lead to a significant difference to final oxidation rates.

Meanwhile, a surface layer of two-inch pavement core specimen was collected in the field and used for X-ray CT scanning and image processing. Final black and white image slices of accessible air voids after image processing at each studied depth were analyzed for air void distribution and total number of air voids. From them, average air void radius (r_i), number of air voids (N_i), and shell distance ($r_{NFB,i}$) were determined for each pavement core layer, as shown in Table 31, Table 32, and Table 33. Here, air void distribution is divided into five size ranges, from 0~0.2 mm, 0.2~0.5 mm, 0.5~1 mm, 1~2 mm, and 2~3 mm. As we can see, average air void radius, though not exactly the same, are rather close from layer to layer. While the number of air voids differs from one layer to another, so does average shell distance that is determined by the number of air void in each layer.

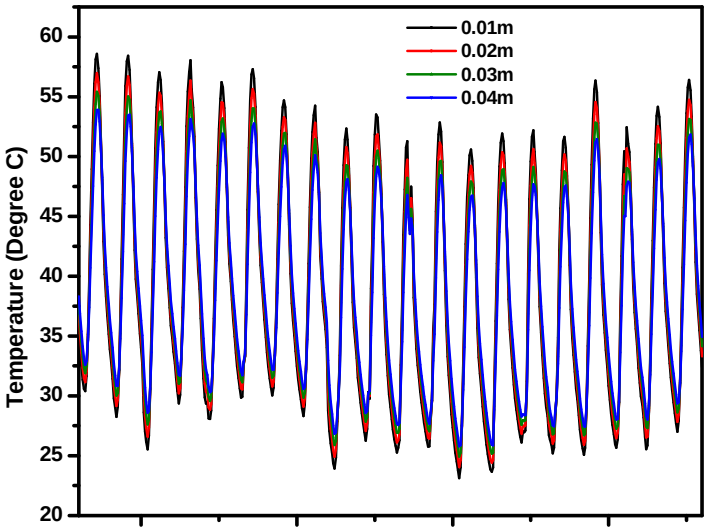


Figure 65. Pavement Temperature of US82 at Different Depths in Pavements in a Summer Period.

Table 31. Average Air Void Radius Calculated for Each Air Void Range at Different Pavement Layers of US82.

Depth	Average Air Void Radius r_i (mm)				
	0~0.2 mm	0.2~0.5 mm	0.5~1 mm	1~2 mm	2~3 mm
0.01 m	0.140	0.351	0.727	1.360	2.377
0.02 m	0.142	0.350	0.722	1.358	2.400
0.03 m	0.144	0.348	0.725	1.337	2.306
0.04 m	0.141	0.351	0.720	1.361	2.405

Table 32. Number of Air Voids Calculated for Each Air Void Range at Different Pavement Layers of US82.

Depth	Number of Air Voids				
	0~0.2 mm	0.2~0.5 mm	0.5~1 mm	1~2 mm	2~3 mm
0.01 m	17	99	130	87	17
0.02 m	13	87	105	57	8
0.03 m	13	89	106	55	6
0.04 m	14	85	104	72	13

Table 33. Shell Distance Calculated for Each Air Void Range at Different Pavement Layers of US82.

Depth	Average Shell Distance r_{NFB} (mm)				
	0~0.2 mm	0.2~0.5 mm	0.5~1 mm	1~2 mm	2~3 mm
0.01 m	12.567	12.567	12.567	12.567	12.567
0.02 m	14.314	14.314	14.314	14.314	14.314
0.03 m	14.369	14.369	14.369	14.369	14.369
0.04 m	13.891	13.891	13.891	13.891	13.891

With the air void radius (r_i) and shell distance ($r_{NFB,i}$) pair at each size range in each layer, a vertical transport model is used to calculate oxygen pressure profiles (P_{av}), both upper and lower limits, as a function of depths. P_{av} values at corresponding layers are read from the plot and summarized in Table 34. The assumption of convection dominated transport process established the upper limits, a constant oxygen pressure at 0.2 atm throughout the air void channel that is independent of depth in pavement. While the assumption of oxygen transport by diffusion only provided lower limit, a decrease of oxygen concentration away from surface of the pavement.

The amount of lower limit P_{av} decreases away from pavement surface varies with the size of the air voids. For air void size range from 2~3 mm, there is nearly no oxygen pressure drop at all layers; For air void size in range from 0.5mm to 1 mm, oxygen pressure drops significantly from 0.2 atm at the surface to 0.198 atm at 0.01 m below the pavement surface, and to 0.192 atm at 0.04 m below the surface; For the smallest air void size range, 0~0.2 mm, oxygen pressure drops tremendously from 0.2 atm at the surface to 0.14 atm at 0.01 m below the surface, and oxygen is completely depleted at 0.04 m below the surface. In the process of diffusion throughout an air void channel, oxygen is also continuously consumed by adjoining asphalt binder-aggregate matrix. Because of that, oxygen concentration in an air void is determined by the balance of supply rate and consumption rate. Considering that the supply rate of oxygen is higher for larger air void size, while the oxygen consumption rate stay the same for all size of air voids (shell distance are nearly the same), oxygen is more easily depleted inside smaller air void than larger ones.

With a known pavement temperature profile, the upper and lower P_{av} values corresponding to an air void radius (r_i) and shell distance ($r_{NFB,i}$) pair, and the air void radius (r_i) and the shell distance ($r_{NFB,i}$) themselves, a horizontal diffusion and reaction model was used to calculate a highest oxidation rate and a lowest oxidation rate for air voids in the size range at given depth. Bulk yearly oxidation rate of each pavement layer is also estimated with Eq. 9 with known oxidation rates for each air void size range and number of air voids in each size range. Figure 66 shows bulk carbonyl content growth for one year period for these four studied pavement layers. Table 35 summarizes yearly oxidation rates calculated for each air void size range and bulk oxidation rates at each layer.

Table 34. P_{av} Calculated for Each Air Void Range at Different Pavement Layers of US82.

		P_{av} (atm)				
Depth	**Condition**	**0~0.2 mm**	**0.2~0.5 mm**	**0.5~1 mm**	**1~2 mm**	**2~3 mm**
0.01 m	Upper	0.2	0.2	0.2	0.2	0.2
	Lower	0.141	0.192	0.198	0.199	0.200
0.02 m	Upper	0.2	0.2	0.2	0.2	0.2
	Lower	0.084	0.184	0.196	0.199	0.200
0.03 m	Upper	0.2	0.2	0.2	0.2	0.2
	Lower	0.030	0.176	0.194	0.198	0.200
0.04 m	Upper	0.2	0.2	0.2	0.2	0.2
	Lower	0.000	0.169	0.192	0.197	0.199

The effect of air void size on oxidation rates is clearly observed. Taking layer 1 as an example, highest oxidation rate increases from 0.0281 CA/year to 0.0394 CA/year with increase of air void size range from 0~0.2 mm to 2~3 mm. This difference becomes greater when lowest oxidation rates are compared where effect of air void size on vertical diffusion is combined (from 0.0256 CA/year to 0.0326 CA/year).

The effect of pavement temperature on oxidation rates is observed by comparing oxidation rates calculated for a certain air void size range or overall bulk oxidation rates at

different pavement layers. Taking overall bulk oxidation rates as an example, oxidation rates decrease with pavement depths, from 0.0329 CA/year at 0.01 m below the surface to 0.0276 CA/year at 0.04 m below the surface if highest oxidation rates are compared. In addition, temperature effect is also shown in Figure 66, as oxidation rates were slow during spring and winter, and increased significantly during the summer due to higher pavement temperatures, as would be expected.

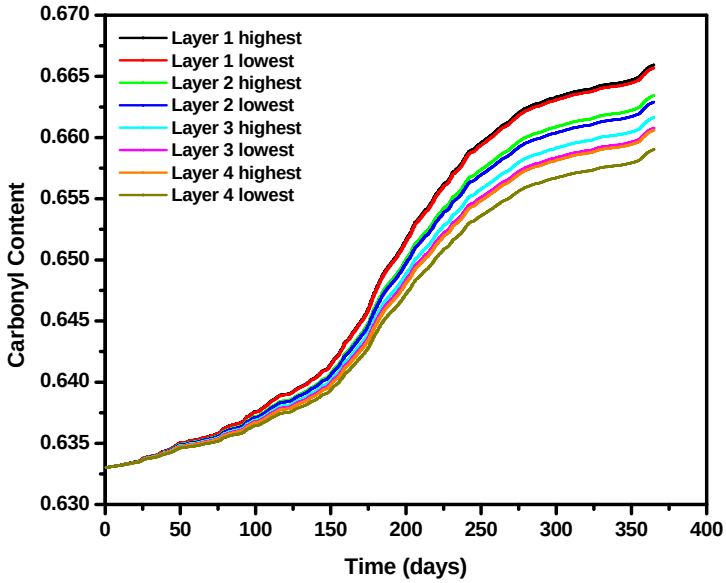


Figure 66. Bulk Carbonyl Growth Rates (Oxidation Rates) of US82 for One-Year Period at Different Pavement Layers.

Table 35. Oxidation Rates Calculated for Each Air Void Range at Different Pavement Layers of US82.

		r_{O2}(CA/year)					
Depth	**Condition**	**0~0.2 mm**	**0.2~0.5 mm**	**0.5~1 mm**	**1~2 mm**	**2~3 mm**	**Bulk**
0.01 m	Highest	0.0281	0.0301	0.0328	0.0359	0.0394	0.0329
	Lowest	0.0256	0.0297	0.0326	0.0359	0.0394	0.0326
0.02 m	Highest	0.0262	0.0281	0.0306	0.0335	0.0368	0.0304
	Lowest	0.0208	0.0275	0.0304	0.0335	0.0369	0.0298
0.03 m	Highest	0.0248	0.0266	0.0289	0.0317	0.0347	0.0286
	Lowest	0.0148	0.0256	0.0286	0.0317	0.0347	0.0277
0.04 m	Highest	0.0236	0.0253	0.0275	0.0302	0.0331	0.0276
	Lowest	0.0000	0.0241	0.0272	0.0301	0.0331	0.0259

Highest and lowest oxidation rates are shown in both Figure 66 and Table 35. Their values are calculated with input of upper and lower limit of P_{av} separately. In each pavement

layer, because the difference in P_{av} of the upper and lower limits is small in a larger air void size and great in smaller air void size, it is not surprising to see that the highest and lowest oxidation rates calculated at larger air void size are rather close. Their difference becomes more and more obvious with decrease of air void size, as shown in Table 32, and Table 33. For some air void size at different pavement layers, lower limit P_{av} decreases away from pavement surface. So, the difference between highest and lowest oxidation rates becomes greater at deeper pavement layers, as we observed in Figure 65 with bulk oxidation rates.

Model Validation

Measured Pavement Oxidation Rates in the Field

Oxidation of the asphalt binders in these pavements in the form of the carbonyl content growth is summarized in Figure 67. This figure shows the bulk carbonyl content of the recovered binders for each pavement core versus the corresponding service age.

Among the six pavements, distinct oxidation rates were obtained. Texas pavements of US277, US290, and US54 have a relatively high oxidation rates from 0.0635 CA/year to 0.0935 CA/year, while Texas pavements of IH35-Waco and US69 and Minnesota pavement Cell 1 have low carbonyl growth rates of 0.0256 CA/year to 0.0334 CA/year. There appears to be a great deal of disorganization of the data. However, when considered in detail and evaluated from the perspective of the key elements that affect asphalt oxidation in pavements including pavement temperature, pavement air void properties, and asphalt oxidation kinetics, the results are, in fact, quite consistent. Texas has higher pavement temperature compared with Minnesota, so it is expected that in general oxidation rates in Texas should be greater than in Minnesota. In fact, for a Texas pavement (US277) with slightly higher air void content and similar value of activation energy as Minnesota Cell 1, the oxidation rate is nearly two-fold of Minnesota Cell 1. Oxidation rates of US290 are further accelerated by extremely high air void content of 12.44 percent, and oxidation rates of US54 are sped up by an exceptional low value of activation energy of 54.95 KJ/mol.

Exceptions in Texas pavements are IH35-Waco and US69 that have oxidation rates comparable to Minnesota Cell 1. IH35-Waco is a 4-inch rich bottom layer that is 16 inch below pavement surface. At this depth, amplitude of daily temperature fluctuation attenuates to a great deal and causes oxidation rate to decrease drastically compared with surface layers. For US69, there is no apparent explanation of the low oxidation rate with pavement information obtained so far. The low oxidation rate is actually caused by a combination of pavement temperature, air voids parameters, and asphalt oxidation kinetics.

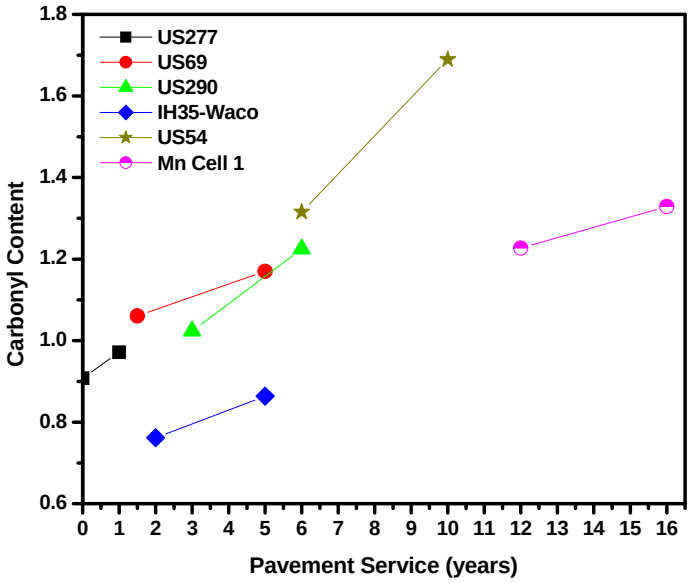


Figure 67. Measured Oxidation Rates of Asphalt Binders in Various Pavements.

Modeled Pavement Oxidation Rates in the Field

While measured field oxidation rates provide some insight on variables that affect asphalt oxidation and values of asphalt oxidation rates in pavements, the data are not detailed enough to serve as a prediction model to pavement engineers. A fundamentals-based oxygen transport and reaction model to predict asphalt binder oxidation in pavements was presented in Chapter 7 and the previous sections of this chapter. However calibration and verification of the pavement oxidation model is required. In this section, pavement temperature, air void properties, and asphalt oxidation kinetics are carefully characterized for pavement cores (sites) listed in Table 29 plus one more pavement site of IH35-LRD. From them, yearly oxidation rates are modeled as a function of time and depths in the pavement cores.

The thickness of validation cores ranges from two to four inches. In this study, each pavement core was divided into 0.5 inch layers, and designated as layer 1 (top layer), layer 2, layer 3, etc. Representative pavement temperature, air void parameters, and P_{av} values for each core layer are obtained to calculate oxidation rates at these individual pavement layers.

Temperature Profile of Pavements

Climate inputs including hourly solar radiation, hourly air temperature, and daily wind speed in hourly format at these pavement sites were collected or interpolated. Annual pavement temperature profiles as a function of depth for these locations were generated using climate data inputs coupled with the pavement temperature prediction model. Temperature profile for the pavement core is a function of the depths in the core, and representative pavement temperature of each 0.5-inch thick pavement layer is calculated with a given depth for each layer.

Figure 68 shows a demonstration of pavement temperature profile calculated for the top layer of studied pavement cores for a period of 15 days in winter and summer. Annual temperature profile of these pavements as different pavement core layers is reported in the Appendix B.

As shown in Figure 68, there is a great deal of difference in these temperature profiles for each pavement core in terms of daily temperature fluctuations and daily average temperatures. These profiles could be categorized into three groups: 1) Minnesota Cell 1, with daily average pavement temperature much lower than other pavements in winter and summer; 2) Rich bottom layer of IH35-Waco and IH35-LRD, with nearly no daily temperature fluctuations in winter and slight fluctuations in summer; and 3) All other Texas pavements. Because pavement temperature are heavily influenced by climate and depths in the pavements, it is not difficult to point out that the difference between group 1 to other pavements is mainly caused by cold climate in Minnesota, and that the difference between group 2 to other pavements is induced by the depth effect.

Even among the four Texas pavements in group 3, there is also a significant variation of daily temperature fluctuations and daily average temperatures that follows climate trend. Climate in these pavement sites change from dry-cold in Amarillo, to wet-warm in Lufkin, and to dry-warm at Laredo, with climate of Bryan in the middle of them. Corresponding to that, US277 at Laredo has the highest daily average temperature with US69 at Lufkin second to it, while US54 at Amarillo and US290 at Bryan have relative lower daily average temperatures. Similar observation follows for daily temperature fluctuations.

The discussion above compares temperature of the top layer of studied pavement cores. Ssimilar observation follows for comparison of temperature at other core layers. Of course, it is expected that daily temperature fluctuation decreases away from top layer for each pavement cores, while average daily temperature do not change too much.

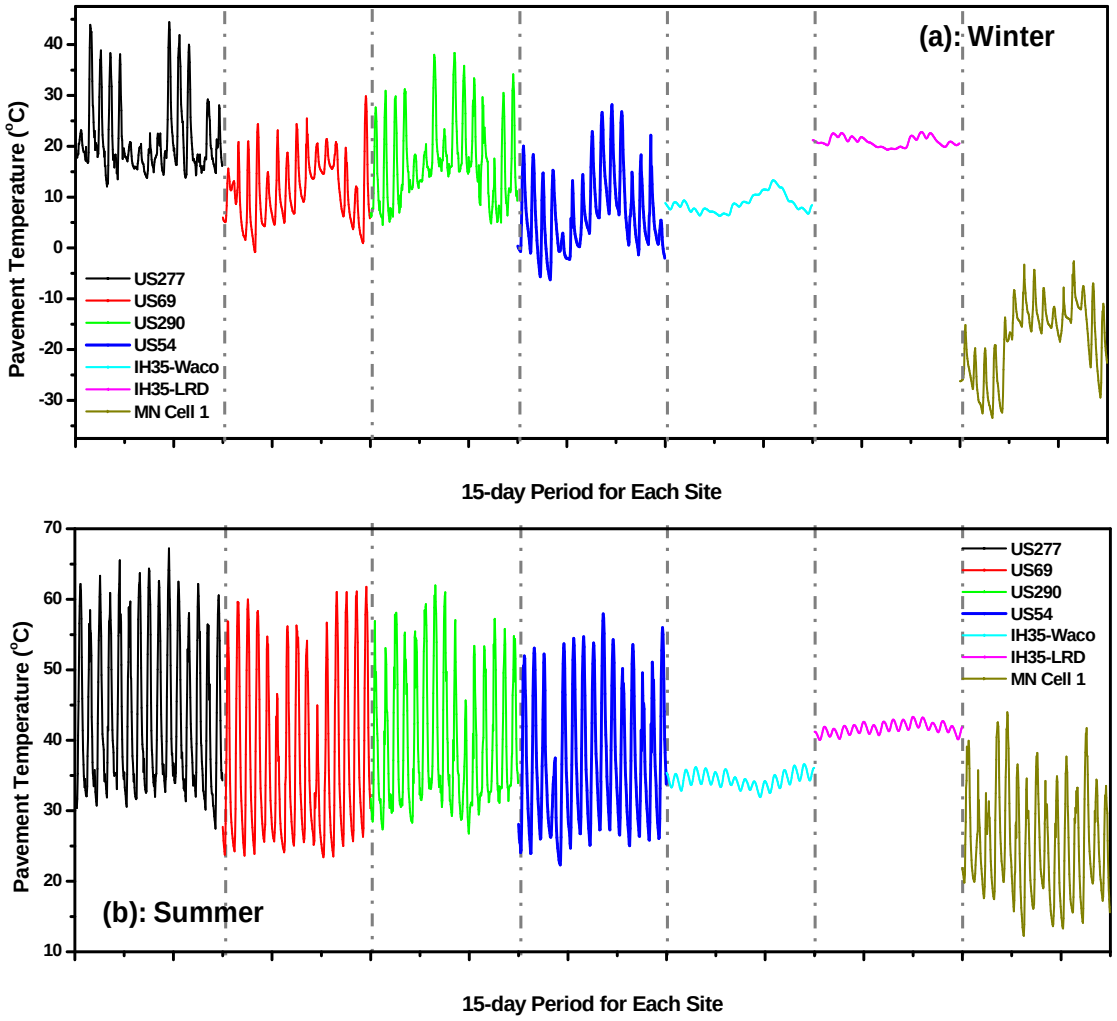


Figure 68. Temperature Profiles of Top Layer of Validation Pavement Core at (a): Winter from January 15 to January 30, 1994, and (b): Summer from July 1 to July 15, 1994.

Characterization of Air Void in Pavements

Pavement cores were collected from these validation sites and scanned with X-ray CT for interior air void structure. A sequence of grey scale images slices are generated with 1 mm interval in depths. These original grey scale images were then converted to black and white images of total air voids after calibration and interconnected air voids after image processing. Figure 69 shows a collection of representative black and white images of total air void after calibration.

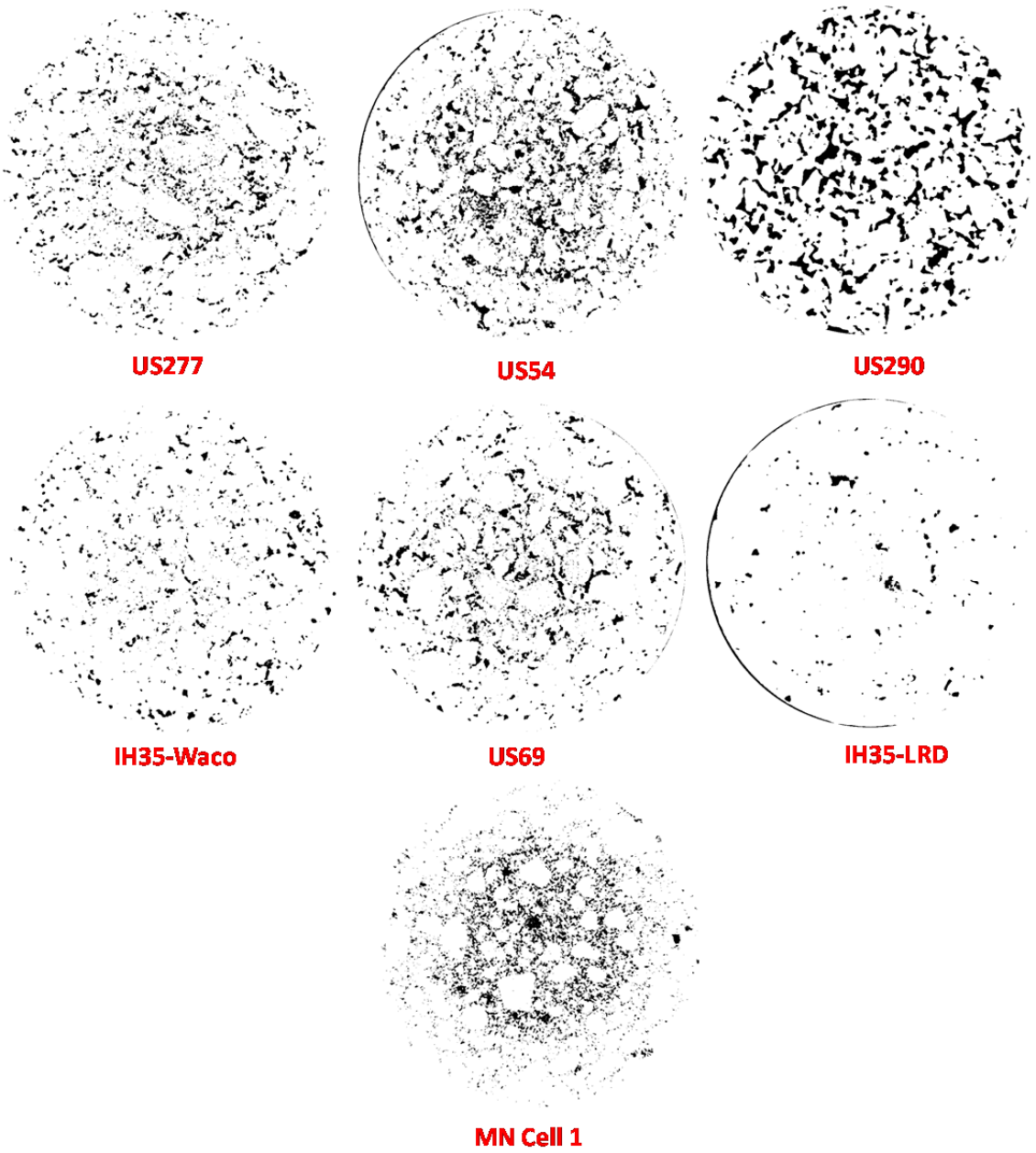


Figure 69. Collection of Representative Images of Total Air Void for Each Field Cores.

Each core exhibits unique air void properties in terms of air void size, number of air voids, and air void distribution. For example, most of the air voids in the field core of US290 have larger air voids than other pavement cores, while the number of air voids is less than most of other cores. Air voids in the field core of IH35-LRD is much less than other field cores.

From these black and white images of total air void, model-required air void parameters including average air void radius (r_i), number of air voids (N_i), and shell distance ($r_{NFB,i}$) for each layer of field cores were determined following procedures demonstrated in Chapter 4. Image slices obtained in each 0.5-inch thick core layer are combined to analyze for air void distribution and total number of air voids in this layer.

Table 36 summarizes air void parameters for the top layer of studied pavement cores. It provides quantitative comparison of average air void radius (r_i) and number of air voids in each air void size range, shell distance (r_{NFB}), and total number of air voids of studied pavement cores. More detailed air void data for each pavement core at different pavement layers are reported in the Appendix C.

Table 36. Summary of Air Void Parameters at the Top Layer of Pavement Cores.

r_i (mm) / # *of AV*		US277	US69	US54	US290	IH35 (Waco)	IH35 (LRD)	MN (Cell 1)
AV Size (mm)	0~0.2	0.140/ 34	0.144/ 52	0.145/ 40	0.144/ 20	0.144/ 23	0.140/ 8	0.144/ 95
	0.2~0.5	0.332/ 672	0.336/ 407	0.332/ 436	0.352/ 92	0.340/ 309	0.350/ 80	0.327/ 909
	0.5~1	0.697/ 211	0.700/ 240	0.736/ 246	0.736/ 128	0.702/ 242	0.713/ 92	0.679/ 327
	1~2	1.338/ 83	1.342/ 84	1.359/ 117	1.414/ 129	1.305/ 85	1.308/ 31	1.336/ 97
	2~3	2.400/ 14	2.663/ 12	2.423/ 27	2.455/ 40	2.276/ 5	2.407/ 2	2.470/ 18
r_{NFB} (mm)		8.931	8.470	8.163	11.924	9.182	16.128	6.226
Total # of AV		1014	795	866	409	664	213	1446

As observed in Table 36, air void properties of each pavement core vary from one to another. Total number of air voids in these seven pavement cores changes from 213 for IH35-LRD to 1446 for MN Cell 1, while average shell distance value changes from 6.226 mm to 16.128mm. There is also a noteworthy difference in air void size distribution among these cores. For example, the majority of air voids in US290 have radii larger than 0.5 mm, while in US277, majority of air void radius falls between 0.2~0.5 mm.

The discussion above is based on air voids at top layer of pavement cores, but the dissimilarity of air void properties among these field cores at other core layers are also observed. One needs to note also that for each pavement core, the number of air voids vary in depths while air void size distribution remains almost the same.

Calculation of P_{av} and Asphalt Binder Oxidation Rates

For each air void radius (r_i) and shell distance ($r_{NFB,i}$) pair at a given air void size range, a vertical transport model is used to calculate oxygen pressure profiles (P_{av}), both upper and lower limits as a function of depths, and P_{av} values at corresponding depth are then read from the plot. The assumption of a convection-dominated transport process established the upper limit; a constant oxygen pressure at 0.2 atm throughout the air void channel is used. While the assumption of oxygen transport by diffusion only provided lower limit; a profile of decrease of

oxygen pressure away from surface of the pavement is obtained. P_{av} values at corresponding depth for each pavement core layer is summarized and reported in the Appendix C.

With a known temperature profile, the upper and lower P_{av} values for each air void radius (r_i) and shell distance ($r_{NFB,i}$) pair, the air void radius (r_i), the shell distance ($r_{NFB,i}$), and asphalt oxidation and hardening kinetic parameters, a horizontal diffusion and reaction model was used to calculate a highest oxidation rate and a lowest oxidation rate for air voids in each given size range at different core layers. Bulk oxidation rate of each core layer is estimated with Eq. 4-8 with known oxidation rates for each air void size range and number of air voids in each size range. Oxidation rates calculated for each air void size range as well as bulk oxidation rates at each core layer for these validation cores is reported in Appendix D.

Table 37 summarize yearly maximum and minimum oxidation rates at different layers of studied pavement cores. Detailed data of modeled oxidation rates for each pavement cores are reported in the Appendix D. As reported in Table 37, yearly oxidation rate could reach as high as 0.1198 CA/year (pavement US54 at top layer) and go as low as 0.0182 CA/year (pavement MN cell 1 at layer 6). The ranking of pavements in order of oxidation rates is US54, US290, US277, IH35-LRD, US69, IH35-Waco, and MN Cell 1 from high to low. This ranking is, in fact, quite consistent from the perspective of the key elements that affect asphalt oxidation in pavements including pavement temperature, pavement air void properties, and asphalt oxidation kinetics.

Minnesota Cell 1 has the lowest oxidation rate calculated among these seven pavement sites, primarily caused by the cold climate in Minnesota. As shown in Figure 67, the daily average temperature of MN cell 1 is much lower than other Texas pavements. Among Texas pavements, asphalt binder in US54 has an exceptional low value of activation energy of 54.95 KJ/mol, as a result, oxidation rate is much higher compared with other asphalt binders under the same oxygen pressure. For US290, air void content of is extremely high (12.44 percent). The majority of air void has an air void radius larger than 0.5 mm, and because of that, it is not surprise to see higher oxidation rate in US290. Texas pavement US277 has intermediate air void content and intermediate value of activation energy compared with other Texas pavements, and a maximum oxidation rate of 0.0526 CA/year is calculated. Exceptions in Texas pavements are IH35-LRD, IH35-Waco, and US69 that have oxidation rates comparable to Minnesota Cell 1. IH35-LRD and IH35-Waco has a rich bottom layer that is 12 to 16 inch below pavement surface. Amplitude of daily temperature fluctuation attenuates to a great deal at these depths, as shown in Figure 68, which causes oxidation rates to decrease drastically compared with surface layers. For US69, it seems the low oxidation rate is caused by the combination of high activation energy of asphalt binders, less favorable air void distribution, and relative low pavement temperature.

Table 37. Summary of Maximum and Minimum Oxidation Rates Calculated for Each Pavement Core Layers.

Oxidation rate (CA/year)		US277	US69	US54	US290	IH35 (Waco)	IH35 (LRD)	MN (Cell 1)
Layer 1	Highest	0.0526	0.0296	0.1198	0.0771	0.0268	0.0384	0.0239
	Lowest	0.0524	0.0294	0.1174	0.0761	0.0253	0.0281	0.0238
Layer 2	Highest	0.0489	0.0267	0.1151	0.0697	0.0266	0.0382	0.0226
	Lowest	0.0480	0.0264	0.1061	0.0674	0.0243	0.0257	0.0224
Layer 3	Highest	0.0460	0.0243	0.1119	0.0639	0.0264	0.0384	0.0215
	Lowest	0.0447	0.0239	0.0976	0.0610	0.0240	0.0221	0.0212
Layer 4	Highest	0.0437	0.0227	0.1075	0.0593	0.0263	0.0384	0.0206
	Lowest	0.0420	0.0223	0.0918	0.0550	0.0240	0.0221	0.0202
Layer 5	Highest	0.0411	--	0.1040	0.0557	0.0262	--	0.0192
	Lowest	0.0382	--	0.0839	0.0506	0.0240	--	0.0188
Layer 6	Highest	--	--	--	--	0.0263	--	0.0187
	Lowest	--	--	--	--	0.0242	--	0.0182

For each pavement core, oxidation rates decrease away from the surface. Taking US277 as an example, maximum oxidation decreases from 0.0526 CA/year at the top layer to 0.0411 CA/year in the fifth layer. These differences in oxidation rates with pavement depths are mainly caused by temperature differences, because model inputs are almost the same in the calculation of maximum oxidation rates at different core layers except pavement temperature. Similarly, a decrease of minimum oxidation rate away from pavement surface could also be observed, but at a greater level. In this case, the decrease of oxidation is not only influenced by pavement temperature but also pressure in air voids (P_{av}); values of P_{av} also decreases away from pavement surface.

Measured Oxidation Rates versus Modeled Oxidation Rates

Because of the limited number of cores that can be obtained, the relatively short time between coring (due to the project length relative to the slow field oxidation rate), and the inherent variability that tends to exist between cores, the ability to make layer-by-layer comparisons of these field oxidation measurements, especially considering the fairly modest layer-by-layer differences indicated by the model calculations, is necessarily limited. Consequently, the overall binder oxidation rates for each pavement core (rather than slice by slice comparisons) were compared using the field measurements and model calculations.

Table 38 summarizes yearly oxidation rates (in terms of carbonyl growth) measured for these six validation cores. Maximum and minimum oxidation rates calculated from the model are also reported. The visual comparison is shown in Figure 70.

Table 38. Comparison of Measured and Modeled Field Oxidation Rates.

State	Site	Oxidation rate modeled (CA/year)		Bulk oxidation rate measured (CA/year)
		Maximum	Minimum	
MN	Cell 1	0.0200	0.0195	0.0256
TX	US277-LRD	0.0465	0.0451	0.0705
	US69-LFK	0.0258	0.0255	0.0370
	IH35-LRD #4	0.0384	0.0245	---
	US290-BRY	0.0651	0.0620	0.0671
	IH35-WAC #4	0.0264	0.0243	0.0340
	US54-AMR	0.1117	0.0994	0.0935

The ranking of predicted oxidation rates from high to low is the same as the ranking established by field measurement except for US277, and the oxidation rates measured in the field can be quite close to the range of predicted oxidation rates that were established by the maximum and minimum oxidation rates. For example, the measured oxidation rate is only three percent higher than the maximum oxidation rate calculated for US290, and for US54 the measured oxidation rate is six percent lower than the minimum oxidation rate predicted.

On the other hand, there are exceptions. For example, for pavements from US277, US69, IH35-Waco, and MN Cell 1, the respective measured oxidation rates are 34, 30, 22, and 21 percent higher than the maximum oxidation rates predicted.

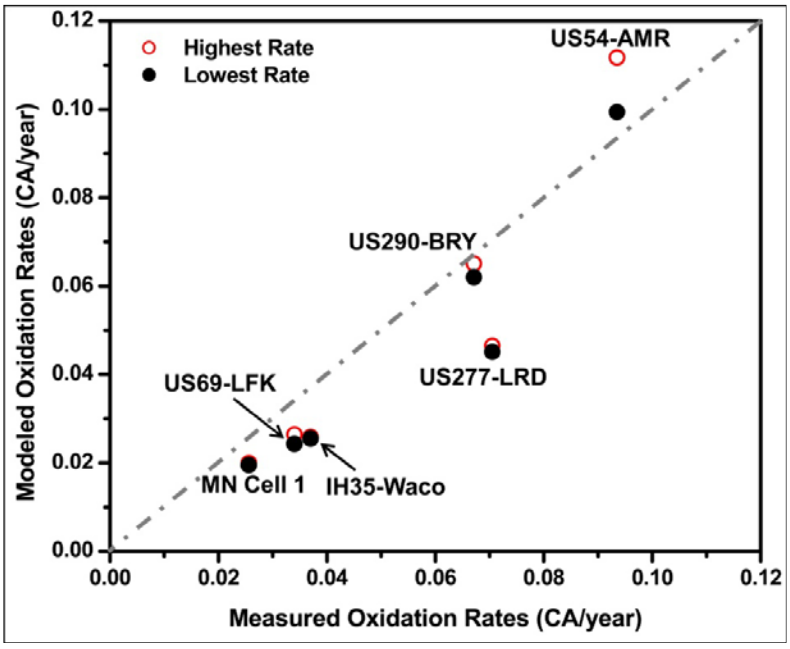


Figure 70. Comparison of Measured and Modeled Field Oxidation Rates.

A possible explanation of these higher rates is that these pavements were all newly constructed pavements, at least relative to their oxidation rates; at the time of their first core, the Texas pavement's respective service lives were 0, 1.5, and 2 years. For Minnesota Cell 1, the first core was taken after 11 years in the road. Oxidation of a neat asphalt binder is characterized by an initial rapid rate period that declines over time until a constant-rate period is reached. It has been estimated that the fast oxidation rate period can last as long as 2~3 years for Texas pavements, and 12 years or longer for Minnesota pavements. Thus, the asphalt binder oxidation for these pavement cores was most likely dominated by the initial rapid oxidation period, rather than the slower constant-rate reaction regime. However, in the model calculations, only the slower constant-rate reaction kinetics parameters were used to calculate the field oxidation rates, thereby likely providing a significant underestimation of the oxidation rates. The reaction rate for the constant rate period can generally be described using an Arrhenius expression for temperature variation and pressure dependence, while the reaction mechanisms are still not fully understood for initial rapid rate period. An extensive understanding of oxidation mechanisms and oxidation kinetics in this rapid oxidation period is essential to incorporating the fast reaction period into this model and to providing a more accurate prediction of oxidation rates during the first several years of service for newly constructed pavements.

In spite of this disagreement of model predictions for pavements that are largely in the fast rate oxidation period, in general this fundamentals-based model provides a very good match with field measurements, suggesting that it captures the critical elements that affect asphalt binder oxidation in pavements.

SUMMARY

Transport through an air void channel and transport and reaction within the asphalt-aggregate matrix associated with an air void channel were modeled separately to calculate an oxidation rate for the finite asphalt-aggregate layer associated with the air void channel. Because oxidation rate calculated with such a model depends heavily on air void properties that varies from pavement layer to layer, methods to characterize pavement air voids are developed. Three air void parameters, including air void radius (r_i), average shell distance ($r_{NFB,i}$), and number of air voids (N_i), were obtained with X-ray CT scanning technique and imaging analysis to use in the model. Combing above developments with pavement temperature, asphalt binder oxidation and hardening kinetics, layer-by-layer asphalt oxidation rate in a pavement is successfully determined.

Asphalt oxidation rates of six pavements with distinct temperature profile, air void properties, asphalt oxidation kinetics, and years in service have been measured and compared with model calculations. Measured bulk oxidation rates of pavement cores vary from 0.0935 CA/year for pavement US54 at Amarillo, Texas, to 0.0256 CA/year for pavement Minnesota Cell 1.

Measured oxidation rates among these pavements are consistent from the perspective of the key elements that affect asphalt oxidation in pavements including pavement temperature, pavement air void properties, and asphalt oxidation kinetics. In general, asphalt binders with high activation energy results in a low oxidation rate in the field; high pavement temperature leads to

an increased oxidation rate (Texas pavements vs. Minnesota pavement; surface cores vs. rich bottom cores); and large air void pore radius and small shell distance produce a higher oxidation rate.

Pavement temperature and air void parameters for these pavement cores were collected as model inputs to predict field oxidation rates on these validation pavement cores. The ranking of predicted oxidation rates is exactly the same as the ranking established by field measurement except US277; and oxidation rates measured in the field, in general, fall in between or close to the range of predicted oxidation rates established by the maximum and minimum oxidation rates, with a few exceptions. The exceptions are newly constructed pavements where asphalt binder oxidation rate most likely are still governed by the initial rapid oxidation period, rather than the low constant reaction rate regime used in the model calculations, which will underestimate the oxidation rates for these new pavements to a great extent.

An extensive understanding of oxidation mechanisms and oxidation kinetics in this rapid oxidation period is essential to incorporate fast reaction period into this model to provide more accurate prediction of oxidation of new constructed pavements.

The importance of this study is to develop an oxidation model for prediction of asphalt oxidation in pavements. Such a model is a critically important tool for pavement design and improvement and for maintenance scheduling.

CHAPTER 9. MODELING ASPHALT OXIDATION IN PAVEMENT WITH FIELD VALIDATION

[Pages 171 through 178 reprinted with permission from Jin, X., Cui, Y., and Glover, C.J. (2013) Modeling Asphalt Oxidation in Pavement with Field Validation. *Petroleum Sci. and Technol*., Volume 31, Issue 13, pp. 1398-1405. Copyright 2013. Reproduced by permission of Taylor & Francis Group, LLC. (http://www.tandfonline.com).]

ABSTRACT

A model for asphalt oxidation in pavement was developed based on fundamentals of oxygen diffusion in the mastic and reaction with asphalt. Diffusion depth, a concept different from the conventional film thickness, defined the oxygen diffusion region in the mastic. A field calibration factor accounted for the factors not considered in the model such as the effect of small aggregate particles on oxygen diffusion. Carbonyl area and viscosity of binders recovered from field cores were measured and used for model calibration and validation. Results demonstrated that the proposed model estimates carbonyl growth over time in pavement, layer-by-layer, quite well.

INTRODUCTION

The mechanistic-empirical pavement design guide is being implemented by many state highway agencies (McCarthy and Liang, 2011). However, the global aging model (Mirza et al., 1995) used in MEPDG is problematic for predicting asphalt hardening in pavements. It fails to recognize that each binder has unique aging and hardening rates (Liu et al., 1996) and that asphalt oxidizes well below the top inch of pavement (Al-Azri et al., 2006). Furthermore, it assumes that the level of oxidation in pavements has a practical limit, an assumption not supported by both laboratory and field data. In summary, a better model for asphalt oxidation in pavements is needed for both design and maintenance purposes.

Lunsford (1994) proposed a highway-pavement aging model, including important concepts such as oxygen diffusion limit, air void, and binder content. Prapaitrakul et al. (2009) improved this model by using average pore radius, average shell thickness, and hourly pavement temperature input. Han (2011a) used five pore radii from X-ray CT measurements of pore size distribution instead of one average value, thus further refining the model.

In this paper, the asphalt oxidation model was significantly improved by: 1) adding the concept of diffusion depth to better define the oxygen diffusion region in the mastic; 2) incorporating both fast-rate and constant-rate asphalt oxidation kinetics; 3) introducing a field calibration factor to account for the factors not considered in the earlier model, for example, the tortuosity of oxygen path around aggregates, oxygen transport enhancement by micro cracks, and binder absorption by aggregates. Furthermore, the improved model was validated using field data and compared with the earlier models.

MODEL DEVELOPMENT

Asphalt oxidation in pavements is a complex process of both oxygen and thermal transport. The pavement is produced as mixing aggregates and asphalts and then compacting the mixture to meet design requirements of air void content. Some of these air voids are trapped air voids while others are accessible air voids. Oxygen in accessible air void channels diffuses from these channels into asphalt films coating aggregate particles; meanwhile, oxygen reacts with asphalt, making the material stiffer and less permeable to oxygen. Both reaction and diffusion processes are affected by pavement temperature which is a function of time and depth.

These complex and interrelated processes were simplified for modeling purposes by making the following assumptions: 1) pavement temperature changes only in the vertical direction, i.e. horizontal variation at the same pavement depth is negligible; 2) oxygen transports horizontally from pore wall into the mastic, i.e. one-dimensional model and no vertical diffusion in the mastic; 3) at the pore wall, oxygen is at 0.2 atmospheric pressure, i.e. negligible oxygen transport resistance within the accessible air void channels from the pavement surface to lower pavement layers (Han, 2011a).

Model Components

Six components were included in the pavement oxidation model:

1. The oxygen transport-reaction model, representing how oxygen partial pressure (equivalent to concentration) changes as a function of position and time in the mastic, influenced by both oxygen diffusion and reaction.
2. The binder oxidation kinetics, describing the formation rate of carbonyl (the main oxidation product that contributes to asphalt hardening) as a function of temperature and oxygen partial pressure.
3. The oxygen diffusivity in the mastic, as a function of both temperature and binder viscosity (in turn influenced by asphalt composition, level of oxidation, and temperature).
4. The accessible air voids, providing the exposed surface area of asphalt to air.
5. Mixture design, providing the volume of binder.
6. Depth-dependent hourly pavement temperatures, as a driving force of pavement oxidation.

The first three components are coupled, because as the diffusivity decreases with oxidative hardening of the binder, the diffusion rate of oxygen through the binder decreases and thus the rate of oxidation is also reduced. The first five components are discussed in more detail below, whereas the pavement temperature model is detailed in the literature (Han et al., 2011a).

Accessible Air Void and Mixture Design

The accessible air void and mixture design components are further discussed because they determine an average diffusion depth for oxygen into the mastic, which is important to the boundary condition for the oxygen transport-reaction model.

The diffusion depth is calculated from the exposed surface area of asphalt to accessible air voids (S_{ea}) and the volume of effective binder (V_{be}): $d_D = \frac{V_{be}}{S_{ea}}$, where V_{be} is the total binder volume in the mix less the absorbed volume. This is similar to assuming that all binder surrounds accessible air voids at a uniform thickness, a reasonable first-order assumption for the purpose of asphalt oxidation. This assumption leads to a Cartesian system oxygen transport-reaction model. The concept of diffusion depth is different from the conventional asphalt film thickness, which is pictured as asphalt coating uniformly the aggregate surfaces. Because the exposed surface area of asphalt is much less than aggregate surface area, the magnitude of average diffusion depth will be greater than the film thickness.

The exposed surface area is estimated from the analysis of X-ray CT images of total air voids in mixture. First, a series of grey-scale images of total air voids were obtained by scanning the field core from top to bottom at 1-mm interval (Prapaitrakul et al., 2009). A threshold value, determined by matching the total air void content from the grey-scale images with that from measurement, converts the grey-scale images into binary images. Then the image processing toolbox in MATLAB® was used to identify objects of connected air voids. Parts of these objects are accessible air voids, depending on the pavement design. For example, if below the asphalt surface course is asphalt base, only objects connecting to the top image (i.e. pavement surface) are considered to be accessible air voids, while the other objects are consider to be trapped air voids with limited oxygen supply from the asphalt base. If below the asphalt surface course is unconsolidated base, objects connecting to the bottom image are also considered to be accessible air voids, the assumption being that atmospheric air is freely accessible through the unconsolidated base. After accessible air voids in each image are identified, the total perimeter of accessible air voids for each image is obtained using MATLAB®. If we assume the same total perimeter for the 1-mm interval, the exposed surface area of binder to accessible air voids in that 1-mm interval is this perimeter times 1 mm. By applying this procedure to all images, the exposed surface area can be obtained for every image. Furthermore, by summing the exposed surface areas of images belonging to a certain layer, the exposed surface area for that layer is obtained.

The mixture design provides binder content (P_b, by weight of mixture), binder specific gravity (G_b), maximum specific gravity of mixture (G_{mm}), and occasionally binder absorption (P_{ba}, by weight of aggregate). The volume of the effective binder can be calculated from these data and measured air void content (AV) using the established volumetric procedure (Asphalt Institute, 2001).

Asphalt Oxidation Kinetics

Asphalt oxidation was characterized by the formation of carbonyl content (Liu et al., 1996). At constant temperature and oxygen pressure, the carbonyl area of asphalt undergoes an

early nonlinear fast-rate period followed by a later constant-rate period (Van Oort, 1956; Liu et al., 1996; Herrington, 1998; Petersen and Harnsberger, 1998). Data for recovered binder from field cores showed that the early fast-rate period might not be passed during hot-mix production and construction (Glover et al., 2005), and an oxidation kinetics model for tank asphalt was developed to simulate both fast-rate and constant-rate reaction periods (Jin, 2011). Herein, a similar model was assumed for short-term aged asphalt. The model consists of two parallel reactions: a first order reaction that terminates when the limiting amount of reactants is depleted, and a zero order constant-rate reaction that lasts indefinitely throughout the pavement service life. The equations for the growth of CA are:

$$\frac{\partial CA(x,t)}{\partial t} = M_{RTFO} k_f e^{-k_f t} + k_c \tag{9-1}$$

$$k_f = A_f P^{\alpha} e^{-E_{af}/RT} \tag{9-2}$$

$$k_c = A_c P^{\alpha} e^{-E_{ac}/RT} \tag{9-3}$$

where x is distance from the pore wall into surrounding mastic (meter), t is time (hour), M_{RTFO} is the limiting amount of carbonyl formation due to the first-order reaction after hot mix production and construction, k_f and k_c are two reaction constants that are temperature dependent according to the Arrhenius equations, P is oxygen partial pressure (atm), and α is reaction order with respect to P. In this work, an average value 0.27 for α was used (Liu et al., 1996; Han et al., 2011a).

The initial condition is $CA(x,0) = CA_{RTFO}$, i.e., the CA of asphalt after hot mix production. It may be obtained by testing binder after the rolling thin film oven (RFTO) or by testing the recovered binder from the loose mix.

Oxygen Transport-Reaction Model and Oxygen Diffusivity

The governing equation for the model is:

$$\frac{\partial P(x,t)}{\partial t} = \frac{\partial}{\partial x}\left(fcf \cdot D_O \frac{\partial P}{\partial x}\right) - \frac{c}{h} \cdot \frac{\partial CA(x,t)}{\partial t} \tag{9-4}$$

where D_O is oxygen diffusivity in pure asphalt (m^2/hour); c is a factor that converts rate of carbonyl formation to rate of oxygen consumption (mol O_2/[mL asphalt]/CA), an average value of 3.71×10^{-4} based on ten asphalts (Liu et al., 1998a) was used in this work; h is the solubility constant of oxygen in asphalt (mol O_2/[mL asphalt]/[atm oxygen pressure in gas phase]), which is a function of temperature (Dickinson, 1984); *fcf* is the field calibration factor adjusting D_O. While the hindering effect of aggregates on oxygen diffusivity makes *fcf* less than unity, the assumption of no binder absorption and the development of cracks make *fcf* greater than unity. Therefore, *fcf* may be greater or less than unity due to the combined effect.

The initial condition is $P(x,0) = 0$. The boundary conditions are $P(0,t) = 0.2$, and $\frac{\partial}{\partial x} P(d_D, t) = 0$, where d_D is the diffusion depth (meter).

The oxygen diffusivity is a function of temperature and asphalt viscosity (Han et al., 2011b):

$$\frac{D_O}{T} = 5.21 \times 10^{-12} LSV^{-0.55} \quad (9\text{-}5)$$

where T is temperature (Kelvin), and LSV is low shear rate limiting viscosity (Pa.s), which is a function that relates asphalt oxidation to hardening (Lau et al., 1992):

$$LSV = e^{m+HS\times CA} \quad (9\text{-}6)$$

where m is the intercept of ln(LSV) versus CA, HS is the hardening susceptibility (ln[Pa·s]/CA). Both m and HS may be functions of temperature (Lunsford, 1994) in general, although experimentally HS is only a very weak function.

In Eq. 9-4, and considering a point in the asphalt mastic, the first term on the right-hand side represents the net input rate of oxygen to that point by diffusion and the second term represents the consumption rate of oxygen due to reaction with asphalt. These terms together give the accumulation rate of oxygen in the asphalt (the left side term). This equation and the rate equation for asphalt oxidation (Eq. 9-1) form the system of partial differential equations for the pavement oxidation model.

FIELD CALIBRATION AND VALIDATION OF PAVEMENT OXIDATION MODEL

Materials

Field cores obtained from two field sites in Texas were used for model calibration and validation, shown in Table 39. The two sites covered two different climate zones. Loose mixes were obtained during pavement construction. Two cores, one from a wheel path and another from the shoulder, were obtained from each site at each coring date, for a total of eight cores.

Table 39. Data of Field Cores, Binders, and Loose Mix.*

Route	Location	Climate Zone	Constructed	Coring Dates	AV%	G_{mm}
US 277	Del Rio, Texas	Dry-Warm	April 2008	1st: 7/28/2008 2nd: 12/14/2009	7.7	2.497
US 82	Lubbock, Texas	Dry-Cold	July 2008	1st: 8/25/2008 2nd: 12/9/2009	7.4	2.264
Route	**E_{ac} (KJ/mol)**	**HS (1/CA)**	**m (ln(Pa.s))**	**CA_{RTFO}**	**P_b**	**G_b**
US 277	75.2	3.97	5.84	0.740	4.2	1.041
US 82	69.6	3.33	6.04	0.814	6.2	1.021

* G_{mm}, P_b, and G_b are provided by mixture design

Methodology

Oxidation kinetics parameters for the binders used in the field were obtained in the laboratory according to the method detailed by Jin et al. (2011). Binders in the loose mix were extracted and recovered, and values for CA_{RTFO} were measured. Next, air void contents were measured for the field cores using the CoreLok method (Instrotek Inc., 2001). After that the field cores were scanned to obtain the grey-scale X-ray CT images, and then sliced into several layers about 12mm thick. The binders from each sliced layer were extracted and recovered for CA and viscosity measurements. The measured air void content, X-ray CT images, and mixture design

information were used to obtain the diffusion depth for each layer. These data (except X-ray CT images) also are shown in Table 39.

Site-specific hourly pavement temperatures for an entire year were calculated using the pavement temperature model developed in Han et al. (2011a). These calculations were used repeatedly assuming they adequately represent pavement temperatures over the other years.

The CA data for the top two layers of the second shoulder cores were used for calibrating the two model parameters: *fcf* and M_{RTFO}. The other CA data for first and second cores (from both wheel path and shoulder) were used for model validation.

Results and Discussion

Table 40 presents the diffusion depth and CA data obtained according to the above methodology.

Table 40. Layer-by-Layer Diffusion Depth (mm) and CA of US 277 and US 82 Field Cores.

Layers of	Wheel Path 1st Core			Wheel Path 2nd Core		
US 277	**d_D (mm)**	**CA data**	**CA calc**	**d_D (mm)**	**CA data**	**CA calc**
1	0.386	0.936	0.961	1.167	1.206	1.110
2	0.615	0.937	0.934	3.072	1.004	0.906
3	0.748	0.971	0.911	0.575	0.970	1.131
4	0.706	0.955	0.901	0.510	0.886	1.106
5	0.462	0.930	0.907	-	-	-
US 82	**d_D (mm)**	**CA**	**CA calc**	**d_D (mm)**	**CA**	**CA calc**
1	0.974	0.879	0.972	1.293	1.201	1.193
2	2.948	0.830	0.868	2.037	1.122	1.063
3	4.360	0.823	0.843	1.846	1.193	1.032
4	3.292	0.831	0.845	-	-	-
Layers of	**Shoulder 1st Core**			**Shoulder 2nd Core**		
US 277	**d_D (mm)**	**CA data**	**CA calc**	**d_D (mm)**	**CA data**	**CA calc**
1	0.663	1.019	0.950	**0.592**	**1.218**	1.240
2	0.636	0.897	0.933	**2.710**	**0.959**	0.918
3	0.790	0.894	0.908	1.579	0.971	0.960
4	0.603	0.923	0.909	0.675	0.949	1.074
5	0.344	0.918	0.913	0.700	1.008	1.039
US 82	**d_D (mm)**	**CA data**	**CA calc**	**d_D (mm)**	**CA data**	**CA calc**
1	0.970	0.876	0.972	**0.883**	**1.218**	1.219
2	3.111	0.771	0.866	**2.550**	**1.015**	1.013
3	3.768	0.798	0.847	11.362	1.026	0.850
4	-	-	-	6.367	1.109	0.863

The recovered binder CA data of the loose mix and the top two layers of shoulder second cores (bolded in Table 40) were used for parameter calibration of *fcf* and M_{RTFO}. For US 277, the optimal values for *fcf* and M_{RTFO} are 1.2 and 0.05, respectively. For US 82, the optimal values for *fcf* and M_{RTFO} are 10 and 0.18, respectively. Because no binder absorption data were available from the mixture designs of these two sites, zero binder absorption was assumed, making *fcf* greater than unity. Due to the long computational time required for solving the system of partial

differential equations, it is recommended to first determine a small range for the two parameters by trial and error, and then use a search at a smaller step for the optimal values that minimize the sum of the absolute errors. A common range of M_{RTFO} is 0.05 to 0.25, while the *fcf* (greater than zero) is case dependent.

Using the calibrated model parameters, CA values of the other layers of both first and second cores were calculated using the pavement oxidation model. Figure 71 compares the model calculations with data layer by layer for US 277 shoulder. The model calculations matched with data of all layers quite well. The top and bottom layers of second core oxidized significantly greater than the second and third layers, due to much smaller diffusion depths (0.592 and 0.700 mm) of the former layers versus 2.710 and 1.579 mm for in the latter layers. Furthermore, the top layer oxidized the most due to the highest temperature at the pavement surface. These data demonstrated the capability of the model to predict the oxidation of asphalt in pavement at different depths.

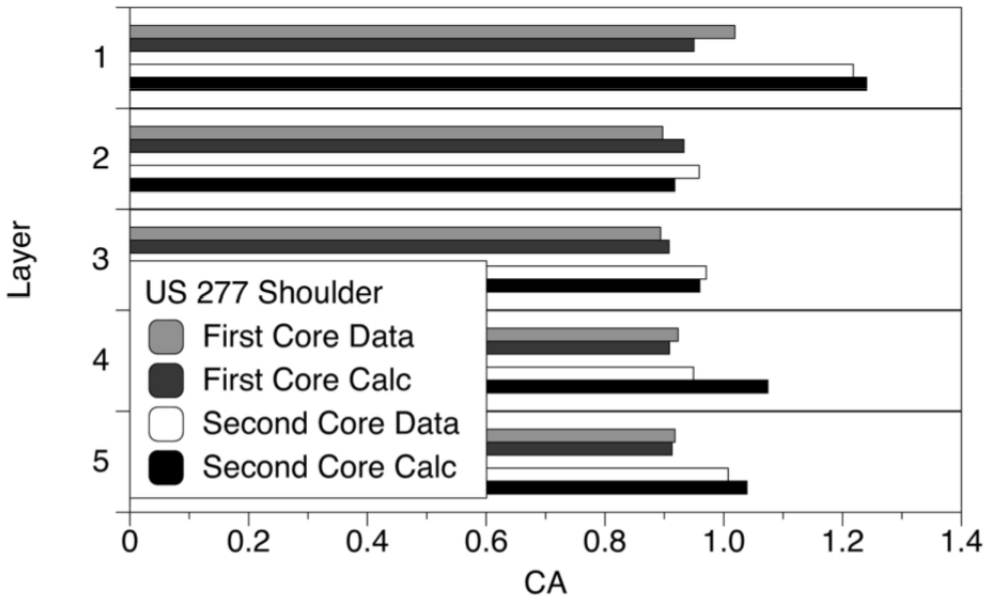


Figure 71. Comparison of Field Data and Model Estimates of CA for US 277 Shoulder.

Figure 72 compares calculations of CA averaged over the whole core for US 277 shoulder. The models compared were 1) the model developed in this work; 2) the thin film model based on this model but assuming no oxygen diffusion resistance in the binder; 3) Han's model that did not include a fast-rate period. The stepwise increases reflect seasonal changes in pavement temperatures. The thin film model agreed with the first core data point, however it overestimated the oxidation at later times when diffusion resistance increases due to age hardening. The calculation of Han's model is based on his calculated oxidation rate for this pavement site (Han, 2011a). Clearly, it did not capture the fast oxidation during the early period. Calculations of the model developed in this work using diffusion depths of the second core showed that the oxidation rate declined over time due to increased diffusion resistance. And the discrepancy between the first core data point and the model calculation was because the actual diffusion depths of the first core were not used for the calculation.

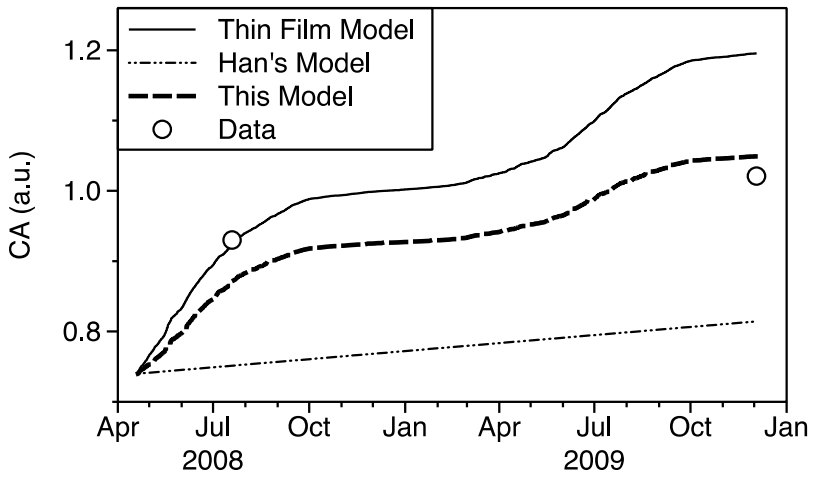


Figure 72. Comparison of CA Calculations using Different Models for US 277 Shoulder.

In summary, a total of 33 model predictions were made for the 33 layers of eight cores. In general, the model predicts asphalt oxidation in pavement as a function of time and depth reasonably well. Most (88 percent) of the absolute percent errors were within 17 percent of CA data. Using a common value of hardening susceptibility (5 ln[Pa.s]/CA), 17 percent error in CA leads to about 8 percent error in ln(*LSV*). Part of the discrepancy between data and estimates was due to measurement error (about 5 percent). Other factors include the effect of asphalt absorption on diffusion depth and change of air voids content over time due to traffic compaction and crack development.

SUMMARY

A pavement oxidation model was developed based on oxygen transport and reaction fundamentals. It requires binder oxidation kinetics and hardening parameters for both fast-rate and constant-rate reaction periods, calibrated oxygen diffusivity in the mastic, accessible air voids characterization in the mixture, and mixture design. The model also requires the input of hourly pavement temperatures. Two model parameters M_{RTFO} and *fcf* were calibrated using field data; the model was capable of predicting asphalt oxidation in pavement after one year of field aging quite well. Ultimately, this model will be used with pavement response models in a pavement design guide for evaluating long-term pavement performance.

CHAPTER 10. AN OXIDATIVE AGING STUDY OF SEAL COAT TREATED PAVEMENT

ABSTRACT

Projecting pavement oxidation over time requires oxidation kinetics and hardening properties of the specific binder used in the pavement. However, obtaining such information on the binder can be complicated by factors such as variation in binder properties throughout pavement construction and the presence of a seal coat, not to mention the fact that prior history of the pavement of interest may not even be available, including samples of the original binder.

By using the Pressure Oxidation Vessel method for measuring a binder's constant-rate oxidation reaction kinetics parameters, along with a pavement oxidation model, measurements on binder recovered from a pavement can be used to project oxidation and hardening in the pavement over time and to assess the effectiveness of a seal coat in extending pavement life.

Using this approach on a seal coat-treated pavement, binder properties for the seal coat binder and the pavement binder were measured and found to be distinctly different, based on observations on field cores. Furthermore, the first layer underneath the seal coat was found to have properties intermediate between the two, reflecting the presence of both binders in that layer but not in deeper layers. Finally, recovered binder strongly supports the hypothesis that a surface seal coat may be able to reduce oxidation of binder underneath the seal coat by blocking the transport of oxygen through the pavement.

INTRODUCTION

There is a need to understand more about binder oxidation in pavements and whether seal coats might be able to retard oxidative hardening and ultimately to predict pavement performance, as affected by seal coat applications. Oxidation of asphalt leads to rheological hardening, manifested by simultaneous increases in dynamic storage modulus and viscosity. It is believed that chip seal (seal coat) treatments may have the capacity to delay age-hardening in pavements by blocking oxygen to the original binder or to rejuvenate in-place binder near the pavement surface. However, definitive data to verify these hypotheses are largely non-existent. Furthermore, in order to predict binder durability in pavements, it is essential to be able to predict asphalt binder oxidation in service based on that binder's oxidation kinetics and accessibility to oxygen.

However, seal coat binders have significantly different properties from the pavement binder and consequently complicate assessing the effectiveness of treatments on the underlying original binder and its in-service oxidation. Such assessments are further complicated by the possible variations in the pavement binder used throughout pavement construction. Each binder, even of the same performance grade, may have different oxidation kinetics (such as activation energy) and hardening parameters and therefore respond to pavement oxidation with different hardening rates.

Further complicating performance predictions is the fact that determining binder oxidation properties typically is not done ahead of construction and is difficult at best as a forensic exercise. Binder performance grade testing prior to construction does not provide the crucial measures of oxidation kinetics and hardening that are required for performance prediction that incorporates oxidative aging. Furthermore, binder samples typically are not obtained at the time of construction in which case subsequent testing for kinetics and hardening properties cannot be done.

Most seal coat research has focused on the immediate effects of restoring pavement properties, such as surface cracks, heaving, and surface raveling (O'Brien, 1989) and surface waterproofing (Brown, 1988). Even for a successfully applied seal coat, the seal coat and underlying pavement serviceability eventually will fall below acceptable levels after a combination of traffic loading and asphalt oxidative hardening over time, but the question remains as to when that failure will occur and to what extent will a seal coat help retard the deterioration in the unlying pavement binder.

This work provides 1) new data on seal coat effectiveness with respect to pavement binder oxidation and hardening and 2) a methodology for assessing binder and seal coat performance in existing pavements for which there is no original binder available. The methodology calls for analyzing binder and seal coat materials recovered from field cores.

OBJECTIVES

The first objective of this work was to test chemical and rheological properties of binders recovered from field cores and to track the aging process on both the seal coat and pavement binders.

The second objective was to conduct laboratory aging of binders recovered from cores for the purpose of determining binder kinetics and hardening parameters, to assess binder oxidation in pavements, and to compare oxidation with and without seal coat treatments.

EXPERIMENTAL METHODOLOGY

Materials

US 82 in the Lubbock District of TxDOT was constructed using a CMHB-F type mixture in July 2008, with Alon PG 76-22 asphalt binder and Texas crushed limestone from Higginbotham quarry (Kiewit Inc.), screenings from Clements Pit (Price Const. Co.), and local field sand. A 300 ft test section was subsequently seal coated August 25, 2008.

Table 41. Pavement Construction and Coring Information.

Item	Details
District	Lubbock, Texas
Highway	US 82
Binder Supplier & PG Grade	Alon 76-22
Seal Coat Binder Type and Spray Rate	AC 20-5TR 0.43gal/sq yd
Construction Date	July 2008
Seal Coat Application Date	August 25, 2008, after 1st coring
1st Coring	Aug. 2008 (without seal coat)
2nd Coring	Dec. 2009 (with and without seal coat)
3rd Coring	Aug. 2010 (with and without seal coat)
Mixture Type	Travel lane: CMHB-F (2.25 inches) Shoulder : CMHB-F (4 inches)

In 2008, sample cores were taken from the field before a seal coat was applied to part of the pavement. In 2009, cores from both seal coat treated and untreated pavement sections were obtained. For analysis of the cores from the seal coat sections, the first step was to carefully separate the seal coat layer with a knife for separate analysis. This layer was a single course layer about 0.25 inches thick as shown in Figure 73. After removing these seal coat layers, all the cores were sliced into 0.5 inch thick layers from top to bottom.



Figure 73. Sample Core with Seal Coat Treatment from US 82 Shoulder Section Collected in 2009.

Binder Extraction and Recovery

Each of the layers obtained from the cores, including seal coat layers, were extracted with solvent to recover the aged binder. The extraction used three successive washes using a mixture of 15 percent ethanol plus 85 percent toluene by volume. After the binder was extracted from the aggregate, the combined solvent from the three washes was allowed to settle in a small beaker for 30 seconds and distributed among four to five 15 mL conical centrifuge tubes and centrifuged at 3100 rpm for about 10 minutes to remove aggregate. The solvent was then filtered to remove all particles from the binder solution. The binder was recovered from the solvent with a Büchi, Re 111 rotovap. During recovery, nitrogen gas was introduced to the vessel to assist removing

the remaining solvent and to prevent contact with oxygen. The bath temperature was maintained at 100°C to avoid hardening or softening of the asphalt in dilute solution. When no more solvent drops on the condenser were detected visually, the bath temperature was increased and after reaching 174°C, the recovery was continued for an additional 45 minutes to ensure sufficient solvent removal.

Recovered Binder Aging in the Pressure Oxidation Vessel (POV)

Second-year core samples were used to obtain binder for use in pressure oxidation vessel determination of binder kinetics and hardening parameters. The seal coat layer, the first layer underneath the seal coat (unavoidably a blend of both seal coat and pavement binder), and additional layers underneath the first layer provided enough binder for kinetics determinations of the pavement binder, seal coat and a mixture of the two.

Recovered binder from the pavement located 0.5 inches and more below the bottom of seal coat layer, was considered pure pavement binder. This conclusion is based on property measurements of binder recovered from field cores.

Pressure oxidation vessel (POV) aging is achieved in five vessels, each maintained at a specific temperature ranging from 60°C to 98°C and 1 atm air (provided by supplying air flow through the temperature bath for pre-heating and then through the POV at a rate of approximately 30 mL/min). Binder samples were placed into 4 cm × 7 cm aluminum trays to form 1 mm-thick uniform films. This thickness was proved to limit the effects of diffusion to a reasonable level while providing a sufficient amount of oxidized binder (Domke et al., 1997). Each capped vessel was then immersed in a constant temperature triethylene glycol bath. Trays were removed from the POV on specific days, chosen to provide an appropriate amount of oxidation for kinetics determination; the aging schedule for each sampling was devised according to the POV temperature.

Fourier Transform Infrared Spectrometer (FTIR)

A Nicolet 6700 FT-IR spectrometer with an attenuated total reflectance ZnSe prism was used to measure carbonyl area (CA), which tracked the oxidation progress in asphalt samples. The CA, reported in arbitrary units, was the area under the absorbance spectrum from 1650–1820 cm^{-1} and above the baseline at 1820 cm^{-1}.

Dynamic Shear Rheometer

A Carri-Med CSL 500 controlled stress rheometer was used to record and analyze the rheological property DSR Function. The DSR Function, calculated from the dynamic storage modulus (G′) and the dynamic viscosity (η′) is defined as:

$$\text{DSR Function} = G'/(\eta'/G'), \text{ at } 15°C, 0.005 \text{ rad/s} \quad (10\text{-}1)$$

If the function cannot be conveniently measured directly, it may be approximated by using G′ and η′ values measured at 44.7°C and 10 rad/s in time sweep mode and then converting the DSR

function to a value at 15°C and 0.005 rad/s by dividing its value at 44.7°C by 2000 (the frequency ratio 10/0.005). The DSR function combines both elastic and viscous properties and has been shown to correlate well with ductility measured at 15°C. Some recent research has shown that DSR Function could reflect the performance of the binder in pavement service.

RESULTS AND DISCUSSION

Oxidation Evaluation

The first objective in the study was to test chemical and rheological properties of the recovered binders.

Previous work on asphalt field aging in Texas Highways (Glover et al., 2005), provided evidence that binder oxidation occurred over many inches of depth into the pavement. Work presented in this report (Chapters 3 through 9 and 11 through 15) provide a better fundamental understanding of binder oxidation in pavements, experimental validation with field cores, the impact of binder oxidation on mixture properties, and computation tools for implementation of the results. The work described in this chapter was directed at addressing the specific impact of seal coats on this binder oxidation and hardening process and in the context of these various tools. It should be noted that measuring and interpreting the effectiveness of seal coats is always problematic because of the unknown extent to which seal coats penetrate into the pavement and blend *in-situ* with the orginal binder. With that in mind, the discussion that follows includes data for both traveled (wheel path) and untraveled (shoulder) lanes and on both treated and untreated sections of pavement.

This study on US 82 in the Lubbock District of TxDOT tracks chemical and rheological property changes due to field aging and seal coat treatment. Untreated cores were collected in both 2008 and 2009, and seal coat treated cores were collected only in 2009.

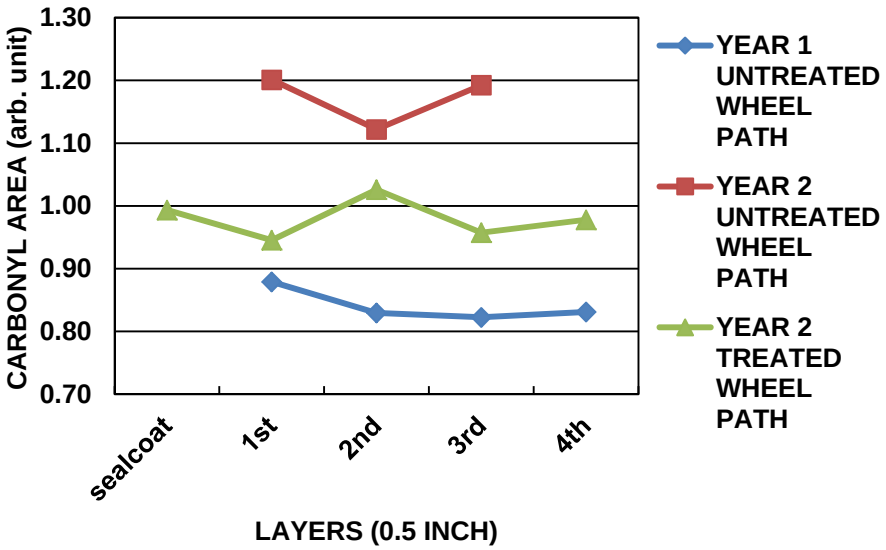


Figure 74. Carbonyl Area Distributions in Wheel Path Cores for Years 1 and 2.

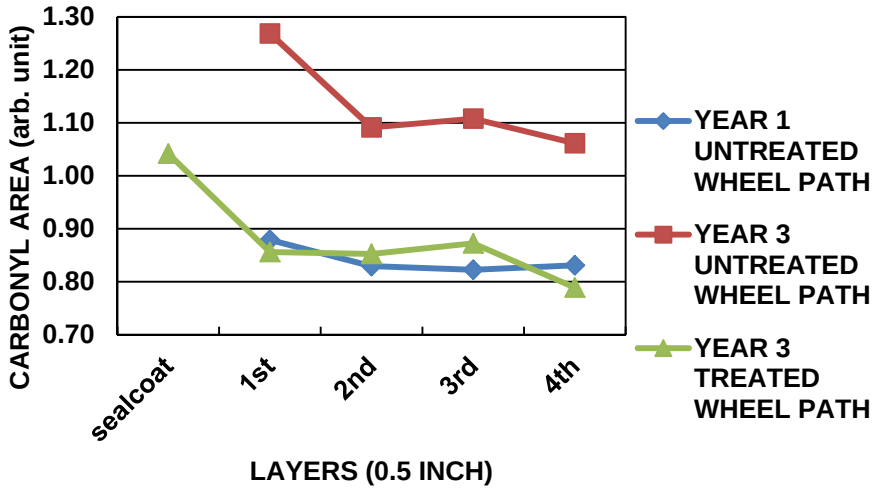


Figure 75. Carbonyl Area Distributions in Wheel Path Cores for Years 1 and 3.

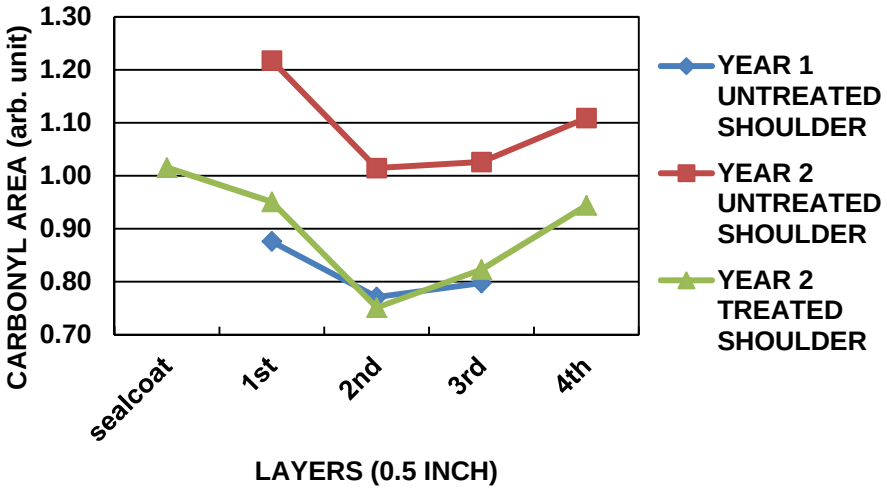


Figure 76. Carbonyl Area Distributions in Shoulder Cores for Years 1 and 2.

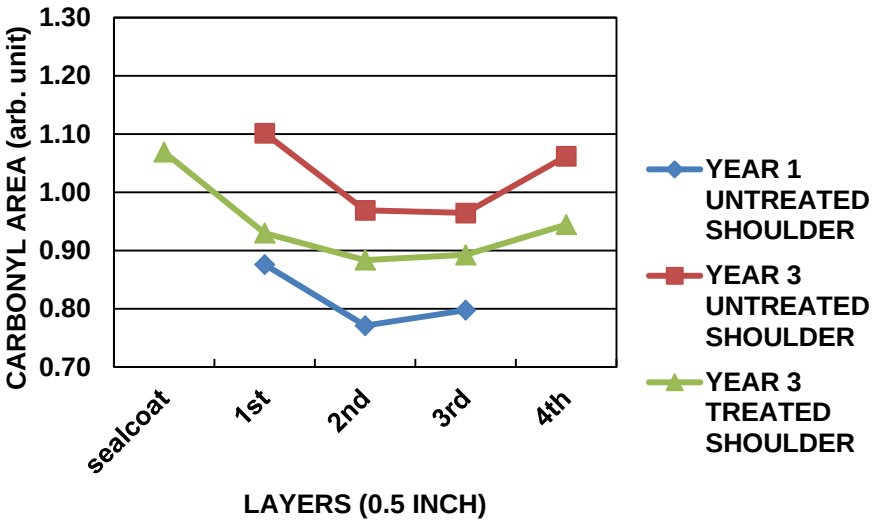


Figure 77. Carbonyl Area Distributions in Shoulder Cores for Years 1 and 3.

Figure 74, Figure 75, Figure 76, and Figure 77 show the carbonyl area (CA) versus pavement depth (in terms of pavement layer) for binder recovered from each field core tested in this study. For both wheel path and shoulder cores, it appears that oxidation was less in the presence of the maintenance seal coat. All of the untreated cores below their surface have significantly higher CA than their corresponding seal coat treated cores, supporting the tentative hypothesis that a seal coat may hinder oxygen penetration below the surface of the pavement. The seal coat binder is different from the pavement binder and thus cannot be compared to the binder in the untreated cores and to the binder below the seal coat layer in the treated cores. This issue is addressed further, below.

Average CA values for each core are shown in Figure 78. These values are mass-weighted averages of all the layers (excluding the seal coat layer because the binder used is different). Loose mix samples were obtained during construction. FTIR measurements gave a loose mix CA value of 0.81 arb. unit (arbitrary units), close to the CA values obtained from pavement cores obtained one month after construction (0.814 for the shoulder and 0.845 for the wheelpath) for the cores. The CA value increased to around 1.10 for the untreated cores after 18 months (2009) and then essentially held that value over the next seven months, which may be an artifact of inevitable core variability. Nevertheless, the CA for the treated cores is always less than that for the untreated cores. There may be two explanations for this phenomenon: 1) seal coat treatment may slow the aging in the lower part of the pavement, which is consistent with Figure 74, Figure 75, Figure 76, and Figure 77; and 2) the seal coat binder may penetrate into the first layer of the treated cores, to be blended with the pavement binder during extraction and recovery, or even blended *in situ*, providing some rejuvenation to the original binder.

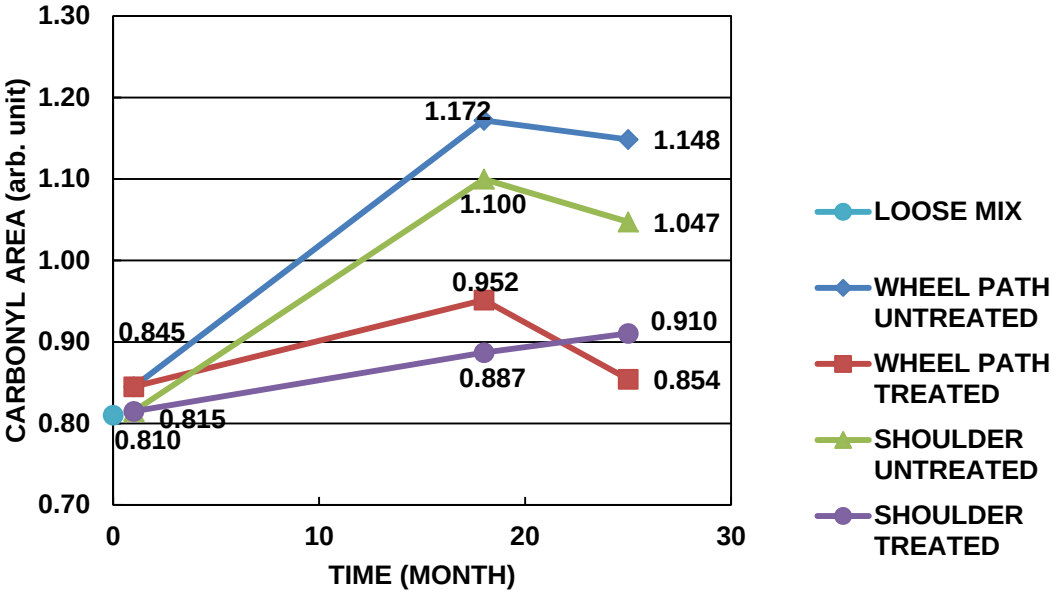


Figure 78. Average Carbonyl Areas for Field Cores.

Figure 79 tells a similar story for the average DSR Function. The DSR Function for treated cores aged in the pavement beyond construction was much lower than the corresponding value for untreated cores for both wheel path and shoulder.

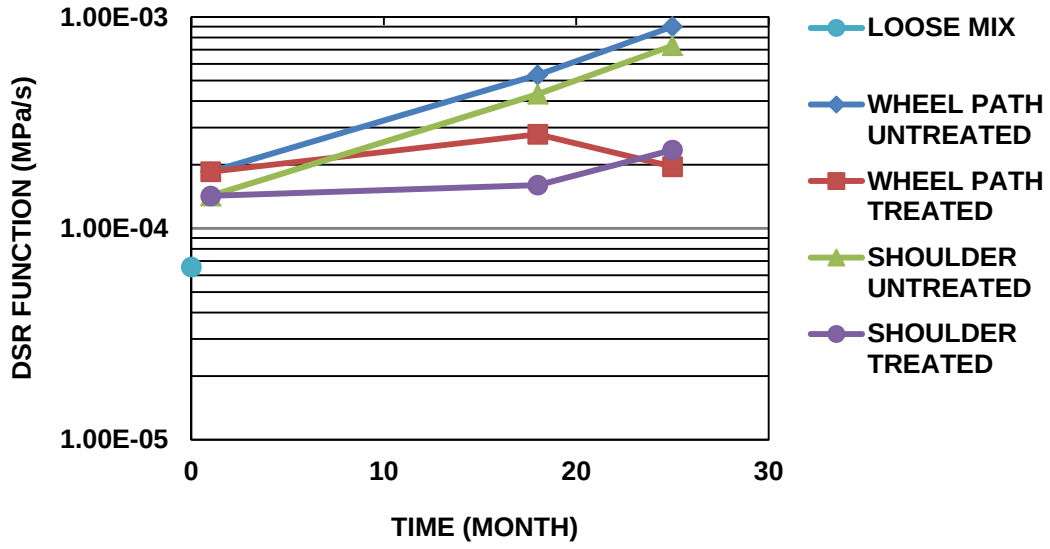


Figure 79. Average DSR Function for Field Cores.

The correlation between DSR Function and CA is characteristic for each asphalt. The slope of ln (viscosity) versus CA is termed the DSR Function harding susceptibility. In Figure 80, recovered binder DSR Function vs. CA data are plotted for each layer for the various treated and untreated cores. For example, the data labeled "untreated shoulder year 2 inches shows four

data points for the four layers in that core, each layer aged for the same amount of time according to when the core was sampled. The asphalt in different layers aged to different CA levels and the DSR function corresponding to each CA generally is higher or lower, consistent with a higher or lower value of the CA. Other untreated pavement cores do not provide as consistent a relationship of increasing oxidation over time, but the trend holds.

For the treated pavements, other observations are noted. First, the seal coat layer binder (all points inside the circle) shows CA values that are offset well below the pavement binder data for a given CA., i.e., the asphalt in these seal coat layers has a lower DSR Function for a given level of oxidation, indicated by the CA. Second, a linear correlation based on all the layers from the untreated section cores plus the lower layers from treated section cores (excluding the seal coat layer but including all pavement layers including the first pavement layer beneath the sealcoat) is:

$$\text{DSR Function} = 3.85 \times 10^{-6}\, e^{(4.59CA)},\ R^2=0.78$$

While there is significant scatter to these data, resulting in the r^2 value of 0.78, the data are consistent with other binder data for this pavement, as noted below. Third, for the first layers (beneath the sealcoat) in two of the treated cores (treated wheel path year 2 and treated shoulder year 3), the points clearly lie between pure pavement asphalt and seal coat asphalt, likely indicating penetration of the seal coat into the top of the original pavement. This observation also would explain the results in Figure 79 if the softer binder (lower DSR Function at the same CA) soaked into the top of the pavement, producing a lower average value for the treated cores compared to the untreated ones.

Another observation from Figure 80 is that cores from the treated pavement sections have CA values that are significantly less than those from the untreated pavements. For example, the least CA from the untreated-shoulder year 2 core (CA=1.015), was more than the highest CA from the treated-shoulder year 2 core (CA=0.944) (not counting the first layer below the seal coat layer, although the statement still would hold). The same statement can be made in comparing the treated shoulder core to the untreated shoulder core, both for year 3 and the other treated versus untreated cores. The consistency of this result in the cores from this pavement appears to be a compelling result, supporting the notion that seal coats may well retard oxidation in pavements for a time. However, it is not observed in the other seal coated pavements studied in this project, suggesting that achieving an effective seal is problematic.

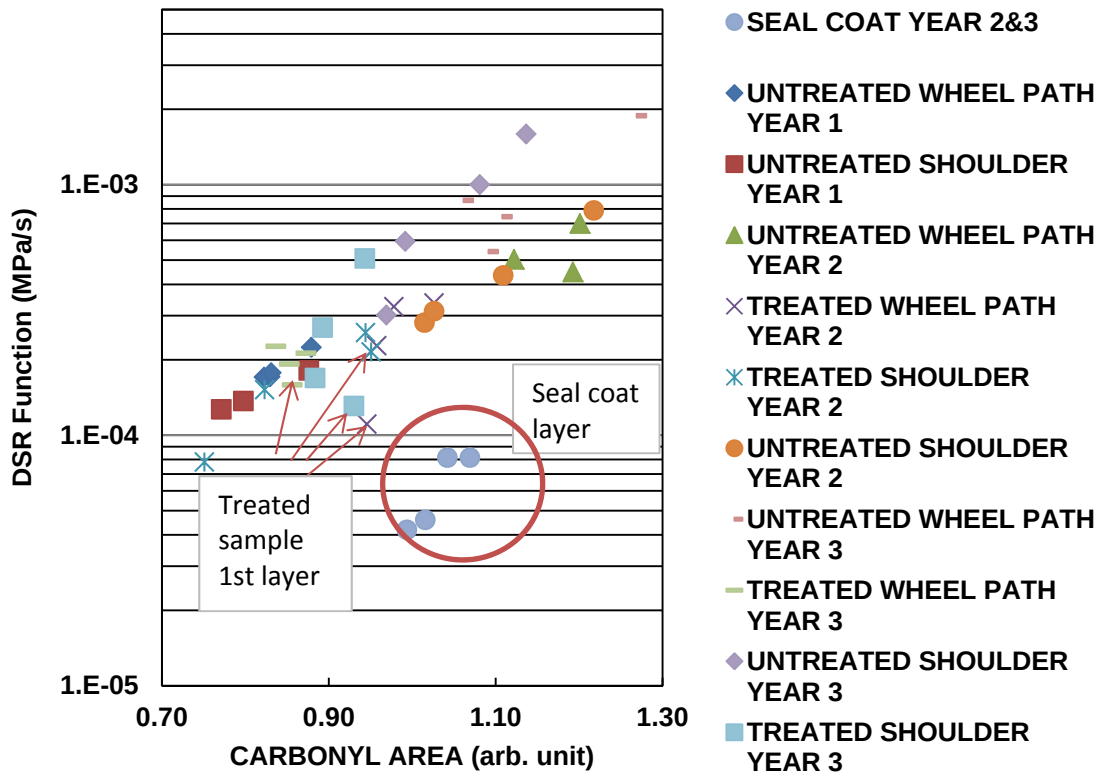


Figure 80. DSR Function Hardening Susceptibility for Each Layer in Field Cores.

Recovered Binder Pressure Oxidation Vessel Testing

Work has been reported previously on the development of an apparatus and procedure for oxidizing unaged asphalt under atmospheric air pressure and at several elevated temperatures in order to evaluate binder oxidation kinetics and hardening. An asphalt oxidation kinetics model was established to describe the formation rate of carbonyl during the constant-rate period, following classical Arrhenius reaction kinetics (Lau et al. 1992). Reaction kinetics parameters such as the activation energy (E_{AC}), the pre-exponential factor (A), and the oxygen reaction order (α), are specific characteristics of each asphalt and the oxidation rate is described in terms of these parameters by

$$r_{CA} = AP^{\alpha} exp\left(\frac{-E_{AC}}{RT}\right) \quad (10\text{-}2)$$

In this current project, field binder recovered from field cores was characterized using this POV method in order to determine binder oxidation kinetics parameters after pavement aging. Such an approach can be used on pavements as a forensics tool, potentially making every pavement a test section, even when the original binder is not available.

Figure 81, Figure 82, and Figure 83 show CA growth of the three recovered binders (the original asphalt, the seal coat asphalt and a mixture of the two) and at three temperatures. In the constant reaction period, the reaction rate (or CA growth rate) is constant at constant

temperature, and this constant rate increases with increasing temperature. The data for all of these recovered binders appear to be in the constant rate period.

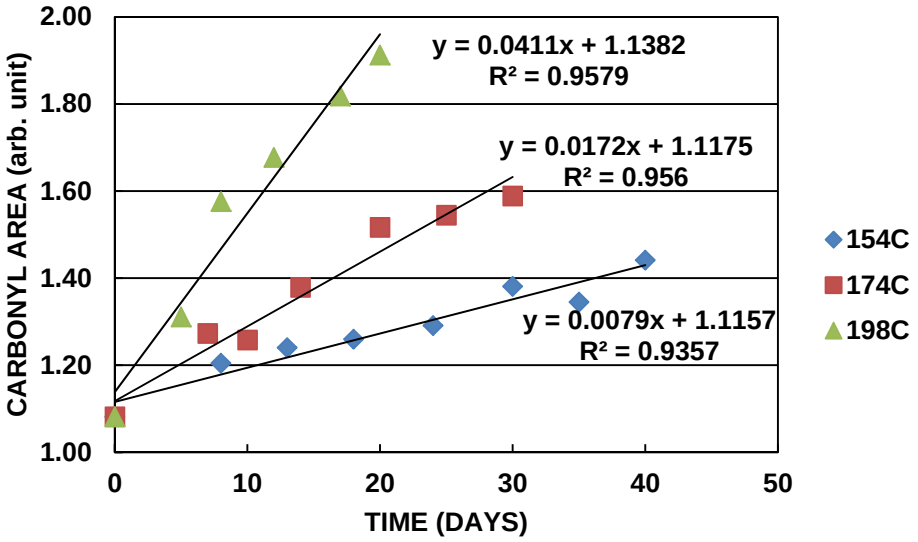


Figure 81. Carbonyl Area Growth for Pavement Binder in POV.

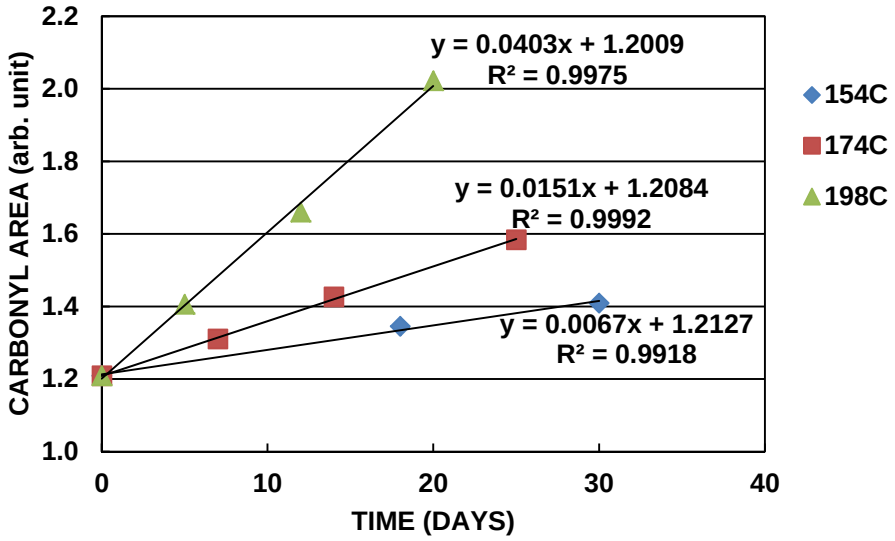


Figure 82. Carbonyl Area Growth for 1st Layer (Mixed) Binder in POV.

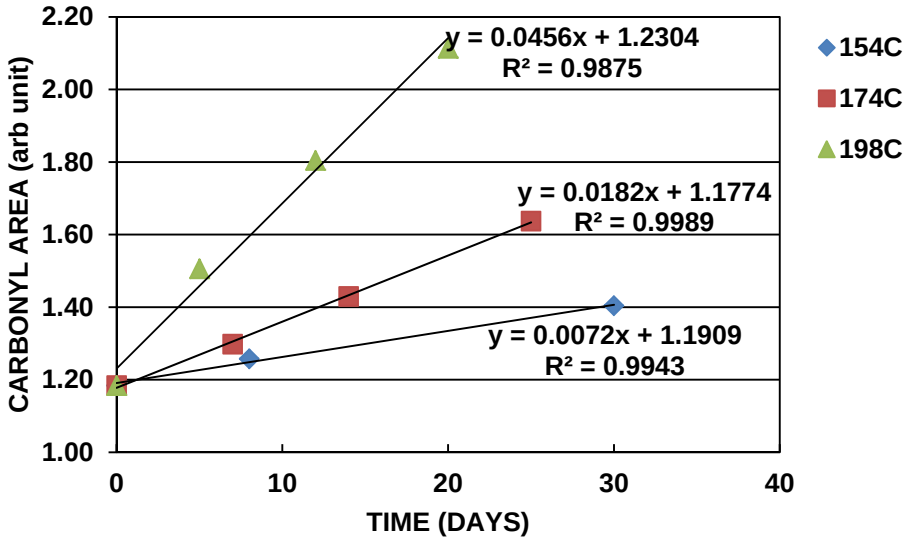
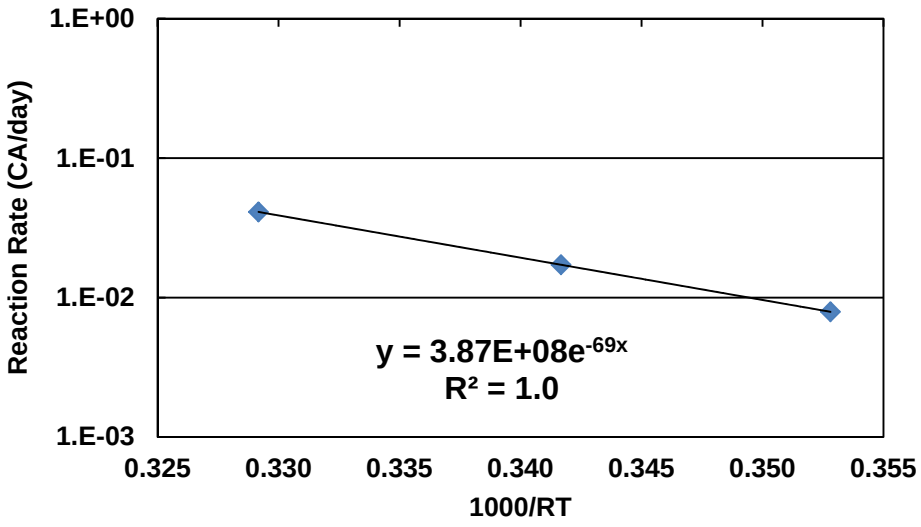
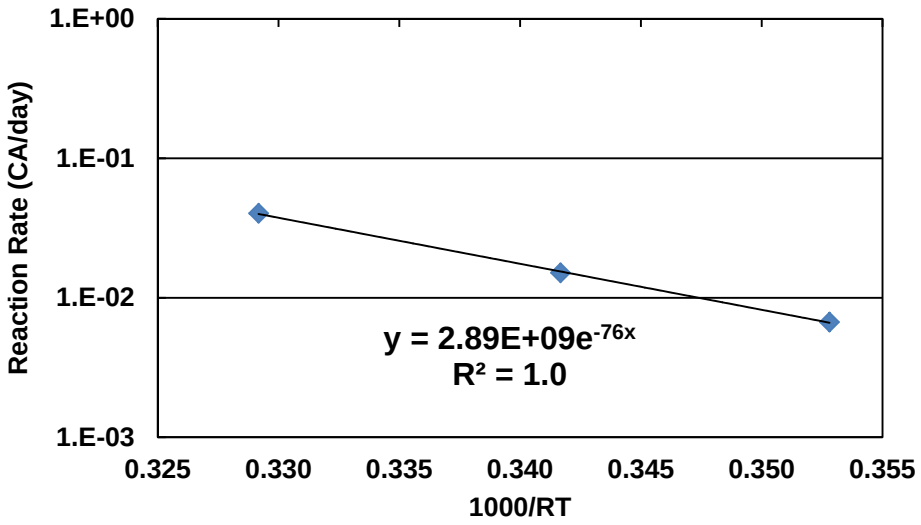


Figure 83. Carbonyl Area Growth for Seal Coat Layer Binder in POV.

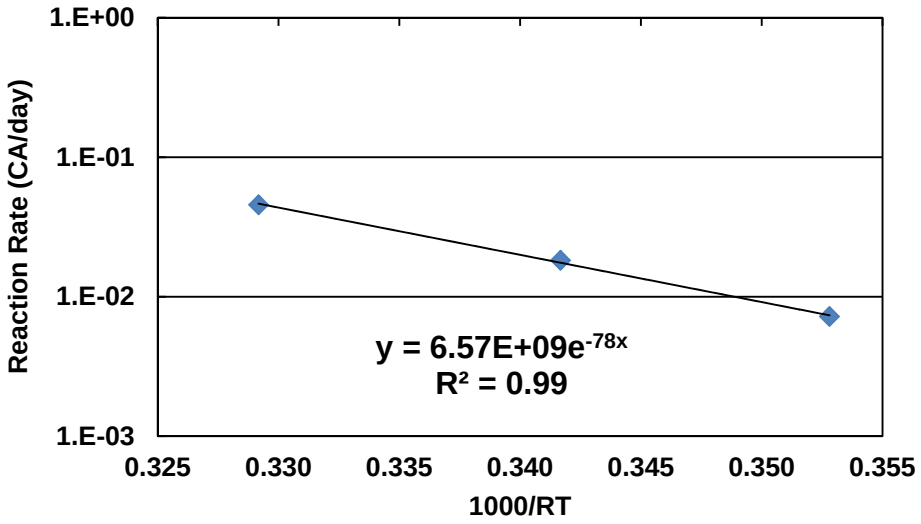
Figure 84 shows activation energy plots for each of the three binders. This experimentally determined parameter is independent of temperature for a given asphalt but establishes the sensitivity of the reaction rate to temperature. Of the recovered binders, the original pavement binder shows the lowest activation energy (69 kJ/mol) compared to 76 and 78 kJ/mol for the first layer and the seal coat binders. For comparison, the work reported in Chapter 4 showed the orginal Alon 76-22 binder with a constant rate activation energy of 77 kJ/mol. The reason for the difference between the recovered binder value of 69 kJ/mol and the original binder value of 77 kJ/mol is unknown.



(a)



(b)



(c)

Figure 84. Activation Energies for Field-recovered (a) Original Binder, (b) 1st Layer Binder, and (c) Seal Coat Layer Binder.

DSR Function hardening susceptibility values were also determined from the POV aging data of the recovered binders. The results are given in Figure 85. The pavement binder has greater DSR Function values for a given CA compared to the seal coat binder, in agreement with the previous observation in Figure 80. Again, the binder recovered from the first pavement layer of treated cores shows a mixed property with the trendline lying between the pavement binder and seal coat binder. Probably coincidentally, the hardening susceptibility values of the seal coat and the pavement binder (thus also for the first layer) are nearly the same.

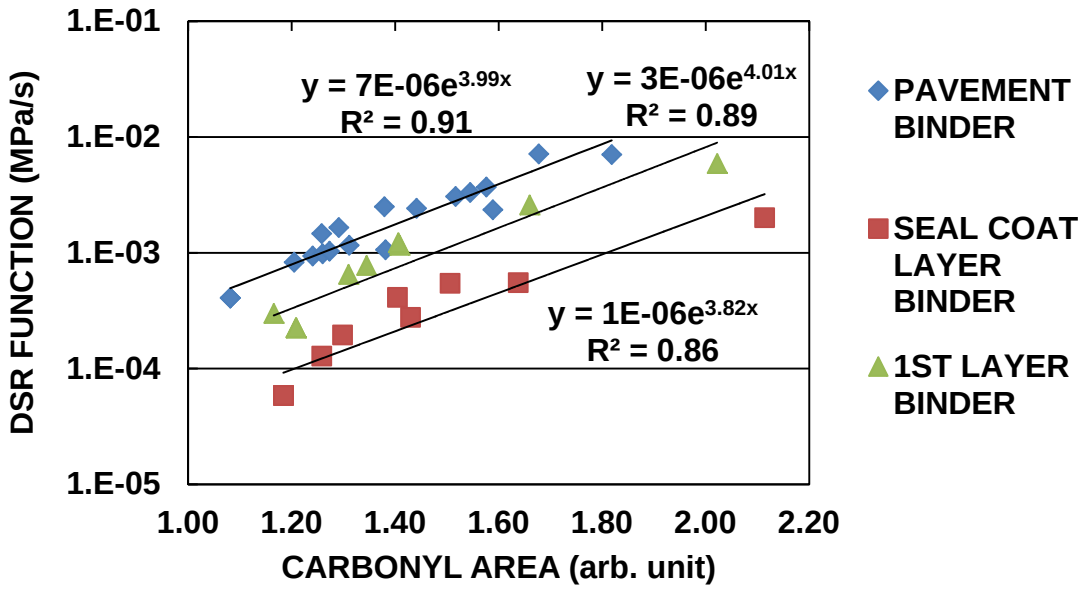


Figure 85. DSR Function Hardening Susceptibilities.

Figure 86 compares the DSR Function hardening susceptibility of binder recovered from untreated cores for years 1, 2, and 3, both as-recovered (labeled as field recovered binder) and after additional aging in the POV. Also shown are data for the original binder (supplied by the manufacturer), both unaged and after POV aging to various levels for binder kinetics determination. Recovered binder with additional aging in the POV follows the same DSR function hardening path as the binder recovered from field cores and as the original binder. This result has been seen before for binder aging in the field and is important because it means that the original binder is not necessary for evaluating past pavement performance (forensics) and for predicting future performance, even for pavements for which original binder is unavailable. Table 42 provides the hardening susceptibility parameters for each of these determinations.

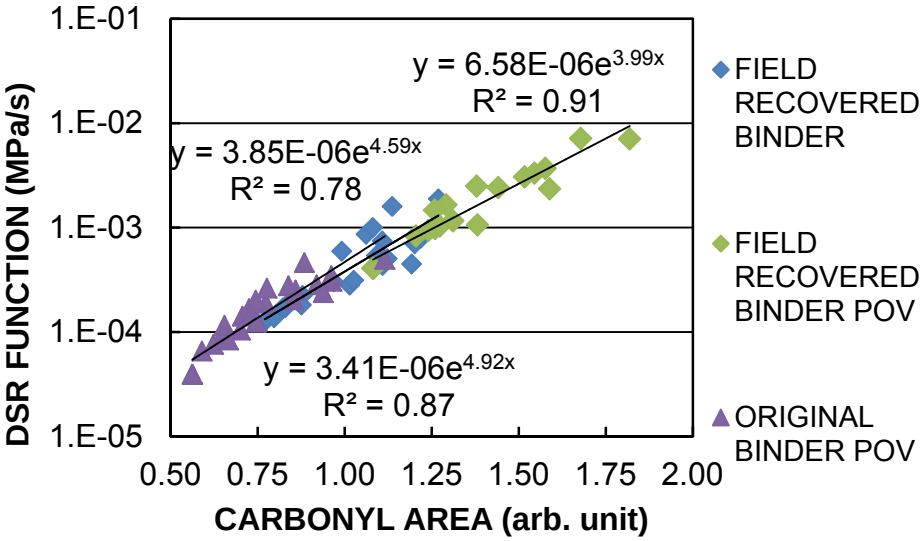


Figure 86. DSR Function Hardening Susceptibility for Recovered Binder and Recovered Binder after POV.

Table 42. DSR Function Parameter Estimates for the Different Binder Data Sets.

Hardening Susceptibility Factors	Field Recovered Binder	Recovered Binder, POV-aged	Manufacturer Sample, POV-aged	All Binder Data Together
Pre-exponential	3.85×10^{-6}	6.58×10^{-6}	3.41×10^{-6}	6.23×10^{-6}
HS	4.59	3.99	4.92	4.09
R^2	0.78	0.91	0.87	0.94

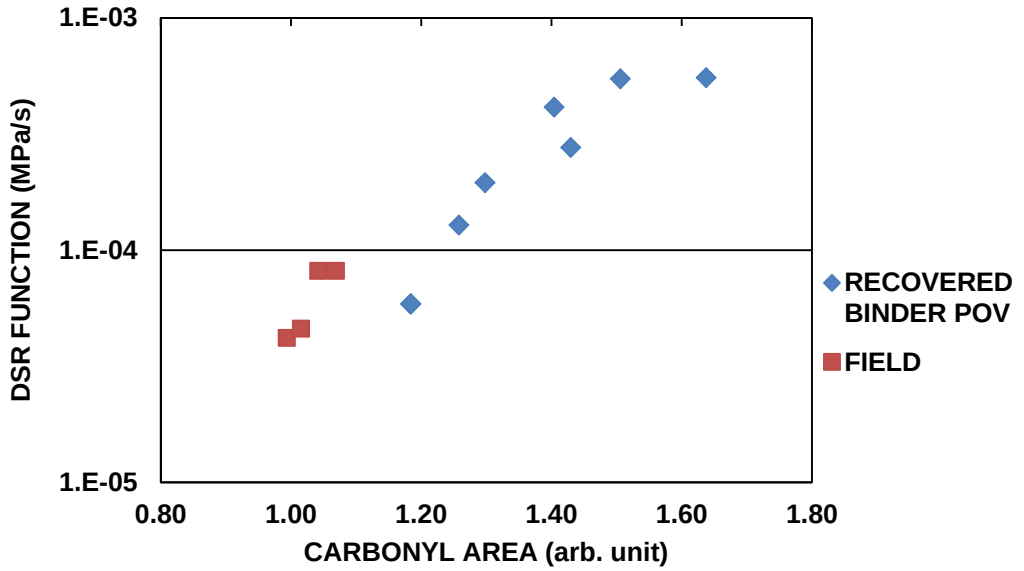


Figure 87. DSR Function Hardening Susceptibility for the Seal Coat Binder.

Figure 87 shows similar results for the seal coat binder. Recovered seal coat was measured to obtain DSR function and CA data. Samples were also further aged in the POV to obtain DSR function values at higher levels of aging (i.e., CA) than existed in the field cores.

SUMMARY

This study provides a systematic method to evaluate seal coat treated pavement oxidation and to predict future changes to the binder rheology. DSR function hardening susceptibility, the ratio between increases in log DSR Function and carbonyl area, is a characteristic of asphalt materials that relates chemical and rheological properties and that is sensitive enough to be used to identify blends of original binder and seal coat material. As such, it can be used to assess seal coat penetration below the pavement surface. Binder extracted and recovered from field cores can be further oxidized in laboratory accelerated aging in order to determine oxidation kinetics. Kinetics measurements of the recovered binder appear to compare well to the original binder, allowing the possibility of analyzing oxidation kinetics as a forensics study of pavements where no original binder is available.

Cores from the treated pavement sections have CA values that are significantly less than those from the untreated pavements, for the same pavement aging level. The consistency of this result in the cores from this pavement appears to be support the hypothesis that seal coats may well retard oxidation in pavements for a time. However, this result has not been observed in the other seal coated pavements studied in this project, suggesting that achieving an effective seal is problematic. More work is needed to consider how effective seals may be achieved.

This work has demonstrated a method for evaluating seal coat effectiveness with respect to binder oxidation and hardening even for pavements that were not initially planned to be test pavements. This strategy therefore provides a very cost-effective strategy for seal coat and pavement oxidation evaluation.

CHAPTER 11. DIRECT TENSION TESTING OF HOT MIX ASPHALT FIELD SAMPLES

A comparison can be made to validate the viscoelastic characterization (VEC) and modified (indicated by the asterisk) repeated direct tension (RDT*) tests by testing the same sample using both tests. The complex modulus at a frequency of 1 Hz (6.28 radians/sec.) can be pulled from the 20°C (68°F) master curve developed from VEC test data and compared with the dynamic modulus from the RDT* test. If the two moduli are similar, then the tests were successful and can be confidently used to determine the undamaged properties of a mixture.

DIRECT TENSION TESTING OF FIELD SAMPLES

The RDT* and VEC tests were originally designed for testing LMLC samples. It is much more of a challenge to test field samples and correctly characterize and compare the material properties. Field samples vary from site to site with respect to layer thickness, air voids, binder type, and aggregate type, among other factors. Even samples taken from the same site have variations from sample to sample. However, if these tests can be successfully applied to field samples, a comparison can be made between the VEC and RDT* tests, validating the tests as viable options for direct tension testing of field samples. To make this possible, changes to the sample configuration had to be made in order to test the HMA layer of interest in the direct way that it experiences tension in the field. In addition, several modifications had to be made to the VEC and RDT* test setup, procedures, and analysis. Various field sites were selected in order to determine the factors that have the greatest impact on differences between VEC and RDT* test results.

Field Sample Selection

Seven field sites throughout Texas were selected from which to take samples for this study. Each site was selected based on differing factors such as sample thickness, composition, and climate. Sample thicknesses range from 1.5 inches (38.1 mm) to 3 inches (76.2 mm). Climates were selected based on geographical regions throughout Texas and include dry-warm (DW), dry-cold (DC), wet-warm (WW), and wet-cold (WC). For six of the seven sites, four cores were taken from each site with two cores from the wheel path (WP) and two cores from the shoulder (SH). For the remaining site, only cores from the shoulder were collected. The defining characteristics of each site are shown in Table 43.

Texas Department of Transportation mixtures Type C and Type D can be found in TxDOT Standard Specification 340 while the CMHB-F mixture is found in TxDOT Standard Specification 344 (TxDOT, 2004). The 25 mm SFHMAC mixture was a special TxDOT speciation, SS3248, prepared for perpetual pavement sections.

Table 43. Field Sample Characteristics.

Route Name	Construction Year	Climate[1]	Mixture Type	Aggregate	Binder	Sample Size (in)	WP/ SH[2]	Air Voids (%)
IH 20	2001	WC	12 mm SP[3]	Sandstone	PG 76-22	1.5	WP	9.6
								8.8
							SH	10.1
								11.1
IH 35	2007	DW	25 mm SFHMAC[4]	Traprock/ River Gravel	PG 76-22	3	SH	3.3
								3.6
US 277	2008	DW	TxDOT Type C	Limestone	PG 70-22	2	WP	14.1
								7.4
							SH	7.2
								7.2
US 82	2008	DC	CMHB-F[5]	Limestone	PG 70-28	1.5	WP	8.6
								10.1
							SH	8.8
								7.6
US 83	2008	DC	TxDOT Type D	Granite	PG 70-28	1.5	WP	5.8
								9.8
						2	SH	9.1
								11.0
SH 36	2006	WW	TxDOT Type D	Limestone	PG 64-22	1.5	WP	4.1
								3.0
							SH	5.3
								6.8
Farm to Market 2994	2002	DW	TxDOT Type D	River Gravel	PG 70-22	2	WP	6.6
								5.6
							SH	8.3
								8.1

[1] WC = Wet Cold, DW = Dry Warm, DC = Dry Cold, WW = Wet Warm
[2] WP = Wheel Path, SH = Shoulder
[3] 12 mm Superpave mix
[4] TxDOT Stone Filled Hot Mix Asphalt Concrete
[5] TxDOT Type F Course Mix-High Binder Mixture

Sample Configuration and Preparation

The cylindrical shape used to test LMLC samples for the VEC and RDT* tests was not conducive to testing field samples. A new sample shape as well as a procedure for gluing the samples to the test platens had to be developed for the testing of field samples.

Sample Cutting

Testing field samples in direct tension requires some modifications to the samples taken from the field. Cores in their original configuration do not lend themselves to direct tension testing in the direction of interest. In order to facilitate this type of testing on field materials collected as cores, they must be trimmed and oriented so that the layer in question can be pulled in the direction for which the tensile properties of the material are sought. In order to determine the tensile properties associated with fatigue failure, collected cores are trimmed to leave only the layer of interest. The resulting circular disk of thickness varying from 1.5 in to 3 inches is trimmed into a rectangular shape. Preliminary attempts were made to test the samples without trimming the ends of the sample as shown in Figure 88(a). However, this proved to be problematic. If the initial lengthwise cuts were not well centered, platens glued to the sample for testing would not align properly causing unwanted moments and occasional failure at the sample/platen interface. In order to address these issues, the rounded ends were removed and the rectangular shape shown in Figure 88(b) was adopted.

Fatigue failure is most often associated with longitudinal cracking which runs parallel to the direction of traffic; therefore the length of the prism runs perpendicular to the traffic direction. For a 6-inch diameter core, this results in a prism with a length of approximately 4 inches and a width of 3 incheas as shown in Figure 88(b). The depth of the prism is dependent on the thickness of the layer under investigation.

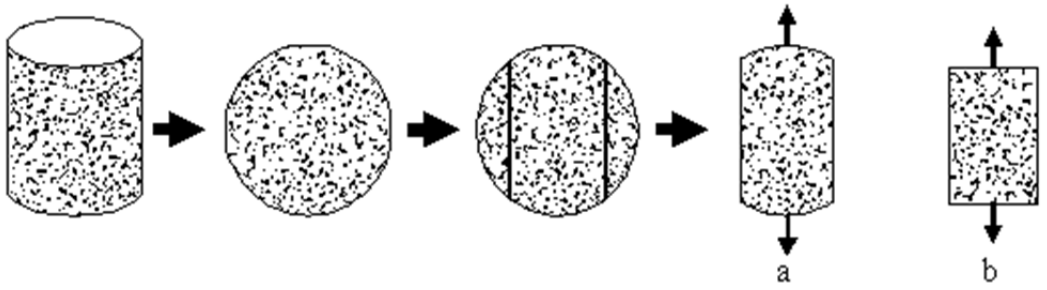


Figure 88. Sample Trimming Procedures with Ends (a) Untrimmed and (b) Trimmed.

Sample Gluing

Initial attempts at gluing platens to the sample for testing were made on the vertical gluing jig shown in Figure 89(a). While this method of gluing centered the sample on the platens with respect to width, it failed to center it with respect to depth. It also failed to properly align the top and bottom platens. Improperly centered samples and misaligned platens tend to cause unwanted moments in the testing process which introduce high variability and unreliability in the test results. In some cases, the moments placed on the sample prevented the test from running to completion due to the platens being peeled from the sample or the sample failing in bending.

In order to better center the samples between platens, a horizontal, magnetic gluing vice, shown in Figure 89(b), was employed. Thickness and width of the samples were carefully measured at each end and at the midpoint of the sample. The platen dimensions were also

measured. The sample measurements were then averaged and divided by two. Gauge metal of appropriate thicknesses was inserted below and beside the sample to position the sample in the center of the platens. Platens were placed flush against the side and bottom of the vice, then brought together to ensure proper alignment with each other. The vice was then reopened and the sample inserted between the platens with the appropriate gauge metal pieces in place. Platens and sample ends were cleaned and a 2 ton (17.8 kN) epoxy was applied to each end of the sample. The vice was then tightened until complete contact was made with the platens and the epoxy. Care was taken to not over tighten the vice, allowing the platens to remain aligned with each other rather than aligning with the sample ends.

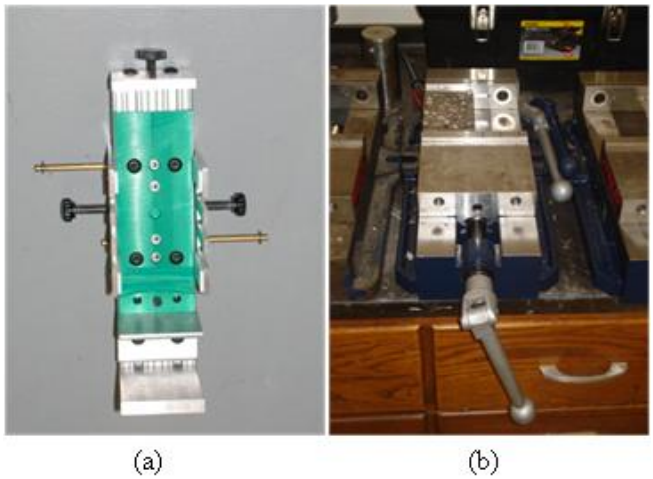


Figure 89. (a) Vertical Gluing Jig and (b) Horizontal Magnetic Gluing Vice with Three Inch Wide Sample.

Unwanted moments were minimized by properly preparing the sample, ensuring proper platen alignment, and centering the sample between the platens.

In order to measure displacement of the sample during testing, linear variable differential transformers (LVDTs) were centered, vertically, on each of the four sides of the sample with a 2 inch (50.8 mm) gauge length. The data collected from these LVDTs was averaged to obtain the approximate sample displacement near the center of the sample.

Machine Modifications

While careful preparation of the field samples greatly reduced the potential for moments during testing, some changes also had to be made to the servo hydraulic testing machine in order to reduce eccentricity. Initial tests used a fixed-fixed connection, where both platens were directly bolted, on both ends, into the testing machine. This tended to exaggerate the small eccentricities inherent in the samples. To remedy this problem, a fixed-pinned connection was used which incorporated a ball and socket joint on one end of the sample, as shown in Figure 90. This allowed the sample to move more freely during testing. The socket base plate was also adjusted horizontally for each test to ensure that the ball was not forced into the joint, causing unwanted bending in the sample. As a result, the ball fit directly into the joint without the application of any horizontal forces. This modification to the servo hydraulic testing machine

further reduced the potential for error in testing caused by eccentric loading and applied moments.

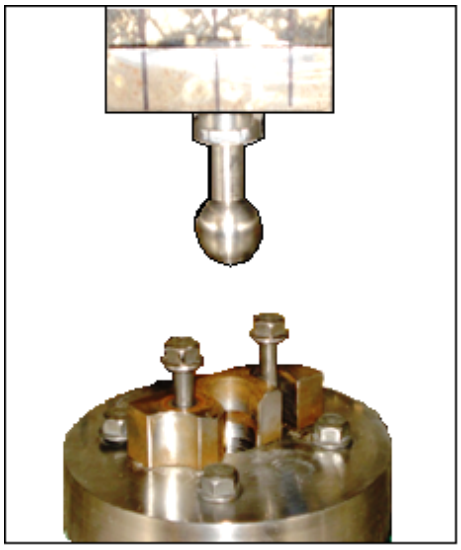


Figure 90. Three-Inch Wide Sample Attached to Ball and Socket Joint Shown with Movable Base Plate.

In addition to the mechanical modifications made to the machine, a program was added to the testing system which would automatically detect when one of the measuring LVDTs for the VEC test reached the 100 με limit. At this point, the test would automatically terminate, reducing the possibility of human error caused by attempting to stop the test manually.

Test Modifications

With adjustments made to sample preparation and the testing machine, modifications could then be made to the tests themselves. VEC test cycles were completed in approximately 5 to 15 seconds at the original rate of 0.01 inches/min. (0.254 mm/min.). This limited amount of data proved to be insufficient for proper analysis and development of the relaxation modulus and complex modulus master curves. In order to provide more test data from the VEC test, the loading rate was adjusted from 0.01 inches/min. (0.254 mm/min.) to 0.004 inches/min. (0.102 mm/min) and finally to 0.002 inches/min. (0.051 mm/min). This provided a minimum of 20 seconds worth of data for most cases.

The RDT* test was adjusted to separate the undamaged and damaged cycles. Other adjustments were also necessary to eliminate the possibility of damaging the samples during the undamaged cycles due to excessive strain. The controlled strain limit for the undamaged cycles was changed from 80 με to 30 με in order to accomplish this. The reduction in this limit made it more difficult for the testing machine to control the test, increasing the amount of noise in the resulting data. However, it prevented the sample from experiencing damaging strains. The number of undamaged cycles was also reduced from 500 to 50. Five hundred cycles was unnecessary when 50 cycles provided sufficient data to perform the necessary analysis. The damaged strain limit was also reduced from 350 με to 175 με. This allowed for collection of

sufficient data to calculate the damaged properties while preventing sample failure or failure at the sample/platen interface.

Analysis Modifications

As mentioned in the previous section, the decrease in strain limits for the undamaged cycles of the RDT* test caused an increase in the noise observed in the recorded data. The analysis of the RDT* data requires that the peaks and valleys of the stress and strain be located. Automation of this process resulted in picking the peaks and valleys of the noise rather than the actual response. Manual identification of these points proved to be far too time consuming and inefficient for adequate and timely analysis. It was observed that the recorded noise occurred at a much higher frequency than the 1 Hz (6.28 radians/sec.) loading frequency. This made it possible to apply a low pass frequency filter to the collected data, removing the unwanted noise occurring at frequencies above 1 Hz (6.28 radians/sec). The result was a much smoother data set that allowed for automated peak picking of the stress and strain curves.

RESULTS

With sample, machine, test, and analysis modifications made, the VEC and RDT* tests could be applied to field samples. The data were collected and test results analyzed for the selected sites listed in Table 43. The results from these tests can be seen Table 44, which include E^* and E_{ve} as well as the absolute percent difference between E^* and E_{ve} for each sample.

A careful inspection of the results from the individual LVDTs indicates that a stiffness gradient occurs between the pavement surface and the bottom of the layer being tested. While further analysis of this gradient is ongoing, it is beyond the scope of this particular study. However, the average response of the four LVDTs was sufficient to give an overall view of the material behavior and performance needed for test comparisons and practical application.

Table 44. Field Sample VEC and RDT* Test Results.

Route Name	Wheel Path /Shoulder	Percent Air Voids	E_{ve} Average (MPa)	E*(1) (MPa)	E_{ve} (MPa)	Absolute % Difference
IH 20	Wheel Path	9.6%	6631	6356	6538	2.8%
		8.8%		8313	7793	6.7%
	Shoulder	10.1%		6240	6072	2.8%
		11.1%		6396	6121	4.5%
IH 35	Shoulder	3.3%	3883	3475	3575	2.8%
		3.6%		3952	4191	5.7%
US 277	Wheel Path	14.1%	4564	4020	4407	8.8%
		7.4%		4589	4928	6.9%
	Shoulder	7.2%		4323	4459	3.0%
		7.2%		4367	4462	2.1%
US 82	Wheel Path	8.6%	6054	5027	4826	4.2%
		10.1%		5496	6190	11.2%
	Shoulder	8.8%		7744	6900	12.2%
		7.6%		7101	6300	12.7%
US 83	Wheel Path	5.8%	1989[1]	1921	3000	**36.0%**
		9.8%		1887	1800	4.8%
	Shoulder	9.1%		2004	1999	0.2%
		11.0%		1981	2169	8.7%
SH 36	Wheel Path	4.1%	8923	8567	9419	9.0%
		3.0%		6254	9061	**31.0%**
	Shoulder	5.3%		7870	8426	6.6%
		6.8%		4682	6962	**32.8%**
Farm to Market 2994	Wheel Path	6.6%	4719	4899	5040	2.8%
		5.6%		5093	5097	0.1%
	Shoulder	8.3%		3966	4140	4.2%
		8.1%		4566	4597	0.7%

[1]Value does not include outlier value of 3000 MPa.

Of the 26 samples tested, only three appeared as outliers in a statistical analysis. These included a sample from US 83 located in the wheel path and two from SH 36, one in the wheel path and one in the shoulder. After reviewing the notes and results associated with US 83, it appears that the unusually large percent differences between E^* and E_{ve} could be the result of poor sample preparation and handling which resulted in eccentric loading during testing. SH 36, however, is a very stiff mixture. This high level of stiffness may have influenced the results of

the VEC test. Mixturees of this level of stiffness may require a higher strain limit than the prescribed 100 με in order for the VEC test to produce viable results. This warrants further evaluation using several samples of high stiffness.

For the remaining 23 samples, the absolute percent difference between E^* and E_{ve} follow a normal distribution with a mean of 5.4 percent and a standard deviation of 3.72 percent, indicating that the results from the VEC and RDT* tests were similar. A study by L. K. Huang suggested that differences between stiffness moduli from SCB and FB test of about 10 percent or less were acceptable (Huang, 2009). Thus, the VEC and RDT* tests are viable direct tension tests for determining the undamaged moduli of a HMA field sample.

It is also important to consider the effects of the different properties of each individual sample. This is necessary in order to determine if the two tests can be applied over a broad range of field samples or if the test results are limited based on the individual properties of the sample. Differences between E^* and E_{ve} were examined based on air void content, binder content, sample thickness, age, and climate conditions to determine what correlations, if any, could be drawn from the results. In each case, correlations were weak, with age having the greatest correlation coefficient of 0.4311, indicating a slight increase in E^* and E_{ve} differences with respect to aging. Binder content and sample thickness appeared to have the next greatest correlations, though they were also weak, with values of 0.3289 and −0.3068, respectively. Climate conditions and air voids tend to have little effect on E^* and E_{ve} differences, with both having correlation coefficients less than 0.18.

A mixed stepwise regression was also run for the above mentioned effects to determine their level of significance. At a 95 percent level of significance, only the age of the sample and sample thickness were shown to have a significant effect on the absolute difference between E^* and E_{ve}. Respective p-values for these effects were 0.014 and 0.045, respectively. It can, therefore, be stated that thicker samples taken early in the life of the pavement minimize the difference between E^* and E_{ve}. As a result, it is important to use as much of the layer in question as possible when using the VEC and RDT* tests for determining field sample properties. As the sample ages, careful evaluation should be made with respect to the change in modulus, in order to ensure that the test results are of sufficient quality for accurate pavement evaluation.

Further evidence for the viability of the VEC and RDT* tests can be seen by examining the resulting modulus values at each individual site. Noting that variability can be found from location to location within a site, the average values of E_{ve} for each site in Table 44. Table 44 values are relatively close to the actual measured values for each individual sample. Standard deviations for the study sites range from 185 MPa (26,800 psi) for US 83 to 876 MPa (127,000 psi) for US 82 with 75 percent of the individual values falling within 10 percent of their respective site mean. The variation that is found can be attributed to factors such as different air void contents, binder contents, and traffic loading rates, among others. The similarities between samples provide some confidence in the consistency of the tests for any given site.

SUMMARY

By comparing VEC and RDT* test results from the same sample as well as the results from different samples taken from the same site, it can be seen that these two tests can be successfully applied to field samples. The VEC and RDT* tests provide a quick and accurate method of determining the material properties necessary to assess fatigue under field conditions. Streamlining of the test preparation and further automation of the analysis will further make the VEC and RDT* tests practical methods for determining the material properties of samples obtained from the field.

Researchers will be able to separate and assess the effects of aging and trafficking on the number of loads to fatigue failure by examining VEC and RDT* test results from the wheel path and shoulder of any given pavement over time. This, in turn, will allow for more accurate development of mechanistic models which incorporate accurate aging prediction and correctly characterize fatigue. Current and future models can be compared and analyzed for accuracy by testing field samples throughout the life of the pavement and comparing the test results to those obtained from the models.

Over the past 100 years, significant progress has been made in the development of an efficient and effective transportation system. The direct tension testing of field samples using the VEC and RDT* tests will help propel the industry forward into the next 100 years of success by allowing for the quick, accurate, and direct determination of the material properties of HMA pavements. As these results are applied, agencies will be better able to determine pavement life and plan for the maintenance, rehabilitation, and reconstruction of the transportation system.

CHAPTER 12. INVESTIGATION OF AGING EFFECTS AT A SINGLE FIELD SITE USING DIRECT TENSION TESTING

In this portion of the study, field samples acquired from a site in south Texas were investigated over time to see if relationships existed between the oxidative aging of the binder and the performance of the mixture. Cores were taken four times, first at construction and then at intervals of approximately one year. Laboratory-aged mixtures were also compared to the field samples. Raw materials collected from the same site in south Texas were used to prepare laboratory mixed, laboratory compacted samples that were artificially aged and tested to determine their material properties. Binder extracted from the LMLC and field samples was also examined.

This chapter discusses materials collected for the study followed by a description of the sample preparation methods and test methodologies used to obtain the material properties of the aged and initial condition samples from the laboratory as well as the field. Binder extraction and test methods are also described. Material properties were then used to estimate N_f using the CMSE* method without the application of shift factors. Results from the binder tests, field sample tests, and LMLC sample tests are reported followed by a cross-comparison of all of the results. From each of these tests, conclusions were made with respect to the effects of aging on the selected HMA mixture.

MATERIALS

Materials for this study were selected from US 277 in the Laredo District of the Texas Department of Transportation. At the time of construction, raw materials from the site were collected for the fabrication of LMLC samples. Field cores were taken immediately following construction and thereafter at approximately one year intervals for a total of four sampling times. Binder used specifically for testing was extracted from selected field cores.

US 277 was constructed in 2008. Aggregates for this mixture consisted of a blend of four different aggregates to create a TxDOT Type C mixture (TxDOT, 2004). Three of the aggregates consist of limestone from the South Texas Aggregates Inc., Sabinal Quarry located in Uvalde County, Texas. They include a coarse limestone aggregate, a blend of Type D and Type F limestone aggregates, and manufactured sand. The fourth aggregate used in the blend is manufactured sand from the Vulcan Materials Company, Knippa Quarry, also located in Uvalde County, Texas.

Binder for the US 277 mixture consisted of a PG 70-22 Valero Asphalt binder with an optimum asphalt content of 4.5 percent by weight of mixture using the Superpave volumetric mixture design method.

Twelve cores were taken from the field in 2008; six from the wheel path, and six from the shoulder. Air void content for all 12 field samples was determined. Two cores from the wheel path and two from the shoulder were used for mixture testing. One field core from the wheel path and one from the shoulder were used for binder extraction. The remaining cores were retained as alternates.

A portion of the test section was treated with a chip seal following the initial core extraction. In 2009, six more field samples were taken from the untreated wheel path and six more from the shoulder, with six additional field samples taken from the treated wheel path. This sampling process was repeated in 2010 and 2011. Field samples were selected from the treated and untreated sections for mixture and binder testing as described for the 2008 samples. The 2011 field wheel path samples all had a chip seal, which was placed on the pavement surface approximately nine months prior to coring.

TESTING METHODOLOGY

Two uniaxial tension tests developed at Texas A&M University were used to determine the material and fatigue properties of the samples. These include the VEC test (Luo and Lytton, 2010) and the Modified Repeated Direct Tension (RDT*) test (Luo et al., 2008). Asphalt binder was extracted from selected field samples and analyzed using a Fourier Transform Infrared Spectrometer to determine the degree of binder oxidation.

Sample Preparation

LMLC and field samples were prepared for uniaxial tension testing in order to minimize eccentricities and to reduce moments during testing. Binders were extracted from selected field cores.

LMLC Samples

LMLC samples used in this study were fabricated based on a D-optimal statistical design which incorporated several combinations of binder contents and AV with 0, 6, 9, and 12-month aging periods in a 60°C accelerated aging room. Table 45 includes the D-optimal design combinations. Ranges used for binder contents and AV are shown in Table 46.

Table 45. D-Optimal Statistical Design for LMLC Samples.

Run	Aging	Binder Content	Air Void
1	0 months	Opt -0.5%	Low
2			High
3		Opt +0.5%	Medium
4			High
5			Low
6		Optimum	Medium
7			High
8	6 months	Opt -0.5%	High
9			Medium
10		Opt +0.5%	Low
11			Medium
12		Optimum	High
13			Low
14			Medium
15	9 months	Opt -0.5%	High
16			Medium
17		Opt +0.5%	Medium
18			Low
19			High
20		Optimum	Medium
21	12 months	Opt -0.5%	Medium
22			Low
23		Opt +0.5%	Low
24			High
25		Optimum	Low
26			High
27			Medium

Table 46. Binder Content and Air Voids for US 277 Samples.

	Binder Content		Air Voids
Low	Optimum −0.5 %	(4.0 %)	< 5%
Medium	Optimum	(4.5 %)	5%–7%
High	Optimum +0.5 %	(5.0 %)	> 7%

Aggregates used for the LMLC samples were placed in an oven at the mixing temperature of 149°C and were left overnight in order to remove any moisture. The binder was also heated to the same mixing temperature for two hours just prior to mixing. The mixture was then short-term oven-aged at the compaction temperature of 135°C for four hours as prescribed by AASHTO R30 for performance testing.

Samples were molded using the Super Gyratory Compactor (SGC) to 152 mm diameter by 152 mm height in order to meet the specified target AV content. The initial AV content found in the 152 mm diameter by 152 mm high samples was slightly higher than the values shown in

Table 46 due to the conditions imposed by the SGC mold (Masad et al., 1999). To obtain a more uniform AV distribution, representative of the typical air void distributions encountered in field samples, LMLC samples were compacted at a higher AV content and then cored to a 102 mm diameter. The samples then had 25 mm trimmed from each end to produce the final 102 mm diameter by 102 mm high sample with the appropriate target low, medium, or high AV content.

The prepared LMLC samples were next placed in vertical gluing jigs (Figure 91a) so that 102 mm diameter steel platens could be affixed to each end. The gluing jigs provided a method of aligning the platens to minimize eccentricities during the tension testing process. Following sufficient drying time, three LVDTs were placed vertically and equidistant around the sample (Figure 91b). The LVDT gauge length was 51 mm.

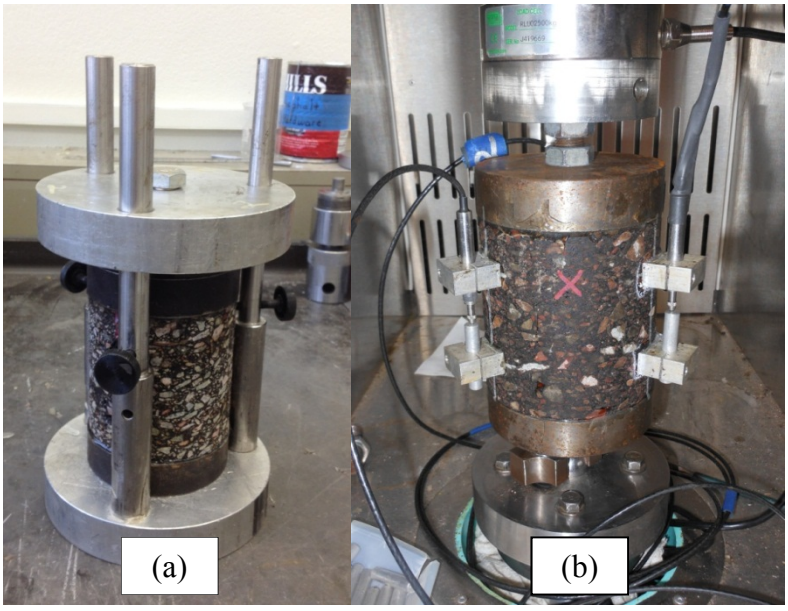


Figure 91. Vertical Gluing Jig (a) and Test Setup (b) for LMLC Samples.

Field Samples

Field cores were trimmed into a prismatic shape as shown in Figure 92. This allowed the samples to be tested in the same direction that they would experience tension forces in the field. Special care was taken during cutting to ensure that the sample sides were as close to parallel as possible.

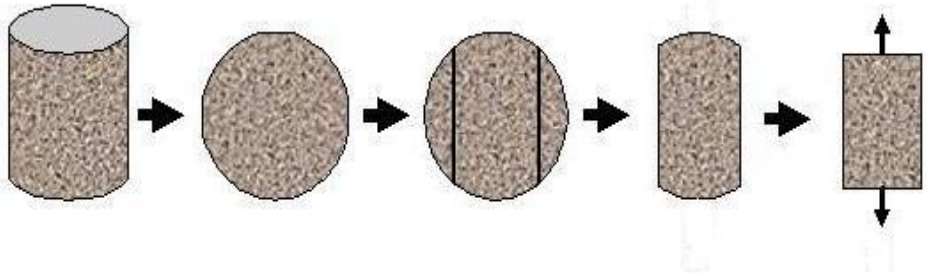


Figure 92. Field Sample Testing Configuration.

A horizontal magnetic gluing vice (Figure 93) was used to affix steel plates to each end of the field samples. The magnetic vice ensured that the platens remained aligned with each other, regardless of any small discrepancies in the sample, which may have occurred during the cutting process.



Figure 93. Magnetic Gluing Vice for Field Samples.

LVDTs were placed at 51 mm gauge length on each of the long sides of the sample to measure the vertical displacement induced during testing.

Binder Extraction

The binder extraction process for the field samples was executed by first separating any applied chip seals from the sample by knife. Field samples were then cut by electric saw into several layers, from top to bottom, with each layer being approximately 12.7 mm thick. These layers were then broken into small pieces.

The extraction used three successive washes of a mixture of 15 percent ethanol plus 85 percent toluene by volume. After the extraction, the solvent was centrifuged and filtered to remove all the aggregate particles from the binder solution.

The asphalt binder was recovered from the solvent with a Büchi RE111 Rotovap. Nitrogen was used to carry off the solvent and prevent further oxidation. During solvent removal, the bath temperature was kept at 100°C to avoid hardening or softening of the asphalt in dilute solution. To ensure total solvent removal, the temperature was increased to 174°C for 45 minutes after the condensing solvent could no longer be detected visually.

HMA Mixture Testing

In order to calculate the fatigue properties of LMLC and field samples, both the VEC and RDT* tests were performed. VEC and RDT* tests were performed using a servo-hydraulic testing machine. A ball and socket joint was used to further minimize the effects of sample eccentricity and undesirable moments for both LMLC and field samples. Figure 94 shows the field sample test setup with LVDT placement and the ball and socket joint.

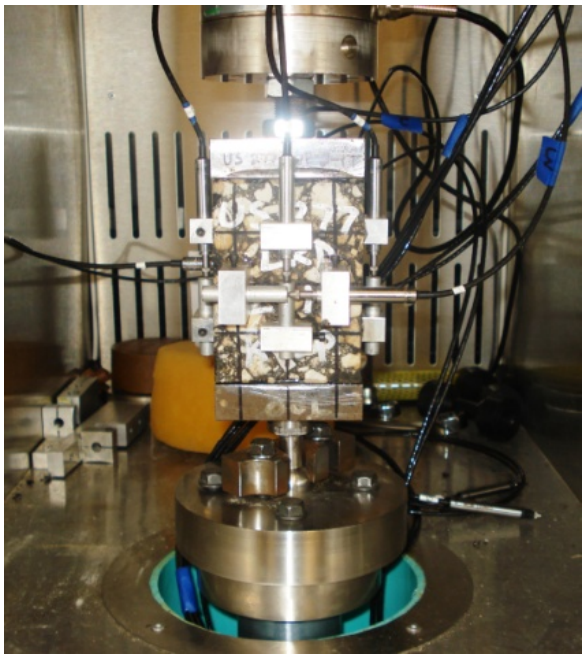


Figure 94. Field Sample Test Setup with Ball and Socket Joint at Base.

VEC TEST

The original VEC test and analysis was developed at Texas A&M University for application to LMLC samples (Luo and Lytton, 2010; Luo et al., 2008). Modifications were later made to this test for application to field samples as described in Chapter 11.

The VEC test was performed by applying a monotonically increasing tensile load to a sample at a strain rate of 50.8 μm per minute. The test continued at this rate until one of the measuring LVDTs reached a strain level of 100 με. It is assumed that at this small strain level, no damage occurs and the sample can used in further testing (Luo and Lytton, 2010).

The sample was initially conditioned and tested at 10°C. Once the test was completed, the sample was reconditioned for a minimum of two hours and retested at 20°C and 30°C using the same procedure.

Recorded load and displacement data from the LVDTs for each temperature were used to calculate stress and strain. These values were averaged and defined using a fitting curve at each temperature. Fitting parameters from these curves were then used, in conjunction with Laplace

transformations and calculated shift factors, to determine the relaxation modulus (E_t) master curve and the complex modulus (E*) master curve at 20°C.

RDT* TEST

The RDT* test was developed at Texas A&M University by Luo et al. (2008). This test was also further refined for application to field samples as described in Chapter 12.

The RDT* test was performed on a sample preconditioned at 20°C. The sample was exposed to a Haversine load in displacement control mode with a maximum vertical strain level of 30 με for 50 cycles at a frequency of 1 Hz. For a 51 mm LVDT gauge length, 30 με is a change in gauge length of approximately 1.5 μm. This portion of the test was used to calculate the undamaged viscoelastic phase angle and the undamaged dynamic modulus of the mixture.

Following the 50 cycles at 30 με, a 1000 cycle Haversine loading was applied at a frequency of 1 Hz with a maximum strain level of 175 με. For a 51 mm LVDT gauge length, 175 με is a change in gauge length of approximately 8.9 μm. At the completion of the test the sample was damaged and could not be retested.

Data obtained from the RDT* test were averaged and filtered using a low pass filter. The filter removed machine noise from the data, allowing for automated data processing.

The damaged portion of the RDT* test (175 με level) was used in combination with the results of the undamaged portion of the test to determine fracture properties, such as Paris' law fracture coefficient, *A*, Paris' law exponent, *n*, and the rate of damage accumulation, *b*. These were then used in the CMSE* model to calculate N_f (Luo et al., 2008; Walubita et al., 2005a, 2006b).

Binder Testing

Extracted binders from field cores and LMLC samples were analyzed using FTIR to determine the degree of oxidation. A Nicolet 6700 FTIR spectrometer with an attenuated total reflectance zinc selenide prism was used to determine the degree of binder oxidation, by measuring carbonyl area (CA). CA is the area under the absorbance peak from 1650–1820cm^{-1}, in arbitrary units, which provides a direct measurement of the oxidation progress in asphalt binder. This property is also strongly correlated to rheological properties measured in the Dynamic Shear Rheometer (Martin et al., 1990).

TEST RESULTS

Mixture and fracture properties for LMLC samples and field samples were calculated using the data obtained from both the VEC and RDT* tests. Binder properties were also determined. The results of these calculations were evaluated and compared as a way of validating the VEC and RDT* testing methods. LMLC and field mixture results and binder results were also evaluated individually and combined in order to provide a preliminary evaluation of the effects of aging and maintenance treatments on HMA mixtures.

Extracted Binder Test Results

Following the testing of the LMLC samples, the binders were extracted and tested using FTIR to determine its chemical properties. Due to the nature of the D-optimal statistical design used in the sample fabrication determination, a full factorial set of data is not available. However, the overall trends can still be observed from the test results.

Figure 95 shows the CA of the samples, which had optimum binder content with each series representing different AV contents. From Figure 95 it can be seen that as the samples age in the laboratory, the CA increases. However, the Low AV samples show less oxidation (lower CA values) as a result of less exposure to oxygen within the sample. The Medium AV and High AV samples appear to experience similar changes in CA as the sample ages. This indicates that there may be a threshold AV content at which the diffusion of oxygen into the binder becomes constant.

In Figure 96 the AV content is held constant at Medium AV with each series representing different binder contents. Figure 96 shows that the change in binder content appears to have little effect on the change in CA.

While it appears that a change in AV content has a greater impact as compared to a change in binder content, the binder from the LMLC samples is aging in a measurable way and trends are as expected, with CA increasing with time.

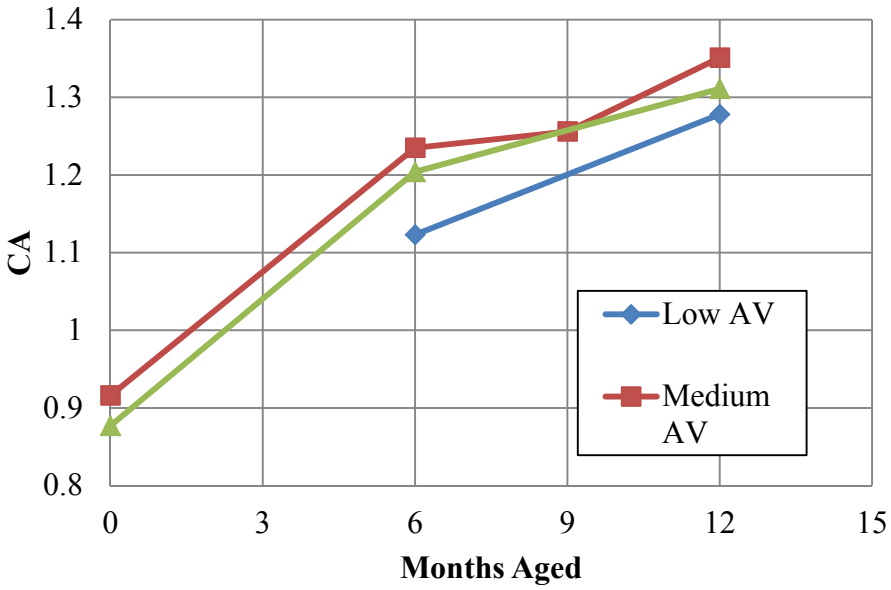


Figure 95. CA of LMLC Samples at Optimum Binder Content.

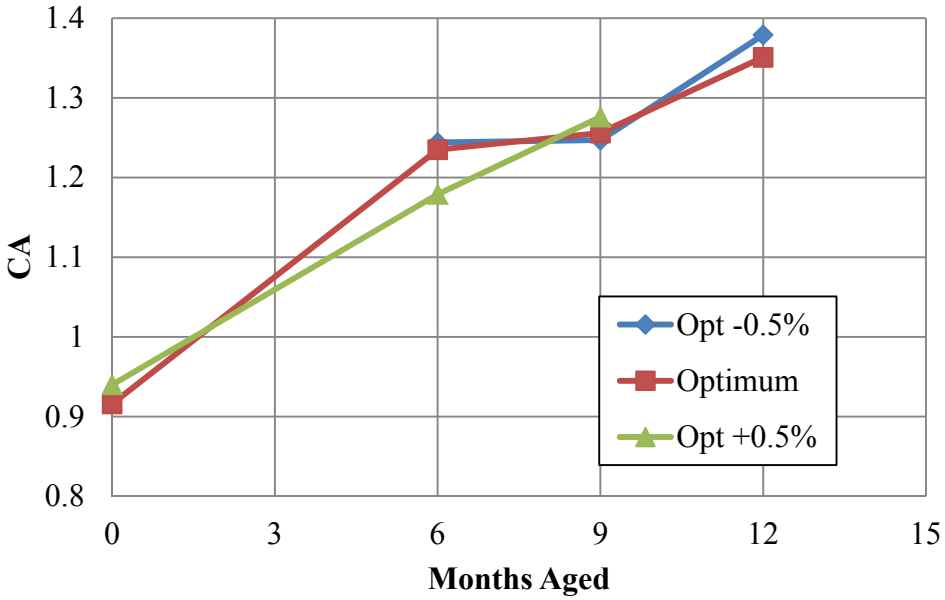


Figure 96. CA of LMLC Samples at Medium AV.

With respect to the field cores, the binder for each layer was tested and its chemical properties determined by FTIR after extraction and recovery. Binder CA growth rates were measured from samples obtained from the wheel path and shoulder for each of the four years from 2008 to 2011. Figure 97 and Figure 98 show the CA with depth for the shoulder and wheel path sections, respectively.

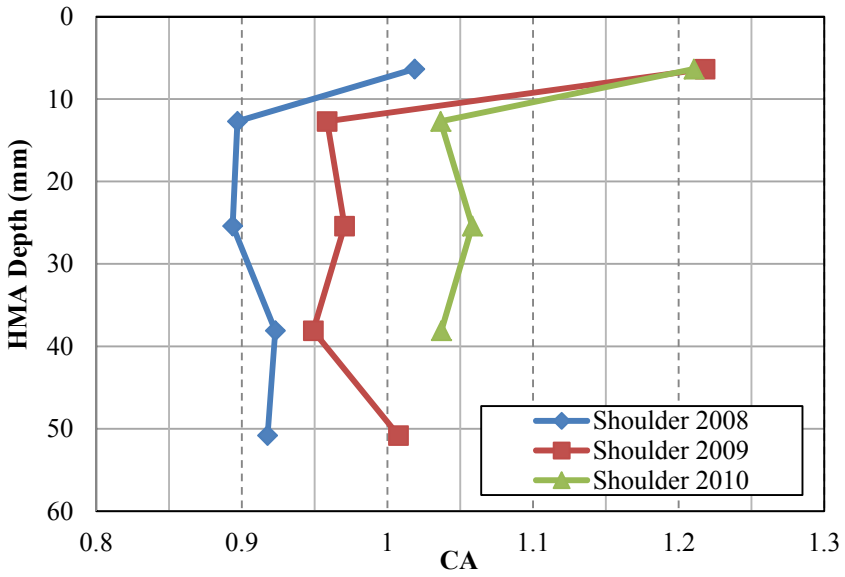


Figure 97. CA Value with Depth and Years for US 277 Shoulder.

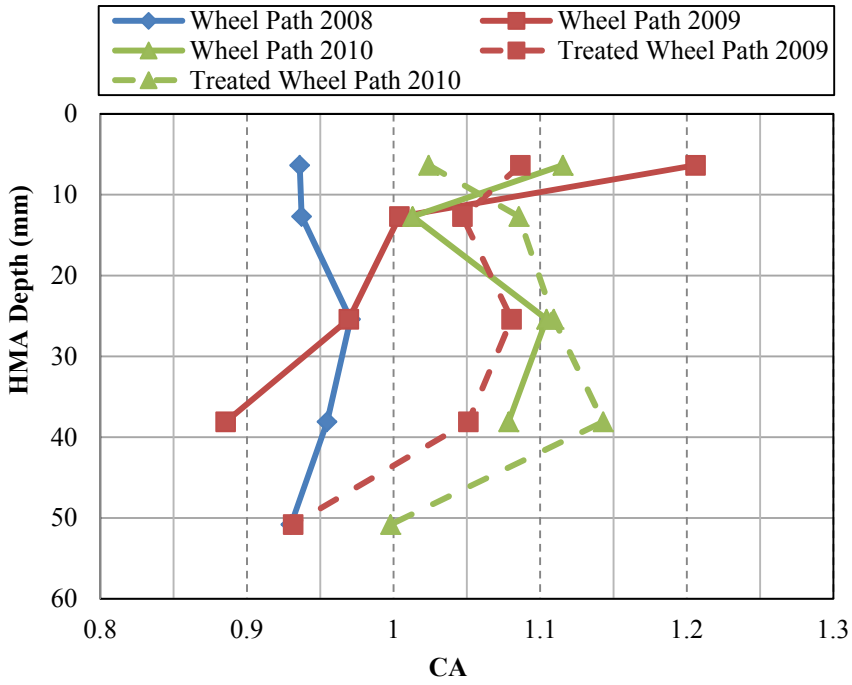


Figure 98. CA Value with Depth and Years for US 277 Wheel Path.

In Figure 97, for the samples taken from the shoulder, there was no chip seal treatment on the surface, indicating that the data represents the natural aging process of the road without traffic. The CA values of the first layer for all of the samples are considerably higher than those for the underlying layers. The 2008 sample was collected three months after construction. The CA value of the first layer for this sample was already over 0.1 higher than the average value for layers 2 through 5 that have a standard deviation of 0.015. This is likely due to direct exposure to oxygen during paving in combination with the three month service period. For the 2009 shoulder sample, the CA values of all the layers had increased as expected. Furthermore, the CA for the first layer, which increased 0.2 compared to 0.08 for the deeper layers, has a much faster aging rate between 2008 and 2009. The CA difference between the top layer and the underlying layers rose to about 0.25. The reason for this phenomenon may be the oxygen diffusion resistance, which plays an important role in field aging. The oxygen diffusion resistance for the surface layer is negligible due to the direct exposure to the air. These conclusions agree with observations made in previous studies (Domke et al., 1999).

Similar results were found from the CA data for the wheel path as shown in Figure 98. As previously mentioned, some of the wheel path sections had a chip seal surface treatment placed on the pavement surface after three months of use; just after the 2008 core collection. The purpose of the chip seal was to protect the HMA from oxidative aging by cutting off the contact between the air and pavement. It is also thought to rejuvenate the binder directly beneath the treatment.

The CA for the chip seal treated wheel path samples had a much lower value for the first layer when compared with the untreated sample from the same year. This is a good indication that the first layer aged much less under the chip seal treatment. However, it is not clear whether this was due to cutting off oxygen flow, binder rejuvenation, or a combination of the two factors.

The CA value for the chip seal binder, which was not included in Figure 97 and Figure 98, was approximately 1.5 to 1.6, which is extremely high. This could be due to direct exposure to air or from high UV radiation and high temperatures that result from the darker exposed area associated with chip seals. With the exception of layer 1, the untreated core in 2009 did not did not behave as expected when compared with the core in 2008. For layer 4 (about 38 mm beneath the surface) the CA of the 2009 core turned out to be less than the CA for the 2008 core. This may be due to the variability of the cores or materials, especially when considering that AV content for the 2009 core was approximately one percent less than the core from 2008. The results shown in Figure 98 also give the impression that the chip seal accelerated the aging beneath the surface, which is not as expected.

Figure 99 shows the average CA results for the shoulder, untreated wheel path, and treated wheel path combined. While there is a difference between results from year to year, there is no evident difference between the wheel path and shoulder until 2010. In 2010, the oxidation occurring in the untreated wheel path is slightly less than that occurring in the shoulder. The treated section's oxidation is less than both the shoulder and untreated wheel path. From these results it appears that the average pavement oxidation is eventually affected by both traffic and maintenance treatments. Also note that the CA increased for all three locations by about 0.07 during the first year, indicating that much of the aging occurs during the first year of the life of the pavement.

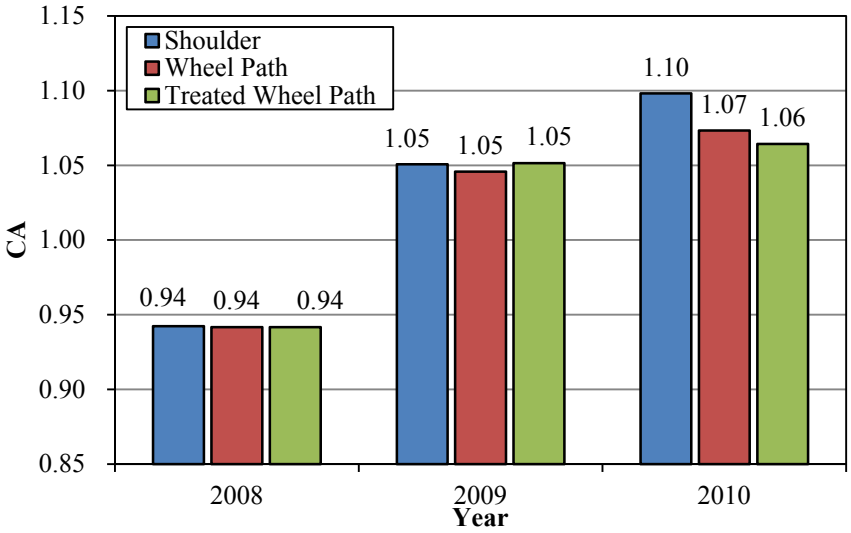


Figure 99. Average Combined CA for All Sections of US 277.

Field Sample Test Results

Results of the VEC and RDT* tests for the field samples were first used to compare the moduli of the various samples taken from the wheel path, treated wheel path, and shoulder from 2008 to 2011.

Figure 100 shows the dynamic modulus (E_{ve}) values obtained from the RDT* test. These values correlate well with the complex modulus (E^*) values from the VEC test which had results that were within 10 percent of E_{ve} (Huang, 2009). From the results shown in Figure 100, it can be

seen that the E_{ve} of the shoulder continues to increase as the pavement ages with the exception of the 2011 sample (Jan-12 in Figure 100), which had a chip seal placed on it shortly after the 2010 sample was collected. The shoulder experiences effectively no traffic, therefore, this result is primarily due to the aging of the HMA.

Both the treated and untreated wheel path experience an initial increase in E_{ve} between 2008 and 2009, however, contrary to the shoulder trend, the modulus then begins to decline for the following three years. From 2008 to 2009, the modulus increases as the pavement ages and is exposed to traffic loading. However, after only the first year, the HMA begins to accumulate damage in the form of fatigue cracking and the modulus declines. Also note that the rate of decline for the untreated wheel path slightly decreased between 2010 and 2011. Again, this may be due to the placement of a chip seal on the surface of the pavement shortly after collection of the 2010 samples.

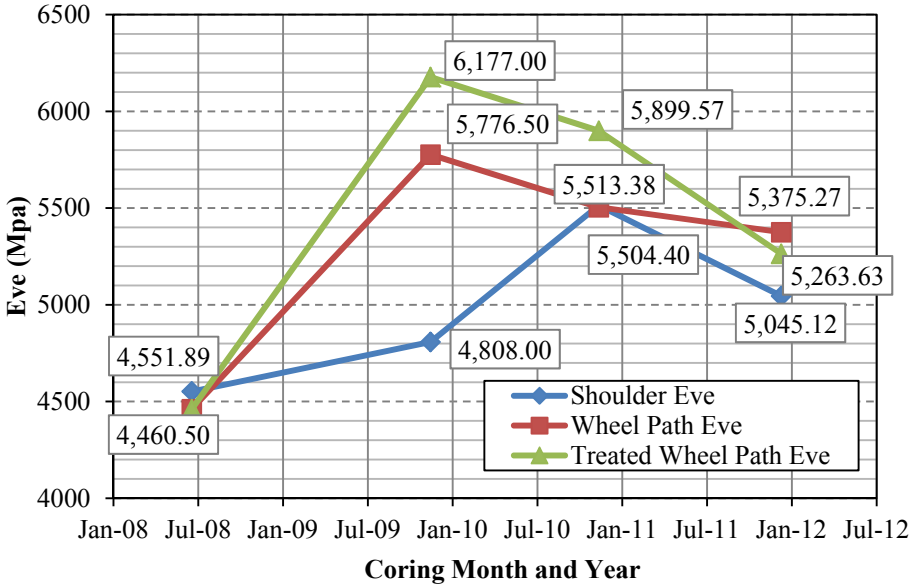


Figure 100. Eve for US 277 Field Samples.

Some other interesting trends can be seen by examining the N_f values calculated for these same samples. N_f values were calculated using the VEC and RDT* results in the CMSE* model. Calculated N_f values are shown in Figure 101. Notice that the N_f values for the shoulder remain relatively flat with a slight decline in N_f values as it ages. The wheel path sections, however, have an initial sharp decline with the rate of change in N_f values slowing as time progresses. Once again, there was a slight increase in N_f for the 2011 wheel path samples, which had the chip seal applied in 2010. It is also important to note that for the treated wheel path section, the N_f values remain at a higher level than the untreated section, suggesting that the chip seal has a positive effect in extending the life of a pavement. It also appears that the placement of a chip seal later in the life of a pavement can also positively affect the pavement life.

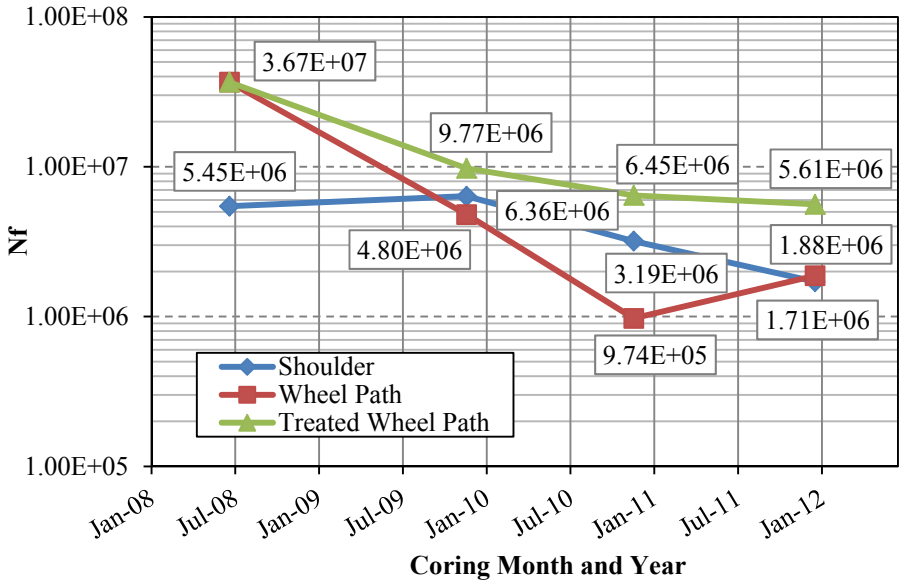


Figure 101. N_f for US 277 Field Samples.

Based on these results, the HMA stiffens with aging, which plays a role in the fatigue failure of pavements. It can also be concluded that a chip seal placed as a maintenance treatment can extend the life of a pavement. However, these results are specific to this particular site. Additional research is recommended using mixtures from other sites in order to determine if these trends are typical of all HMA and if the trends can be predicted.

LMLC Sample Test Results

The VEC and RDT* tests were also performed on LMLC samples. Test data collected allowed for a comparison of the material properties and performance of the LMLC samples at different AV and binder contents for the initial condition and aged samples. An Analysis of Variance test concluded that there are statistically significant effects of aging level, binder content, and air voids on E_{ve} while there are no statistically significant interaction effects among them (i.e., the rate of change in E_{ve} over different aging levels are not statistically different over different AV or over different binder contents). A Tukey HSD statistical test confirmed that E_{ve} was statistically different at each aging level. As seen in the field samples, it is safe to conclude that E_{ve} increases with age. Figure 102 shows how E_{ve} changes over time with low, medium, and high AV contents. As expected, the modulus increases as the sample ages. Low AV samples had a higher E_{ve} value, followed by that for the medium and high AV samples. While the medium and high AV samples appeared to have very similar E_{ve}'s at 6 months, the Tukey HSD analysis for the effect of AV indicated E_{ve} was significantly different overall among all three AV contents. Also, notice that the rate of change in E_{ve} over time is similar for all three AV contents as expected from the insignificant interaction effect test results between aging levels and AV contents.

Figure 103 shows the change in the E_{ve} values for three different binder contents: optimum, optimum −0.5 percent, and optimum +0.5 percent. From Figure 103 the rate of change in E_{ve} appears approximately the same for the optimum and optimum −0.5 percent binder

contents but is slightly slower for the optimum +0.5 percent binder content. However, as mentioned above, the ANOVA test on the interaction effect between binder contents and aging levels indicated that the rate of change in E_{ve} across three binder contents was not statistically significantly different. Tukey HSD analysis on the main effect of binder content indicated that overall there was no significant difference in E_{ve} based on binder content for optimum and optimum +0.5 percent while a significant difference did exist between these two and the optimum −0.5 percent.

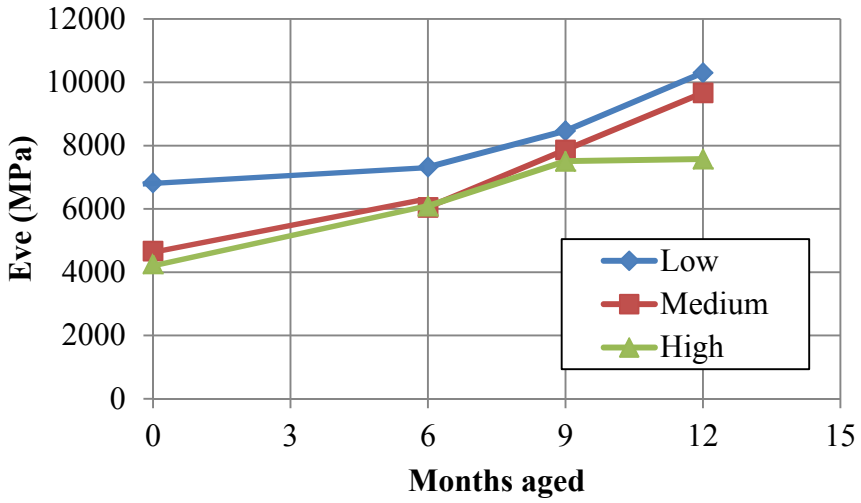


Figure 102. E_{ve} for LMLC Samples at Differing AV.

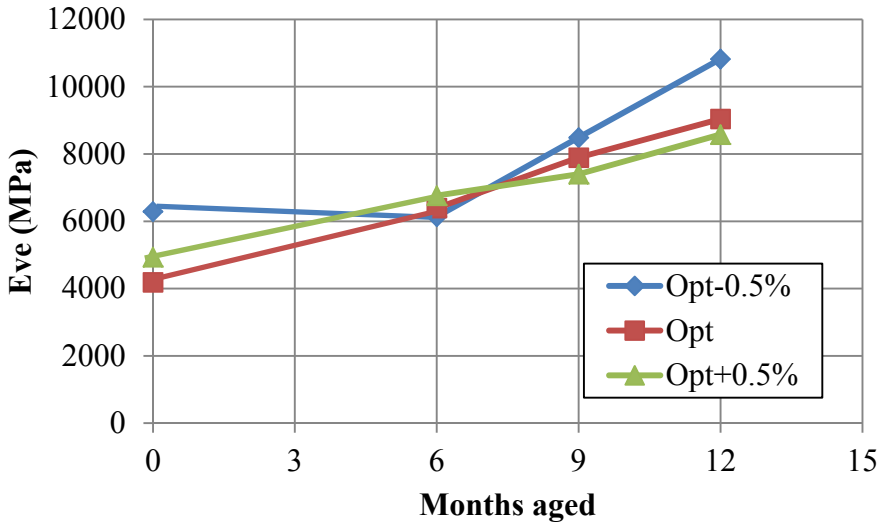


Figure 103. E_{ve} for LMLC Samples at Differing Binder Contents.

Finally, Figure 104 shows N_f for the LMLC samples prepared and tested at the optimum binder content and medium AV. As the samples age and stiffen, N_f slightly increases, indicating that aging is affecting the mixture performance, though its effect is small. A linear fit of the data indicates that N_f changes at a rate of approximately 180,500 loads per month of artificial aging. While this may seem significant, it must be remembered that this is associated with accelerated aging, meaning that one month in the laboratory aging room could be equivalent to several

months in the field. One study of nine different binders found that one month of laboratory aging was equivalent to a range of 13 to 19 months in the field (Woo et al., 2007). However, that relationship was developed with respect to binders under different aging conditions and cannot be directly compared to the mixture aging conducted in this study. Nevertheless, the E_{ve} and N_f values collected for both LMLC and field samples allowed for some relationships to be developed, as discussed in the subsequent section.

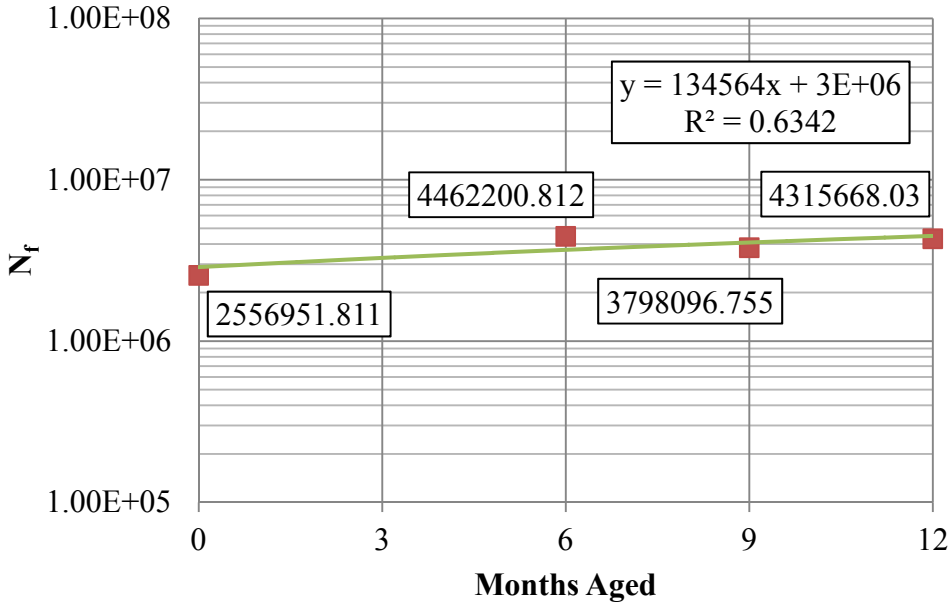


Figure 104. Number of Loads to Fatigue Failure for LMLC Samples with Medium AV and Optimum Binder Content.

COMPARISON OF TEST RESULTS

With testing and analysis results obtained for binders, field samples, and LMLC samples, it is possible to make some comparisons between the results. A connection between binder aging and field performance along with a correlation between field and LMLC mixture performance may provide the information required to predict the effects of aging on the performance of HMA in the field.

LMLC vs. Field Samples

LMLC samples were only exposed to accelerated laboratory aging and experienced no traffic loading prior to testing. In order to make an equivalent comparison to performance in the field, it is important to compare the LMLC sample results with field results from samples which had minimal exposure to traffic loading. To accomplish this, a comparison was made between the LMLC samples and the field samples taken from the shoulder of US 277. Figure 105 shows this comparison of E_{ve} values. The 2011 field sample is not shown because the chip seal placement altered the resulting E_{ve} value, making it incompatible. Plotting the two lines representing the linear fit of E_{ve} for the LMLC and field samples on the same graph, the shows the relationship between field and LMLC samples . With the age of the LMLC samples in

months listed at the top of the graph and the number of months that spanned between field samples acquisition listed at the bottom, it can be determined that one month of aging in the laboratory is equivalent to approximately 10.5 months in the field for US 277. This is less than the 13 to 19 months found in previous studies (Woo et al., 2007), but the Laredo climate is a case of extreme heat which may have affected the rate of aging.

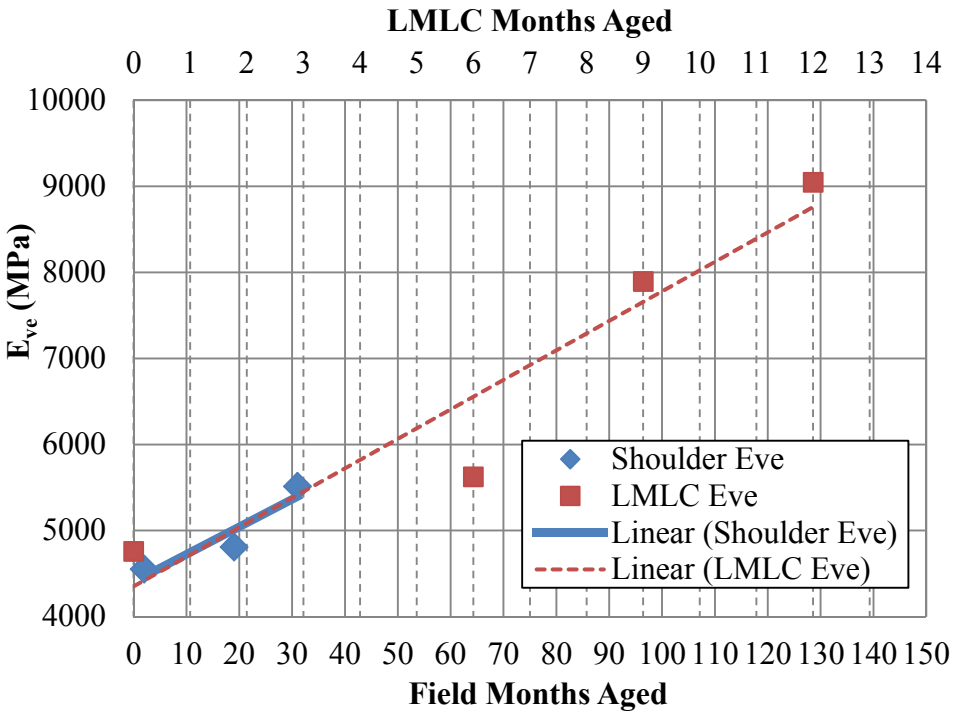


Figure 105. Laboratory to Field E_{ve} Comparison.

LMLC Samples vs. Extracted Binder

Comparing the E_{ve} values of the LMLC samples versus the corresponding CA from their respective extracted binders it can be seen that the two properties are related (Figure 106, Figure 107). Figure 106 shows the relationship between E_{ve} and CA for the LMLC samples at low, medium, and high AV. All three sets of samples show that a correlation exits between CA and E_{ve} for mixtures, with a strong correlation for the high AV samples.

The same can be said when viewing the LMLC samples at optimum, optimum −0.5 percent, and optimum +0.5 percent binder contents as seen in Figure 107. Optimum and optimum +0.5 percent binder contents appear to show an acceptable correlation between CA and E_{ve}, with the higher binder content having a much stronger correlation. Thus, it can be stated that there is a strong relationship between binder oxidation, resulting binder stiffening, and ultimate mixture stiffening with aging.

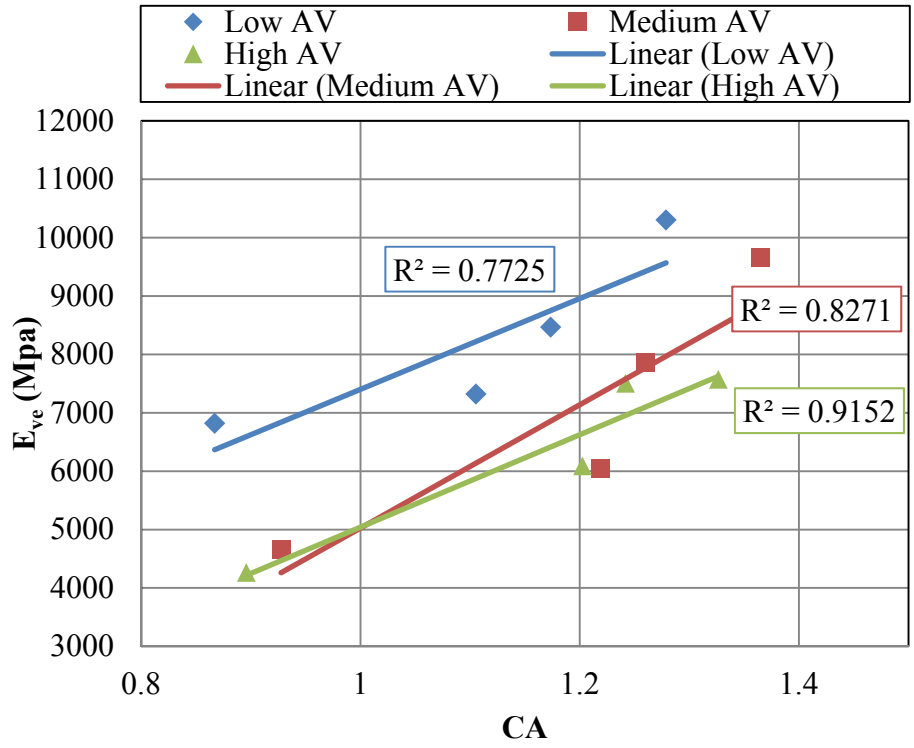


Figure 106. E_{ve} vs. CA for LMLC Samples with Different AV and Increasing Age.

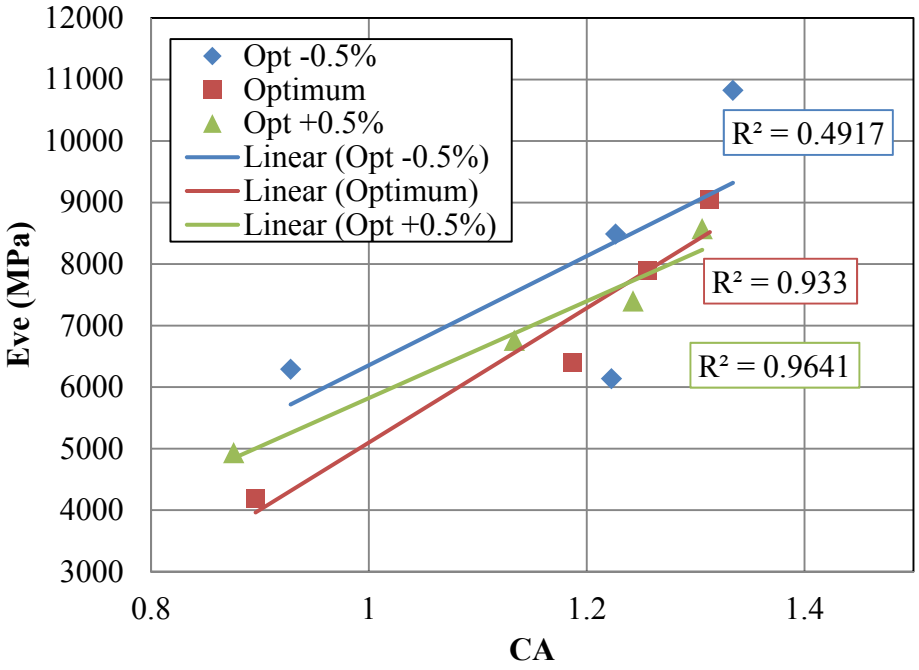


Figure 107. E_{ve} vs. CA for LMLC Samples with Different Binder Contents and Increasing Age.

Field Samples vs. Extracted Binders

As a LMLC mixture ages, it stiffens, which will ultimately affect pavement performance. The next step is to be able to predict the role of aging on pavement performance in the field. The effects of aging on HMA field mixtures can also be viewed by taking the CA results from the binders extracted from the field cores and comparing them with the E_{ve} results obtained from the field samples.

The stiffness of a mixture is affected by much more than just the aging process. Traffic, AV content, aggregate type, and climate, among other things, all play a role in how a mixture will change stiffness and, ultimately, how the pavement will perform. With so many factors playing a role in field performance, the correlation between E_{ve} and CA for field samples cannot be made. Some generalized conclusions, however, can be made.

Figure 108 is a combined plot of E_{ve} and CA with respect to the month the sample was obtained, with E_{ve} shown on the left axis and CA on the right. E_{ve} trends are represented by solid lines, while CA results are shown as dashed lines. Based on this comparison, the oxidation of the binder, as represented by CA of the corresponding extracted binder, plays a role in the stiffness of the mixture. This is especially apparent when viewing the response of the shoulder, which has little or no exposure to traffic loading. With the exception of the 2011 sample, which, as stated previously, had a chip seal placed on it, the shoulder's mixture stiffness continues to increase over time as the CA increases. In the case of the treated and untreated wheel path, this phenomenon is apparent between 2008 and 2009, but the mixture loses stiffness as it begins to experience damage and cracks begin to accumulate throughout the HMA. This is also shown by the fact that N_f continues to decrease with time as was seen in Figure 101.

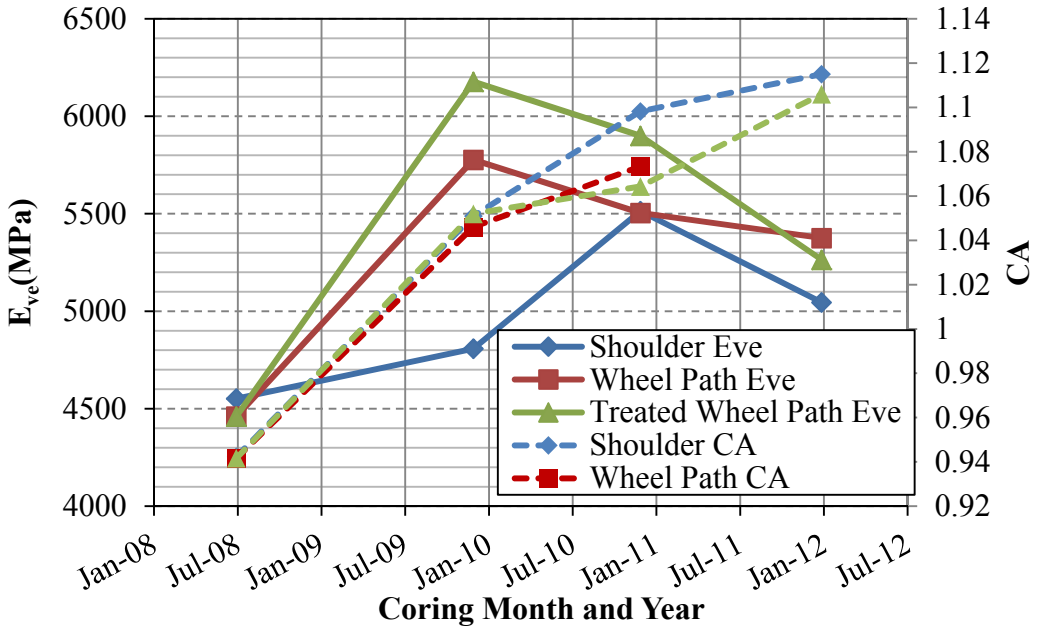


Figure 108. E_{ve} vs. CA of Field Samples for US 277 between 2008 and 2011.

The laboratory test results from LMLC and field samples and corresponding extracted binders lead to the following important conclusions regarding HMA aging as well as the effects of chip seals on pavement performance:

- Aging does play a role in the fatigue failure of HMA as evidenced by the performance of field samples, taken over time, from the shoulder. The stiffening of a mixture also coordinates well with an increase in oxidation, represented by CA development in corresponding extracted binders.

- While both AV and binder content play a role in mixture aging, AV plays a much more significant role.

- For US 277, much of the HMA aging occurs during the first year. In general, the rate of aging for US 277 decreases over time.

- Chip seals appear to slow HMA aging and, as a result, slow the rate of damage accumulation due to fatigue. However, this effect takes place primarily at the surface of the HMA where the chip seal is placed.

- It is possible to develop a relationship between binder aging and mixture aging. A relationship can also be drawn between *artificially*-aged LMLC samples and *realistically*-aged field samples.

These generalized conclusions are an important first step in moving toward mechanistic models which incorporate and quantify aging. A relationship between binders and LMLC samples and between LMLC samples and field samples lends itself to the potential development of prediction models which incorporate aging. The next step in this development requires a deeper investigation into other field sites with different mixture and environmental conditions. While the findings in this chapter are a good starting point, a quality fatigue failure prediction model must be applicable to a wide range of HMA mixtures in all types of climates and conditions.

CHAPTER 13. COMPARISON OF AGING IN THE FIELD WITH ACCELERATED LABORATORY AGING

This chapter examines HMA mixture aging at three different sites across Texas based on the properties of field samples cut from cores and corresponding LMLC samples made from raw materials used during construction. A description of the materials collected from each site is included along with a brief description of the test methods used to determine the mixture properties of the samples. The CMSE* method (Luo et al., 2008, Walubia et al., 2006) was used to determine the loads to failure in fatigue for both the LMLC and field samples. The results associated with the LMLC samples are discussed. Next, the field sample test results are presented followed by an examination of the relationships between the LMLC, artificially laboratory-aged samples, and the naturally-aged field samples.

MATERIALS AND TESTING

Materials were collected from three Texas sites where HMA was utilized in the construction of new pavement surface layers. Enough binder and aggregate was collected for LMLC samples to be fabricated and tested. Field cores were also collected immediately after construction and then three more times at approximately one, two, and three years after construction.

Site Selection

Each of the sites selected had different characteristics which distinguished it from the others, such as climate, aggregate type, and binder type. This allowed for a more broad study. A description of each site follows.

US 277 Laredo District

US 277 is located in the Laredo District of TxDOT and is in the southernmost part of the state. The climate is dry and warm (DW) with an annual average of the high temperatures of 86.3°F (30.2°C) and 21.5 inches (545 mm) of average annual precipitation (U.S. Climate Data, Accessed July 2, 2012). The mixture was a TxDOT Type C mixture (TxDOT, 2004) with a PG 70-22 binder. The optimum binder content was 4.5 percent by weight of the mixture. The aggregate consisted of a well graded blend of limestone and manufactured sand from Uvalde County, Texas.

US 83 Childress District

US 83 is located in the Childress District of TxDOT and is located in the northernmost part of the state. The climate is dry and cool (DC) with an annual average of the high temperatures of 74.3°F (23.5°C) and 22.7 inches (576 mm) of average annual precipitation (Belsoft and Styleshout, 2012). The mixture consisted of a TxDOT Type D mixture (TxDOT, 2004) with a PG 70-28 binder. The optimum binder content was 5.3 percent by weight of the mixture. The aggregate consisted of a well graded granite material from Snyder, OK.

SH 24 Paris District

SH 24 is located in the Paris District of TxDOT, in the northeastern portion of the state. The climate is wet – cold (WC) with an annual average of the high temperatures of 74.0°F (23.4°C) and 47.8 inches (1214 mm) of average annual precipitation (U.S. Climate Data, Accessed July 2, 2012). The mixture consisted of a TxDOT Type D mixture (TxDOT, 2004) with a PG 64-22 binder. The optimum binder content was 5.4 percent by weight of the mixture. The aggregate consisted of a well graded sandstone material from Sawyer, OK.

X-Ray CT Analysis

X-ray computed tomography is a non-destructive technique used to capture the internal structure of granular materials and other composites. Various applications of this method to asphalt mixtures can be found in the literature (Masad, 2004; Braz et al., 1999; Shashidhar, 1999). Among other applications, X-ray CT has been used successfully in asphalt mixtures for characterizing the influence of compaction on the internal structure (Masad et al., 2009), assessing internal structure of open-graded mixes (Alvarez et al., 2010a; Muraya, 2007), analyzing water transport characteristics (Kassem et al., 2008; Masad et al., 2007), and assessing stone-on-stone contact (Alvarez et al., 2010b; Watson et al., 2004). Figure 109 illustrates the equipment used in this study.

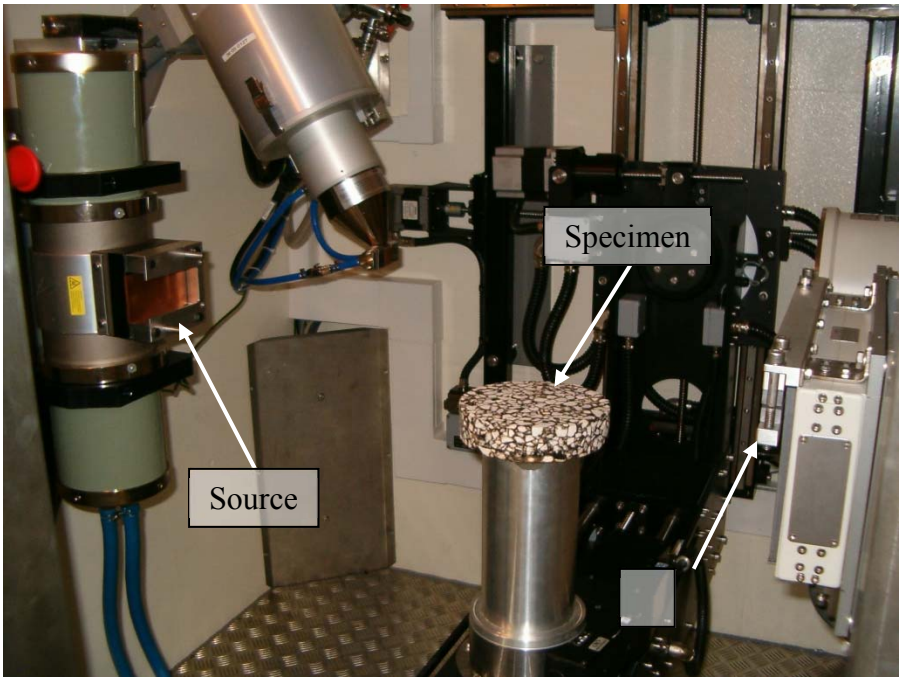


Figure 109. X-ray CT Equipment.

The equipment consists of a mini-focus 350 kV X-ray source and a linear detector. The setup for X-ray image acquisition involved positioning a test specimen between the source and the linear detector (see Figure 109). Due to the absorption and scattering, the intensity of the x-rays changes from I_0 at the source to I_1 at the detector (after penetrating the specimen). The

correlation between I_0 and I_1 is related to the linear attenuation coefficients of the material and allows estimating the density distribution of the specimen constituents. The variations in density are represented in a grayscale cross sectional image of the specimen, with lower density materials constituents shown in darker colors (i.e., air voids are shown in black in Figure 110).

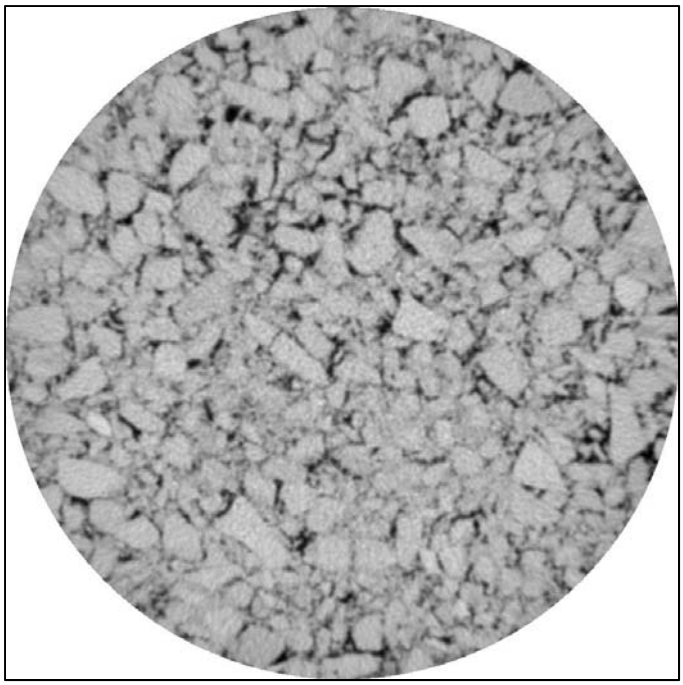


Figure 110. Sample of X-ray CT Image.

In this study, images were captured every 1 mm in the vertical direction of the specimen. The array of images was analyzed using a grayscale intensity threshold value to separate the AV from the solid constituents in the mixture (i.e., aggregate and asphalt binder). The threshold value represents a boundary value below which pixels in the analyzed image are considered as part of the AV, whereas pixels that have intensity values above the threshold value are considered to belong to the solid constituents. The threshold was calibrated using the laboratory-measured total AV content of the specimen. For AV interconnectivity, a procedure described by Masad et al. (2007) was used to identify the AV paths connected all the way from the top to the bottom of the specimen (Masad et al. 2007). During the analysis, the AV in contact with the edge of the specimen were discarded as part of the possible connected paths.

The results of the analysis were the vertical distribution of the total and interconnected AV. The results are presented by measurement year and also grouped by treated and untreated sections for both the wheelpath (RWP) and shoulder (NBS or SBS). The average total and interconnected AV for each case are summarized at the bottom right corner of the figures.

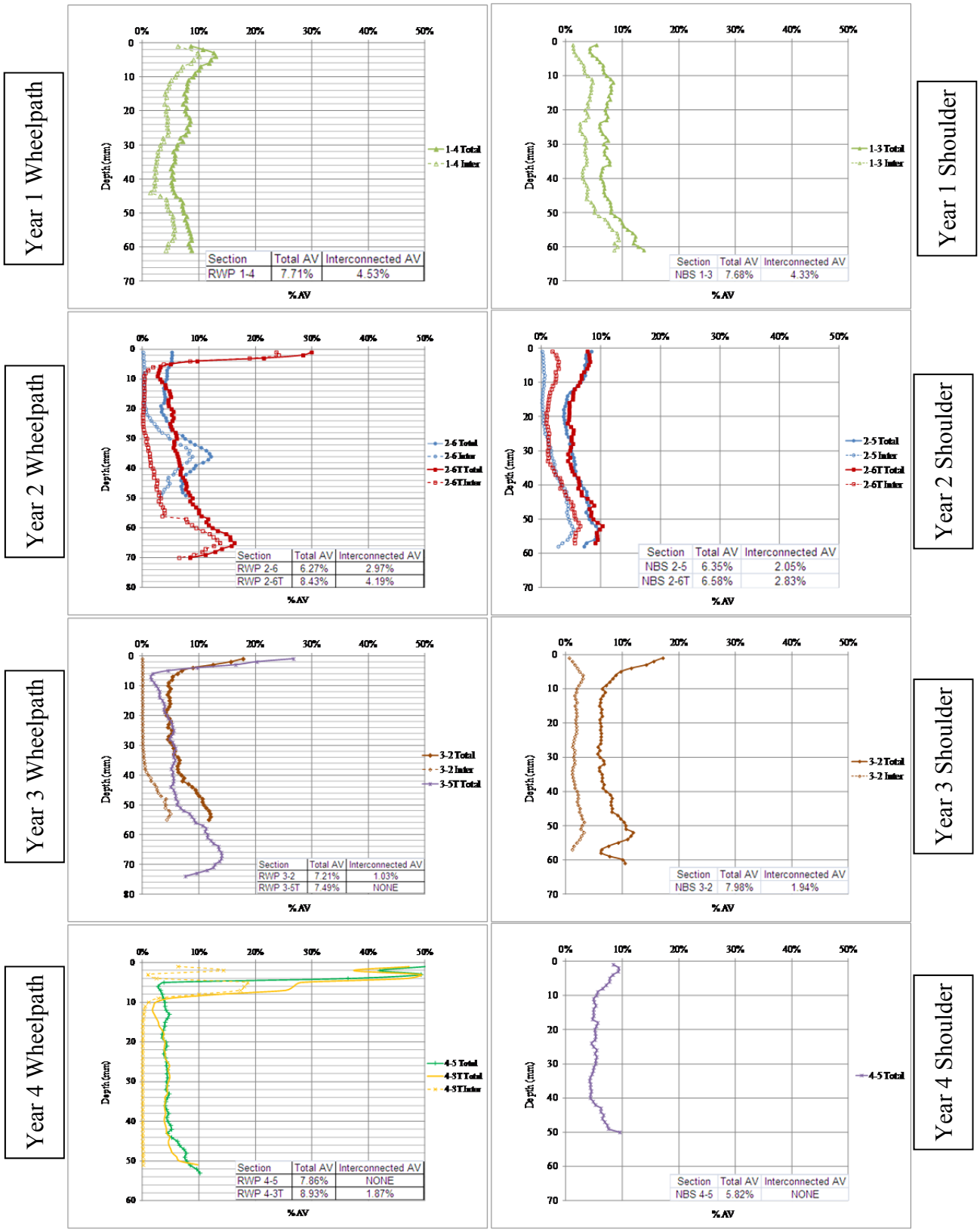


Figure 111. Total and Interconnected AV Yearly Results for US 277.

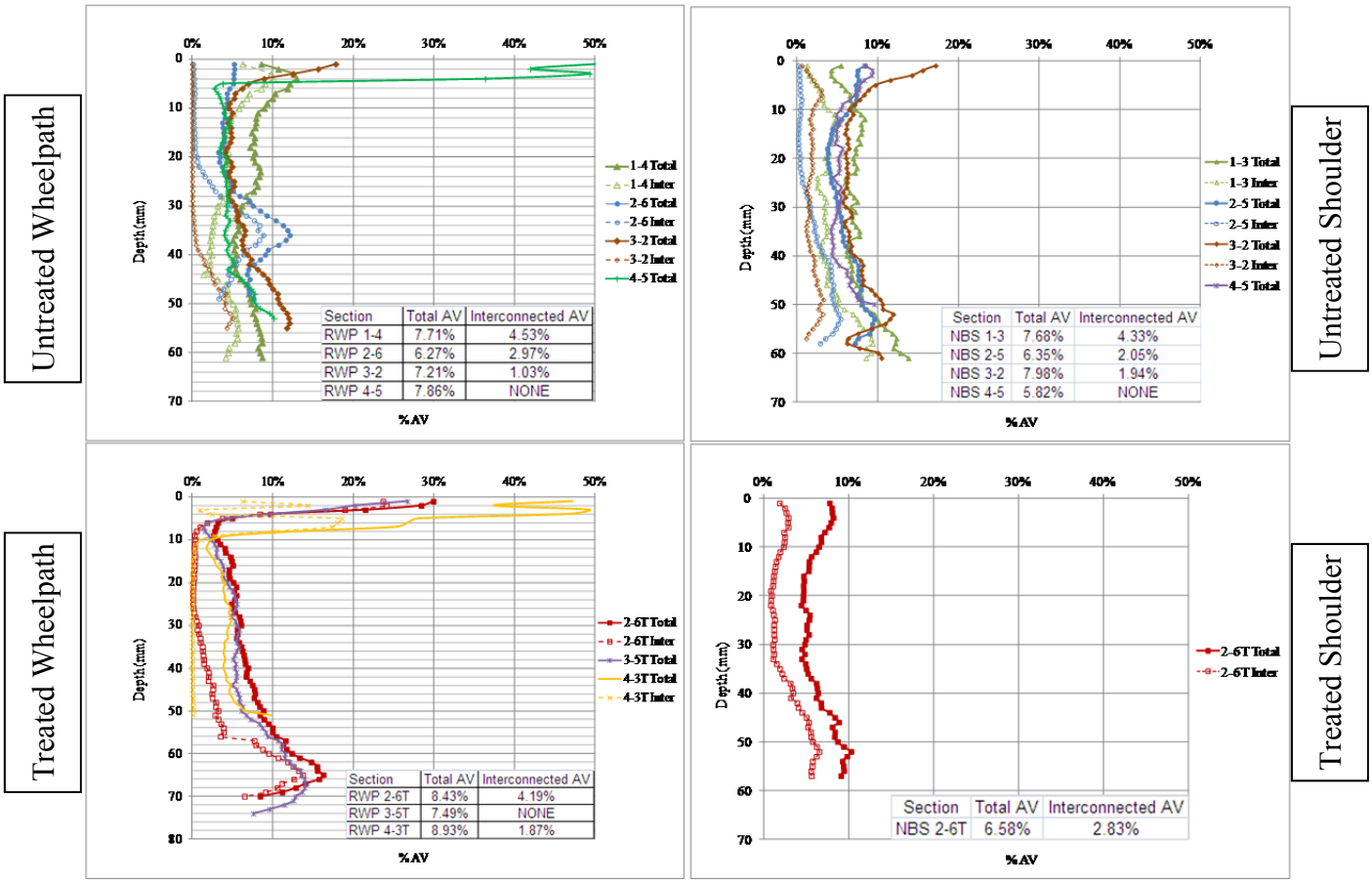


Figure 112. Total and Interconnected AV Results for Untreated and Treated Sections on US 277.

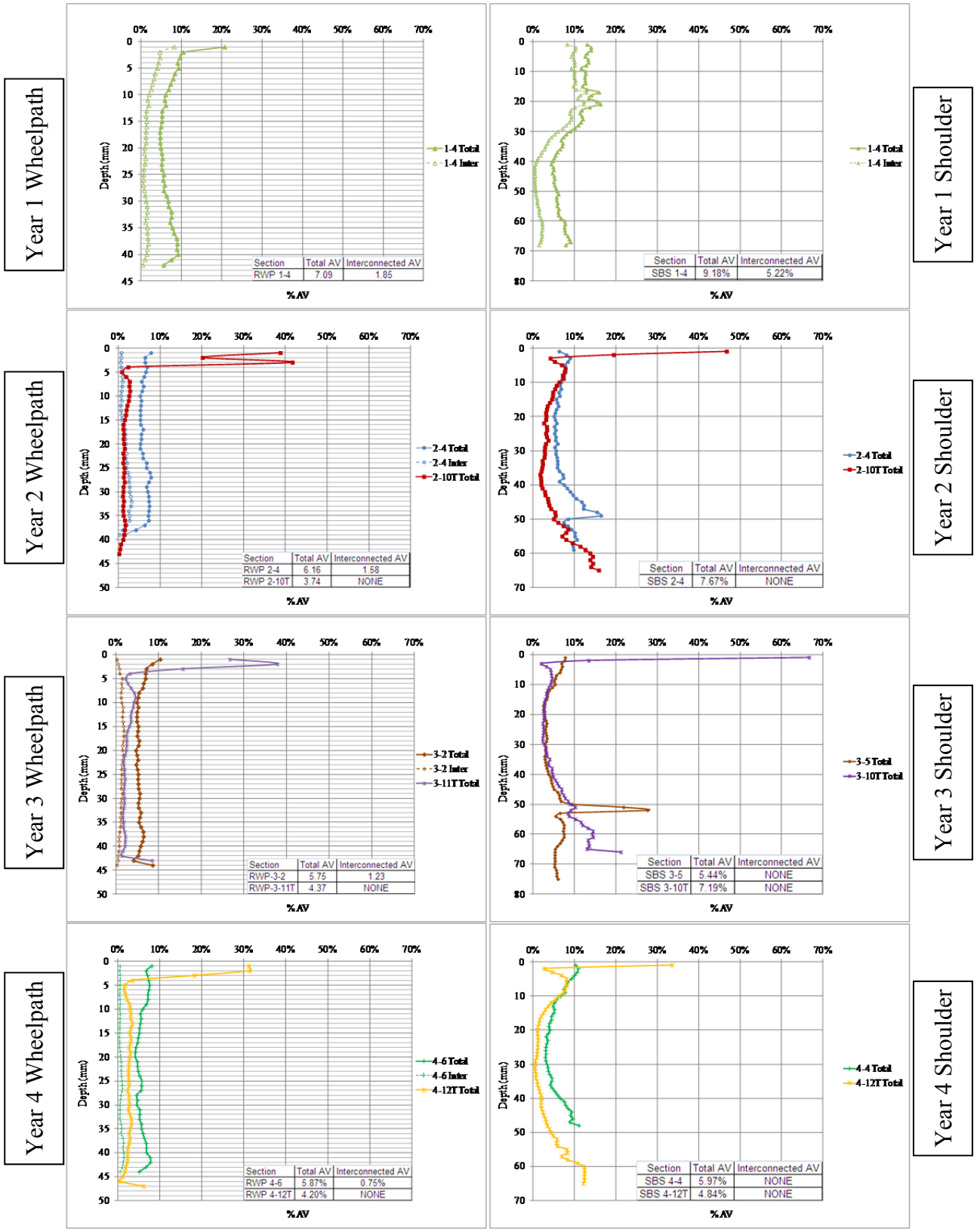


Figure 113. Total and Interconnected AV Yearly Results for US 83.

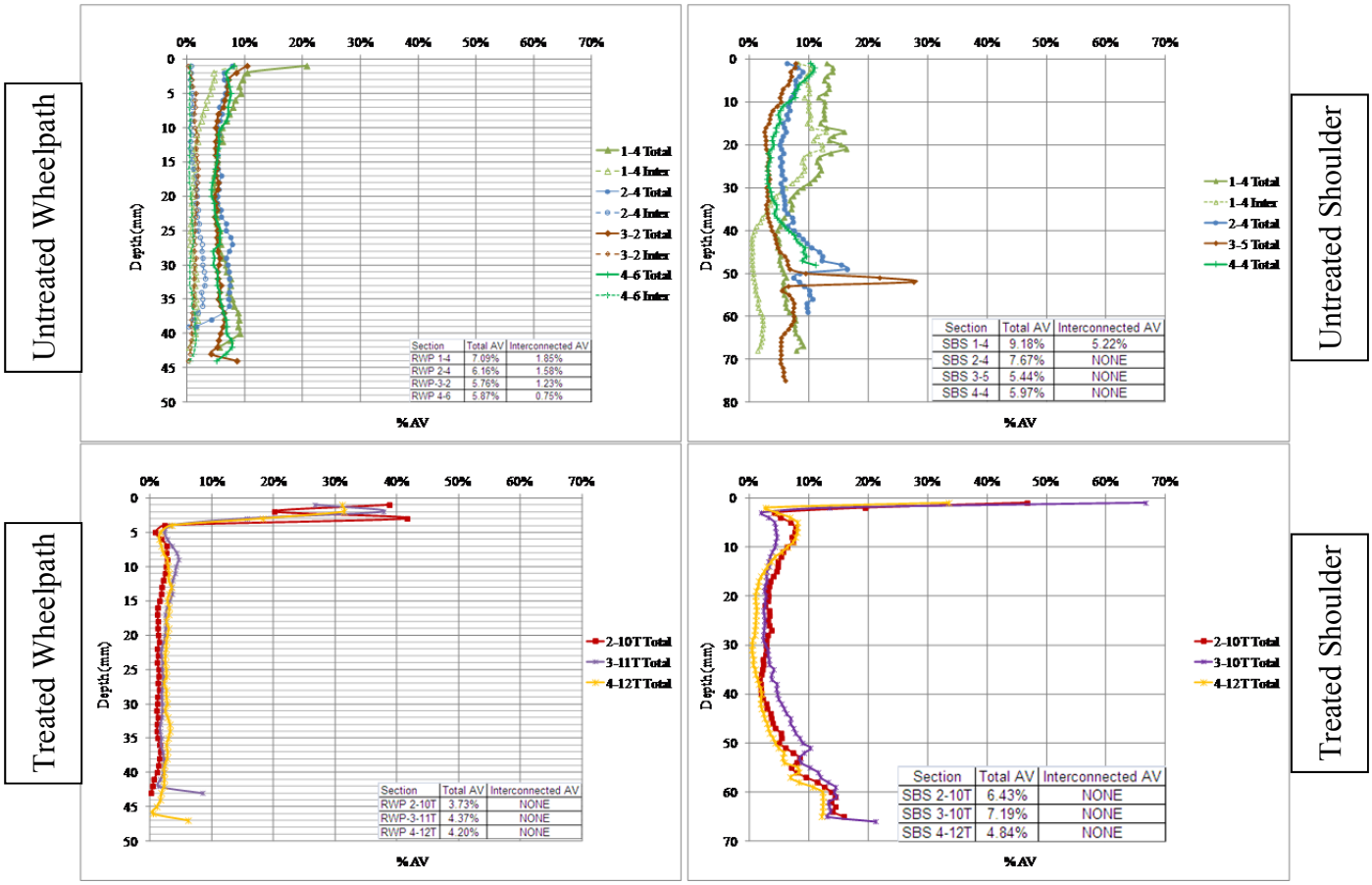


Figure 114. Total and Interconnected AV Results for Untreated and Treated Sections on US 83.

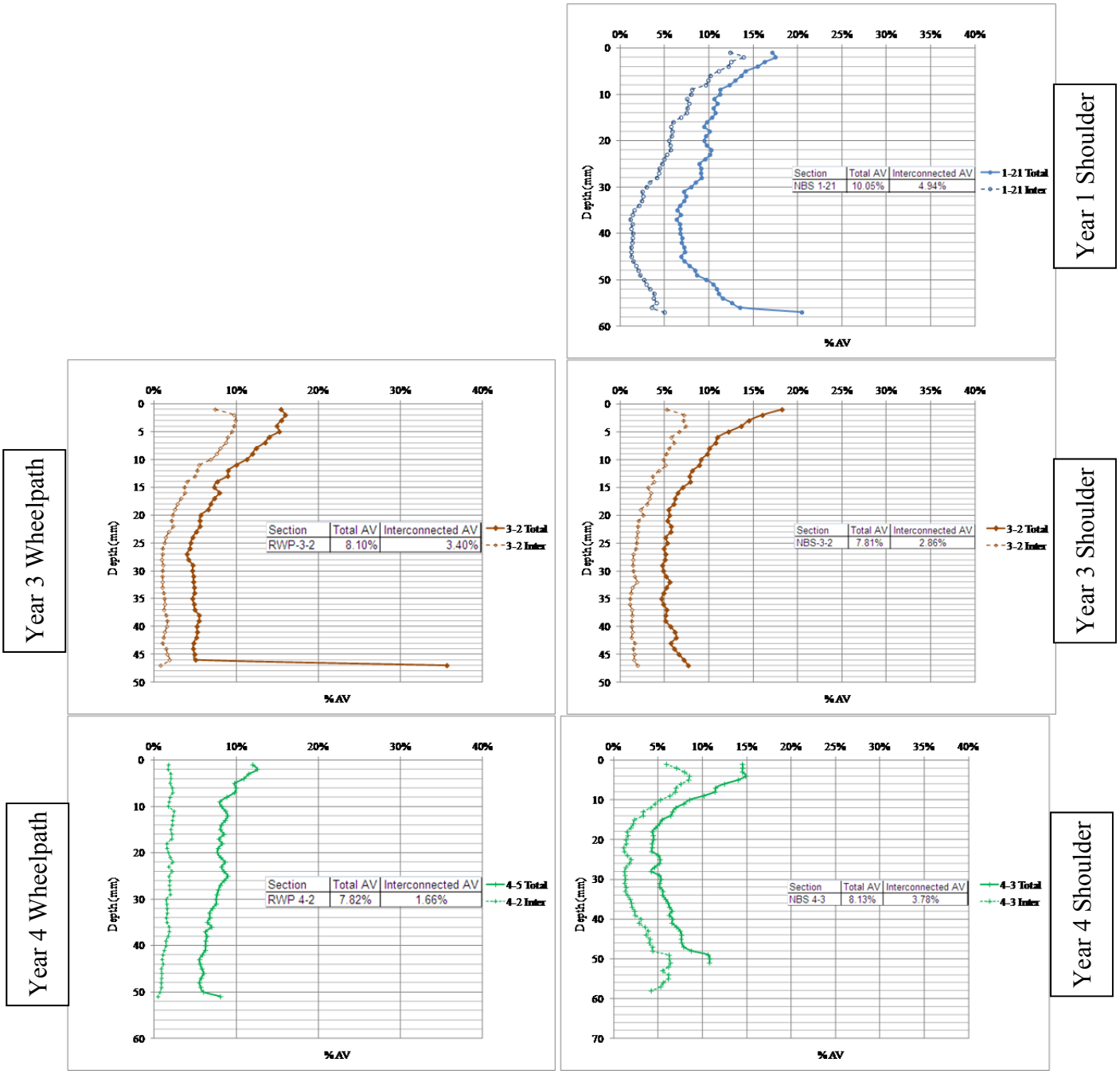


Figure 115. Total and Interconnected AV Yearly Results for SH 24.

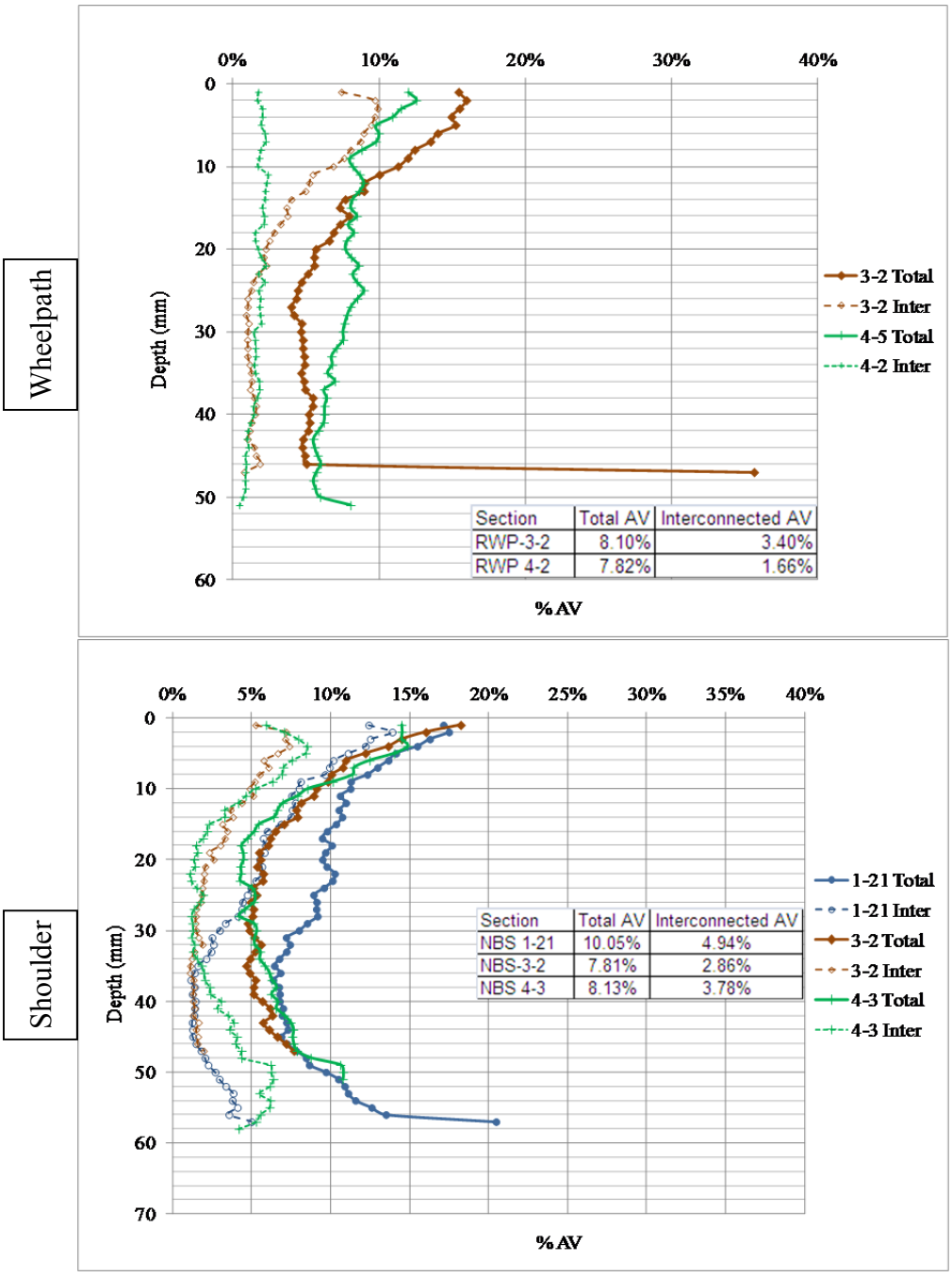


Figure 116. Total and Interconnected AV Results for Untreated Sections on SH 24.

Discussion

Observations of the X-ray CT AV analysis for the US 277 field cores include:

1. Steady decline in interconnected AV despite total AV staying relatively constant with time (i.e., measurement year). In some instances there is no interconnectivity after one or two years.

2. For wheelpath cores, treatment seems to increase the air voids at the surface of the core, within the first 5–10 mm from the top of the specimen. This increase is not apparent in the case of the shoulder cores.

3. The AV distributions for untreated cores (except for specimens 2-6 and 4-5) are fairly constant (i.e., flat lines) with specimen depth which is typical of field cores.

For the US 83 field cores, the X-ray CT analysis revealed the following trends:

1. There is a steady decline in both total and interconnected AV with time for the untreated sections. The interconnected AV for the shoulder cores were null after the second measurement year.

2. There was no AV interconnectivity for any of the treated sections (wheelpath and shoulder).

3. There was an apparent increase in the total AV within the first 5mm of the surface of the core for treated wheelpath and shoulder cores.

4. For untreated sections (both wheelpath and shoulder) there is an apparent increase in total AV between measurement years 3 and 4, which could be due to pavement distress such as raveling. This trend was not observed in the treated cores.

5. The AV distributions for the untreated cores are fairly flat throughout the depth of the specimens with just a slightly higher AV content towards the top of the specimen. This type of AV distribution is typical of field cores.

In the case of SH 24 only untreated sections were available. A summary of the results of the AV analysis is provided next:

1. A steady decline in total and interconnected air voids was observed for the wheelpath cores. For the shoulder cores, after a decline between years 1 and 3 there was a slight increase.

2. Most of the AV distributions follow a C-shaped curve, with more AVs towards the top and bottom of the specimen. This type of distribution is commonly observed in laboratory-compacted specimens rather than field cores.

LMLC Sample Preparation

LMLC samples were fabricated using the Super Gyratory Compactor. A blended aggregate gradation was used, and a mixture design was prepared in accordance with Superpave requirements. HMA mixture designs included the materials described in the preceding section. The aggregates used for the samples were heated to a temperature of 300°F (149°C) and left overnight to remove any moisture. The binder was also heated to the same temperature for two hours before mixing. The mixture was then short-term oven-aged at the molding temperature of

275°F (135°C) for four hours. This short term aging is intended to capture the aging that takes place during mixing, transport, and placement of HMA in the field.

The samples were compacted into cylinders of 6 inch (152 mm) height by 6 inch (152 mm) diameter to the required AV content in the SGC. The initial AV content in these compacted samples was measured to be higher than the specified content due to the conditions imposed by the mold. To remedy this problem, the samples were molded at a higher AV content and then cored to a 4-inch (102 mm) diameter. The sample had 1 inch (25 mm) trimmed from each end to produce the final 4 inch (102 mm) diameter by 4 inch (102 mm) high sample with the specified range of AV. The coring and trimming of the LMLC samples provided samples with a more uniform distribution of AV, similar to what would be found in the field (Masad et al., 1999). The AV content used for each of the three mixtures had an average AV content of 5 to 7 percent. Optimum binder content, as described in the preceding section for each site, was used in this study.

Prior to laboratory testing, the samples were subjected to artificial laboratory aging for periods of 6, 9, and 12 months at a constant temperature of 140°F (60°C) in an environmental room. Samples tested immediately after fabrication represent the initial aging condition and approximate the pavement condition at the time of placement.

After artificial laboratory aging, the sample was centered and glued to steel platens using a vertical gluing jig with high strength 2-ton epoxy glue. The freshly glued sample was left in the jig for a minimum of four hours to ensure complete setting of the glue. Three LVDTs were attached at 120° from each other along the sample diameter.

Field Sample Preparation

In order to obtain a good representation of HMA mixture behavior under varying conditions and ages, field cores were taken from the wheel path, shoulder, and where possible, from adjoining wheel path and shoulder sections which had been treated with a chip seal. Field cores were taken from each site at approximately one year intervals following an initial coring shortly after construction for the purpose of examining the effects of aging.

For US 277, field cores were taken from the wheel path, shoulder, and treated wheel path in July 2008, December 2009, December 2010, and January 2012. The initial coring in 2008 took place just prior to the placement of the chip seal and did not include a treated field core. It is assumed that the treated section would exhibit the same properties as the untreated section at the time of chip seal treatment.

US 83 field cores were collected from the wheel path and shoulder in 2008 with subsequent coring from the wheel path, shoulder, treated wheel path, and treated shoulder in 2009, 2010, and 2011.

SH 24 field cores were collected from the shoulder and wheel path in 2009, 2010, and 2011. This site did not include a treated section.

All collected field cores were photographed, catalogued, and trimmed to obtain the surface layer of HMA. The AV content for the surface layer from each core was determined. The layers were then trimmed to the sample shape shown in Figure 92. This allowed the samples to be tested in direct tension perpendicular to the direction of traffic, in the same manner they experienced tension in the field under traffic loading.

Following trimming, the samples were placed in a magnetic gluing vice and steel platens were affixed to each end. Imperfections in the trimming process produced samples with ends which were not always perfectly parallel. The magnetic vice provided a way to ensure that the platens were aligned with each other, and not with the imperfectly trimmed samples. This helped to eliminate eccentricities in the testing process and minimized undesirable moments. Finally, LVDTs were affixed to each side of the sample with a 2-inch (50.8 mm) gauge spacing for a total of four LVDTs.

Testing Procedures

LMLC and field samples were tested following the same procedure. Samples were place in a servo-hydraulic testing machine with a fixed connection at the top of the sample. A pinned connection, by way of a ball and socket joint, was used for the bottom of the sample to help align the sample in the testing machine and further minimize undesired moments during testing. The test setup for both LMLC and field samples is shown in Figure 117, which also shows the LVDT placement.

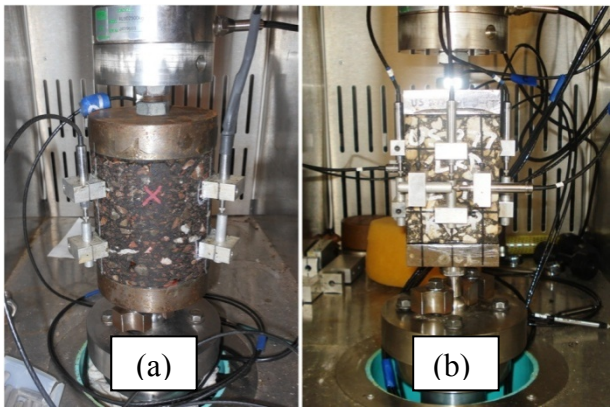


Figure 117. Test Setup for (a) LMLC and (b) Field Samples.

The samples were tested using two uniaxial test methods developed at Texas A&M University. These include the VEC (Luo and Lytton, 2010) and the RDT* tests (Luo et al., 2008).

For the VEC test, a monotonically increasing load is applied to the sample at a machine displacement rate of 0.002 inches per minute (50.8 μm per minute). This continued until one of the measuring LVDTs recorded a displacement of 100 με. It was assumed that at 100 με the sample is not damaged and can subsequently be retested (Luo and Lytton, 2010). Each sample

was tested with load and displacement data collected at 50°F (10°C), 68°F (20°C), and 86°F (30°C). The load and displacement data were used to calculate the respective stresses and strains.

Stresses and strains calculated from the VEC test were then processed using fitting parameters and Laplace transformations to create relaxation and complex modulus master curves at 68°F (20°C) (Luo and Lytton, 2010).

Following the VEC tests, the samples were reconditioned to 68°F (20°C) and tested using the RDT* test. For the RDT* test, the samples were subjected to repeated, strain-controlled loading. Strain levels were controlled by one of the sample-mounted LVDTs.

Initially, the samples were subjected to a tensile load resulting in an undamaging strain level of 30 με. The sample was then compressed back to its original configuration. This haversine loading cycle was repeated for 50 cycles at a frequency of 1 Hz in order to obtain the undamaged properties of the mixture, including the dynamic modulus (E_{ve}). The results of this portion of the test were also used to verify the results of the VEC test.

Following a short resting period of 5 to 10 minutes, the samples were then subjected to 1000 cycles of a 175 με strain level at a frequency of 1 Hz. These cycles were used to capture the damaged behavior of the mixture.

By using both the undamaged mixture properties and the results of the damaged portion of the uniaxial repeated load test, the dissipated pseudo-strain energy (DPSE) associated with fracture was calculated. The DPSE associated with fracture, AV contents, and binder film thicknesses (based on aggregate gradation and binder content) were then used to calculate damage parameters such as Paris' Law fracture coefficient (A) and exponent (n) (Luo et al., 2008) .

All of these mixture properties were then used in the CMSE* performance prediction model (Luo et al., 2008, Walubia et al., 2006) to calculate N_f.

LMLC SAMPLE TEST RESULTS

VEC and RDT* tests were carried out on LMLC samples at different AV and binder content combinations selected by a D-optimal statistical design. The design aimed to evaluae the effects of these two mixture parameters on mixture properties and performance.

Figure 118 shows the E_{ve} values for the three different sites at optimum binder content and medium AV. E_{ve} increases considerably with age confirming that the mixture becomes stiffer with time. US 277 was the stiffest of the three sites, while US 83 had the lowest stiffness. Also, US 277 continued to show an increase in the modulus after nine months while the other two sites start to level off.

An Analysis of Variance test of the data showed that AV, binder content, and aging level had statistically significant effects on E_{ve} with no statistically significant interaction effects among them. A Tukey Honest Significant Differences analysis for each of significant factors was

also performed, which confirmed that the overall E_{ve} was statistically different for all three AV contents. Mixtures with low AV (less than 4 percent) exhibited higher E_{ve} values than those with medium (5 to 7 percent) and high (great than 7 percent) AV. The insignificant interaction effects between AV and aging level is evidenced by the similar rate of change in E_{ve} over time.

A Tukey HSD analysis of binder content showed that there was no statistically significant difference between optimum and optimum +0.5 percent. However, a significant difference was found between optimum −0.5 percent and optimum as well as between optimum −0.5 percent and optimum +0.5 percent.

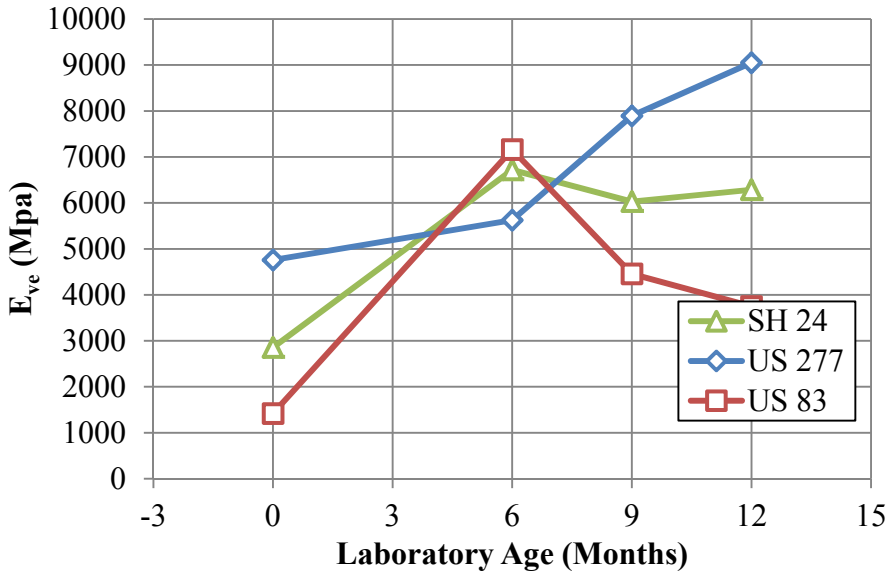


Figure 118. E_{ve} Trends for Artificially Laboratory-Aged LMLC Samples.

Figure 119 shows the N_f for the three mixtures at optimum binder content and medium AV. N_f for US 83 decreases with age which is consistent with the observation that the mixture stiffens with age and becomes more susceptible to failure. US 277 and SH 24 show slight increases in N_f with time; however, the overall trends are relatively stable when compared with that for US 83. Based on these results, the US 83 mixture is more sensitive to the effects of aging.

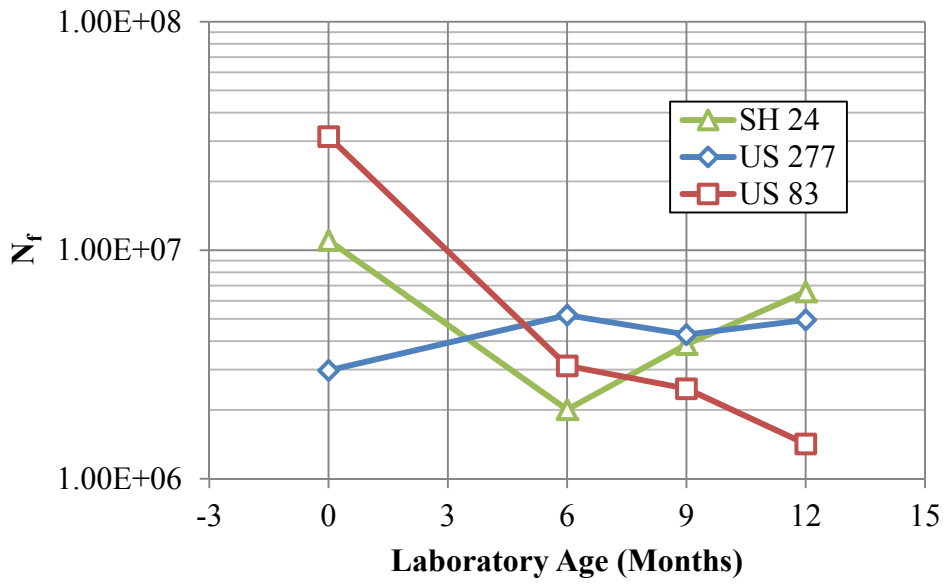


Figure 119. N_f Trends for Artificially Laboratory-Aged LMLC Samples.

FIELD SAMPLE TEST RESULTS

Data collected from the tests performed on the field samples for US 277, US 83, and SH 24 were analyzed and evaluated. Results from both the wheel path and shoulder were examined. Figure 120 shows the E_{ve} values for the treated and untreated wheel path sections. As with the LMLC samples, the E_{ve} values for US 83 continue to increase with age. However, the E_{ve} values for US 277 exhibit a sharp increase followed by a gradual decrease. This may be a result of the formation of micro cracks in the trafficked wheel path, which are resulting in a weakening of the layer. The same can be said for the results of the E_{ve} values for the SH 24 samples. Note that the treated wheel path E_{ve} values for US 277 are similar to those found in the untreated wheel path, indicating that the treatment had minimal effect on the overall stiffness of the HMA layer. However, there appears to be a significant benefit from the chip seal treatment on the trafficked wheel path section of US 83, which is located in a cooler climate than US 277.

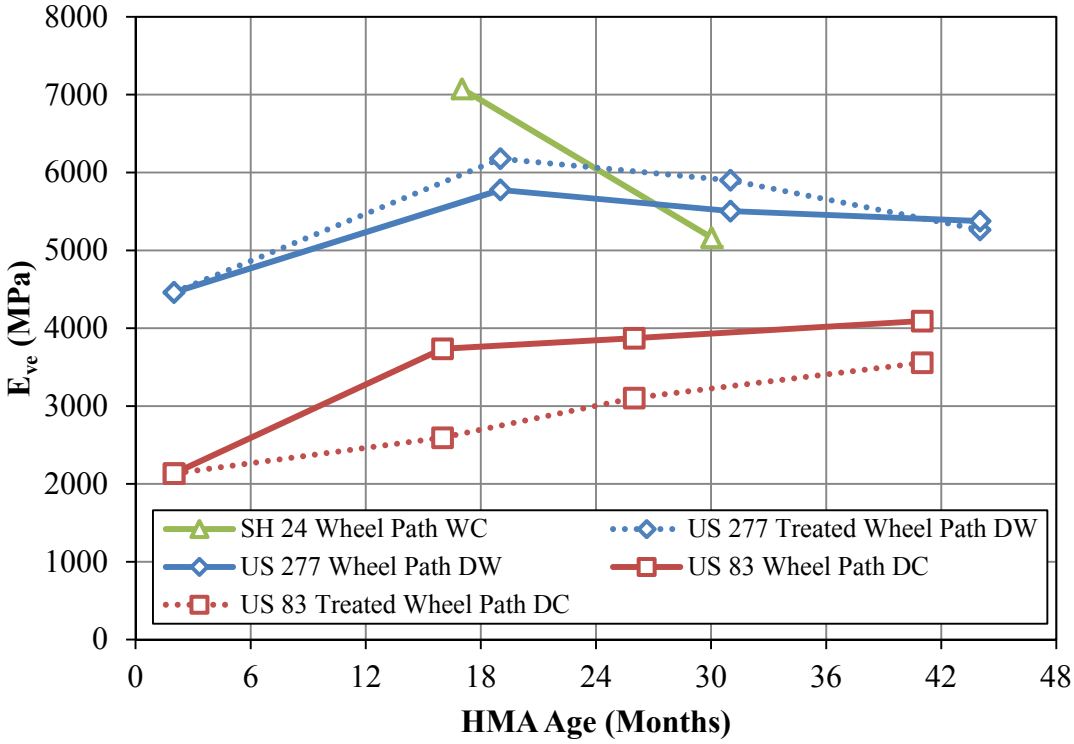


Figure 120. E_{ve} for Field Samples Taken from the Wheel Path.

In order to more directly examine the effects of aging without the confounding effects of traffic, the shoulder samples were analyzed and evaluated. Figure 121 shows E_{ve} for the shoulders of US 277, US 83, and SH 24. Each site shows an initial increase in E_{ve} to a maximum value followed by a slight decrease. This minimal change in E_{ve} after the initial jump may be associated with a more steady, level trend which continues in the future and is similar to previous results found in aged binder testing (Glover et al., 2005, Jin et al., 2011). Also note that the treatment placed on the shoulder of US 83 appears to have no major effect on the overall E_{ve} of the HMA layer. For both the wheel path and shoulder, there is a sharp increase in E_{ve} over the first 18 months. For the US 277 and US 83 shoulder samples, this upward trend continues past 24 months. While some of this increase may be due to the impact of traffic loading on the wheel path samples, the increase in E_{ve} for the shoulder samples can be attributed more directly to mixture aging.

While the E_{ve} value provides an indication of the HMA mixture response to oxidative aging of the binder, which also plays a role in the fatigue failure of HMA, it is important to examine the N_f values calculated from the CMSE* method. N_f includes other influential factors such as binder film thickness, AV content, binder content, and pavement structure as well as damage properties including Paris' Law fracture coefficient and exponent and the rate of fracture damage accumulation. Figure 122 shows the calculated values of N_f for the wheel paths of US 277, US 83, and SH 24. Boxes near the data points indicate the AV content of the HMA layer in the field.

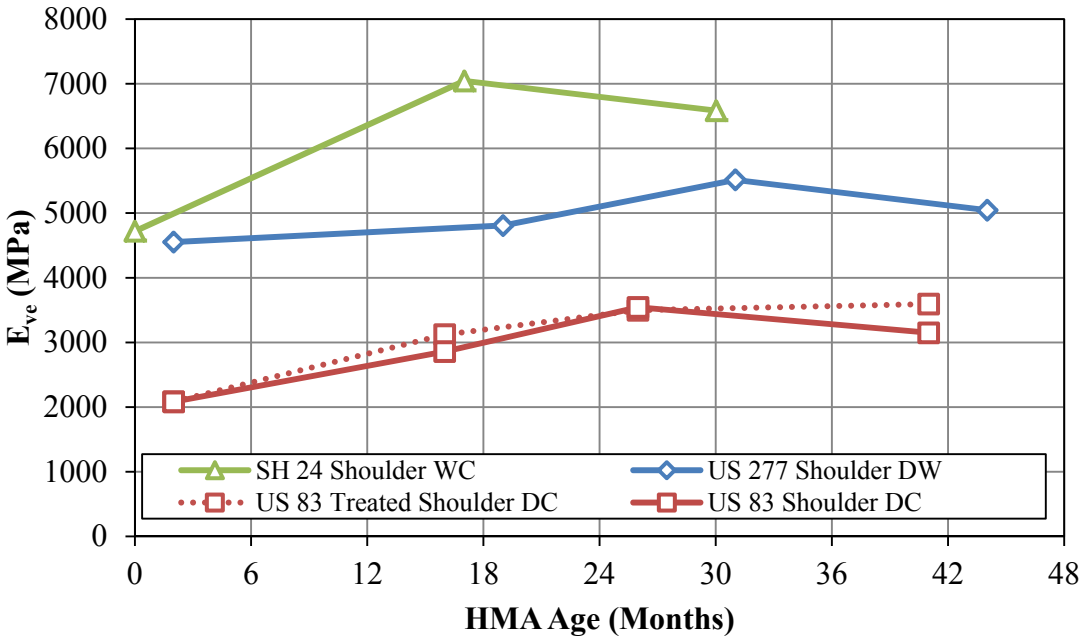


Figure 121. E_{ve} for Field Samples Taken from the Shoulder.

As expected, US 277 and SH 24 show a continued decrease in N_f values as the pavement ages and is subjected to traffic. For both of these cases, the AV content in the field remains relatively constant. Following the collection of the third core, the US 277 N_f values increase slightly. This may be attributed to the placement of a chip seal shortly after the third core collection, indicating a small benefit from a treatment placed a few years after the pavement is constructed. The N_f values for the treated section of US 277 decrease at a slower rate than those for the untreated section, indicating that the chip seal slows the rate of damage to the pavement due to fatigue.

US 83 shows an increase in N_f over the first couple years of cores. Note, however, that the AV content decreases considerably from the first year. As the HMA was exposed to traffic, further compaction occurred, causing the mixture to further stiffen, which resulted in an extension of the pavement life. In other words, N_f increased with further compaction and lower AV.

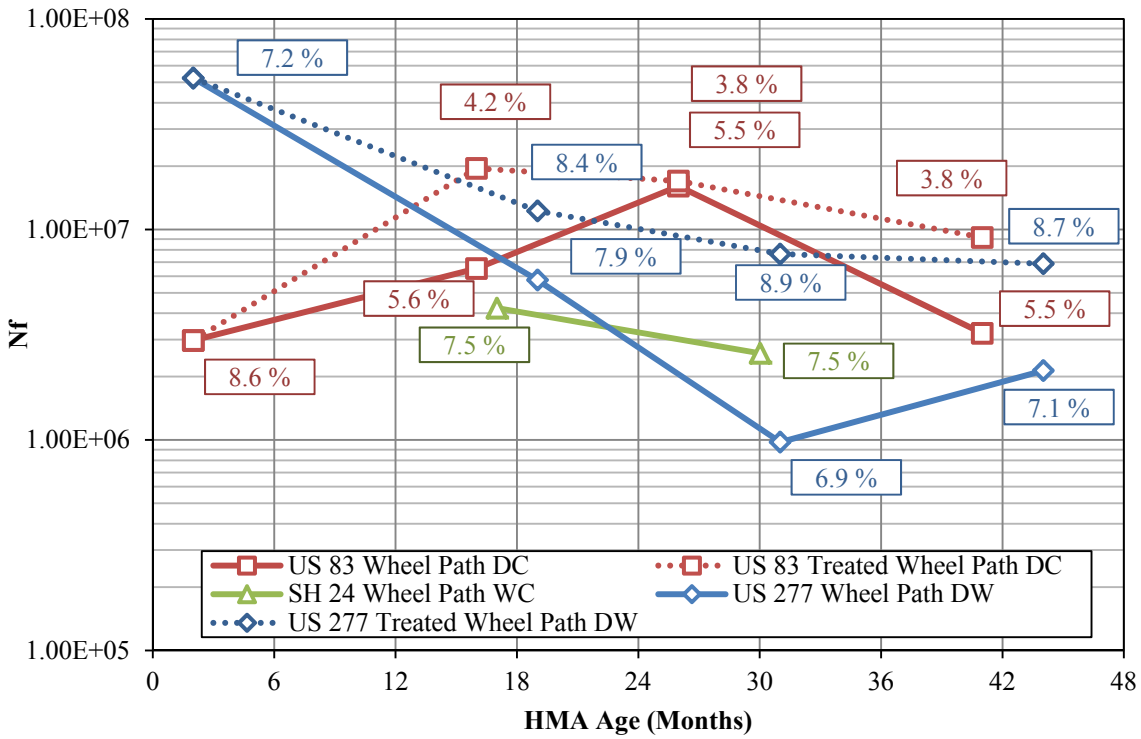


Figure 122. N_f for Field Samples Taken from the Wheel Path.

Shoulder N_f values for US 277, US 83, and SH 24 are shown in Figure 123. As previously mentioned, the shoulder values provide more focus on the effects of aging by eliminating the effects due to traffic. Once again, N_f decreases as the HMA ages but at a slower rate than for the wheel path samples subjected to traffic. The US 83 values see an increase in N_f in the early stages (higher AV in the first cores than in the following years) but then follow the slowly decreasing trend exhibited by US 277 and SH 24. The chip seal placed on the shoulder of US 83 seems to have little effect on extending the pavement life. While the downward trend on the shoulders is less than that for the wheel paths, it is still significant, indicating that HMA aging does have a significant impact on fatigue failure in HMA.

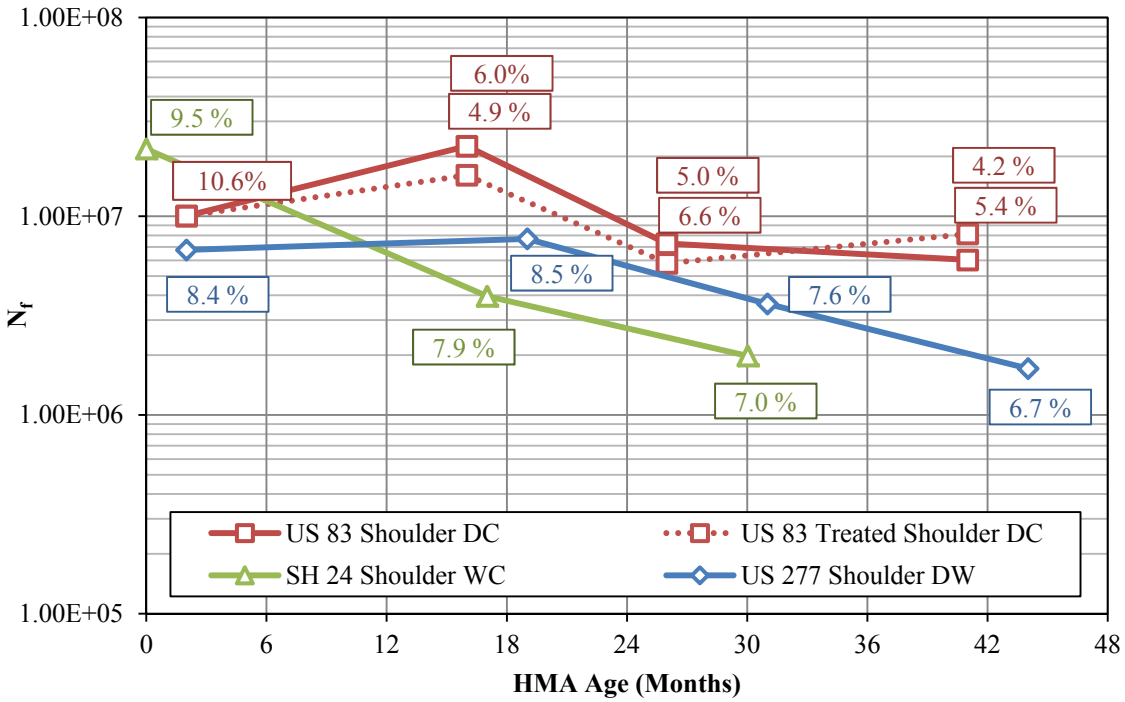


Figure 123. N_f for Field Samples Taken from the Shoulder.

COMPARISON OF FIELD AND LMLC SAMPLE RESULTS

With both LMLC and field sample data analyzed and examined separately, an evaluation of the combined results was made in order to determine if relationships can be seen between artificially laboratory-aged samples and naturally-aged field cores.

Figure 124 shows the combined results of the LMLC and field sample E_{ve} values. The top axis represents the artificial aging period for the LMLC samples while the bottom axis is the actual age of the HMA layer in the field. By adjusting the axes to fit the field E_{ve} to the LMLC E_{ve}, it was determined that one month of aging in the laboratory was equivalent to 10.5 months of aging in the field for both US 277 and US 83. SH 24 data could not be aligned without a vertical shift in the LMLC results; however, the trends between laboratory and field with the 1:10.5 comparison are similar.

The combined graphical results for N_f are not as easily interpreted as the E_{ve} results. While all of the combined N_f results shown in Figure 125 either decrease or remain relatively constant, as expected, any correlations between LMLC and field sample results could not be made directly. This may be due to the number of factors which play a role in the calculation of N_f. In order to relate the LMLC sample N_f results to the field N_f results, a more complex model needs to be developed.

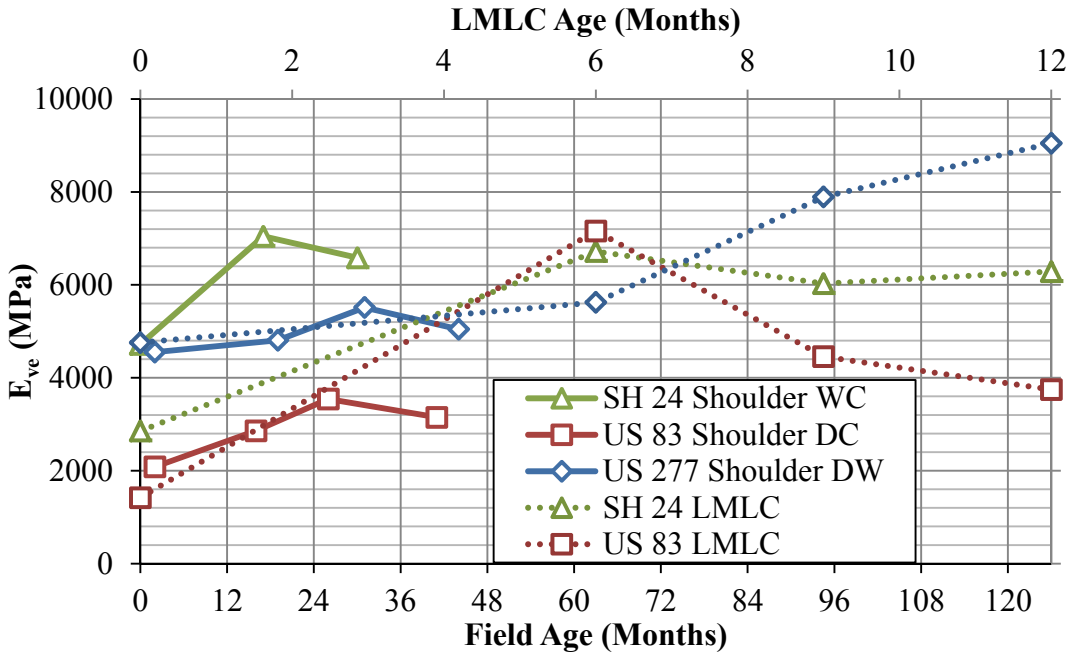


Figure 124. LMLC and Field Sample Combined E_{ve} Results.

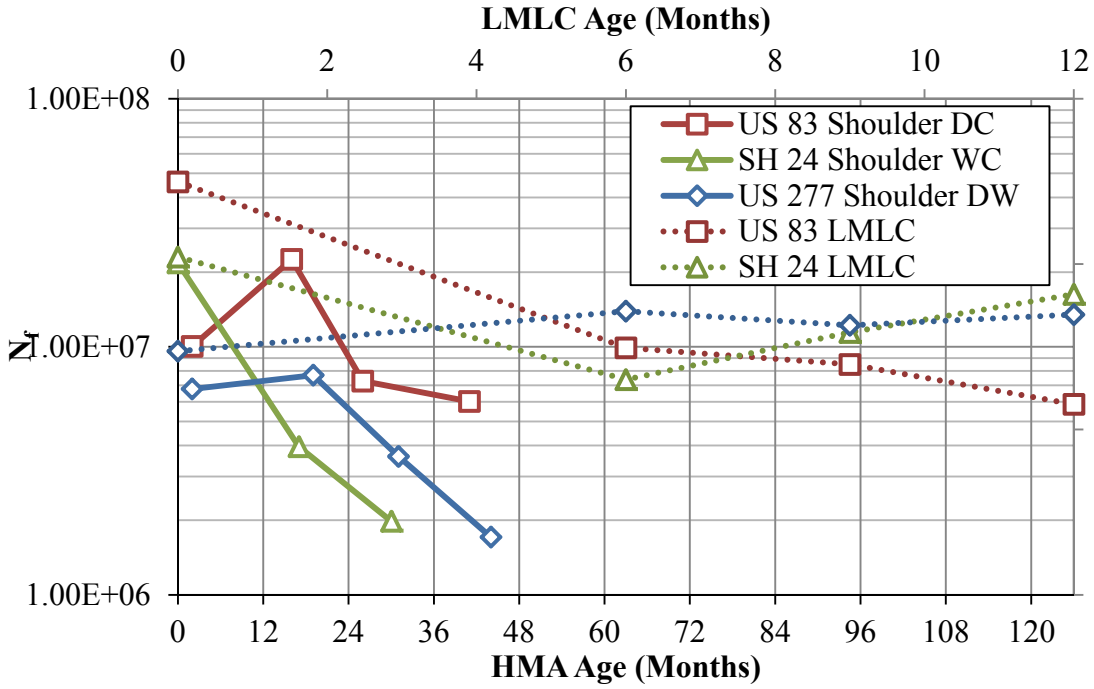


Figure 125. LMLC and Field Sample Combined N_f Results.

SUMMARY

Characterizing the role of aging in the development of fatigue failure in HMA mixtures is not a simple task. Many factors play a role, not only in fatigue cracking as a whole, but also in the aging process. In order to effectively characterize and predict the effect on mixture properties of HMA aging in the field, aging in LMLC mixtures must be understood and correlated with actual field performance.

This chapter showed that HMA aging through binder oxidation not only occurs but also plays a significant role in the development of fatigue failure. A comparison can be made between artificially laboratory-aged LMLC samples and naturally-aged field cores taken from the shoulder, where minimal trafficking has occurred. For the sites in Texas included in this study, when comparing E_{ve}, one month of artificial aging in the laboratory is equivalent to 10.5 months in the field.

Future studies should include the further development of a more mechanistic model to predict N_f in the field from mixture data collected from unaged LMLC samples available during mixture design and collected unaged binder data, in combination with accelerated laboratory-aged binder data or aged binder data calculated using existing models (Jin et al., 2011). This can be accomplished by developing the relationship between artificially laboratory-aged LMLC N_f values and N_f values obtained from naturally-aged field samples. By developing this relationship with field cores taken from the shoulder, the impact of aging without the confounding effects of traffic can be better understood and predicted. With these components, a pavement prediction model that accounts for aging and its impact on N_f in the field can be fully developed.

CHAPTER 14. AN ACCELERATED METHOD FOR COMPARING BINDERS FOR PAVEMENT DURABILITY (AN ACCELERATED BINDER AGING TEST)

ABSTRACT

The measurement of binder oxidation kinetics parameters allows estimates of binder oxidation rates at specific pavement sites and for specific pavement characteristics by using the kinetics information in an appropriate thermal and oxygen transport model. From these calculations, binders can be compared as part of an oxidative hardening pavement durability test. However, measuring kinetics parameters requires up to three months of oxidation experiments at atmospheric air pressure and multiple temperatures, so the technique is neither rapid nor readily applicable.

A new accelerated aging test using the pressure aging vessel (PAV, ASTM D6521-08) under high temperatures (between 90°C and 100°C), and elevated pressure (2.1 MPa), needs significantly less time, 50 hours, to estimate the required kinetics parameters. Due to the higher pressure, both the oxidation activation energies and pre-exponential factors are different from those determined at 1 atm, likely because of a different balance of reaction products that is not fully understood. Consistent correlations exist between data at the two pressures. These correlations provide the basis for estimating reaction kinetics parameters at pavement conditions from measurements at PAV conditions. These parameters can then be used in a pavement oxidation and hardening model to compare different binders for their impact on pavement durability at specific pavement climates.

INTRODUCTION

Many studies have been conducted on the issue of predicting pavement performance based on asphalt concrete mixture and asphalt binder physical and chemical properties. Oxidative aging is the main reason for chemical component changes (Martin et al., 1990; Hagos, 2009), and the changes accumulate with time, with effects appearing after many years of usage (Petersen, 1998; Liu, 1998; Woo, 2008; Siddiqui, 2009).

Carbonyl-containing compounds are one kind of major product of oxidation, so tracking carbonyl formation is commonly used to represent oxidative changes (Liu, 1996). It is also confirmed that after a short nonlinear fast-rate period, the carbonyl growth is linear over time at constant temperature but varies for different asphalts. This kinetics period is called the constant-rate period and over the life of a pavement is considered the major form of field aging (Herrington, 1998; Petersen, 1998). Numerous accelerated aging tests have been developed to simulate the aging that occurs in the field by raising either temperature or pressure or both (Liu, 1996; Huh and Robertson, 1996). Inevitably, elevated pressure changes the reaction process causing binder aging comparisons obtained from these aging tests to deviate from comparisons at pavement aging conditions (Domke et al., 1999; Domke et al., 2000).

An Arrhenius function of both temperature and pressure that includes asphalt-specific kinetics parameters has been determined to describe the carbonyl formation rate in asphalt materials (Lau, 1991; Lunsord et al., 1992):

$$r_{CA} = AP^{\alpha} exp\left(\frac{-E_{AC}}{RT}\right) \quad (14\text{-}1)$$

A system including measuring reaction rates, calculating the factors and tracking oxidation level has been established. This system has been integrated into an oxidation model, which also combined concrete structure, field temperature and binder rheological properties information, to predict oxidation level (Prapaitrakul et al., 2009).

In this study, oxidation rates have been measured for eight asphalts at two temperatures to determine the reaction kinetics parameters at PAV conditions. A reliable activation energy correlation between PAV (20.7 atm air gauge) and POV (1 atm air absolute) pressures provides a method for determining pavement oxidation and hardening rates for use in an accelerated durability comparison of asphalt binders. Such an accelerated aging test has been a long-sought and elucive goal of asphalt materials testing. Application of this method is presented in Chapter 16.

EXPERIMENTAL METHODS

Eight different asphalts commonly used in Texas, were studied. Table 47 lists the asphalts . The selection of the asphalt binders covered four different manufacturers, four different PG grades, and two straight binders plus six modified binders. All of them were neat binders and came directly from manufacturers' plants and thus were without any of the aging that occurs in the hot mix plant or field service.

Table 47. Asphalts Used in the Study.

Name	Modification	Name	Modification
Lion PG64-22	None	Martin PG64-22	None
Lion PG70-22	Yes	Martin PG70-22	Yes
Alon PG70-22	Yes	SEM PG70-22	Yes
Alon PG76-22	Yes	SEM PG70-28	Yes

Pressure Aging Vessel*

The standard PAV apparatus was designed to simulate the binder oxidation in a pavement over a number of years of service. According to AASHTO R 28, Accelerated Aging of Asphalt Binder Using a Pressurized Aging Vessel, several 3.2-mm thick asphalt film samples are placed in a cylindrical chamber containing dry, clean compressed air at 305 psi (20.7 atm) air pressure and different temperatures.

For the purposes of this study, this standard test was modified. The oxidation reactions at 110°C, at which the final product may have a significant weight loss, apparently are different from the reactions at pavement service temperature. Thus, for the modified method only 90°C and 100°C conditions were adopted from the standard PAV test. An additional modification of

the standard method was to use a number of 38 mm diameter tin containers instead of the standard pans described in AASHTO R 28. In these containers, asphalt samples of 3.65 grams form a 3.2 mm film, as required by the standard method. Another modification was to obtain samples aged for several different periods at the same condition in order to obtain an oxidation rate. Each replicate sample, subjected to aging in the PAV was removed after its appropriate specified time and measured for chemical and physical properties changes.

Pressure Oxidation Vessel

Five pressure oxidation vessels, each immersed in a triethylene glycol bath, provides a constant flow of preheated replacement air at one atmosphere pressure and a constant temperature for binder oxidation. The temperatures varied from 60°C to 98°C. Researchers placed 2.4 grams of asphalt into a 4 cm x 7 cm aluminum tray to form a film about 0.08 mm thick. This thickness reduced the effects of diffusion to an acceptable level (Domke et al., 1997). A numbers of trays were removed from each POV at prescribed intervals, dependent upon the POV temperature, for sample analysis.

Fourier Transform Infrared Spectrometer

Carbonyl area was measured using a Nicolet 6700 FTIR spectrometer with an attenuated total reflectance zinc selenide prism. Carbonyl area, reported in arbitrary units, is the area under the absorbance peak from 1650-1820cm^{-1}, which provides a direct measurement of the oxidation progress in asphalt.

Dynamic Shear Rheometer

A Carri-Med CSL 500 controlled stress rheometer was used to measure and analyze the rheological properties. Approximate values for the low shear rate limiting viscosity (η*) at 60°C and 0.1 rad/s of asphalt binders were obtained by using the time-temperature superposition correlation. Dynamic storage modulus (G′) and viscosity (η') both at 44.7°C and 10 rad/s in time sweep mode were measured to calculate the DSR Function, expressed as (G′)/(η′/G′). The DSR Function combines both elastic and viscous properties of asphalts and correlates with ductility at 15°C, 1 cm/min and as such is believed to relate to binder durability (Ruan et al., 2003).

RESULTS AND DISCUSSION

Reaction Rate

Lau et al. (1992) determined that, for a neat asphalt binder at constant temperature, after an initial fast-rate aging period, the rate of carbonyl formation declines and transitions to become constant. Liu et al. (1996) reported that for both the fast-rate and constant-rate reaction periods, the reaction rate depends on oxygen partial pressure; increasing the pressure while keeping the temperature constant causes oxidation rate increases.

Figure 126 and Figure 127 show example PAV (20.7 atm air gauge) and POV (1 atm air absolute) data for the Martin PG70-22 binder . The constant-temperature reaction rate is higher

at higher temperatures in both apparatuses and faster at the higher air pressure of the PAV compared to the POV (e.g., compare the 90°C data). Note that the time unit in Figure 126 (PAV) is hours whereas for the POV conditions, the time units in Figure 127 are days.

Table 48 summarizes the measured coknstant-rate reaction rates for the two methods. Even disregarding the film thickness difference, which would provide more diffusion resistance to the PAV sample, oxidation still occurs much more rapidly at 20.7 atm air pressure than at one atmosphere air. To facilitate comparison, the time unit in Table 48 is days for both POV and PAV.

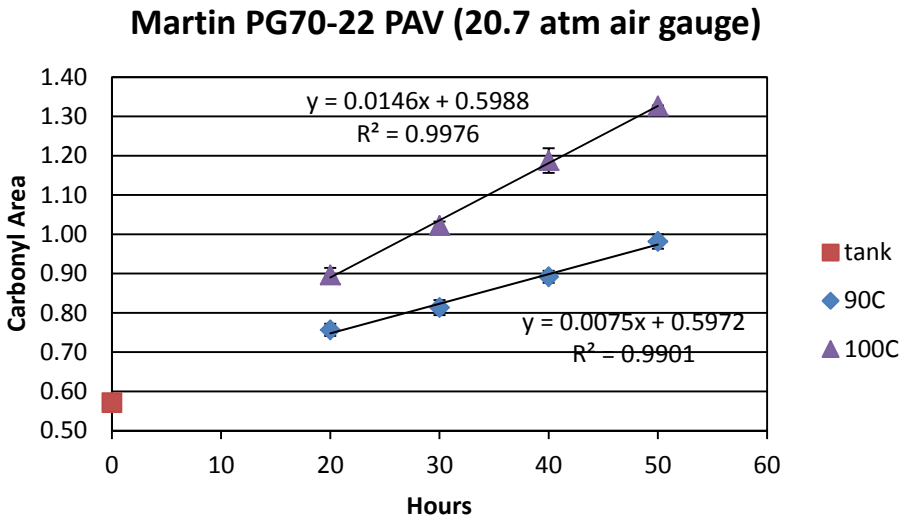


Figure 126. Carbonyl Area Increases with Hours of PAV Aging.

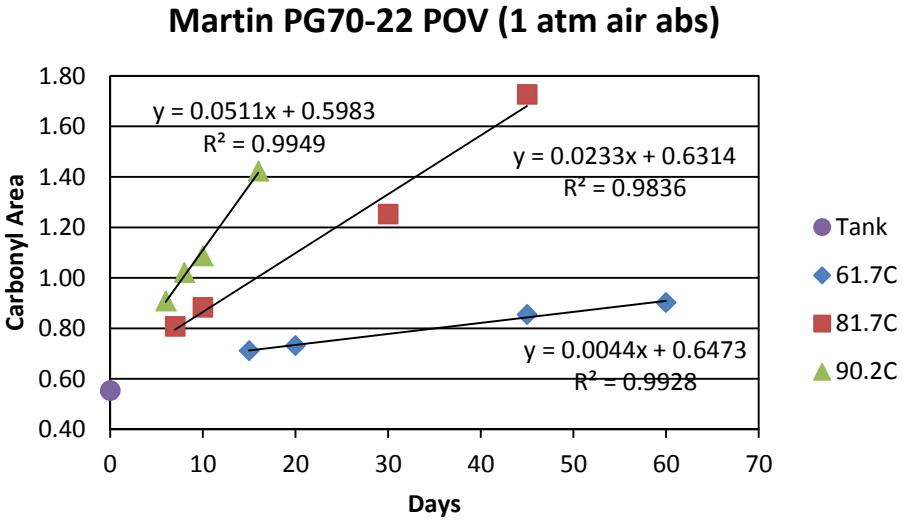


Figure 127. Carbonyl Area Increases with Days of POV Aging.

Table 48. Constant-Rate Reaction Rates for Eight Binders.

	POV(Temperature: CA/Days)	PAV(Temperature: CA/Days)
Lion PG64-22	61°C: 0.0048	90°C: 0.2472
	72°C: 0.0131	100°C: 0.3024
	81°C: 0.0201	
	92°C: 0.0626	
Lion PG70-22	60°C: 0.0055	90°C: 0.2376
	68°C: 0.0084	100°C: 0.3264
	79°C: 0.0162	
	97°C: 0.0691	
Martin PG64-22	62°C: 0.0054	90°C: 0.1872
	82°C: 0.0181	100°C: 0.2856
	90°C: 0.0333	
Martin PG70-22	62°C: 0.0043	90°C: 0.1800
	82°C: 0.0231	100°C: 0.3504
	90°C: 0.0524	
Alon PG70-22	56°C: 0.0029	90°C: 0.2232
	68°C: 0.0071	100°C: 0.3384
	79°C: 0.0217	
	88°C: 0.0410	
	96°C: 0.0578	
Alon PG76-22	62°C: 0.0037	90°C: 0.2040
	70°C: 0.0082	100°C: 0.3360
	79°C: 0.0150	
	87°C: 0.0266	
	97°C: 0.0540	
SEM PG70-22	60°C: 0.0028	90°C: 0.1848
	70°C: 0.0067	100°C: 0.3264
	79°C: 0.0270	
	89°C: 0.0431	
	98°C: 0.0468	
SEM PG70-28	60°C: 0.0020	90°C: 0.1824
	70°C: 0.0094	100°C: 0.2904
	88°C: 0.0270	
	98°C: 0.0332	

An Arrhenius model that describes the rate of carbonyl increase as a function of temperature and pressure during the constant-rate period has been proposed by Liu et al. (1996). Taking the natural logarithm of both sides of Eq. 14-1 results in the following equation:

$$\ln(r_{CA}) = \ln A + \alpha \ln P - E_{AC}/RT \tag{14-2}$$

At a specified temperature (usually chosen to be less than 100°C), if pressure (P) is fixed, then the pre-exponential factor (AP^{α}) and activation energy (E_{AC}) are constant for each asphalt

but independent of temperature (*T*). Figure 128 shows the correlation between the rate of CA increase (POV data) and temperature (in the form of 1000/RT) for one asphalt and the pre-exponential and activation energy parameters that were obtained from the correlation. From these measurements for the asphalts in Table 47, constant-rate period kinetics parameters were determined. Then, using these parameters in Eq. 14-2, POV condition reaction rates were calculated at 90°C and 100°C for comparison to the PAV rates that were measured at these temperatures. These comparisons are shown in Figure 129 and Figure 130.

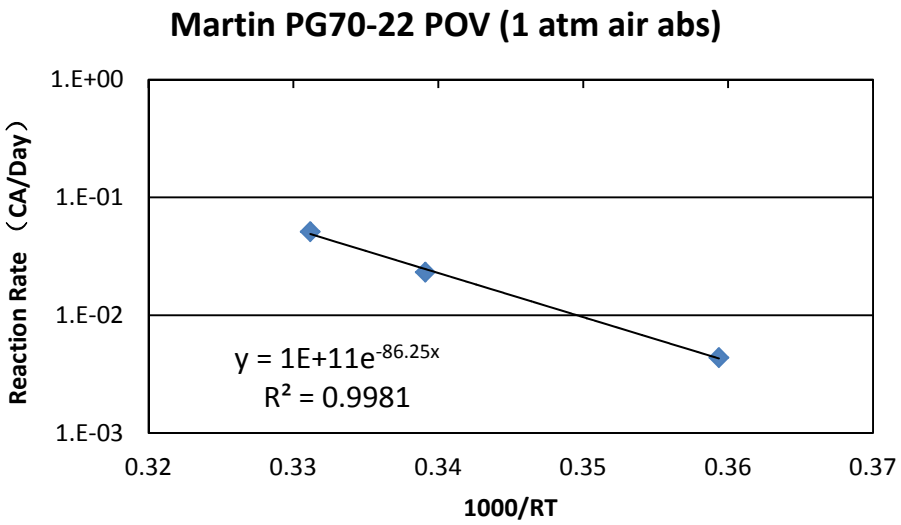


Figure 128. CA Rate vs. 1/RT, Activation Energy for Martin PG70-22 is 86.25 kJ/mol.

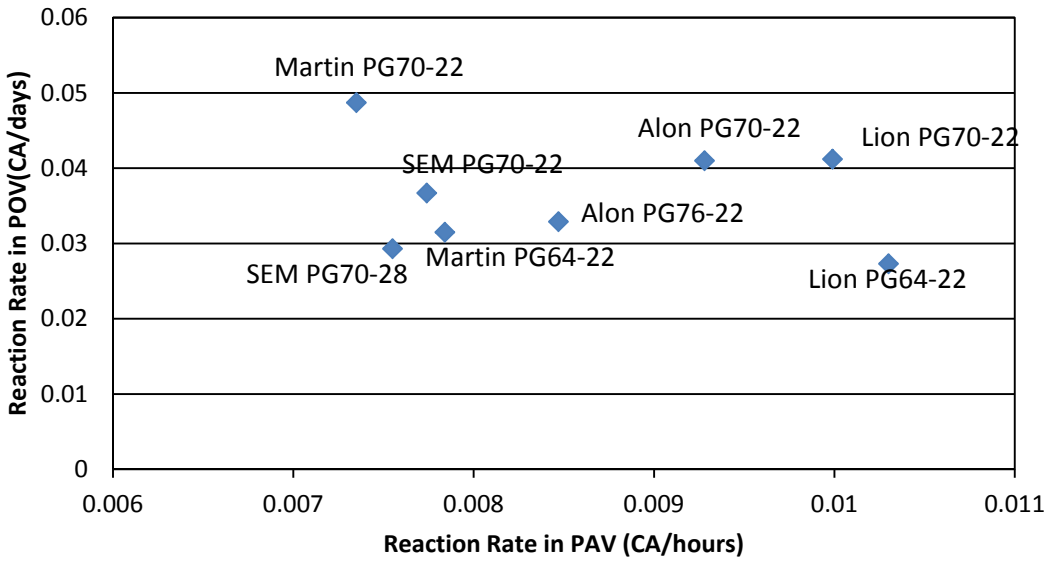


Figure 129. Comparison of 90°C Reaction Rates Determined from PAV and POV Methods.

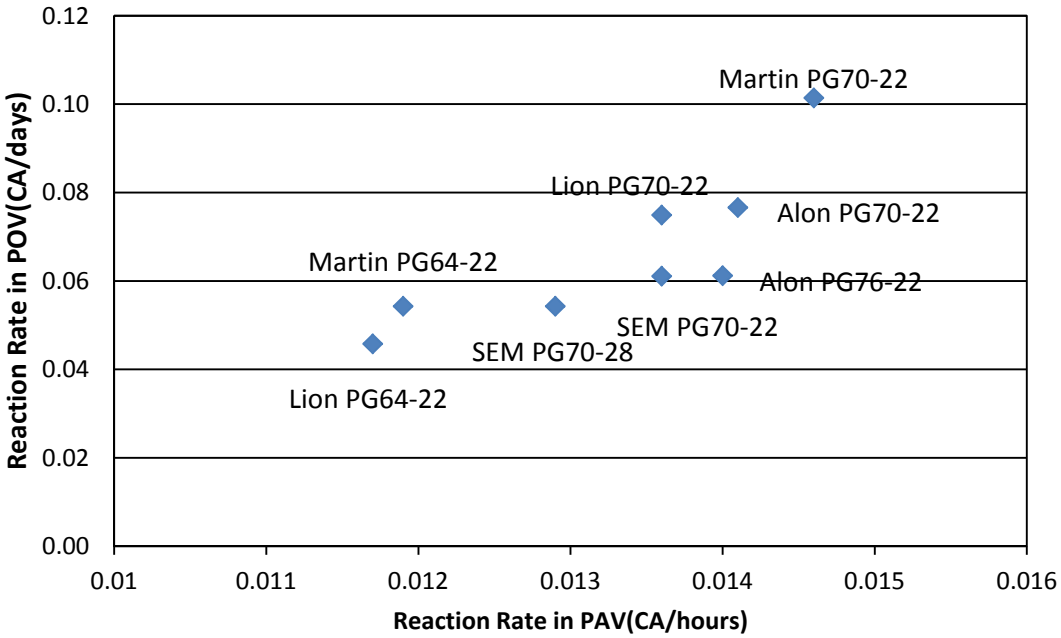


Figure 130. Comparison of 100°C Reaction Rates Determined from PAV and POV Methods.

Two observations are noted from Figure 129 and Figure 130. First, at a fixed temperature (90 or 100°C), the reaction rate rankings of each binder in the two different devices are different because of the different oxygen pressures. For example, at 90°C, of the eight asphalts evaluated in this study, the Martin PG 70-22 has the highest oxidation rate in the POV but the lowest in the PAV. Second, at different temperatures, the reaction rate ranking of a binder was not always the same in a particular device. For example, Lion 64-22 has the highest oxidation rate in the PAV at 90°C but the lowest rate at 100°C. This effect is the result of the different activation energies for the different asphalts and emphasizes, once again, the futility of measuring the relative reaction rates of asphalts at an elevated temperature and using those rates to predict rankings at pavement conditions.

From the reaction rate data for both POV and PAV apparatuses, constant-rate period activation energy and pre-exponential factors were determined. These values are summarized in Table 49.

Table 49. Summary of Constant-Rate Kinetics Parameters at POV and PAV Conditions.

Binder	POV Kinetics Parameters[a]		PAV Kinetics Parameters[b]	
	Pre-exponential Factor (AP^{α}) (CA/day)	Activation Energy (kJ/mol)	Pre-exponential Factor (AP^{α}) (CA/day)	Activation Energy (kJ/mol)
Lion PG64-22	3.0×10^{6}	56	1.2	14
Lion PG70-22	5.1×10^{8}	70	1.0×10^{3}	35
Alon PG70-22	6.46×10^{9}	78.3	5.5×10^{4}	47
Alon PG76-22	4.71×10^{9}	77	1.2×10^{6}	56
Martin PG64-22	8.81×10^{8}	72	4.5×10^{4}	47
Martin PG70-22	1.98×10^{11}	88	4.0×10^{8}	74.5
SEM PG70-22	1.09×10^{10}	80	1.1×10^{7}	63
SEM PG70-28	1.03×10^{9}	72.5	3.3×10^{5}	53

[a]POV conditions: 1 atm air absolute, 0.8 mm film
[b]PAV conditions: 20.7 atm air gauge, 3.2 mm film

Rheological Properties

Low shear rate limiting viscosity hardening susceptibility and DSR Function hardening susceptibility data are given in Table 50. The hardening susceptibility is the slope of the ln viscosity (or ln DSRFn) versus CA and as such reflects the extent of rheological hardening to oxidation. Such rheological stiffening is a direct result of the chemical changes caused by oxidation and has been well noted previously in the literature (Martin et al.1990; Lau et al., 1992; Petersen et al., 1993; Liu et al., 1996; Petersen, 1998).

Figure 131, Figure 132, Figure 133, and Figure 134 show viscosity and DSRFn hardening susceptibility relationships for both the POV and PAV methods for the Martin PG 70-22 material. The relationship is clearly defined and the slope is characteristic of each asphalt. Quantitatively understanding these relationships is critical to predicting changes to pavement durability under the influence of oxidation. Based on these data we conclude that the hardening susceptibility parameters must be determined at atmospheric air pressure in order to accurately reflect pavement hardening; apparently no correlation between PAV and POV conditions is evident for these materials.

Table 50. Hardening Susceptibility for Eight Binders.

		POV Conditions[a]	PAV Conditions[b]
Lion PG64-22	Limiting Viscosity HS:	2.33	3.29
	DSR Function HS:	4.23	4.93
Lion PG70-22	Limiting Viscosity HS:	2.46	3.12
	DSR Function HS:	3.48	4.20
Martin PG64-22	Limiting Viscosity HS:	5.12	4.16
	DSR Function HS:	5.52	4.50
Martin PG70-22	Limiting Viscosity HS:	2.35	2.53
	DSR Function HS:	4.22	3.87
Alon PG70-22	Limiting Viscosity HS:	3.04	3.14
	DSR Function HS:	5.95	4.02
Alon PG76-22	Limiting Viscosity HS:	5.03	2.71
	DSR Function HS:	5.45	3.63
SEM PG70-22	Limiting Viscosity HS:	4.51	4.17
	DSR Function HS:	6.11	4.83
SEM PG70-28	Limiting Viscosity HS:	4.53	3.58
	DSR Function HS:	5.50	4.51

[a]POV conditions: 1 atm air absolute, 0.8 mm film
[b]PAV conditions: 20.7 atm air gauge, 3.2 mm film

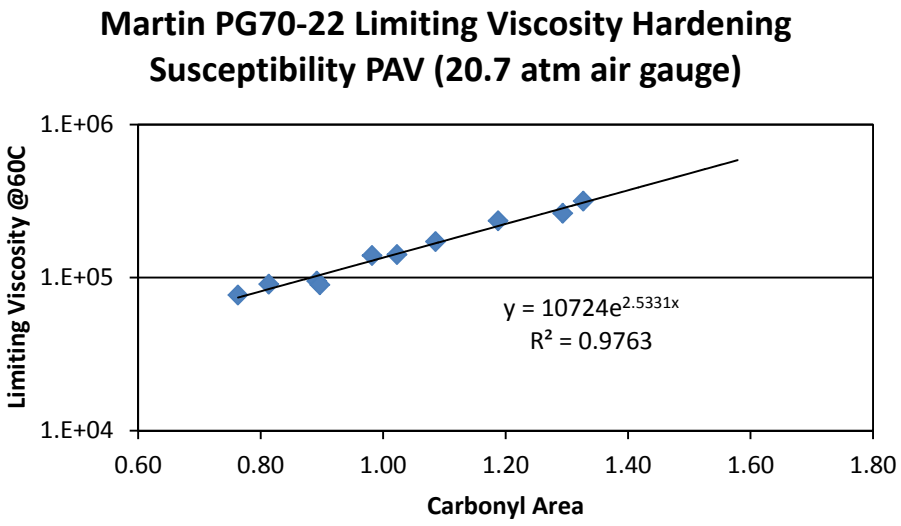


Figure 131. Limiting Viscosity HS of Martin PG 70-22 from PAV.

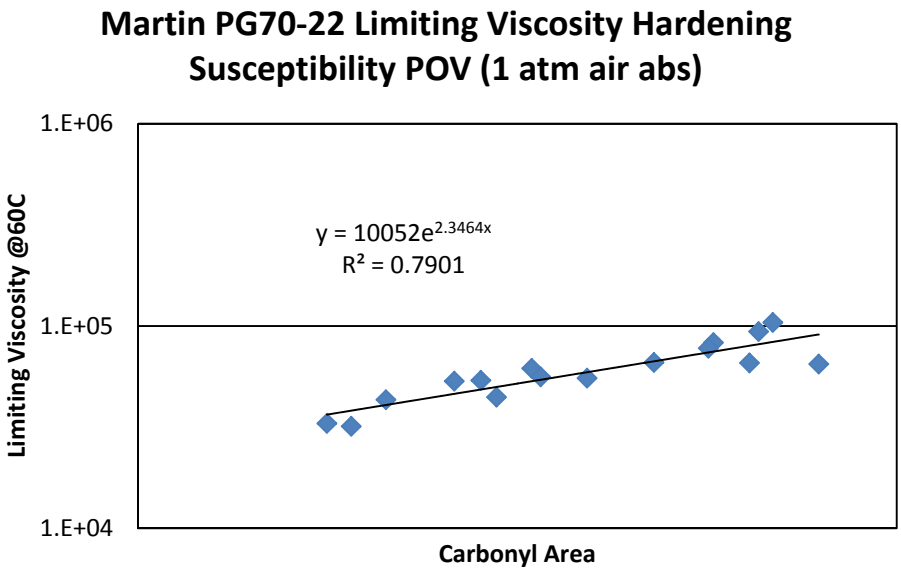


Figure 132. Low Shear Rate Limiting Viscosity HS of Martin PG 70-22 from POV.

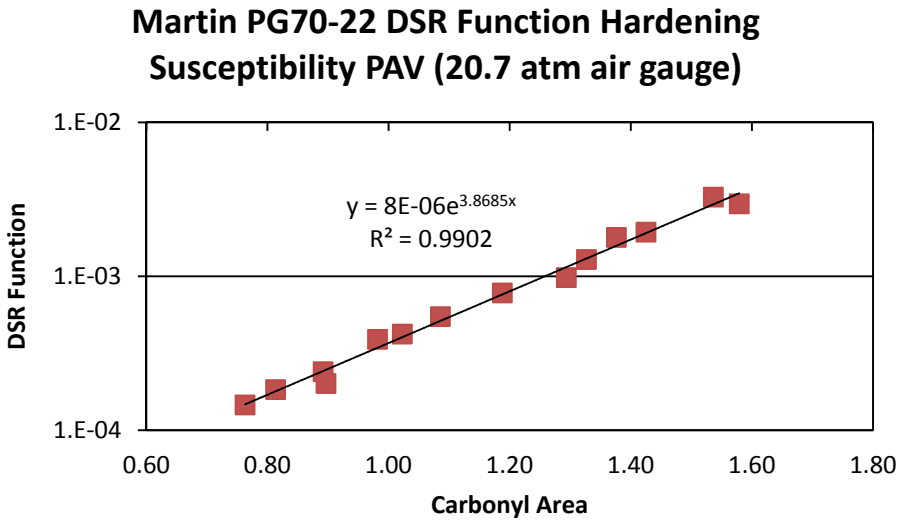


Figure 133. DSR Function HS of Martin PG 70-22 from PAV.

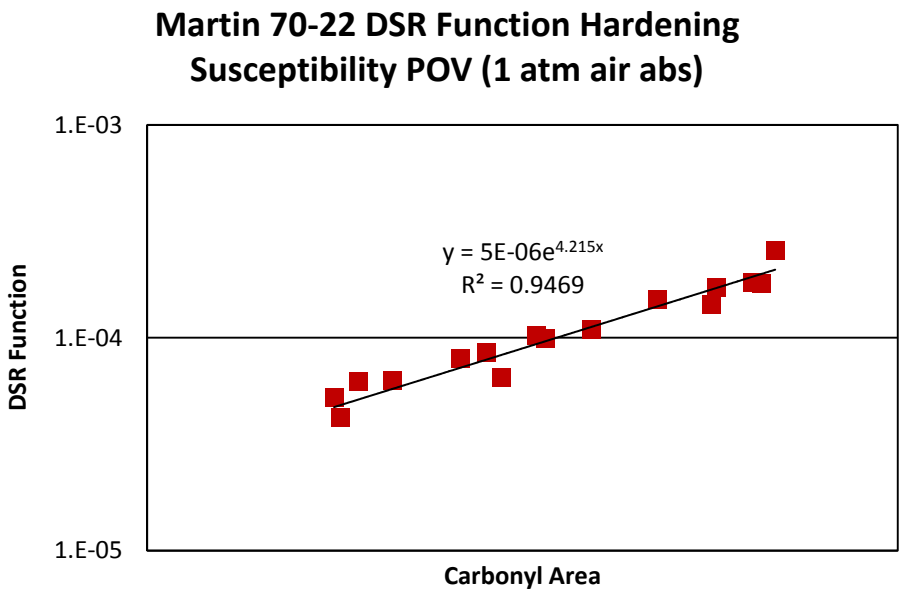


Figure 134. DSR Function HS of Martin PG 70-22 from POV.

Activation Energy Comparison

Eq. 14-2 defines the activation energy E_{AC} at a fixed pressure. Literature reports support the conclusion that a similar balance of reactions occurs for a given asphalt aged below 100°C. Thus, E_{AC} is assumed to be independent of temperature below 100°C even though it varies from one asphalt to the next. Domke et al. (2000) reported that oxidation rates are affected by the nature of the supply of oxygen (pure oxygen versus air) and the total pressure. To illustrate this effect, Figure 135 compares the activation energies for asphalt oxidation at one atmosphere air to those at elevated pure oxygen pressures. The figure is created from data for 11 asphalts reported by Domke et al. (2000) and Liu et al. (1996). In each case, asphalt was oxidized in films nominally 1 mm thick. Linear correlations are seen in Figure 135 between high pressure pure oxygen aging (at either 4 atm or 20 atm pure oxygen) and one atmosphere air aging. The existence of such correlations is important to the development of an aging test that can provide predictions of binder performance in the presence of oxidative aging in a reasonable amount of time and that are founded on fundamental principles of binder oxidation and hardening.

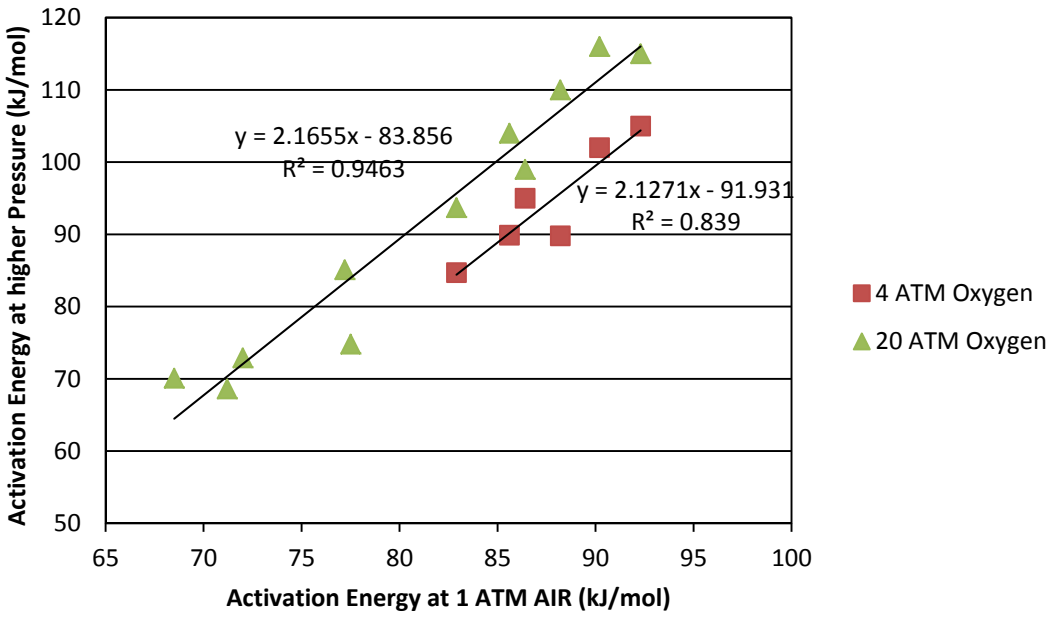


Figure 135. E_{AC} (4 atm and 20 atm, abs O_2) vs. E_{AC} (1 atm abs air).

For this project, we used both PAV and POV apparatuses to measure oxidation kinetics parameters for the same asphalts at two oxidation conditions. Figure 136 compares the activation energies from both the POV (1 atm air absolute, 0.8 mm thick films) and PAV (20.7 atm air gauge, 3.2 mm thick films) oxidation conditions. Two sets of data are shown in the figure. One set of data, consisting of the eight asphalts shown in Table 47, was obtained for this study. The other set, consisting of six SHRP asphalts (AAA, AAB, AAD, AAF, AAG, and AAM) was previously reported in the literature from two sources. The POV data at 1 atm air, 0.8 mm films, are from Domke et al. (2000), and the PAV data at 20.7 atm air, 3.2 mm films, are from Huh and Robertson (1996).

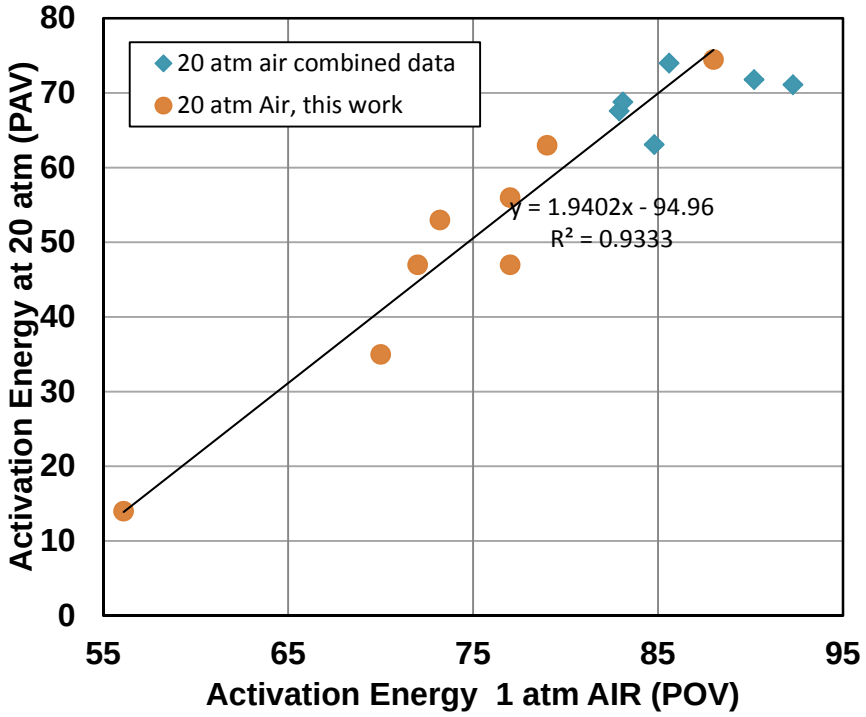


Figure 136. PAV (20.7 atm Air Gauge) vs. POV (1 atm Air abs) Activation Energy.

From Figure 136, it is seen that for these asphalts the relationship between activation energies measured at the two conditions is linear, and includes effects of the film thickness differences to the extent they affect reaction rates (and therefore activation energies) through mass transfer resistance. The slope is close to that for the data in Figure 135 but the activation energy values using pure oxygen (Figure 131, Figure 132, Figure 133, and Figure 134) were about 30 kJ/mol higher than that using air at the same oxygen partial pressure (4 atm) (Figure 136). This difference may occur because of oxygen transport resistance due to the film thickness.

Kinetics Parameters Correlation

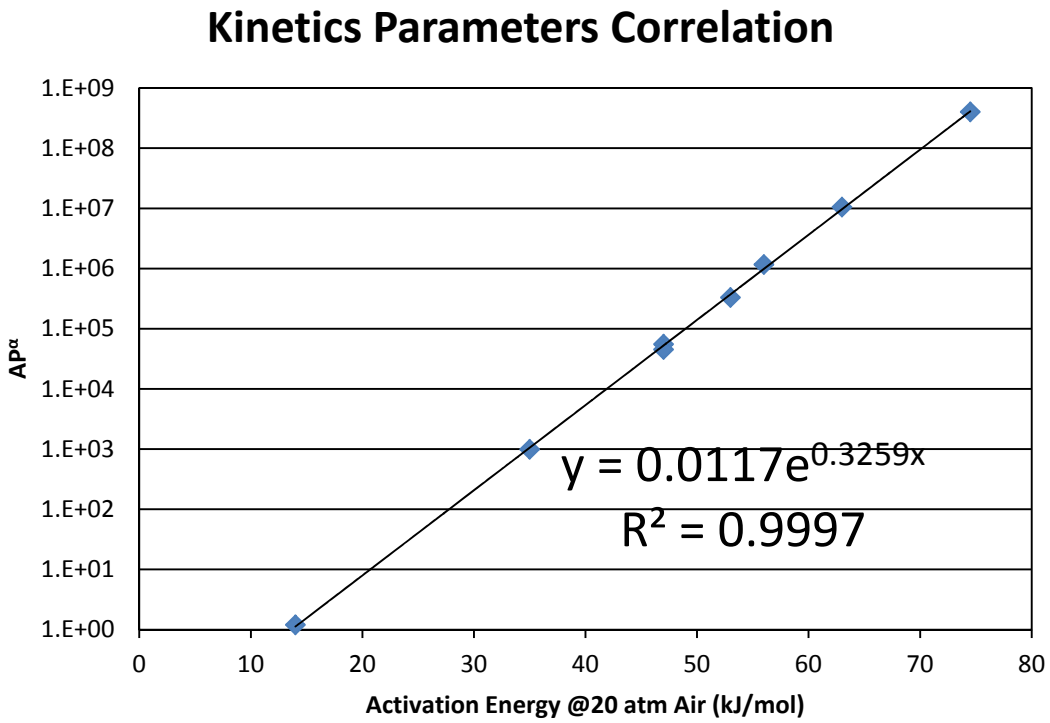


Figure 137. AP^{α} vs. E_{AC} from PAV Data.

Just as was true for the POV data at 1 atm air (Figure 20), the PAV data at 20 atm air also provided a correlation between activation energies and pre-exponential factors, shown in Figure 137. The POV data imply an isokinetic temperature of 359 K for the asphalts at 1 atm while the PAV data provide an isotkinetic temperature of 369 K at 20 atm air. As discussed in Chapter 3, the isokinetic temperature is that at which all asphalts have the same reaction rate. While the existence of an isokinetic temperature is neither required nor strictly in accord with the data, that the results are so uniform for all asphalts tested seems quite remarkable and may simplify an accelerated aging test in the future as data are gathered at PAV conditions for more asphalts.

AN ACCELERATED BINDER AGING TEST

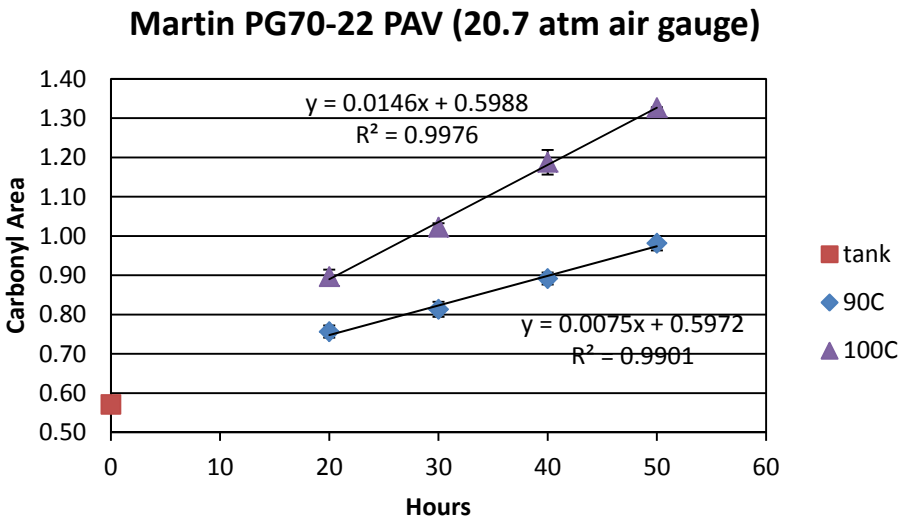
The work presented in this and previous chapters provide the basis for an accelerated binder aging test. As noted in Chapter 1, "… developing an accelerated binder aging test that ranks asphalts the same as pavement aging is challenging at best and fundamentally impossible at worst because of the different effects of time, temperature, and pressure on different materials." Such a test has been long sought.

The approach developed in this work has been to develop an accelerated method of determining a binder's oxidation kinetics parameters and then to use those parameters in a pavement oxidation model to predict binder oxidation specific to each pavement (e.g., air voids) and location (climate), binder hardening in response to oxidation, and each binder's impact on

pavement performance (e.g., mixture fatigue). In this way, the accelerated test can compare binders for their oxidation characteristics and their impact on pavement performance. Thus, the test consists of laboratory measurements (using PAV, FTIR, DSR, and mixture characterization tests) and computer simulations, using thermal and oxygen transport models of binder oxidation in pavements.

To summarize the binder oxidation portion of the test, the following steps will be conducted:

- Age binders in the PAV apparatus at 90°C and 100°C for several aging times, sufficient to establish a constant-rate aging period (e.g., 20, 30, 40, 50 hours),
- Measure FTIR CA for each of the aged binder samples,
- From these measurements, calculate CA aging rates (



- Figure 126) and from rate as a function of 1/RT determine an activation energy (Figure 128),
- Using the activation energy correlation relating PAV to POV aging (Figure 136), convert the PAV aging constant-rate activation energy to a POV constant-rate activation energy, E_{ac},
- Using the pre-exponential factor – activation-energy correlation (Figure 20) and E_{ac}, estimate A_c,
- Using the fast-rate – constant-rate activation energy correlation (Figure 19), estimate E_{af},
- Using the pre-exponential factor – activation energy correlation or the fast-rate reaction (Figure 21), estimate A_f,
- From constant-rate reaction data and an initial tank (unaged) CA value, estimate M, the ultimate contribution of the fast-rate reaction to increases in CA.
- With estimates for all of the kinetics parameters (E_{ac}, A_c, E_{af}, A_f, M), use the pavement oxidation model to predict binder pavement oxidation for comparison with the various binders of interest.

Kinetics parameters determined using this approach for the eight binders presented in this chapter are summarized in Table 51. For these data, measured POV data are shown for comparison in addition to the calculated POV values (based on the PAV measurements).

Besides binder oxidation, other data will be needed: binder hardening susceptibility and mixture fatigue response to binder hardening. Incorporation of the work of this project into a software user interface that automates these calculations is presented in Chapter 16.

Table 51. Measured and Calculated Kinetics Parameters Based on PAV Activation Energies and Fast-Rate-Constant-Rate Correlations.

Binder	POV Conditions[a]				PAV Cond[b]	POV Conditions[a]			
	Measured Eac (KJ/mol)	Measured Ac (CA/day)	Measured Eaf (KJ/mol)	Measured Af (CA/day)	Measured Eac (KJ/mol)	Calculated Eac (KJ/mol)	Calculated Ac (CA/day)	Calculated Eaf (KJ/mol)	Calculated Af (CA/day)
Martin PG64-22	72	8.81×10^{8}	51.9	7.37×10^{6}	47	73.1	1.12×10^{9}	51.7	1.56×10^{7}
Martin PG70-22	88	1.98×10^{11}	60.9	2.64×10^{8}	74.5	87.3	1.29×10^{11}	63.8	8.57×10^{8}
Alon PG76-22	77	4.71×10^{9}	52.6	2.21×10^{7}	56	77.7	5.30×10^{9}	55.7	5.79×10^{7}
Alon PG70-22	78.3	6.46×10^{9}	60.8	3.50×10^{8}	47	73.1	1.12×10^{9}	51.7	1.56×10^{7}
SEM PG70-28	72.5	1.03×10^{9}	49.1	3.34×10^{7}	53	76.2	3.16×10^{9}	54.4	3.74×10^{7}
SEM PG70-22	80	1.09×10^{10}	54.4	3.83×10^{7}	63	81.3	1.77×10^{10}	58.7	1.61×10^{8}
Lion PG64-22	56.1	2.97×10^{6}	37.3*	1.27×10^{5}*	14	56.1	3.81×10^{6}	37.3	1.28×10^{5}
Lion PG70-22	70	5.09×10^{8}	49.1*	6.50×10^{6}*	35	66.9	1.42×10^{8}	46.5	2.72×10^{6}

[a]POV conditions: 1 atm air absolute, 0.8 mm film

[b]PAV conditions: 20.7 atm air gauge, 3.2 mm film

*These values for these asphalts were calculated from measured E_{ac} and measured A_c at 1 atm air, using fast-rate-constant-rate kinetics parameters correlation (Jin et al., 2011; Jin, 2012). Other calculated values in this table (for all asphalts) were based on the 1 atm-air – 20 atm-air activation energy correlation from this study and the fast-rate-constant-rate kinetics parameters correlation by Jin et al. (2011) and Jin et al. (2012).

SUMMARY

This chapter draws on earlier chapters to develop an accelerated method for comparing binders in their ability to provide a durable pavement mixture. With the kinetics work from Chapter 3, a strategy was developed and demonstrated for making a 50-hour PAV determination of a binder's constant-rate activation energy at PAV elevated pressure conditions. With that measurement and correlations from Chapter 3, plus a further correlation developed in this chapter between PAV high-pressure conditions and pavement-pressure conditions, extimates of a complete set of binder oxidation fast-rate and constant-rate kinetics parameters can be made. These parameters can then be used in the pavement oxidation models of binder oxidation and hardening presented in Chapters 7 through 9. With the results of these models, binders can be compared in their expected pavement performance.

Thus, the accelerated PAV method for determining binder oxidation kinetics parameters, coupled with the thermal and oxygen transport model of pavment oxidation, and with data on the impact of binder oxidative hardening on mixture durability, provide an accelerated aging test of a binder's performance. This test is specific to a pavement's location and incorporates elements of the particular pavement's structural design and materials and therefore provides results that are specific to each pavement in a way that has not been possible previously.

This work and its implantation in a software product that automates the various elements of the test is further discussed in Chapter 16.

CHAPTER 15. TOWARD A FRAMEWORK FOR INCORPORATING AGING IN MIXTURE DESIGN

In order to move toward a framework for incorporating aging in mixture design and predicting N_f, it is necessary to determine how a mixture responds to oxidative aging and subsequent binder hardening and which factors have the greatest effect on mixture stiffening susceptibility and loss of fatigue resistance.

In this chapter, data collected from 21 field sites across the state of Texas are examined as a first step. Three of the sites are US 277, US 83, and SH 24, which were described previously. A description of the 18 additional sites is also given. Cores from these sites were trimmed and analyzed in the same fashion as those from the preceding chapters. For a limited number of these field sites, mixture response to oxidative aging and subsequent binder hardening was determined in terms of two characteristic slopes that represent how the mixture changes as a result of changes in binder properties. Next, one of these slopes was selected for further study, and a predictive method for estimating this selected characteristic slope was formulated. Finally, recommendations for using this predictive method or directly measuring this characteristic slope in a mixture design system are provided.

MATERIAL SELECTION

Twenty-one sites across Texas were used in this part of the study. Sites were selected from five different climate zones which include DW, DC, WW, WC, and moderate (M). Each site had different characteristics, such as aggregate type, binder type, binder content, and layer of interest. All binders were classified as Superpave Performance Grade binders. Cores were taken from the shoulder, wheel path, treated and untreated shoulder and wheel path where possible. Each site and its associated characteristics are listed in Table H1 of Appendix H. An abbreviated list showing location, climate, and construction date is shown in Table 51.

Testing and subsequent data collection for several cores collected from US 190 was not possible due to the stiffness of the samples. The high modulus values (ranging from 7500 to 11,000 MPa) discovered during the non-damaging tests caused the samples to fail prematurely during the damaging portions of testing, leaving an incomplete data set for this site. A similar situation occurred for US 54. This site was constructed in 1998 resulting in samples which were extremely brittle. Again, failure occurred during the damaging portion of the RDT* test, resulting in an incomplete data set. SH 59 and US 69 had similar problems with a few samples but not to the same degree as US 190 and US 54. However, of the 218 samples tested from the shoulder and wheel path of the listed sites, 191 ran to completion and provided enough data to calculate N_f.

Table 52. Field Sample Collection Sites.

TxDOT District	Location	Climate	Construction Date	TxDOT District	Location	Climate	Construction Date
Bryan	US 290	M	2002	Lubbock	US 84	DC	2009
Atlanta	IH 20	WC	2001	Childress	US 83	DC	2008
Waco	IH 35 Layer #5	M	2002	Yoakum	SH 36	WW	2006
Wichita Falls	SH 59	DC	2007	Atlanta	US 259	WC	2005
Laredo	IH 35 Layer #3	DW	2007	Paris	SH 24	WC	2009
Laredo	IH 35 Layer #4	DW	2007	Odessa	Farm to Market 1936	DW	2002
Lufkin	US 69	WW	2003	Pharr	Farm to Market 2994	DW	2002
Laredo	Farm to Market 649	DW	2006	Amarillo	US 54	DC	1998
Laredo	US 277	DW	2008	Paris	SH 19/24	WC	2000
Tyler	US 259	WC	2007	Bryan	SH 6	M	2000
Lubbock	US 82	DC	2008				

FIELD SAMPLE TEST RESULTS

Figure 138 and Figure 139 show the E_{ve} and N_f results for the shoulders of all field sites and indicate that E_{ve} decreases and N_f increases with aging time under field conditions for the majority of the mixtures examined. Wheelpath data in Figure 140 and Figure 141 follow these same general trends, and the effects of surface treatments (chip seals) serve to protect the surface and extend (or improve) N_f and decrease E_{ve} as shown by more detailed data in Appendix H. In this chapter shoulder data are examined in more detail to isolate the effects of binder oxidative aging and the subsequent hardening of the binder, stiffening of the mixture, and loss of mixture resistance to fatigue.

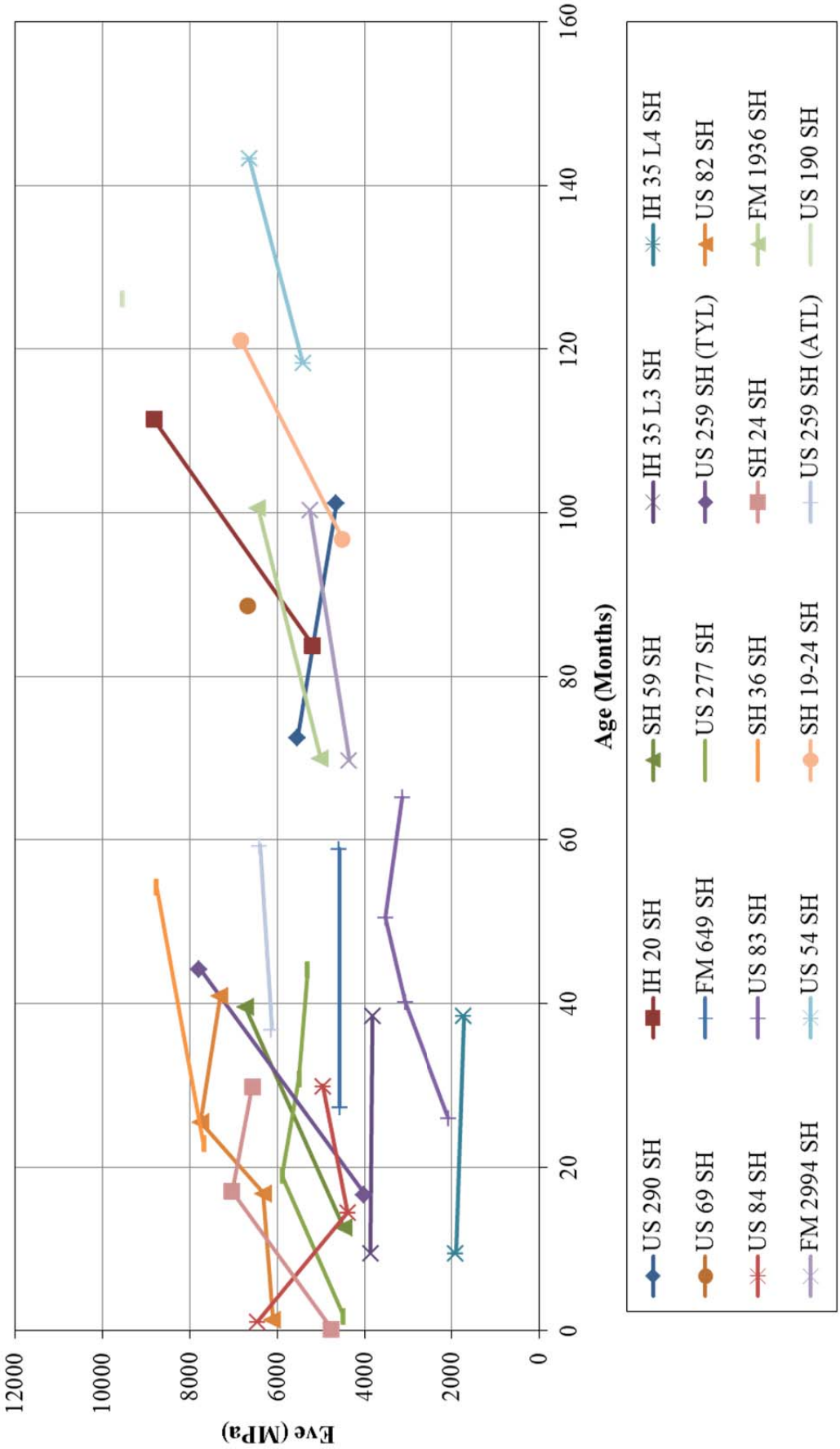


Figure 138. E_{ve} for Shoulders of All Field Sites.

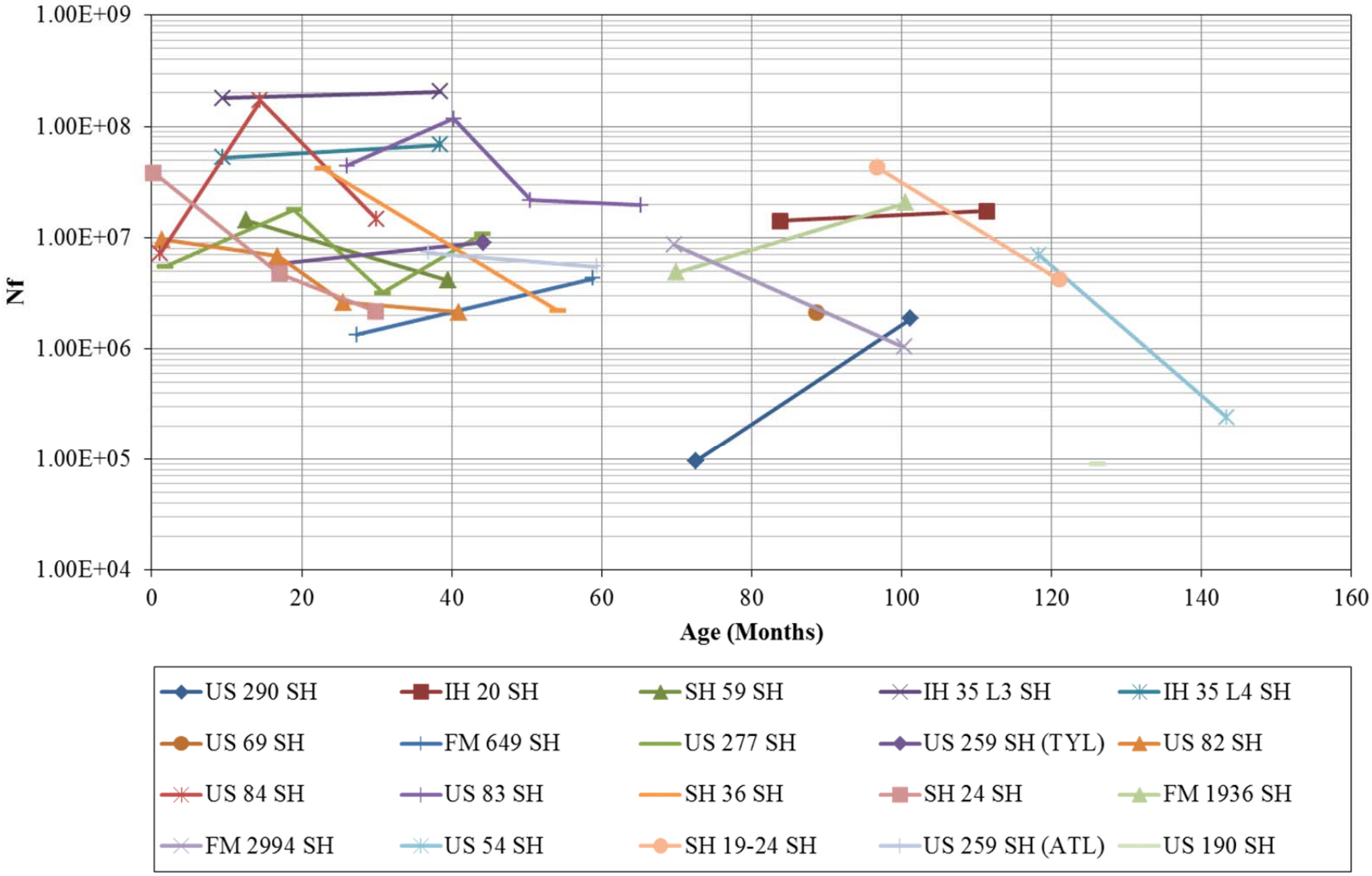


Figure 139. N_f for Shoulders of All Field Sites.

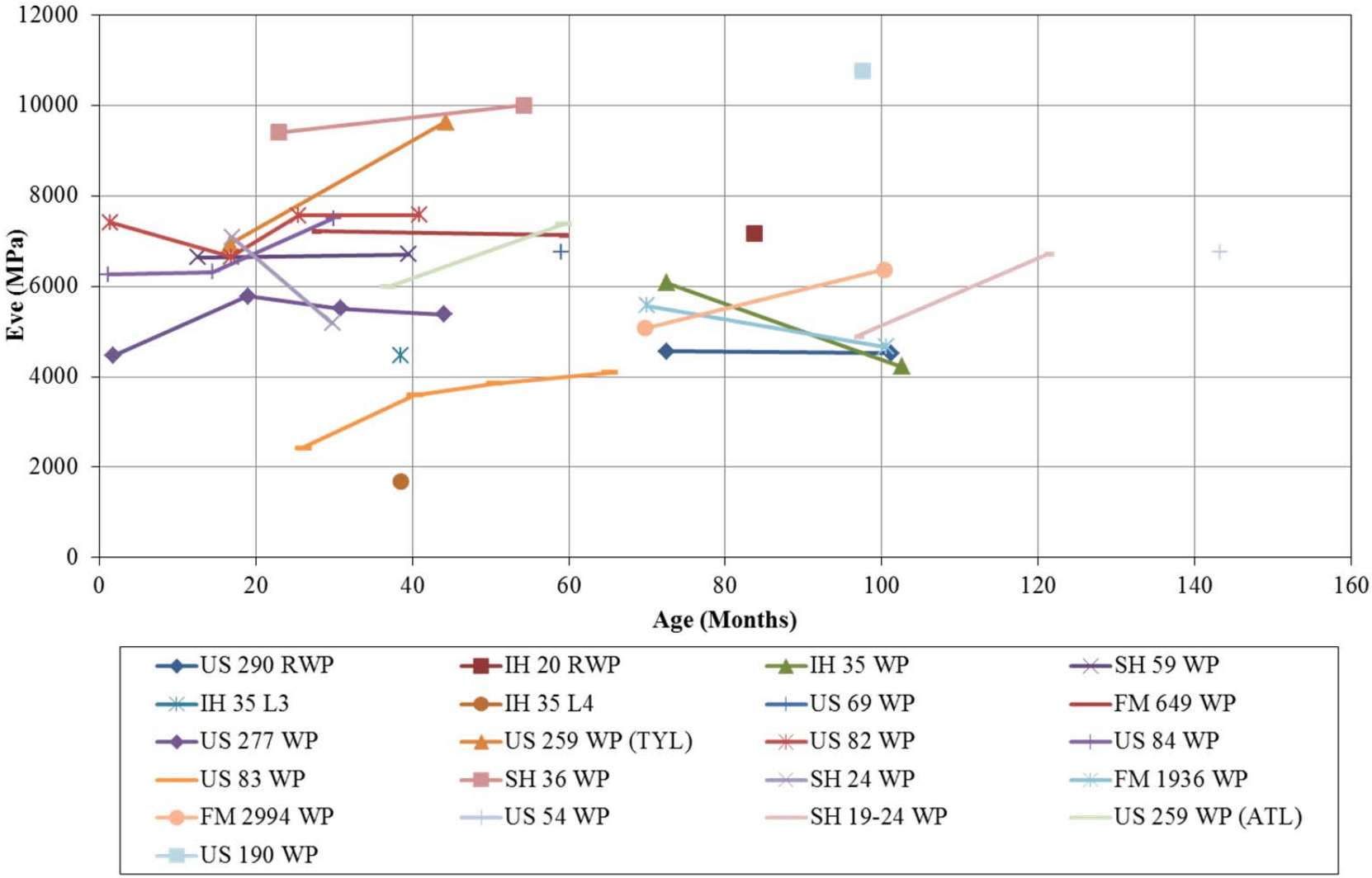


Figure 140. E_{ve} for Wheelpaths of All Field Sites.

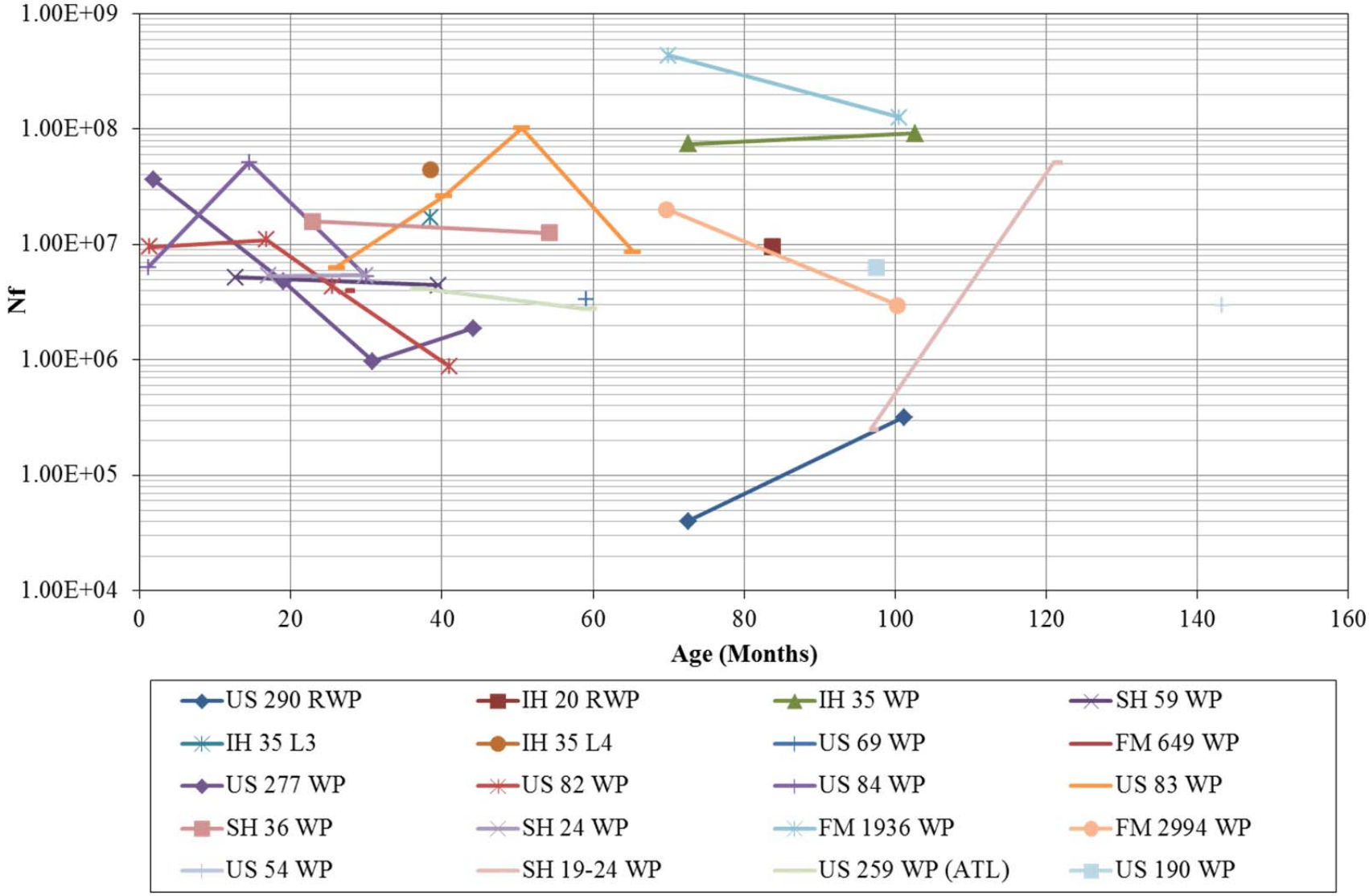


Figure 141. N_f for Wheelpaths of All Field Sites.

BINDER VS. MIXTURE RESULTS

To more closely examine the direct effects of binder oxidative aging on mixture stiffening and loss of fatigue resistance in any of the different climates and different mixtures evaluated, changes in binder physical properties in terms of DSR function (DSR_f) replaced aging time as shown in Figure 138, Figure 139, Figure 140, and Figure 141. For each of the three field sites studied in more detail through examination of the effects of AV and binder content with aging with LMLC specimens (US 277, US 83, and SH24), E_{ve} versus DSR_f and N_f versus DSR_f were examined on log-log plots. The slopes of these plots provide an indication of the mixture stiffening susceptibility (slope of E_{ve} versus DSR_f plot) and loss of mixture fatigue resistance (slope of N_f and DSR_f plot) in response to binder hardening due to oxidative aging.

Figure 142 and Figure 143 show examples of these E_{ve} versus DSR_f plots for US 277, and Figure 144 and Figure 145 show examples of these N_f versus DSR_f plots for this same section. Although the effect of AV on each of these mixture response variables (E_{ve} and N_f) was statistically significant and that of binder content was not statistically significant as noted previously in Chapter 13 for each LMLC mixture, the effects of these two mixture parameters do not appear to significantly affect the slopes (mixture stiffening susceptibility or the slope of E_{ve} versus DSR_f plot and loss mixture fatigue resistance or the slope of N_f and DSR_f plot), especially given the variability in the measured E_{ve} or calculated N_f and the lack of replicate slopes due to the extensive effort required to obtain the slope based on testing replicate specimens over time.

The slopes of the log-log plots of E_{ve} versus DSR_f and N_f versus DSR_f for all three LMLC mixtures with different AV and binder contents are shown in Table 53 with mixture characteristics that may play a role in changing these slopes. These mixture characteristics include a qualitative AV level representing a range of values as described previously in the experiment design in Chapter 11, binder content (P_b), percent binder absorbed (P_{ba}) that is a function of aggregate type and binder content, the resulting effective binder content (P_{be}) that remains to coat aggregate particles, and an effective film thickness (FT_e) that is a function of aggregate type, aggregate gradation, and binder content as the effective binder content (P_{be}) is distributed to coat the surface area of the aggregates. The corresponding slopes for the field cores are also shown for the field conditions (optimum binder content and medium AV).

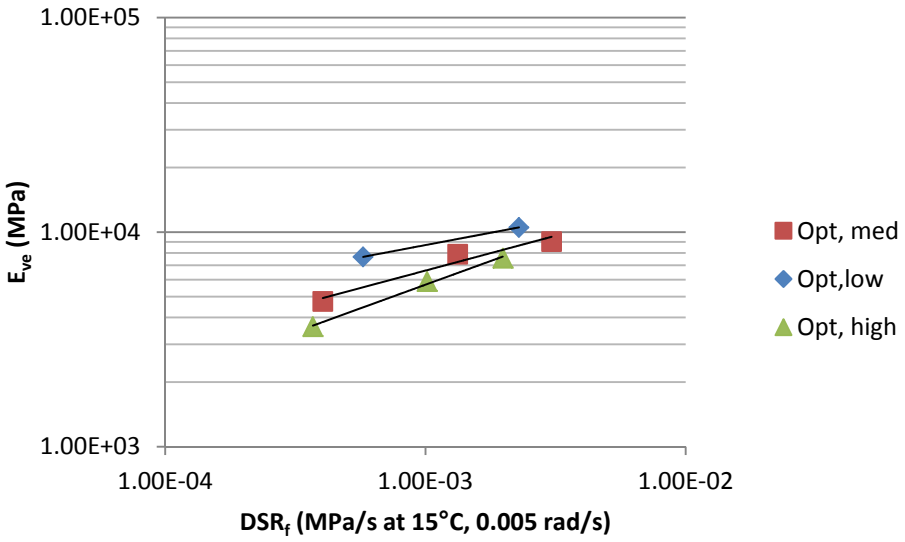


Figure 142. Example Plot of E_{ve} vs. DSR_f to Examine AV Effect (US 277).

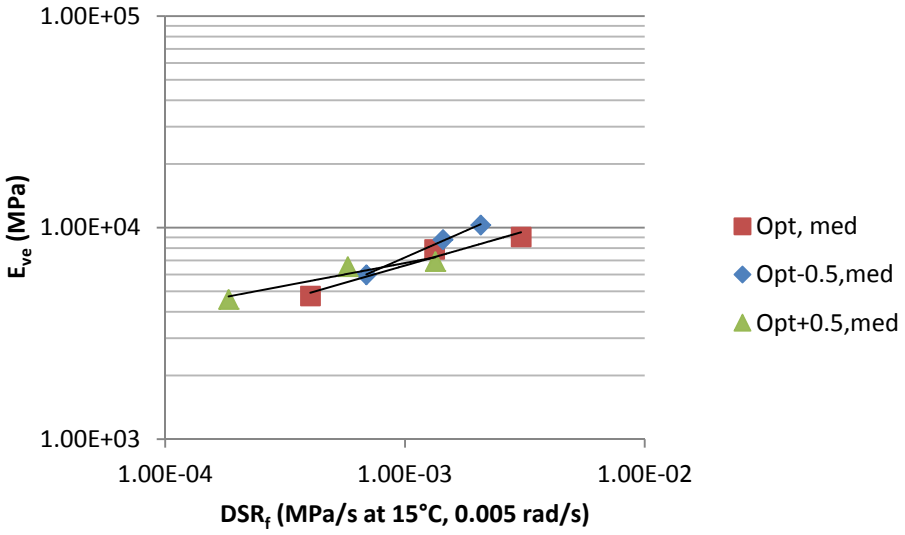


Figure 143. Example Plot of E_{ve} vs. DSR_f to Examine Binder Content Effect (US 277).

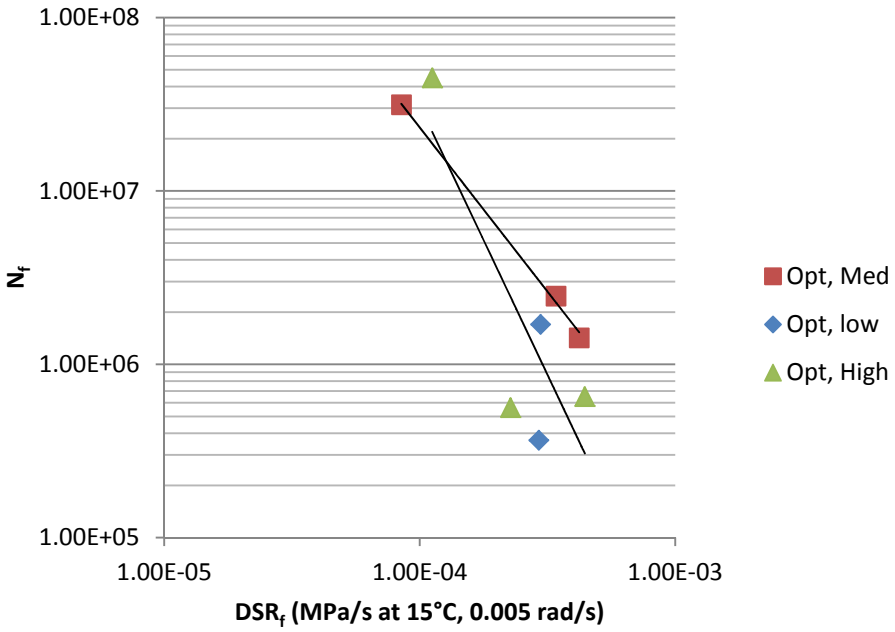


Figure 144. Example Plot of N_f vs. DSR_f to Examine AV Effect (US 277).

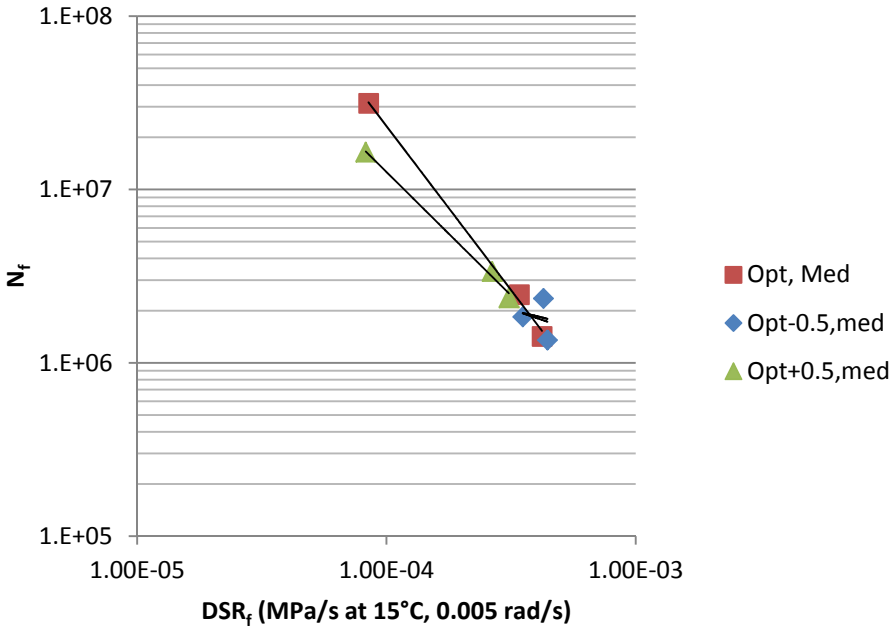


Figure 145. Example Plot of N_f vs. DSR_f to Examine Binder Content Effect (US 277).

Table 53. Slopes of E_{ve} vs. DSR_f and N_f vs. DSR_f for LMLC Samples (Log-Log).

Field Site	AV	Binder Content	P_b (%)	P_{ba} (%)	P_{be} (%)	FT_e (µm)	Log-Log Slope E_{ve} vs DSR_f	Log-Log Slope N_f vs DSR_f	Log-Log Field Slope N_f vs DSR_f
US 277	Low	Optimum	4.5	0.97	3.6	4.4	0.23	0.22	
US 277	Medium	Optimum	4.5	0.97	3.6	4.4	0.32	0.25	-1.35
US 277	High	Optimum	4.5	0.97	3.6	4.4	0.44	-0.37	
US 277	Medium	Opt-0.5%	4.0	0.97	3.1	3.5	0.50	-1.76	
US 277	Medium	Opt+0.5%	5.0	0.97	4.1	5.2	0.21	-1.98	
US 277	Low	Opt-0.5%	4.0	0.97	3.1	3.5	0.17	-0.40	
US 277	Low	Opt+0.5%	5.0	0.97	4.1	5.2	0.12	-0.51	
US 277	High	Opt-0.5%	4.0	0.97	3.1	3.5	0.42	-0.69	
US 277	High	Opt+0.5%	5.0	0.97	4.1	5.2	0.23	-0.32	
US 277	AVERAGE					***4.4***	***0.29***	***-0.86***	
US 83	Low	Optimum	5.3	0.04	5.3	9.7	-22.89	100.30	
US 83	Medium	Optimum	5.3	0.04	5.3	9.7	0.68	-1.89	0.11
US 83	High	Optimum	5.3	0.04	5.3	9.7	0.33	-3.11	
US 83	Medium	Opt-0.5%	4.8	0.04	4.8	8.7	2.15	-0.49	
US 83	Medium	Opt+0.5%	5.8	0.04	5.8	10.7	0.49	-1.43	
US 83	Low	Opt-0.5%	4.8	0.04	4.8	8.7	0.42	-0.83	
US 83	Low	Opt+0.5%	5.8	0.04	5.8	10.7	0.95	-1.51	
US 83	High	Opt-0.5%	4.8	0.04	4.8	8.7	0.75	18.08	
US 83	High	Opt+0.5%	5.8	0.04	5.8	10.7	0.76	-2.88	
US 83	AVERAGE					***9.7***	***0.82***	***-1.73***	
SH 24	Low	Optimum	5.4	0.68	4.8	6.4	-2.08	-4.09	
SH 24	Medium	Optimum	5.4	0.68	4.8	6.4	0.25	-0.36	-1.71
SH 24	High	Optimum	5.4	0.68	4.8	6.4	0.25	-1.34	
SH 24	Medium	Opt-0.5%	4.9	0.68	4.3	5.5	-0.51	-1.10	
SH 24	Medium	Opt+0.5%	5.9	0.68	5.3	7.2	0.20	-0.85	
SH 24	Low	Opt-0.5%	4.9	0.68	4.3	5.5	0.18	-0.21	
SH 24	Low	Opt+0.5%	5.9	0.68	5.3	7.2	0.23	-0.75	
SH 24	High	Opt-0.5%	4.9	0.68	4.3	5.5	0.21	-0.98	
SH 24	High	Opt+0.5%	5.9	0.68	5.3	7.2	0.30	-0.48	
SH 24	AVERAGE					***6.4***	***0.23***	***-1.13***	

As each individual mixture from a given field site did not show significant differences in the characteristic slopes with changes in AV that are assumed to allow for sufficient oxygen availability for aging and changes in binder content over a small range, average values were obtained as shown in Table 53. These averages were obtained without the yellow highlighted outliers that showed trends in binder versus mixture properties in the opposite direction as the

majority of samples tested. These outliers are assumed related to the significant variability associated with obtaining these slopes. These average slopes appear to be mixture specific, and the range of values matches those found for other mixtures in TxDOT Project 0-4468 Evaluate the Fatigue Resistance of Rut Resistant Mixes and TxDOT Project 0-4688 Development of a Long-Term Durability Specification for Modified Asphalt (Walubia et al., 2006, Woo et al., 2007). TxDOT Project 0-4468 included two mixtures with slopes approximately equal to −1.0, and TxDOT Project 0-4688 included four mixtures with slopes of −0.9, −1.0, −2.1, and −2.5.

To determine which characteristic slope is most useful in incorporating aging in a mixture design system, the effects of E_{ve} on N_f were examined. Using the CMSE* approach described previously in the experiment design in Chapter 11, an increase in mixture stiffness with aging is not sufficient to understand the loss of mixture fatigue resistance with aging, as increases in stiffness while holding all other mixture variables constant results in an increase in N_f. Thus the prediction of N_f in the CMSE* approach simultaneously accounts for other key mixture parameters that also change with aging and impact loss of mixture fatigue resistance. These key variables include the Paris' law fracture parameters, A and n, the rate of damage accumulation, b, and the initial crack size c_0.

Based on the average values for the loss in mixture fatigue resistance as shown in Figure 146, there appears to be a very strong relationship with effective film thickness (FT_e) that accounts for many mixture parameters simultaneously (aggregate type through P_{ba} which is utilized with binder content or P_b to calculate P_{be} that is then distributed over the surface area of the aggregate represented by the aggregate gradation). Another important variable in how aging affects mixture loss of fatigue resistance is binder type, and this is accounted for through the change in DSR_f that forms the denominator of the characteristic slopes.

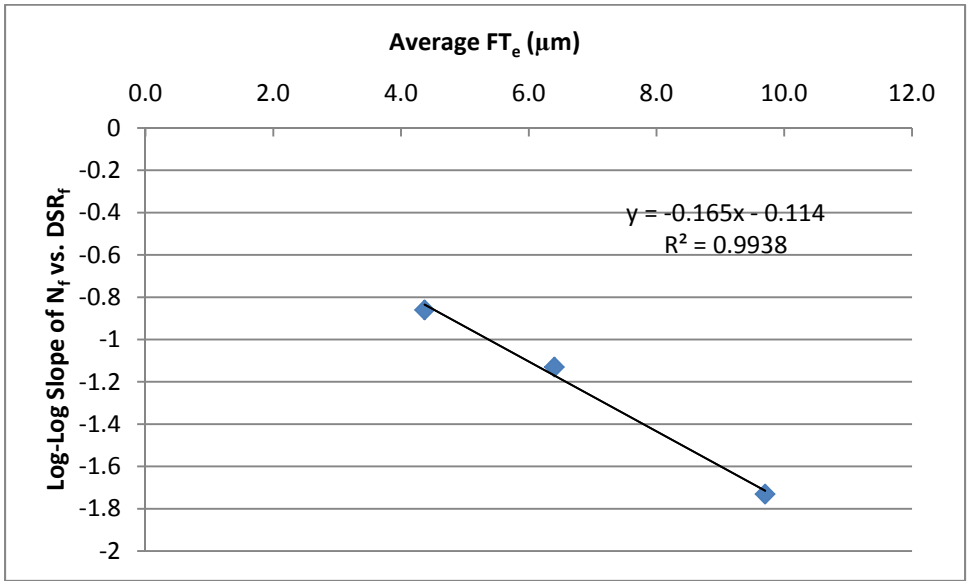


Figure 146. Average Log-Log Slope of N_f vs. DSR_f versus Average FT_e.

Using the correlation provided in Figure 146 based on laboratory data, loss of mixture fatigue resistance with binder oxidative aging (log-log slope of N_f vs. DSR_f) can be predicted for four different field sites (including corresponding field sites utilized in the laboratory

experiment) where the pavement is relatively young, data were available to calculate FT_e, and reasonable trends were obtained to obtain the characteristic slope with DSR_f increasing with time and N_f decreasing with time. The results of this prediction are shown in Table 54. The predicted characteristic slopes are all smaller than the measured slopes by an average factor of 1.6. This value can be thought of as a shift factor between laboratory and field conditions that accounts for differences in artificial laboratory aging at 60°C and natural field aging. For a fourth field site constructed earlier in 2007, the predicted slope is high, but the measured slope is significantly larger with a laboratory to field shift factor of approximately 6.8. These results indicate that caution should be utilized if predicting the characteristic slope for FT_e values outside those used to formulate the predictive equation shown in Figure 146 or outside the range of approximately 4–10μm.

Table 54. Predicted vs. Measured Log-Log Field Slopes of N_f vs. DSR_f.

Field Site	Measured Log-Log Field Slope N_f vs DSR_f	FT_e (μm)	Predicted Log-Log Field Slope N_f vs DSR_f	Lab to Field Shift Factor
US 277	−1.35	4.4	−0.84	1.6
SH 24	−1.71	6.4	−1.17	1.5
SH 59	−2.32	7.3	−1.32	1.8
FM 2994	−12.95	10.9	−1.91	6.8

RECOMMENDATIONS FOR MIXTURE DESIGN SYSTEM

When aged mixture properties are not available, the average laboratory to field shift factor of 1.6 may be utilized in a mixture design system and applied to the predicted loss of mixture fatigue resistance with binder stiffening (slope of N_f vs. DSR_f). Thus with the ability to predict changes in DSR_f with depth and climate as outlined previously in Chapter 12, the corresponding changes in N_f from an initial value measured on unaged mixtures can be estimated. However, based on the limited results shown in this chapter, it is recommended that both unaged and aged mixture properties be measured for high traffic volume facilities where a high level of reliability in the design is desired. The aged mixture properties may be obtained after a long-term aging procedure for compacted samples such as that in AASHTO R 30 (5 days at 85°C) or another procedure to be developed in the upcoming NCHRP Project 9-54 Long-Term Aging of Asphalt Mixtures for Performance Testing and Prediction. The characteristic slope or loss of mixture fatigue resistance can then be estimated using measured changes in N_f and measured changes in DSR_f or measured changes in N_f and predicted changes in DSR_f tied directly to a specific climate.

Figure 147 provides a flow chart of the recommended mixture design system to incorporate aging for both low traffic and high traffic volume facilities. It should be noted that traffic is not currently considered. Further analysis of the data generated by this project may provide additional insight on the effects of traffic on further damaging and decreasing mixture loss of fatigue resistance as shown previously in Chapter 12 for one field site.

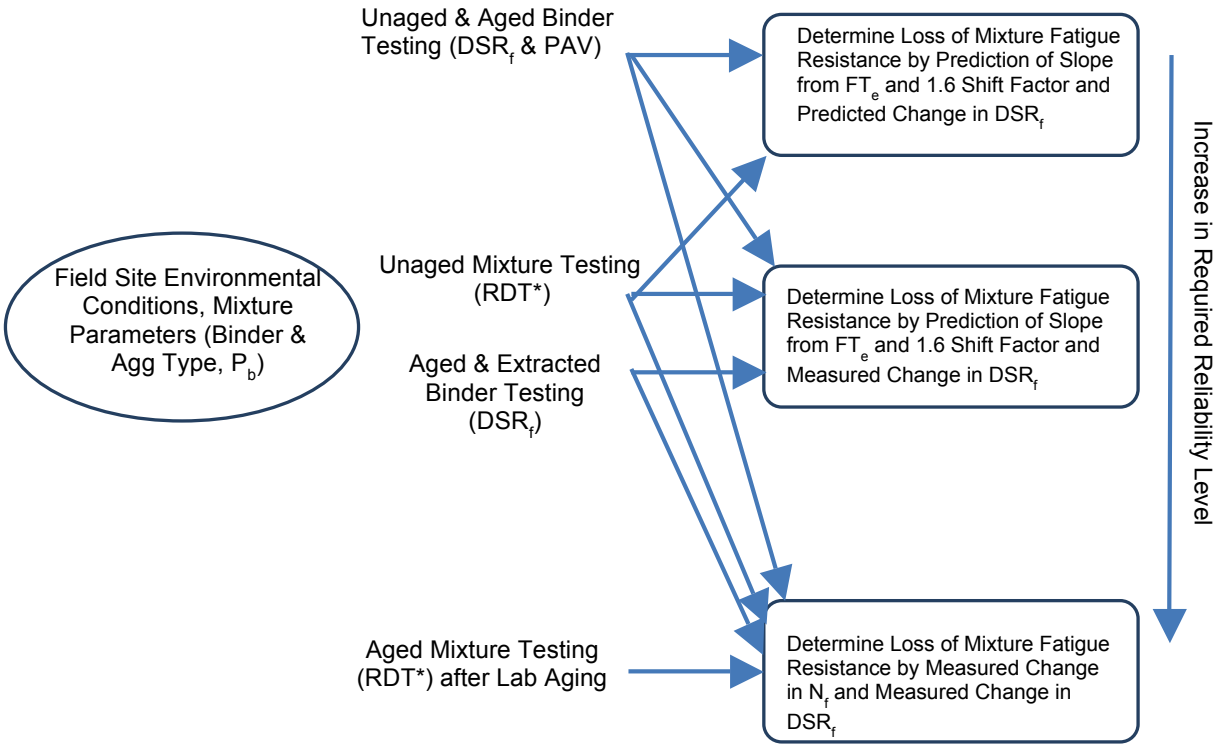


Figure 147. Flow Chart of Recommended Mixture Design System with Aging.

CHAPTER 16. PAVEMENT AGING MODEL GRAPHICAL USER INTERFACE AND SUPPORTING SOFTWARE

INTRODUCTION TO THE AGING MODEL GRAPHICAL USER INTERFACE AND SUPPORTING SOFTWARE

Overview of Software

The software package described in this chapter facilitates implementation of the asphalt aging model developed in this work. The software prompts for the required input data and the mathematical solutions are automatically computed. The software package consists of three sub-packages. The first sub-package is the aging model graphical user interface (AMG) and is the primary graphical user interface supplied in this software package. Two additional graphical user interfaces (GUIs) support the AMG. The first supporting GUI is a Reaction Kinetics Parameters GUI (RKPG). The second supporting GUI is a temperature profile GUI (TPG).

Inputs to the AMG include binder properties, the temperature profile in the pavement, and reaction kinetics parameters. The primary output of the AMG is carbonyl area as a function of time. DSR Function vs. time is an optional output. The AMG is based on the aging models developed in Chapters 7 through 9 and draws heavily on the model described in Chapter 9. The model also incorporates other elements of this project: fast-rate, constant-rate reaction kinetics (Chapter 3); oxygen diffusion in asphalt mateials (Chapter 4); modeling temperature in pavments (Chapters 5 and 6); and development of an accelerated aging procedure for comparing asphalts and their durability in pavements (Chapter 14).

There are four major sections to this chapter. The first section is this introduction that outlines the chapter and provides introductory information on the software package.

The second major section of this chapter (*Using the Aging Model Graphical User Interface [AMG])* describes the use of the AMG.

The third major section (*Using the Reaction Kinetics Parameters Graphical User Interface [RKPG])* describes the GUI used for extracting kinetics reaction parameters from data supplied to the software. Inputs to the RKPG can be either 1 atmosphere air POV test results or 20 atmosphere air PAV test results. If POV results are input, the RKPG optimizes the fit of the reaction model to the experimental results by adjusting the five reaction kinetics parameters. Then, the optimized parameters and a graphical display of the fit are shown. One disadvantage of POV testing is that an approximately 90-day test time is required. An alternative, requiring only a few days of test time, is PAV testing. Using the results of PAV testing as inputs, the RKPG will supply an estimate of the constant rate activation energy at 1 atm. Then either the full set of reaction kinetics parameters from POV testing or only the constant rate activation energy from PAV testing can be input to the AMG. If only the constant rate activation energy is available, the AMG will estimate the other reaction kinetics parameters. The RKPG is based on the work described in Chapter 3 (Jin et al., 2011) and the work described in Chapter 14.

The fourth section of this chapter (*Using the Temperature Profile Graphical User Interface[(TPG]),* describes the use of the TPG. Inputs to the TPG include environmental inputs (wind speed, air temperature, and solar radiation) as well as pavement solar absorption and reflection characteristics. The TPG outputs a pavement temperature profile to an Excel worksheet. The temperature profile is a two-dimensional array which provides pavement temperature as a function of pavement depth and hour of the year. It is anticipated that the output from this GUI, in particular, will have uses beyond the AMG. This GUI and the corresponding suggested methods are applicable to all US locations. A database of pavement temperature profiles for several locations in Texas has already been built and is being supplied with this software package. The TPG is only required when the user desires to model a pavement for which the temperature profile cannot be reasonably approximated by one of the provided profiles. The TPG is based on the work described in Chapter 6 (Han et al., 2011a).

Software Packages Supplied

Introduction

Each of the three graphical user interfaces supplied has been built with MATLAB using the GUIDE application. After creation, the code (.m) and figure (.fig) files for each GUI were jointly compiled into a single executable file using the deploytool application. Executable MATLAB files may be run using the MATLAB Compiler Runtime (MCR), which is also supplied with this software package.

A few rules apply generally when working with these MATLAB GUIs:

- Close Excel® spreadsheets before attempting to run a GUI that will write data to those spreadsheets. It is not necessary to close Excel spreadsheets that the GUI will read data from.
- Close all MATLAB figure windows created by a GUI before rerunning that GUI or any GUI that produces a figure. It is not necessary to close the GUI figure window itself before rerunning the GUI.
- Push enter after typing new data into a GUI text box. This ensures that the GUI reads the new data value and resets the corresponding variable.

MATLAB Compiler Runtime (MCR)

Prior to attempting to use any of the GUIs the user should install the MCR. Even if the user has MATLAB installed it is best to install the MCR supplied with this package. This is because the MCR corresponds to the version of MATLAB (including any additional toolboxes) that was used to create the provided GUIs. If the user already has another version of the MCR installed, it is still suggested to separately install the provided MCR version, or to verify that the installed version is the same version as the provided MCR. Multiple MCR versions may be simultaneously installed on a single computer. The GUIs have had their paths modified to access the MCR even if MATLAB is installed on the computer. Once the MCR is installed, to run a GUI the user simply clicks on the application file (.exe) icon in the relevant sub-package folder.

Aging Model Graphical User Interface Sub-Package

The aging model graphical user interface sub-package includes the following components:

1. The executable application file: AMG.exe.
2. The original MATLAB files that were compiled to produce the executable file: AMG.m and AMG.fig. These file are not needed for the use of the software package but are provided in case the user would like to read the details of the code and/or modify the code. Use of these files requires MATLAB software.
3. A folder containing several temperature profiles for locations in Texas. Each temperature profile is located in a different Excel workbook. The profiles are in the format required for input into the AMG. If one of the provided profiles is for a location close to the location of interest for aging simulation, then that profile may be used directly in the AMG. On the other hand, if none of the profiles provided are for a location close to the location of interest, then the TPG may be used to develop a new temperature profile for a pavement in the location of interest.

Reaction Kinetics Parameters GUI Sub-Package

The reaction kinetics parameters graphical user interface sub-package includes the following components:

1. The executable application file: RKPG.exe.
2. The original MATLAB files that were compiled to produce the executable file: RKPG.m and RKPG.fig. These file are not needed for the use of the software package, but are providing in case the user would like to read the details of the code and/or modify the code. Use of these files requires MATLAB software.
3. An example Excel workbook: ExperimentalResults.xls. This workbook has two sheets. The first sheet, "POV," contains example POV experimental results in the format required for input into the RKPG. The second sheet, "PAV," contains example PAV experimental results in the format required for input into the RKPG. Refer to the third major section of this chapter for more detail.

Temperature Profile GUI Sub-Package

The temperature profile graphical user interface sub-package includes the following components:

1. The executable application file: TPG.exe.
2. The original MATLAB files that were compiled to produce the executable file: TPG.m and TPG.fig. These file are not needed for the use of the software package but are provided in case the user would like to read the details of the code and/or modify the code. Use of these files requires MATLAB software.
3. An example Excel workbook: DataAndResults.xls. This workbook has seven sheets. The sheets are developed when following the procedures suggested for use of the TPG. An

outline of the sheets is provided here and more detail is provided in the fourth major section of this chapter.

a. "Processed" This sheet contains the pre-processed solar radiation, wind speed, and air temperature data. These data are obtained from specified internet sites, and some pre-processing is required prior to using the data as input to the TPG. This page shows the pre-processed form required by the TPG.
b. "NSRD Raw" This sheet contains raw environmental data as obtained from the National Solar Radiation Database website. Hourly solar radiation and ground albedo (not pavement albedo) are obtained from this sheet.
c. "NCDC Raw" This sheet contains raw environmental data obtained from the National Climatic Data Center website. The hourly wind speed and hourly air temperature are obtained from this sheet.
d. "NCDC Time Slotted" This sheet is used to process the time column data taken from NCDC Raw sheet. The processed form is then pasted into the Processed sheet.
e. "Summer" This sheet contains the output from the TPG when summer values are used for certain input variables.
f. "Winter" This sheet contains the output from the TPG when winter values are used for certain input variables.
g. "Final" This sheet contains portions of the data from the Summer and Winter sheets, which are appropriately combined. The data in this sheet are the final pavement temperature profile and may be used as an input to the AMG.

USING THE AGING MODEL GRAPHICAL USER INTERFACE (AMG)

Introduction

The aging model graphical user interface may be used to simulate field aging in pavements. Inputs to the AMG include properties of the binder, properties of the compacted mixture, and pavement temperature. The primary output from the AMG is binder carbonyl area as a function of time. If DSR function hardening susceptibility data are available the AMG may also be used to predict DSR function values. The AMG is based on the modeling work described in Chapters 7–9 , with emphasis on the work described in Chapter 9 (Prapaitrakul et al., 2009; Han, 2011; Jin et al., 2011).

The AMG is the primary graphical user interface in this software package. The two supporting graphical user interfaces, the RKPG and the TPG, are described in the third and fourth major sections of this chapter, respectively. These supporting GUIs are intended to help the user obtain the inputs required by the AMG. If the user already has the required inputs from another source, there is no need to use the supporting GUIs.

The AMG is based on a numerical solution to the partial differential equation describing conservation of oxygen through the diffusion depth in the binder. The equation is shown below. With the oxygen concentration in the binder known, it is possible to find the reaction rate, and ultimately the carbonyl increase. The details of this model may be found in Chapter 9:

$$\frac{\partial P(x,t)}{\partial t} = \frac{\partial}{\partial x}\left(\text{fcf} \cdot D_0 \frac{\partial P}{\partial x}\right) - \frac{c}{h} \cdot \frac{\partial \text{CA}(x,t)}{\partial t}$$

where P is the oxygen partial pressure that would be in equilibrium with the oxygen concentration in the binder under the given conditions, t is the time, x is the distance in to the diffusion depth, fcf is a field Calibration factor, D_o is the oxygen diffusivity in asphalt, c is the relation between CA production and oxygen consumption, and h is henry's constant for oxygen dissolving into the binder.

An image of the AMG is shown below in Figure 148. The required inputs and the GUI outputs are described in the sections that follow.

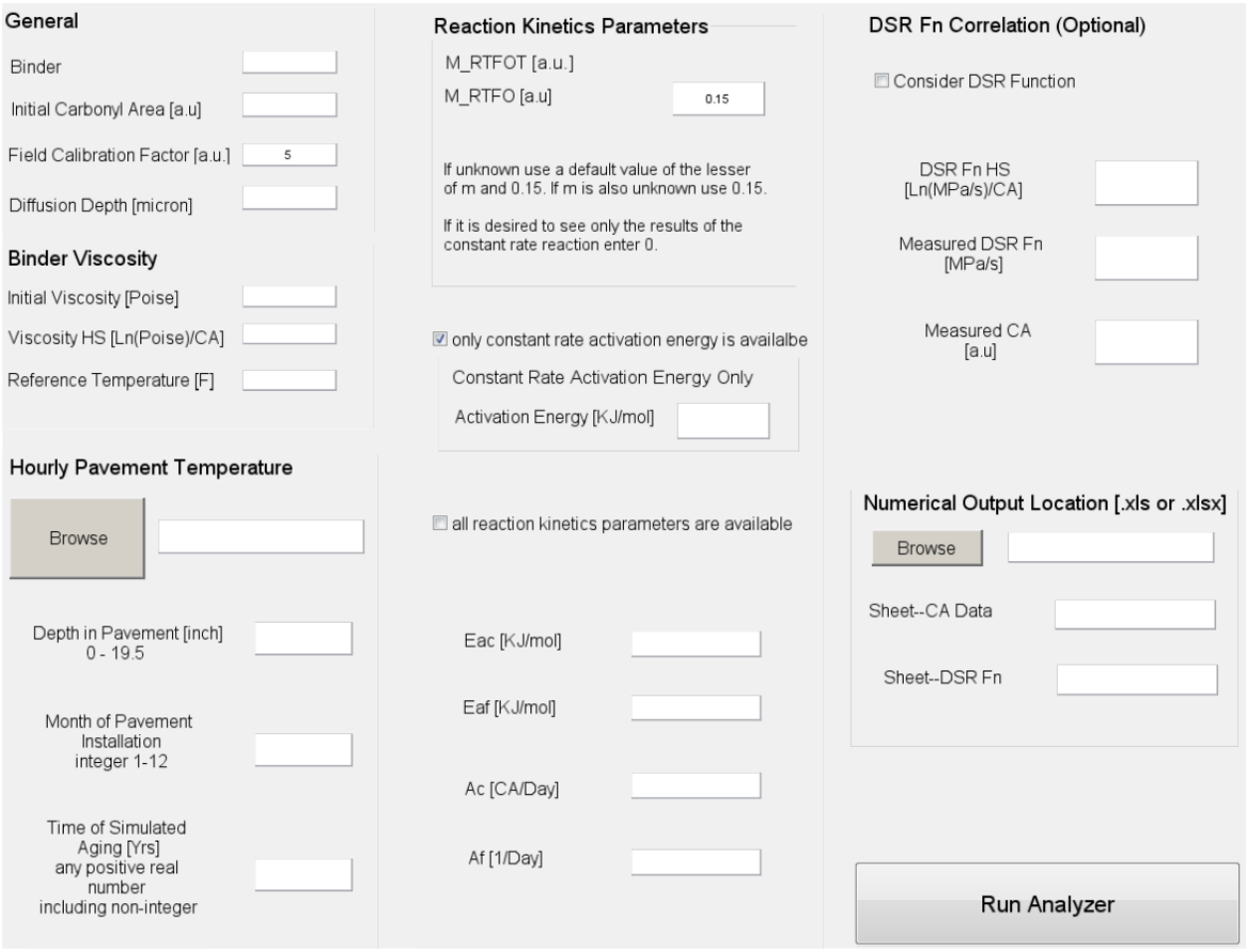


Figure 148. Image of Aging Model Graphical User Interface (AMG).

Inputs

The AMG requires five categories of inputs: general, binder viscosity, hourly pavement temperature, reaction kinetics parameters, and numerical output location. The inputs for each of these categories are grouped together in individual panels within the AMG. Each required input is described below under its respective panel heading.

General Panel

The general input panel is located in the top left of the AMGUI, and specific inputs include: binder type [arb. unit], initial carbonyl area [arb. unit], field calibration factor (fcf) [dimensionless], and Diffusion Depth [μm].

Binder Type. The binder type is simply an identifier for the binder. The user may type any identifier or leave the input box empty.

Initial Carbonyl Area. The initial carbonyl area is the carbonyl area in the binder just after the pavement has been installed. This level of aging is typically approximated by the thin film oven test or the rolling thin film oven test. CA is reported in arbitrary units (i.e., unitless). This CA level is different from the tank CA, which is the level in the binder prior to any aging associated with mixing of the binder with aggregate to form the asphalt mixture.

Field Calibration Factor. The field calibration factor is a scalar with arbitrary units (i.e., unitless) that is intended to adjust the calculated value of oxygen diffusivity in the binder. This factor is mixture dependent and can only be found by comparing the model results with actual field measurements, and then adjusting the fcf so that the model matches the field measurements. The fcf may be greater than or less than unity. If field aged cores are not available for determination of the fcf, then two alternate methods for determining the fcf are suggested below.

Diffusion Depth Known, but fcf Unknown. A default value of 5 [dimensionless] for the fcf is suggested if the diffusion depth is known and there are no field cores that can be used to determine the fcf.

Neither fcf nor Diffusion Depth Known. If neither the fcf nor the diffusion depth is known, then it is suggested to use a default value of unity for the fcf and estimate the diffusion depth as suggested below.

Diffusion Depth (d_D). The diffusion depth [μm] is defined as the volume of asphalt in the mix divided by the surface area of the accessible air voids. It is suggested that this determination be made on a layer-by-layer basis, with each layer approximately 10 mm thick. Determination of the surface area of the accessible air voids requires X-ray CT images of representative cores. Additionally, the images must be processed using image processing software. The methods are more thoroughly described in Chapter 9.

Estimation of Diffusion Depth from Film Thickness. If it is not possible to measure the d_D using the methods described in above, the diffusion depth may be estimated from the film thickness. The film thickness referred to here is the parameter commonly used to describe HMA. It refers to the theoretical thickness of the asphalt film that would result if the asphalt where uniformly spread over the entire aggregate surface area. To estimate the d_D, use the formula below and also set the fcf value in the AMG to unity.

$$d_D[\mu m] = (\text{film thickness } [\mu m]) \cdot 250$$
set: fcf = 1

Binder Viscosity Panel

The binder viscosity panel is located directly below the general input panel. The required inputs include: initial viscosity [Poise], viscosity hardening susceptibility (HS) [1/CA], and reference temperature [°F].

Initial Viscosity. The initial viscosity is the low sheer rate limiting viscosity measured at the reference temperature and reported in units of Poise [Poise].

Viscosity HS. The viscosity hardening susceptibility relates the natural log of the low sheer rate limiting viscosity (LSV) (measured at the reference temperature) to the carbonyl area:

$$\ln(LSV) = HS \cdot CA + m$$

where *m* is the theoretical natural log of viscosity when CA equals zero. The form of the HS is $[\text{Ln}(\text{Poise}_2/\text{Poise}_1)/(\text{CA}_2\text{-CA}_1)]$. Note that if LSV is reported in Pa·s, and the HS is calculated as the slope relating ln(LSV) to CA, then the numerical value of the HS will be the same as if the LSV had been in units of Poise.

Reference Temperature. The reference temperature is the temperature at which the low sheer rate limiting viscosity is measured. This measurement is typically made using a dynamic sheer viscometer (DSR) instrument. The measurement temperature set on this instrument while making the viscosity measurement is the reference temperature. The temperature should be reported in degrees Fahrenheit [°F].

Hourly Pavement Temperature Panel

The hourly pavement temperature panel is located directly below the binder viscosity panel. The required inputs are: the pavement temperature array [°C], the depth in pavement [inch], the month of installation [1-12], and the time period of simulated aging [Yrs].

Pavement Temperature Profile. The pavement temperature profile represents the pavement temperature throughout a representative year, as a function of depth and time. Using the browse button the user can select the Excel file containing the pavement temperature profile. The temperature profile must be contained in the first worksheet in the Excel workbook. The data should begin in the top left cell of the worksheet, and no additional information, such as headings, may be present in the worksheet. The temperature profile values must be in degrees C.

A temperature profile may be obtained using the TPG, described in the fourth major section of this chapter, below. That section includes a detailed explanation of the profile. A brief description is presented here. Each row of the profile represents an hour of the year, with the first row representing the first hour of the year, and the last row representing the last hour of the year. Each column represents a one-half inch difference in pavement depth. The first column represents the surface; the second column represents one-half inch below the surface, and so on. In a profile produced using the TPG there are 40 columns, representing 19.5 inches of depth below the surface. Despite this profile, the AMG will function with any number of columns so

long as sufficient columns are present to reach the simulated pavement depth entered in the AMG.

The description above is the expected form of the temperature profile input, but the AMG can process input of a different form. The caveat is that the user must carefully interpret the results if a different form of input is used. The AMG will function so long as it finds temperature values in the column specified. Recall that each column represents one-half inch of pavement depth; this means that by setting the pavement depth the user is really specifying a column of the temperature profile. For example, if the user only has a single column of temperatures, these may be used by setting the Depth in Pavement to 0. Likewise, the total number of rows need not be equal to the number of hours in a year, but the output will need to be interpreted accordingly. The number of rows will be treated as the number of hours in a year. If, for example, only 100 rows are present in the profile, the program will define a year as having 100 hours. Therefore, if 5 years is input as the simulated aging time, the actual simulated aging will only be 500 hours. Likewise, the effect of the month of installation parameter will be different. One month will be interpreted at $1/12^{th}$ of 100 hours.

Depth in Pavement. The depth in pavement parameter is the depth at which the user would like to simulate the aging. The depth should be entered in units of inches [inch]. Assuming the temperature profile is obtained using the TPG, the user may input a depth between 0 and 19.5 inches below the pavement surface. The AMG rounds the user input down to the nearest half inch. If the temperature profile is not obtained by using TPG, the user is referred to the section directly above for a description of the effects of non-typical temperature profile inputs.

The depth in pavement parameter is included in the Hourly Pavement Temperature Panel because it is the depth below the surface that controls the column of the temperature array used in the simulation. Beyond this, the depth in the pavement also controls the diffusion depth, when the diffusion depth is calculated layer by layer, but the diffusion depth has been placed in the general parameters panel. This is because the method of calculating the diffusion depth is at the discretion of the user, and is not controlled by the AMG.

Month of Installation. The month of installation is the month the road was physically placed. The program assumes the pavement was installed on the first day of the month. Therefore, if 1 is entered the program will assume the pavement was installed at the beginning of the year. It will then use the temperature profile exactly as provided. Alternatively if, for example, the number 7 is entered, the program will rearrange relevant column of the temperature profile so that the representative year begins in July.

Time of Simulated Aging. The user must designate the duration of the simulated aging in units of years [Yrs]. The AMG will replicate the relevant portion of the temperature profile as needed. Any positive number may be entered.

Limitations: Computation Time. On a personal computer, a 10 year aging simulation will take approximately 10–15 minutes to run. Longer simulations will require proportionally longer running times.

Limitations: Numerical Output. If the simulated aging time is greater than approximately 7.4 years (65,000 hrs), the output will be limited to a graphical form.

Reaction Kinetics Parameters Panel

The reaction kinetics parameters panel is located in the middle of the AMG. The user must input an M_{RTFOT} value [arb. unit] and a constant rate activation energy value [KJ/mol]. If the user enters an activation energy in the "Constant Rate Activation Energy Only" subpanel, the AMG will calculate estimated values for the additional reaction kinetics parameters. Alternatively, the user may choose to enter a full set of reaction kinetics parameters if they are available. All of these parameters are briefly discussed below. For more detail the reader is referred to the third major section of the chapter: *Using the Reaction Kinetics Parameters Graphical User Interface*.

M_{RTFOT} Subpanel. In general the M value represents the amount of CA that can be produced by the "fast-rate" reaction in the binder. The M value, as opposed to the M_{RTFOT} value, represents the total amount of CA that can be produced by unaged binder from the fast-rate reaction. During the asphalt mixing and installation processes some binder aging occurs. After this binder aging, a reduced portion of M remains because a portion of the fast-rate reactants has already been reacted. The amount of aging that occurs during the mixing and installation processes is approximated by the rolling thin film oven test. Therefore, the M_{RTFOT} value represents that amount of CA that can still be produced by the fast-rate reactants after the pavement installation. The units of the M_{RTFOT} value are arbitrary units, the same as CA.

Typically, the M_{RTFOT} value must be found by optimization using field cores. For more detail see Chapter 9. If the M_{RTFOT} value is not known, it is suggested that the lesser of 0.15 and the M value be used. The M value may be determined from POV testing as described in the third major section of the chapter, below. If neither the M_{RTFOT} value nor the M value is known, it is suggested that a value of 0.15 be used for the M_{RTFOT} value.

If the user would like to simulate aging with only the constant rate reaction occurring (ignoring the fast-rate reaction), then a value of zero should be entered for the M_{RTFOT} value.

Constant Rate Activation Energy Only Subpanel. If the user has the constant rate activation energy but does not have a full set of reaction kinetics parameters then the user should check the "only constant rate activation energy is available" box. The constant rate activation energy should be entered in units of kilojoules per mole [KJ/mol]. When the user enters the constant rate activation energy in this subpanel the AMG automatically estimates the remaining reaction kinetics parameters.

The constant rate activation energy is the activation energy obtained from aging at atmospheric pressure. If PAV aging at 20 atmospheres air is conducted the user is directed to use the RKPG to obtain an estimate of the atmospheric pressure constant rate activation energy.

Full Set of Reaction Kinetics Parameters Subpanel. If the user has a full set of reaction kinetics parameters, then the user should check the "all reaction kinetics parameters are

available" checkbox. The "Full Set of Reaction Kinetics Parameters" subpanel will become visible. The parameters required are: constant rate activation energy [KJ/mol], fast rate activation energy [KJ/mol], constant rate pre-exponential factor [CA/Day], and fast rate pre-exponential factor [1/Day]. Each of these parameters is described briefly below, but a more detailed explanation can be found in the third major section of this chapter under "Reaction Kinetics Parameters from Full POV Lab Testing."

Constant Rate Activation Energy. The constant rate activation energy should be entered in units of kilojoules per mole [KJ/mol]. The constant rate activation energy refers to the activation energy obtained from atmospheric pressure aging.

Fast-Rate Activation Energy. The fast rate activation energy should be entered in units of kilojoules per mole [KJ/mol]. The fast rate activation energy refers to the fast rate activation energy obtained from atmospheric pressure aging.

Constant Rate Pre-exponential Factor. The constant rate pre-exponential factor should be entered in units of CA per day [CA/Day]. The constant rate pre-exponential factor refers to the constant rate pre-exponential factor obtained from atmospheric pressure aging. The AMG obtains the more general constant rate pre-exponential factor by dividing by $0.2^{0.27}$, where 0.2 is the partial pressure of oxygen in air and 0.27 is the order of the reaction with respect to oxygen.

Fast Rate Pre-exponential Factor. The fast rate pre-exponential factor should be entered in units of 1 over day [1/Day]. The fast rate pre-exponential factor refers to the fast rate pre-exponential factor obtained from atmospheric pressure aging. The AMG obtains the more general fast rate pre-exponential factor by dividing by $0.2^{0.27}$, where 0.2 is the partial pressure of oxygen in air, and 0.27 is the order of the reaction with respect to oxygen.

DSR Fn Correlation (Optional) Panel

The DSR Fn Correlation panel is located in the top right of the AMG. The DSR Fn can be correlated with the carbonyl content of the binder. The inputs required include the binder specific data needed to correlate DSR Fn with carbonyl area, see below. If these inputs are supplied the AMG can be used to predict DSR function increase with time.

Consider DSR Function. If the user selects the "Consider DSR Function" checkbox the "DSR Function" panel will become visible. If the user does not have the requested input, then the box should be unchecked to avoid an error. The DSR Function panel requires three inputs: (1) DSR Function Hardening Susceptibility, (2) Measured DSR Function, and (3) Measured Carbonyl.

The DSR Function may be correlated to the carbonyl content as follows:

$$\ln(DSR\ Fn) = (DSR\ Fn\ HS) \cdot CA + \ln(m_{DSR})$$

The DSR Fn HS relates the natural log of the DSR Fn to the carbonyl area. The Measured DSR Fn and Measured CA represent a point on this correlation line, therefore the meaning of

measured here is that both are measured on the same sample of binder. The units of the measured DSR Fn value should be mega-pascals per second [MPa/s]. The units of the measured CA value are arbitrary [arb. unit]. The form of the DSR fn HS is ln(MPa/s)/CA. For more information about the DSR Function see Ruan et al. (2003), Juristyarini et al. (2011a), and Juristyarini et al. (2011b).

Numerical Output Location Panel

The numerical output location panel is located on the bottom right of the AMG. The user must specify an Excel workbook into which the AMG may write the numerical output. Additionally, the user must specify one sheet into which to write the CA output, and a second sheet into which to write the DSR Function output.

Excel Output File. The user may use the browse button to select an Excel file into which the AMG will write the numerical output. Alternatively, the user may type the path and filename directly in the edit box to the right of the browse button. If the browse button is used and a selection is made, the path and file name will appear in the edit box to the right of the browse button.

Sheet—CA Data. The user must type the name of the sheet within the selected Excel workbook into which the AMG should write the CA data. The specified sheet should be blank. If the specified sheet does not exist in the workbook, the AMG will create a new sheet within the workbook that has the name of the specified sheet.

Sheet—DSR Fn Data. The user must type the name of the sheet within the selected Excel workbook into which the AMG should write the DSR Fn data. The specified sheet should be blank. If the specified sheet does not exist in the workbook, the AMG will create a new sheet within the workbook that has the name of the specified sheet.

Outputs

The AMG numerically solves the partial differential equation for oxygen partial pressure presented in the introduction of this section. The oxygen partial pressure is a function of time and depth, where depth is the diffusion depth, not the depth in the pavement. As part of the solution path, it is simultaneously possible to calculate CA as a function of time and depth. The calculated CA values are averaged over the diffusion depth for each time reported. The resulting primary output from the AMG is CA vs. time. CA is reported in arbitrary units [arb. unit], and the time is reported in hrs or hrs$\cdot 10^4$. The results are provided graphically and numerically.

Graphical Output

After the user presses the "Run Analyzer" button, a graphical display of the primary results will pop up in a new figure window on the screen. This figure, labeled Figure 2 in the AMG software output display, shows CA vs. time. In addition, a second figure window, labeled Figure 2 in the software display, shows DSR function vs. time as a semilog plot if the DSR function option was selected.

Carbonyl Area vs. Time. This figure window will pop up every time the analyzer is run. The graph displays carbonyl area vs. time. Carbonyl area is shown in arbitrary units [arb. unit], and time is shown in units of $hr \cdot 10^4$. An example result for a two-year aging simulation is shown in Figure 149. This example resulted from the use of the following example values and inputs: initial CA 0.8, fcf 5, d_D 800, initial viscosity 10000, viscosity HS 8, reference temp. 140, El Paso temperature profile (from database), depth in pavement 0.5 inches, month of installation 1, the time of simulated aging 2, M_{RTFOT} 0.15, and constant rate activation energy 80.

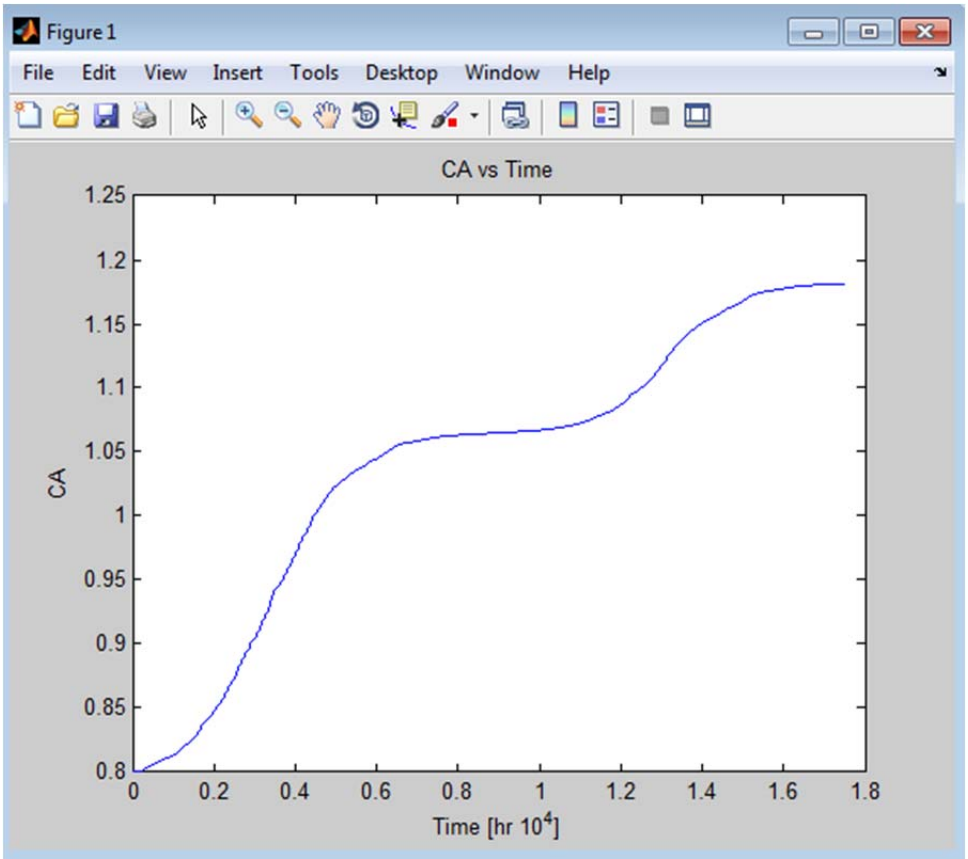


Figure 149. Image of CA vs. Time Pop up Window Graphical Result.

The trends shown in this graph are characteristic of asphalt aging. Each year will typically have periods of slower and faster CA increase. The slower periods result from cooler temperatures during the cooler seasons and the faster periods result from warmer temperatures during the warmer seasons. Additionally, aging will generally be faster in younger pavements. One reason for this is because as carbonyl levels increase oxygen diffusivity decreases. Therefore, initially the oxygen diffusivity is relatively high allowing oxygen to quickly diffuse into the binder.

DSR Fn vs. Time. If the user selected the check box "Consider DSR Function" and supplied the necessary inputs, then a second figure window showing the DSR Function vs. Time on a semilog plot will be displayed. The DSR function is in units of mega-pascals per second [MPa/s]. Time is in units of hours multiplied by ten to the fourth power [$hr \cdot 10^4$]. A sample figure is shown in Figure 150. This example resulted from the same numerical inputs used to produce

Figure 149. The following additional inputs were used: DSR HS 9, Measured DSR Function 0.0001 MPa/s, and measured carbonyl 0.8.

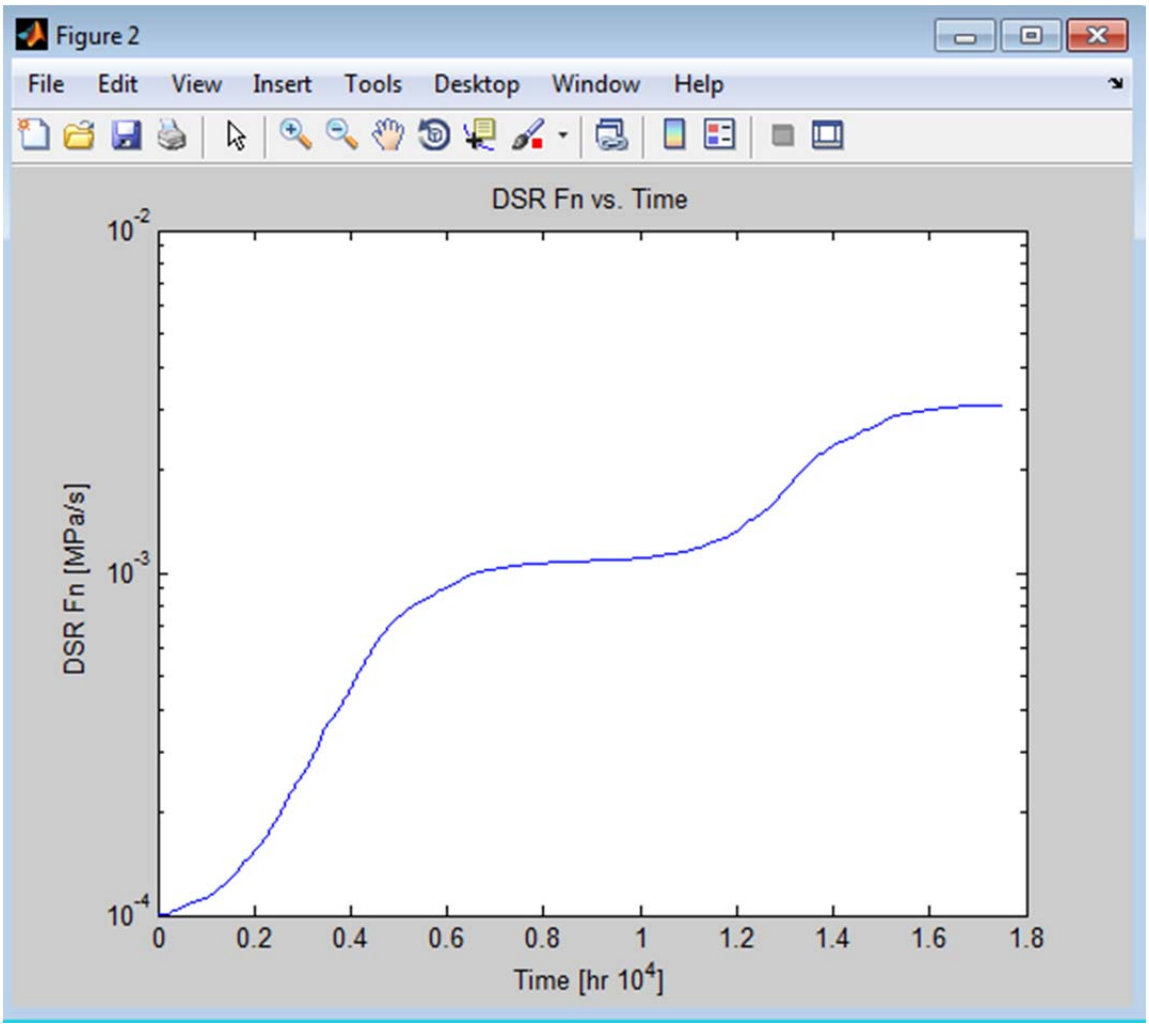


Figure 150. Image of DSR Fn vs. Time Pop up Window Graphical Result.

The natural log of the DSR function is linearly related to the CA content. Therefore, when DSR function is plotted on a semilog plot with time as the independent variable, the shape of the plot will be similar to the shape of a plot of CA vs. time as shown in Figure 149.

Numerical Output

In addition to the graphical results described above, the AMG also writes the numerical results to an Excel workbook if the simulated aging time is less than approximately 7.4 years. The Excel workbook is the one specified using the browse button in the Numerical Output Location Panel of the AMG.

The primary numerical output is CA vs. time data. This numerical output will be in the form of two columns. The first column will be the simulated aging time, and the second column will be the corresponding CA value. This numerical output is the same data that is presented

graphically in the first pop up window described above. The two columns of data will be written to the sheet of the Excel workbook specified in the Numerical Output Location Panel.

If the user selected the check box "Consider DSR Function" then a second set of numerical data will be written to a second sheet of the same Excel workbook. The numerical output will again be in the form of two columns. The first column will be time, and the second column will be the corresponding DSR function values. These data are the same data that are presented graphically in the second pop up window. The two columns of data will be written to the sheet of the Excel workbook specified in the Numerical Output Location Panel.

USING THE REACTION KINETICS PARAMETERS GRAPHICAL USER INTERFACE

Introduction

The aging model graphical user interface requires reaction kinetics parameters as inputs. In addition to the M_{RTFOT} value, at least the constant rate activation energy (E_{ac}) must be supplied. If only the M_{RTFOT} and E_{ac} values are available, the AMG will estimate the additional reaction kinetics parameters. Alternatively, the user may directly enter the full set of reaction kinetics parameters if available. Depending on the experimental results available, either the E_{ac} value or the full set of reaction kinetics parameters may be determined using the Reaction Kinetics Parameters Graphical User Interface. The RKPG is based on the kinetics work described in Chapter 3, (Jin et al., 2011), and on the work described in Chapter 14.

The model CA growth curve for carbonyl area increase with time is shown below:

$$CA = CA_t + M\left(1 - e^{-k_f t}\right) + k_c t$$

$$k_f = A_f e^{\frac{-E_{af}}{RT}}$$

$$k_c = A_c e^{\frac{-E_{ac}}{RT}}$$

where the fundamental reaction kinetics parameters are: the fast rate pre-exponential factor, A_f [1/Day]; the constant rate pre-exponential factor, A_c [CA/Day]; the constant rate activation energy, E_{ac} [KJ/mole]; and fast rate activation energy, E_{af} [KJ/mol]. The total amount of carbonyl area increase due to the fast rate reaction is M and is determined from the difference between CA_0 and CA_t. CA_0 is the intercept the of the constant rate portion of the growth curve, and CA_t is the CA level in of the asphalt "in the tank" prior to any aging. In the AMG model it is suggested to use an M Rolling Thin Film Oven Test (M_{RTFOT} and RTFOT) value rather than an M value, because actual pavement is aged during the mixing and compaction processes, and this level of aging is approximated by the RTFOT. The M_{RTFOT} value may be chosen as the lesser of 0.15 and the M value commuted by the RKPG if an optimized value of M_{RTFOT} is not available. Similar reasoning to that discussed for the M value applies to the other reaction kinetics parameters as well, but the values provided by the RKPG model are sufficiently accurate for use in the AMG.

Reaction kinetics parameters may be determined using either the pressure oxidation vessel or the pressure aging vessel. In this work POV testing refers to the aging of asphalt films at atmospheric pressure and at least two different temperatures. Four to five temperatures are suggested (e.g., 140°F, 160°F, 180°F, 190°F, and 200°F). PAV testing refers to aging of asphalt

films at 20 atmospheres of air and two temperatures, 90°C and 100°C. For more complete details see Chapters 3 and 14. After aging with either test method, CA levels are measured using FTIR. The results may be processed to yield the reaction kinetics parameters using the RKPG, as described below.

The RKPG is shown below in Figure 151. The upper panel, "Rxn Kinetics Parameters from POV [1 atm air] Data," allows the user to input POV testing results and calculates a full set of reaction kinetics parameters. The lower panel, "Estimated POV [1 atm air] Constant Rate Activation Energy From PAV [20 atm air] Data and Correlation," allows the user to input results from PAV testing and calculates an estimate of the constant rate activation energy at 1 atm.

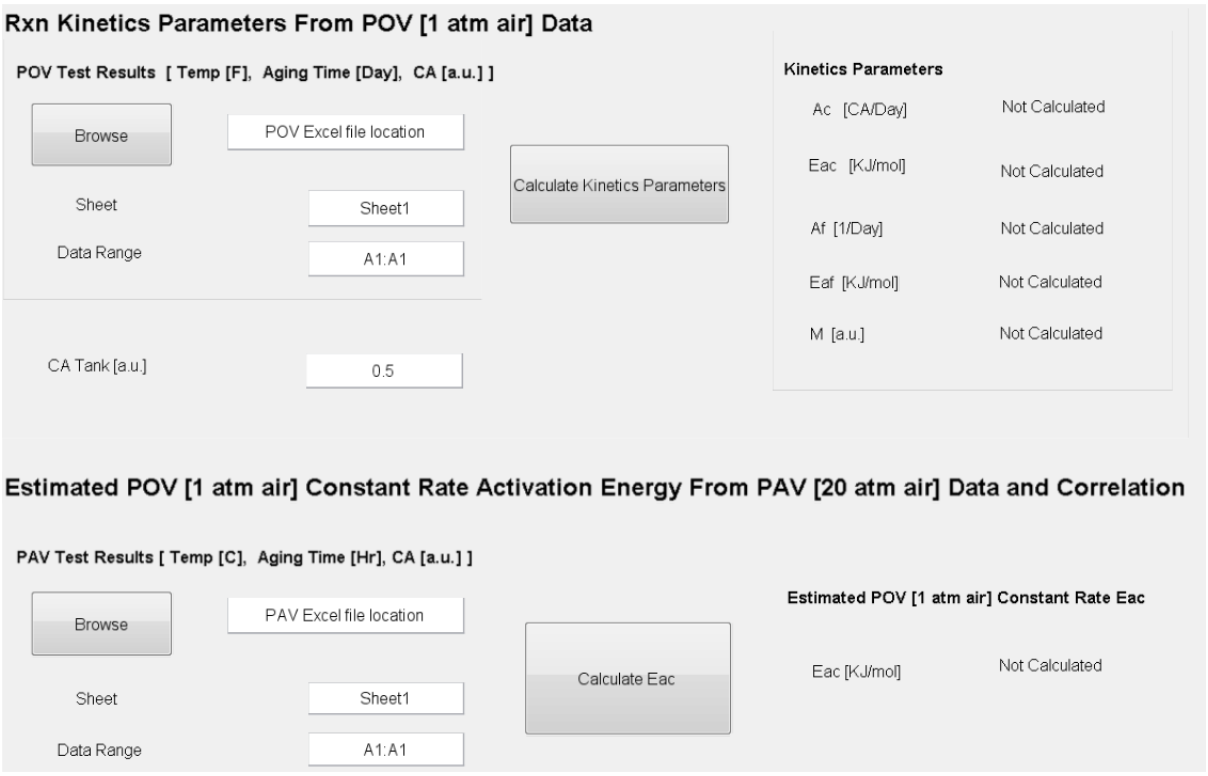


Figure 151. Reactions Kinetics Parameters Graphical User Interface.

Reaction Kinetics Parameters from Full POV Lab Testing

The upper panel, "Rxn Kinetics Parameters From POV [1 atm air] Data," should be used when experimental results from POV testing are available. The inputs include the experimental results and the initial carbonyl area of the asphalt. The required form for the experimental results is described below. The output includes a full set of reaction kinetics parameters and a graphical display of the optimized model fit to the data.

Inputs

The location of the POV testing results must be specified. The browse button may be used to specify the location of an Excel Workbook containing the POV testing results. The location of the data within the Excel workbook must be specified by entering the worksheet and

data range in the corresponding text boxes. The required format of the data is described below. Additionally, an example Excel workbook, which shows the required format, is provided with the Reaction Kinetics Parameters GUI sub-package. The example workbook is named ExperimentalResults.xls. For the example workbook, the specific sheet containing the POV data is named "POV Input," and the data range is "C2:E34."

The POV testing results must be contained in the Excel workbook and appropriately formatted. The results should be stored in three adjacent columns in a single worksheet. The first column should list the temperature in degrees Fahrenheit [°F], the second column should list the aging time in days [Day], and the third column should list the average carbonyl area [arb. unit] for duplicate binder films aged under the corresponding temperature and time conditions. The aging temperatures should be grouped together and should start from the lowest temperature and increase to the highest temperature. The total number of aging temperature must be at least 2 and no more than 5. The number of aging times per aging temperature must be at least 2 and is not limited.

After specifying the location of the POV data, the user should click the button "Calculate Kinetics Parameters."

Visual Aging Results Review and Visual Estimate of the Beginning of the Constant Rate Period

After pressing the "Calculate Kinetics Parameters" button, two new figure windows will pop up on the screen. An example of the larger window labeled "Results from Aging Experiments" is shown below in Figure 152. This figure was obtained by using the data in the example Excel workbook provided. This figure shows separate graphs of CA versus aging time for each aging temperature. The total number of graphs depends on the number of aging temperatures in the input data. The first graph will be labeled POV # 1 with the corresponding temperature, the second POV # 2 with the corresponding temperature, and so on. The smaller figure is labeled "Visual Determination of Data to Include and Beginning of Constant Rate Period" and is shown in Figure 153 below. This figure is for user input. The input required is described below.

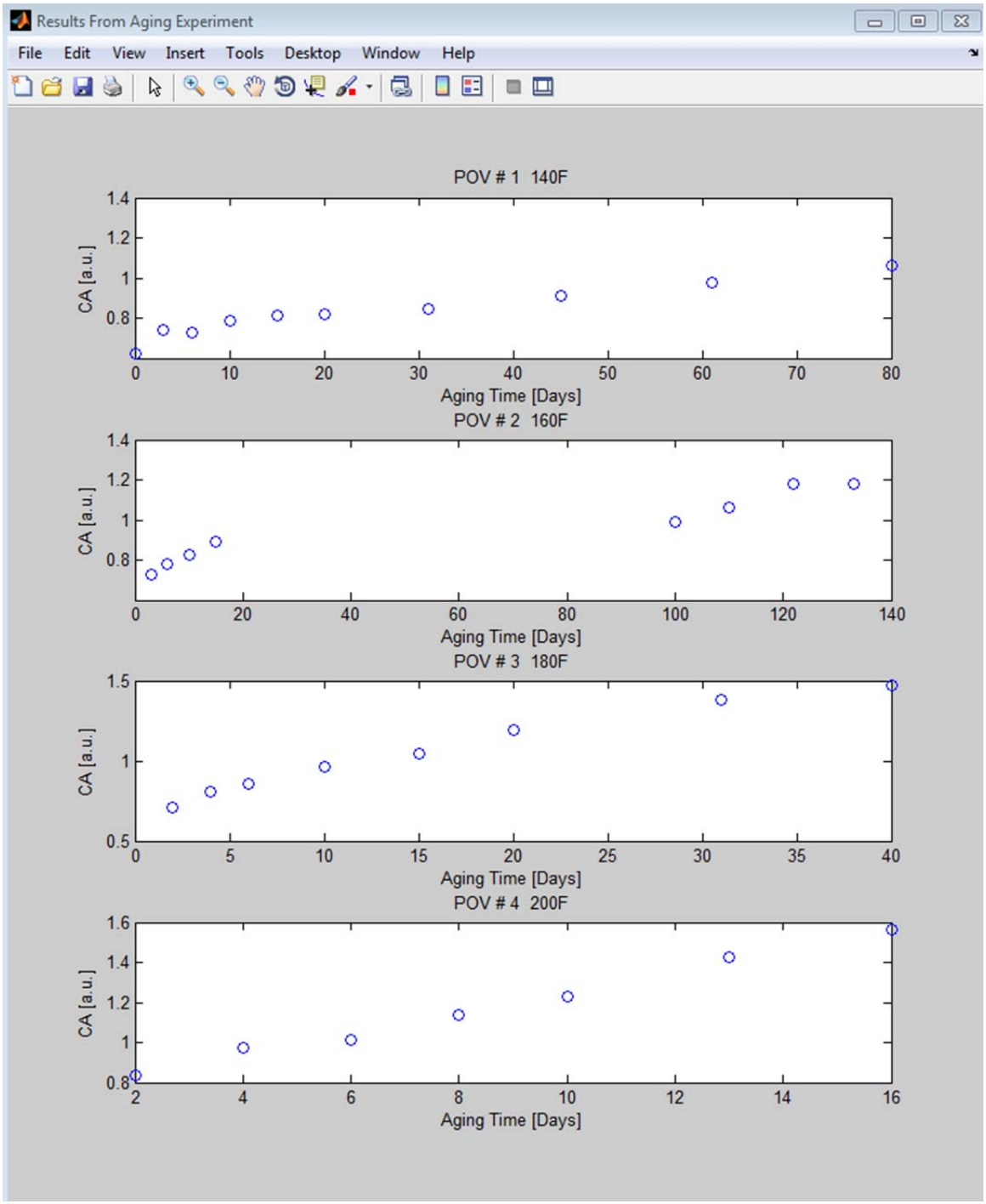


Figure 152. Results from Aging Experiment Window.

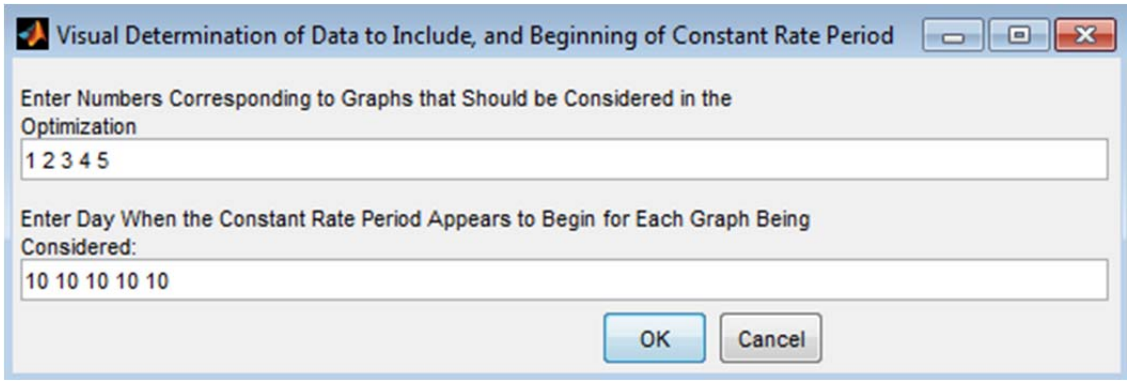


Figure 153. Window for Visual Determination of Which Data Should Be Considered in the Optimization and the Apparent Beginning of the Constant Rate Period.

Referring to the pop up user input box, the first section asks the user to "Enter Numbers Corresponding to Graphs that Should be Considered in the Optimization." The graphs referred to are the individual graphs in the larger figure "Results From Aging Experiment." The default entry is "1 2 3 4 5." Retaining this entry and clicking "OK" tells the RKPG to consider the results in graphs one through five. In the example above, only four graphs are shown; therefore at most the user may enter "1 2 3 4." Ideally, all of the data will be included in the optimization calculations, but sometimes from the graphical results it is apparent that some portion of the data should not be included. Any graph displaying bad data should be excluded from the optimization.

In the example above, it appears that the data from POV # 2 may not be good. Several aging tray results seem to be missing from the middle aging period. The values reported for aging times at and beyond 100 days appear excessively low. In this case the user may choose to enter "1 3 4." If this choice is made the optimization process will use the data from POVs #1, #3, and #4, but will not use the data from POV #2. The final plot (described below) will still show the results from POV #2 and the model fit. The user always has the option to rerun the RKPG after seeing the final fit of the model to the data. This procedure may be useful to determine if the best fit is obtained by rejecting or retaining the data from a particular POV.

Still referring to the user input box, the second section asks the user to "Enter Day When the Constant Rate Period Appears to Begin for Each Graph Being Considered." The default entry is "10 10 10 10 10." This entry corresponds to a situation where data from five aging temperatures were provided, and the constant rate period for each graph appears to begin on the 10^{th} day of aging. To select the beginning of the constant rate period the user must look at an individual graph and make a visual determination of the day when the data appear to begin to fall on a line.

Consider the constant rate determinations based on the results shown in Figure 152 In the graph POV # 1 140°F above, it appears that the constant rate period may begin around day 20. The second graph should be ignored in this example, because the data were excluded from consideration. For the third graph, the constant rate period appears to begin around day 5. For the final graph the rate appears almost constant over the entire period, so day 2 may be selected. Based on these choices, the user should input "20 5 2" in the second box.

The calculated constant rates, based on the visual determinations, are used by the RKPG to make an initial guess during the optimization calculations. If it is not clear where the constant rate period begins, it is suggested that the user run the RKPG several times making different choices and looking for the best fit in the final graph. Although the choices are only used to calculate a guess, it is possible that the optimization process will find a local minimum rather than a global minimum based on the guess. Ultimately, as long as the final fit appears reasonable, the reactions kinetics parameters determined will be satisfactory for input into the AMG.

Once the user has completed the visual determinations and entered the results, the "OK" button should be clicked. The outputs are described below.

Outputs

After the user clicks the "OK" button as described above: (1) constant rate lines will be drawn on the graphs in the "Results From Aging Experiments" window, (2) a model fit figure window called "Original Data and Optimized Model Shown Together" will appear, and (3) the calculated reaction kinetics parameter results will replace the corresponding "Not Calculated" text in the RKPG. The graphical output section below describes numbers (1) and (2), with (2) being described first. A numerical output section describing (3) follows the graphical output section.

Graphical Output. The "Original Data and Optimized Model Shown Together" window shows the original data and the optimized model on a single graph. The resulting figure from the example POV aging test discussed above is shown below in Figure 154.

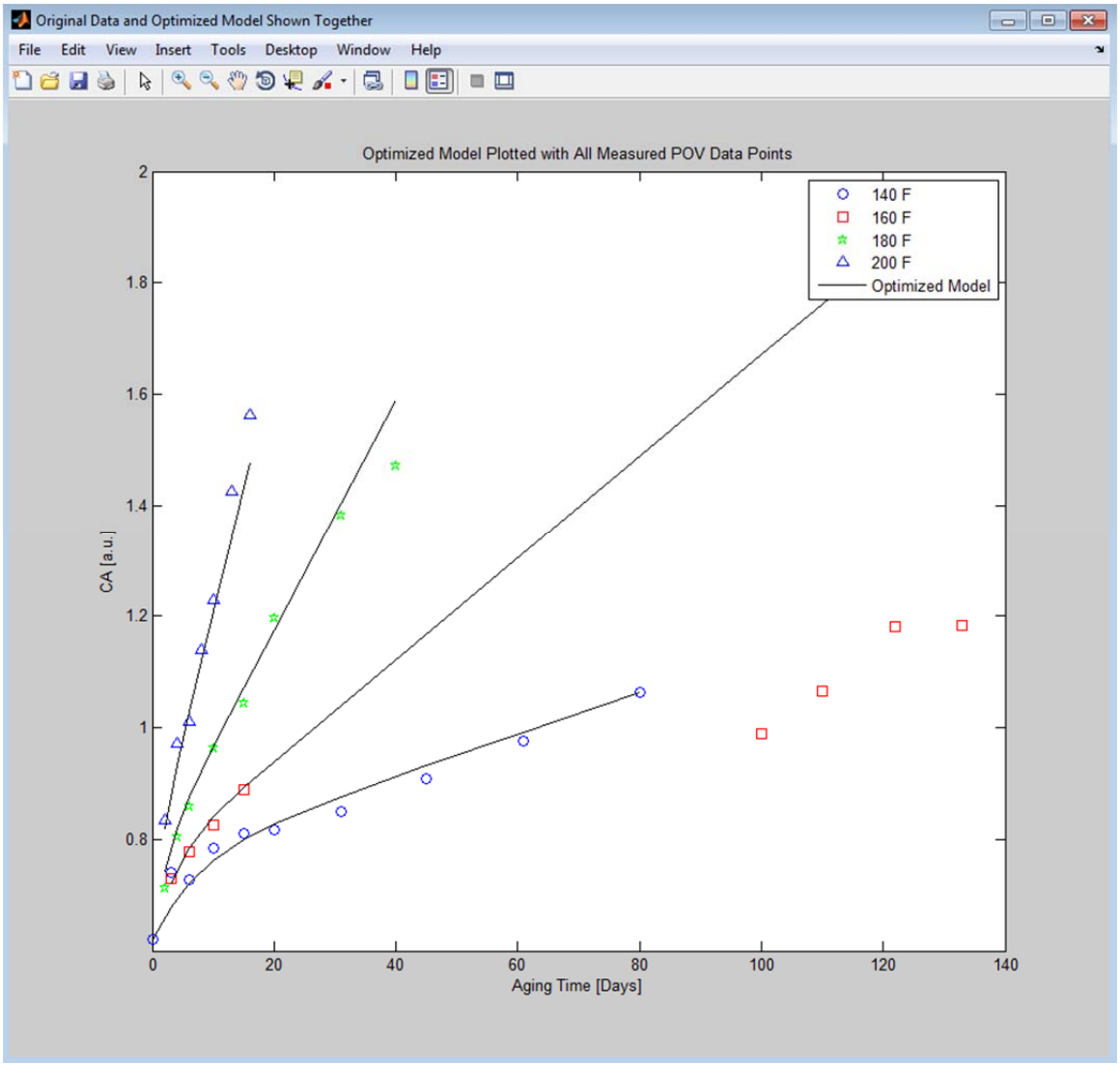


Figure 154. Original Data and Optimized Model Shown Together Window.

In this example, the model appears to fit the data fairly well. The data from POV #2 (160°F), represented by the red squares, were not used in the optimization process. Despite this, the model appears to fit the early 160°F data well. It appears likely that some experimental or recording error occurred with respect the red squares at aging times of 100 and greater days. It was almost certainly a correct choice, in this example, to ignore the data from POV #2 in the optimization process.

By minimizing or closing the "Original Data and Optimized Model Shown Together" window, the user will again be able to see the "Results From Aging Experiment" window. This figure has now been updated to include constant rate lines. These lines are linear regression lines based on the data points after the user-selected beginning of the constant rate period. The result for the example discussed is shown below in Figure 155. The second graph, POV # 2 160°F, does not have a regression line. This is because it was determined (see above) that these data should be ignored in the optimization process. If the final model fit appears poor (in the Original Data and Optimized Model Shown Together window) then the user may choose to look back at

the now updated Results from Aging Experiment figure and try to determine if the any choice for the beginning of the constant rate period can be improved. If so, the user should rerun the RKPG using any revised constant rate period beginning choices.

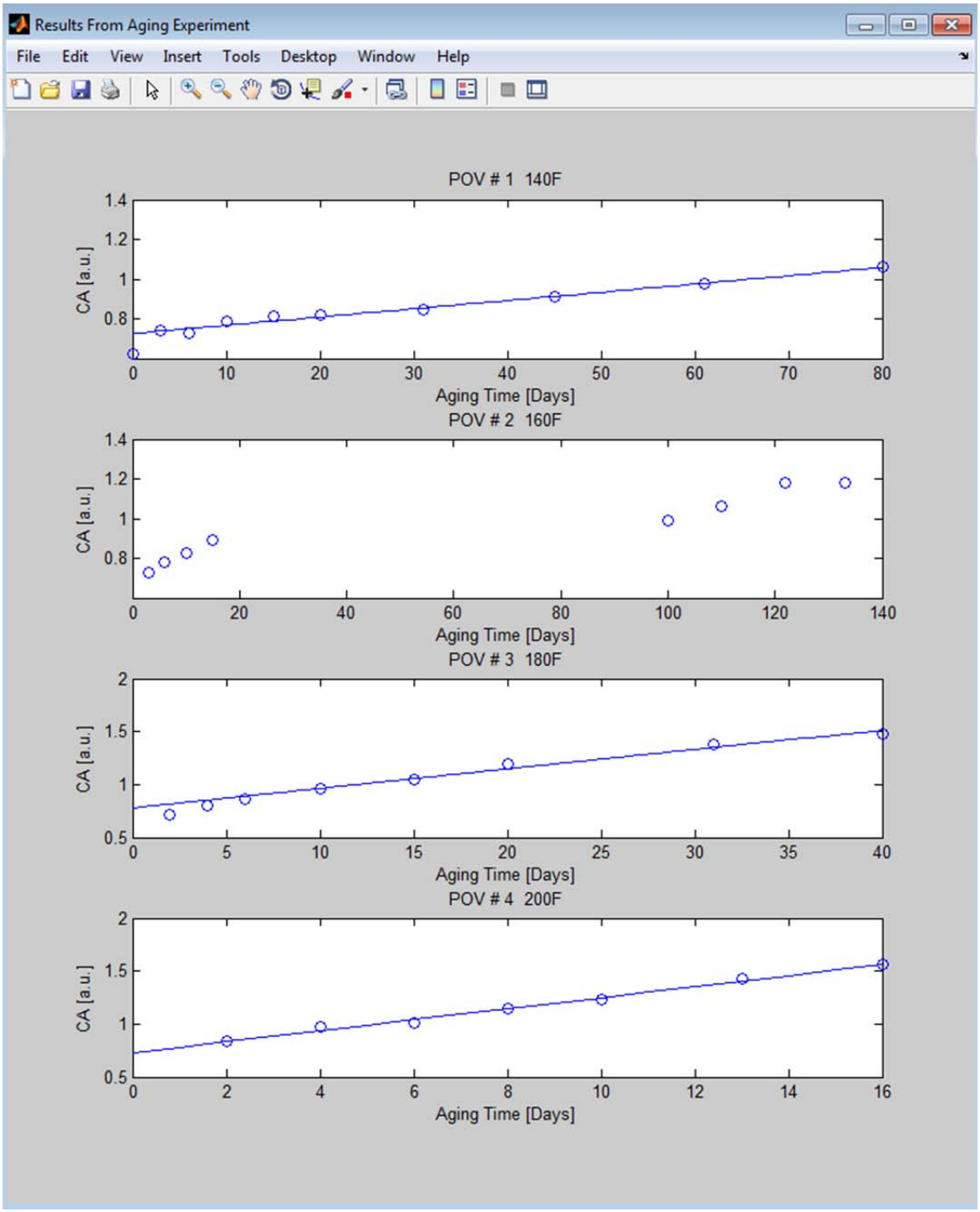


Figure 155. Results from Aging Experiment, with Constant Rate Regression Lines.

Numerical Output. The optimized results for the reaction kinetics parameters replace the corresponding "Not Calculated" text in the RKPG. The parameters: A_c, A_F, E_{ac}, E_{af}, and M are

the parameters corresponding to the carbonyl area growth model described in the introduction section of this chapter. These parameters are provided in the appropriate units for direct entry into the AMG.

Constant Rate Activation Energy from PAV Lab Test Results

Introduction

If the results from a POV test are not available it is possible to estimate the constant rate activation energy from the results of a PAV test. The additional reaction kinetics parameters A_c, A_F, E_{ac}, and E_{af} can be estimated by the AMG. The primary advantage of PAV testing is that it is significantly faster than POV testing. A typical PAV test requires less than 100 hours, while a POV test requires around 90 days.

Looking at the RKPG shown in Figure 151 above, the lower panel "Estimated POV Constant Rate Activation Energy From PAV Data and Correlation" is provided to process the results from PAV testing. The required inputs and the outputs are discussed below.

Inputs

The format for the input to the PAV section is analogous to the format of the input to the POV section discussed above. The input format required is shown in the "PAV" sheet of the example Excel workbook ExperimentalResults.xls. As above, the input should be contained in three adjacent columns of an Excel worksheet. The first column should contain the temperature. Note that the temperature input to the PAV section should be in units of degrees C [°C], while the POV section required temperature to be in units of degrees F [°F]. There should be two aging temperatures, the same aging temperatures should be grouped together, and the lower temperatures should be listed first. The second column must contain the aging time. Note here that the aging time should be in units of hours [Hr], while the aging time in the POV section was in units of days [Day]. The third column should contain the average carbonyl area of the binder aged according to the corresponding temperature and time.

Once the input is in the appropriate format, the file must be identified in the RKPG. The browse button may be used to specify the file location and file name. The sheet name and data range must be specified by using the corresponding text boxes. For the example data contained in ExperimentalResults.xls, the sheet name is "PAV," and the data range is "A2:C11."

After the PAV test data location has been specified, the user should click the "Calculate Eac" button.

Outputs

The output from the PAV section of the RKPG is an estimated value of the constant rate activation energy, E_{ac}, at 1 atmosphere of air. PAV testing is conducted at 20 atmospheres of air. The PAV section of the RKPG takes the PAV testing results, computes the corresponding E_{ac}, and converts this value to a 1 atmosphere air E_{ac}. This conversion is done using the correlation

described in Chapter 14. The 1 atmosphere air E_{ac} value is in the appropriate units to be directly input into the AMG.

USING THE TEMPERATURE PROFILE GRAPHICAL USER INTERFACE (TPG)

Introduction

The AMG requires a representative one-year pavement temperature profile as an input. A database of temperature profiles has been provided with this software package. The provided profiles may be used directly as inputs to the AMG. The database of temperature profiles covers approximately 20 locations in Texas. A user may desire to model aging in a pavement for which the temperature profile cannot be approximated by one of the provided profiles. In this case the user can use the Temperature Profile GUI to create the needed temperature profile. The TPG can be used to create a pavement temperature profile for any location in the United States. Figure 156 shows the TPG. Inputs required include three site-specific hourly parameters and three site specific single value parameters. The hourly parameters required are solar radiation, wind speed, and air temperature. The single value parameters are albedo, algebraic difference between absorption coefficient and emission coefficient, and absorption coefficient. There are several additional site specific parameters, but a study of these parameters has shown that non-site specific approximations can be used to create a temperature profile that is sufficiently accurate for use in the AMG. The non-site specific approximations of these additional parameters are built into the TPG. The TPG and the suggested methods described in this section are based on the work described in Chapter 6 (Han et al., 2011a).

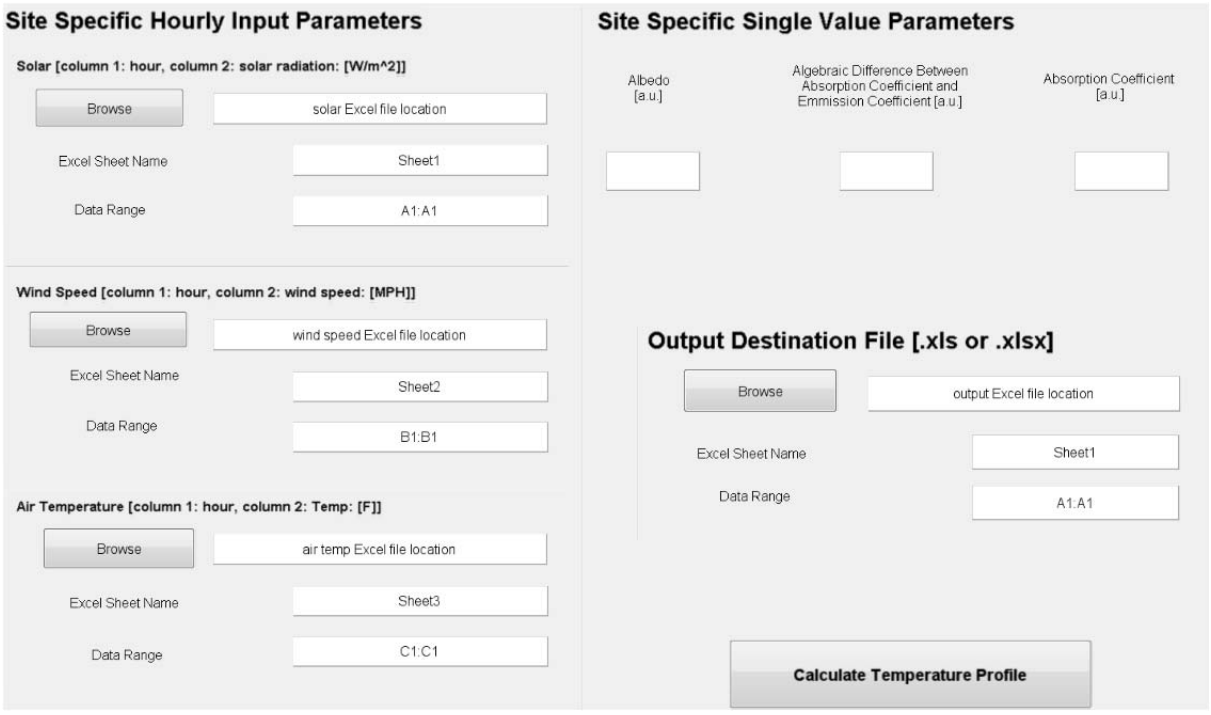


Figure 156. Temperature Profile Graphical User Interface.

This section of the chapter has been divided into two parts: (1) Using the TPG (inputs already determined), and (2) Suggested Methods of: Determining Input Parameters, Determining the Summer and Winter Period, and Formatting Inputs. Part 1 focuses on the use of the TPG. It assumes that the user has or knows how to obtain the required inputs. Part 2 focuses on obtaining the required inputs using online sources and the methods generally described in Chapter 6. Part 1 has been put before part 2 to give the reader an understanding of the use of the TPG before diving into the details of obtaining the inputs.

Part 1: Using the TPG (Inputs Already Determined)

Introduction

Part 1 of this section describes use of the TPG. There are three categories of inputs: (1) site specific hourly parameters, (2) site specific single value parameters, and (3) the location of the Excel file to which the TPG should write the output. The hourly inputs should be stored within one or more Excel worksheets. The location of these data must be identified in the TPG. The single value parameters are typed directly into the TPG. In addition to an explanation of the inputs, this part of the chapter explains the temperature profile output. Finally, if the pavement location has summer and winter periods, two temperature profiles must be produced and then combined. This combination process is explained.

An example Excel workbook, DataAndResults.xls, has been provided as part of the Temperature Profile GUI sub-package. The workbook contains seven worksheets. The contents of these worksheets are not entirely explained until part 2 of this section, below, but it may be helpful to refer to this workbook while reading part 1 as well. In particular the sheets "Processed," "Summer," "Winter," and "Final" are partially described in part 1.

Site Specific Hourly Parameters

The site specific hourly parameters that must be input into the TPG include: solar radiation [W/m^2], wind speed [MPH], and air temperature [°F]. Each of these input data sets must be contained in an Excel worksheet. In the TPG the user specifies where the data set is stored by specifying the file path and filename, the worksheet name in the Excel workbook, and the range of cells within the Excel worksheet. Suggested methods of determining each of these input data sets are explained in part 2 of this section. In this part the format of the input required by the TPG is explained.

Solar Radiation. The solar radiation input must be in two adjacent columns. The first column must contain the hour of the year and the second column must contain the corresponding solar radiation during that hour. The hour values may be in any form, but no hour may be skipped or repeated. The solar radiation values must be in units of watts per square meter [W/m^2]. The number or entries (i.e., rows) in each column should correspond to the number of hours in a year. If the number of entries does not perfectly correspond to the number of hours in a year, the TPG will still calculate a temperature profile, but the profile will be for a period slightly different than one year. Likewise, this output will work in the AMG, but the aging prediction will be for a period slightly different than one year. More important than the total number of hours is that the number of hours in the solar radiation input corresponds to the

number of distinct hours in the wind speed and air temperature inputs. If the number of distinct hours for each type of input do not match an error message will result.

Wind Speed. Like the solar radiation, the wind speed input must be in two adjacent columns. The first column must contain the hour of the year and the second column must contain the corresponding wind speed. The wind speed must be in units of mph.

The source of online wind speed data that is suggested (see part 2 below) often supplies several values for a single hour and may skip hours. Additionally, a wind speed value may be missing. The TPG will automatically convert repeat values to a single value by averaging. If an hour is missing, the TPG will report an error message telling the user where the hour is missing. The user can then manually insert an estimation value, for example by using the previous hour's value. If the hour appears but the wind speed value is missing, the TPG will automatically fill in the missing value using the value from the previous hour. The processing described above requires the form of the hour input to be: "YYYYMMDD.HH." For example, to specify the first hour of the first day of the first month of January 2005 the following number sequence and format should be used: 20050101.01. (The final period ends the sentence and is not part of the format.)

Air Temperature. The air temperature data must follow the form of the wind speed data, as discussed immediately above. The air temperature must be in units of degrees Fahrenheit.

Final Form of Processed Hourly Data for TPG Input. The form of the hourly data sets required by the TPG is shown below in Figure 157. Although shown in a single sheet, it is not necessary that the solar radiation, wind speed, and air temperature data sets are in the same sheet, or even in the same workbook. Although only 28 rows are shown in Figure 157, there are approximately 8759 rows in total (i.e., one row for each hour of the year).

The user is cautioned to be sure that the initial hour for each set and the final hour for each set match. It is typically necessary to delete and/or add columns to get the initial and final hours to match for each data set. Matching the initial and final hours does not mean that the total number of rows in each data set will match. This is because the wind speed and air temperature sets from the suggested source (see part 2 below) often have repeated hours. The TPG automatically accounts for repeated hours. In the image below it can be seen that each set begins at hour 1. The raw data for one or more of the sets may have a zero hour. Unless all three sets have a zero hour, the zero hours should be deleted so that the initial hours all match. A similar procedure should be applied to the final hours.

The user is also cautioned to visually inspect the last few entries of the solar radiation data. The suggested online source (see part 2 below) often provides values for the last few entries that are unreasonable (e.g., −9999). Any unreasonable values should be manually replaced with zeros.

	A	B	C	D	E	F	G	H	I	J
1	YYYY-MM-DD	HH:MM (LS	SUNY Glo (Wh/m^2)		Wind Speed [MPH]			Temperature [F]		
2	1/1/05	1:00	0		20050101.01	14		20050101.01	45	
3	1/1/05	2:00	0		20050101.02	13		20050101.02	46	
4	1/1/05	3:00	0		20050101.03	13		20050101.03	46	
5	1/1/05	4:00	0		20050101.04	13		20050101.04	48	
6	1/1/05	5:00	0		20050101.04	***		20050101.04	****	
7	1/1/05	6:00	0		20050101.05	11		20050101.05	47	
8	1/1/05	7:00	0		20050101.06	11		20050101.06	47	
9	1/1/05	8:00	0		20050101.06	14		20050101.06	47	
10	1/1/05	9:00	120		20050101.07	9		20050101.07	45	
11	1/1/05	10:00	242		20050101.08	10		20050101.08	47	
12	1/1/05	11:00	344		20050101.09	13		20050101.09	46	
13	1/1/05	12:00	395		20050101.10	14		20050101.10	43	
14	1/1/05	13:00	404		20050101.10	9		20050101.10	41	
15	1/1/05	14:00	354		20050101.11	10		20050101.11	37	
16	1/1/05	15:00	257		20050101.12	10		20050101.12	37	
17	1/1/05	16:00	133		20050101.12	9		20050101.12	35	
18	1/1/05	17:00	7		20050101.13	9		20050101.13	36	
19	1/1/05	18:00	0		20050101.14	10		20050101.14	35	
20	1/1/05	19:00	0		20050101.15	10		20050101.15	37	
21	1/1/05	20:00	0		20050101.16	13		20050101.16	38	
22	1/1/05	21:00	0		20050101.17	15		20050101.17	37	
23	1/1/05	22:00	0		20050101.18	15		20050101.18	37	
24	1/1/05	23:00	0		20050101.18	13		20050101.18	37	
25	1/1/05	24:00:00	0		20050101.19	14		20050101.19	36	
26	1/2/05	1:00	0		20050101.20	14		20050101.20	36	
27	1/2/05	2:00	0		20050101.21	11		20050101.21	33	
28	1/2/05	3:00	0		20050101.22	7		20050101.22	33	

Figure 157. Site Specific Hourly Inputs Formatted as Required by the TPG.

Site Specific Single Value Parameters

The site specific single value parameters that must be input into the TPG include: albedo, the algebraic difference between absorption coefficient and emission coefficient, and the absorption coefficient. The values are entered directly into the TPG. Each of these values is dimensionless. A suggested method for determining these values is explained in part 2 of this section, below.

Temperature Profile Output

The TPG uses the supplied inputs to compute a temperature profile in the pavement for a period of one year. The user must specify the destination location. The output is in degrees Celsius [°C], as required by the AMG.

Destination File. The user must specify an Excel file into which the TPG may write the temperature profile. The user must also specify the worksheet within the Excel file. Finally, the user must specify the data range within the worksheet. Regarding the data range, it is sufficient and generally easiest to enter only the location of the top left cell of the data range, for example "A1." Attempting to enter the entire data range requires knowledge of the exact size of the output data set.

Understanding the Output. The output data will have 40 columns and a number of rows equal to the number of hours in the year (more precisely, the number of hours input in the site specific hourly parameters section). Each cell in the data set will be filled with a temperature value in degrees C [°C]. Each row of the data represents a single hour and each column of the data represents a single depth in the pavement. The depth increment between columns is 0.5 inches. The data are now described in more detail.

The first row of the data represents the pavement temperature profile during the first hour of the year. Starting from the left, the first value in this row represents the temperature at the pavement surface during the first hour of the year. The second value from the left represents the temperature 0.5 inches (12.7 mm) below the pavement surface during the first hour of the year. The third value represents the temperature 1 inch below the surface during the first hour of the year, and so on. The value on the far right side (40^{th} value) of the first row represents the pavement temperature 19.5 inches below the surface during the first hour of the year. It is assumed that few applications will require a temperature more than 19.5 inches below the surface. The model calculations do not rely on the actual pavement being 19.5 inches deep, or any specific depth.

Likewise, the second row of the data represents the pavement temperature profile during the second hour of the year. The values in the second row correspond to specific depth values in the pavement as explained for the first row in the paragraph above. The total number of rows will correspond to the number of hours in the year. Therefore, the temperature profile in the pavement during a specific hour of the year may be found by looking at the corresponding row.

Dealing with Sites with Summer and Winter Seasons

Many pavements, particularly outside of Texas, have summer and winter seasons. Winter seasons correspond to seasons of snow and ice coverage. A suggested method of determining whether a pavement has a winter season and the specific time period of the winter season is explained in part 2 of this section, below. This section describes how to use the TPG when the user knows there is a winter season and knows the time period of the winter season.

If the pavement location has distinct summer and winter seasons, then albedo, and the algebraic difference between absorption and emission coefficients may have different summer and winter values. The site specific hourly inputs and the absorption coefficient do not change with summer and winter seasons.

If there are different values for summer and winter seasons, then it will be necessary to run the TPG two times and combine the winter and summer outputs to get a single temperature profile. First, run the TPG using the summer season input values and set the destination file location to an Excel worksheet named “Summer.” Then run the TPG using the winter season input values and set the destination file location to an Excel worksheet, in the same workbook, named “Winter”. Finally, create a third worksheet named “Combined T Profile.” Copy the results from the Summer Sheet into the Combined T Profile sheet. Then, copy the rows in the Winter sheet that correspond to the winter season. Paste these copied rows over the existing summer values in the corresponding rows in the Combined T Profile worksheet.

Part 2: Suggested Methods of: Determining Input Parameters, Determining the Summer and Winter Period, and Formatting Inputs

Introduction

Part 1 of this section described the use of the TPG and pavement temperature profile produced by the TPG. This part explains suggested methods for determining the input parameters, and the summer and winter seasons. Suggested methods for formatting the inputs using Excel are also provided. The suggested methods described here in detail are based on the general methods described in Chapter 6, "Modeling Pavement Temperature."

Recall that an example Excel workbook, DataAndResults.xls, has been provided as part of the Temperature Profile GUI sub-package. The workbook contains seven worksheets. A brief overview of each sheet was provided in the introduction to this chapter. The methods below describe how to produce a workbook of this form.

Hourly Parameters

Solar Radiation. Hourly solar radiation values in units of watts per square meter [W/m^2] can be obtained directly from the National Solar Radiation Database (http://rredc.nrel.gov/solar/old_data/nsrdb/). Once on this site, select the National Solar Radiation Database 1991–2005 Update link. Scroll down to the subheading "Hourly Solar Data and Statistical Summaries, Individual site-years by:" and select the "State and site name" link. Select the state and site that is closest to the location of the road of interest. After this, select a year under the data subheading. For example, select year 2005. It is not critical which year is selected because the objective of the TPG is only to provide a representative pavement temperature profile for one year. On the other hand, if the year had atypical temperature conditions it would not be a good choice.

After selecting a year, a spreadsheet will open on the desktop. Select all of the contents and paste them into an Excel worksheet. Alternatively, the spreadsheet may already be in Excel. Even if the spreadsheet is already in Excel, it may be more convenient to paste into another worksheet in a separate workbook in order to follow the example Excel workbook, DataAndResults.xls, provided with the Temperature Profile GUI sub-package. In the example workbook the sheet is labeled "NSRD Raw." However the downloaded data are saved, the hourly data may be taken from the second column, and the solar radiation data may be taken from the seventh column (G in Excel).

This same downloaded spreadsheet is used for determining the summer and winter seasons as discussed below (see Summer and Winter Period Determination).

Wind Speed and Air Temperature. The wind speed and the air temperature can both be downloaded from the National Climatic Data Center (NCDC) National Oceanic and Atmospheric Administration (NOAA) website (http://www.ncdc.noaa.gov/cdo-web/). The wind speed should be in units of miles per hour (MPH), and the air temperature should be in units of degrees Fahrenheit [°F]. From the home page of the NOAA website, it is possible to use the

interactive map application to request the wind speed and air temperature data. The map application is updated somewhat frequently, making it likely that the steps required to find this information will be slightly different than the steps described below.

From the home page, go to the interactive map application. In the pop-up box select "Time-Related maps" and then select Hourly/Sub-Hourly, because hourly input data are needed for the TPG. Take a few minutes to become familiar with usage of the interactive map. Once sufficiently familiar, select the dot, using the "select tools" that is "closest" to the road of interest. The term closest does not refer simply to distance. The user should also consider likely climate. For example, if the user's pavement of interest is located in a valley and the closest dot is on a nearby mountain, it may make sense to select a further dot that also located in the valley. Once a dot (or multiple dots) has been selected a pop-up box will appear requesting the user to select the specific site and general time range of interest. Check the site desired, select "get selected data," and then choose "Simplified." The user will be taken to another page and asked to select the date range of the data desired. Select the same date range as was selected for the solar radiation data above. For example, select data from the first hour of 2005 until the last hour of 2005, and press continue. Then check the "Inventory Review" box, and enter an email address for receipt of the links to the data, and press "Submit Request."

An e-mail will be received, typically within a few minutes, from cdo@noaa.gov. The e-mail will contain several links, all containing the same data, but in different formats. The second link provides the data in a format that can be copied and pasted into Excel. One disadvantage of this link is that each link within it only provides a single month of data. The user must open each sub-link separately and copy the data into Excel. Deleting the repeated headings after pasting into Excel is also required.

The columns of interest are the 3rd column (C), which contains the time information, the 5th column (E), which contains the wind speed information, and the 22nd column (V), which contains the air temperature information.

The column containing the time information will require further processing before it can be used as an input to the TPG. To understand the processing required it may help to look at the included example Excel Workbook named "DataAndResults.xls." In particular, the user may follow the method that was used in the fourth worksheet "NCDC Time Slotted." The details are now explained.

First, copy the column containing the time information into a blank Excel worksheet. The number in the time column must be split into two columns. The first column should contain the first 8 digits (YYYYMMDD) of the number and the second column should contain the last 4 digits (HHMM) of the number. This can be done by selecting the data tab in Excel, and then the "Text to Columns" icon. Choose the "fixed width" option and click next. Use the mouse to click between the fourth and fifth columns, counting from the right. In other words, put a vertical bar separating the HHMM section from the YYYYMMDD section. Then click finish. The original number should be split into two columns in the Excel sheet. The user may copy the formulas in the example Excel worksheet, NCDC Time Slotted, to create the next three columns. The formulas are also briefly explained here. The third column is the second column divided by

10,000. The forth column is the third column rounded to the hundredths decimal place. The final column is the sum of the first and fourth columns. The number in the final column is in the hour format that can be used in the TPG. The hours are separated from the rest of the information by a decimal place, and no minute information is retained. The final column can be used twice, once for the hours for the wind speed, and a second time for the hours for the air temperature.

The needed columns of data are ready and the user must just put them together. It is recommended that the user follow the format in the example Excel workbook (DataAndResults.xls) in the "Processed" sheet. The TPG requires that the hour and corresponding data for each hourly input are in two adjacent columns, but does not require that the different hourly inputs be in the same spreadsheet. Nevertheless, it is recommended that all 6 columns [hour, corresponding solar rad., hour, corresponding wind speed, hour, corresponding air temp.] be placed in a single spreadsheet, as in the example, for ease of review.

Single Value Parameters

Introduction. The single value input parameters that must be determined are albedo, the algebraic difference between absorption coefficient and emission coefficient (ADBAE), and the absorption coefficient. Suggested methods for determining these parameters are discussed below. The albedo and the ADBAE may each have different summer and winter values. To develop a representative temperature profile both values must be taken into account. Several U.S. maps that have 29 study site locations are shown and discussed below. For a detailed listing of the study sites refer to Chapter 6.

Albedo. The albedo represents the fraction of the solar radiation that is reflected. As such, it has arbitrary units [a.u.] (aka unitless). The albedo may have different summer and winter values. The steps to determine the albedo value are now discussed.

The first step is to divide the US into northern and southern regions based on average annual snowfall. It is recommended that the northern region be defined as areas having a mean total snowfall of greater than 12.0 inches, and the southern region be defined as areas having a mean total snowfall of 12.0 inches or less. An average snowfall map is available on the NCDC website (http://cdo.ncdc.noaa.gov/cgi-bin/climaps/climaps.pl). A copy of this map is provided below as Figure 158.

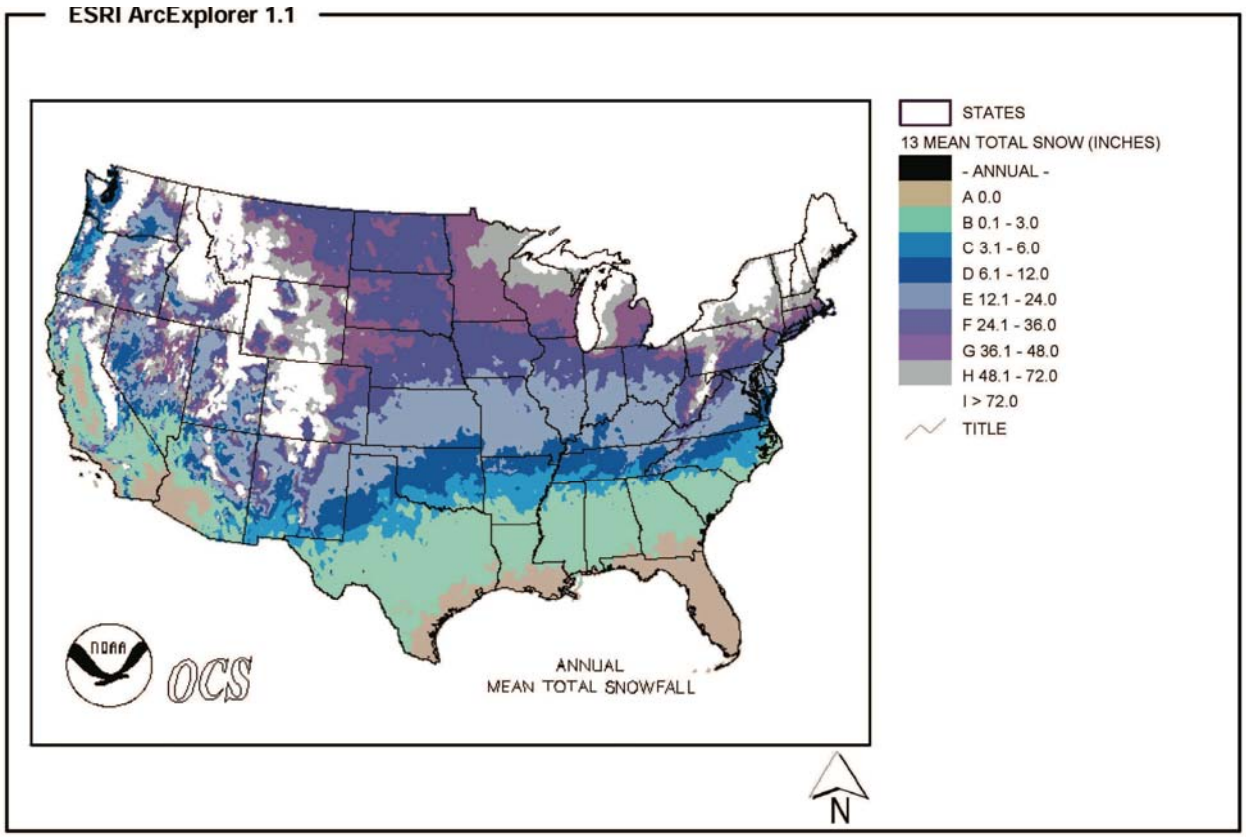


Figure 158. Annual Mean Total Snowfall Map Taken from the NCDC Website (http://cdo.ncdc.noaa.gov/cgi-bin/climaps/climaps.pl).

The second step is to identify the study site on the maps in Figure 159, below, that is the closest site to the pavement of interest and is also in the same snowfall region as the pavement of interest. The albedo values for the summer and winter seasons may then be read directly from the maps. If the summer and winter values are different, the site has summer and winter seasons. If the pavement of interest is physically close to a study site but in a geographically distinct region (other than snowfall), the user may choose to average the albedo values from the three closest study sites. This averaged albedo value may be used in place of a single value from the map below. This same type of averaging may be used for the ADBAE and absorption coefficient values discussed below.

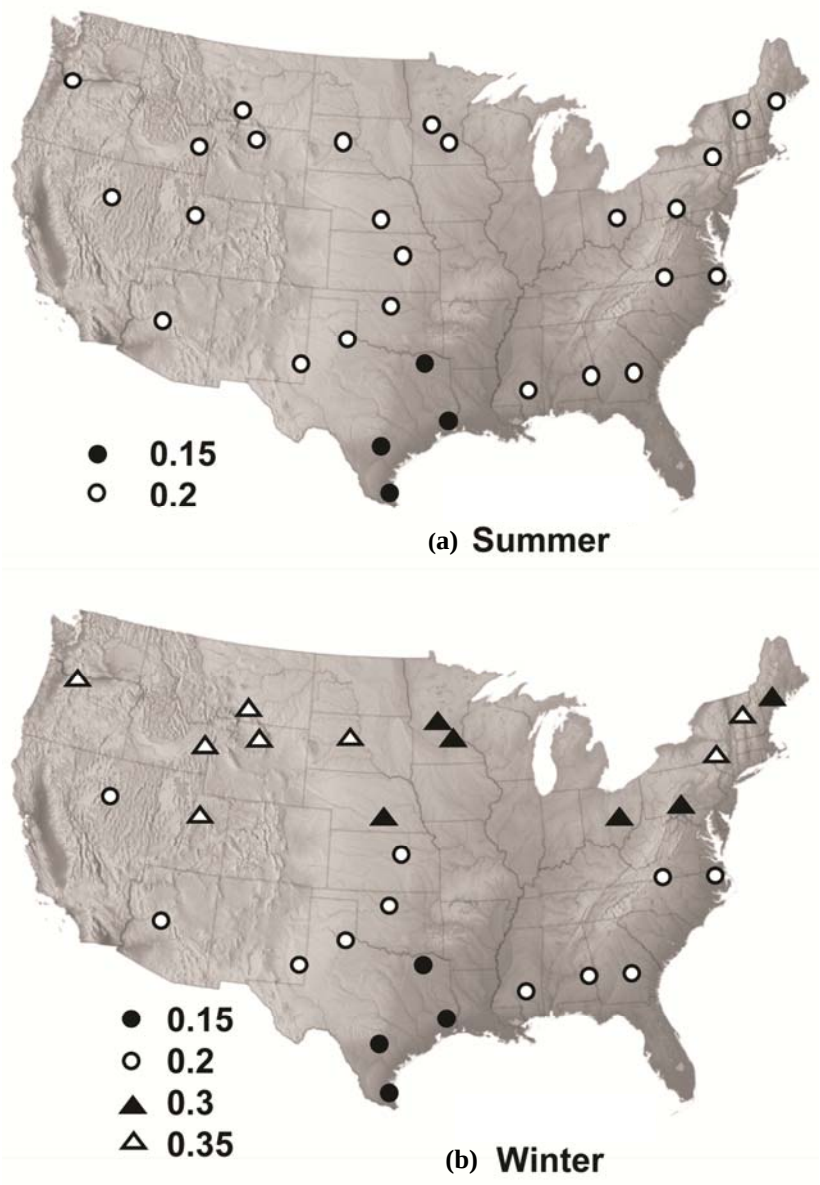


Figure 159. Distribution of Optimized Albedo Values.
Taken from Chapter 6 (Han et al., 2011a).

Algebraic Difference between Absorption Coefficient and Emission Coefficient. The method of determining the ADBAE is analogous to the method of determining the albedo as discussed above. The process is simplified for the ADBAE values because the U.S. maps having the study sites also identify the relevant regions. Choose the study site on the maps in Figure 160 that is closest to the pavement of interest and is also in the same region as the pavement of interest. It is possible that the study site will be different than the study site selected above because the regions are different. For details about the selection of these regions see Chapter 6.

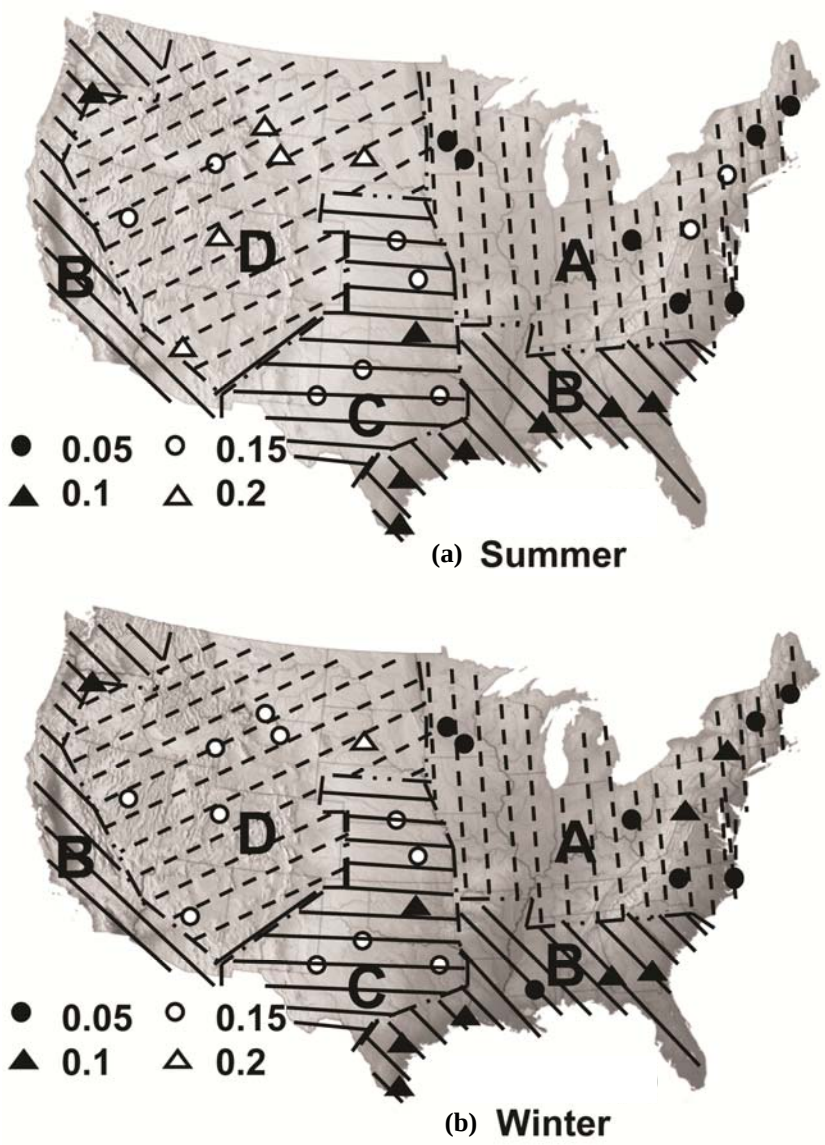


Figure 160. Distribution of Optimized Values of ADBAE. Taken from Chapter 6 (Han et al., 2011a).

Absorption Coefficient. Determination of the absorption coefficient is also analogous to the determination of the albedo value, but the relevant regions are different and there is no difference between summer and winter values.

The relevant regions are mean relative humidity regions. It is suggested that the U.S. be divided into two regions: one region having a mean annual relative humidity of at least 66 percent and another region having a mean annual average relative humidity of less than 66 percent. A mean annual relative humidity map can be found on the NCDC website (http://cdo.ncdc.noaa.gov/cgi-bin/climaps/climaps.pl), and this map is provided below as Figure 161.

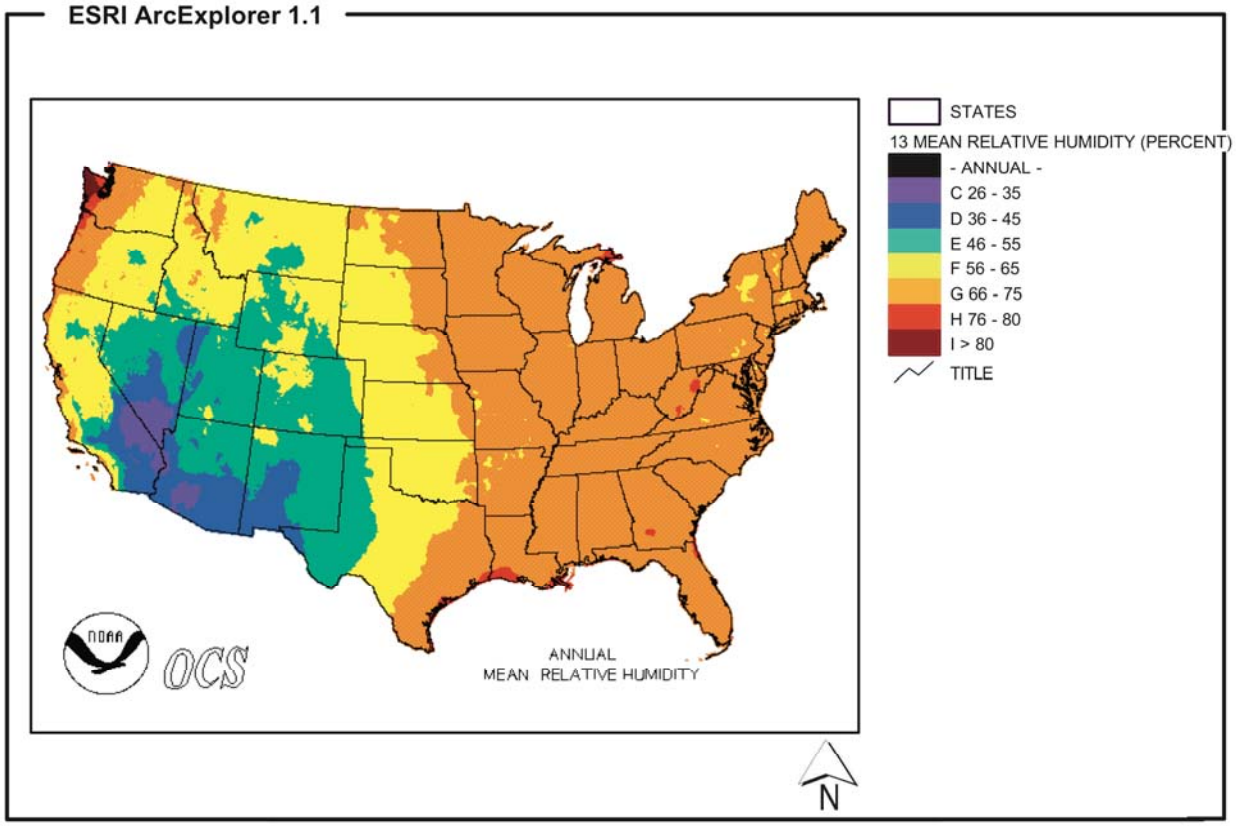


Figure 161. Annual Mean Relative Humidity Map. Taken from the NCDC Website (http://cdo.ncdc.noaa.gov/cgi-bin/climaps/climaps.pl).

After determination of the humidity regions, select the study site in the maps in Figure 162 below that is closest to the pavement of interest and in the same humidity region. Then read the absorption coefficient directly from the map.

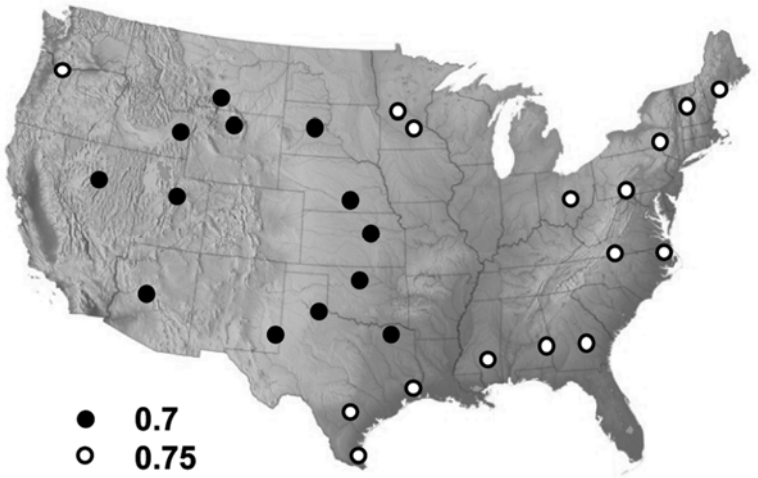


Figure 162. Distribution of Optimized Values of Absorption Coefficient. Taken from Chapter 6 (from Han et al., 2011a).

Summer and Winter Period Determination

If either the albedo or the ADBAE values are different for summer and winter seasons, then the pavement must be considered to have both summer and winter seasons. As a result, it is necessary to determine the portion of the year that is the summer season and the portion of the year that is the winter season.

For purposes of the TPG the summer season may be defined as the time period having relatively low ground albedo values, and the winter season may be defined as the time period having relatively high ground albedo values. Ground albedo values are distinct from pavement albedo values, which are entered into the TPG. The hourly ground albedo values may be read directly from the spreadsheet data downloaded from the NSRD, as described in the section *Solar Radiation* above. The relevant column is the second column from the right (AM). Ground albedo values of around 0.4 correspond to a winter period, while ground albedo values of around 0.2 correspond to a summer period. The winter period is typically limited to a month or two, such as January and February.

SUMMARY

This chapter provides a practical explanation of the use of the software package provided with this report. The software package includes a Pavement Aging Model Graphical User Interface sub-package and two supporting sub-packages. The first supporting sub-package is a Reaction Kinetics Parameters Graphical User Interface sub-package, and the second supporting sub-package is a Temperature Profile Graphical User Interface sub-package. For the purposes of this work, the sub-packages are intended to be used to create inputs that may be used in the AMG. Alternatively, the supporting sub-packages may be used as stand-alone software packages. In particular, it is thought that a yearly pavement temperature profile, as provided by the TPG, will likely have practical applications beyond use in the AMG. A detailed listing of the components of each sub-package is provided in the introduction section of this chapter.

The AMG is the primary graphical user interface. Inputs include: reaction kinetics parameters, a pavement temperature profile, and additional inputs. The RKPG may be used to provide the reaction kinetics parameters for the specific asphalt used in the pavement if experimental POV or PAV results are available. Ideally, the user will provide a full set of reaction kinetics parameters to the AMG but if only constant rate activation energy is available the AMG will estimate the additional parameters. A database of pavement temperature profiles for Texas locations is provided with the TPG sub-package. These temperature profiles may be used directly in the AMG. If the database does not contain a pavement temperature profile for the location of interest, the TPG may be used to create a new pavement temperature profile for any location in the U.S. In addition to kinetics parameters and a temperature profile, the user must also specify the desired length of the simulated aging and the month of pavement installation. Additional inputs include general information about the asphalt mix, viscosity information, and the desired output location for the numerical output. Full details are provided in the second major section of this chapter, *Using the Aging Model Graphical User Interface*.

The AMG provides a prediction of the increase in carbonyl area with aging time as the primary output. This result is provided in a graphical format. The result is also output numerically to an Excel file if the simulated aging time is less than approximately 7.4 years. In addition to carbonyl area vs. time, the AMG can also provide predicted DSR function vs. time values if the DSR function correlation parameters are provided.

The RKPG is designed to support usage of the AMG by aiding the user in obtaining the reaction kinetics parameters. The RKPG requires experimental POV or PAV results and based on these results provides reaction kinetics parameters. If POV results are provided, the RKPG will estimate a full set of reaction kinetics parameters. These parameters include: constant rate activation energy, fast rate activation energy, constant rate pre-exponential factor, fast-rate pre-exponential factor, and the total amount of carbonyl area increase possible due to the fast rate reaction. If only PAV testing results are provided, the RKPG will estimate the constant rate activation energy at one atmosphere air. If only the constant rate activation energy is input to the AMG, the AMG will estimate the additional reaction kinetics parameters. Full details regarding the RKPG are provided in the third major section of this chapter, *Using the Reactions Kinetics Parameters Graphical User Interface*.

The TPG is designed to support usage of the AMG by aiding the user in obtaining a pavement temperature profile. Inputs to the TPG include environmental parameters and parameters based on pavement location. The output is a pavement temperature profile in the format required by the AMG. The environmental inputs include hourly solar radiation, hourly wind speed, and hourly air temperature. The pavement location inputs include albedo, the algebraic difference between the absorption coefficient and the emission coefficient, and the absorption coefficient. Methods of determining these inputs from online sources and provided maps are explained. No experimental inputs are required. The TPG is only required if the supplied database of temperature profiles does not include a profile for a location near the road of interest. The output from the TPG is a pavement temperature profile which is a function of time of year and depth below the pavement surface. The time period covered depends on the input, but ideally the input will cover a period of one year and the output will likewise provide a representative temperature profile for a one-year period. Full details regarding the TPG are provided in the fourth major section of this chapter, *Using the Temperature Profile Graphical User Interface*.

For a more detailed theoretical explanation of the concepts embodied by the software the reader is referred to the body of this report. In particular, the following works provide the foundation for this software package. For the AMG, refer to the works described in Chapters 7 (Prapaitrakul et al., 2009), 8 (Han, 2011), and 9 (Jin et al., 2011), with the focus on Chapter 9. For the RKPG, refer to the works described in this report, Chapter 3 (Jin et al., 2011), and Chapter 14. For the TPG, refer to the work described in Chapter 6 (Han et al., 2011a).

CHAPTER 17. SUMMARY AND RECOMMENDATIONS

SUMMARY

This project has been a comprehensive research effort designed to provide the capability of predicting changes in binder properties in pavements due to oxidative hardening and the impact of this oxidative hardening on mixture properties, such as fatigue, that are important to long-term pavement performance. This effort has incorporated many interrelated research and development accomplishments, grouped below according to the larger elements to which they contribute:

- Development of a Pavement Binder Oxidation Model
    - Characterization of the ***binder oxidation kinetics parameters*** for fast-rate and constant-rate portions of the oxidation reactions for 24 binders used by TxDOT, including their characteristic changes in binder rheology in response to the oxidation.
    - An improved fundamental understanding of ***oxygen diffusivity in asphalt and mastics*** for both unmodified and polymer modified binders.
    - Improved ***air temperature modeling***
    - The development of an ***improved pavement temperature model*** that provides temperature of the pavement as a function of time and depth, and specific to the climate and hourly weather of interest.
    - The development of a transport and computational ***model for predicting binder oxidation in pavements*** over time and as a function of depth below the pavement surface, a model that incorporates each of the above elements and can be applied to a specific climate and hourly weather of interest.

- Mixture Test Development and Measurements
    - The development of a test device and ***method for testing prismatic specimens cut from pavement cores*** that is applicable to determining the rheological properties of three inch pavement lifts.
    - ***Measurements of binder oxidation in pavements***, over the course of the project and the impact of these changes on mixture properties.
    - ***Measurements of binder oxidation in laboratory mixtures*** and the impact of these changes on the laboratory mixture properties.
    - An ***evaluation of seal coat effectiveness.***

- An HMA Mixture Design Approach That Includes Binder Oxidation
    - An ***accelerated binder aging test*** for comparing binders with respect to their oxidative hardening durability.
    - Initial development of a ***mixture design and analysis system*** that incorporates binder oxidative aging in pavements and the accompanying increased stiffness of mixtures that results in a deterioration of mixture durability.

- The development of an executable ***software user interface*** that incorporates the various elements above in an HMA mix design component to provide insight into binder oxidative hardening and mixture durability in pavements.

The third item above, the mixture design approach, is the culmination of the work in the other two areas. A detailed summary of each of these items follows.

Development of a Pavement Oxidation Model

Binder Oxidation Kinetics

Twenty-four binders were aged in pressure oxidation vessels, but at one atm air conditions, at multiple temperatures from which constant-rate oxidation kinetics data were obtained. For 15 of these binders, additional data were obtained that allowed evaluation of a dual "fast-rate, constant-rate" model.

Empirical correlations were found between the fast-rate and constant-rate model parameters. The importance of these correlations is that they allow estimating fast-rate kinetics parameters from the constant-rate parameters, thereby reducing the number of model parameters from six to three: CA_{tank} (the carbonyl area of the unaged tank asphalt), M (the CA jump from the tank asphalt to the intercept of the constant-rate period), and E_{ac} (the constant-rate activation energy). This reduction of parameters not only simplifies the kinetics model, but also saves the time and effort required to obtain the fast-rate oxidation kinetics data.

Rheological data confirmed previous reports that hardening susceptibilities of each binder were independent of aging temperature and independent of whether the oxidation occurred in the fast-rate or constant-rate aging period.

Comprehensive oxidation kinetics parameters and hardening susceptibility data, together with the dual kinetics model, provide a sound basis for predicting binder oxidation and hardening as a function of time and temperature. Such a capability is fundamentally important to pavement oxidation models, to improving pavement design, and to predicting pavement performance.

Oxygen Diffusivity in Asphalt and Mastics

Measurements of the diffusivity oxygen in binders were determined based on laboratory oxidation experiments in binder films of known reaction kinetics. For neat asphalts, oxygen diffusivities (D) ranged from10^{-10} to 10^{-11} m^2/s, varying with temperature (T) and asphalt low shear rate limiting viscosity (η_o*); log(D/T) varied linearly with log(η_o*) for both base asphalts and polymer-modified binders. For asphalt mastics, oxygen diffusivity decreased as filler volume fraction increased. Quantitatively, this effect followed theoretical predictions reported in the literature of the effect of a dilute suspension of spherical inclusions on diffusivity. Quantitatively understanding the diffusion of oxygen in asphalt binders and mastics is an essential element of a comprehensive model of binder oxidation in pavements.

Air Temperature Modeling

Accurate hourly air temperature values are important for accurate hourly calculations of pavement temperature. Sensitivity analysis showed that the annual mean air temperature strongly affects the annual mean pavement temperature, and daily variations in air temperature affect daily variations in pavement temperatures, although to a much less extent than solar radiation. Five air temperature models (annual mean, monthly means, daily means, single-sine, and sine-sine) were studied for their effect on pavement temperature and asphalt oxidation. Comparisons were made for three pavement sites.

The model estimates provided the highest level of accuracy, while daily averages perform better than monthly and yearly averages. The method using a single-sine model together with measurements of daily high, low, and average temperatures is recommended for its simplicity. When more accurate estimates are required, the pattern model, coupled with daily high, low, and average temperatures, is an excellent method.

Pavement Temperature Modeling

An accurate model for pavement temperature prediction is critical in the study of asphalt material properties and pavement performance. The model developed in this work provided significant improvements over previous temperature models and can be used to obtain accurate estimates of hourly pavement temperatures as a function of depth at a desired pavement site, not just in Texas but also across the nation. The model employs commonly recorded hourly solar radiation, daily average wind speed, and interpolated hourly air temperature as climate input data. Three key site-specific model parameters were identified and national distribution of their values correlates with climatic patterns, suggesting possible interpolation strategies based on climate. The temperature model, proposed data sources and interpolated model parameters provided calculations that agreed well with experimental measurements, suggesting a general approach to predicting pavement temperatures nationwide with acceptable accuracy. This model is a powerful tool for engineers for pavement design, performance modeling, and predicting pavement durability. In the context of this work, it provides significantly better temperatures for calculating pavement oxidation than previous models.

Pavement Binder Oxidation Modeling

Three versions of a pavement oxidation model have been developed as the cornerstone to a model for predicting pavement durability. These methods all include the effect of oxygen diffusion and pavement temperature as a function of time and depth and oxidation kinetics but represent a progression of developing capability. The first effort adopted a coarse approach to considering air voids and worked quite well, simply because the air voids in mixtures typically are high enough that variations in air voids are not critical to the calculated results. This result is likely aided by the fact that temperature in the pavement changes throughout the day, providing a mechanism (expansion and contraction of the air in the pavement) for replenishing air in the mixture voids throughout the daily cycle.

The second approach included the air voids distribution in mixtures and as a function of layers in the pavement. As such, a more refined calculation that accounted more precisely for the air voids distribution in pavements was developed. Thus, transport through an air void channel and transport and reaction within the asphalt-aggregate matrix associated with an air void channel were modeled separately to calculate an oxidation rate for the finite asphalt-aggregate layer associated with the air void channel. Asphalt oxidation rates of six pavements with distinct temperature profile, air void properties, asphalt oxidation kinetics, and years in service were measured and compared with model calculations. In general, asphalt binders with high activation energy results in a low oxidation rate in the field; high pavement temperature leads to an increased oxidation rate (Texas pavements versus Minnesota pavement; surface cores versus rich bottom cores); and large air void pore radius and small shell distance produce a higher oxidation rate. Furthermore, comparisons of field oxidation rates compare well to those calculated using the model.

A third version of the pavement oxidation model requires binder oxidation kinetics and hardening parameters for both fast-rate and constant-rate reaction periods and has the capability of calibrating oxygen diffusivity in the mastic, accessible air voids, and mixture design by introducing additional model parameters. This approach provides a method for pavements for which data on these characteristics are not available, for example, for in–place pavements for which original data are not available. Initial evaluations suggest that the model is capable of predicting asphalt oxidation in pavements quite well, even after one year of field aging when the effects of the fast-rate oxidation period dominate those of the constant-rate period.

Mixture Test Development and Measurements

Testing of HMA Field Samples

Development by comparing VEC and RDT* test results from the same sample as well as the results from different samples taken from the same site shows that these two tests can be successfully applied to field samples. The VEC and RDT* tests provide a quick and accurate method of determining the material properties necessary to assess fatigue under field conditions. Streamlining the test preparation and further automation of the analysis will further make the VEC and RDT* tests practical methods for determining the material properties of samples obtained from the field.

Researchers will be able to separate and assess the effects of aging and trafficking on the number of loads to fatigue failure by examining VEC and RDT* test results from the wheel path and shoulder of any given pavement over time. This in turn will allow for more accurate development of mechanistic models that incorporate accurate aging prediction and correctly characterize fatigue. Current and future models can be compared and analyzed for accuracy by testing field samples throughout the life of the pavement and comparing the test results to those obtained from the models.

Over the past 100 years, significant progress has been made in the development of an efficient and effective transportation system. The direct tension testing of field samples using the VEC and RDT* tests will help propel the industry forward into the next 100 years of success by

allowing for the quick, accurate, and direct determination of the material properties of HMA pavements. As these results are applied, agencies will be better able to determine pavement life and plan for the maintenance, rehabilitation, and reconstruction of the transportation system.

A Field Site Study of Mixture Aging

The laboratory test results from LMLC and field samples and corresponding extracted binders lead to the following important conclusions regarding HMA aging as well as the effects of chip seals on pavement performance:

- Aging plays a role in the fatigue failure of HMA as evidenced by the performance of field samples, taken over time, from the shoulder. The stiffening of a mixture also coordinates well with an increase in oxidation, represented by CA development in corresponding extracted binders.

- While both AV and binder content play a role in mixture aging, AV plays a much more significant role.

- For US 277, much of the HMA aging occurs during the first year. In general, the rate of aging for US 277 decreases over time.

- Chip seals appear to slow HMA aging and as a result slow the rate of damage accumulation due to fatigue. However, this effect takes place primarily at the surface of the HMA where the chip seal is placed.

- It is possible to develop a relationship between binder aging and mixture aging. A relationship can also be drawn between *artificially*-aged LMLC samples and *realistically*-aged field samples.

These generalized conclusions are an important first step in moving toward mechanistic models that incorporate and quantify aging. The relationships between binders and LMLC samples and between LMLC samples and field samples lends themselves to the potential development of prediction models that incorporate aging. The next step in this development requires a deeper investigation into other field sites with different mixture and environmental conditions. While the findings in this chapter are a good starting point, a quality fatigue failure prediction model must be applicable to a wide range of HMA mixtures in all types of climates and conditions.

Field versus Laboratory Mixture Aging

Characterizing the role of aging in the development of fatigue failure in HMA mixtures is not a simple task. Many factors play a role, not only in fatigue cracking as a whole but also in the aging process. In order to effectively characterize and predict the effect on mixture properties of HMA aging in the field, aging in LMLC mixtures must be understood and correlated with actual field performance.

This work showed that HMA aging through binder oxidation not only occurs but also plays a significant role in the development of fatigue failure. A comparison can be made between artificially laboratory aged LMLC samples and naturally aged field cores taken from the shoulder, where minimal trafficking has occurred. For the sites in Texas included in this study, when comparing E_{ve}, one month of artificial aging in the laboratory was equivalent to 10.5 months in the field.

Future studies should include the further development of a more mechanistic model to predict N_f in the field from mixture data collected from unaged LMLC samples available during mixture design and collected unaged binder data, in combination with accelerated laboratory aged binder data or aged binder data calculated using existing models. This can be accomplished by developing the relationship between artificially laboratory aged LMLC N_f values and N_f values obtained from naturally aged field samples. By developing this relationship with field cores taken from the shoulder, the impact of aging without the confounding effects of traffic can be better understood and predicted. With these components, a pavement prediction model that accounts for aging and its impact on N_f in the field can be fully developed.

Seal Coat Evaluation

This study provides a systematic method to evaluate seal coat treated pavement oxidation and to predict future changes to the binder rheology. DSR function hardening susceptibility, the ratio between increases in log DSR Function and carbonyl area, is a characteristic of asphalt materials that relates chemical and rheological properties and that is sensitive enough to be used to identify blends of original binder and seal coat material. As such, it can be used to assess seal coat penetration below the pavement surface. Binder extracted and recovered from field cores can be further oxidized in laboratory accelerated aging in order to determine oxidation kinetics. Kinetics measurements of the recovered binder appear to compare well to the original binder, allowing the possibility of analyzing oxidation kinetics as a forensics study of pavements where no original binder is available.

Cores from the treated pavement sections have CA values that are significantly less than those from the untreated pavements, for the same pavement aging level. The consistency of this result in the cores from this pavement appears to be support the hypothesis that seal coats may well retard oxidation in pavements for a time. However, this result has not been observed in the other seal coated pavements studied in this project, suggesting that achieving an effective seal is problematic. More work is needed to consider how effective seals may be achieved.

This work has demonstrated a method for evaluating seal coat effectiveness with respect to binder oxidation and hardening even for pavements that were not initially planned to be test pavements. This strategy therefore provides a very cost-effective strategy for seal coat and pavement oxidation evaluation.

An HMA Mixture Design Approach That Includes Binder Oxidation

An Accelerated Binder Aging Test

The measurement of binder oxidation kinetics parameters allows estimates of binder oxidation rates at specific pavement sites and for specific pavement characteristics by using the kinetics information in an appropriate thermal and oxygen transport model. From these calculations, binders can be compared as part of an oxidative hardening pavement durability test. However, measuring kinetics parameters requires up to three months of oxidation experiments at atmospheric air pressure and multiple temperatures, so the technique is neither rapid nor readily applicable.

A new accelerated aging test using the pressure aging vessel (PAV, ASTM D6521-08) at elevated temperatures (90°C and 100°C, for example), and elevated pressure (2.1 MPa), needs significantly less time, 50 hours, plus analysis time to estimate the required kinetics parameters. Due to the higher pressure, both the oxidation activation energies and pre-exponential factors are different from those determined at 1 atm, likely because of a different balance of reaction products that is not fully understood. Consistent correlations exist between data at the two pressures. These correlations provide the basis for estimating reaction kinetics parameters at pavement conditions from measurements at PAV conditions. These parameters can then be used in a pavement oxidation and hardening model to compare different binders for their impact on pavement durability at specific pavement climates.

Such an accelerated aging test will provide binder comparisons at pavement conditions that are specific to each climate and pavement design, and that are far better than conventional standard tests. The total time for such comparisons is estimated to be one week.

Mix Design and Analysis System

When aged mixture properties are not available, the average laboratory to field shift factor of 1.6 may be utilized in a mixture design system and applied to the predicted loss of mixture fatigue resistance with binder stiffening (slope of log N_f vs. log DSR_f). Thus with the ability to predict changes in DSR_f with depth and climate as outlined previously in Chapters 8 through 9, the corresponding changes in N_f from an initial value measured on unaged mixtures can be estimated. However, based on the limited results shown in this chapter, it is recommended that both unaged and aged mixture properties be measured for high traffic volume facilities where a high level of reliability in the design is desired. The aged mixture properties may be obtained after a long-term aging procedure for compacted samples such as that in AASHTO R 30 (5 days at 85°C) or another procedure to be developed in the upcoming NCHRP Project 9-54 Long-Term Aging of Asphalt Mixtures for Performance Testing and Prediction. The characteristic slope or loss of mixture fatigue resistance can then be estimated using measured changes in N_f and measured changes in DSR_f or measured changes in N_f and predicted changes in DSR_f tied directly to a specific climate.

Software User Interface

The software package includes a Pavement Aging Model Graphical User Interface (AMG) sub-package and two supporting sub-packages. The first sub-package is a Reaction Kinetics Parameters Graphical User Interface (RKPG) sub-package, and the second is a Temperature Profile Graphical User Interface (TPG) sub-package. The sub-packages create inputs to the AMG. Alternatively, the supporting sub-packages may be used as stand-alone software packages. For example, the pavement temperature profile provided by the TPG likely will have practical applications beyond use in the AMG.

The AMG provides a prediction of the increase in carbonyl area with aging time as the primary output and in a graphical format. The result also is tabulated numerically in an Excel file if the simulated aging time is less than approximately 7.4 years. In addition to carbonyl area vs. time, the AMG also can provide predicted values of the DSR function vs. time if DSR function correlation parameters are provided.

The RKPG aids the user in obtaining reaction kinetics parameters from either POV or PAV laboratory data.

The TPG aids the user in obtaining a pavement temperature profile for the designated pavement location based on environmental climate and weather data and modell parameters.

RECOMMENDATIONS

This project provided significant contributions towards achieving an integrated understanding of the decline of pavement durability over the course of its life. Implementation and future work are recommended:

- Implementation
    - Introduce the software user interface to TxDOT engineers as a pavement mixture design tool through a workshop with TxDOT personnel conducted by project researchers
    - Adopt the accelerated aging test as a means of comparing binders in their oxidative hardening
    - Implement a strategy for evaluating existing pavements by testing recovered binders for their oxidation and hardening kinetics parameters and projecting future hardening and fatigue resistance changes for the purpose of optimizing maintenance resources
- Future Work
    - Incorporate the pavement transport and thermal oxidation model into a new pavement design guide
    - Continue to evaluate the effectiveness of maintenance treatments

- Continue to validate the pavement oxidation and hardening model with data from field pavements
- Improve our fundamental understanding of oxidation kinetics chemistry and reaction kinetics, including both the fast-rate and constant-rate reactions and the correlations between their several parameters.
- Improve our fundamental understanding of the correlation between PAV reaction kinetics parameters at 20 atm and POV determinations at 1 atm

REFERENCES

Highway Statistics 2008, Table HM 220 - Highway Statistics 2008 - FHWA. http://www.fhwa.dot.gov/policyinformation/statistics/2008/hm220.cfm. Accessed June 2011.

AASHTO. (2004) (NCHRP 1-37A) Guide for Mechanistic-Empirical Design of New and Rehabilitated Pavement Structures. http://trb.org/mepdg. Accessed November 2004.

Ahmed, Z., I. Marukic, S. Zaghloul, and N. Vitillo. (2005) Validation of Enhanced Intergrated Climatic Model Predictions with New Jersey Seasonal Monitoring Data. *Transportation Research Record*, No. 1913, pp. 148–161.

Al-Azri, N.A., S.H. Jung, K.M. Lusford, A. Ferry, J.A. Bullin, R.R. Davison, and C.J. Glover. (2006) Binder Oxidative Aging in Texas Pavements: Hardening Rates, Hardening Susceptibilities, and the Impact of Pavement Depth. *Transportation Research Record*, Vol.1962, pp. 12–20.

Al-Omari, A., L. Tashman, E. Masad, L. A. Cooley, Jr. and T. Harman. (2002) Proposed Methodology for Predicting HMA Permeability. *Journal of the Association of Asphalt Paving Technologists*, Vol. 71, pp. 30–58.

Arabani, M., and B. Ferdowsi. Laboratory Evaluating and Comparison of the SCB Test Results with Other Common Tests for HMA Mixtures. (2007) *Advanced Characterisation of Pavement Soil Engineering Materials, Vol. 1&2*, pp. 15–64.

Asphalt Institute. (2001) Superpave Mix Design. *Superpave Series No. 2* (SP-2). Asphalt Institute, Lexington, KY.

ASTM D 2041. (2003) Standard Test Method for Theoretical Maximum Specific Gravity and Density of Bituminous Paving Mixtures. 2003 Annual Book of ASTM Standards, 04.03, West Conshohocken, PA .

ASTM D 6752. (2004) Standard Test Methods for Bulk Specific Gravity and Density of Compacted Bituminous Mixtures Using Automatic Vacuum Sealing Method. 2004 Annual Book of ASTM Standards, 04.03, West Conshohocken, PA.

Baek, C., B. S. Underwood, and Y. R. Kim. (2012) Effects of Oxidative Aging on Asphalt Mixture Properties. In *Transportation Research Board 91st Annual Meeting*, Washington, D. C.

Baker, J., D. Reicosky, and D. Baker. (1988) Estimating the Time Dependence of Air Temperature Using Daily Maxima and Minima: A Comparison of Three Methods. *Journal of Atmospheric and Oceanic Technology*, Vol. 5 (6), pp. 736–742.

Barber, E.S. (1957) Calculation of Maximum Pavement Temperatures from Weather Reports. *Bulletin (Highway Research Board)*, Vol. 168, pp. 1–8.

Basmadjian, D. (2004) Mass Transfer: Principles and Applications, CRC Press LLC, Boca Raton, FL.

Belsoft and Styleshout. (2012) U.S. Climate Data, Temperature-Precipitation-Sunshine. http://www.usclimatedata.com/. Accessed July 2012.

Bird, R.B., W.E. Stewart, and E.N. Lightfoot. (2002) Transport Phenomena. Second Edition. John Wiley & Sons, New York, NY.

Bosscher P. J., H.U. Bahia, S. Thomas, and J.S. Russell. (1998) Relationship Between Pavement Temperature and Weather Data Wisconsin Field Study to Verify Superpave Algorithm. *Transportation Research Record*, No. 1609, pp. 1–11.

Brockwell, P. J. and R. A. Davis. (2002). Introduction to Time Series and Forecasting. Second Edition. Springer-Verlag, New York, NY.

Brown, E. R. (1988) Preventive Maintenance of Asphalt Concrete Pavements. *Transportation Research Record*, No.1205, pp. 6–11.

Brown A.B., J.W Sparks, O. Larsen. (1957) Rate of Change of Softening Point, Penetration, and Ductility of Asphalt in Bituminous Pavement. *Proceedings AAPT*, Vol. 26 (66).

Burr B.L., R.R. Davison, C.J. Glover, and J.A. Bullin. (1990) Solvent Removal from Asphalt. *Transportation Research Record*, No. 1269, pp. 1–8.

Burr B.L., R.R. Davison, C.J. Glover, and J.A. Bullin. (1994) Softening of Asphalts in Dilute Solutions at Primary Distillation Conditions. *Transportation Research Record*, No. 1436, pp. 47–53.

Burr B.L., C.J. Glover, R.R. Davison, J.A. Bullin. (1993) New Apparatus and Procedure for the Extraction and Recovery of Asphalt Binder from Pavement Mixtures. *Transportation Research* Record, No. 1391, pp. 20–29.

Burr, B. L., R. R. Davison, H. B. Jemison, C. J. Glover, and J. A. Bullin. (1991) Asphalt Hardening in Extraction Solvents. *Transportation Research Record*, 1323, pp. 70-76.

Carslaw, H.S., and J.C. Jaeger. (1959) Conduction of Heat in Solids. 2nd edition, Oxford Science Publications.

Cipione C.A., R.R. Davison, B.L. Burr, C.J. Glover, and J.A. Bullin. (1991) Evaluation of Solvents for the Extraction of Residual Asphalt from Aggregates., *Transportation Research* Record, No. 1323, pp. 47–52.

Clark, R.C. (1958). Practical Results of Asphalt Hardening on Pavement Life. *Association of Asphalt Paving Technol*ogists. Vol. 27, pp. 196–208.

Conseugra, A., D.N. Little, H. V. Quintus, and J. Burati. (1989) Comparative Evaluation of Laboratory Compaction Devices Based on Their Ability to Produce Mixtures With Engineering Properties Similar To Those Produced In The Field. *Transportation Research Record*, Vol. 1228, pp. 80–87.

Coons, R.F. and P.H. Wright. (1968) An Investigation of the Hardening of Asphalt Recovered from Pavements of Various Ages. *Association of Asphalt Paving Technologists*, Vol. 37, pp. 510.

Debele, B., R. Srinivasan, and J. Parlange. (2007) Accuracy Evaluation of Weather Data Generation and Disaggregation Methods at Finer Timescales. *Advances in Water Resources*, Vol. 30 (5), pp. 1286–1300.

Dempsey, B. J. (1970) A Heat Transfer Model for Evaluating Frost Action and Temperature Related Effects in Multilayered Pavement Systems. *Highway Research Record*, Vol. 342, pp. 39–56.

Dickinson E. J. and J. H. Nicholas. (1949) The Reaction of Oxygen with Tar Oils, *Road Research,* RN/843, No. 16.

Dickinson, E.J. (1984). The Diffusion Controlled Reaction of Oxygen with Films of Bituminous Binders. *Australian Road Research*, Vol. 14, pp. 121–132.

Diefenderfer, B.K., A.M. Asce, I.L. AL-Qadi, and S.D. Diefenderfer. (2006) Model to Predict Pavement Temperature Profile: Development and Validation. *Journal of Transportation Engineering*, Vol. 132, pp. 162–167.

Domke, C. H., R.R. Davison, and C.J. Glover. (1999). Effect of Oxidation Pressure on Asphalt Hardening Susceptibility. *Transportation Research Record*, No. 1661, pp. 114–121.

Domke, C. H., R.R Davison, and C.J. Glover. (2000). Effect of Oxygen Pressure on Asphalt Oxidation Kinetics. *Industrial and Engineering Chemistry Research*, Vol. 39 (3), pp. 592–598.

Domke, C., M. Liu, R.R. Davison, J.A. Bullin, and C.J Glover. (1997) Study of Strategic Highway Research Program Pressure Aging Vessel Procedure using Long-Term, Low-Temperature Aging Experiments and Asphalt Kinetics. *Transportation Research Record*, Vol. 1586 (1), pp. 10–15.

Doyle, P.C. (1958). Cracking Characteristic of Asphalt Cement. *Association of Asphalt Paving Technol*ogists, Vol. 27, pp. 581–597.

Glover, C. J., R.R. Davison, C.H. Domke, Y. Ruan, P. Juristyarini, D.B. Knorr, and S.H. Jung. (2005). Development of a New Method for Assessing Asphalt Binder Durability with Field Validation. Report FHWA/TX-05/1872-2. Texas Transportation Institute, College Station, TX.

Gui, J., P.E. Phelan, K.E. Kaloush, and J.S. Golden. (2007). Impact of Pavement Thermophysical Properties on Surface Temperature. *Journal of Materials in Civil Engineering*, Vol. 19 (8), pp. 683–690.

Hagos, E. T. (2009). Chemical Characterization of Laboratory and Field Bitumen Aging in Porous Asphalt Concrete. *Advanced Testing and Characterisation of Bituminous Materials*, Vol. 1&2, pp. 173–184.

Halstead, W.J. (1963). The Relation of Asphalt Ductility to Pavement Performance. *Association of Asphalt Paving Technol*ogists. Vol. 32, pp. 247–270.

Han, R. (2011). Improvement to a Transport Model of Asphalt Binder Oxidation in Pavements: Pavement Temperature Modeling, Oxygen Diffusivity in Asphalt Binders and Mastics, and Pavement Air Void Characterization. Chapter IV Improved Modeling of Asphalt Binder Oxidation in Pavements and Pavement Air Void Characterization. Ph.D. Dissertation, Texas A&M University, College Station, TX.

Han, R., X. Jin, and C.J. Glover. (2011a). Modeling of Pavement Temperature History for Use in Binder Oxidation Models and Pavement Performance Prediction. *Journal of Materials in Civil Engineering*, Vol. 23, pp. 351–359.

Han, R., X. Jin, and C.J. Glover. (2011b). Oxygen Diffusivity in Asphalts and Mastics, *Petroleum Science and Technology.* In press.

Hermansson, A. (2000). Simulation Model for Calculating Pavement temperatures, Including Maximum Temperature. *Transportation Research Record*, Vol. 1699, pp. 134–141.

Hermansson, A. (2004). Mathematical Model for Paved Surface Summer and Winter Temperature: Comparison of Calculated and Measured Temperatures. *Cold Regions Science and Technology*, Vol. 40, pp. 1–17.

Herrington, P. R. (1998). Oxidation of Bitumen in the Presence of a Constant Concentration of Oxygen. *Petroleum Science and Technology*, Vol. 16 (9-10), pp. 1061-1084.

Highter, W.H., and D.J. Wall. (1984). Thermal Properties of Some Asphalt Concrete Mixes. *Transportation Research Record*. No. 968, pp. 38–45.

Huang, L. K. (2009). Evaluation of Semicircular Bending Test for Determining Tensile Strength and Stiffness Modulus of Asphalt Mixtures. *Journal of Testing and Evaluation*, Vol. 37 (2), pp. 122–128.

Huh, J.-D. and R. Robertson. (1996). Modeling of Oxidative Aging Behavior of Asphalts from Short-Term, High-Temperature Data as a Step Toward Prediction of Pavement Aging. *Transportation Research Record*, No. 1535 (1), pp. 91–97.

Instrotek Incorporated. (2001). *Corelok® Operator's Guide*, Version 10, Raleigh, NC.

Jin, X. (2012). Asphalt Oxidation Kinetics and Pavement Oxidation Modeling. Chapter IV Modeling Asphalt Oxidation in Pavements with Field Validation. Ph.D. Dissertation, Texas A&M University, College Station, TX.

Jin, X., R. Han, Y. Cui, and C.J. Glover. (2011). Fast-Rate-Constant-Rate Oxidation Kinetics Model for Asphalt Binders. *Industrial & Engineering Chemistry Research*, Vol. 50 (23), pp. 13,373–13,379.

Juristyarini P., R.R. Davison, and C.J. Glover. (2011a). Oxidation Hardening Kinetics of the Rheological Function G′/(η′/G′) in Asphalts. *Petroleum Science and Technology*, Vol. 29 (19), pp. 2027–2036.

Juristyarini P., R.R. Davison, and C.J. Glover. (2011b). Development of an Asphalt Aging Procedure to Assess Long-Term Binder Performance. *Petroleum Science and Technology*, Vol. 29 (21), pp. 2258–2268.

Kandhal, P.S. (1977). Low-Temperature Ductility in Relation to Pavement Performance. In ASTM STP 628: Low-Temperature Properties of Bituminous Materials and Compacted Bituminous Paving Mixtures, C.R. Marek (Ed.), American Society for Testing and Materials, Philadelphia, PA, pp. 95–106.

Kandhal, P.S., and W.C. Koehler. (1984). Significant Studies on Asphalt Durability: Pennsylvania Experience. *Transportation Research Rec*ord, Vol. 999, pp. 41–50.

Kandhal, P.S., and M.E. Wenger. (1975). Asphalt Properties in Relation to Pavement Performance. *Transportation Research Rec*ord, Vol. 544, pp. 1–13.

Klein, A.G., and S. Julienne. (2002). Development and Validation of a Snow Albedo Algorithm for the MODIS Instrument. *Annals of Glaciology*, Vol. 34, pp. 45–52.

Lau, C.K., (1991). Photo- and Moderate- Temperature Oxidation Reactions and their Impacts on the Properties and Performance on Asphalt as a Pavement Binder. M.S. Thesis, Texas A&M University, College Station, TX.

Lau, C.K., K.M. Lunsford, C.J. Glover, R.R. Davison, and J.A. Bullin. (1992). Reaction Rates and Hardening Susceptibilities as Determined from POV Aging of Asphalts. *Transportation Research Record*, Vol. 1342, pp. 50–57.

Lee, D.Y. and R.J. Huang. (1973). Weathering of Asphalts as Characterized by Infrared Multiple Internal Reflection Spectra. *Analytical Chemistry*, Vol. 46, p. 2242.

Liang, R.Y., S. Rabab'ah, and K. Al-Akhras. (2006). Validation of Enhanced Integrated Climatic Model Prediction over Different Drainable Base Materials. Transportation Research Board Annual Meeting 2006 CD-ROM.

Lin M.S., J.M Chaffin, M. Liu, C.J. Glover, R.R Davison, J.A. Bullin. (1996). The Effect of Asphalt Composition on the Formation of Asphaltenes and their Contribution to Asphalt Viscosity. *Fuel Science and Technology International*, Vol. 14 (1&2), pp. 139–162.

Lin, M.S. (1995). The Formation of Asphaltenes and its Impact on Chemical and Physical Properties of Asphalts. Ph.D. Dissertation, Texas A&M University, College Station, TX.

Lin, M.S., J.M. Chaffin, R.R. Davison, C.J. Glover, and J.A. Bullin. (1998). A New Suspension Viscosity Model and Its Application to Asphaltene Association Thermodynamics and Structures. In *Structure and Dynamics of Asphaltenes*, M. Iino, and T. Takanohashi (Eds.), Plenum Press, NY.

Lin, M.S., K.M. Lunsford, C.J. Glover, R.R. Davison, and J.A. Bullin. (1995). The Effects of Asphaltenes on the Chemical and Physical Characteristics of Asphalts. In *Asphaltenes: Fundamentals and Applications*, E.Y. Sheu and O.C. Mullins (Eds.), Plenum Press, NY.

Liu, M., J.M. Chaffin, R.R. Davison, C.J. Glover, and J.A. Bullin. (1997). Reactivity of Asphalt Supercritical Fractions. *Industrial & Engineering Chemistry Research*, Vol. 36 (6), pp. 2177–2183.

Liu, M., M.S. Lin, J.M. Chaffin, R.R Davison, C.J. Glover, C.J. and J.A. Bullin. (1998a). Oxidation Kinetics of Asphalt Corbett Fractions and Compositional Dependence of Asphalt Oxidation. *Petroleum Science and* Technology, Vol. 16 (7&8), pp. 827–850.

Liu, M., K. M. Lunsford, R. R. Davison, C. J. Glover, and J. A. Bullin. (1996). The Kinetics of Carbonyl Formation in Asphalt. *AIChE J.*, Vol. 42 (4), pp. 1069–1076.

Liu, M., M.A. Ferry, R.R. Davison, C.J. Glover, and J.A. Bullin. (1998b). Oxygen Uptake as Correlated to Carbonyl Growth in Aged Asphalts and Asphalt Corbett Fractions. *Industrial & Engineering Chemistry Research*, Vol. 37, pp. 4669–4674.

Luca, J., and D.M. Mrawira. (2005). New Measurement of Thermal Properties of Superpave Asphalt Concrete. *Journal of Materials in Civil Engineering*, Vol. 17, pp. 72–79.

Lunsford, K.M. (1994). The Effect of Temperature and Pressure on Laboratory Oxidized Asphalt Films with Comparison to Field Aging. Ph.D. Dissertation, Texas A&M University, College Station, TX.

Luo, R., and R. L. Lytton. (2010). Characterization of the Tensile Viscoelastic Properties of an Undamaged Asphalt Mixture. *Journal of Transportation Engineering*, Vol. 136 (3), pp. 173–180.

Luo, X. (2012). Characterization of Fatigue Cracking and Healing of Asphalt Mixtures. Ph.D. Dissertation, Texas A&M University, College Station, TX.

Luo, X., A. E. Martin, R. Luo, R. L. Lytton, and C. J. Glover. (2008). *Aging Experiment Design Including Revised CMSE* Testing Protocols and Analysis to Characterize Mixture Fatigue Resistance.* FHWA-DTFH61-07H-0009, U.S. Department of Transportation Federal Highway Administration, McLean, VA.

Lytton, R.L., D.E. Pugahl, C.H. Michalak, H.S. Liang, and B.J. Dempsey. (1989). An Integrated Model of the Climatic Effects on Pavements. Report FHWA-RD-90-033, Texas Transportation Institute, College Station, TX.

Martin, K. L., R.R. Davison, C.J. Glover, and J.A. Bullin. (1990). Asphalt Aging in Texas Roads and Test Sections. *Transportation Research Record*, Vol. 1269, pp. 9–19.

Masad E, E. Arambula, R. Ketcham, A. Abbas, A.E. Martin. (2007). Nondestructive Measurements of Moisture Transport in Asphalt Mixtures. *Asphalt Paving Technology*, Vol. 76, pp. 919–952.

Masad E. (2004). X-Ray Computed Tomography of Aggregates and Asphalt Mixes. *Materials Evaluation*, Vol. 62 (7), pp. 775–783.

Masad, E., B. Muhunthan, N. Shashidhar, and T. Harman. (1999a). Internal Structure Characterization of Asphalt Concrete Using Image Analysis. *Journal of Computing in Civil Engineering*, Vol. 13(2), pp. 88–95.

Masad, E., B. Muhunthan, N. Shashidhar, and T. Harman. (1999b). Effect of Compaction Procedure on the Aggregate Structure in Asphalt Concrete. *Transportation Research Record*, Vol. 1681, pp. 179–184.

Masad, E., V. K. Jandhyala, N. Dasgupta, N. Somadevan, and N. Shashidhar. (2002). Characterization of Air Void Distribution in Asphalt Mixes using X-ray Computed Tomography. *Journal of Materials in Civil Engineering*, Vol. 14 (2), pp. 122–129.

Masad, E., S. Saadeh, T. Al-Rousan, E. Garboczi, and D. Little. (2005). Computations of Particle Surface Characteristics using Optical and X-ray CT Images. *Journal of Computational Materials Science*, Vol. 34, pp. 406–424.

Maxwell, E.L. (1998). METSTAT: The Solar Radiation Model Used in the Production of the National Solar Radiation Data Base (NSRDB). *Solar Energy*, Vol. 62, pp.263–279.

McCarthy, L. M. and J. Liang (2011). Sensitivity Analysis for Flexible Pavement Design Using the Mechanistic-Empirical Pavement Design Guide. *Transportation Research E-Circular,* E-C155.

Minhoto, M.J.C., J.C Pais, P.A.A. Pereira, and L.G. Picado-Santos. (2005) Predicting Asphalt Pavement Temperature with a Three-Dimensional Finite Element Method. *Transportation Research Record*, No. 1919, pp. 96–110.

Mirza, M.W., and M.W. Witczak. (1995). Development of a Global Aging System Short and Long Term Aging of Asphalt Cements. *Asphalt Paving Technology, Vol.* 64, pp. 393–430.

Mrawire, D.M, and J. Luca. (2006). Effect of Aggregate Type, Gradation, and Compaction Level on Thermal Properties of Hot-Mix Asphalts. *Canadian Journal of Civil Engineering*, Vol. 33, pp. 1410–1417.

National Climatic Data Center (NCDC). (2005). Climate Maps of United States-Mean Snow Depth. http://cdo.ncdc.noaa.gov/cgi-bin/climaps/climaps.pl. Accessed March 2008.

National Climatic Data Center (NCDC). (2005). Climate Maps of United States-Mean Relative Humidity. http://cdo.ncdc.noaa.gov/cgi-bin/climaps/climaps.pl. Accessed March 2008.

North Dakota Agricultural Weather Network. (2011). *Data Information, http://ndawn.ndsu.nodak.edu/help.html?topic=datainfo*. Accessed January 2011.

Perez, R., P. Ineichen, K. Moore, M. Kmiecik, C. Chain, R. George, and F. Vignola. (2002). A New Operational Model for Satellite-Derived Irradiances: Description and Validation. *Solar Energy*, Vol.73, pp. 307–317.

Petersen, J. C. (1998). Asphalt Aging - Dual Oxidation Mechanism and its Interrelationships with Asphalt Composition and Oxidative Age Hardening. *Asphalt Mixture Components*, Vol.1638, pp. 47–55.

Petersen, J.C. (1986). Quantitative Function Group Analysis of Asphalts Using Differential Infrared Spectrometry and Selective Chemical Reaction-Theory and Applications. *Transportation Research Record*, No. 1096, pp. 1-11.

Petersen, J. C. (2009). A Review of the Fundamentals of Asphalt Oxidation Chemical, Physicochemical, Physical Property, and Durability Relationships. *Transportation Research Circular, Number E-C140.* Transportation Research Board of the National Academies, Washington, D.C.

Petersen, J. C. and P.M. Harnsberger. (1998). Asphalt Aging: Dual Oxidation Mechanism and Its Interrelationships with Asphalt Composition and Oxidative Age Hardening. *Transportation Research Record*, No. 1638, pp. 47–55.

Petersen, J. C., J.F. Branthaver, R.E. Robertson, P.M. Harnsberger, J.J. Duvall, and E.K. Ensley. (1993). Effects of Physiochemical Factors on Asphalt Oxidation Kinetics. *Transportation Research Record*, No. 1391, pp. 1–10.

Prapaitrakul N., X. Jin., R. Han, and C.J. Glover. (2009). A Transport Model of Asphalt Binder Oxidation in Pavements. *Road Materials and Pavement Design,* Vol. 10 (Special Issue), pp. 95–113.

R Development Core Team. (2011). *R: A Language and Environment for Statistical Computing.* http://www.r-project.org/. R Foundation for Statistical Computing: Vienna, Austria.

Radisic, M., W. Deen, R. Langer, and G. Vunjak-Novakovic. (2005). Mathematical Model of Oxygen Distribution in Engineered Cardiac Tissue with Parallel Channel Array Perfused with Culture Medium Containing Oxygen Carriers. *American Journal of Physiology - Heart and Circulatory Physiology*, Vol. 288, pp. H1278–H1289.

Reid R.C., J.M. Prausnitz, and T.K. Sherwood. (1977). The Properties of Gases and Liquids, 3rd ed., New York, McGraw-Hill, p. 567.

Ruan, Y., R.R. Davison, and C.J. Glover. (2003). An Investigation of Asphalt Durability: Relationships Between Ductility and Rheological Properties for Unmodified Asphalts. *Petroleum Science and Technology*, Vol. 21(1&2), pp. 231–254.

Rumney, T.N., and R.A. Jimenez. (1969). "Pavement Temperatures in the Southwest". *Highway Research Record*, Vol. 361, pp. 1–13.

Senadheera, S., D.D. Gransberg, and T. Kologlu. (2000). Statewide Seal Coat Constructability Review. Report TX-97/0-1787-3, Texas Department of Transportation, Austin, TX.

Siddiqui, M.N. (2009). NMR Finger Printing of Chemical Changes in Asphalt Fractions on Oxidation. *Petroleum Science & Technology*, Vol. 27(17), pp. 2033–2045.

Simpson, A. L., B.K. Ostrom, and P.N. Schmalzer. (2006). Guidelines for The Collection of Long-Term Pavement Performance Data. Report FHWA-HRT-06-067, MACTEC Engineering and Consulting, Inc., Beltsville, MD.

Solaimanian, M., and T.W. Kennedy. (1993). Predicting Maximum Pavement Surface Temperature Using Maximum Air Temperature and Hourly Solar Radiation. *Transportation Research Record*, Vol. 1417, pp. 1–11.

Sousa, J. B., J. Harvey, L. Painter, J.A. Deacon, and C.L. Monismith. (1991). Evaluation of Laboratory Procedures for Compacting Asphalt-Aggregate Mixtures. Report SHRP-A-UWP = 91-523, Strategic Highway Research Program, National Research Council, Washington, D.C.

Torres A.C. (2004). Probabilistic Analysis of Air Void Structure and its Relationship to Permeability and Moisture Damage of Hot Mix Asphalt. M.S. thesis, Texas A&M University, College Station, TX.

TxDOT. (2004). Texas Department of Transportation Standard Specifications for Construction and Maintenance of Highways, Streets, and Bridges. Austin, TX.

U.S. Geological Survey. A Global Crustal Model. http://www.usgs.gov. Accessed October 2006.

Van Oort, W.P. (1956). Durability of Asphalt. *Industrial and Engineering Chemistry*, Vol. 48, pp. 1196–1201.

Viswanadham, Y., and R. Ramanadham. (1970). Estimation of Long Wave Radiation by an Empirical Method. *Pure and Applied Geophysics*, Vol. 81, pp. 272–278.

Walubita, L.F. (2006). Comparison of Fatigue Analysis Approaches for Predicting Fatigue Lives of Hot Mix Asphalt Concrete Mixtures (HMA). Ph.D. Dissertation, Texas A&M University, College Station, TX.

Walubita, L.F., A.E. Martin, C.J. Glover, S.H. Jung, G.C. Cleveland, and R.L. Lytton. (2005a). Fatigue Characterization of Asphalt Concrete Using Mechanistic Empirical and Calibrated Mechanistic Approaches Including the Effects of Aging. ASCE/GSP- R. Lytton Symposium June 1-3, 2005, Asphalt Concrete: Simulation, Modeling, and Experimental Characterization (Geotechnical Special Publication 146), Volume 185, No. 11, pp.103–114.

Walubita, L.F., A.E. Martin, S.H. Jung, C.J. Glover, E.S. Park, A. Chowdhury, and R.L. Lytton (2005b). Comparison of Fatigue Analysis Approaches for Two Hot Mix Asphalt Concrete (HMA) Mixtures. Report FHWA/TX-05/0-4468-2, Texas Transportation Institute, College Station, TX.

Walubita L.F., A.E. Martin, and G.S. Cleveland. (2006a). Application of the New M-E Pavement Design Guide Software for Fatigue Characterization of Three Texas Asphalt Mixtures, Paper accepted for presentation at the *10th ICAP Conference 2006*, 12-17 August 2006, Quebec, Canada.

Walubita, L.F., A. Epps Martin, C.J. Glover, S.H. Jung, G.C. Cleveland, R.L. Lytton, and E.S. Park. (2006b). Application of the Calibrated Mechanistic Approach with Surface Energy (CMSE) Measurements for Fatigue Characterization of Asphalt Mixtures. *Association of Asphalt Paving Technologists*, Vol. 75, pp. 457–490.

Walubita L.F., A.E. Martin, S.H. Jung, C.J. Glover, and E.S. Park. (2006c). Application of Calibrated Mechanistic Fatigue Analysis with Aging Effects. Report FHWA/TX-06/0-4468-3, 2006, Texas Transportation Institute, College Station, TX.

Woo WJ, A. Chowdhury, C.J. Glover. (2008). Field Aging of Unmodified Asphalt Binder in Three Texas Long-Term Performance Pavements. *Transportation Research Record: Journal of the Transportation Research Board*, Vol. 2051, pp. 11–22.

Woo WJ, E. Ofori-Abebresse, A. Chowdhury, J. Hilbrich, Z. Kraus, A.E. Martin, and C.J. Glover. (2007). Polymer Modified Asphalt Durability in Pavements. Publication FHWA/TX-07/0-4688-1, FHWA/TX-07, Texas Transportation Institute, College Station, TX.

Yavuzturk, C., K. Ksaibati., and A.D.Chiasso. (2005). Assessment of Temperature Fluctuations in Asphalt Pavement Due to Thermal Environmental Conditions Using a Two-Dimensional, Transient Finite-Difference Approach. *Journal of Materials in Civil Engineering*, Vol. 17, pp. 465–475.

APPENDIX A

CARBONYL CONTENT AT ES AND SI: EXPERIMENTAL MEASUREMENT VERSUS MODEL CALCULATION

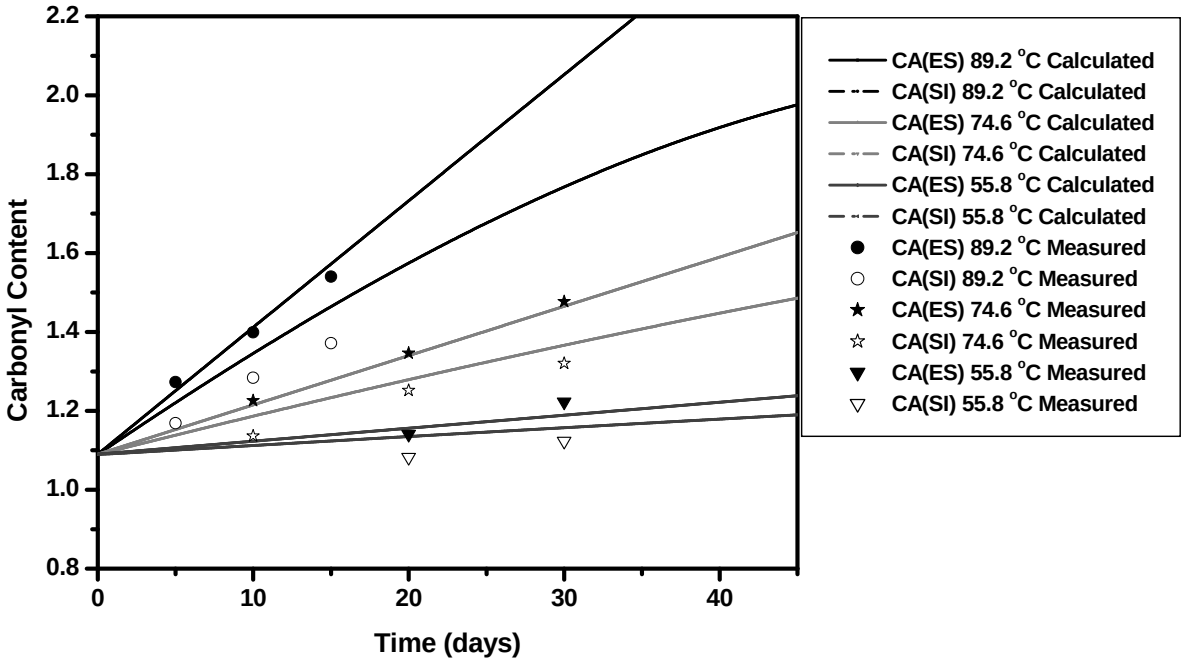


Figure A1. Carbonyl Growth at ES and SI of Asphalt Film of Valero-Houston 64-22: Experimental Measurement versus Model Calculation.

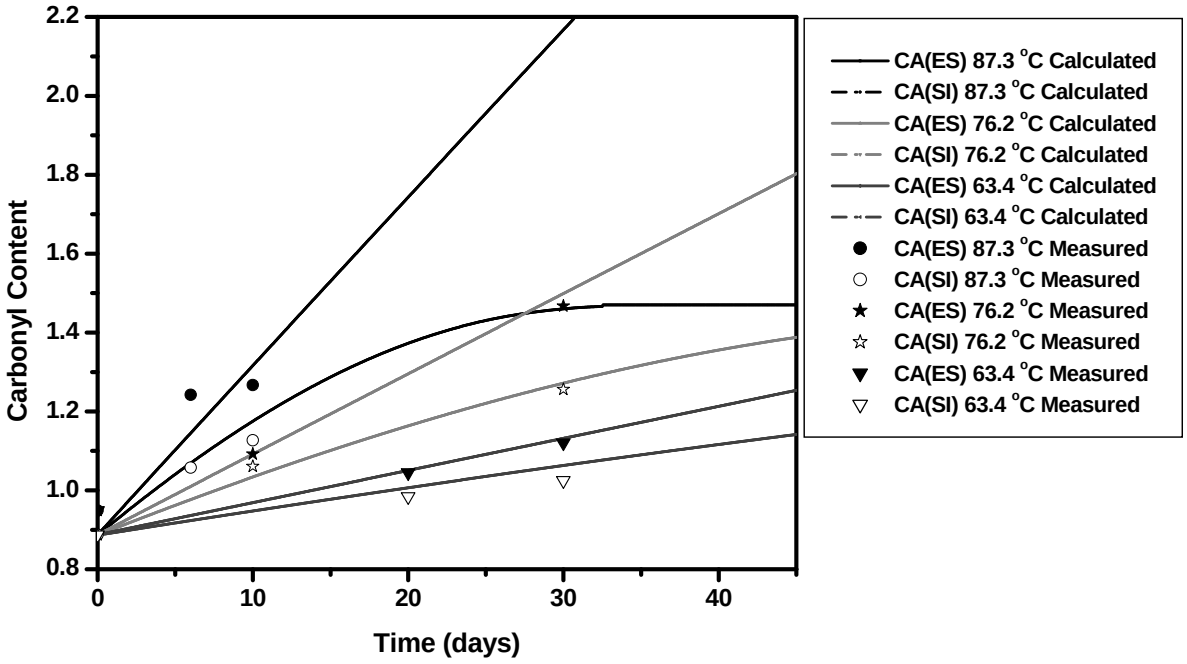


Figure A2. Carbonyl Growth at ES and SI of Asphalt Film of Martin 64-22: Experimental Measurement versus Model Calculation.

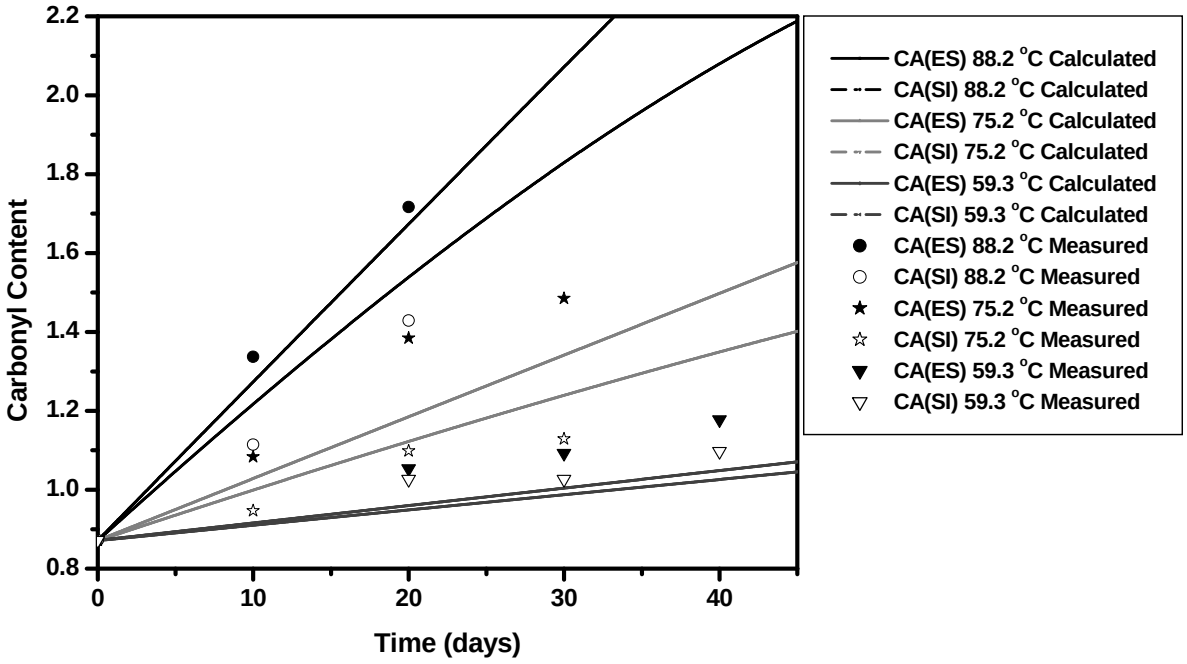


Figure A3. Carbonyl Growth at ES and SI of Asphalt Film of Alon 64-22: Experimental Measurement versus Model Calculation.

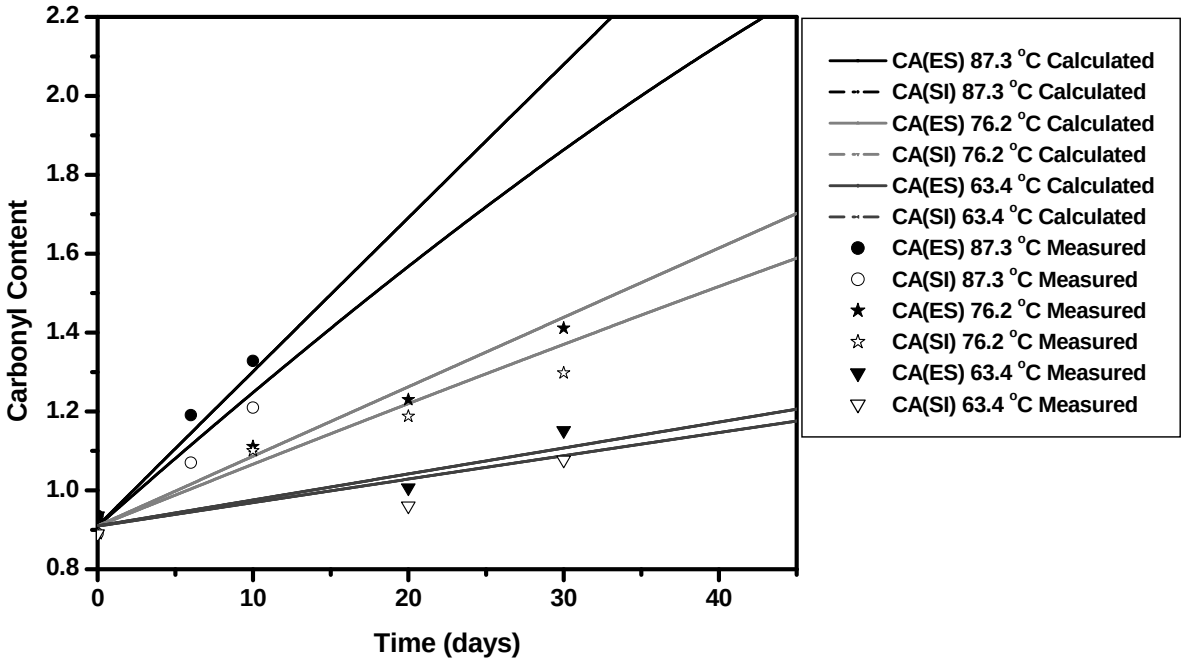


Figure A4. Carbonyl Growth at ES and SI of Asphalt Film of Alon 76-22: Experimental Measurement versus Model Calculation.

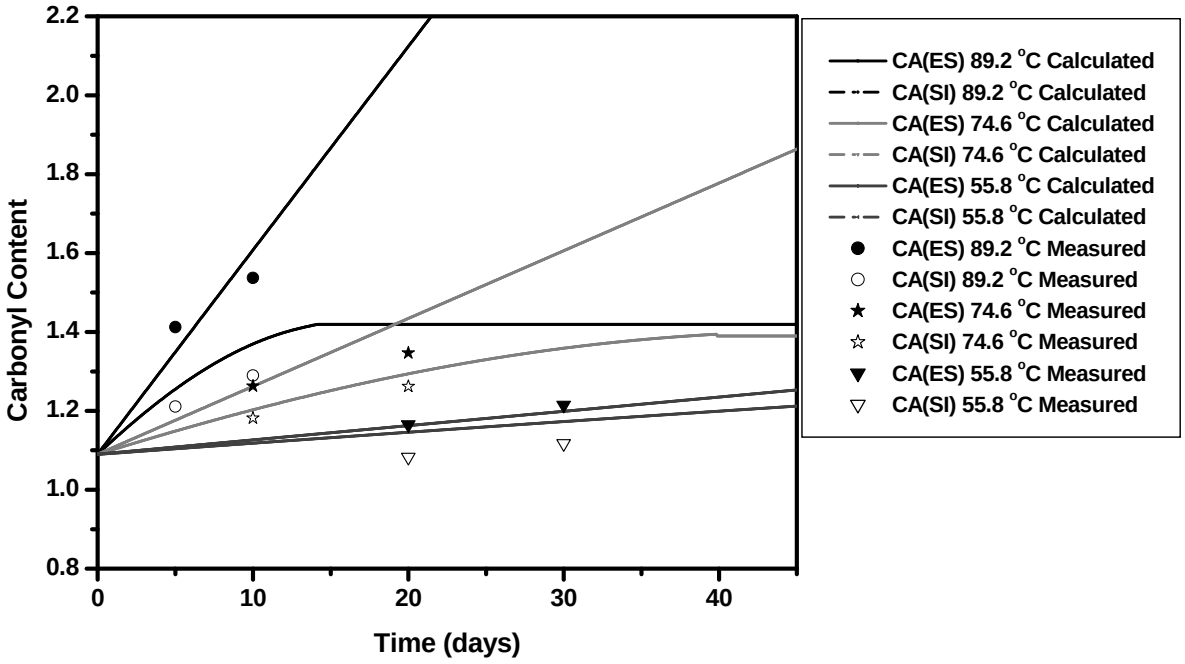


Figure A5. Carbonyl Growth at ES and SI of Asphalt Film of Lion 64-22: Experimental Measurement versus Model Calculation.

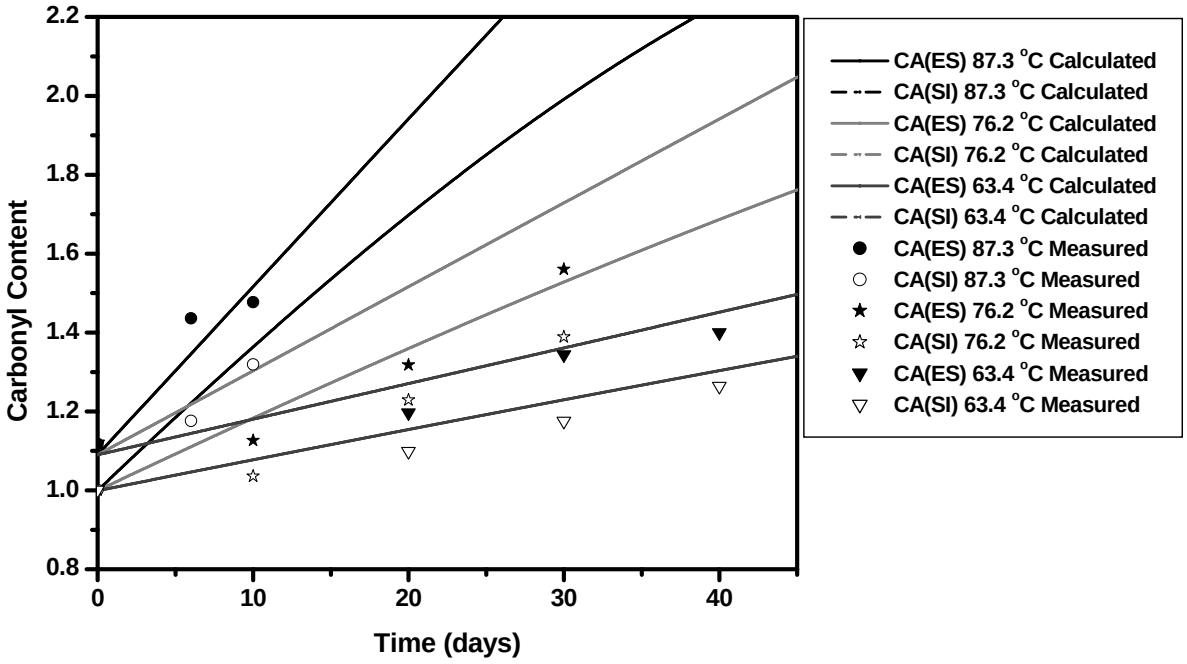


Figure A6. Carbonyl Growth at ES and SI of Asphalt Film of Lion 70-22: Experimental Measurement versus Model Calculation.

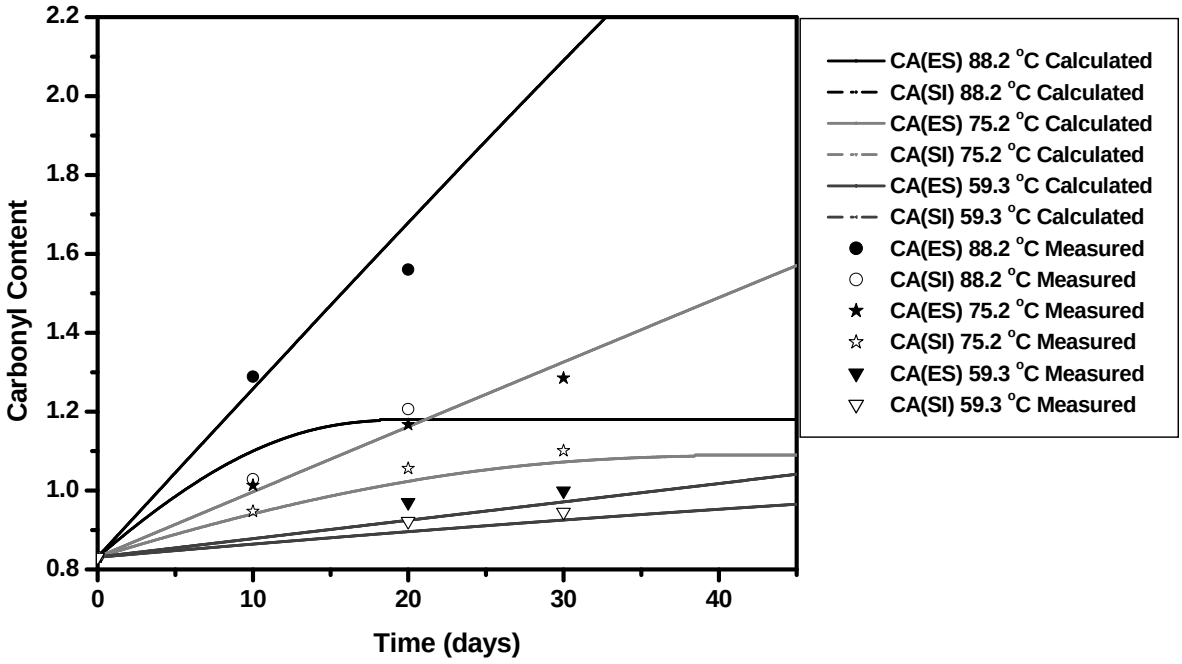


Figure A7. Carbonyl Growth at ES and SI of Asphalt Film of SEM 70-22: Experimental Measurement versus Model Calculation.

APPENDIX B

PAVEMENT TEMPERATURE

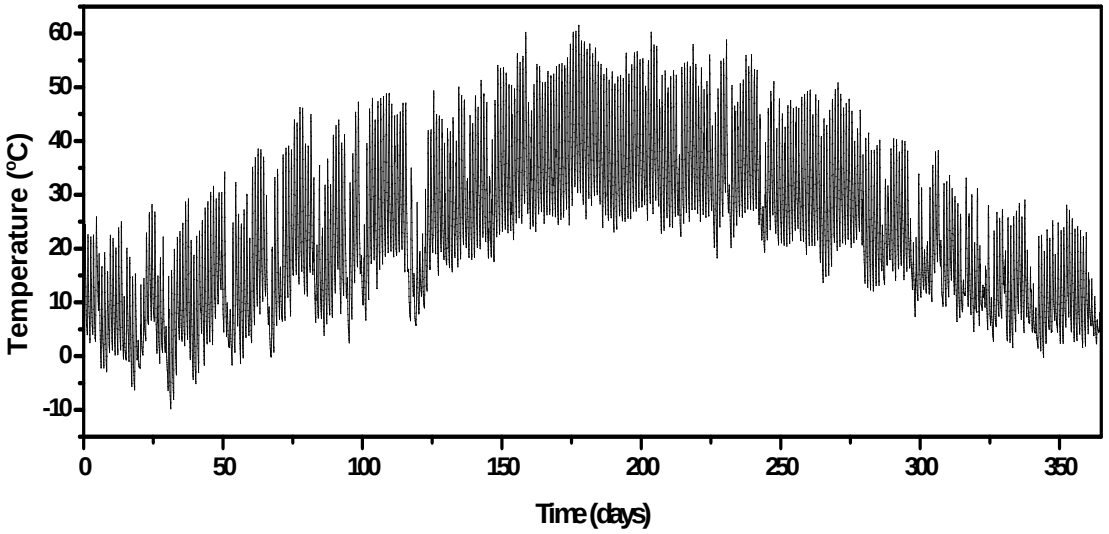


Figure B1. Pavement Temperature of US290 at Layer 1.

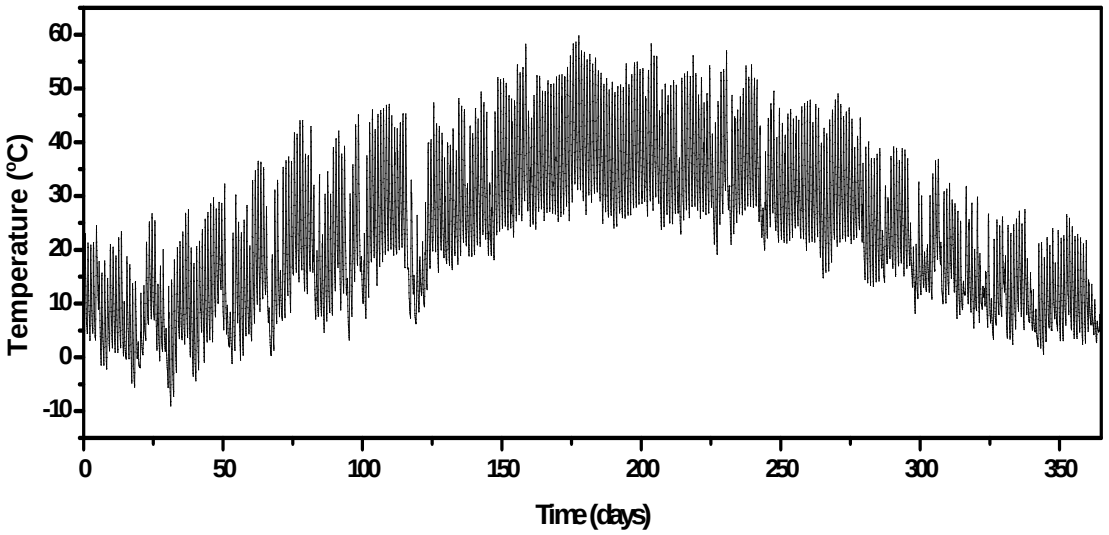


Figure B2. Pavement Temperature of US290 at Layer 2.

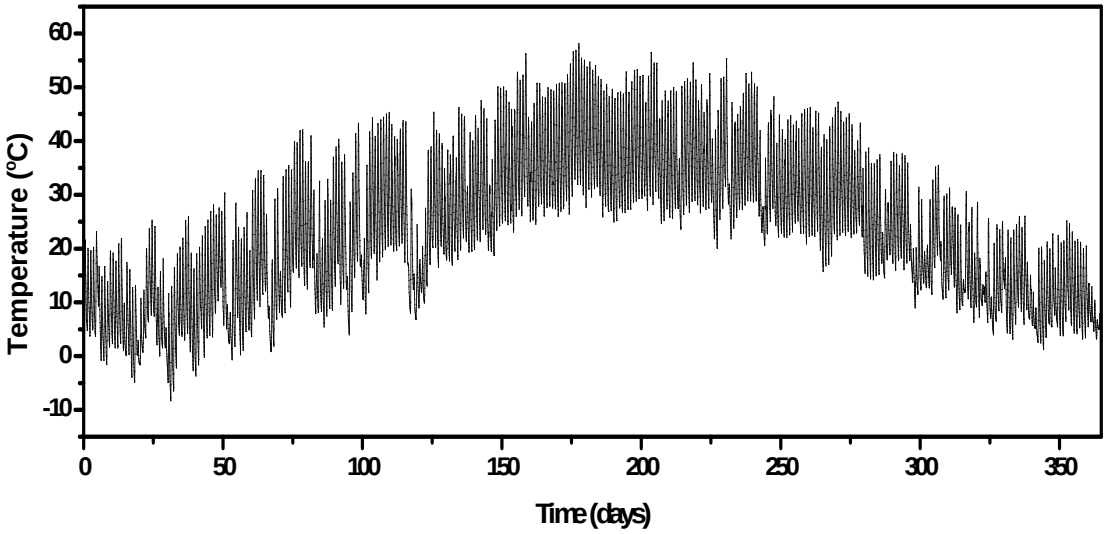


Figure B3. Pavement Temperature of US290 at Layer 3.

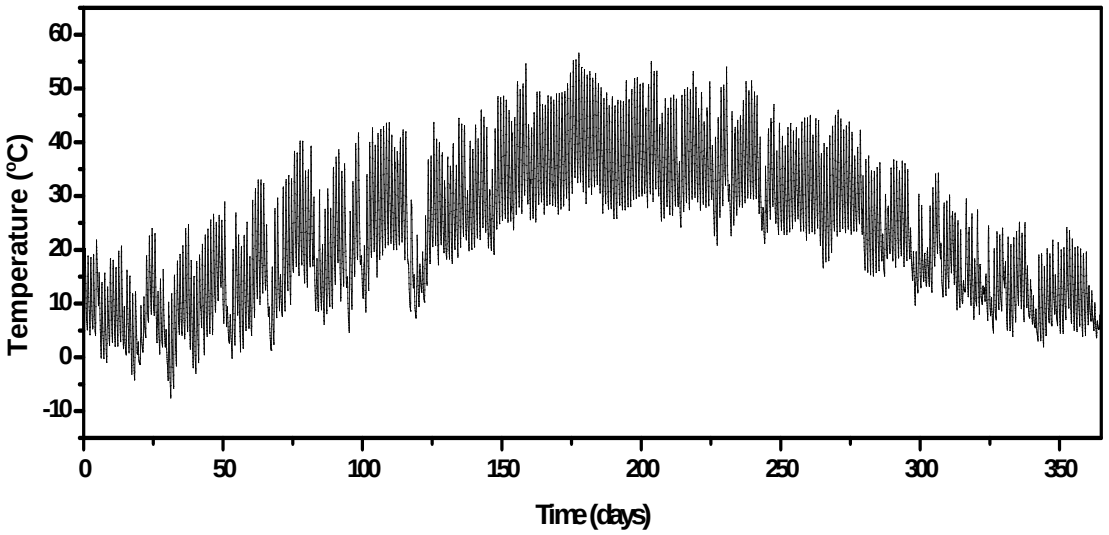


Figure B4. Pavement Temperature of US290 at Layer 4.

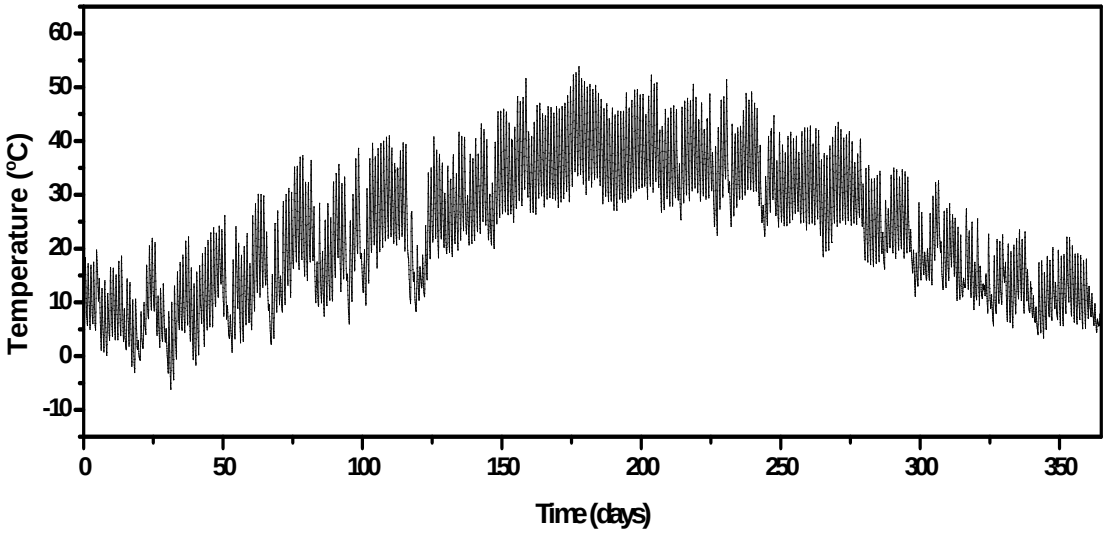


Figure B5. Pavement Temperature of US290 at Layer 5.

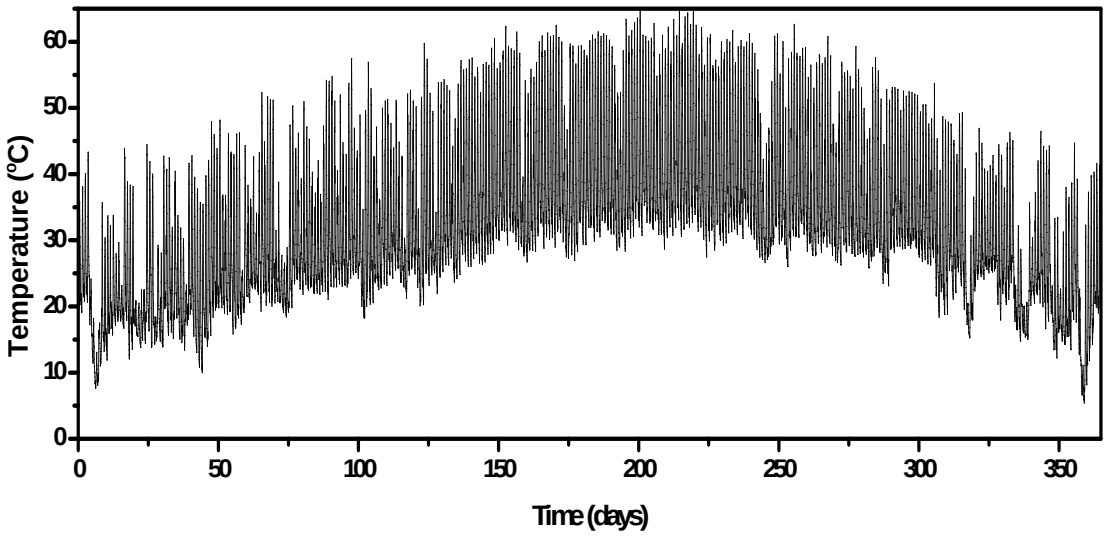


Figure B6. Pavement Temperature of US277 at Layer 1.

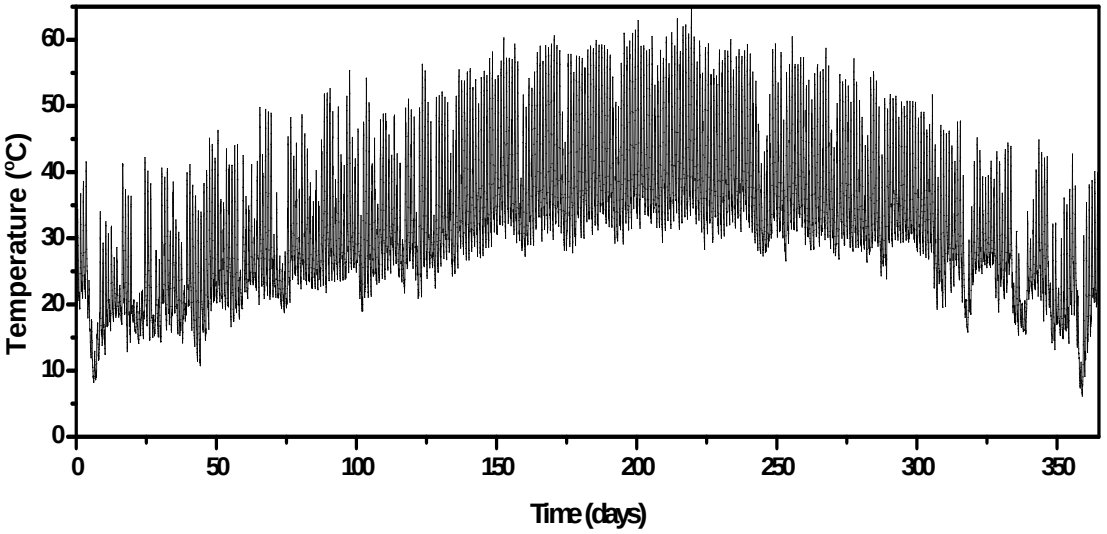


Figure B7. Pavement Temperature of US277 at Layer 2.

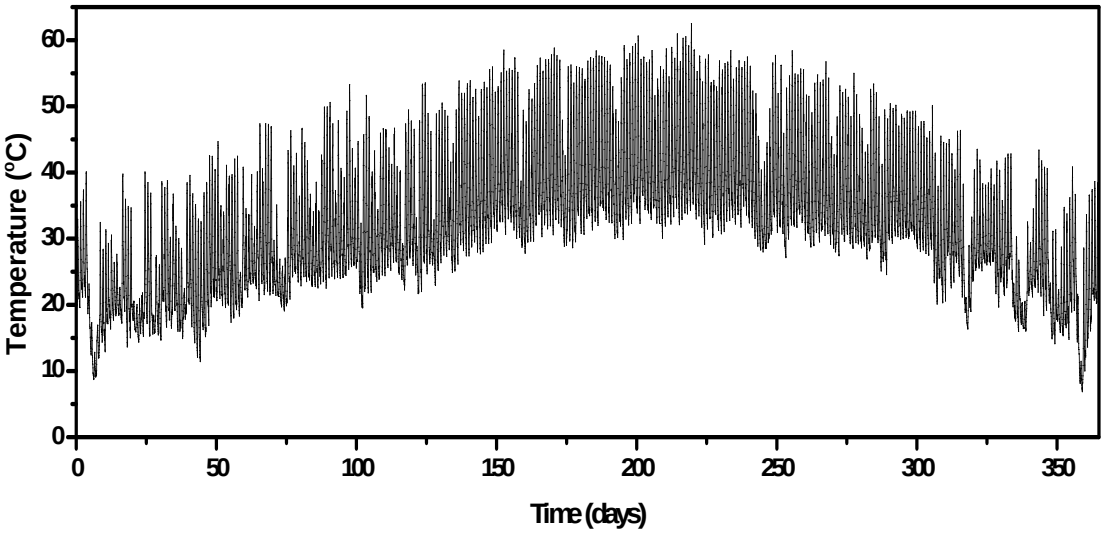


Figure B8. Pavement Temperature of US277 at Layer 3.

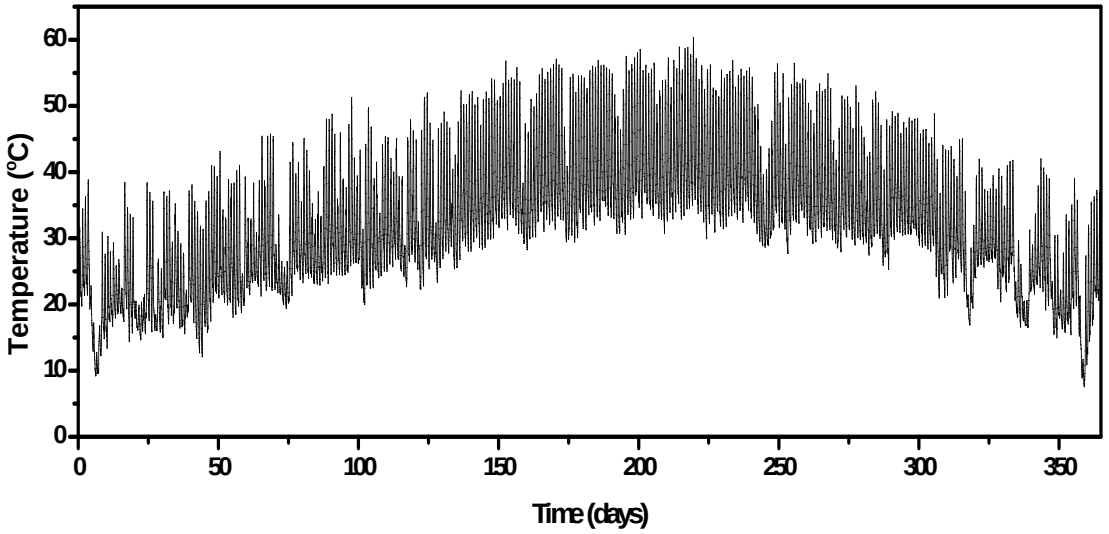


Figure B9. Pavement Temperature of US277 at Layer 4.

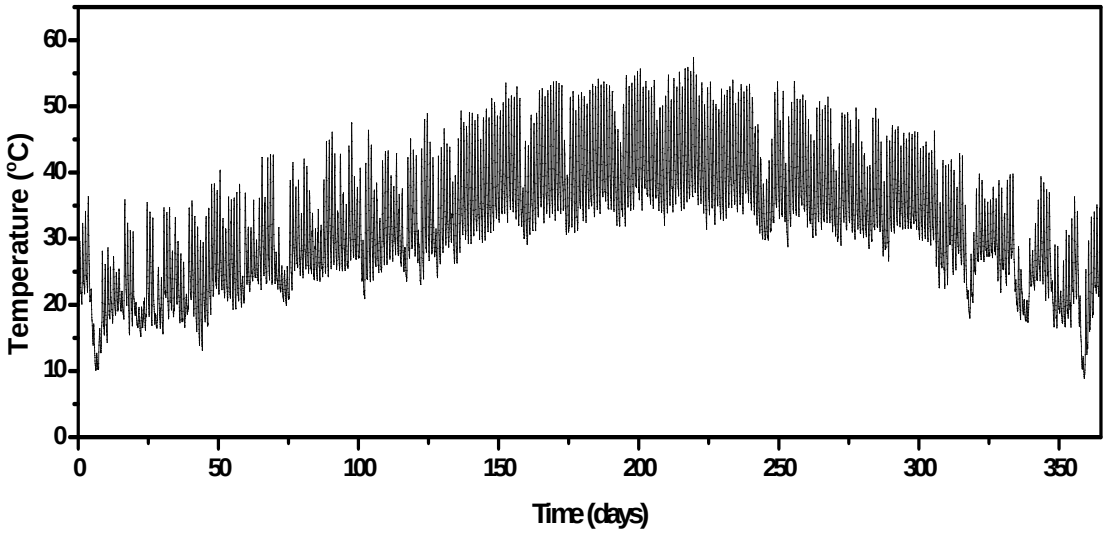


Figure B10. Pavement Temperature of US277 at Layer 5.

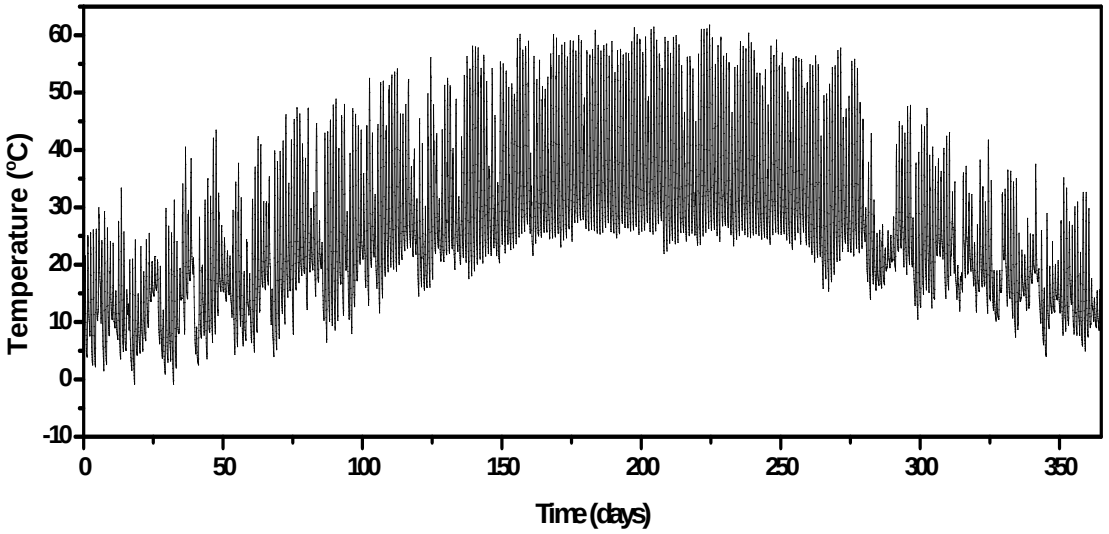


Figure B11. Pavement Temperature of US69 at Layer 1.

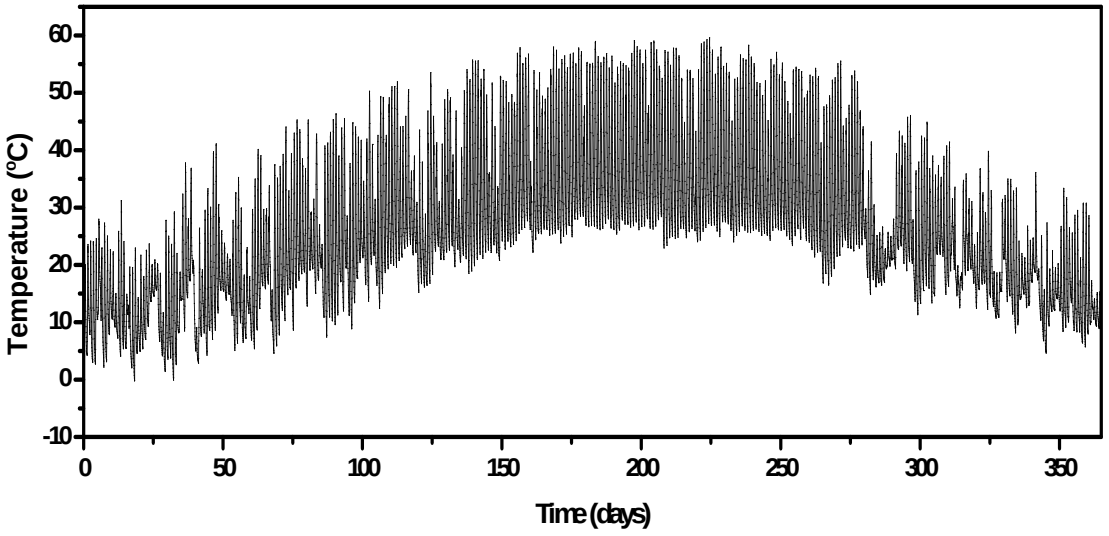


Figure B12. Pavement Temperature of US69 at Layer 2.

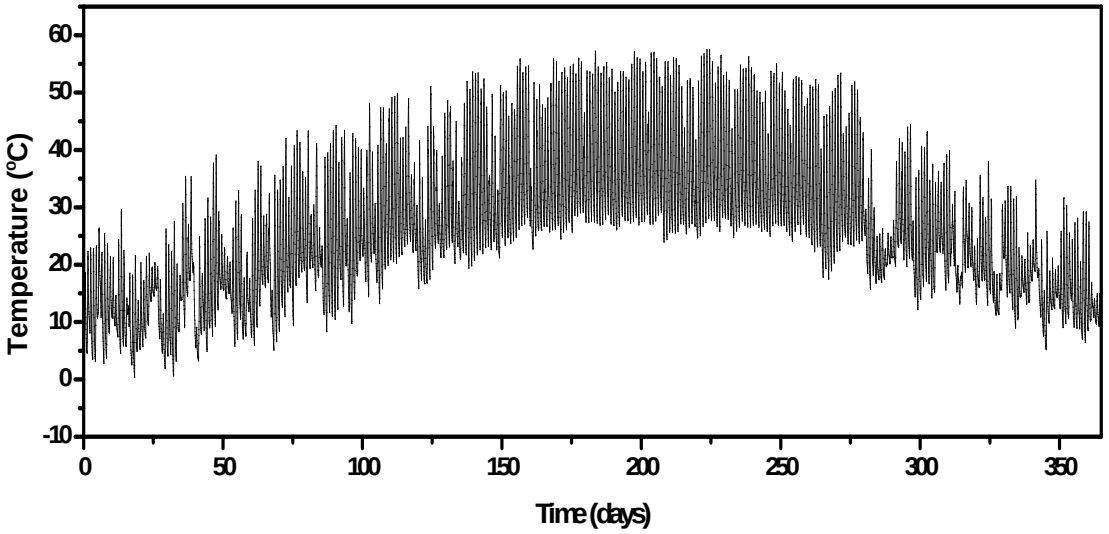


Figure B13. Pavement Temperature of US69 at Layer 3.

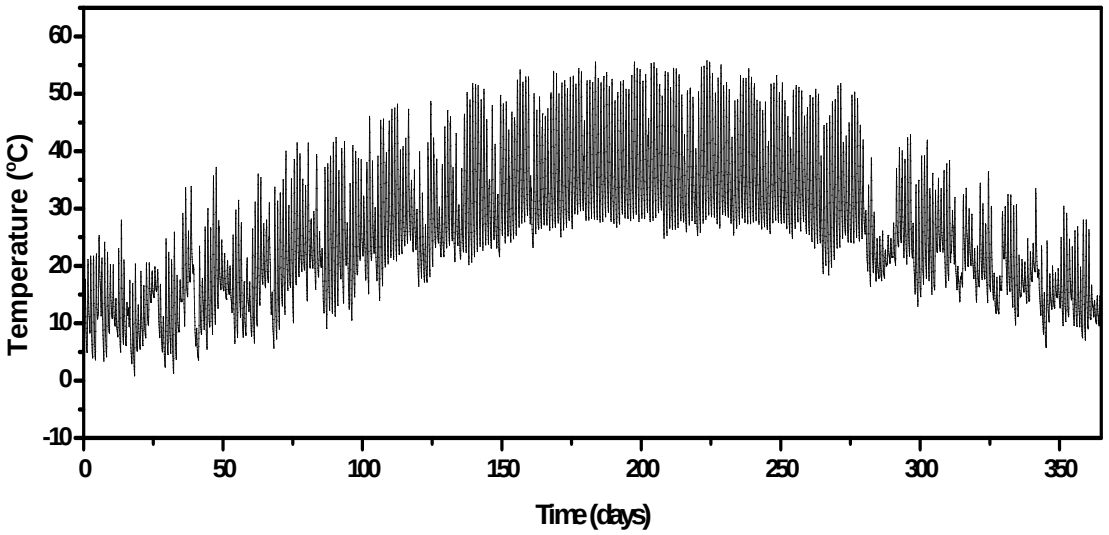


Figure B14. Pavement Temperature of US69 at Layer 4.

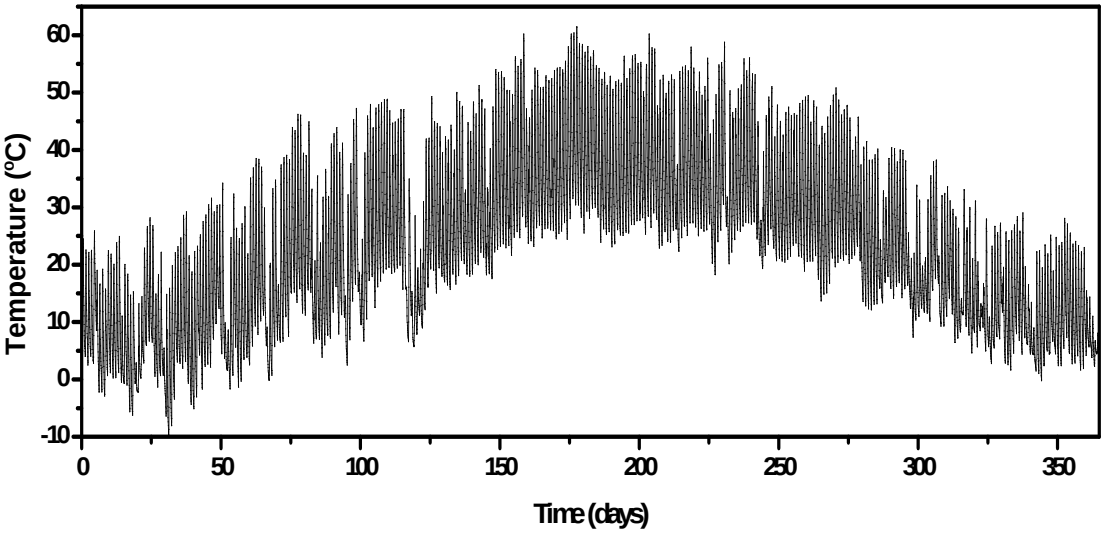


Figure B15. Pavement Temperature of US54 at Layer 1.

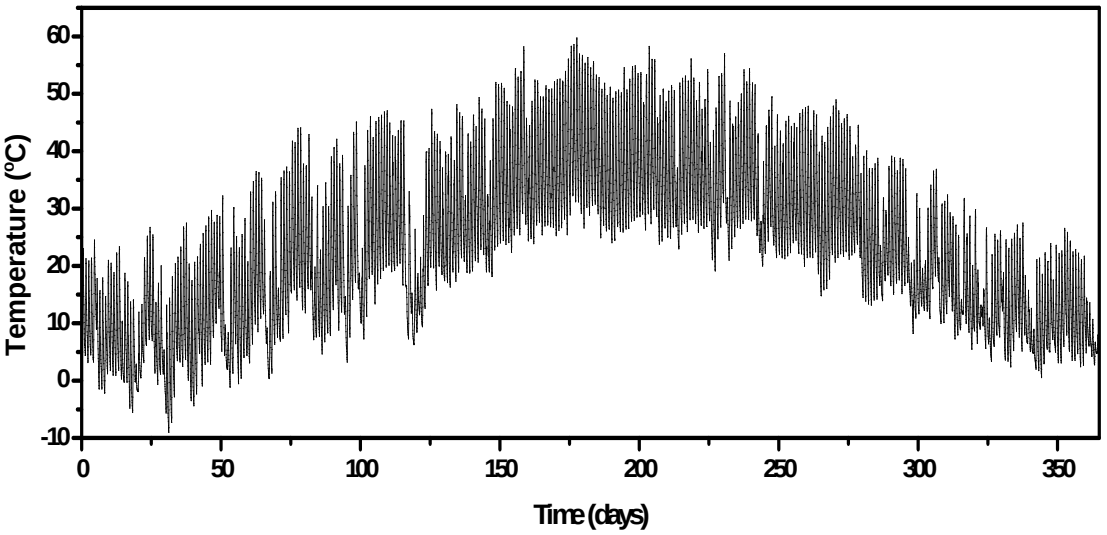


Figure B16. Pavement Temperature of US54 at Layer 2.

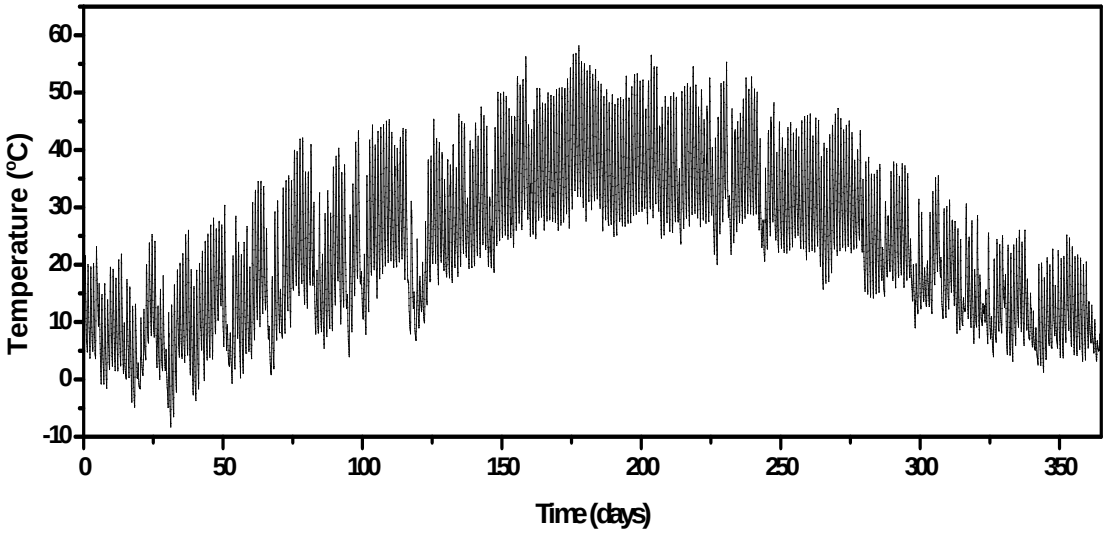


Figure B17. Pavement Temperature of US54 at Layer 3.

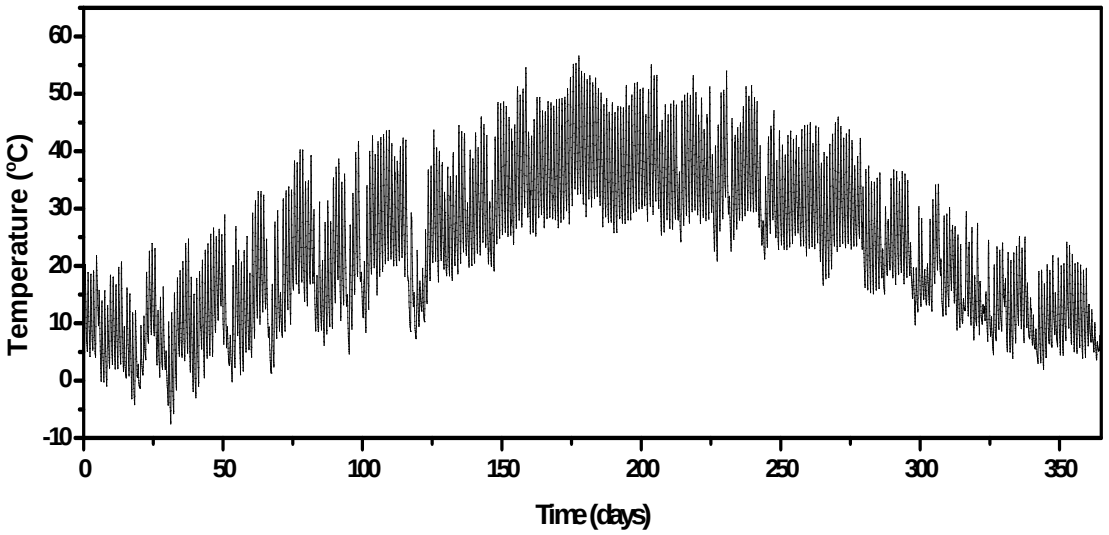


Figure B18. Pavement Temperature of US54 at Layer 4.

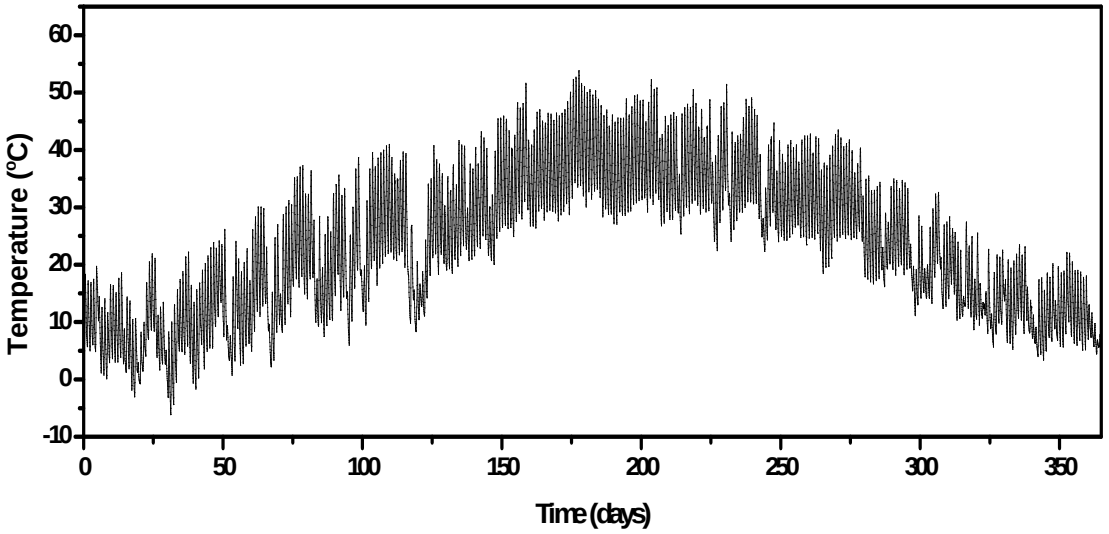


Figure B19. Pavement Temperature of US54 at Layer 5.

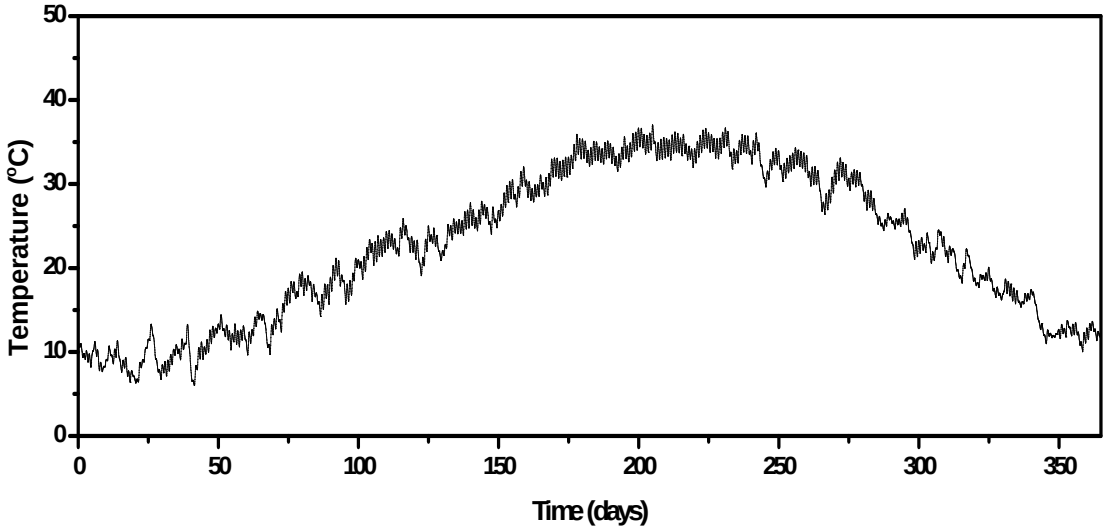


Figure B20. Pavement Temperature of IH35-Waco at Layer 1.

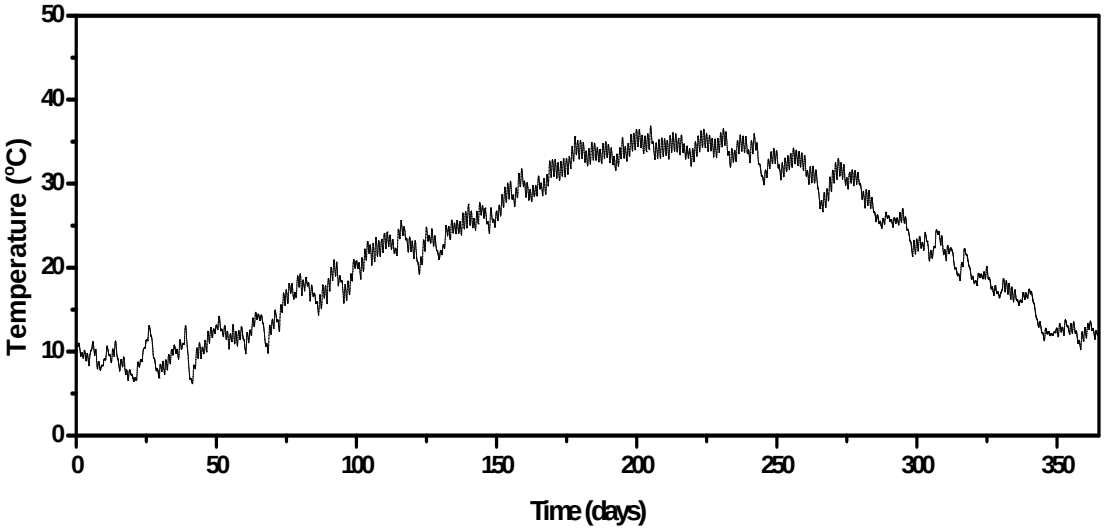


Figure B21. Pavement Temperature of IH35-Waco at Layer 2.

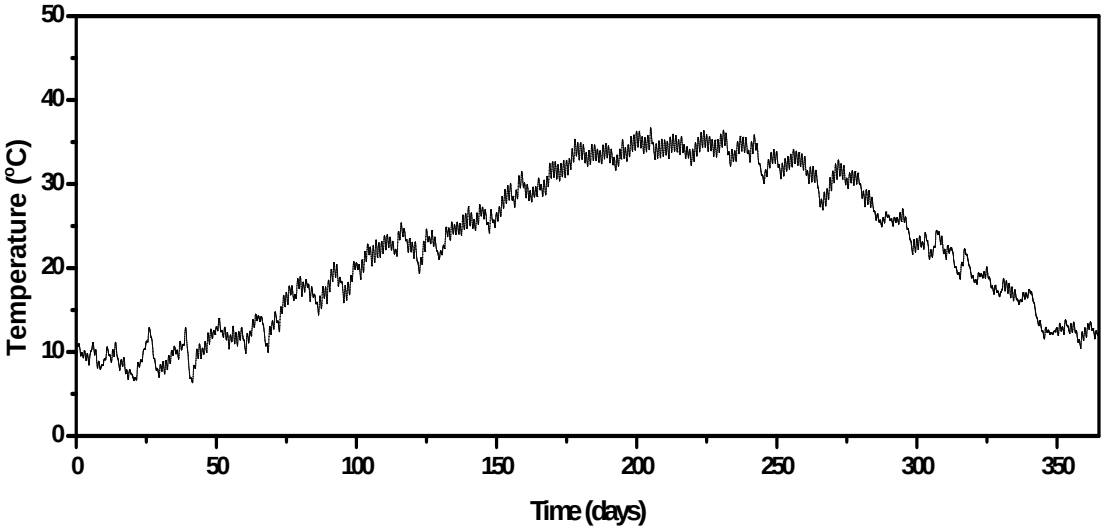


Figure B22. Pavement Temperature of IH35-Waco at Layer 3.

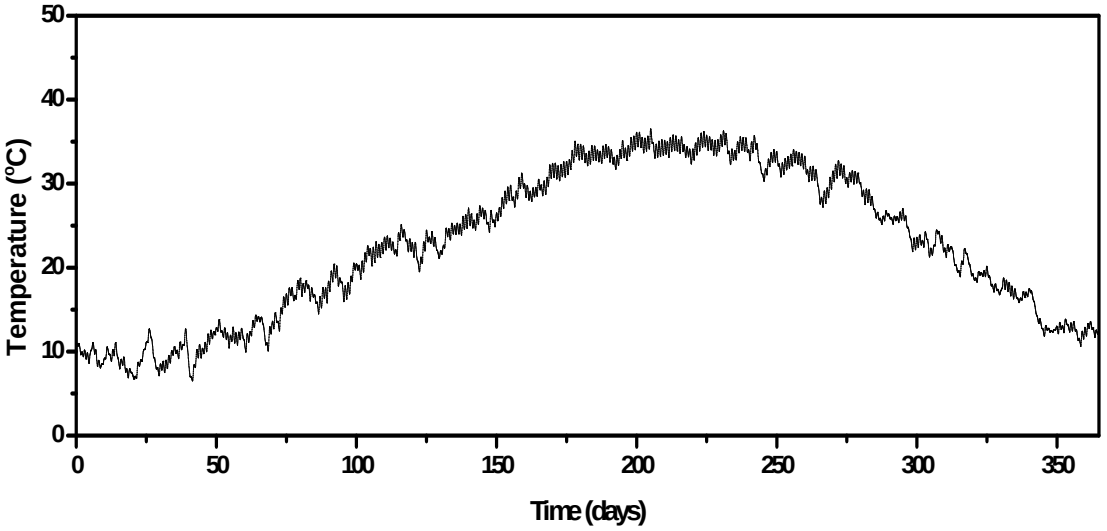


Figure B23. Pavement Temperature of IH35-Waco at Layer 4.

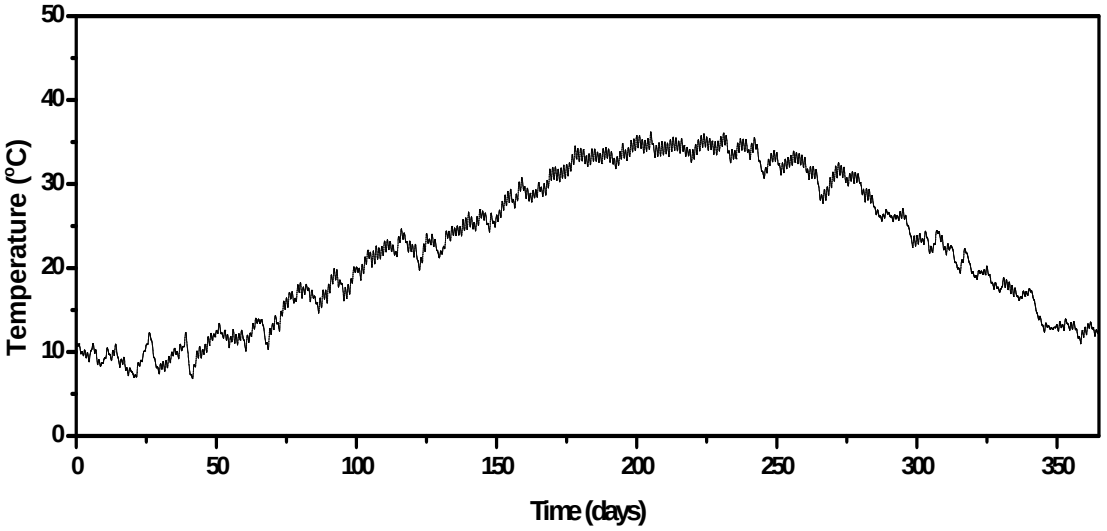


Figure B24. Pavement Temperature of IH35-Waco at Layer 5.

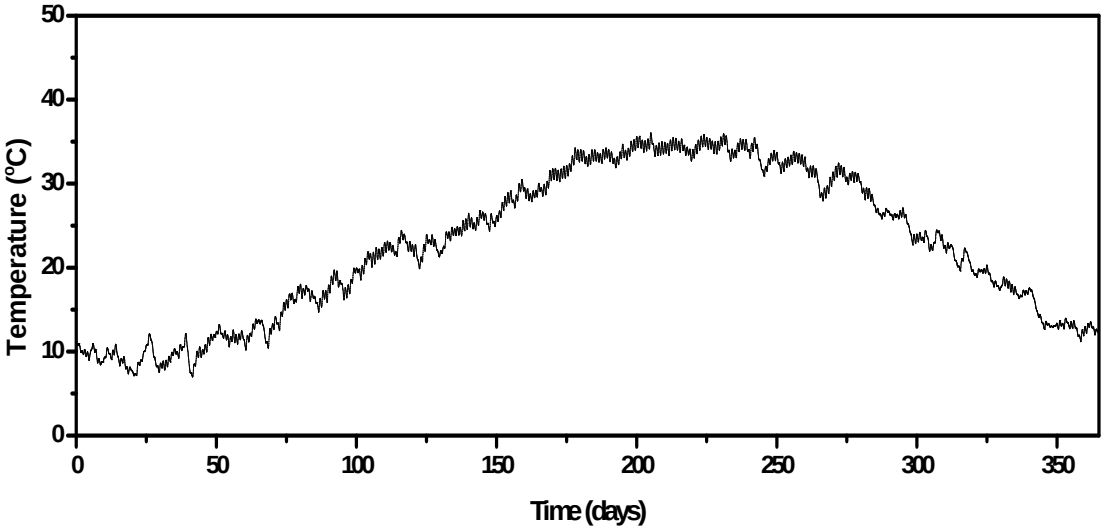


Figure B25. Pavement Temperature of IH35-Waco at Layer 6.

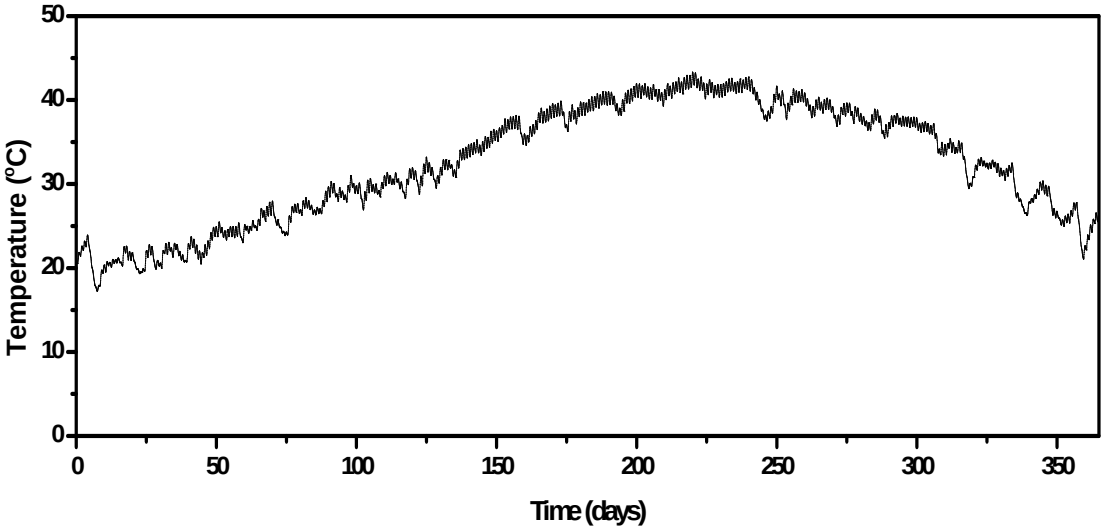


Figure B26. Pavement Temperature of IH35-LRD at Layer 1.

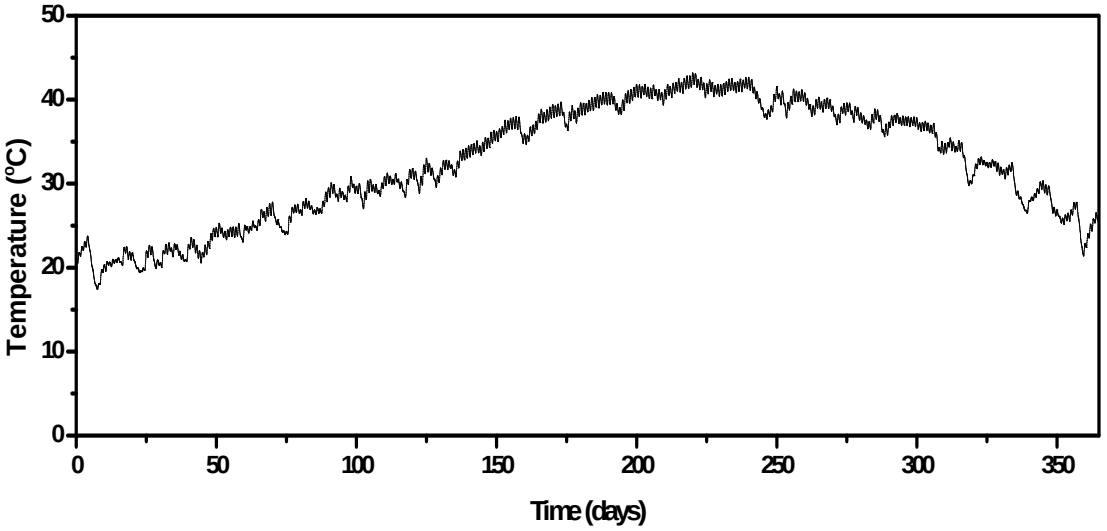


Figure B27. Pavement Temperature of IH35-LRD at Layer 2.

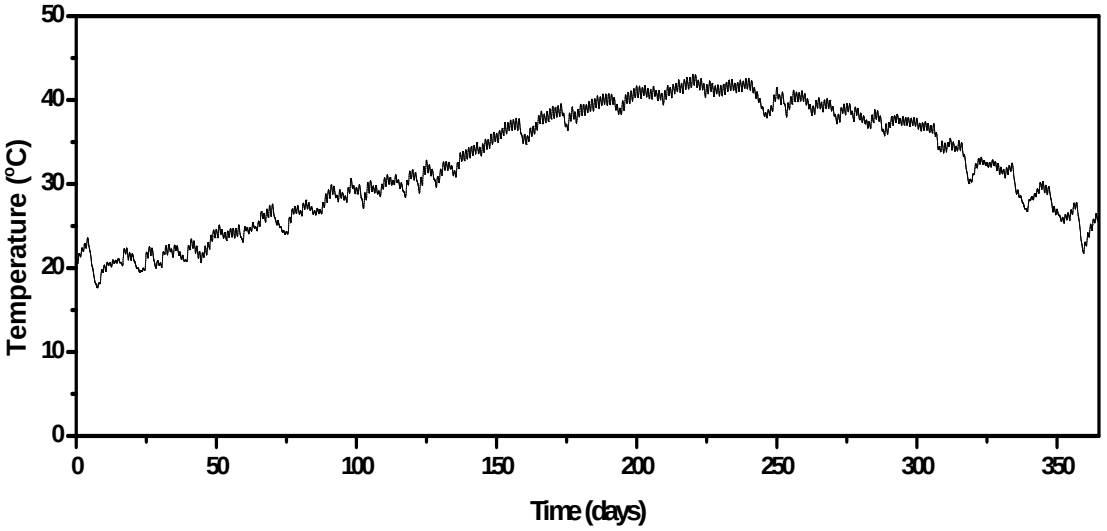


Figure B28. Pavement Temperature of IH35-LRD at Layer 3.

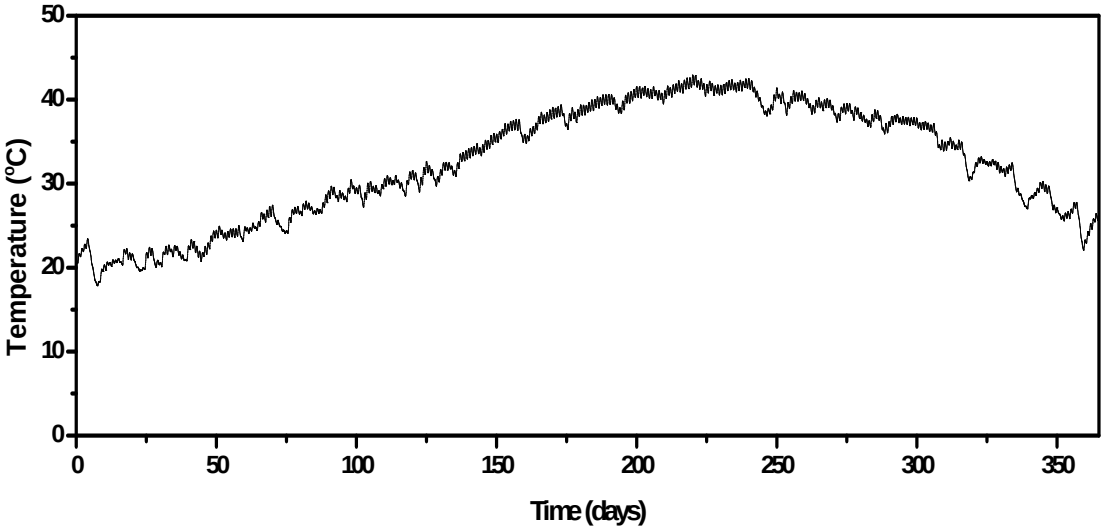


Figure B29. Pavement Temperature of IH35-LRD at Layer 4.

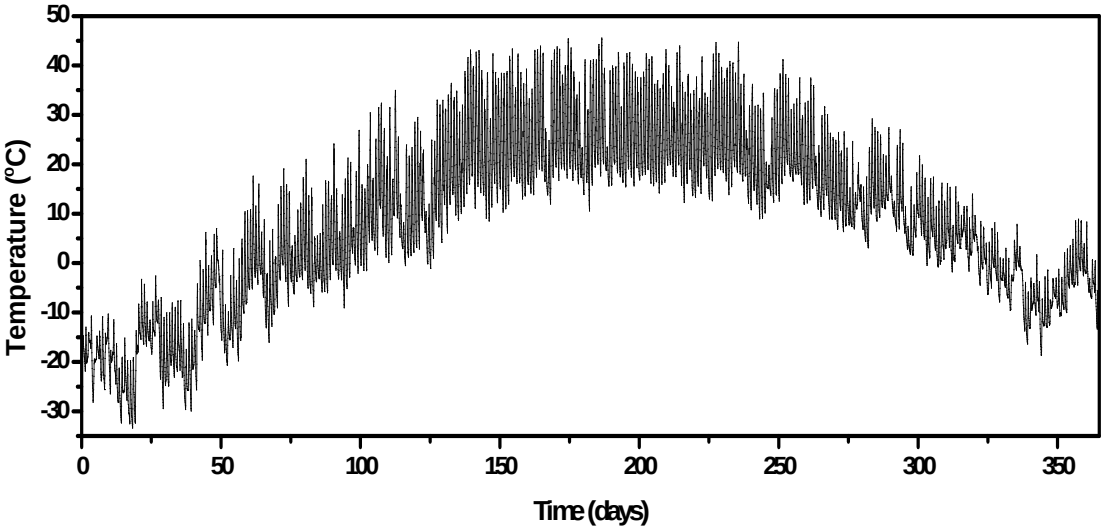


Figure B30. Pavement Temperature of MN CELL 1 at Layer 1.

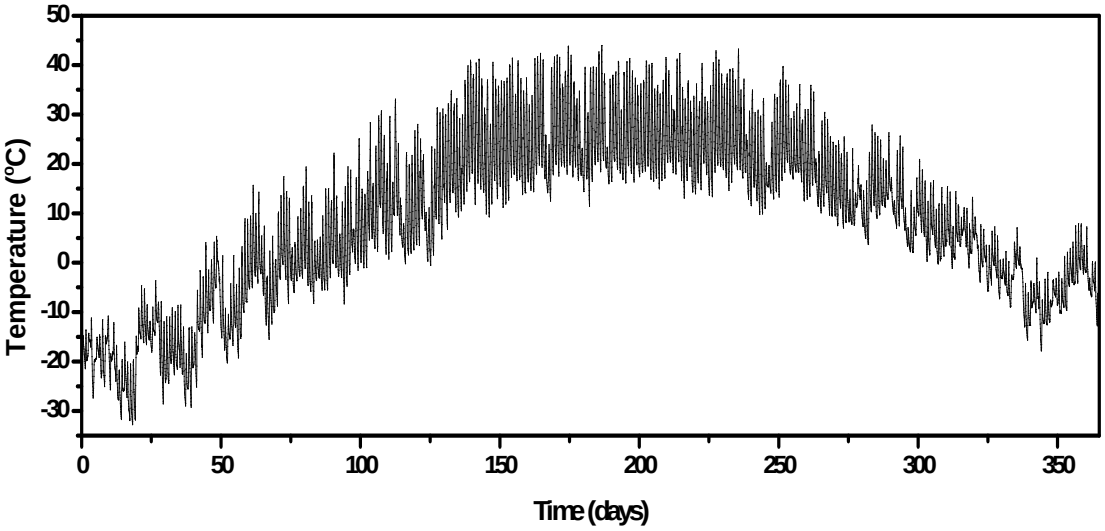


Figure B31. Pavement Temperature of MN CELL 1 at Layer 2.

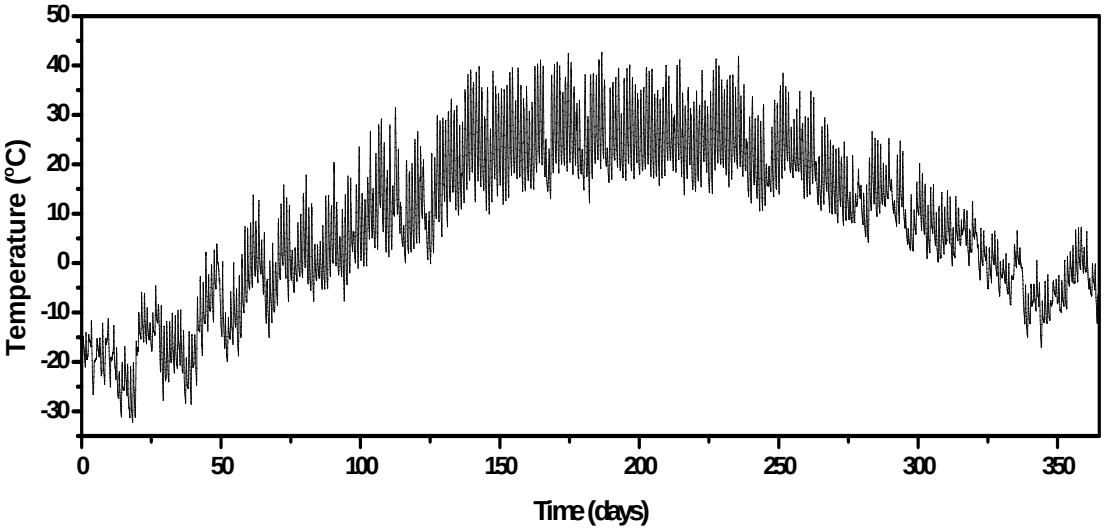


Figure B32. Pavement Temperature of MN CELL 1 at Layer 3.

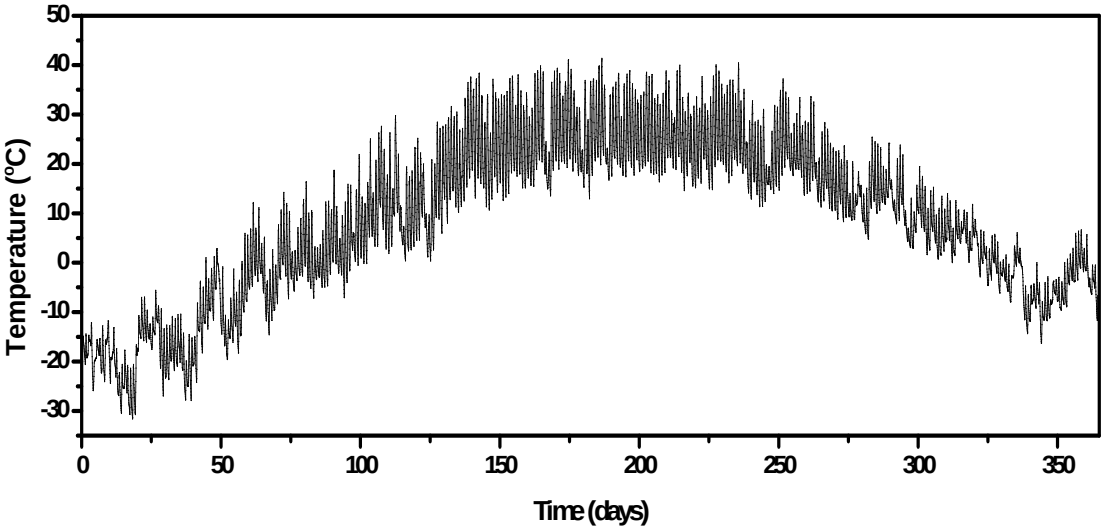


Figure B33. Pavement Temperature of MN CELL 1 at Layer 4.

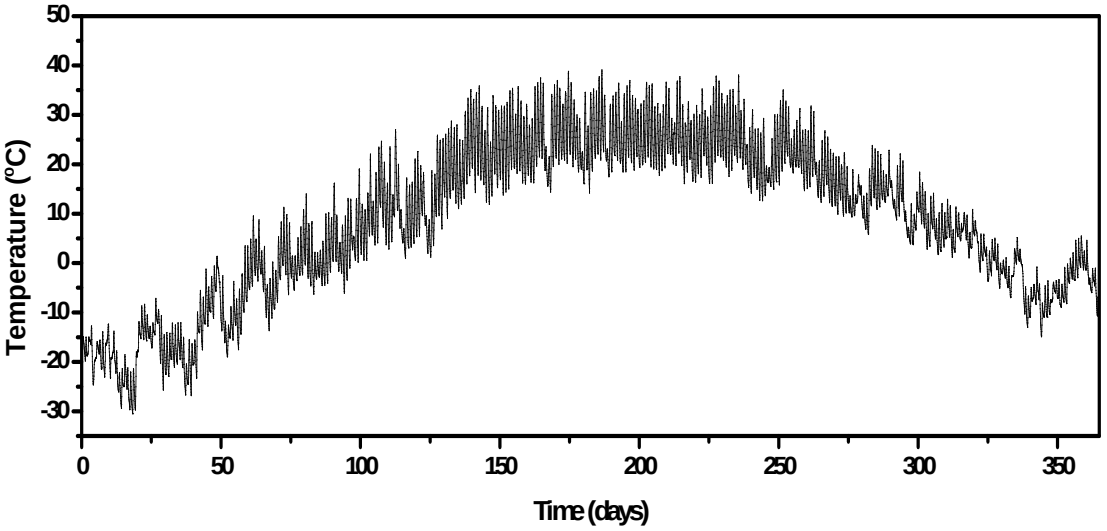


Figure B34. Pavement Temperature of MN CELL 1 at Layer 5.

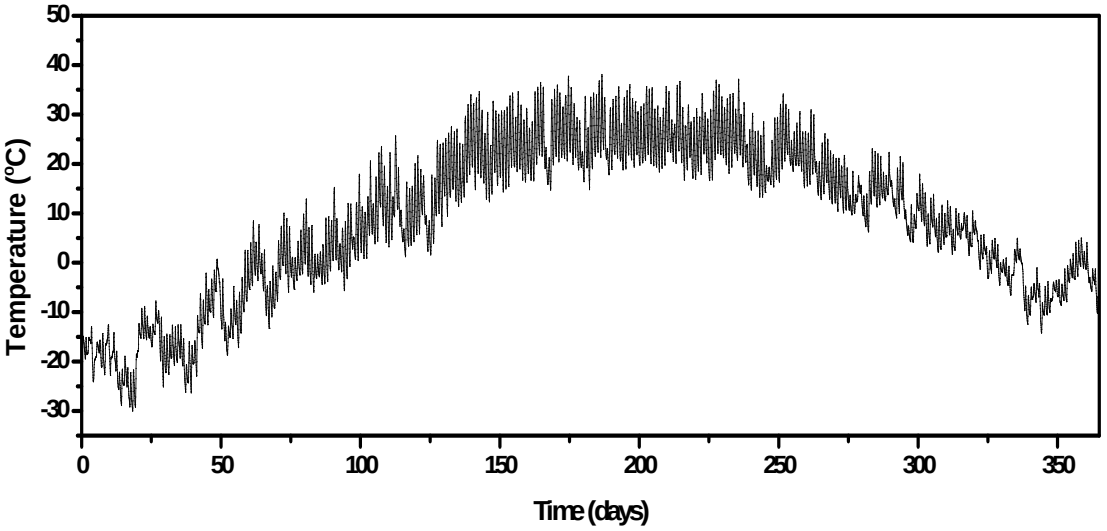


Figure B35. Pavement Temperature of MN CELL 1 at Layer 6.

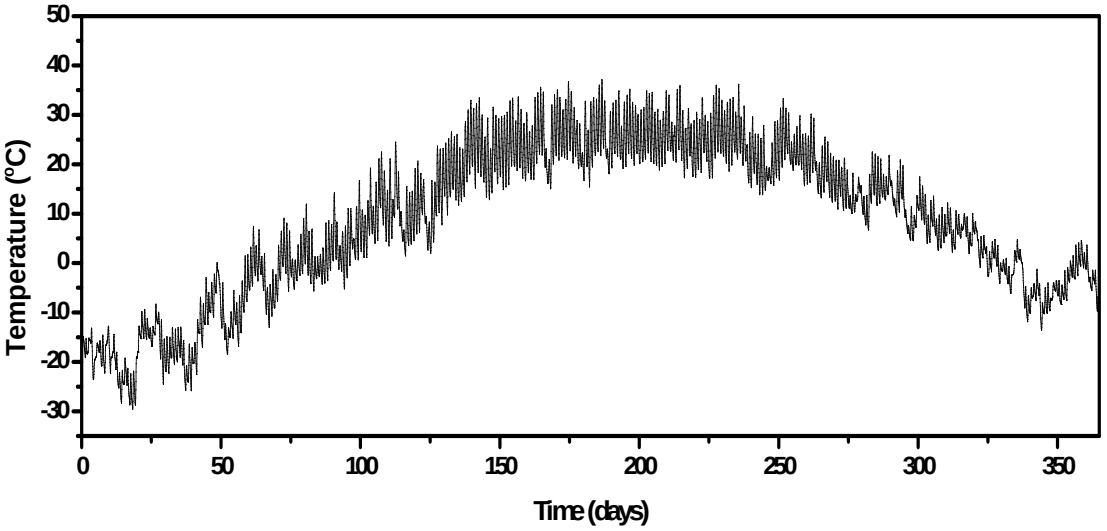


Figure B36. Pavement Temperature of MN CELL 1 at Layer 7.

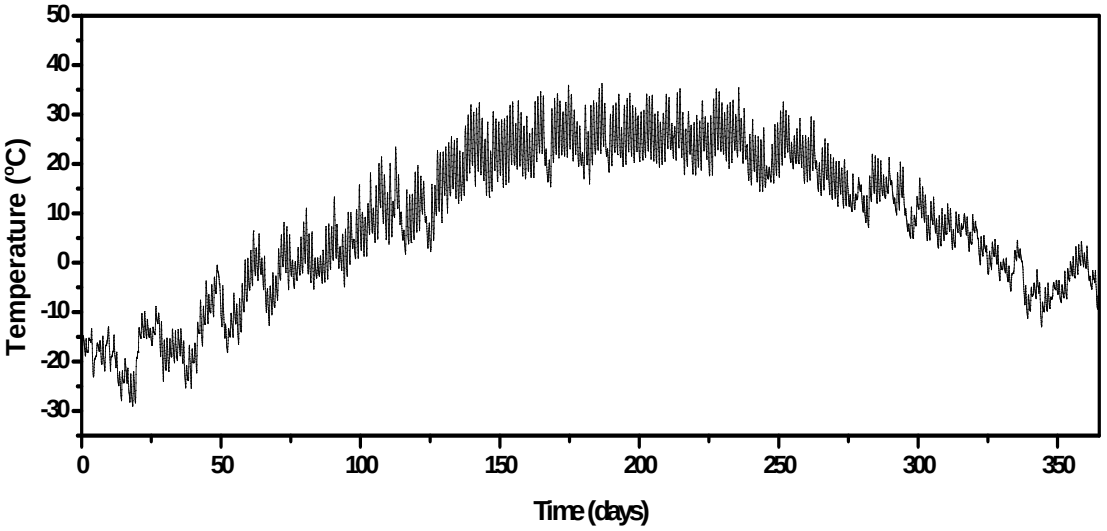


Figure B37. Pavement Temperature of MN CELL 1 at Layer 8.

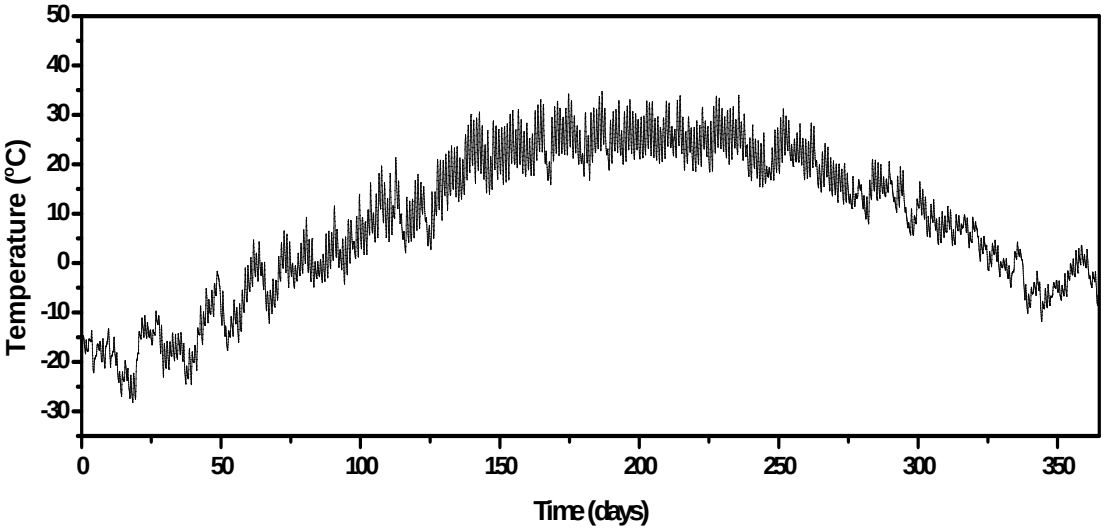


Figure B38. Pavement Temperature of MN CELL 1 at Layer 9.

APPENDIX C

AIR VOID CHARACTERIZATION

Table C1. Average Air Void Radius at Different Pavement Layers of US290.

Depth	Average Air Void Radius r_i (mm)				
	0~0.2 mm	0.2~0.5 mm	0.5~1 mm	1~2 mm	2~3 mm
Layer 1	0.144	0.352	0.736	1.414	2.455
Layer 2	0.143	0.351	0.739	1.415	2.428
Layer 3	0.145	0.351	0.736	1.422	2.433
Layer 4	0.142	0.353	0.736	1.415	2.443
Layer 5	0.142	0.351	0.721	1.422	2.453

Table C2. Number of Air Voids at Different Pavement Layers of US290.

Depth	Number of Air Voids				
	0~0.2 mm	0.2~0.5 mm	0.5~1 mm	1~2 mm	2~3 mm
Layer 1	20	92	128	129	40
Layer 2	19	76	119	115	44
Layer 3	19	66	109	113	41
Layer 4	20	71	104	113	41
Layer 5	18	74	94	89	32

Table C3. Shell Distance at Different Pavement Layers of US290.

Depth	Average Shell Distance r_{NFB} (mm)				
	0~0.2 mm	0.2~0.5 mm	0.5~1 mm	1~2 mm	2~3 mm
Layer 1	11.924	11.924	11.924	11.924	11.924
Layer 2	12.210	12.210	12.210	12.210	12.210
Layer 3	12.421	12.421	12.421	12.421	12.421
Layer 4	12.197	12.197	12.197	12.197	12.197
Layer 5	12.805	12.805	12.805	12.805	12.805

Table C4. P_{av} Calculated for Each Air Void Range at Different Pavement Layers of US290.

Depth	Condition	P_{av} (atm)				
		0~0.2 mm	0.2~0.5 mm	0.5~1 mm	1~2 mm	2~3 mm
Layer 1	Upper	0.2	0.2	0.2	0.2	0.2
	Lower	0.107	0.185	0.197	0.199	0.2
Layer 2	Upper	0.2	0.2	0.2	0.2	0.2
	Lower	0.025	0.171	0.193	0.198	0.198
Layer 3	Upper	0.2	0.2	0.2	0.2	0.2
	Lower	0.008	0.158	0.190	0.197	0.197
Layer 4	Upper	0.2	0.2	0.2	0.2	0.2
	Lower	0.000	0.145	0.187	0.196	0.197
Layer 5	Upper	0.2	0.2	0.2	0.2	0.2
	Lower	0.000	0.121	0.183	0.195	0.196

Table C5. Average Air Void Radius at Different Pavement Layers of US277.

Depth	Average Air Void Radius r_i (mm)				
	0~0.2 mm	0.2~0.5 mm	0.5~1 mm	1~2 mm	2~3 mm
Layer 1	0.140	0.332	0.697	1.338	2.400
Layer 2	0.142	0.331	0.700	1.314	2.290
Layer 3	0.138	0.326	0.695	1.289	2.306
Layer 4	0.141	0.326	0.682	1.284	2.290
Layer 5	0.142	0.330	0.688	1.303	2.385

Table C6. Number of Air Voids at Different Pavement Layers of US277.

Depth	Number of Air Voids				
	0~0.2 mm	0.2~0.5 mm	0.5~1 mm	1~2 mm	2~3 mm
Layer 1	34	672	211	83	14
Layer 2	37	744	237	81	6
Layer 3	36	710	216	58	4
Layer 4	37	737	203	47	3
Layer 5	39	781	242	73	7

Table C7. Shell Distance at Different Pavement Layers of US277.

Depth	Average Shell Distance r_{NFB} (mm)				
	0~0.2 mm	0.2~0.5 mm	0.5~1 mm	1~2 mm	2~3 mm
Layer 1	8.931	8.931	8.931	8.931	8.931
Layer 2	8.487	8.487	8.487	8.487	8.487
Layer 3	8.686	8.686	8.686	8.686	8.686
Layer 4	8.530	8.530	8.530	8.530	8.530
Layer 5	8.280	8.280	8.280	8.280	8.280

Table C8. P_{av} Calculated for Each Air Void Range at Different Pavement Layers of US277.

Depth	Condition	P_{av} (atm)				
		0~0.2 mm	0.2~0.5 mm	0.5~1 mm	1~2 mm	2~3 mm
Layer 1	Upper	0.2	0.2	0.2	0.2	0.2
	Lower	0.159	0.193	0.199	0.199	0.200
Layer 2	Upper	0.2	0.2	0.2	0.2	0.2
	Lower	0.112	0.186	0.197	0.199	0.200
Layer 3	Upper	0.2	0.2	0.2	0.2	0.2
	Lower	0.082	0.179	0.195	0.199	0.200
Layer 4	Upper	0.2	0.2	0.2	0.2	0.2
	Lower	0.047	0.172	0.194	0.198	0.200
Layer 5	Upper	0.2	0.2	0.2	0.2	0.2
	Lower	0.000	0.161	0.192	0.197	0.199

Table C9. Average Air Void Radius at Different Pavement Layers of US69.

Depth	Average Air Void Radius r_i (mm)				
	0~0.2 mm	0.2~0.5 mm	0.5~1 mm	1~2 mm	2~3 mm
Layer 1	0.144	0.336	0.700	1.342	2.663
Layer 2	0.144	0.332	0.695	1.328	2.458
Layer 3	0.145	0.330	0.695	1.354	2.625
Layer 4	0.144	0.331	0.704	1.346	2.711

Table C10. Number of Air Voids at Different Pavement Layers of US69.

Depth	Number of Air Voids				
	0~0.2 mm	0.2~0.5 mm	0.5~1 mm	1~2 mm	2~3 mm
Layer 1	52	407	240	84	12
Layer 2	49	369	230	86	13
Layer 3	50	390	222	85	15
Layer 4	45	337	194	91	20

Table C11. Shell Distance at Different Pavement Layers of US69.

Depth	Average Shell Distance r_{NFB} (mm)				
	0~0.2 mm	0.2~0.5 mm	0.5~1 mm	1~2 mm	2~3 mm
Layer 1	8.470	8.470	8.470	8.470	8.470
Layer 2	8.742	8.742	8.742	8.742	8.742
Layer 3	8.660	8.660	8.660	8.660	8.660
Layer 4	9.100	9.100	9.100	9.100	9.100

Table C12. P_{av} Calculated for Each Air Void Range at Different Pavement Layers of US69.

		P_{av} (atm)				
Depth	Condition	0~0.2 mm	0.2~0.5 mm	0.5~1 mm	1~2 mm	2~3 mm
Layer 1	Upper	0.2	0.2	0.2	0.2	0.2
	Lower	0.193	0.196	0.198	0.200	0.2
Layer 2	Upper	0.2	0.2	0.2	0.2	0.2
	Lower	0.189	0.192	0.196	0.199	0.2
Layer 3	Upper	0.2	0.2	0.2	0.2	0.2
	Lower	0.184	0.188	0.194	0.199	0.2
Layer 4	Upper	0.2	0.2	0.2	0.2	0.2
	Lower	0.181	0.185	0.192	0.199	0.2

Table C13. Average Air Void Radius at Different Pavement Layers of US54.

Depth	Average Air Void Radius r_i (mm)				
	0~0.2 mm	0.2~0.5 mm	0.5~1 mm	1~2 mm	2~3 mm
Layer 1	0.145	0.322	0.736	1.359	2.423
Layer 2	0.143	0.322	0.693	1.349	2.413
Layer 3	0.145	0.320	0.692	1.355	2.443
Layer 4	0.141	0.323	0.700	1.355	2.432
Layer 5	0.141	0.322	0.700	1.356	2.431

Table C14. Number of Air Voids at Different Pavement Layers of US54.

Depth	Number of Air Voids				
	0~0.2 mm	0.2~0.5 mm	0.5~1 mm	1~2 mm	2~3 mm
Layer 1	40	436	246	117	27
Layer 2	45	537	265	108	20
Layer 3	44	542	251	105	21
Layer 4	29	315	172	91	22
Layer 5	29	315	172	91	22

Table C15. Shell Distance at Different Pavement Layers of US54.

Depth	Average Shell Distance r_{NFB} (mm)				
	0~0.2 mm	0.2~0.5 mm	0.5~1 mm	1~2 mm	2~3 mm
Layer 1	8.163	8.163	8.163	8.163	8.163
Layer 2	7.722	7.722	7.722	7.722	7.722
Layer 3	7.763	7.763	7.763	7.763	7.763
Layer 4	9.543	9.543	9.543	9.543	9.543
Layer 5	9.543	9.543	9.543	9.543	9.543

Table C16. P_{av} Calculated for Each Air Void Range at Different Pavement Layers of US54.

Depth	Condition	P_{av} (atm)				
		0~0.2 mm	0.2~0.5 mm	0.5~1 mm	1~2 mm	2~3 mm
Layer 1	Upper	0.2	0.2	0.2	0.2	0.2
	Lower	0.113	0.181	0.196	0.199	0.200
Layer 2	Upper	0.2	0.2	0.2	0.2	0.2
	Lower	0.004	0.163	0.193	0.198	0.199
Layer 3	Upper	0.2	0.2	0.2	0.2	0.2
	Lower	0.000	0.146	0.190	0.197	0.199
Layer 4	Upper	0.2	0.2	0.2	0.2	0.2
	Lower	0.000	0.129	0.186	0.196	0.199
Layer 5	Upper	0.2	0.2	0.2	0.2	0.2
	Lower	0.000	0.099	0.182	0.195	0.199

Table C17. Average Air Void radius at Different Pavement Layers of IH35-Waco.

Depth	Average Air Void Radius r_i (mm)				
	0~0.2 mm	0.2~0.5 mm	0.5~1 mm	1~2 mm	2~3 mm
Layer 1	0.144	0.340	0.702	1.305	2.276
Layer 2	0.145	0.334	0.690	1.258	2.335
Layer 3	0.145	0.335	0.696	1.284	2.250
Layer 4	0.143	0.334	0.692	1.272	2.315
Layer 5	0.144	0.331	0.706	1.311	2.341
Layer 6	0.144	0.333	0.720	1.351	2.379

Table C18. Number of Air Voids at Different Pavement Layers of IH35-Waco.

Depth	Number of Air Voids				
	0~0.2 mm	0.2~0.5 mm	0.5~1 mm	1~2 mm	2~3 mm
Layer 1	23	309	242	85	5
Layer 2	21	287	185	53	3
Layer 3	19	280	161	39	2
Layer 4	19	265	153	42	2
Layer 5	19	248	159	68	5
Layer 6	20	210	177	97	17

Table C19. Shell Distance at Different Pavement Layers of IH35-Waco.

Depth	Average Shell Distance r_{NFB} (mm)				
	0~0.2 mm	0.2~0.5 mm	0.5~1 mm	1~2 mm	2~3 mm
Layer 1	9.182	9.182	9.182	9.182	9.182
Layer 2	10.121	10.121	10.121	10.121	10.121
Layer 3	10.600	10.600	10.600	10.600	10.600
Layer 4	10.820	10.820	10.820	10.820	10.820
Layer 5	10.610	10.610	10.610	10.610	10.610
Layer 6	10.366	10.366	10.366	10.366	10.366

Table C20. P_{av} Calculated for Each Air Void Range at Different Pavement Layers of IH35-Waco.

Depth	Condition	P_{av} (atm)				
		0~0.2 mm	0.2~0.5 mm	0.5~1 mm	1~2 mm	2~3 mm
Layer 1	Upper	0.2	0.2	0.2	0.2	0.2
	Lower	0.039	0.125	0.185	0.195	0.199
Layer 2	Upper	0.2	0.2	0.2	0.2	0.2
	Lower	0.000	0.123	0.185	0.195	0.199
Layer 3	Upper	0.2	0.2	0.2	0.2	0.2
	Lower	0.000	0.120	0.184	0.195	0.199
Layer 4	Upper	0.2	0.2	0.2	0.2	0.2
	Lower	0.000	0.119	0.184	0.195	0.199
Layer 5	Upper	0.2	0.2	0.2	0.2	0.2
	Lower	0.000	0.117	0.184	0.194	0.199
Layer 6	Upper	0.2	0.2	0.2	0.2	0.2
	Lower	0.000	0.113	0.183	0.194	0.199

Table C21. Average Air Void Radius at Different Pavement Layers of IH35-LRD.

Depth	Average Air Void Radius r_i (mm)				
	0~0.2 mm	0.2~0.5 mm	0.5~1 mm	1~2 mm	2~3 mm
Layer 1	0.140	0.350	0.713	1.308	2.407
Layer 2	0.144	0.347	0.716	1.302	2.434
Layer 3	0.145	0.343	0.722	1.285	2.301
Layer 4	0.144	0.344	0.723	1.188	2.305

Table C22. Number of Air Voids at Different Pavement Layers of IH35-LRD.

Depth	Number of Air Voids				
	0~0.2 mm	0.2~0.5 mm	0.5~1 mm	1~2 mm	2~3 mm
Layer 1	8	80	92	31	2
Layer 2	7	70	70	25	2
Layer 3	7	71	81	31	3
Layer 4	7	72	82	33	2

Table C23. Shell Distance at Different Pavement Layers of IH35-LRD.

Depth	Average Shell Distance r_{NFB} (mm)				
	0~0.2 mm	0.2~0.5 mm	0.5~1 mm	1~2 mm	2~3 mm
Layer 1	16.128	16.128	16.128	16.128	16.128
Layer 2	17.826	17.826	17.826	17.826	17.826
Layer 3	16.891	16.891	16.891	16.891	16.891
Layer 4	17.001	17.001	17.001	17.001	17.001

Table C24. P_{av} Calculated for Each Air Void Range at Different Pavement Layers of IH35-LRD.

		P_{av} (atm)				
Depth	Condition	0~0.2 mm	0.2~0.5 mm	0.5~1 mm	1~2 mm	2~3 mm
Layer 1	Upper	0.2	0.2	0.2	0.2	0.2
	Lower	0.000	0.012	0.135	0.181	0.194
Layer 2	Upper	0.2	0.2	0.2	0.2	0.2
	Lower	0.000	0.004	0.132	0.181	0.194
Layer 3	Upper	0.2	0.2	0.2	0.2	0.2
	Lower	0.000	0.000	0.130	0.180	0.194
Layer 4	Upper	0.2	0.2	0.2	0.2	0.2
	Lower	0.000	0.000	0.129	0.180	0.194

Table C25. Average Air Void Radius at Different Pavement Layers of MN Cell 1.

Depth	Average Air Void Radius r_i (mm)				
	0~0.2 mm	0.2~0.5 mm	0.5~1 mm	1~2 mm	2~3 mm
Layer 1	0.144	0.327	0.679	1.336	2.470
Layer 2	0.143	0.323	0.675	1.311	2.340
Layer 3	0.145	0.322	0.678	1.316	2.394
Layer 4	0.142	0.324	0.676	1.313	2.401
Layer 5	0.142	0.321	0.679	1.334	2.407
Layer 6	0.143	0.320	0.678	1.331	2.462
Layer 7	0.142	0.320	0.674	1.320	2.417
Layer 8	0.146	0.320	0.683	1.326	2.423
Layer 9	0.146	0.322	0.677	1.339	2.428

Table C26. Number of Air Voids at Different Pavement Layers of MN Cell 1.

Depth	Number of Air Voids				
	0~0.2 mm	0.2~0.5 mm	0.5~1 mm	1~2 mm	2~3 mm
Layer 1	95	909	327	97	18
Layer 2	94	921	321	84	8
Layer 3	91	894	305	87	12
Layer 4	93	916	310	83	12
Layer 5	93	911	309	87	14
Layer 6	95	953	309	79	13
Layer 7	92	921	302	73	10
Layer 8	77	748	263	68	10
Layer 9	73	707	238	77	16

Table C27. Shell Distance at Different Pavement Layers of MN Cell 1.

Depth	Average Shell Distance r_{NFB} (mm)				
	0~0.2 mm	0.2~0.5 mm	0.5~1 mm	1~2 mm	2~3 mm
Layer 1	6.226	6.226	6.226	6.226	6.226
Layer 2	6.273	6.273	6.273	6.273	6.273
Layer 3	6.357	6.357	6.357	6.357	6.357
Layer 4	6.301	6.301	6.301	6.301	6.301
Layer 5	6.296	6.296	6.296	6.296	6.296
Layer 6	6.224	6.224	6.224	6.224	6.224
Layer 7	6.337	6.337	6.337	6.337	6.337
Layer 8	6.926	6.926	6.926	6.926	6.926
Layer 9	7.089	7.089	7.089	7.089	7.089

Table C28. P_{av} for Each Air Void Range at Different Pavement Layers of MN Cell 1.

		P_{av} (atm)				
Depth	**Condition**	**0~0.2 mm**	**0.2~0.5 mm**	**0.5~1 mm**	**1~2 mm**	**2~3 mm**
Layer 1	Upper	0.2	0.2	0.2	0.2	0.2
	Lower	0.184	0.197	0.199	0.2	0.2
Layer 2	Upper	0.2	0.2	0.2	0.2	0.2
	Lower	0.168	0.194	0.199	0.2	0.2
Layer 3	Upper	0.2	0.2	0.2	0.2	0.2
	Lower	0.154	0.191	0.198	0.2	0.2
Layer 4	Upper	0.2	0.2	0.2	0.2	0.2
	Lower	0.140	0.188	0.198	0.2	0.2
Layer 5	Upper	0.2	0.2	0.2	0.2	0.2
	Lower	0.120	0.185	0.197	0.199	0.2
Layer 6	Upper	0.2	0.2	0.2	0.2	0.2
	Lower	0.101	0.181	0.197	0.199	0.2
Layer 7	Upper	0.2	0.2	0.2	0.2	0.2
	Lower	0.088	0.178	0.196	0.199	0.2
Layer 8	Upper	0.2	0.2	0.2	0.2	0.2
	Lower	0.073	0.175	0.196	0.198	0.2
Layer 9	Upper	0.2	0.2	0.2	0.2	0.2
	Lower	0.066	0.173	0.196	0.198	0.2

APPENDIX D

CALCULATED FIELD OXIDATION RATES OF FIELD VALIDATION SITES

Table D1. Oxidation Rates Calculated at Different Pavement Layers of US290.

		r_{O2} (CA/year)					
Depth	**Condition**	**0~0.2 mm**	**0.2~0.5 mm**	**0.5~1 mm**	**1~2 mm**	**2~3 mm**	**Bulk**
Layer 1	Highest	0.0723	0.0741	0.0765	0.0793	0.0820	0.0771
	Lowest	0.0611	0.0726	0.0760	0.0792	0.0820	0.0761
Layer 2	Highest	0.0651	0.0667	0.0689	0.0715	0.0740	0.0697
	Lowest	0.0371	0.0639	0.0682	0.0713	0.0738	0.0674
Layer 3	Highest	0.0596	0.0611	0.0632	0.0656	0.0679	0.0639
	Lowest	0.0250	0.0573	0.0623	0.0652	0.0676	0.0610
Layer 4	Highest	0.0554	0.0568	0.0587	0.0610	0.0632	0.0593
	Lowest	0.0000	0.0520	0.0576	0.0607	0.0629	0.0550
Layer 5	Highest	0.0520	0.0534	0.0553	0.0574	0.0595	0.0557
	Lowest	0.0000	0.0466	0.0539	0.0570	0.0592	0.0506

Table D2. Oxidation Rates Calculated at Different Pavement Layers of US277.

		r_{O2} (CA/year)					
Depth	**Condition**	**0~0.2 mm**	**0.2~0.5 mm**	**0.5~1 mm**	**1~2 mm**	**2~3 mm**	**Bulk**
Layer 1	Highest	0.0450	0.0500	0.0566	0.0636	0.0709	0.0526
	Lowest	0.0420	0.0497	0.0565	0.0636	0.0709	0.0524
Layer 2	Highest	0.0420	0.0467	0.0529	0.0595	0.0700	0.0489
	Lowest	0.0356	0.0457	0.0526	0.0594	0.0700	0.0480
Layer 3	Highest	0.0398	0.0442	0.0500	0.0562	0.0696	0.0460
	Lowest	0.0357	0.0428	0.0498	0.0562	0.0696	0.0447
Layer 4	Highest	0.0380	0.0422	0.0478	0.0537	0.0693	0.0437
	Lowest	0.0263	0.0405	0.0473	0.0535	0.0693	0.0420
Layer 5	Highest	0.0355	0.0394	0.0446	0.0501	0.0689	0.0411
	Lowest	0.0000	0.0370	0.0441	0.0496	0.0689	0.0382

Table D3. Oxidation Rates Calculated at Different Pavement Layers of US69.

		r_{O2} (CA/year)					
Depth	**Condition**	**0~0.2 mm**	**0.2~0.5 mm**	**0.5~1 mm**	**1~2 mm**	**2~3 mm**	**Bulk**
Layer 1	Highest	0.0252	0.0277	0.0312	0.0352	0.0391	0.0296
	Lowest	0.0247	0.0275	0.0311	0.0352	0.0391	0.0294
Layer 2	Highest	0.0226	0.0249	0.0280	0.0316	0.0351	0.0267
	Lowest	0.0219	0.0246	0.0278	0.0316	0.0351	0.0264
Layer 3	Highest	0.0206	0.0228	0.0256	0.0288	0.0320	0.0243
	Lowest	0.0197	0.0224	0.0254	0.0288	0.0320	0.0239
Layer 4	Highest	0.0191	0.0211	0.0237	0.0267	0.0297	0.0227
	Lowest	0.0181	0.0206	0.0234	0.0267	0.0297	0.0223

Table D4. Oxidation Rates Calculated at Different Pavement Layers of US54.

		r_{O2} (CA/year)					
Depth	**Condition**	**0~0.2 mm**	**0.2~0.5 mm**	**0.5~1 mm**	**1~2 mm**	**2~3 mm**	**Bulk**
Layer 1	Highest	0.1050	0.1145	0.1226	0.1323	0.1408	0.1198
	Lowest	0.0946	0.1114	0.1219	0.1321	0.1408	0.1174
Layer 2	Highest	0.1069	0.1108	0.1186	0.1280	0.1362	0.1151
	Lowest	0.0691	0.1048	0.1039	0.1276	0.1362	0.1061
Layer 3	Highest	0.1040	0.1079	0.1154	0.1246	0.1324	0.1119
	Lowest	0.0000	0.0991	0.0977	0.1239	0.1323	0.0976
Layer 4	Highest	0.0983	0.1034	0.1094	0.1168	0.1242	0.1075
	Lowest	0.0000	0.0919	0.0901	0.1161	0.1241	0.0918
Layer 5	Highest	0.0952	0.1001	0.1058	0.1129	0.1200	0.1040
	Lowest	0.0000	0.0828	0.0807	0.1121	0.1198	0.0839

Table D5. Oxidation Rates Calculated at Different Pavement Layers of IH35-Waco.

		r_{O2} (CA/year)					
Depth	**Condition**	**0~0.2 mm**	**0.2~0.5 mm**	**0.5~1 mm**	**1~2 mm**	**2~3 mm**	**Bulk**
Layer 1	Highest	0.0251	0.0262	0.0272	0.0280	0.0304	0.0268
	Lowest	0.0171	0.024	0.0266	0.0277	0.0304	0.0253
Layer 2	Highest	0.0249	0.0260	0.0270	0.0278	0.0302	0.0266
	Lowest	0.0000	0.0239	0.0264	0.0275	0.0302	0.0243
Layer 3	Highest	0.0248	0.0259	0.0269	0.0277	0.0301	0.0264
	Lowest	0.0000	0.0237	0.0263	0.0275	0.0301	0.0240
Layer 4	Highest	0.0247	0.0258	0.0268	0.0276	0.0300	0.0263
	Lowest	0.0000	0.0237	0.0262	0.0274	0.0300	0.0240
Layer 5	Highest	0.0244	0.0256	0.0265	0.0273	0.0297	0.0262
	Lowest	0.0000	0.0235	0.0259	0.0271	0.0297	0.0240
Layer 6	Highest	0.0243	0.0255	0.0264	0.0272	0.0296	0.0263
	Lowest	0.0000	0.0234	0.0257	0.0271	0.0296	0.0242

Table D6. Oxidation Rates Calculated at Different Pavement Layers of IH35-LRD.

		r_{O2} (CA/year)					
Depth	**Condition**	**0~0.2 mm**	**0.2~0.5 mm**	**0.5~1 mm**	**1~2 mm**	**2~3 mm**	**Bulk**
Layer 1	Highest	0.0331	0.0357	0.0393	0.0432	0.0486	0.0384
	Lowest	0.0000	0.0167	0.0353	0.0420	0.0483	0.0281
Layer 2	Highest	0.0330	0.0357	0.0392	0.0431	0.0485	0.0382
	Lowest	0.0000	0.0124	0.0351	0.0419	0.0482	0.0257
Layer 3	Highest	0.0330	0.0356	0.0392	0.0431	0.0485	0.0384
	Lowest	0.0000	0.0000	0.0349	0.0419	0.0482	0.0221
Layer 4	Highest	0.0330	0.0356	0.0391	0.0430	0.0484	0.0384
	Lowest	0.0000	0.0000	0.0348	0.0419	0.0482	0.0221

Table D7. Oxidation Rates Calculated at Different Pavement Layers of MN Cell 1.

		r_{O2} (CA/year)					
Depth	**Condition**	**0~0.2 mm**	**0.2~0.5 mm**	**0.5~1 mm**	**1~2 mm**	**2~3 mm**	**Bulk**
Layer 1	Highest	0.0236	0.0239	0.0242	0.0234	0.0239	0.0239
	Lowest	0.0231	0.0238	0.0241	0.0234	0.0239	0.0238
Layer 2	Highest	0.0223	0.0225	0.0229	0.0221	0.0225	0.0226
	Lowest	0.0213	0.0223	0.0228	0.0221	0.0225	0.0224
Layer 3	Highest	0.0212	0.0215	0.0219	0.0210	0.0215	0.0215
	Lowest	0.0198	0.0212	0.0217	0.0210	0.0215	0.0212
Layer 4	Highest	0.0203	0.0206	0.0210	0.0201	0.0206	0.0206
	Lowest	0.0185	0.0202	0.0208	0.0201	0.0206	0.0202
Layer 5	Highest	0.0190	0.0192	0.0196	0.0188	0.0192	0.0192
	Lowest	0.0165	0.0188	0.0194	0.0188	0.0192	0.0188
Layer 6	Highest	0.0185	0.0187	0.0189	0.0183	0.0187	0.0187
	Lowest	0.0153	0.0181	0.0188	0.0182	0.0187	0.0182
Layer 7	Highest	0.0180	0.0182	0.0186	0.0179	0.0183	0.0182
	Lowest	0.0144	0.0177	0.0184	0.0178	0.0183	0.0176
Layer 8	Highest	0.0176	0.0178	0.0182	0.0175	0.0179	0.0178
	Lowest	0.0134	0.0172	0.0180	0.0174	0.0179	0.0171
Layer 9	Highest	0.0169	0.0172	0.0176	0.0168	0.0172	0.0172
	Lowest	0.0126	0.0165	0.0173	0.0166	0.0172	0.0164

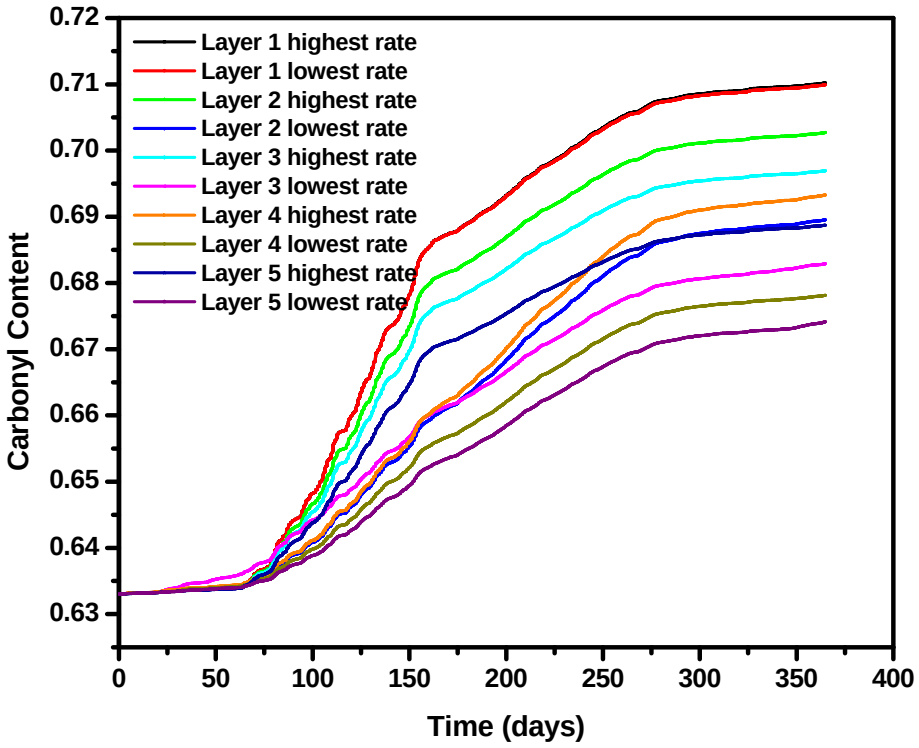


Figure D1. Bulk Carbonyl Growth Rates (Oxidation Rates) of US290 for One-year Period at Different Pavement Layers.

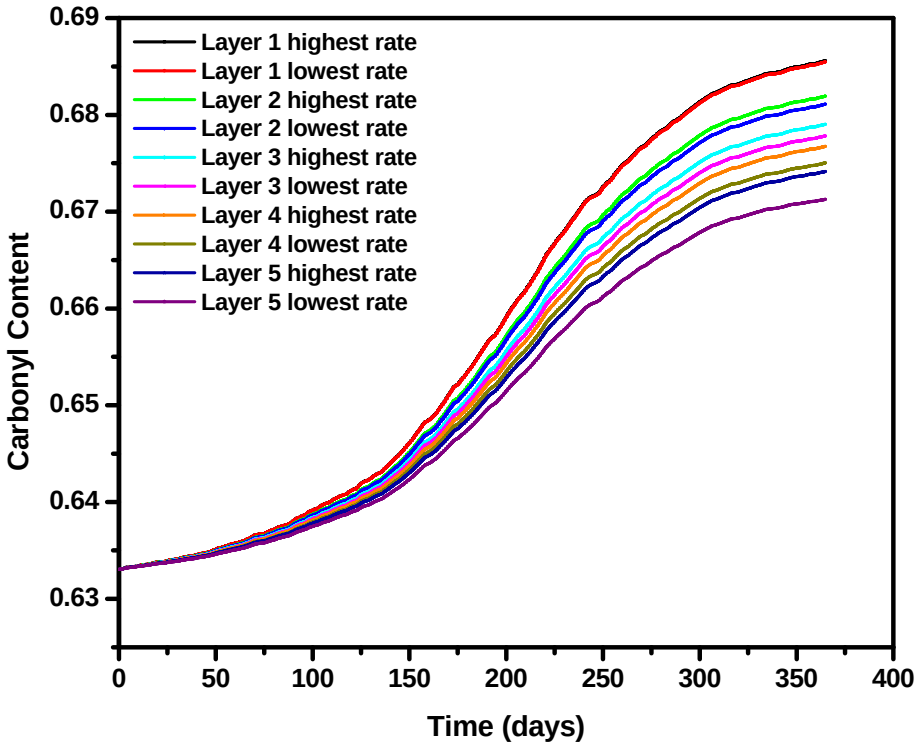


Figure D2. Bulk Carbonyl Growth Rates (Oxidation Rates) of US277 for One- year Period at Different Pavement Layers.

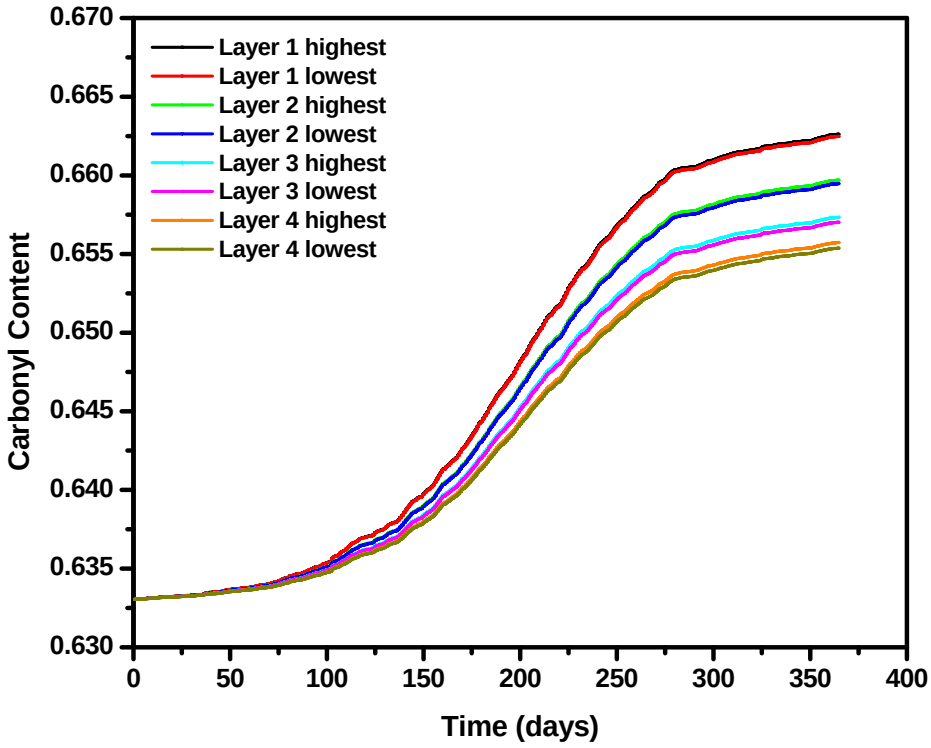


Figure D3. Bulk Carbonyl Growth Rates (Oxidation Rates) of US69 for One-year Period at Different Pavement Layers.

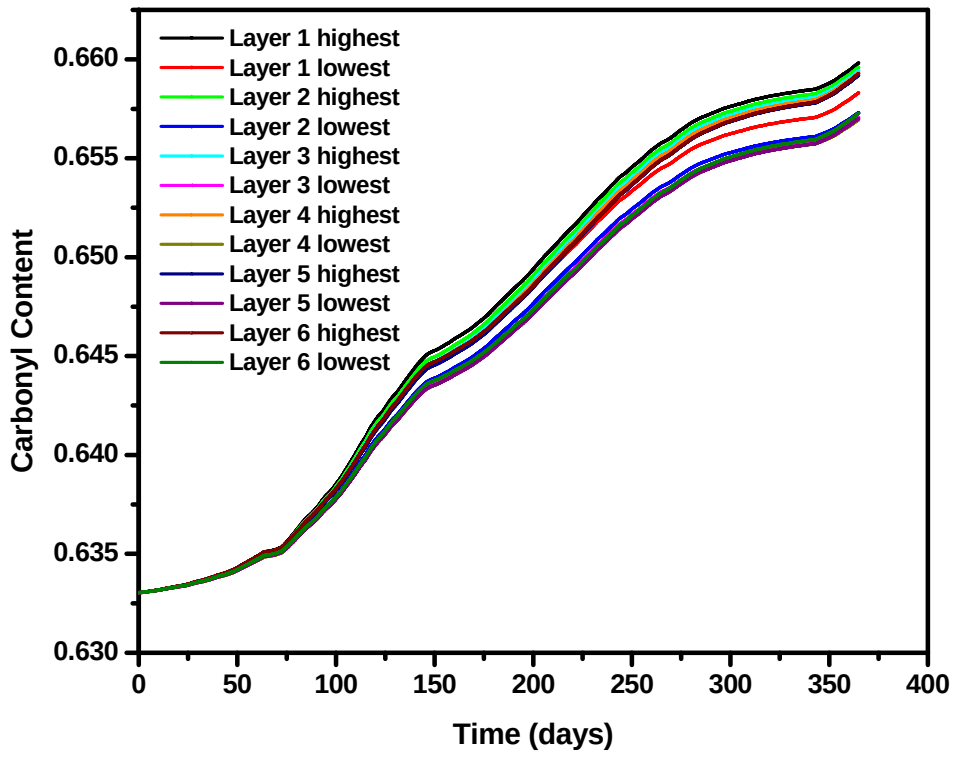


Figure D4. Bulk Carbonyl Growth Rates (Oxidation Rates) of IH35-Waco for One-year Period at Different Pavement Layers.

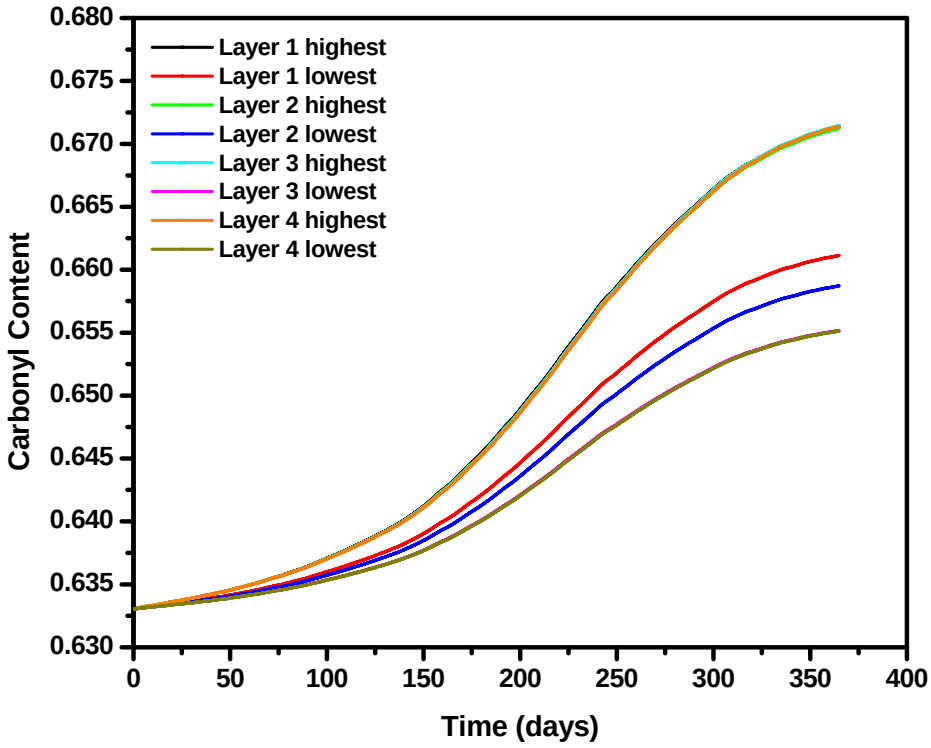


Figure D5. Bulk Carbonyl Growth Rates (Oxidation Rates) of IH35-LRD for One-year Period at Different Pavement Layers.

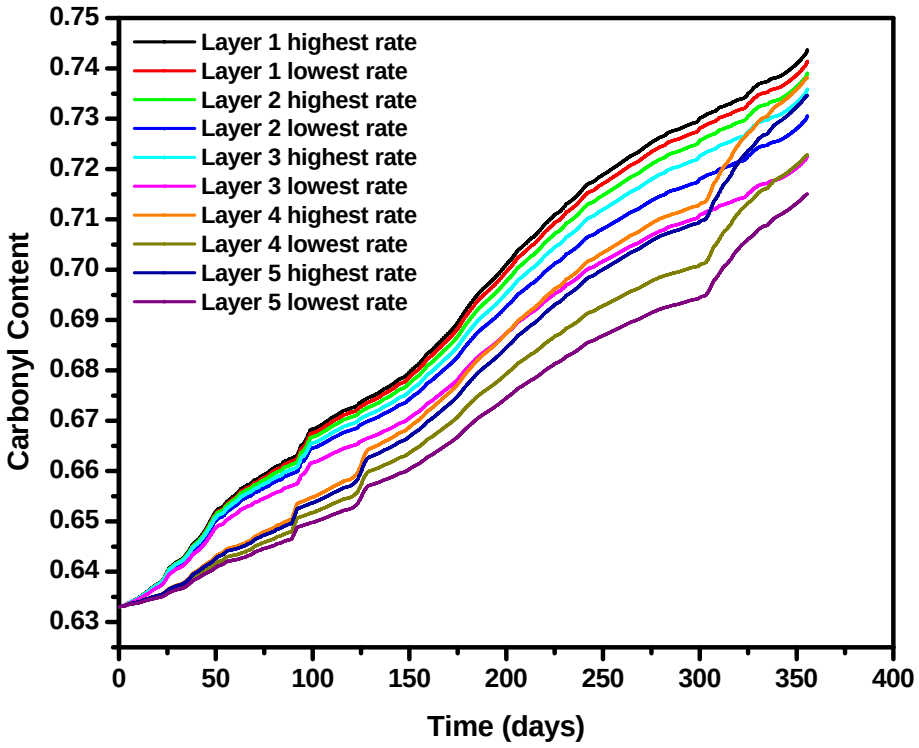


Figure D6. Bulk Carbonyl Growth Rates (Oxidation Rates) of US54-AMR for One-year Period at Different Pavement Layers.

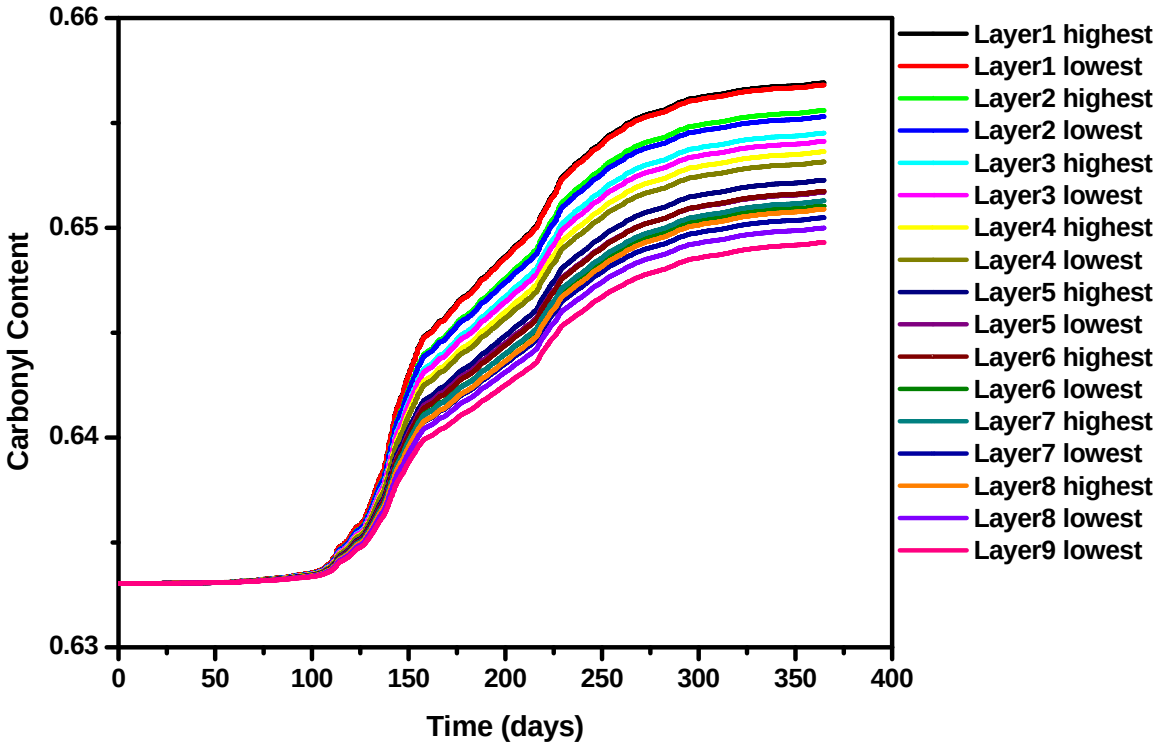


Figure D7. Bulk Carbonyl Growth Rates (Oxidation Rates) of MN Cell1 for One-year Period at Different Pavement Layers.

APPENDIX E

TABLES OF REHEOLOGICAL PROPERTIES, CARBONYL AREA, AND DSR FUNCTION HARDENING WITH PAVEMENT SERVICE TIME DATA

In the graphs below the following terms are used in their abbreviated forms: Carbonyl Area (CA), DSR Function (DSR Fn.). DSR Fn. was measured at 44.7°C, 10 rad/s in time sweep mode and then converted to the DSR Fn. value at 15 °C , 0.005 rad/s.

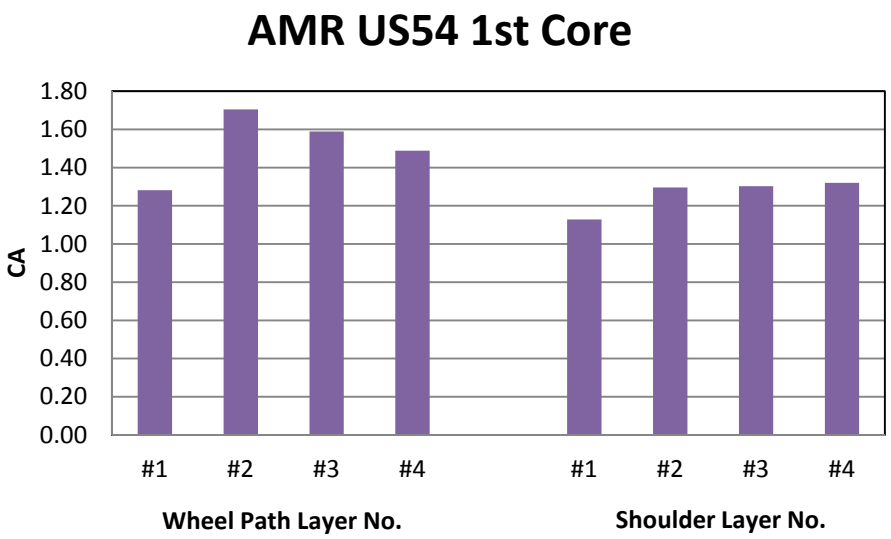
Table E1. US54 AMR Field Core (Wheel Path)

Binder: Unknown Activation Energy: 55 KJ/mol Cons.: 1998		**η_o* (Poise) @60°C 0.1 rad/s**	**G'/(η'/G') (MPa/s) @15°C 0.005 rad/s**	**Carbonyl Area**
1st Core Seal Coat Treated (07/2008)	1st layer &Seal Coat*	60000	0.0002	1.282
	2nd	1200000	0.0106	1.705
	3rd	300000	0.0022	1.590
	4th	160000	0.001	1.489
	1st to 4th	219000	0.0015	1.508

Table E2. US54 AMR Field Core (Shoulder)

Binder: Unknown Activation Energy: 55 KJ/mol Cons.: 1998		**η_o* (Poise) @60°C 0.1 rad/s**	**G'/(η'/G') (MPa/s) @15°C 0.005 rad/s**	**Carbonyl Area**
1st Core Seal Coat Treated (07/2008)	1st layer & Seal Coat*	60000	0.0001	1.128
	2nd	300000	0.0011	1.296
	3rd	280000	0.0012	1.303
	4th	280000	0.001	1.320
	1st to 4th	280000	0.0006	1.245

*Seal Coat layer was too thin to cut off.


AMR US54 1st Core
CA
1.80
1.60
1.40
1.20
1.00
0.80
0.60
0.40
0.20
0.00
#1
#2
#3
#4
#1
#2
#3
#4
Wheel Path Layer No.
Shoulder Layer No.

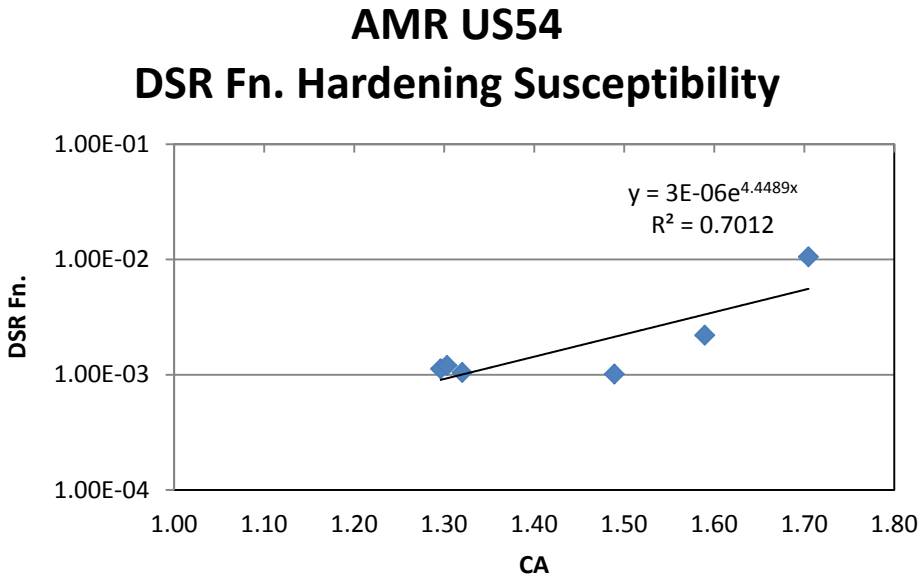

AMR US54
DSR Fn. Hardening Susceptibility
DSR Fn.
1.00E-01
1.00E-02
1.00E-03
1.00E-04
y = 3E-06e4.4489x
R² = 0.7012
1.00
1.10
1.20
1.30
1.40
1.50
1.60
1.70
1.80
CA

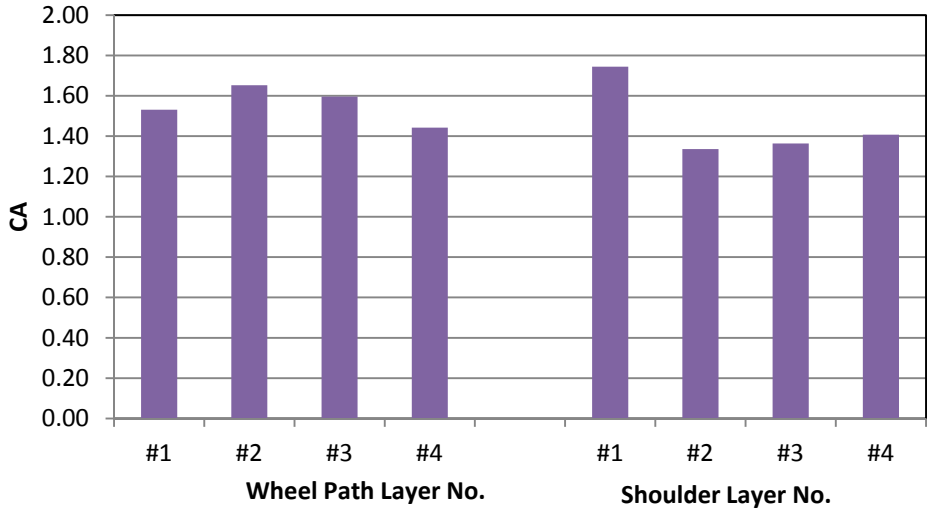
Table E3. IH20 ATL Field Core (Wheel Path)

Binder: Wright PG76-22 Activation Energy: Unknown Cons.: 2003		η_o* (Poise) @60°C 0.1 rad/s	G'/(η'/G') (MPa/s) @15°C 0.005 rad/s	Carbonyl Area
1st Core (07/2008)	1st layer	Too high to measure	Too high to measure	1.531
	2nd	Too high to measure	Too high to measure	1.653
	3rd	1300000	0.0117	1.596
	4th	2000000	0.0157	1.442
	1st to 4th	-	-	1.568

Table E4. IH20 ATL Field Core (Shoulder)

Binder: Wright PG76-22 Activation Energy: Unknown Cons.: 2003		η_o* (Poise) @60°C 0.1 rad/s	G'/(η'/G') (MPa/s) @15°C 0.005 rad/s	Carbonyl Area
1st Core (07/2008)	1st layer	Too high to measure	Too high to measure	1.7445
	2nd	180000	0.0024	1.336
	3rd	210000	0.0029	1.364
	4th	320000	0.0058	1.407
	1st to 4th	-	-	1.489

ATL IH20 1st Core



ATL IH20
DSR Fn. Hardening Susceptibility

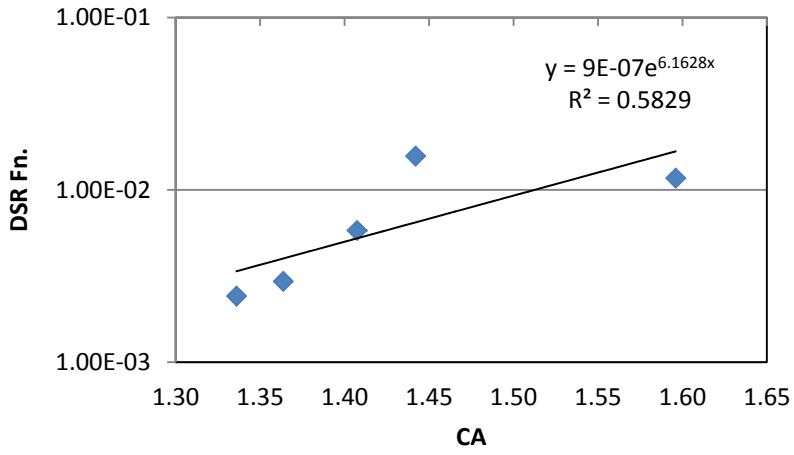
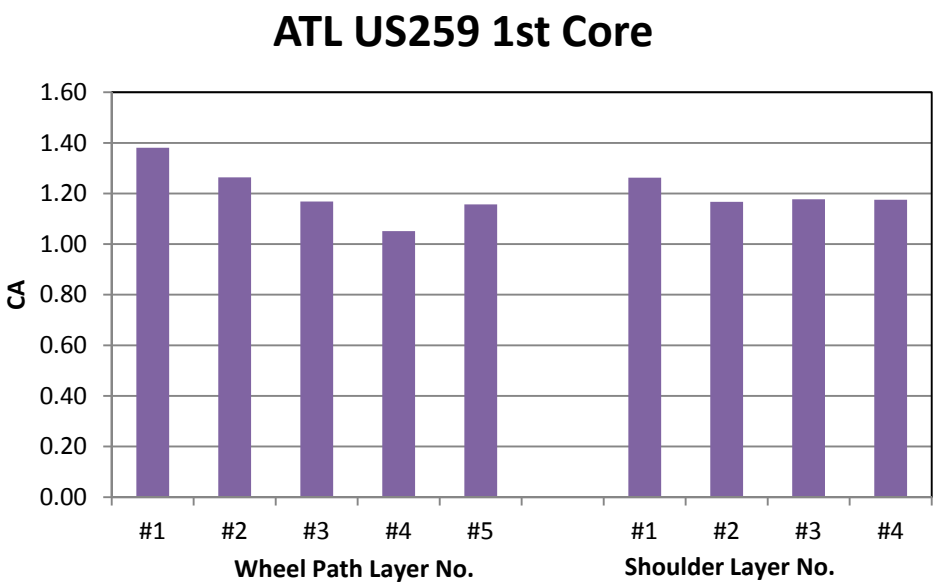


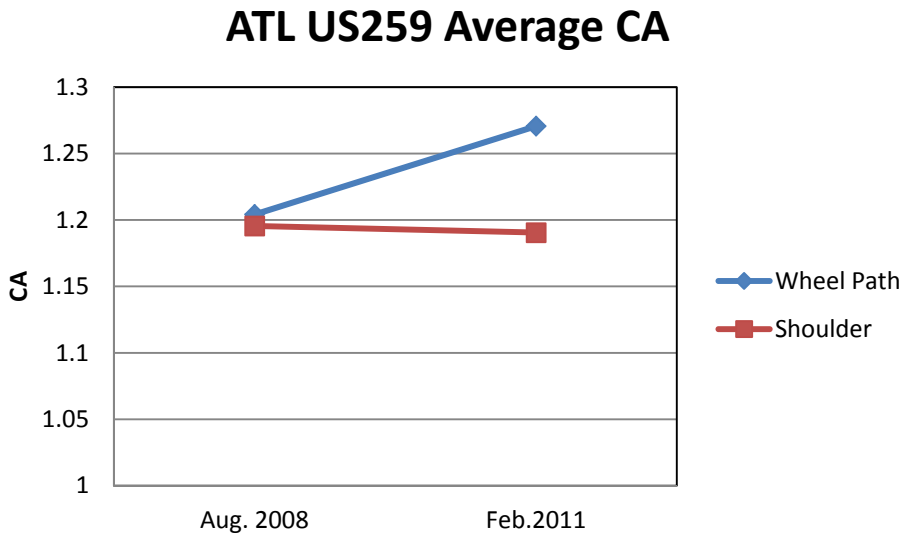
Table E5. US259 ATL Field Core (Wheel Path)

Binder: Lion PG76-22 Activation Energy: 97.4 KJ/mol Cons.: 2005		η_o* (Poise) @60°C 0.1 rad/s	G'/(η'/G') (MPa/s) @15°C 0.005 rad/s	Carbonyl Area
1st Core (12/2008)	1st layer	16000	0.0012	1.381
	2nd	100000	0.00060	1.264
	3rd	100000	0.00050	1.168
	4th	80000	0.00032	1.051
	5th	65000	0.00031	1.157
	1st to 5th	50000	0.00071	1.257
2nd Core (10/2010)	1st to 5th	121000	0.00070	1.271

Table E6. US259 ATL Field Core (Shoulder)

Binder: Lion PG76-22 Activation Energy: 97.4 KJ/mol Cons.: 2005		η_o* (Poise) @60°C 0.1 rad/s	G'/(η'/G') (MPa/s) @15°C 0.005 rad/s	Carbonyl Area
1st Core (12/2008)	1st layer	38000	0.0004	1.263
	2nd	33000	0.0003	1.167
	3rd	30000	0.0003	1.177
	4th	28000	0.0002	1.176
	1st to 4th	30000	0.0003	1.202
2nd Core (10/2010)	1st to 4th	50500	0.00046	1.191


ATL US259 1st Core
1.60
1.40
1.20
1.00
0.80
0.60
0.40
0.20
0.00
CA
#1
#2
#3
#4
#5
Wheel Path Layer No.
#1
#2
#3
#4
Shoulder Layer No.


ATL US259 Average CA
1.3
1.25
1.2
1.15
1.1
1.05
1
CA
Aug. 2008
Feb.2011
Wheel Path
Shoulder

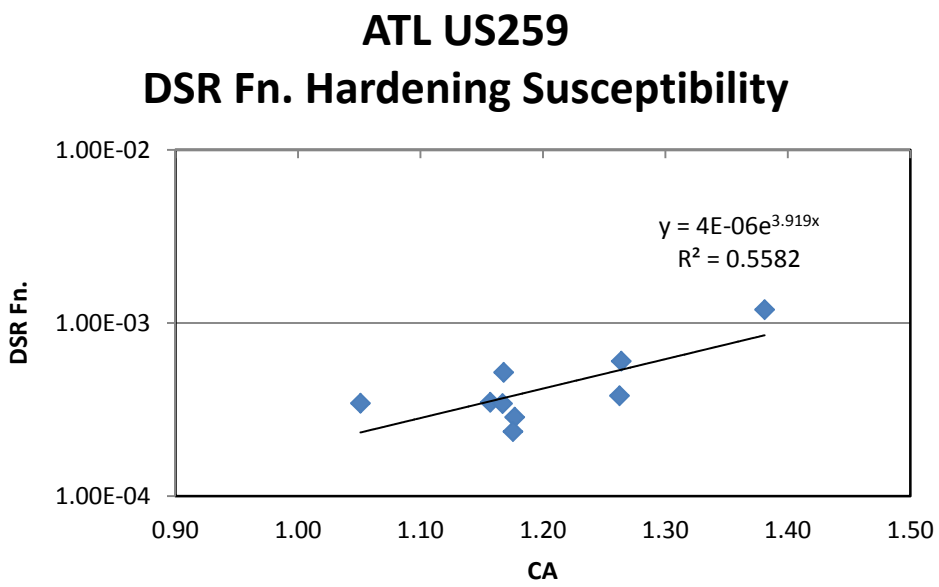
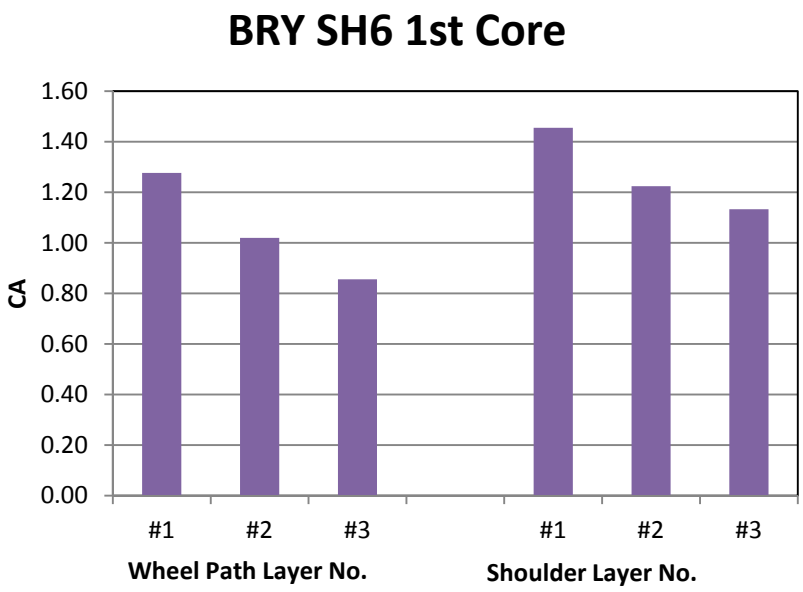

ATL US259
DSR Fn. Hardening Susceptibility
1.00E-02
1.00E-03
1.00E-04
DSR Fn.
y = 4E-06e3.919x
R² = 0.5582
0.90
1.00
1.10
1.20
1.30
1.40
1.50
CA

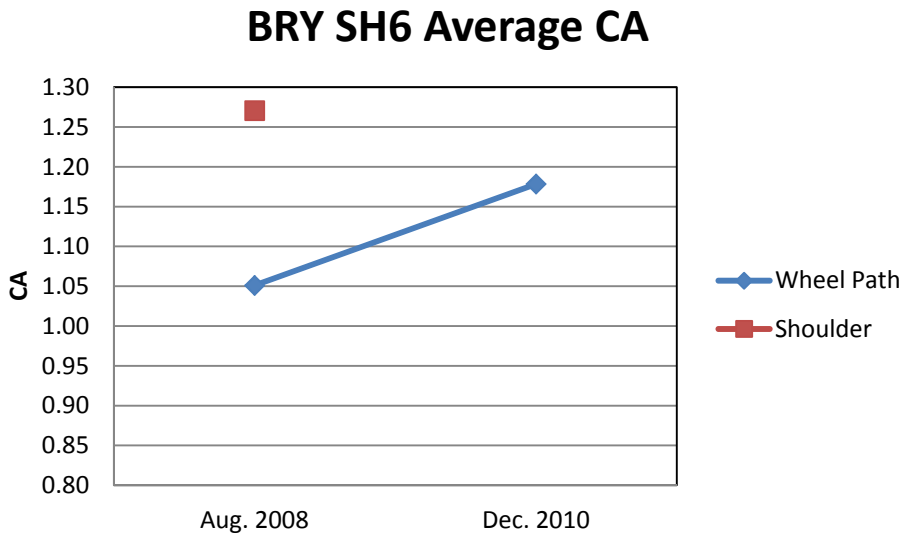
Table E7. SH6 BRY Field Core (Wheel Path)

Binder: Unknown Activation Energy: 52.6 KJ/mol Cons.: 2000		η_o* (Poise) @60°C 0.1 rad/s	G'/(η'/G') (MPa/s) @15°C 0.005 rad/s	Carbonyl Area
1st Core (08/2008)	1st layer	100000	0.001	1.277
	2nd	45000	0.0003	1.020
	3rd	19000	0.0001	0.856
	1st to 3rd	44000	0.0003	1.051
2nd Core (12/2010)	1st to 3rd	87000	0.00072	1.178

Table E8. SH6 BRY Field Core (Shoulder)

Binder: Unknown Activation Energy: 52.6 KJ/mol Cons.: 2000		η_o* (Poise) @60°C 0.1 rad/s	G'/(η'/G') (MPa/s) @15°C 0.005 rad/s	Carbonyl Area
1st Core (08/2008)	1st layer	220000	0.0027	1.455
	2nd	110000	0.0011	1.224
	3rd	70000	0.0007	1.133
	1st to 3rd	119000	0.0012	1.271


BRY SH6 1st Core
1.60
1.40
1.20
1.00
0.80
0.60
0.40
0.20
0.00
CA
#1
#2
#3
#1
#2
#3
Wheel Path Layer No.
Shoulder Layer No.


BRY SH6 Average CA
1.30
1.25
1.20
1.15
1.10
1.05
1.00
0.95
0.90
0.85
0.80
CA
Aug. 2008
Dec. 2010
Wheel Path
Shoulder

BRY SH6
DSR Fn. Hardening Susceptibility

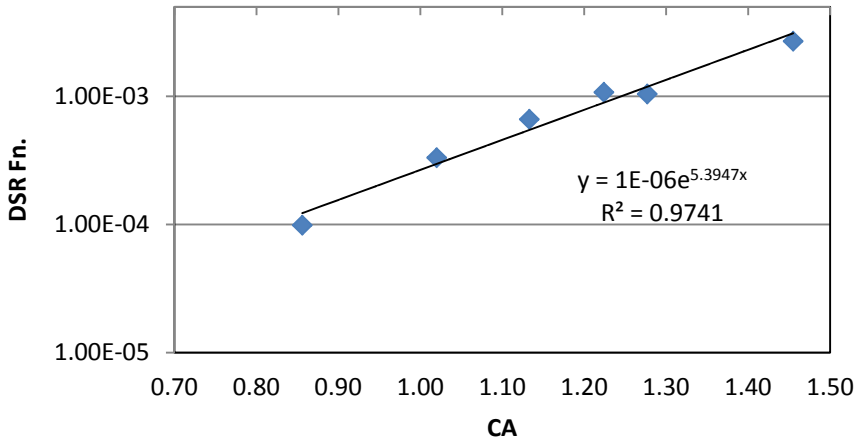
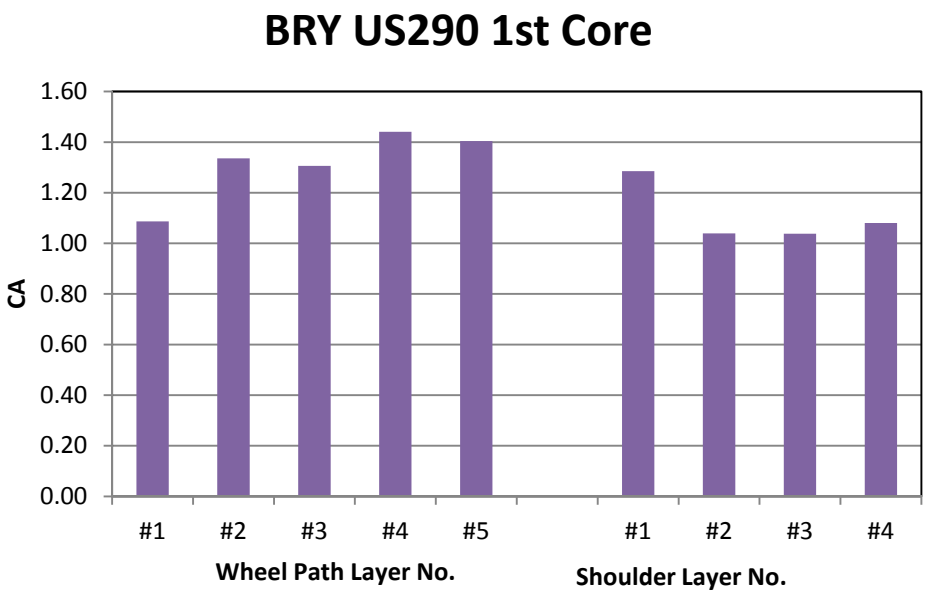


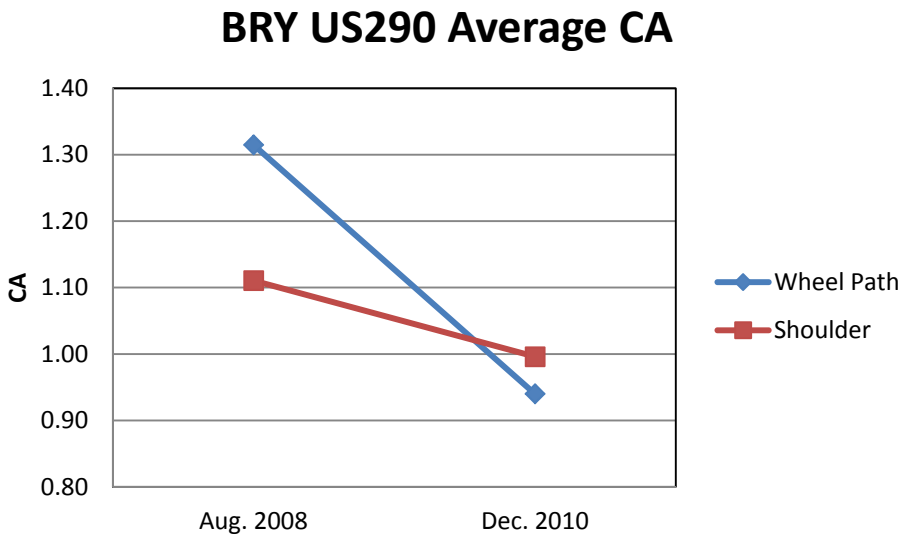
Table E9. US290 BRY Field Core (Wheel Path)

Binder: Eagle PG64-22 Activation Energy: 84.8 KJ/mol Cons.: 2002		η_o* (Poise) @60°C 0.1 rad/s	G'/(η'/G') (MPa/s) @15°C 0.005 rad/s	Carbonyl Area
1st Core (08/2008)	1st layer	80000	0.0006	1.087
	2nd	1000000	0.0106	1.336
	3rd	1100000	0.0123	1.306
	4th	1000000	0.0128	1.441
	5th	800000	0.0159	1.404
	1st to 5th	425000	0.0045	1.269
2nd Core (12/2010)	1st to 5th	54000	0.00026	0.940

Table E10. US290 BRY Field Core (Shoulder)

Binder: Eagle PG64-22 Activation Energy: 84.8 KJ/mol Cons.: 2002		η* (Poise) @60°C 0.1 rad/s	G'/(η'/G') (MPa/s) @15°C 0.005 rad/s	Carbonyl Area
1st Core (08/2008)	1st layer	200000	0.0016	1.285
	2nd	60000	0.0003	1.039
	3rd	58000	0.0003	1.038
	4th	60000	0.0004	1.080
	1st to 4th	89000	0.0005	1.128
2nd Core (12/2010)	1st to 4th	64000	0.00033	0.996


BRY US290 1st Core
1.60
1.40
1.20
1.00
0.80
0.60
0.40
0.20
0.00
CA
#1
#2
#3
#4
#5
#1
#2
#3
#4
Wheel Path Layer No.
Shoulder Layer No.


BRY US290 Average CA
1.40
1.30
1.20
1.10
1.00
0.90
0.80
CA
Aug. 2008
Dec. 2010
Wheel Path
Shoulder

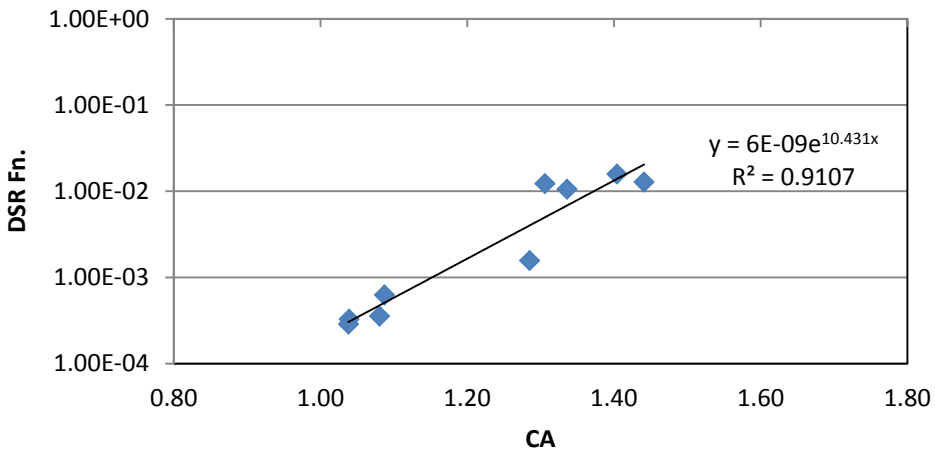

BRY US290
DSR Fn. Hardening Susceptibility
1.00E+00
1.00E-01
1.00E-02
1.00E-03
1.00E-04
DSR Fn.
0.80
1.00
1.20
1.40
1.60
1.80
CA
y = 6E-09e10.431x
R² = 0.9107

Table E11. US83 CHS Field Core (Wheel Path)

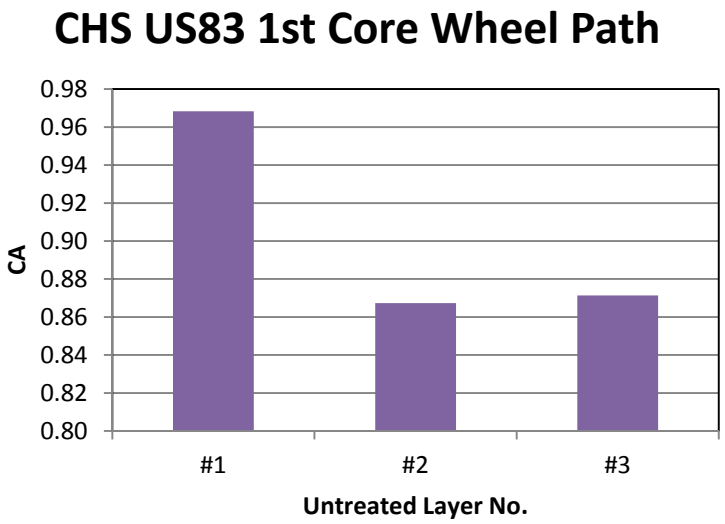
Binder: SEM PG70-28 Activation Energy: 72.5 KJ/mol Cons.: 2008		η_o* (Poise) @60°C 0.1 rad/s	G'/(η'/G') (MPa/s) @15°C 0.005 rad/s	Carbonyl Area
1st Core (08/2008)	1st layer	60000	0.00013	0.968
	2nd	36000	0.00008	0.867
	3rd	31000	0.00007	0.871
	1st to 3rd	40600	0.00009	0.902
2nd Core (10/2009)	1st layer	139000	0.00023	1.129
	2nd	103000	0.00017	1.012
	3rd	86000	0.00016	1.029
	1st to 3rd	107000	0.00018	1.056
3rd Core (08/2010)	1st layer	135000	0.00023	1.097
	2nd	141000	0.00013	1.043
	3rd	112000	0.00021	0.934
	1st to 3rd	128000	0.00019	1.024
4th Core (11/2011)	1st layer	109600	0.00018	1.134
	2nd	93000	0.00015	0.971
	3rd	100000	0.00020	0.946
	1st to 3rd	100000	0.00018	1.017
2nd Core Seal Coat Treated (10/2009)	Seal Coat layer	20000	0.000043	1.311
	1st layer	62000	0.00011	1.034
	2nd	58000	0.000079	0.975
	3rd	64000	0.000092	0.936
	4th	45000	0.000069	0.884
	5th	56000	0.000088	1.012
	1st to 5th	58000	0.000089	0.984
3rd Core Seal Coat Treated (08/2010)	Seal Coat layer	45000	0.00016	1.329
	1st layer	40000	0.000079	0.990
	2nd	82000	0.00013	0.842
	3rd	57000	0.000085	0.807
	1st to 3rd	49000	0.000095	0.880
4th Core Seal Coat Treated (11/2011)	Seal Coat layer	37000	0.00012	1.523
	1st layer	61000	0.00012	1.052
	2nd	103000	0.00016	0.982
	3rd	103000	0.00014	0.905
	1st to 3rd	86000	0.00014	0.980

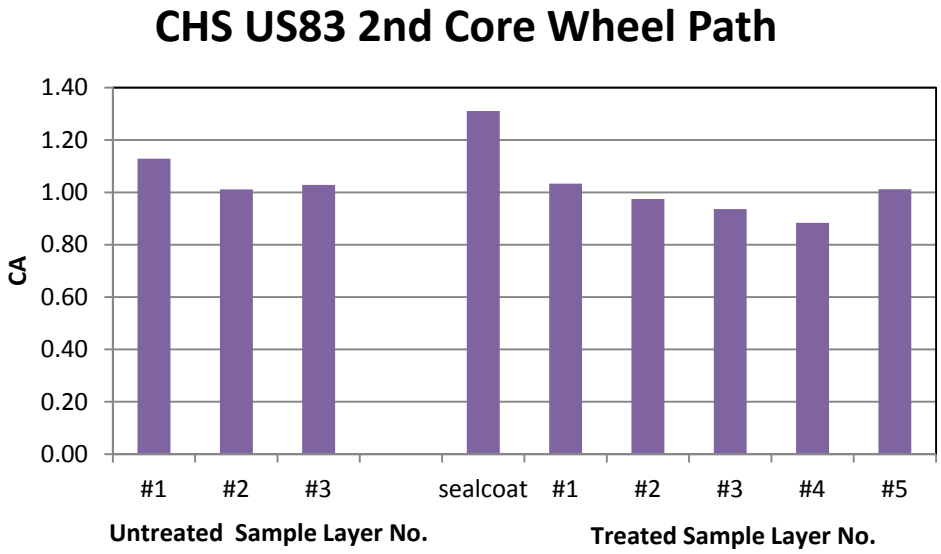
Table E12. US83 CHS Field Core (Shoulder)

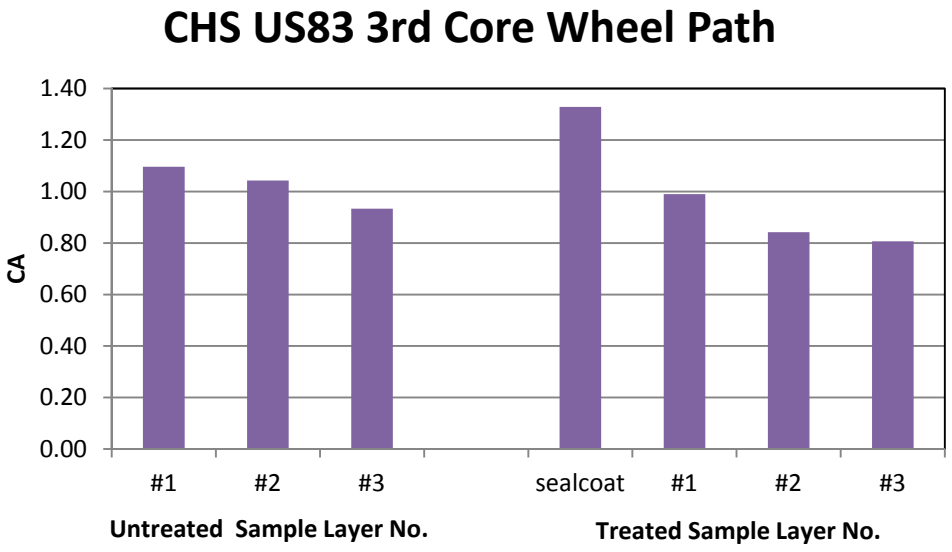
Binder: SEM PG70-28 Activation Energy: 72.5 KJ/mol Cons.: 2008		η_o* (Poise) @60°C 0.1 rad/s	G'/(η'/G') (MPa/s) @15°C 0.005 rad/s	Carbonyl Area
1st Core (08/2008)	1st layer	45000	0.0001	0.924
	2nd	35000	0.00007	0.860
	3rd	35000	0.00007	0.861
	4th	36000	0.00008	0.885
	5th	35000	0.00007	0.900
	1st to 5th	38000	0.00008	0.889
2nd Core (10/2009)	1st layer	270000	0.00045	1.105
	2nd	28000	0.000084	0.937
	3rd	53000	0.000077	0.983
	4th	63000	0.000095	1.039
	5th	54000	0.000080	0.892
	1st to 5th	96000	0.00015	1.004
3rd Core (08/2010)	1st layer	80000	0.00016	0.967
	2nd	72000	0.00012	0.887
	3rd	69000	0.00010	0.894
	4th	92000	0.00018	0.897
	5th	48000	0.000076	0.878
	6th	66000	0.00012	0.925
	1st to 6th	73000	0.00013	0.917
4th Core (11/2011)	1st layer	140000	0.00025	0.983
	2nd	80000	0.00013	0.898
	3rd	71000	0.00013	0.882
	1st to 3rd	92000	0.00016	0.921
2nd Core Seal Coat Treated (10/2009)	Seal Coat layer	20000	0.000042	1.080
	1st layer	41000	0.000069	0.968
	2nd	48000	0.000062	0.900
	3rd	50000	0.000076	0.859
	1st to 3rd	46000	0.000069	0.909
3rd Core Seal Coat Treated (08/2010)	Seal Coat layer	70000	0.000098	1.313
	1st layer	61000	0.000098	0.895
	2nd	55000	0.000081	0.847
	3rd	74000	0.00011	0.919
	4th	100000	0.00017	0.914
	1st to 4th	66000	0.00010	0.886

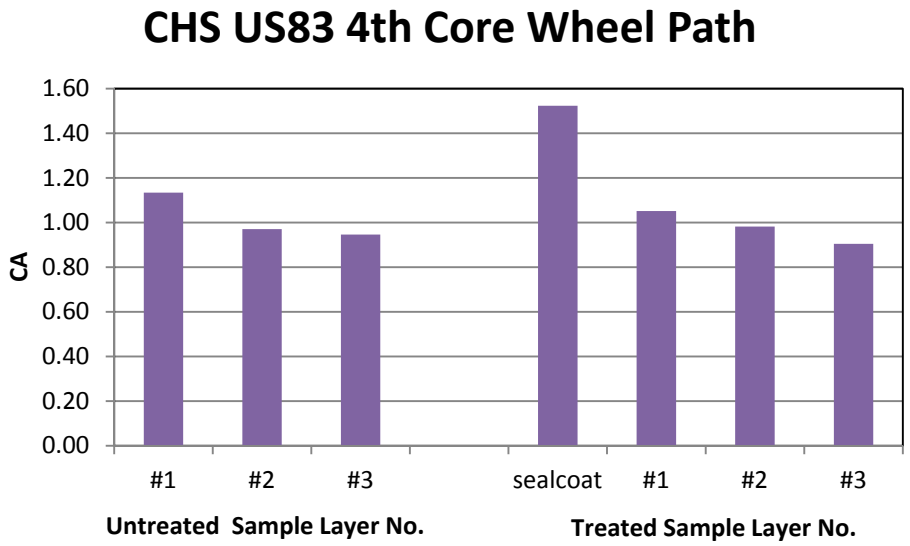
Table E12. US83 CHS Field Core (Shoulder) (continued)

Binder: SEM PG70-28 Activation Energy: 72.5 KJ/mol Cons.: 2008		η_o* (Poise) @60°C 0.1 rad/s	G'/(η'/G') (MPa/s) @15°C 0.005 rad/s	Carbonyl Area
4th Core Seal Coat Treated (11/2011)	Seal Coat layer	50000	0.00022	1.483
	1st layer	100000	0.00021	1.005
	2nd	33000	0.000044	0.734
	3rd	68000	0.00011	0.887
	4th	110000	0.00019	0.950
	1st to 4th	66000	0.00011	0.886

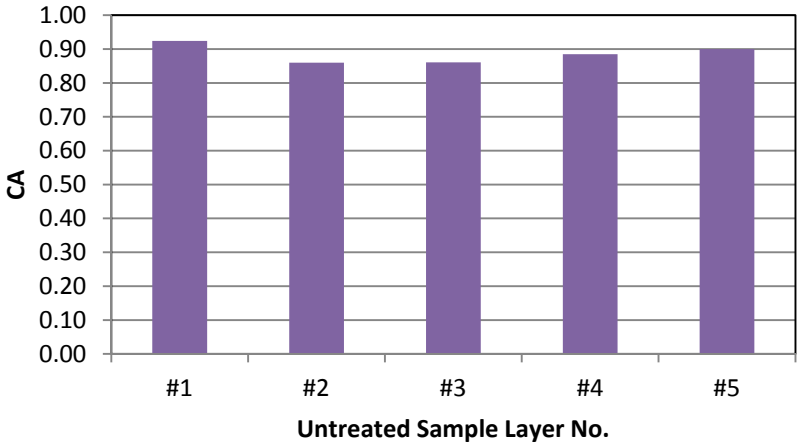

CHS US83 1st Core Wheel Path
0.98
0.96
0.94
0.92
0.90
0.88
0.86
0.84
0.82
0.80
CA
#1
#2
#3
Untreated Layer No.


CHS US83 2nd Core Wheel Path
1.40
1.20
1.00
0.80
0.60
0.40
0.20
0.00
CA
#1
#2
#3
sealcoat
#1
#2
#3
#4
#5
Untreated Sample Layer No.
Treated Sample Layer No.

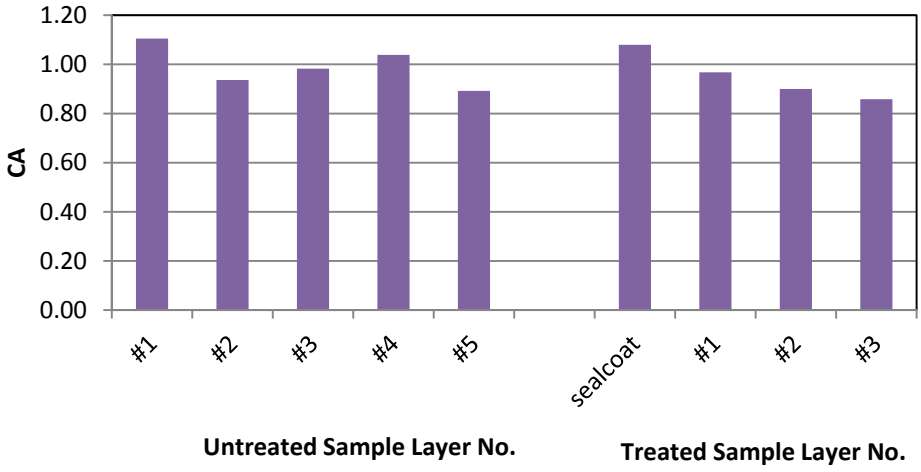

CHS US83 3rd Core Wheel Path
1.40
1.20
1.00
0.80
0.60
0.40
0.20
0.00
CA
#1
#2
#3
sealcoat
#1
#2
#3
Untreated Sample Layer No.
Treated Sample Layer No.

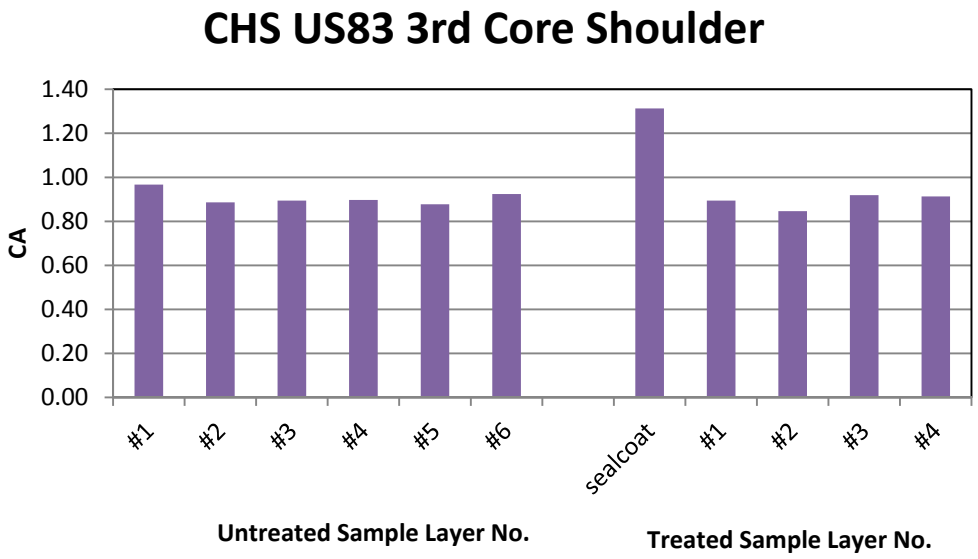

CHS US83 4th Core Wheel Path
1.60
1.40
1.20
1.00
0.80
0.60
0.40
0.20
0.00
CA
#1
#2
#3
sealcoat
#1
#2
#3
Untreated Sample Layer No.
Treated Sample Layer No.

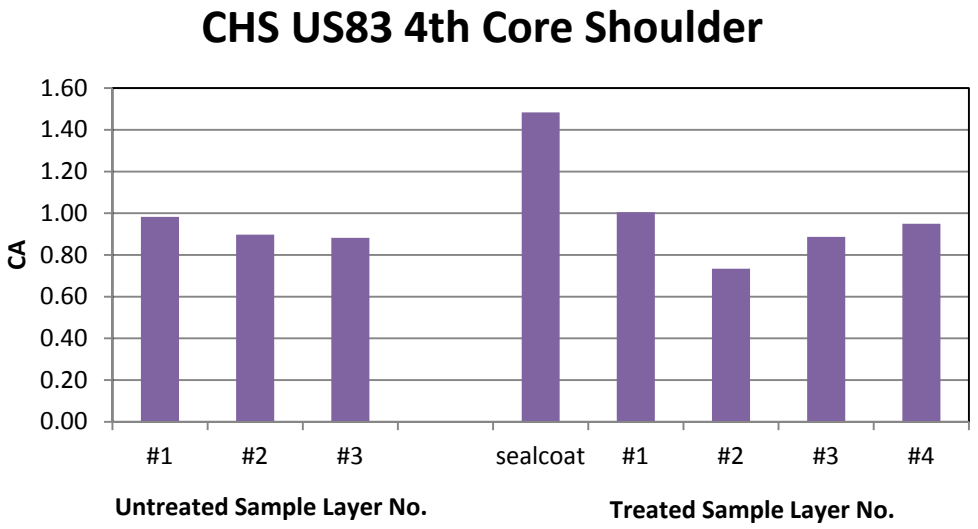
CHS US83 1st Core Shoulder

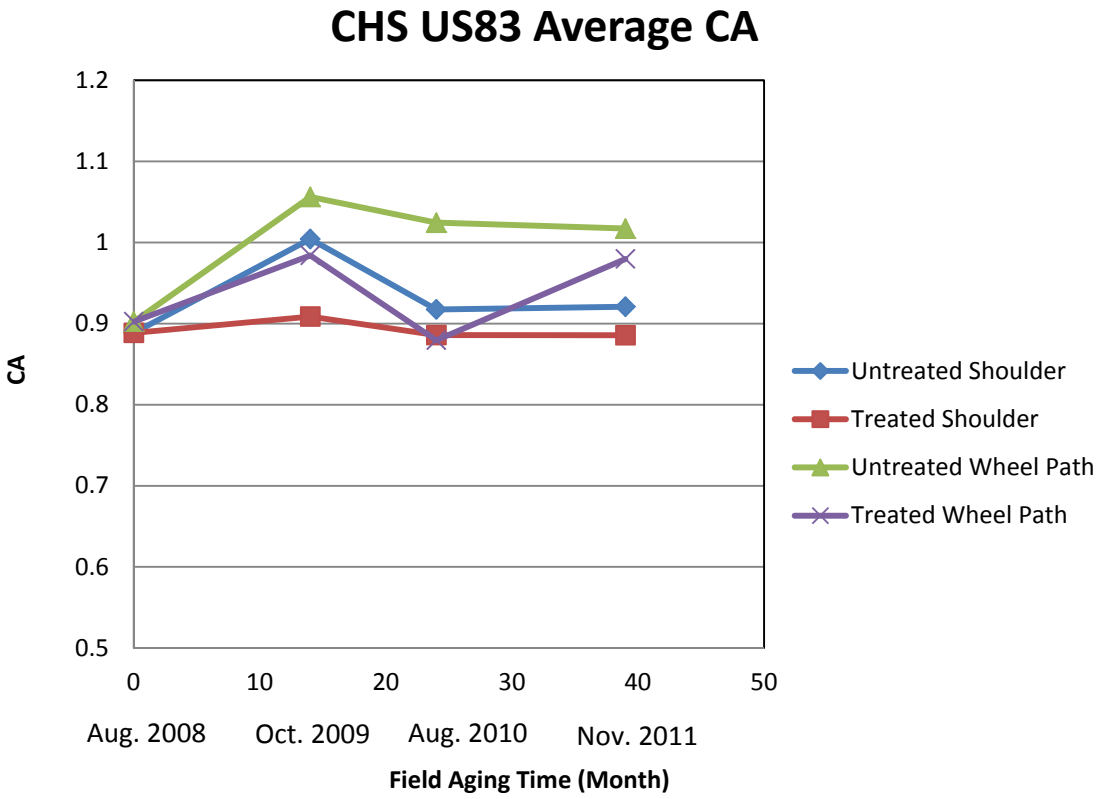


CHS US83 2nd Core Shoulder




CHS US83 3rd Core Shoulder
CA
1.40
1.20
1.00
0.80
0.60
0.40
0.20
0.00
#1
#2
#3
#4
#5
#6
sealcoat
#1
#2
#3
#4
Untreated Sample Layer No.
Treated Sample Layer No.


CHS US83 4th Core Shoulder
CA
1.60
1.40
1.20
1.00
0.80
0.60
0.40
0.20
0.00
#1
#2
#3
sealcoat
#1
#2
#3
#4
Untreated Sample Layer No.
Treated Sample Layer No.


CHS US83 Average CA
1.2
1.1
1
0.9
0.8
0.7
0.6
0.5
CA
0
10
20
30
40
50
Aug. 2008
Oct. 2009
Aug. 2010
Nov. 2011
Field Aging Time (Month)
Untreated Shoulder
Treated Shoulder
Untreated Wheel Path
Treated Wheel Path

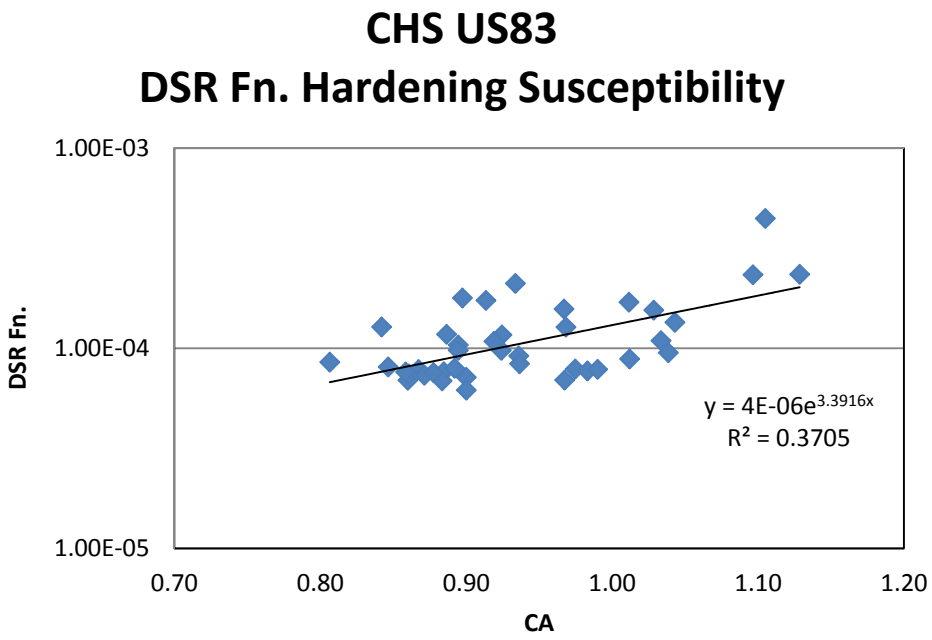

CHS US83
DSR Fn. Hardening Susceptibility
1.00E-03
1.00E-04
1.00E-05
DSR Fn.
0.70
0.80
0.90
1.00
1.10
1.20
CA
y = 4E-06e3.3916x
R² = 0.3705

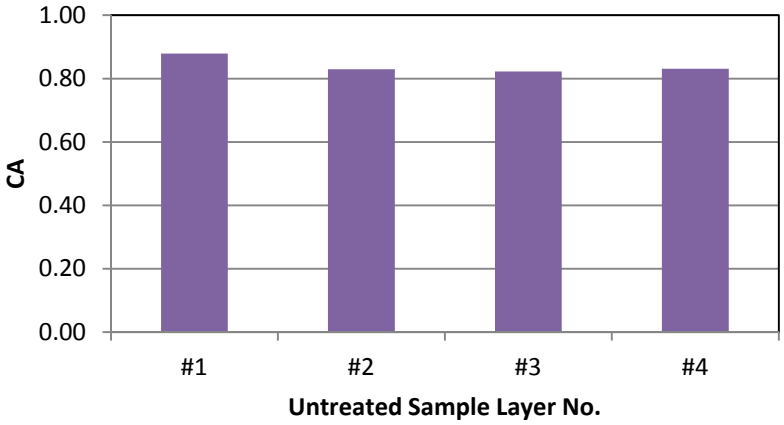
Table E13. US82 LBB Field Core (Wheel Path)

Binder: Alon PG76-22 Activation Energy: 69.8 KJ/mol Cons.: 2008		η_o* (Poise) @60°C 0.1 rad/s	G'/(η'/G') (MPa/s) @15°C 0.005 rad/s	Carbonyl Area
1st Core (08/2008)	1st layer	80000	0.0002	0.879
	2nd	65000	0.0002	0.830
	3rd	70000	0.0002	0.823
	4th	65000	0.0002	0.831
	1st to 4th	70000	0.0002	0.845
2nd Core (12/2009)	1st layer	230000	0.00070	1.201
	2nd	200000	0.00050	1.122
	3rd	170000	0.00045	1.193
	1st to 3rd	190000	0.00053	1.172
3rd Core (08/2010)	1st layer	400000	0.0019	1.269
	2nd	170000	0.00054	1.092
	3rd	230000	0.00075	1.108
	4th	240000	0.00087	1.062
	1st to 4th	250000	0.00090	1.148
2nd Core Seal Coat Treated (12/2009)	Seal Coat layer	19000	0.000042	0.994
	1st layer	62000	0.00011	0.946
	2nd	160000	0.00034	1.026
	3rd	110000	0.00023	0.958
	4th	150000	0.00033	0.978
	1st to 4th	110000	0.00023	0.980
3rd Core Seal Coat Treated (08/2010)	Seal Coat layer	30000	0.000082	1.042
	1st layer	78000	0.00016	0.856
	2nd	100000	0.00019	0.853
	3rd	110000	0.00021	0.873
	4th	120000	0.00022	0.837
	1st to 4th	100000	0.00020	0.854

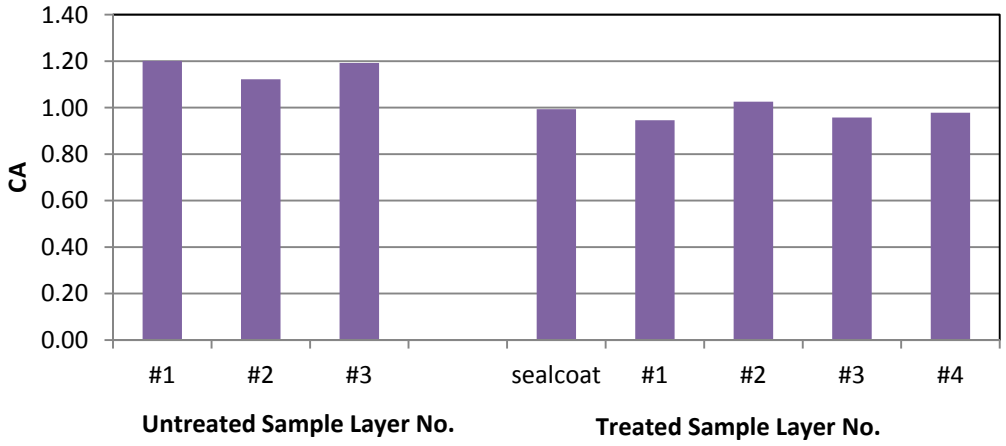
Table E14. US82 LBB Field Core (Shoulder)

Binder: Alon PG76-22 Activation Energy: 69.8 KJ/mol Cons.: 2008		η_o* (Poise) @60°C 0.1 rad/s	G'/(η'/G') (MPa/s) @15°C 0.005 rad/s	Carbonyl Area
1st Core (08/2008)	1st layer	70000	0.0002	0.876
	2nd	52000	0.0001	0.771
	3rd	60000	0.0001	0.798
	1st to 3rd	60000	0.0001	0.815
2nd Core (12/2009)	1st layer	260000	0.00079	1.218
	2nd	130000	0.00028	1.015
	3rd	150000	0.00031	1.026
	4th	170000	0.00044	1.109
	1st to 4th	180000	0.00043	1.100
3rd Core (08/2010)	1st layer	Too high to measure	0.00160	1.137
	2nd	130000	0.00030	0.969
	3rd	210000	0.00059	0.992
	4th	300000	0.0010	1.081
	1st to 4th	-	0.00073	1.047
2nd Core Seal Coat Treated (12/2009)	Seal Coat layer	20000	0.000046	1.016
	1st layer	100000	0.00022	0.951
	2nd	69000	0.000078	0.751
	3rd	120000	0.00015	0.823
	4th	150000	0.00025	0.944
	1st to 4th	100000	0.00016	0.887
3rd Core Seal Coat Treated (08/2010)	Seal Coat layer	25000	0.000082	1.069
	1st layer	67000	0.00013	0.930
	2nd	95000	0.00017	0.884
	3rd	120000	0.00027	0.893
	4th	180000	0.00051	0.943
	1st to 4th	110000	0.00023	0.910

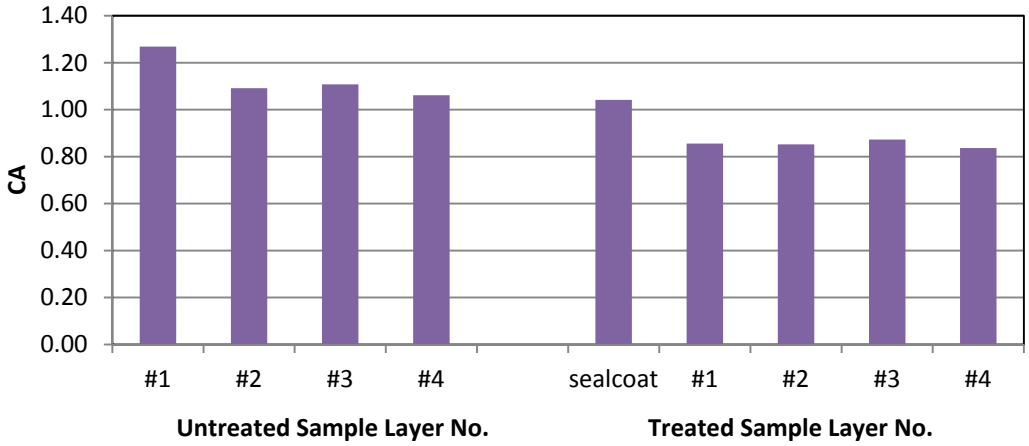
LBB US82 1st Core Wheel Path



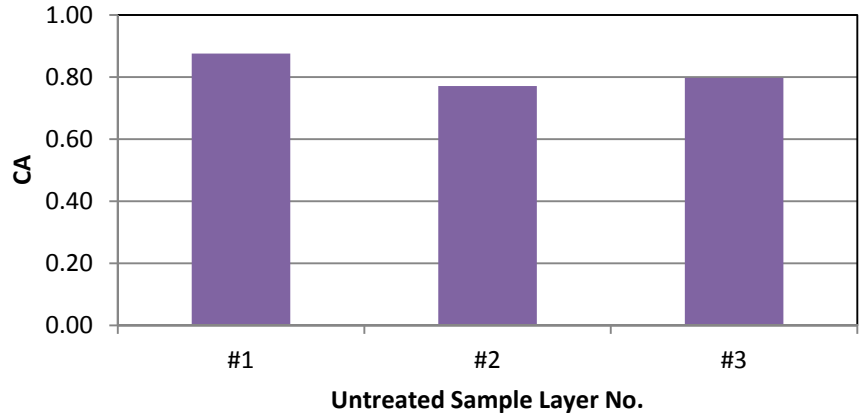
LBB US82 2nd Core Wheel Path



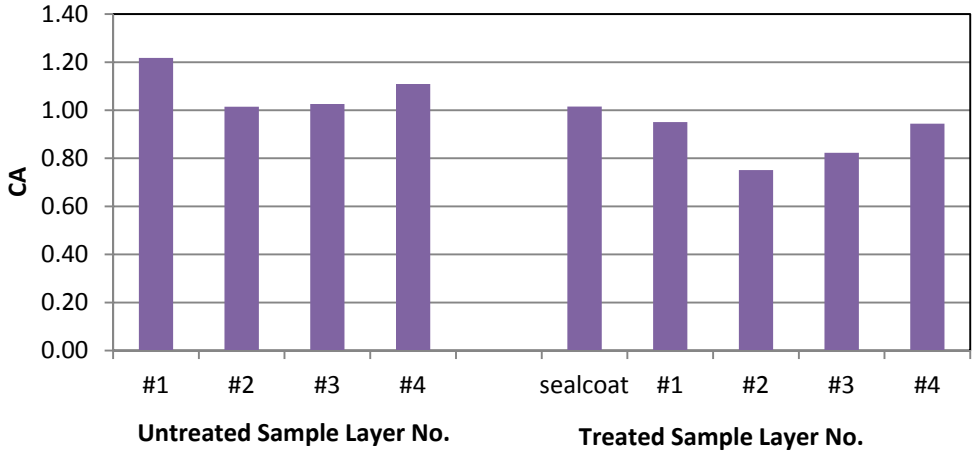
LBB US82 3rd Core Wheel Path



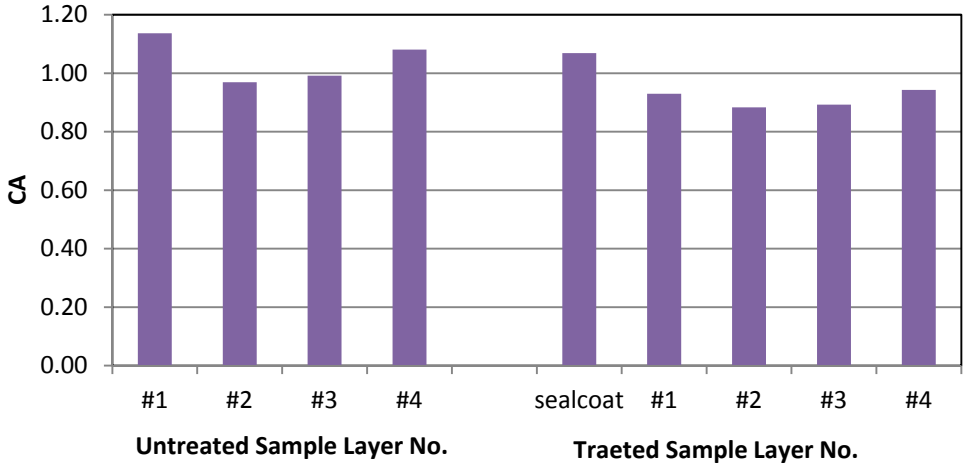
LBB US82 1st Core Shoulder

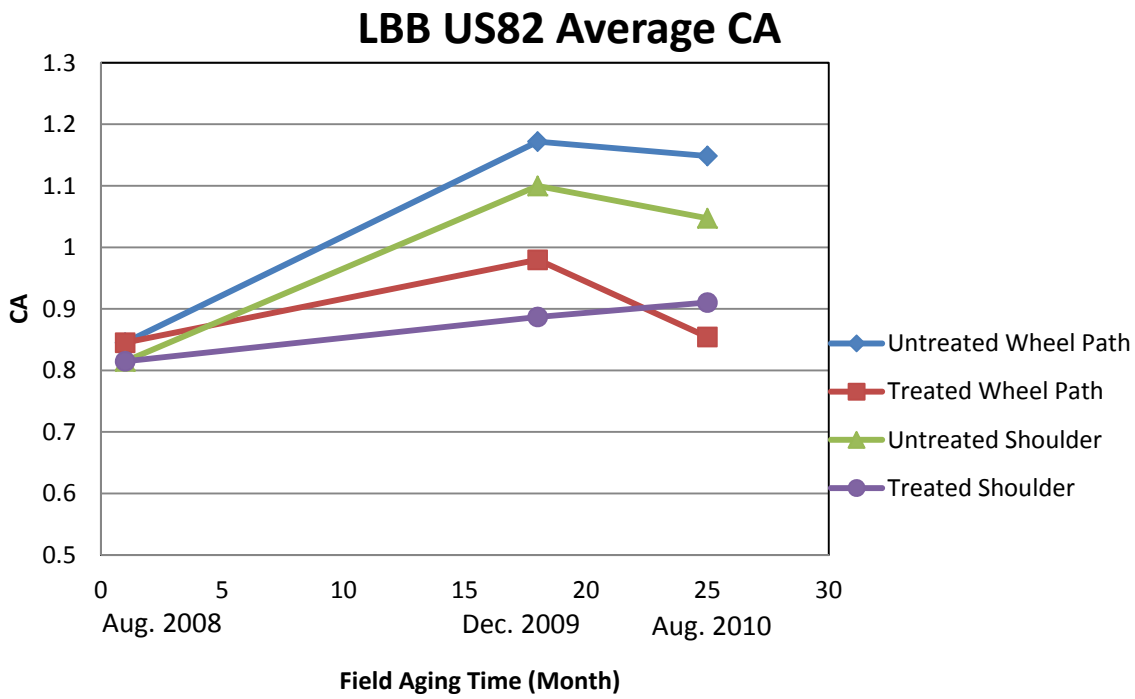


LBB US82 2nd Core Shoulder



LBB US82 3rd Core Shoulder




LBB US82 Average CA
1.3
1.2
1.1
1
0.9
0.8
0.7
0.6
0.5
CA
0
5
10
15
20
25
30
Aug. 2008
Dec. 2009
Aug. 2010
Field Aging Time (Month)
Untreated Wheel Path
Treated Wheel Path
Untreated Shoulder
Treated Shoulder

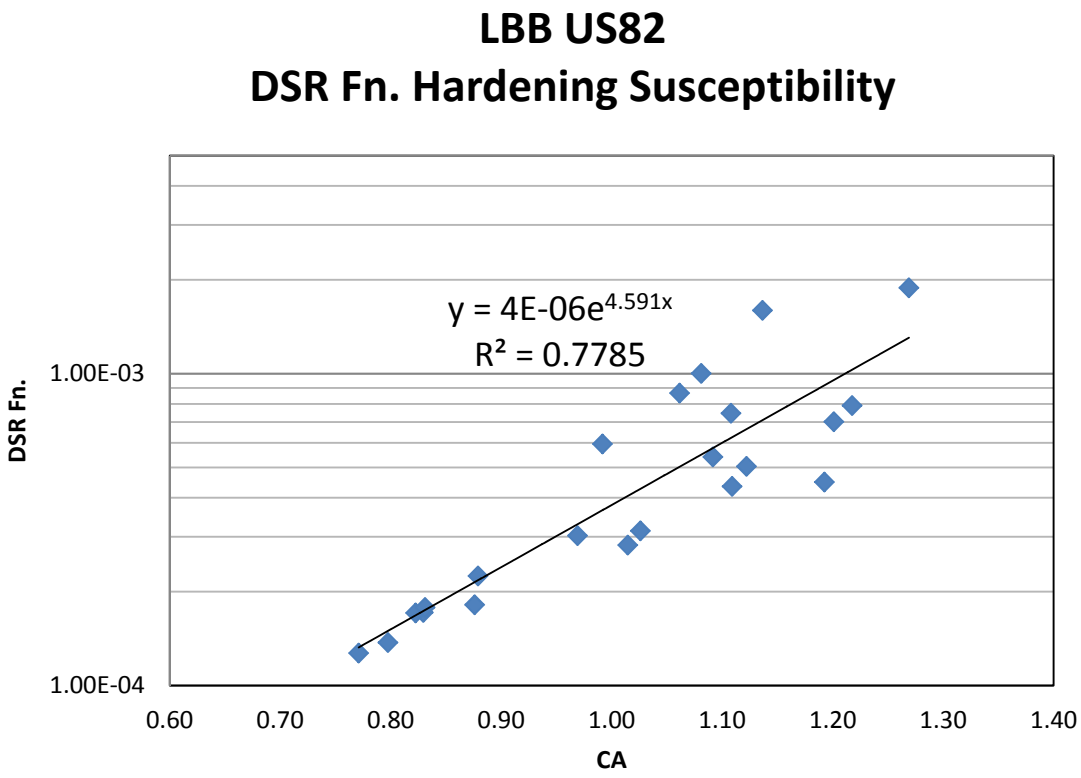
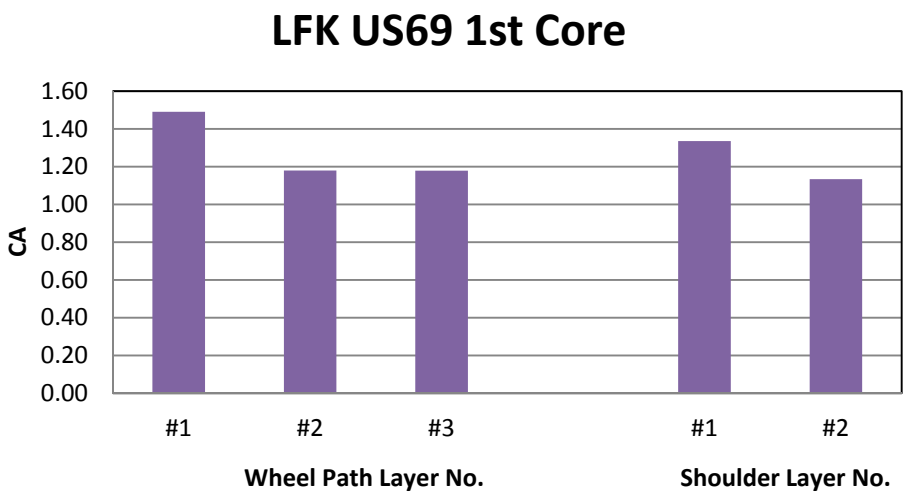

LBB US82
DSR Fn. Hardening Susceptibility
y = 4E-06e4.591x
R² = 0.7785
1.00E-03
1.00E-04
DSR Fn.
0.60
0.70
0.80
0.90
1.00
1.10
1.20
1.30
1.40
CA

Table E15. US69 LFK Field Core (Wheel Path)

Binder: Martin PG70-22 Activation Energy: 64.3 KJ/mol Cons.: 2003		η_o* (Poise) @60°C 0.1 rad/s	G'/(η'/G') (MPa/s) @15°C 0.005 rad/s	Carbonyl Area
1st Core (06/2008)	1st layer	Too high to measure	Too high to measure	1.491
	2nd	200000	0.0015	1.180
	3rd	160000	0.0011	1.179
	1st to 3rd	-	-	1.283

Table E16. US69 LFK Field Core (Shoulder)

Binder: Martin PG70-22 Activation Energy: 64.3 KJ/mol Cons.: 2003		η_o* (Poise) @60°C 0.1 rad/s	G'/(η'/G') (MPa/s) @15°C 0.005 rad/s	Carbonyl Area
1st Core (06/2008)	1st layer	500000	0.002	1.336
	2nd	120000	0.00057	1.134
	1st to 2nd	240000	0.0011	1.235


LFK US69 1st Core
1.60
1.40
1.20
1.00
0.80
0.60
0.40
0.20
0.00
CA
#1
#2
#3
#1
#2
Wheel Path Layer No.
Shoulder Layer No.

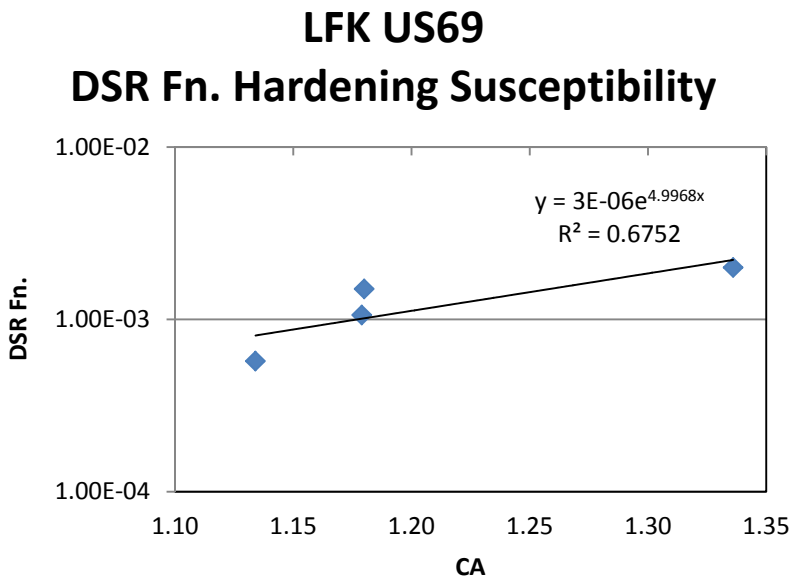
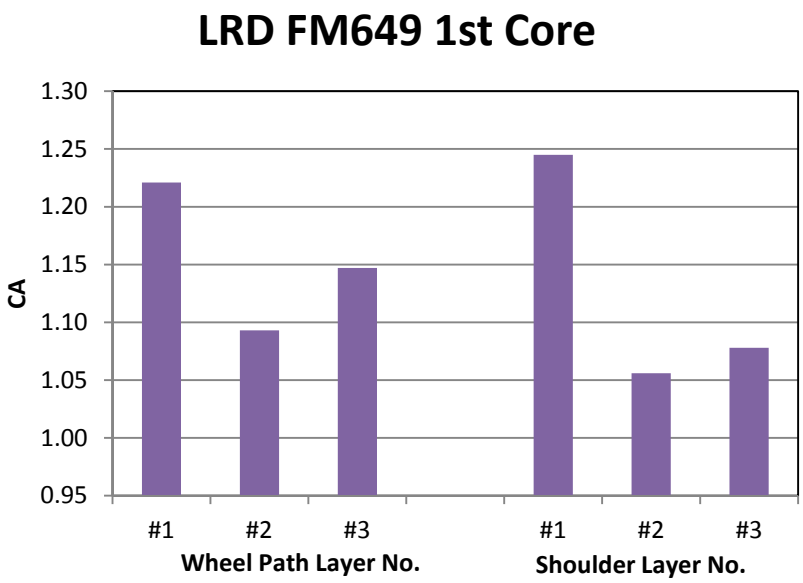

LFK US69
DSR Fn. Hardening Susceptibility
1.00E-02
1.00E-03
1.00E-04
DSR Fn.
y = 3E-06e4.9968x
R² = 0.6752
1.10
1.15
1.20
1.25
1.30
1.35
CA

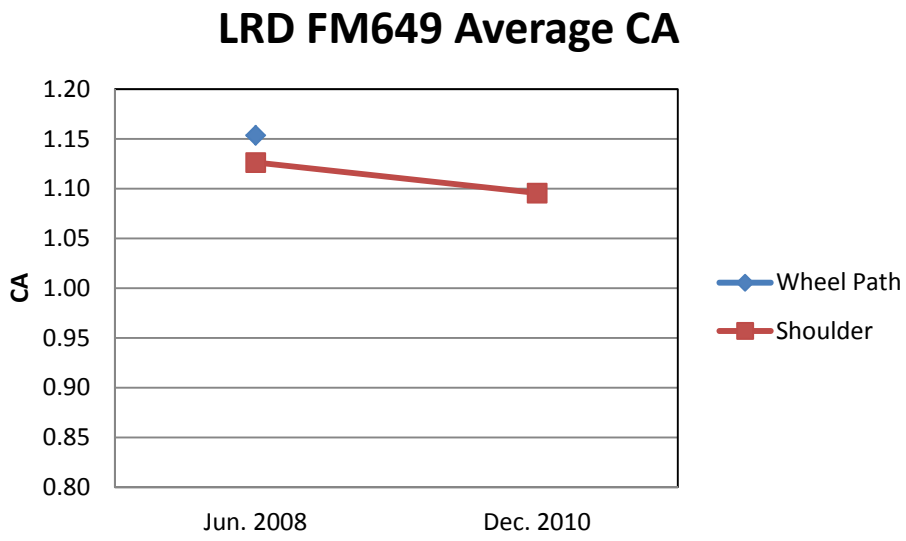
Table E17. FM649 LRD Field Core (Wheel Path)

Binder: Valero-Corpus PG76-22 Activation Energy: 80.1 KJ/mol Cons.: 2006		η_o* (Poise) @60°C 0.1 rad/s	G'/(η'/G') (MPa/s) @15°C 0.005 rad/s	Carbonyl Area
1st Core (06/2008)	1st layer	500000	0.0015	1.221
	2nd	220000	0.0009	1.093
	3rd	200000	0.0008	1.147
	1st to 3rd	280000	0.001	1.154

Table E18. FM649 LRD Field Core (Shoulder)

Binder: Valero-Corpus PG76-22 Activation Energy: 80.1 KJ/mol Cons.: 2006		η_o* (Poise) @60°C 0.1 rad/s	G'/(η'/G') (MPa/s) @15°C 0.005 rad/s	Carbonyl Area
1st Core (06/2008)	1st layer	520000	0.0019	1.245
	2nd	200000	0.0007	1.056
	3rd	160000	0.0006	1.078
	1st to 3rd	255000	0.0009	1.126
2nd Core (02/2010)	1st to 3rd	180000	0.00068	1.096


LRD FM649 1st Core
1.30
1.25
1.20
1.15
1.10
1.05
1.00
0.95
CA
#1
#2
#3
Wheel Path Layer No.
#1
#2
#3
Shoulder Layer No.


LRD FM649 Average CA
1.20
1.15
1.10
1.05
1.00
0.95
0.90
0.85
0.80
CA
Jun. 2008
Dec. 2010
Wheel Path
Shoulder

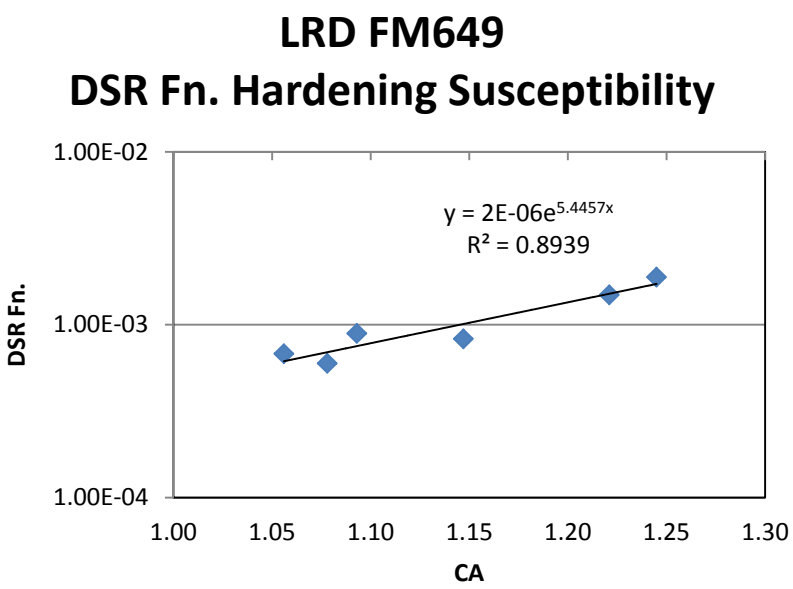

LRD FM649
DSR Fn. Hardening Susceptibility
1.00E-02
1.00E-03
1.00E-04
DSR Fn.
y = 2E-06e5.4457x
R² = 0.8939
1.00
1.05
1.10
1.15
1.20
1.25
1.30
CA

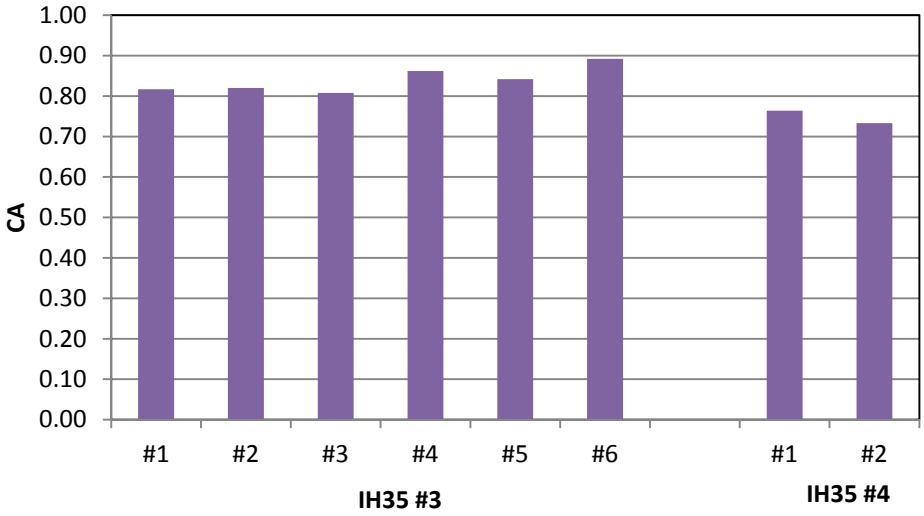
Table E19. IH35 #3 LRD04 Field Core (Shoulder)

Binder: Valero-Corpus PG76-22 Activation Energy: 68.1 KJ/mol Cons.: 2007		η_o* (Poise) @60°C 0.1 rad/s	G'/(η'/G') (MPa/s) @15°C 0.005 rad/s	Carbonyl Area
1st Core (06/2008)	1st layer	100000	0.00028	0.817
	2nd	80000	0.00027	0.820
	3rd	80000	0.00023	0.808
	4th	80000	0.00019	0.862
	5th	150000	0.00035	0.842
	6th	70000	0.00024	0.892
	1st to 6th	90000	0.00027	0.829
2nd Core (12/2010)	1st to 6th	56000	0.00014	0.631

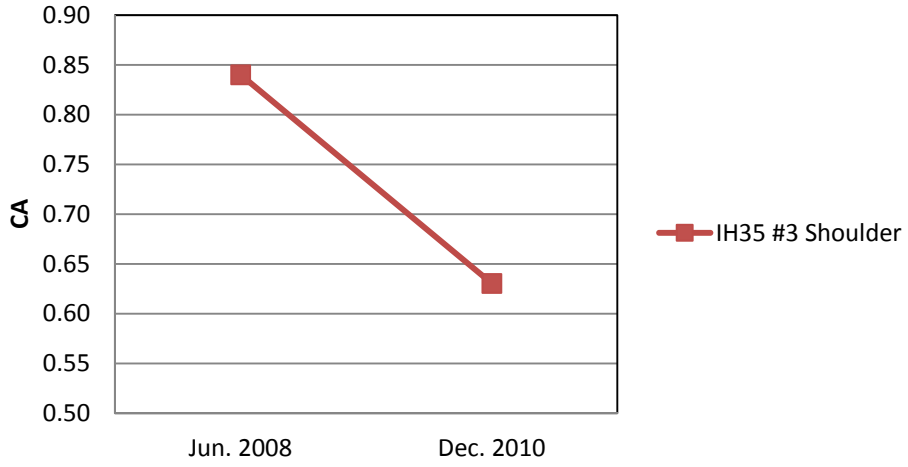
Table E20. IH35 #5 LRD04 Field Core (Shoulder)

Binder: Valero-Corpus PG70-22 Activation Energy: 103.8 KJ/mol Cons.: 2007		η_o* (Poise) @60°C 0.1 rad/s	G'/(η'/G') (MPa/s) @15°C 0.005 rad/s	Carbonyl Area
1st Core (06/2008)	1st layer	30000	0.000092	0.764
	2nd	31000	0.000097	0.733
	1st to 2nd	30500	0.000093	0.749

LRD IH35 #3&#4 1st Core



LRD FM649 Average CA



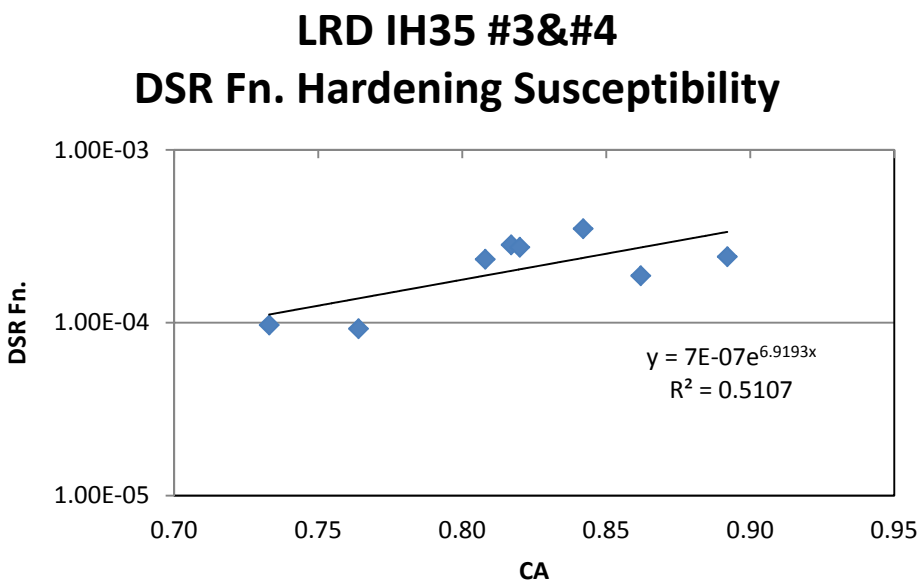

LRD IH35 #3&#4
DSR Fn. Hardening Susceptibility
1.00E-03
1.00E-04
1.00E-05
DSR Fn.
0.70
0.75
0.80
0.85
0.90
0.95
CA
y = 7E-07e6.9193x
R² = 0.5107

Table E21. US277 LRD Field Core (Wheel Path)

Binder: Valero-Corpus PG70-22 Activation Energy: 83.0 KJ/mol Cons.: 2008		η_o* (Poise) @60°C 0.1 rad/s	G'/(η'/G') (MPa/s) @15°C 0.005 rad/s	Carbonyl Area
1st Core (07/2008)	1st layer	82000	0.0003	0.936
	2nd	100000	0.0003	0.937
	3rd	120000	0.0004	0.971
	4th	100000	0.0003	0.954
	5th	80000	0.0003	0.930
	1st to 5th	93000	0.0003	0.942
2nd Core (12/2009)	1st layer	160000	0.00080	1.206
	2nd	150000	0.00042	1.004
	3rd	120000	0.00032	0.970
	4th	37000	0.00014	0.886
	1st to 4th	120000	0.00042	1.046
3rd Core (12/2010)	1st layer	320000	0.00091	1.116
	2nd	150000	0.00043	1.013
	3rd	230000	0.00068	1.104
	4th	140000	0.00045	1.079
	1st to 4th	200000	0.00060	1.073
4th Core (01/2012)	1st layer*	140000	0.00046	1.135
	2nd	200000	0.00062	1.026
	3rd	280000	0.00093	1.175
	4th	130000	0.00047	1.053
	1st to 4th	170000	0.00057	1.091
2nd Core Seal Coat Treated (12/2009)	Seal Coat layer	Too high to measure	0.0030	1.218
	1st layer	170000	0.00047	1.087
	2nd	160000	0.00051	1.047
	3rd	160000	0.00047	1.081
	4th	140000	0.00043	1.051
	5th	83000	0.00029	0.932
	1st to 5th	150000	0.00045	1.052
3rd Core Seal Coat Treated (12/2010)	Seal Coat layer	Too high to measure	0.0027	1.541
	1st layer	110000	0.00037	1.024
	2nd	170000	0.00057	1.086
	3rd	140000	0.00046	1.109
	4th	190000	0.00067	1.143
	5th	72000	0.00030	0.998
	1st to 5th	130000	0.00046	1.064

Table E21. US277 LRD Field Core (Wheel Path) (continued)

Binder: Valero-Corpus PG70-22 Activation Energy: 83.0 KJ/mol Cons.: 2008		η_o* (Poise) @60°C 0.1 rad/s	G'/(η'/G') (MPa/s) @15°C 0.005 rad/s	Carbonyl Area
4th Core Seal Coat Treated (01/2012)	1st layer & Seal Coat*	250000	0.00081	1.226
	2nd	140000	0.00047	1.043
	3rd	170000	0.00066	1.050
	1st to 3rd	180000	0.00063	1.106

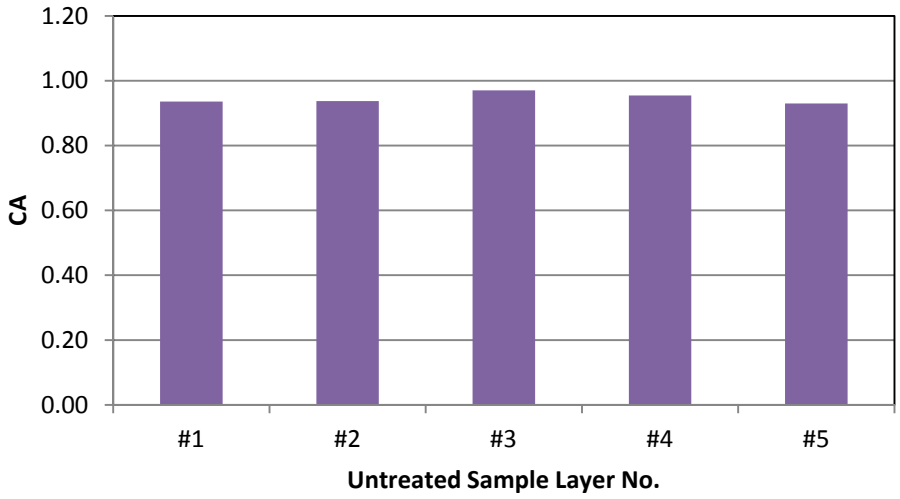
* Another Seal Coat layer was applied, and it was too thin to cut off.

Table E22. US277 LRD Field Core (Shoulder)

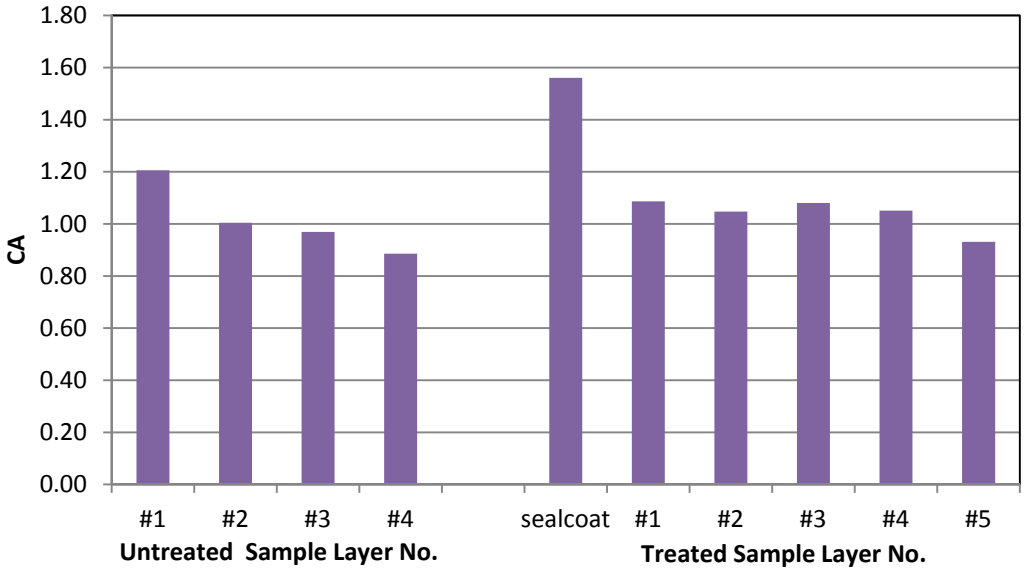
Binder: Valero-Corpus PG70-22 Activation Energy: 83.0 KJ/mol Cons.: 2008		η_o* (Poise) @60°C 0.1 rad/s	G'/(η'/G') (MPa/s) @15°C 0.005 rad/s	Carbonyl Area
1st Core (07/2008)	1st layer	120000	0.0005	1.019
	2nd	85000	0.0004	0.897
	3rd	100000	0.0003	0.894
	4th	100000	0.0004	0.923
	5th	80000	0.0003	0.918
	1st to 5th	98000	0.0004	0.942
2nd Core (12/2009)	1st layer	Too high to measure	0.00087	1.218
	2nd	170000	0.00050	0.959
	3rd	190000	0.00061	0.971
	4th	200000	0.00054	0.949
	5th	160000	0.00047	1.008
	1st to 5th	-	0.00062	1.051
3rd Core (12/2010)	1st layer	310000	0.00098	1.211
	2nd	160000	0.00055	1.037
	3rd	200000	0.00069	1.058
	4th	82000	0.00041	1.037
	1st to 4th	180000	0.00066	1.098
4th Core (01/2012)	1st layer*	340000	0.00104	1.211
	2nd	250000	0.00089	1.037
	3rd	250000	0.00087	1.099
	1st to 3rd	280000	0.00093	1.115

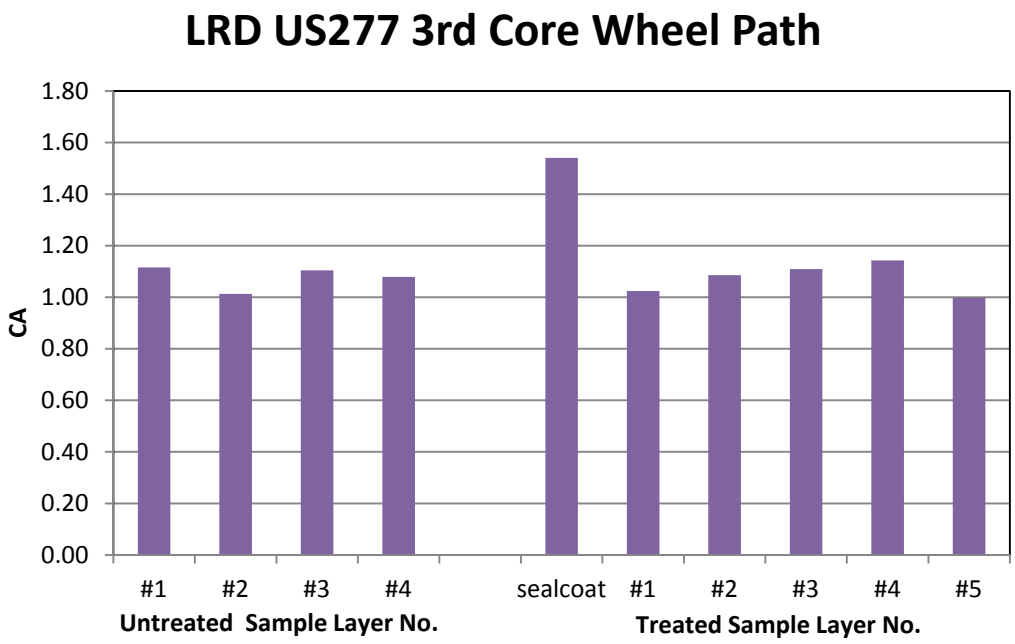
* Another Seal Coat layer was applied, and it was too thin to cut off.

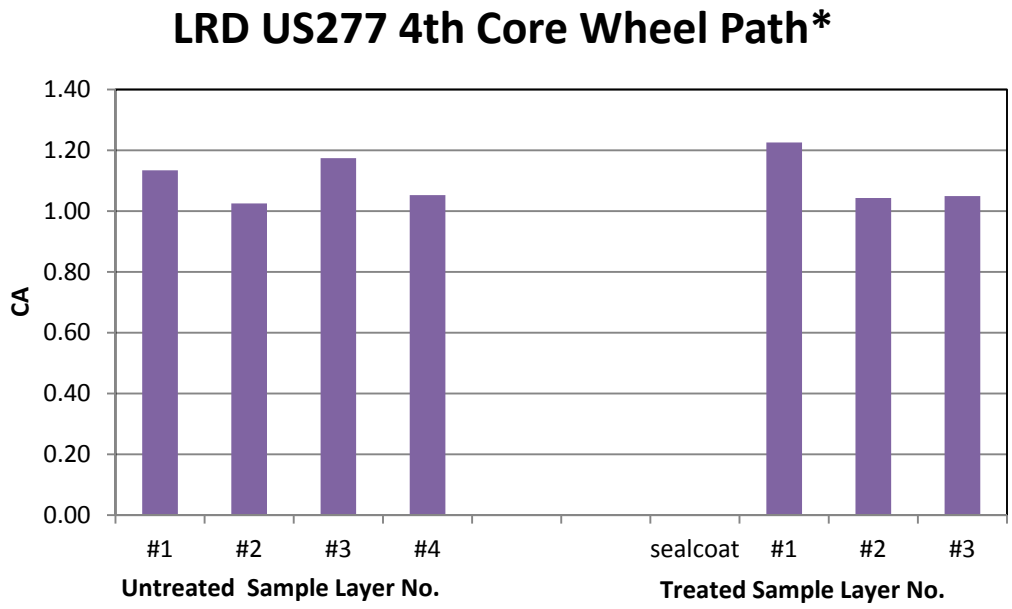
LRD US277 1st Core Wheel Path



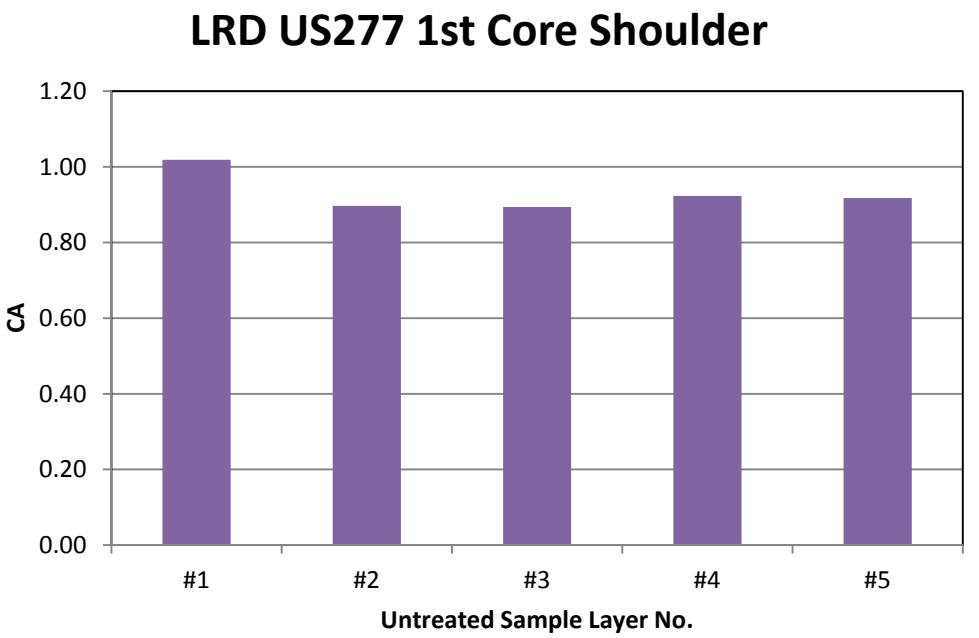
LRD US277 2nd Core Wheel Path

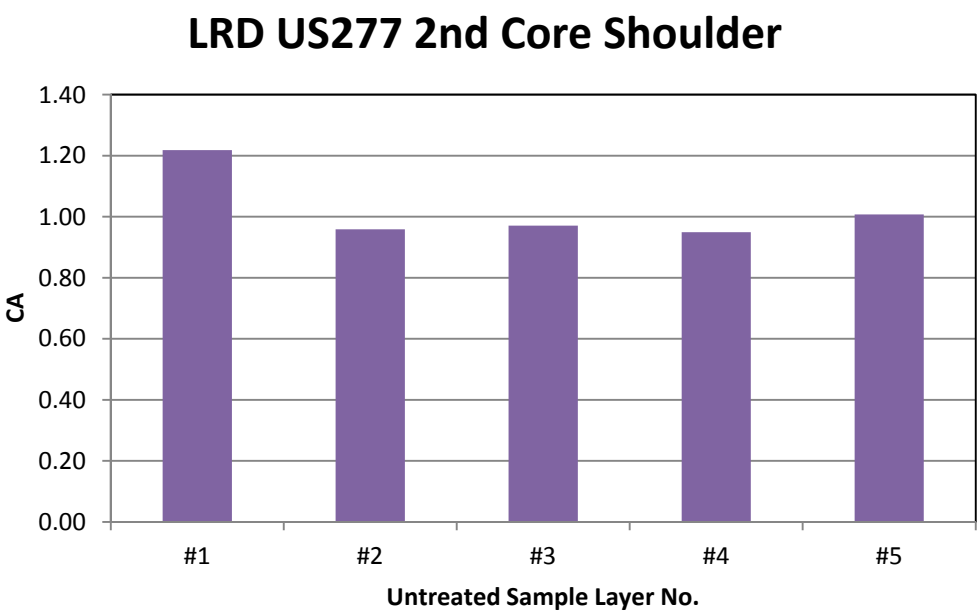


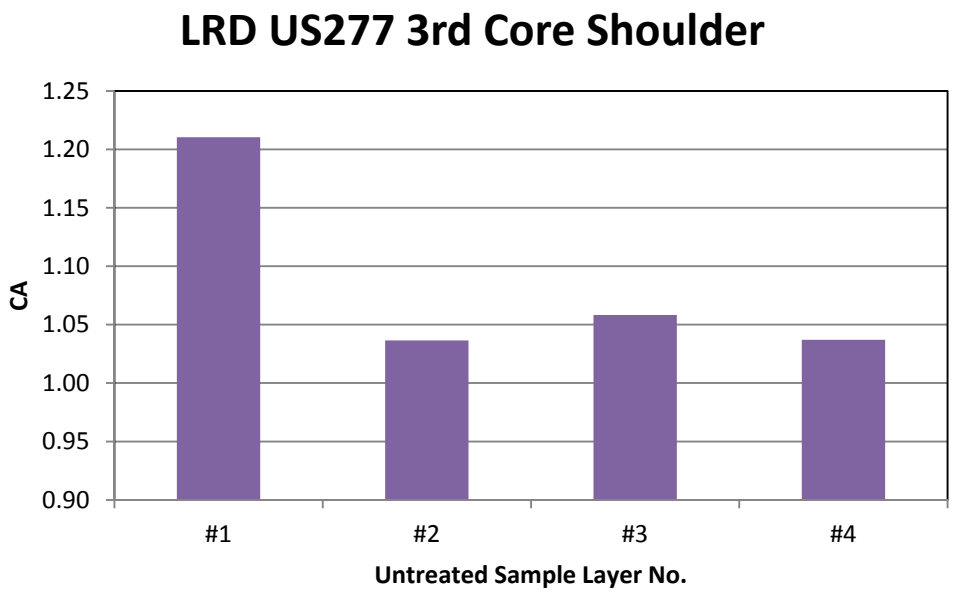


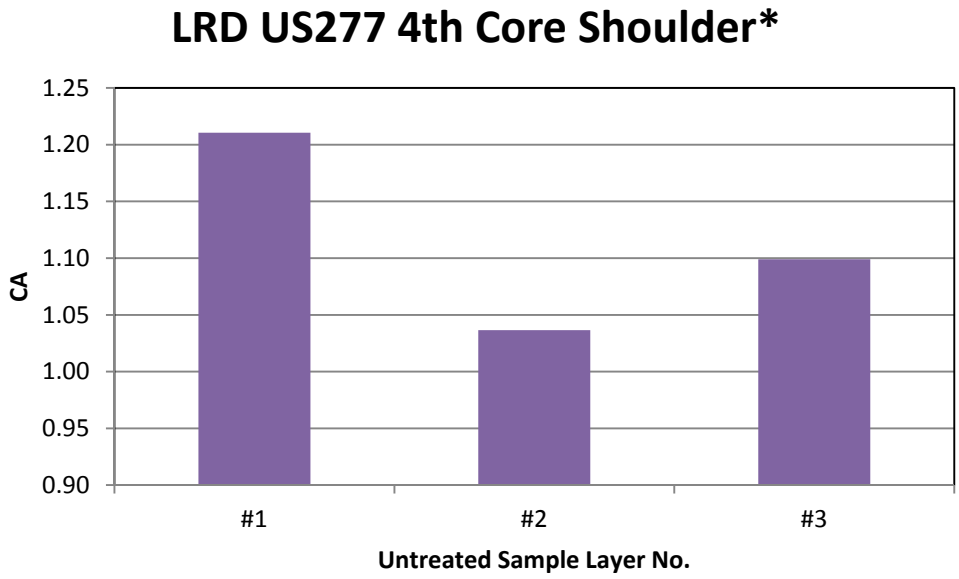


* Another Seal Coat layer was applied on both treated and untreated field sections, and it was too thin to cut off.

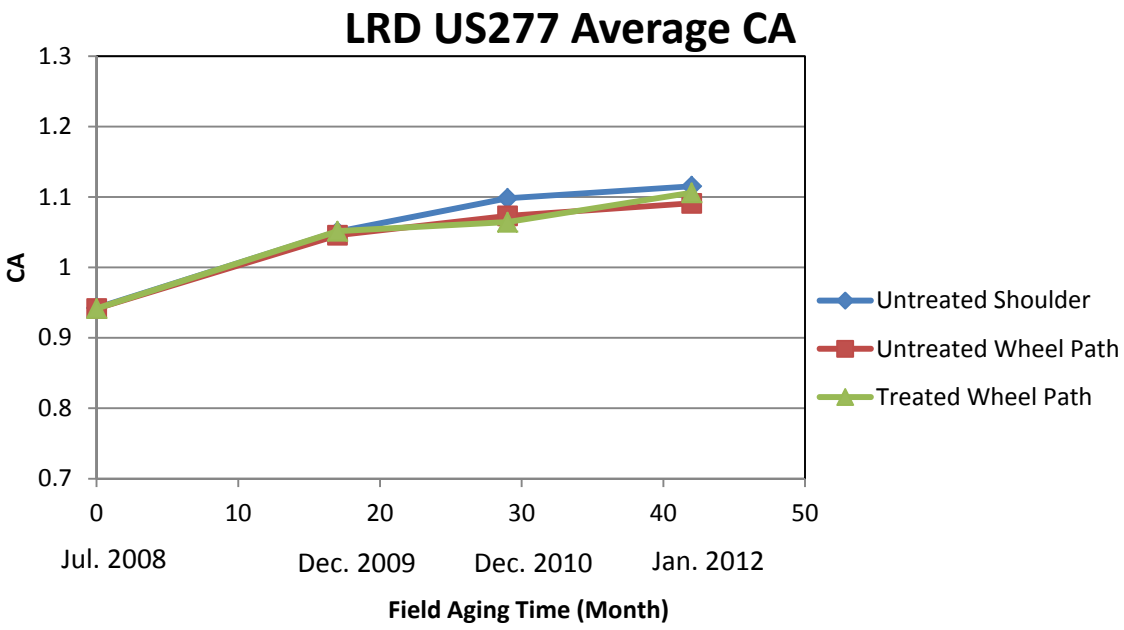

LRD US277 1st Core Shoulder
1.20
1.00
0.80
0.60
0.40
0.20
0.00
CA
#1
#2
#3
#4
#5
Untreated Sample Layer No.


LRD US277 2nd Core Shoulder
1.40
1.20
1.00
0.80
0.60
0.40
0.20
0.00
CA
#1
#2
#3
#4
#5
Untreated Sample Layer No.





* Another Seal Coat layer was applied, and it was too thin to cut off.


LRD US277 Average CA
1.3
1.2
1.1
1
0.9
0.8
0.7
CA
0
10
20
30
40
50
Jul. 2008
Dec. 2009
Dec. 2010
Jan. 2012
Field Aging Time (Month)
Untreated Shoulder
Untreated Wheel Path
Treated Wheel Path

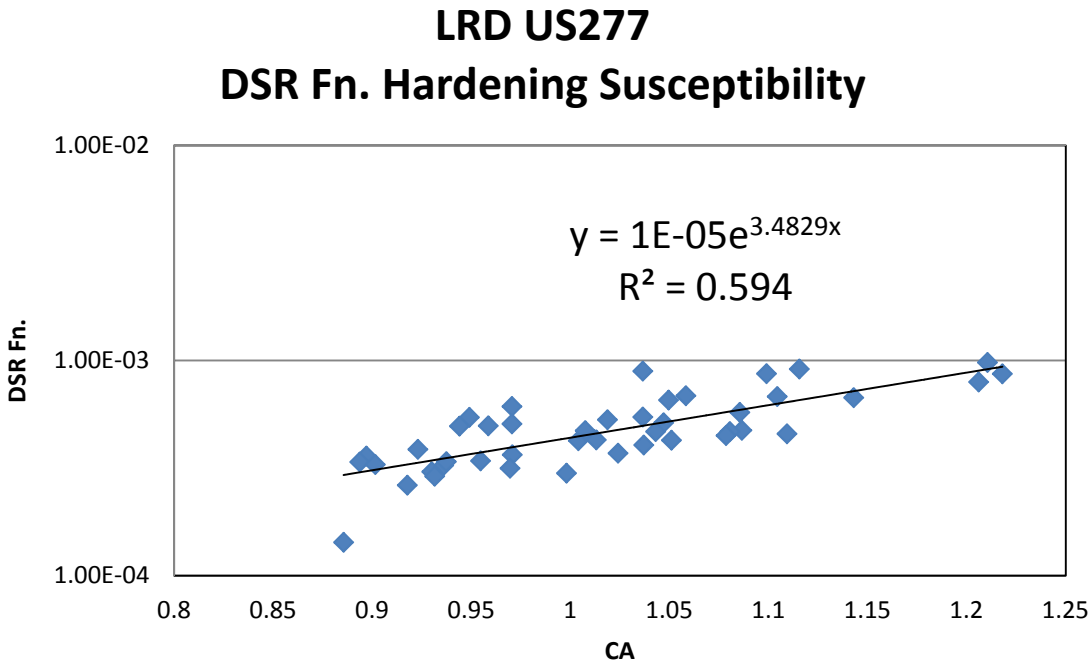
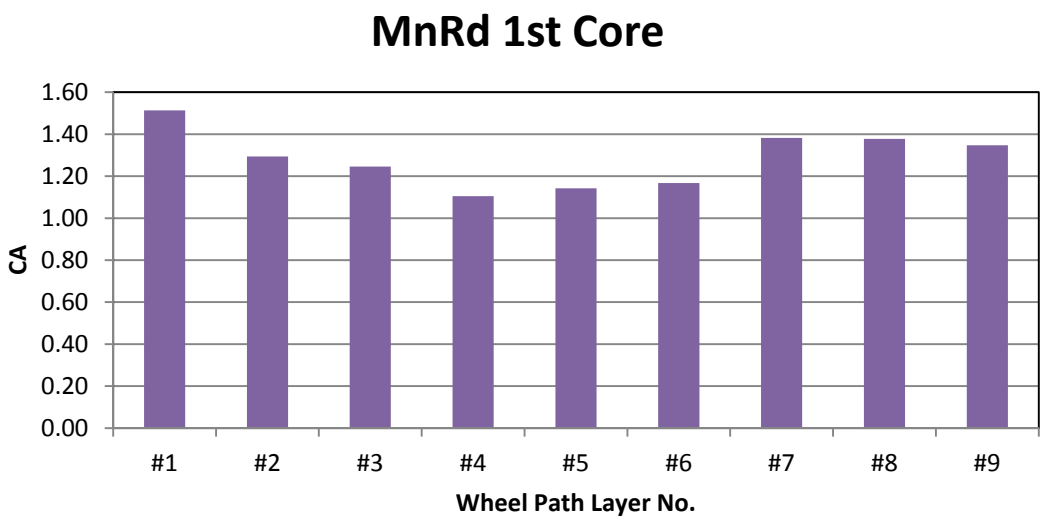

LRD US277
DSR Fn. Hardening Susceptibility
1.00E-02
1.00E-03
1.00E-04
DSR Fn.
y = 1E-05e3.4829x
R² = 0.594
0.8
0.85
0.9
0.95
1
1.05
1.1
1.15
1.2
1.25
CA

Table E23. MnRoad Field Core (Wheel Path)

Binder: Unknown Activation Energy: Unknown Cons.: Unknown		η_o* (Poise) @60°C 0.1 rad/s	G'/(η'/G') (MPa/s) @15°C 0.005 rad/s	Carbonyl Area
1st Core (11/2008)	1st layer	40000	0.00030	1.513
	2nd	20000	0.00012	1.294
	3rd	11000	0.000054	1.246
	4th	11000	0.000052	1.105
	5th	9000	0.000038	1.142
	6th	13000	0.000072	1.168
	7th	17000	0.00011	1.382
	8th	22000	0.00016	1.378
	9th	27000	0.00021	1.347
	1st to 9th	23000	0.00015	1.353


MnRd 1st Core
1.60
1.40
1.20
1.00
0.80
0.60
0.40
0.20
0.00
CA
#1
#2
#3
#4
#5
#6
#7
#8
#9
Wheel Path Layer No.

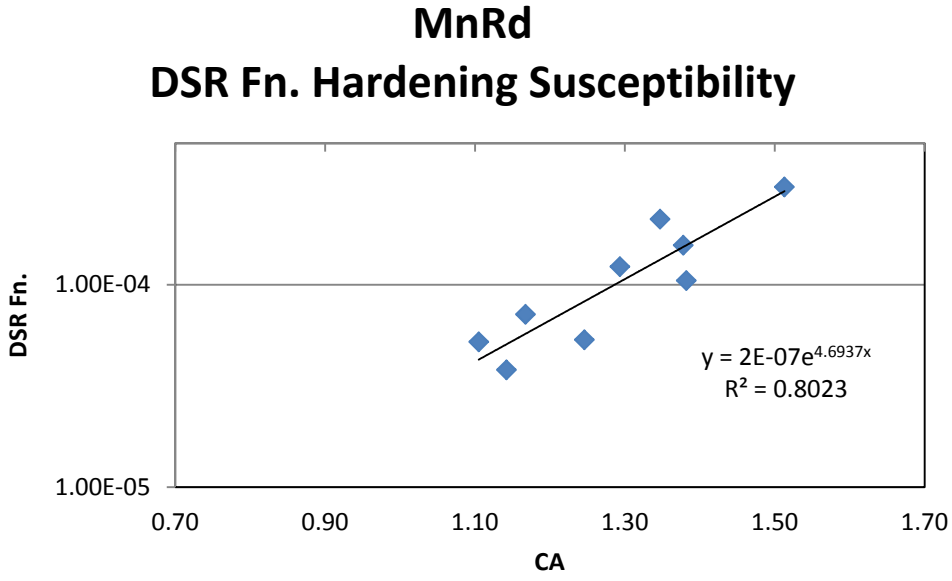
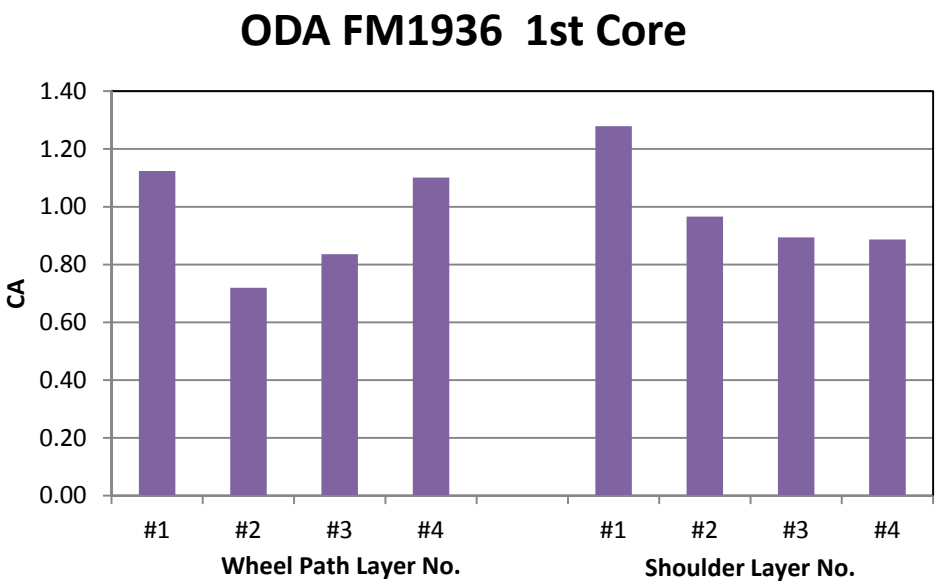

MnRd
DSR Fn. Hardening Susceptibility
DSR Fn.
1.00E-04
1.00E-05
y = 2E-07e4.6937x
R² = 0.8023
0.70
0.90
1.10
1.30
1.50
1.70
CA

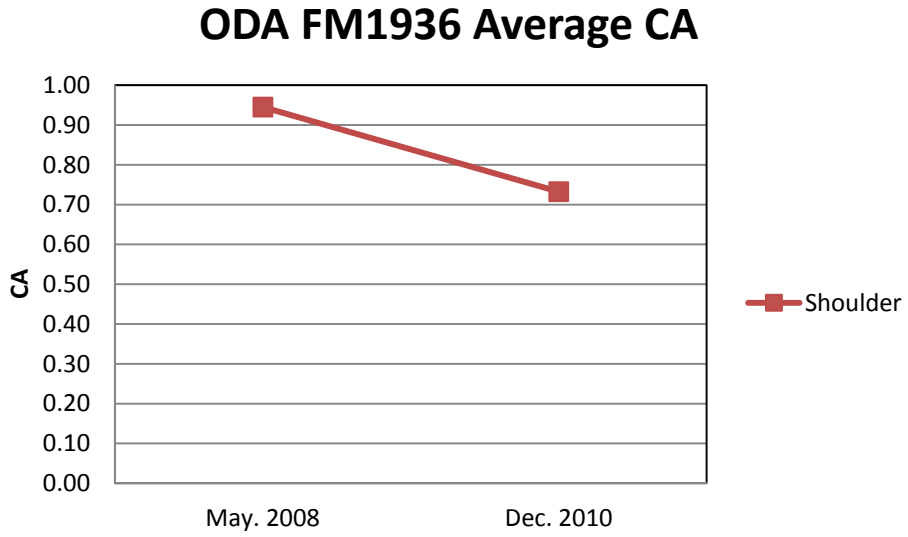
Table E24. FM1936 ODA Field Core (Wheel Path)

Binder: Alon PG70-22 Activation Energy: 47.2 KJ/mol Cons.: 2002		η_o* (Poise) @60°C 0.1 rad/s	G'/(η'/G') (MPa/s) @15°C 0.005 rad/s	Carbonyl Area
1st Core (05/2008)	1st layer	140000	0.00163	1.279
	2nd	30000	0.000157	0.966
	3rd	7900	0.0000141	0.894
	4th	21000	0.0000576	0.887
	1st to 4th	38000	0.00019	1.045

Table E25. FM1936 ODA Field Core (Shoulder)

Binder: Alon PG70-22 Activation Energy: 47.2 KJ/mol Cons.: 2002		η_o* (Poise) @60°C 0.1 rad/s	G'/(η'/G') (MPa/s) @15°C 0.005 rad/s	Carbonyl Area
1st Core (05/2008)	1st layer	55000	0.00038	1.124
	2nd	13000	0.000033	0.920
	3rd	15000	0.000047	0.836
	4th	19000	0.000050	1.101
	1st to 4th	23000	0.000085	0.937
2nd Core (12/2010)	1st to 4th	23000	0.00066	0.733


ODA FM1936 1st Core
1.40
1.20
1.00
0.80
0.60
0.40
0.20
0.00
CA
#1
#2
#3
#4
Wheel Path Layer No.
#1
#2
#3
#4
Shoulder Layer No.


ODA FM1936 Average CA
1.00
0.90
0.80
0.70
0.60
0.50
0.40
0.30
0.20
0.10
0.00
CA
May. 2008
Dec. 2010
Shoulder

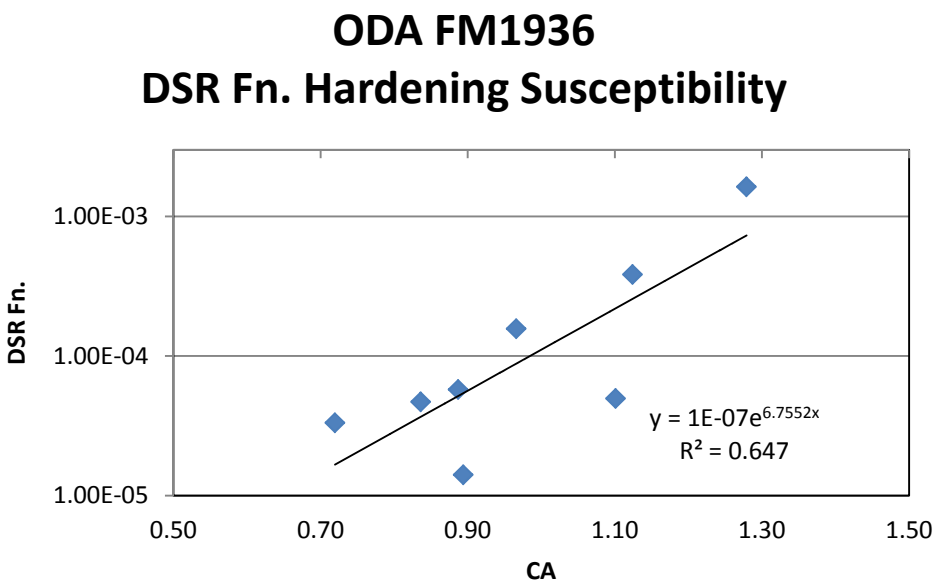

ODA FM1936
DSR Fn. Hardening Susceptibility
DSR Fn.
1.00E-03
1.00E-04
1.00E-05
0.50
0.70
0.90
1.10
1.30
1.50
CA
y = 1E-07e6.7552x
R² = 0.647

Table E26. SH24 PAR Field Core (Wheel Path)

Binder: Lion PG64-22 Activation Energy: 56.1 KJ/mol Cons.: 2009		η_o* (Poise) @60°C 0.1 rad/s	G'/(η'/G') (MPa/s) @15°C 0.005 rad/s	Carbonyl Area
1st Core (07/2009)	1st layer	32000	0.00025	1.171
	2nd	37000	0.00033	1.330
	3rd	44000	0.00043	1.142
	1st to 3rd	37000	0.00033	1.214
2nd Core (12/2010)	1st layer	50000	0.00051	1.471
	2nd	50700	0.00056	1.292
	3rd	41400	0.00036	1.107
	1st to 3rd	47000	0.00047	1.290

Table E27. SH24 PAR Field Core (Shoulder)

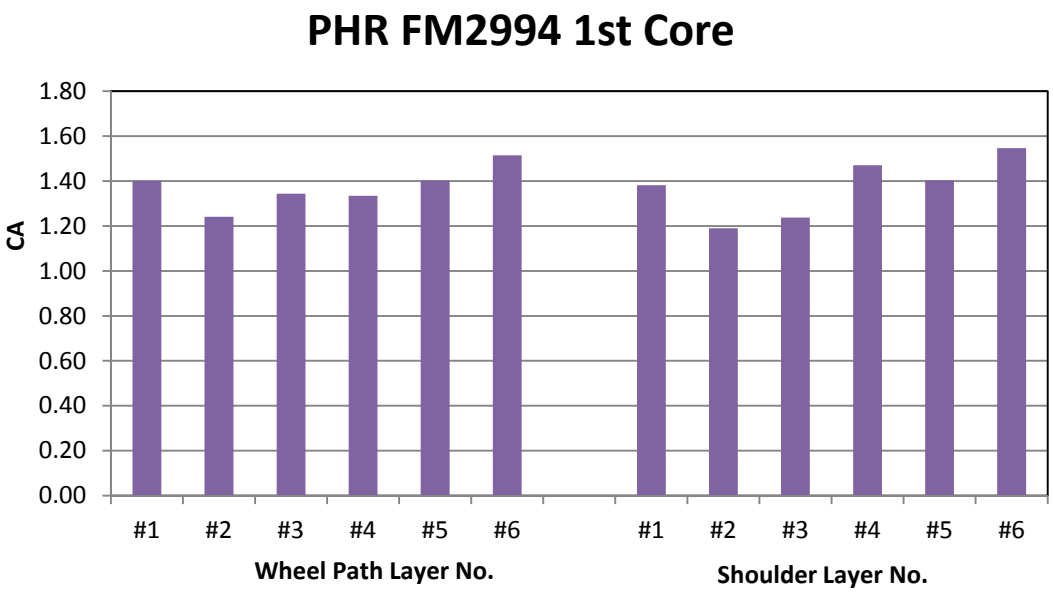
Binder: Lion PG64-22 Activation Energy: 56.1 KJ/mol Cons.: 2009		η_o* (Poise) @60°C 0.1 rad/s	G'/(η'/G') (MPa/s) @15°C 0.005 rad/s	Carbonyl Area
1st Core (06/2009)	1st layer	25000	0.00016	1.149
	2nd	33000	0.00025	1.144
	3rd	25000	0.00016	1.173
	4th	48000	0.00047	1.272
	1st to 4th	30000	0.00022	1.172
2nd Core (12/2010)	1st layer	44000	0.00043	1.296
	2nd	38000	0.00033	1.179
	3rd	57000	0.00060	1.315
	1st to 3rd	45000	0.00044	1.263

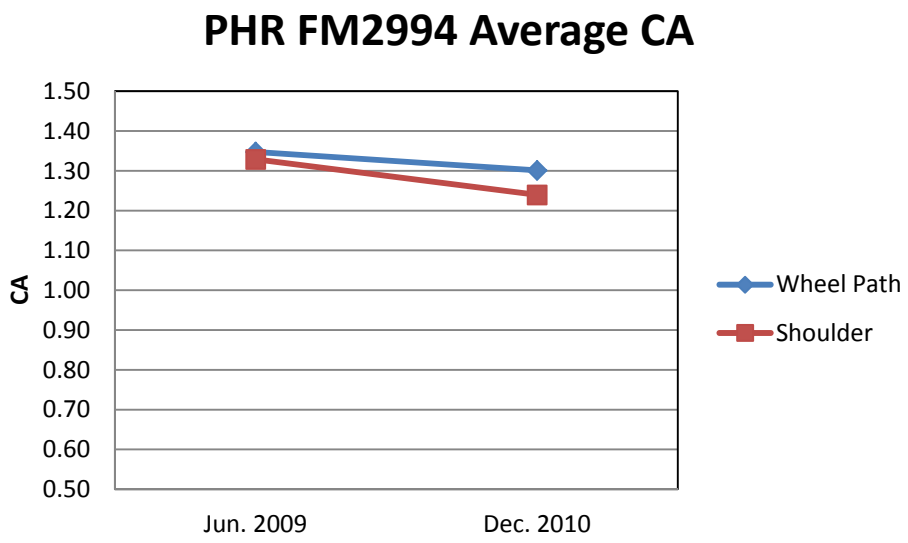
Table E28. FM2994 PHR Field Core (Wheel Path)

Binder: Eagle PG70-22 Activation Energy: 55.0 KJ/mol Cons.: 2002		η_o* (Poise) @60°C 0.1 rad/s	G'/(η'/G') (MPa/s) @15°C 0.005 rad/s	Carbonyl Area
1st Core (05/2008)	1st layer	700000	0.0023	1.402
	2nd	300000	0.0011	1.242
	3rd	400000	0.0018	1.344
	4th	300000	0.0017	1.335
	5th	400000	0.0018	1.403
	6th	300000	0.0017	1.515
	1st to 6th	420000	0.0017	1.347
2nd Core (11/2010)	1st to 6th	330000	0.0019	1.301

Table E29. FM2994 PHR Field Core (Shoulder)

Binder: Eagle PG70-22 Activation Energy: 55.0 KJ/mol Cons.: 2002		η_o* (Poise) @60°C 0.1 rad/s	G'/(η'/G') (MPa/s) @15°C 0.005 rad/s	Carbonyl Area
1st Core (05/2008)	1st layer	1100000	0.0048	1.382
	2nd	400000	0.0016	1.190
	3rd	400000	0.0017	1.237
	4th	400000	0.0021	1.471
	5th	300000	0.0017	1.403
	6th	300000	0.0028	1.547
	1st to 6th	530000	0.0025	1.329
2nd Core (11/2010)	1st to 6th	540000	0.0029	1.240


PHR FM2994 1st Core
CA
1.80
1.60
1.40
1.20
1.00
0.80
0.60
0.40
0.20
0.00
#1
#2
#3
#4
#5
#6
Wheel Path Layer No.
#1
#2
#3
#4
#5
#6
Shoulder Layer No.


PHR FM2994 Average CA
CA
1.50
1.40
1.30
1.20
1.10
1.00
0.90
0.80
0.70
0.60
0.50
Jun. 2009
Dec. 2010
Wheel Path
Shoulder

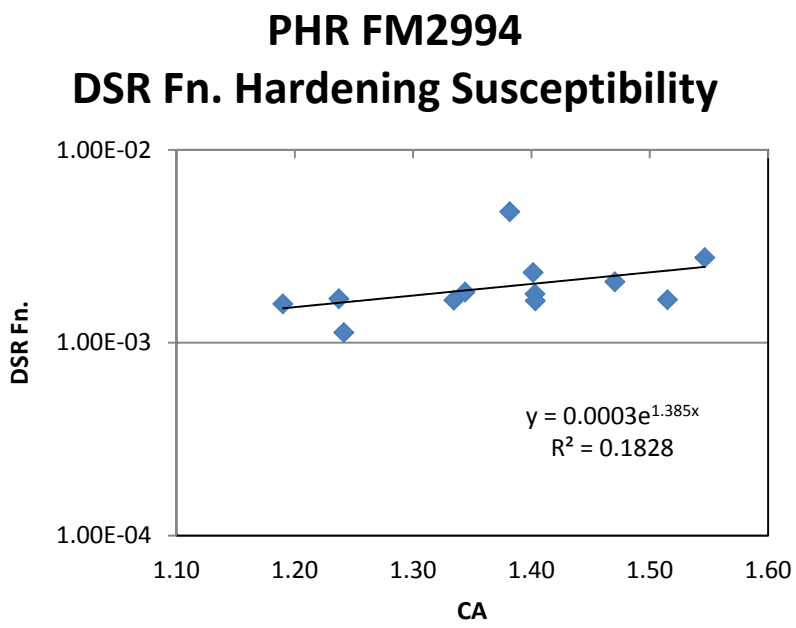
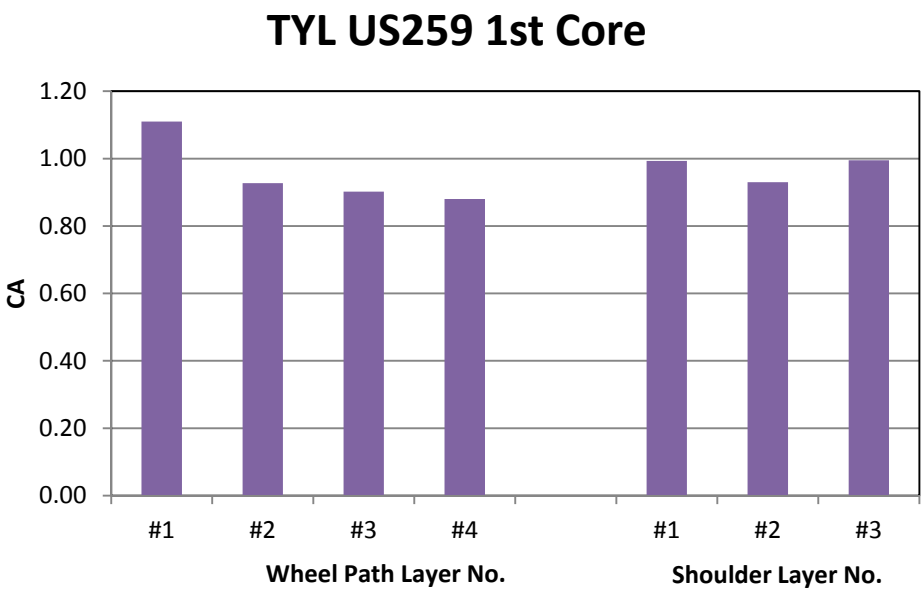

PHR FM2994
DSR Fn. Hardening Susceptibility
1.00E-02
1.00E-03
1.00E-04
DSR Fn.
y = 0.0003e1.385x
R² = 0.1828
1.10
1.20
1.30
1.40
1.50
1.60
CA

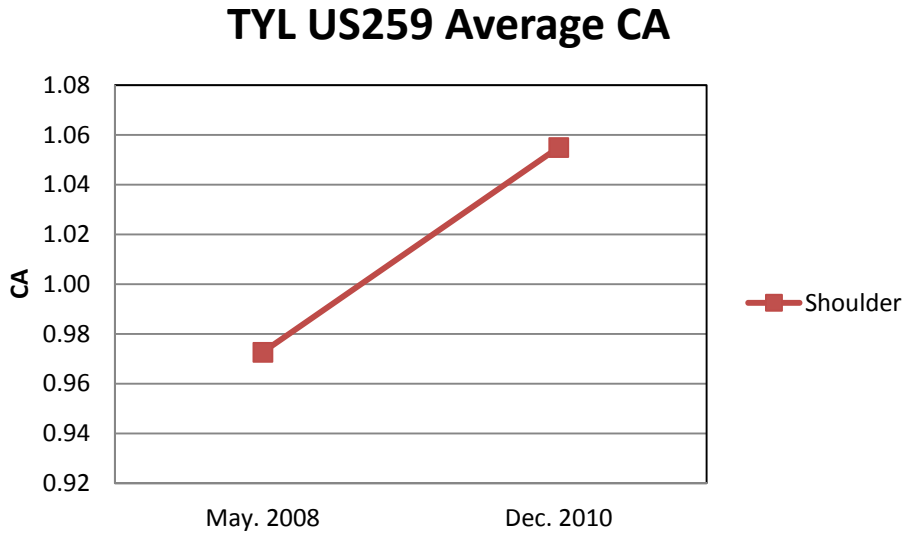
Table E30. US259 TYL Field Core (Wheel Path)

Binder: Lion PG70-22 Activation Energy: 70.2 KJ/mol Cons.: 2007		η* (Poise) @60°C 0.1 rad/s	G'/(η'/G') (MPa/s) @15°C 0.005 rad/s	Carbonyl Area
1st Core (07/2008)	1st layer	50000	0.00041	1.110
	2nd	32000	0.00020	0.927
	3rd	27000	0.00015	0.902
	4th	26000	0.00014	0.880
	1st to 4th	35000	0.00023	0.976

Table E31. US259 TYL Field Core (Shoulder)

Binder: Lion PG70-22 Activation Energy: 70.2 KJ/mol Cons.: 2007		η_o* (Poise) @60°C 0.1 rad/s	G'/(η'/G') (MPa/s) @15°C 0.005 rad/s	Carbonyl Area
1st Core (07/2008)	1st layer	40000	0.00026	0.993
	2nd	25000	0.00013	0.930
	3rd	30000	0.00019	0.995
	1st to 3rd	31000	0.00019	0.973
2nd Core (10/2010)	1st to 3rd	20000	0.000093	1.055


TYL US259 1st Core
1.20
1.00
0.80
0.60
0.40
0.20
0.00
CA
#1
#2
#3
#4
#1
#2
#3
Wheel Path Layer No.
Shoulder Layer No.


TYL US259 Average CA
1.08
1.06
1.04
1.02
1.00
0.98
0.96
0.94
0.92
CA
May. 2008
Dec. 2010
Shoulder

TYL US259
DSR Fn. Hardening Susceptibility

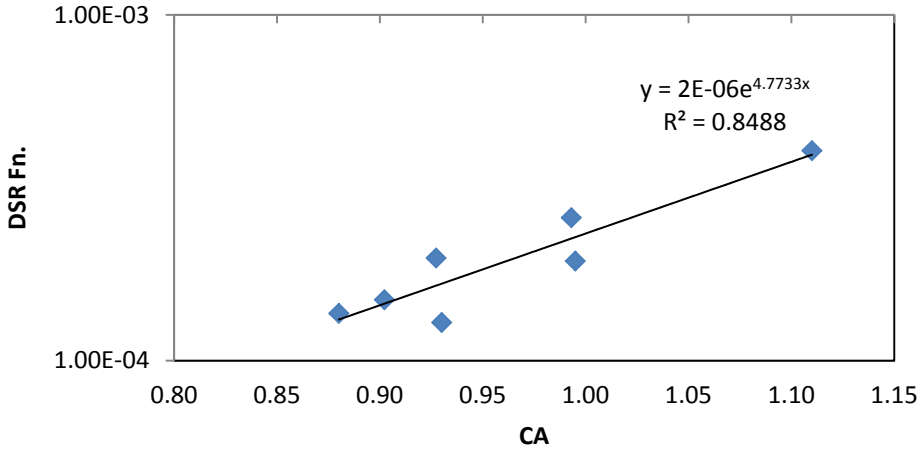
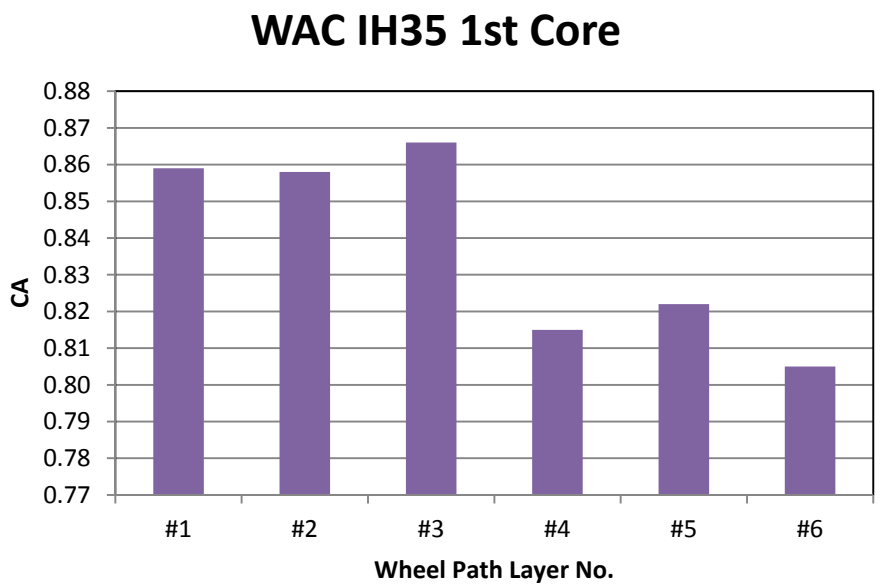
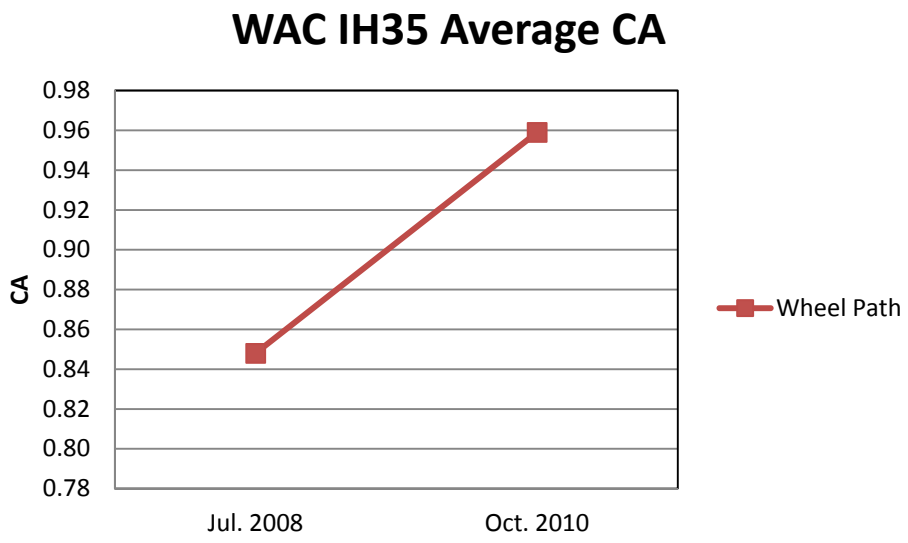


Table E32. IH35 WAC Field Core (Wheel Path)

Binder: Fina PG70-22 Activation Energy: 98.7 KJ/mol Cons.: 2003		η_o* (Poise) @60°C 0.1 rad/s	G'/(η'/G') (MPa/s) @15°C 0.005 rad/s	Carbonyl Area
1st Core (08/2008)	1st layer	26000	0.000075	0.859
	2nd	26000	0.000074	0.858
	3rd	26000	0.000077	0.866
	4th	26000	0.000078	0.815
	5th	31000	0.000090	0.822
	6th	25000	0.000061	0.805
	1st to 6th	26000	0.000075	0.848
2nd Core (02/2011)	1st to 6th	Too high to measure	0.00039	0.959


WAC IH35 1st Core
0.88
0.87
0.86
0.85
0.84
0.83
0.82
0.81
0.80
0.79
0.78
0.77
CA
#1
#2
#3
#4
#5
#6
Wheel Path Layer No.


WAC IH35 Average CA
0.98
0.96
0.94
0.92
0.90
0.88
0.86
0.84
0.82
0.80
0.78
CA
Jul. 2008
Oct. 2010
Wheel Path

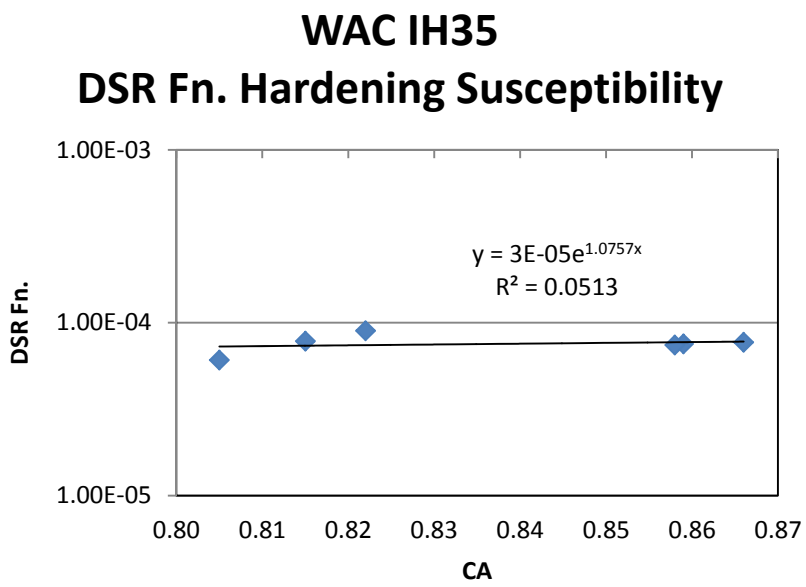
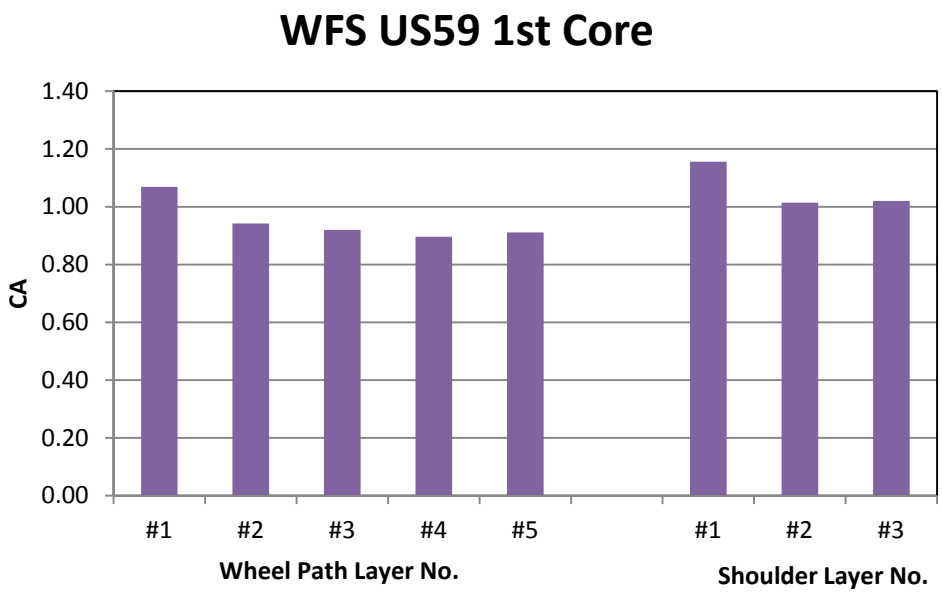

WAC IH35
DSR Fn. Hardening Susceptibility
1.00E-03
1.00E-04
1.00E-05
DSR Fn.
y = 3E-05e1.0757x
R² = 0.0513
0.80
0.81
0.82
0.83
0.84
0.85
0.86
0.87
CA

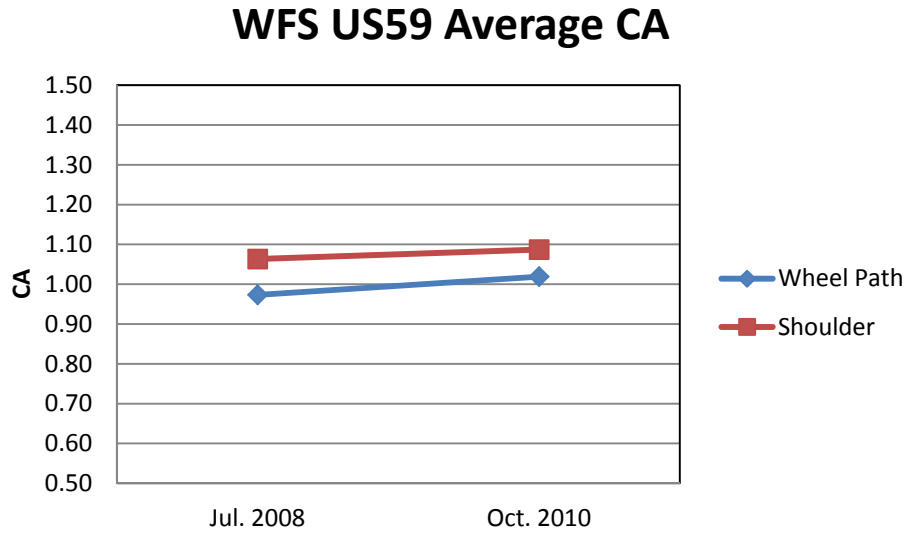
Table E33. US59 WFS Field Core (Wheel Path)

Binder: SEM PG70-22 Activation Energy: 79.9 KJ/mol Cons.: 2007		η_o* (Poise) @60°C 0.1 rad/s	G'/(η'/G') (MPa/s) @15°C 0.005 rad/s	Carbonyl Area
1st Core (07/2008)	1st layer	58000	0.00050	1.069
	2nd	53000	0.00025	0.942
	3rd	52000	0.00026	0.920
	4th	50000	0.00022	0.896
	5th	50000	0.00020	0.911
	1st to 5th	54000	0.00031	0.973
2nd Core (10/2010)	1st to 5th	66000	0.00027	1.019

Table E34. US59 WFS Field Core (Shoulder)

Binder: SEM PG70-22 Activation Energy: 79.9 KJ/mol Cons.: 2007		η_o* (Poise) @60°C 0.1 rad/s	G'/(η'/G') (MPa/s) @15°C 0.005 rad/s	Carbonyl Area
1st Core (07/2008)	1st layer	80000	0.00092	1.156
	2nd	72000	0.00040	1.014
	3rd	50000	0.00044	1.020
	1st to 3rd	66000	0.00054	1.063
2nd Core (10/2010)	1st to 3rd	147000	0.00093	1.087


WFS US59 1st Core
1.40
1.20
1.00
0.80
0.60
0.40
0.20
0.00
CA
#1
#2
#3
#4
#5
Wheel Path Layer No.
#1
#2
#3
Shoulder Layer No.


WFS US59 Average CA
1.50
1.40
1.30
1.20
1.10
1.00
0.90
0.80
0.70
0.60
0.50
CA
Jul. 2008
Oct. 2010
Wheel Path
Shoulder

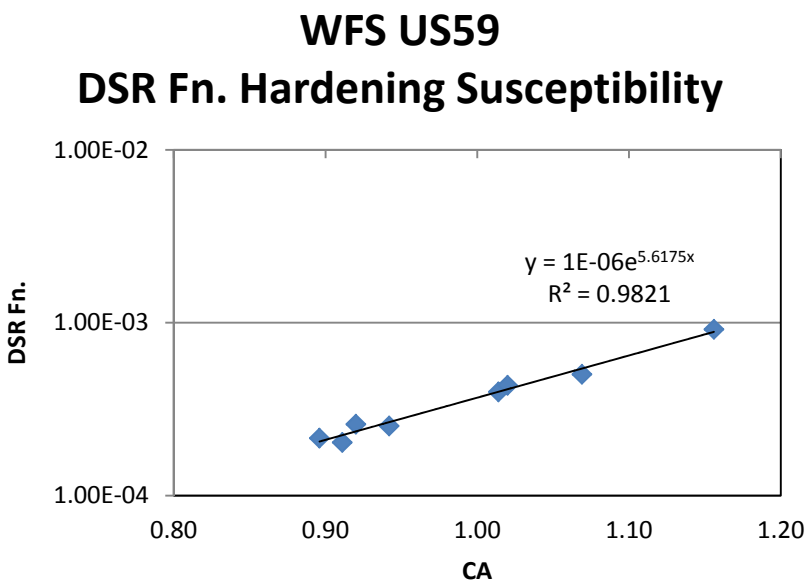
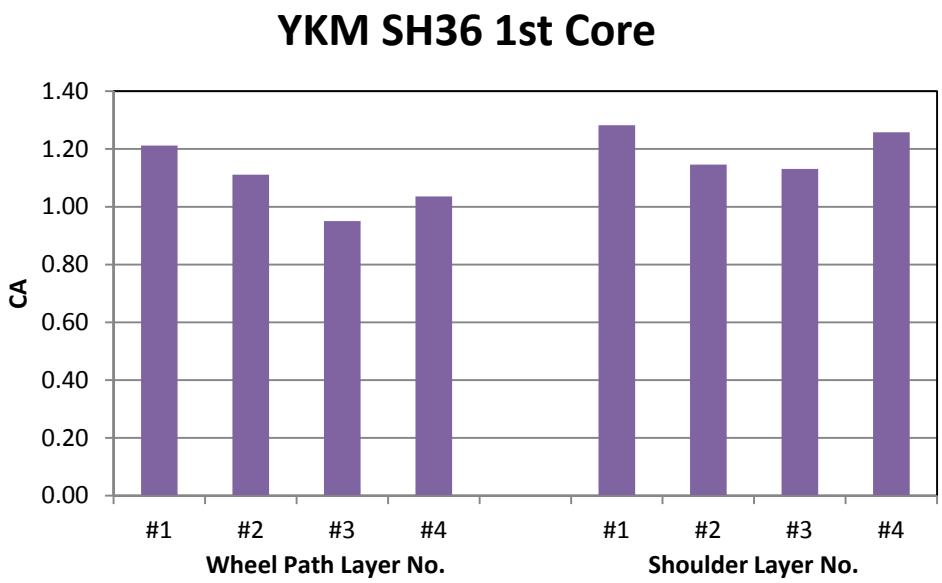

WFS US59
DSR Fn. Hardening Susceptibility
1.00E-02
1.00E-03
1.00E-04
DSR Fn.
y = 1E-06e5.6175x
R² = 0.9821
0.80
0.90
1.00
1.10
1.20
CA

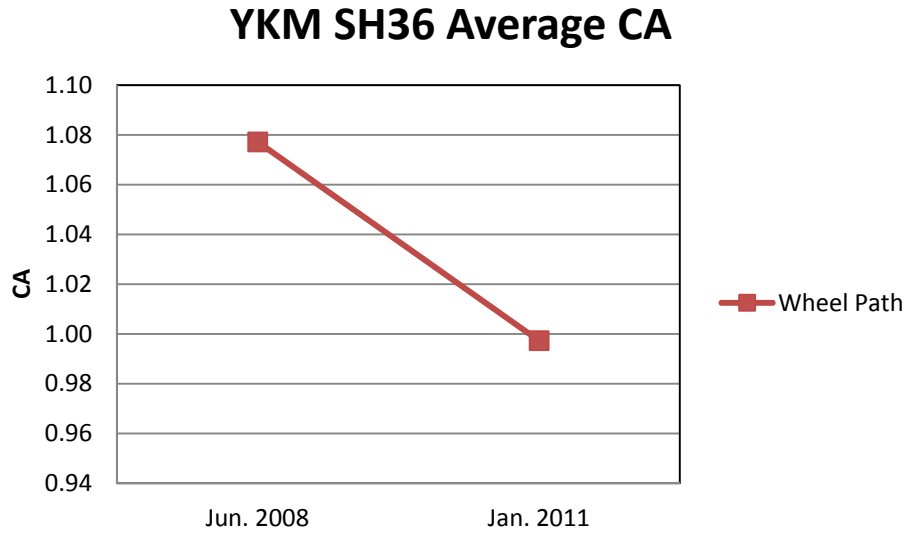
Table E35. SH36 YKM Field Core (Wheel Path)

Binder: Martin PG64-22 Activation Energy: 72.5 KJ/mol Cons.: 2006		η_o* (Poise) @60°C 0.1 rad/s	G'/(η'/G') (MPa/s) @15°C 0.005 rad/s	Carbonyl Area
1st Core (06/2008)	1st layer	70000	0.00054	1.212
	2nd	45000	0.00038	1.111
	3rd	30000	0.00030	0.951
	4th	27000	0.00019	1.036
	1st to 4th	45000	0.00035	1.077
2nd Core (01/2011)	1st to 4th	48000	0.00034	0.997

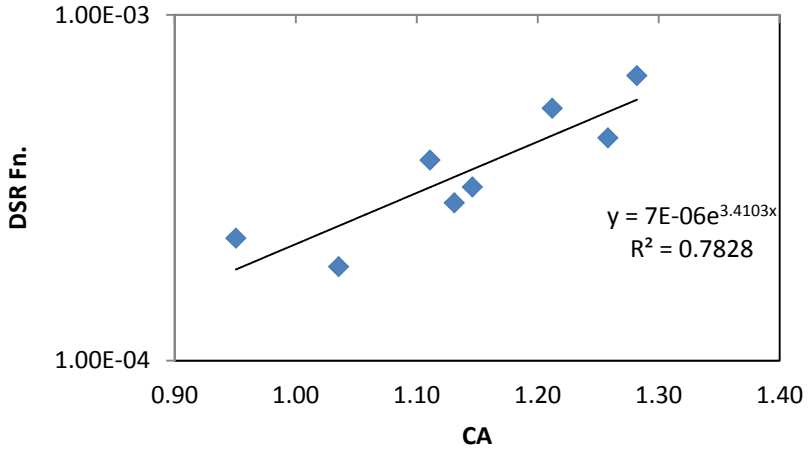
Table E36. SH36 YKM Field Core (Shoulder)

Binder: Martin PG64-22 Activation Energy: 72.5 KJ/mol Cons.: 2006		η_o* (Poise) @60°C 0.1 rad/s	G'/(η'/G') (MPa/s) @15°C 0.005 rad/s	Carbonyl Area
1st Core (06/2008)	1st layer	70000	0.00067	1.282
	2nd	40000	0.00032	1.146
	3rd	35000	0.00029	1.131
	4th	52000	0.00044	1.258
	1st to 4th	49000	0.00042	1.208


YKM SH36 1st Core
1.40
1.20
1.00
0.80
0.60
0.40
0.20
0.00
CA
#1
#2
#3
#4
Wheel Path Layer No.
#1
#2
#3
#4
Shoulder Layer No.


YKM SH36 Average CA
1.10
1.08
1.06
1.04
1.02
1.00
0.98
0.96
0.94
CA
Jun. 2008
Jan. 2011
Wheel Path

YKM SH36
DSR Fn. Hardening Susceptibility



APPENDIX F
TABLES OF BULK S.G., AIR VOID, AND BINDER CONTENT DATA

In the graphs below the following terms are used in their abbreviated forms: Total Air Void (TAV), Accessible Air Void by Corelok Method (AAV CL), and Accessible Air Void by Saturated Surface Dry Method (AAV SSD).

Table F1. US54 AMR Field Core (Wheel Path)

Cons.: 1998		Bulk S.G.	Maximum S.G.	Total Air Voids	Accessible A.V.		Binder Content
					Corelok	SSD	
1st Core Seal Coat Treated (07/2008)	1st	2.03	2.32	12.36	12.27	4.20	- (Seal Coat attached)
	2nd	2.21	2.46	10.26	10.40	8.23	2.0
	3rd	2.26	2.44	7.62	5.62	4.36	3.6
	4th	2.27	2.45	7.54	7.16	6.41	3.6

Table F2. US54 AMR Field Core (Shoulder)

Cons.: 1998		Bulk S.G.	Maximum S.G.	Total Air Voids	Accessible A.V.		Binder Content
					Corelok	SSD	
1st Core Seal Coat Treated (07/2008)	1st	1.98	2.29	13.81	13.20	5.12	- (Seal Coat attached)
	2nd	2.20	2.49	11.67	10.60	8.40	3.6
	3rd	2.20	2.49	11.67	10.72	8.79	3.6
	4th	2.21	2.50	11.82	10.66	8.17	4.3

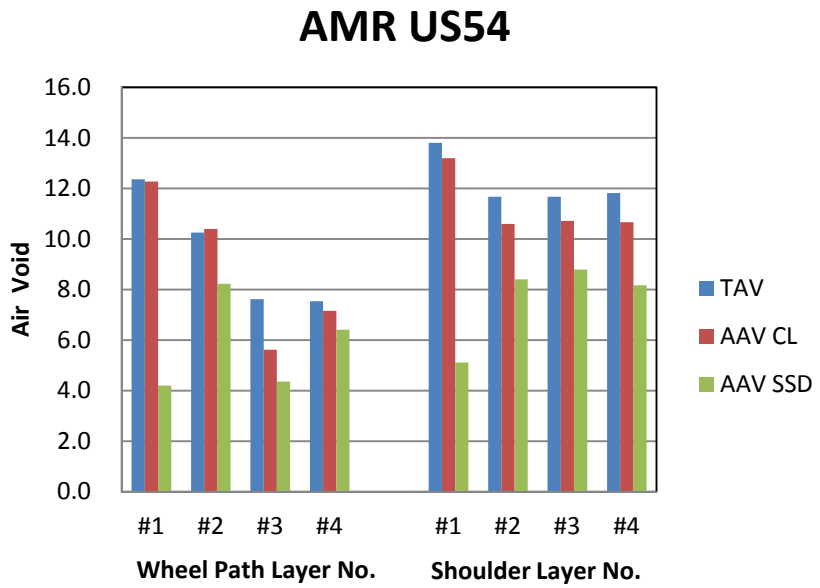


Table F3. IH20 ATL Field Core (Wheel Path)

Cons.: 2003		Bulk S.G.	Maximum S.G.	Total Air Voids	Accessible A.V.		Binder Content
					Corelok	SSD	
1st Core (07/2008)	1st	2.02	2.39	15.62	14.87	12.00	4.8
	2nd	2.16	2.42	10.86	10.41	7.20	4.0
	3rd	2.16	2.43	10.90	9.81	8.09	4.0
	4th	2.06	2.41	14.30	13.88	9.13	3.2

Table F4. IH20 ATL Field Core (Shoulder)

Cons.: 2003		Bulk S.G.	Maximum S.G.	Total Air Voids	Accessible A.V.		Binder Content
					Corelok	SSD	
1st Core (07/2008)	1st	2.03	2.26	10.31	15.48	8.58	Average 4.1
	2nd	2.12	2.41	11.93	11.22	7.89	
	3rd	2.15	2.42	10.98	10.02	7.28	
	4th	2.05	2.37	13.48	13.08	7.56	

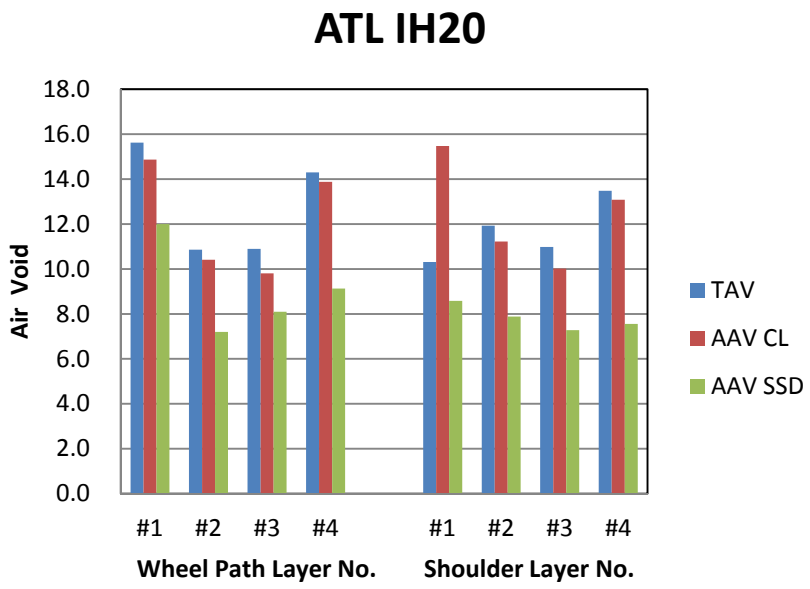


Table F5. US259 ATL Field Core (Wheel Path)

Cons.: 2005		Bulk S.G.	Maximum S.G.	Total Air Voids	Accessible A.V.		Binder Content
					Corelok	SSD	
1st Core (12/2008)	1st	2.20	2.42	9.16	7.94	5.41	4.8
	2nd	2.27	2.41	5.75	4.88	4.45	3.2
	3rd	2.28	2.42	5.85	4.93	4.24	4.4
	4th	2.28	2.41	5.48	4.26	4.01	4.8
	5th	2.22	2.42	8.16	7.65	6.33	4.0

Table F6. US259 ATL Field Core (Shoulder)

Cons.: 2005		Bulk S.G.	Maximum S.G.	Total Air Voids	Accessible A.V.		Binder Content
					Corelok	SSD	
1st Core (12/2008)	1st	2.20	2.42	9.39	9.03	6.79	4.8
	2nd	2.23	2.41	7.30	7.03	5.95	4.8
	3rd	2.26	2.42	6.83	6.55	5.45	4.8
	4th	2.23	2.41	7.15	7.27	6.00	4.4

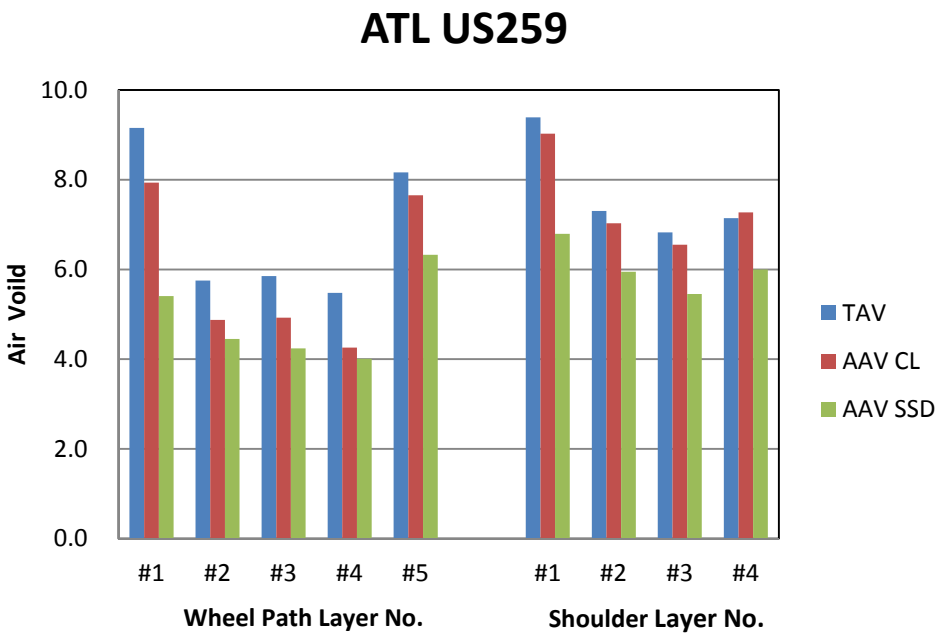


Table F7. SH6 BRY Field Core (Wheel Path)

Cons.: 2000		Bulk S.G.	Maximum S.G.	Total Air Voids	Accessible A.V.		Binder Content
					Corelok	SSD	
1st Core (08/2008)	1st	2.26	2.46	7.91	6.52	4.12	Average 3.9
	2nd	2.32	2.47	5.91	5.35	3.83	
	3rd	2.33	2.47	5.87	4.52	3.63	

Table F8. SH6 BRY Field Core (Shoulder)

Cons.: 2000		Bulk S.G.	Maximum S.G.	Total Air Voids	Accessible A.V.		Binder Content
					Corelok	SSD	
1st Core (08/2008)	1st	2.14	2.46	12.88	13.20	6.62	Average 3.6
	2nd	2.20	2.47	10.67	9.74	5.86	
	3rd	2.23	2.45	8.95	9.48	6.82	

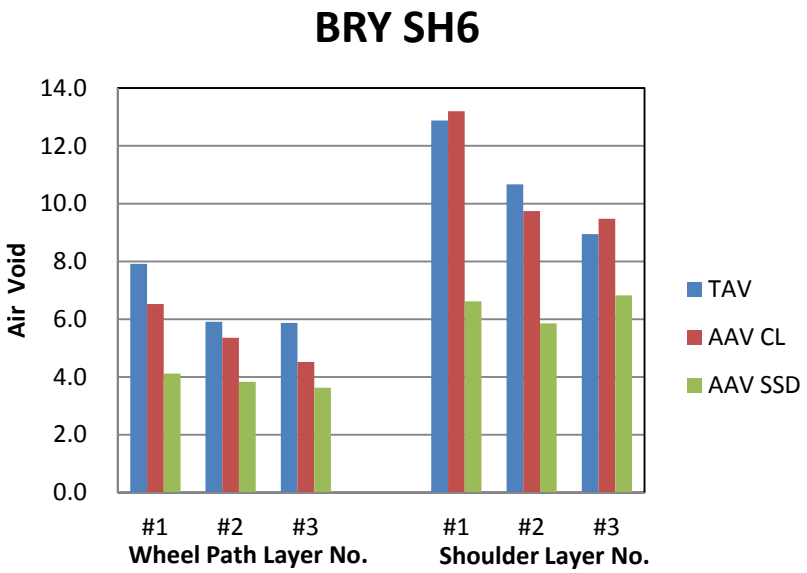


Table F9. US290 BRY Field Core (Wheel Path)

Cons.: 2002		Bulk S.G.	Maximum S.G.	Total Air Voids	Accessible A.V.		Binder Content
					Corelok	SSD	
1st Core (08/2008)	1st	1.84	2.13	13.71	11.54	7.13	-
	2nd	2.06	2.46	16.51	15.94	8.11	
	3rd	2.05	2.46	16.41	16.21	8.20	
	4th	2.03	2.35	13.39	16.56	9.16	
	5th	1.90	2.44	22.02	21.24	10.34	

Table F10. US290 BRY Field Core (Shoulder)

Cons.: 2002		Bulk S.G.	Maximum S.G.	Total Air Voids	Accessible A.V.		Binder Content
					Corelok	SSD	
1st Core (08/2008)	1st	2.14	2.47	13.24	12.36	10.16	Average 3.2
	2nd	2.26	2.46	8.41	6.98	7.14	
	3rd	2.26	2.48	8.92	7.10	7.26	
	4th	2.21	2.48	10.66	9.62	8.86	

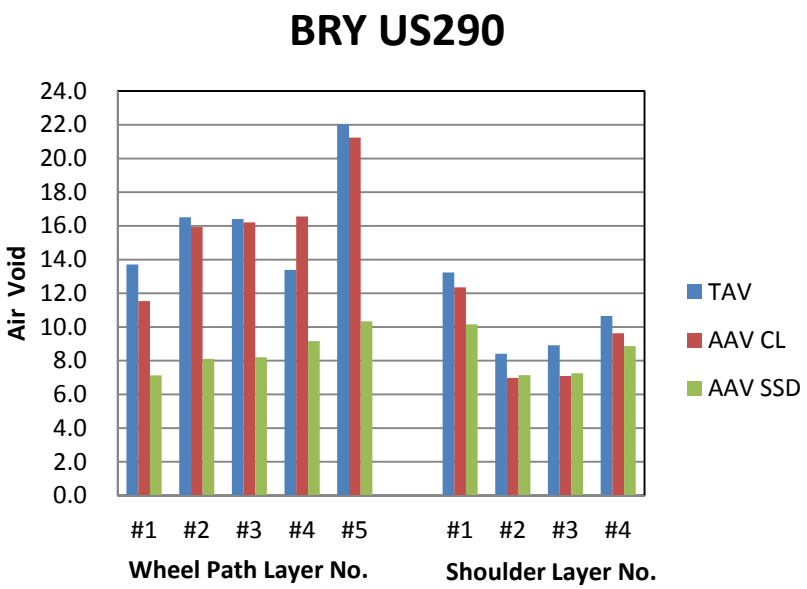


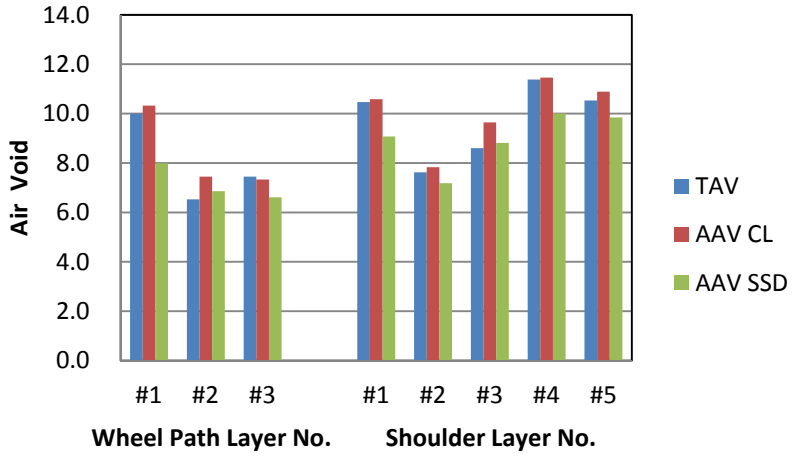
Table F11. US83 CHS Field Core (Wheel Path)

Cons.: 2008		Bulk S.G.	Maximum S.G.	Total Air Voids	Accessible A.V.		Binder Content
					Corelok	SSD	
1st Core (08/2008)	1st	2.18	2.43	9.99	10.32	7.99	Average 4.0
	2nd	2.25	2.40	6.53	7.45	6.86	
	3rd	2.25	2.43	7.45	7.33	6.62	
2nd Core (10/2009)	1st	2.20	2.43	9.55	8.77	6.03	3.6
	2nd	2.25	2.41	6.91	6.60	5.49	3.2
	3rd	2.26	2.40	5.90	5.08	4.02	4.7
3rd Core (08/2010)	1st	2.23	2.46	9.33	7.94	6.19	3.8
	2nd	2.27	2.46	7.39	5.97	4.76	3.5
	3rd	2.29	2.42	5.44	5.07	4.50	3.6
2nd Core Seal Coat Treated (10/2009)	Seal Coat layer & 1st layer	2.05	2.32	11.49	7.28	3.13	5.2
	2nd	2.24	2.41	7.09	5.25	3.69	3.6
	3rd	2.23	2.37	6.05	4.04	2.92	3.6
	4th	2.23	2.41	7.63	5.00	3.78	3.2
	5th	2.17	2.40	9.59	10.76	9.34	2.4
3rd Core Seal Coat Treated (08/2010)	Seal Coat layer & 1st layer	2.13	2.29	7.28	6.13	4.04	7.4
	2nd	2.25	2.42	6.96	6.26	5.03	4.0
	3rd	2.30	2.41	4.62	3.13	2.35	4.0

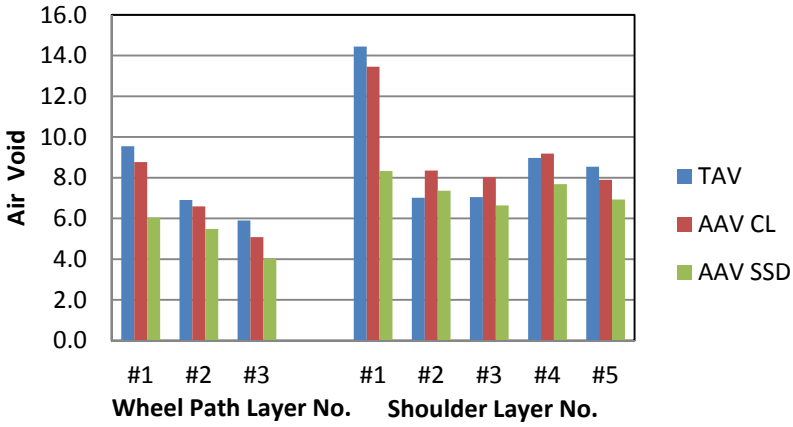
Table F12. US83 CHS Field Core (Shoulder)

Cons.: 2008		Bulk S.G.	Maximum S.G.	Total Air Voids	Accessible A.V.		Binder Content
					Corelok	SSD	
1st Core (08/2008)	1st	2.16	2.42	10.47	10.58	9.07	Average 4.4
	2nd	2.23	2.42	7.62	7.83	7.19	
	3rd	2.20	2.40	8.60	9.64	8.82	
	4th	2.15	2.42	11.38	11.46	10.01	
	5th	2.17	2.43	10.53	10.89	9.84	
2nd Core (10/2009)	1st	2.08	2.43	14.44	13.45	8.33	4.1
	2nd	2.20	2.37	7.02	8.36	7.36	3.4
	3rd	2.20	2.37	7.05	8.02	6.64	4.0
	4th	2.19	2.40	8.97	9.19	7.69	3.6
	5th	2.17	2.38	8.54	7.90	6.93	3.6
3rd Core (08/2010)	1st	2.20	2.44	10.06	9.62	7.92	3.8
	2nd	2.26	2.43	7.13	6.38	5.65	3.9
	3rd	2.25	2.44	7.82	6.59	5.20	3.8
	4th	2.11	2.40	12.16	11.68	8.89	4.6
	5th	2.20	2.42	9.17	9.40	7.50	3.8
	6th	2.22	2.41	7.52	7.84	6.38	3.9
2nd Core Seal Coat Treated (10/2009)	Seal Coat layer & 1st layer	2.11	2.31	8.46	6.16	3.02	6.5
	2nd	2.29	2.41	4.92	4.33	3.30	3.6
	3rd	2.32	2.40	3.28	2.76	2.52	4.0
3rd Core Seal Coat Treated (08/2010)	Seal Coat layer & 1st layer	2.19	2.40	8.41	5.55	4.28	4.4
	2nd	2.27	2.44	6.98	5.70	4.51	4.0
	3rd	2.22	2.44	8.94	9.07	7.68	4.2
	4th	2.11	2.43	12.97	12.65	10.83	3.4

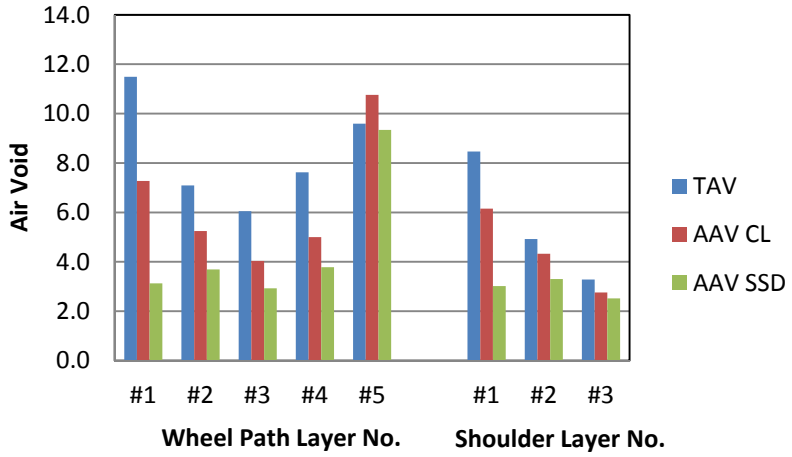
CHS US83
1st Core (2008) Untreated



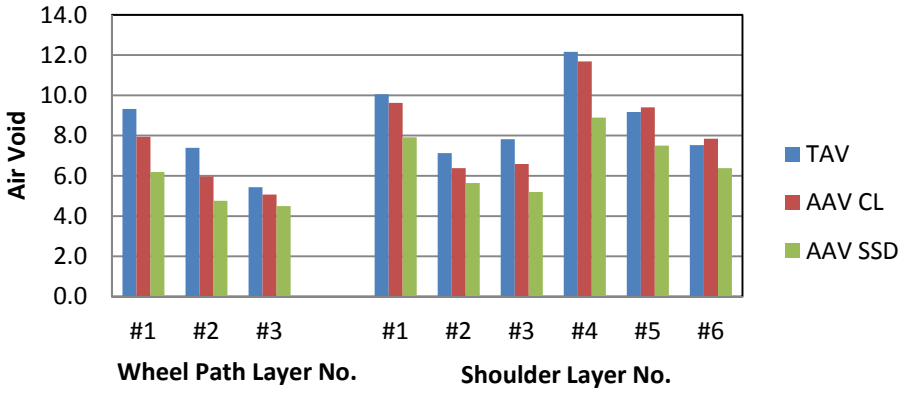
CHS US83
2nd Core (2009) Untreated



CHS US83
2nd Core (2009) Treated



CHS US83
3rd Core (2010) Untreated



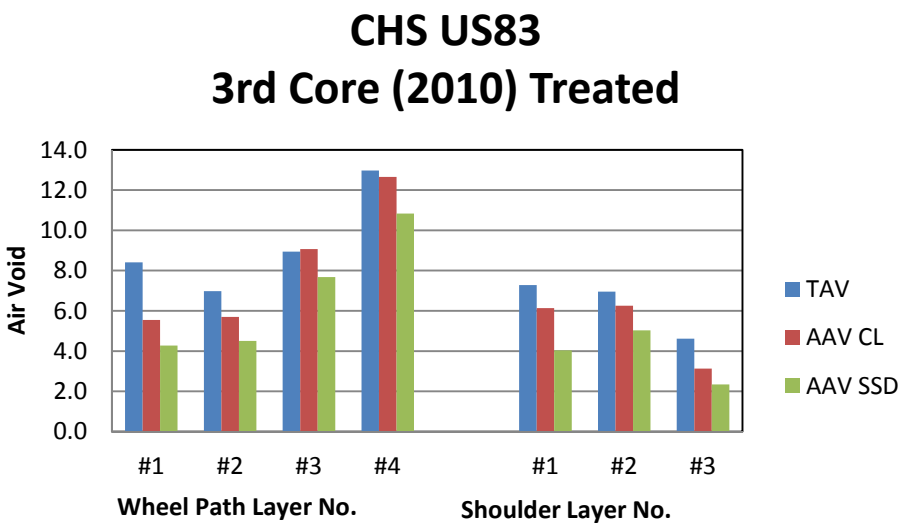

CHS US83
3rd Core (2010) Treated
14.0
12.0
10.0
8.0
6.0
4.0
2.0
0.0
Air Void
#1
#2
#3
#4
Wheel Path Layer No.
#1
#2
#3
Shoulder Layer No.
TAV
AAV CL
AAV SSD

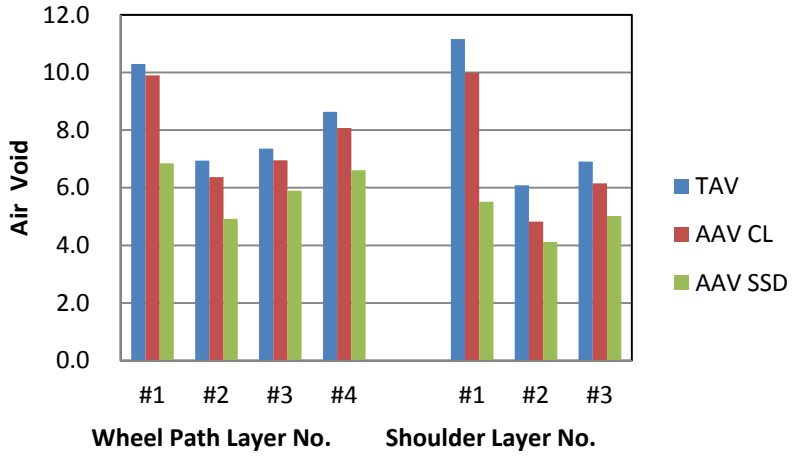
Table F13. US82 LBB Field Core (Wheel Path)

Cons.: 2008		Bulk S.G.	Maximum S.G.	Total Air Voids	Accessible A.V.		Binder Content
					Corelok	SSD	
1st Core (08/2008)	1st	2.08	2.31	10.29	9.90	6.84	Average 4.8
	2nd	2.15	2.31	6.94	6.37	4.92	
	3rd	2.14	2.31	7.36	6.95	5.89	
	4th	2.12	2.32	8.63	8.07	6.61	
2nd Core (12/2009)	1st	2.10	2.32	9.33	7.97	7.01	2.6
	2nd	2.14	2.33	8.32	7.25	6.52	2.8
	3rd	2.11	2.32	8.94	7.04	5.88	3.6
2nd Core Seal Coat Treated (12/2009)	Seal Coat layer & 1st layer	1.74	2.20	20.72	19.09	2.11	4.9
	2nd	2.04	2.32	11.83	10.55	7.72	4.0
	3rd	1.97	2.30	14.23	9.91	4.04	3.6
	4th	2.06	2.27	9.05	8.08	6.46	4.8

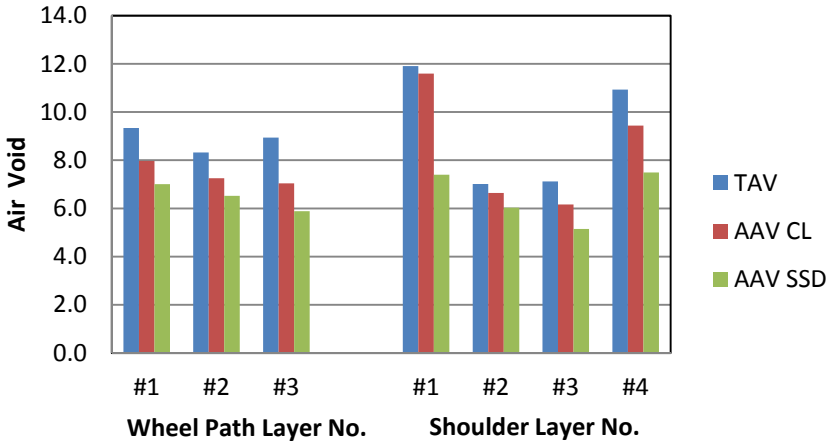
Table F14. US82 LBB Field Core (Shoulder)

Cons.: 2008		Bulk S.G.	Maximum S.G.	Total Air Voids	Accessible A.V.		Binder Content
					Corelok	SSD	
1st Core (08/2008)	1st	2.06	2.32	11.16	9.99	5.51	Average 4.8
	2nd	2.18	2.32	6.08	4.82	4.12	
	3rd	2.15	2.31	6.91	6.15	5.02	
2nd Core (12/2009)	1st	2.02	2.30	11.90	11.60	7.40	3.6
	2nd	2.15	2.31	7.02	6.64	6.03	4.0
	3rd	2.14	2.31	7.12	6.16	5.15	4.4
	4th	2.08	2.33	10.93	9.44	7.49	3.6
2nd Core Seal Coat Treated (12/2009)	Seal Coat layer & 1st layer	1.95	2.20	11.26	11.86	5.69	7.2
	2nd	1.99	2.32	13.88	13.10	9.51	3.6
	3rd	1.98	2.25	12.10	11.57	10.04	4.6

LBB US82
1st Core (2008) Untreated



LBB US82
2nd Core (2009) Untreated



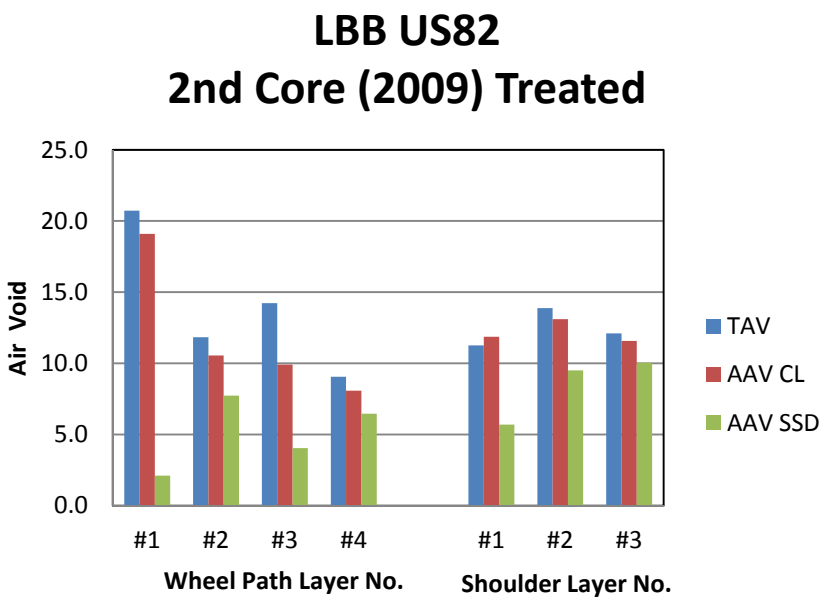

LBB US82
2nd Core (2009) Treated
25.0
20.0
15.0
10.0
5.0
0.0
Air Void
#1
#2
#3
#4
Wheel Path Layer No.
#1
#2
#3
Shoulder Layer No.
TAV
AAV CL
AAV SSD

Table F15. US69 LFK Field Core (Wheel Path)

Cons.: 2003		Bulk S.G.	Maximum S.G.	Total Air Voids	Accessible A.V.		Binder Content
					Corelok	SSD	
1st Core (06/2008)	1st	2.20	2.52	12.68	12.04	7.09	Average 5.6
	2nd	2.30	2.51	8.28	7.59	6.66	
	3rd	2.30	2.49	7.59	7.25	6.81	

Table F16. US69 LFK Field Core (Shoulder)

Cons.: 2003		Bulk S.G.	Maximum S.G.	Total Air Voids	Accessible A.V.		Binder Content
					Corelok	SSD	
1st Core (06/2008)	1st	2.18	2.49	12.61	12.65	9.65	Average 3.2
	2nd	2.26	2.48	8.90	8.54	8.12	

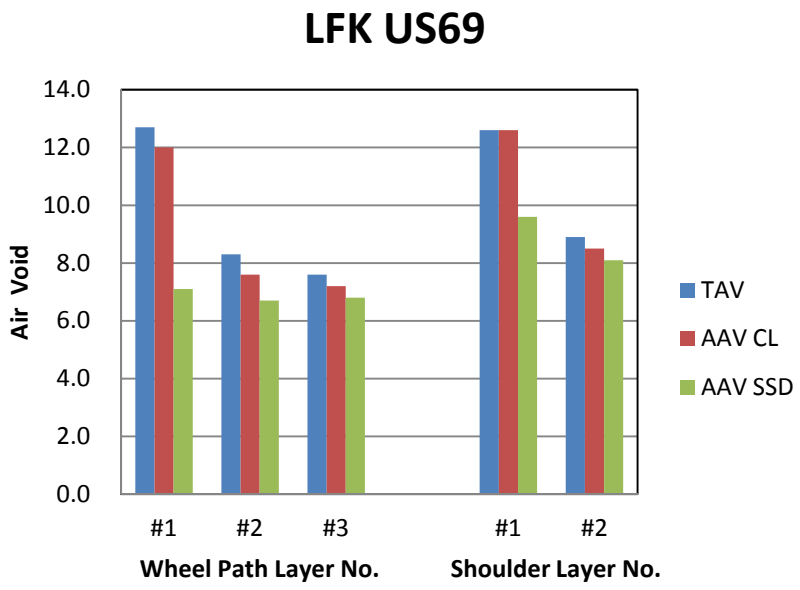


Table F17. FM649 LRD Field Core (Wheel Path)

Cons.: 2006		Bulk S.G.	Maximum S.G.	Total Air Voids	Accessible A.V.		Binder Content
					Corelok	SSD	
1st Core (06/2008)	1st	2.15	2.47	13.03	12.14	9.54	3.6
	2nd	2.17	2.47	12.20	11.34	10.49	3.6
	3rd	2.14	2.48	13.54	12.87	11.92	3.2

Table F18. FM649 LRD Field Core (Shoulder)

Cons.: 2006		Bulk S.G.	Maximum S.G.	Total Air Voids	Accessible A.V.		Binder Content
					Corelok	SSD	
1st Core (06/2008)	1st	2.04	2.47	17.29	16.63	12.20	3.6
	2nd	2.12	2.47	14.15	13.38	12.10	4.0
	3rd	2.14	2.47	13.36	12.97	11.81	3.6

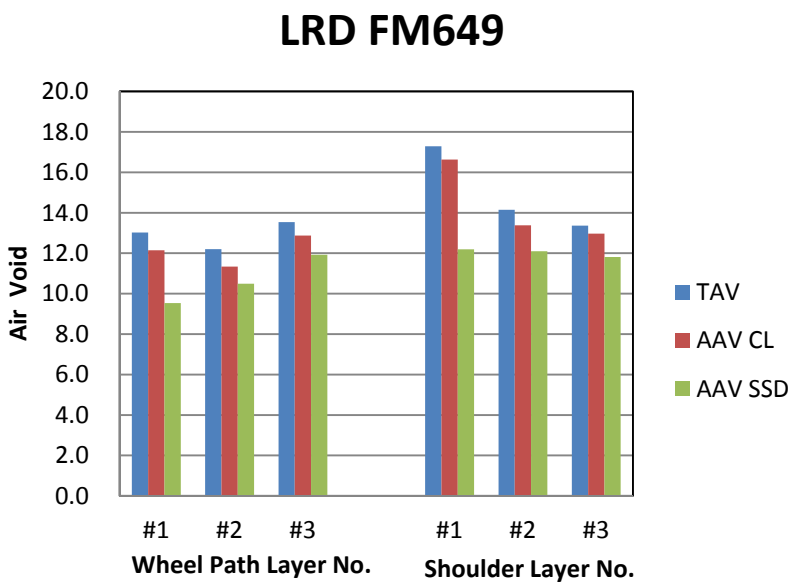


Table F19. IH35 #3 LRD04 Field Core (Shoulder)

Cons.: 2007		Bulk S.G.	Maximum S.G.	Total Air Voids	Accessible A.V.		Binder Content
					Corelok	SSD	
1st Core (06/2008)	1st	2.47	2.63	6.06	5.13	3.43	2.8
	2nd	2.48	2.59	4.36	3.46	2.35	4.0
	3rd	2.50	2.63	4.76	3.74	2.42	-
	4th	2.47	2.61	5.52	4.65	3.23	4.0
	5th	2.44	2.68	8.82	8.69	5.61	3.6
	6th	2.37	2.55	6.91	6.45	5.22	4.8

Table F20. IH35 #5 LRD04 Field Core (Shoulder)

Cons.: 2007		Bulk S.G.	Maximum S.G.	Total Air Voids	Accessible A.V.		Binder Content
					Corelok	SSD	
1st Core (06/2008)	1st	2.30	2.36	2.62	2.42	1.56	Average
	2nd	2.30	2.36	2.50	2.02	2.06	3.2

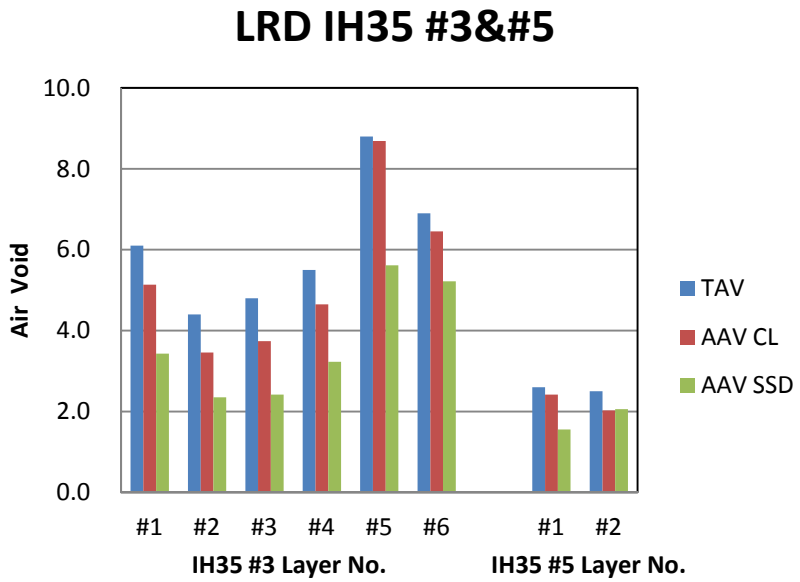


Table F21. US277 LRD Field Core (Wheel Path)

Cons.: 2008		Bulk S.G.	Maximum S.G.	Total Air Voids	Accessible A.V.		Binder Content
					Corelok	SSD	
1st Core (07/2008)	1st	2.33	2.56	8.99	7.40	6.15	2.8
	2nd	2.36	2.56	7.95	6.62	6.22	4.4
	3rd	2.34	2.57	8.78	7.18	6.60	4.0
	4th	2.31	2.55	9.24	8.40	7.76	4.0
	5th	2.29	2.53	9.36	8.36	7.97	6.0
2nd Core (12/2009)	1st	2.33	2.53	8.03	5.54	2.84	4.0
	2nd	2.35	2.55	7.69	6.12	4.18	3.6
	3rd	2.30	2.55	9.65	8.30	7.07	3.6
	4th	2.30	2.47	6.61	4.92	3.38	5.2
3rd Core (12/2010)	1st	2.39	2.56	6.81	3.97	2.82	3.6
	2nd	2.36	2.56	7.60	4.65	2.97	3.9
	3rd	2.37	2.56	7.60	4.74	4.29	3.6
	4th	2.32	2.55	9.15	7.49	6.46	3.4
4th Core* (01/2012)	1st	2.19	2.34	6.78	3.36	2.99	-
	2nd	2.38	2.59	8.76	4.94	3.67	
	3rd	2.37	2.57	8.48	4.29	3.21	
	4th	2.34	2.55	8.97	5.91	5.59	
2nd Core Seal Coat Treated (12/2009)	Seal Coat layer & 1st layer	2.20	2.47	11.09	5.84	3.11	4.4
	2nd	2.31	2.54	9.20	7.66	5.32	4.0
	3rd	2.30	2.55	9.66	8.68	7.66	4.0
	4th	2.30	2.55	9.80	9.34	9.11	3.6
	5th	2.25	2.51	10.40	7.83	6.19	4.0
3rd Core Seal Coat Treated (12/2010)	Seal Coat layer & 1st layer	2.25	2.52	10.80	4.00	2.92	3.9
	2nd	2.30	2.56	10.24	8.11	7.31	3.4
	3rd	2.30	2.54	9.67	8.77	7.95	3.5
	4th	2.21	2.55	13.52	12.49	10.04	3.1
	5th	2.23	2.49	10.43	8.08	5.43	3.7
4th Core Seal Coat Treated* (01/2012)	Seal Coat layer & 1st layer	2.13	2.28	7.25	4.02	2.58	-
	2nd	2.36	2.56	8.59	3.90	2.79	
	3rd	2.36	2.55	8.08	4.59	4.05	

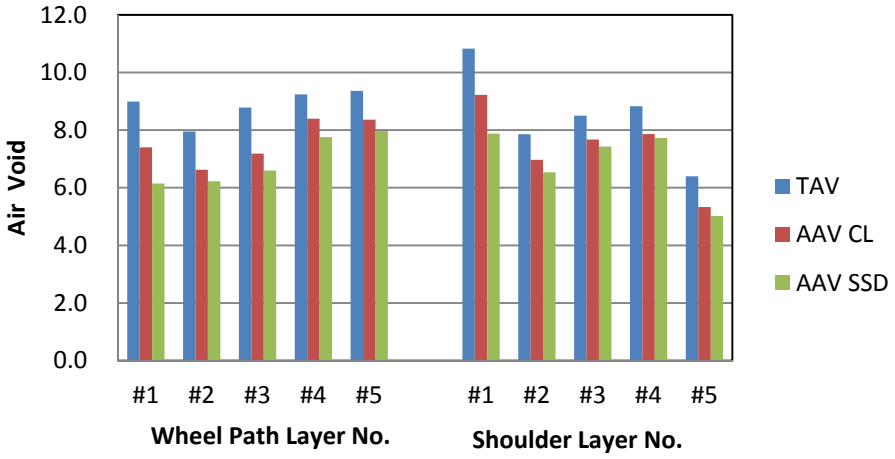
* Another Seal Coat layer was applied, and it was too thin to cut off.

Table F22. US277 LRD Field Core (Shoulder)

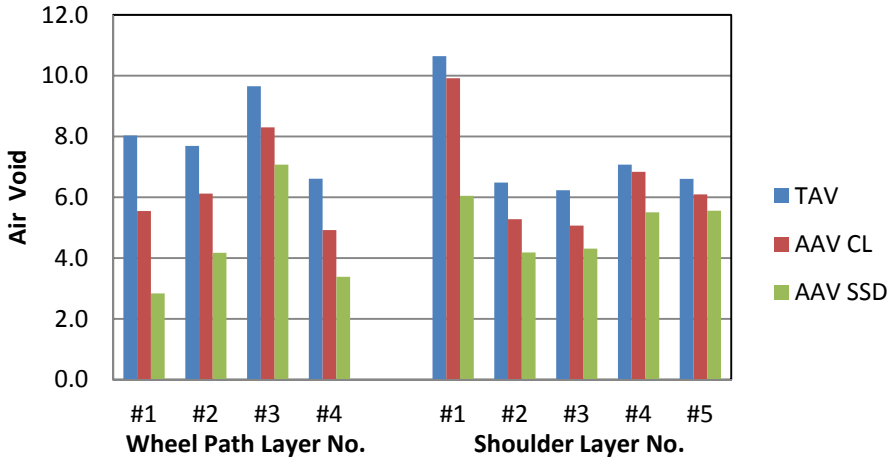
Cons.: 2008		Bulk S.G.	Maximum S.G.	Total Air Voids	Accessible A.V.		Binder Content
					Corelok	SSD	
1st Core (07/2008)	1st	2.28	2.56	10.83	9.22	7.88	4.0
	2nd	2.35	2.55	7.85	6.97	6.53	4.0
	3rd	2.33	2.55	8.50	7.68	7.43	4.0
	4th	2.32	2.55	8.83	7.86	7.73	4.0
	5th	2.33	2.49	6.40	5.33	5.02	6.0
2nd Core (12/2009)	1st	2.28	2.56	10.64	9.91	6.04	3.2
	2nd	2.39	2.56	6.48	5.28	4.18	2.8
	3rd	2.39	2.55	6.23	5.07	4.31	3.6
	4th	2.36	2.53	7.08	6.83	5.51	3.6
	5th	2.35	2.52	6.61	6.09	5.56	4.4
3rd Core (12/2010)	1st	2.32	2.56	9.29	8.10	7.36	3.6
	2nd	2.36	2.56	7.62	5.01	4.28	3.6
	3rd	2.34	2.55	8.17	6.00	5.18	3.6
	4th	2.26	2.43	7.04	5.74	4.98	5.7
4th Core* (01/2012)	1st	2.33	2.57	10.22	7.25	5.34	
	2nd	2.37	2.57	8.18	5.06	3.79	-
	3rd	2.39	2.55	6.66	4.07	3.38	

* Another Seal Coat layer was applied, and it was too thin to cut off.

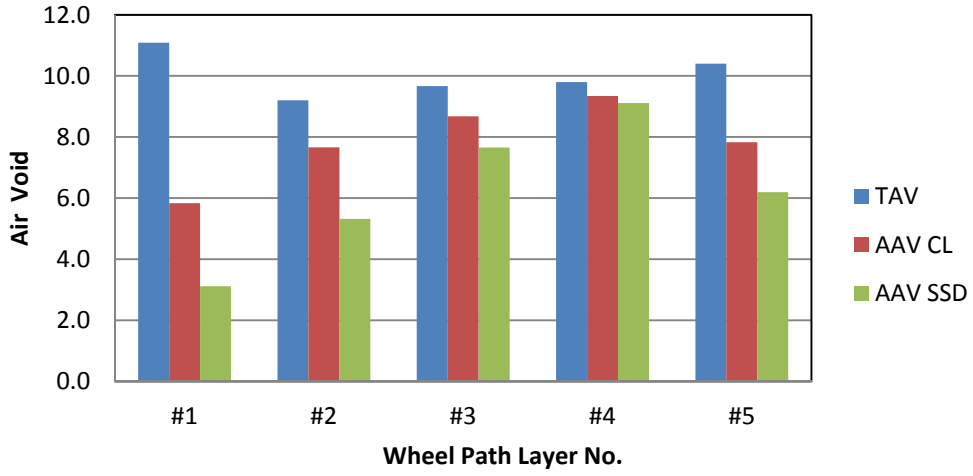
LRD US277
1st Core (2008) Untreated



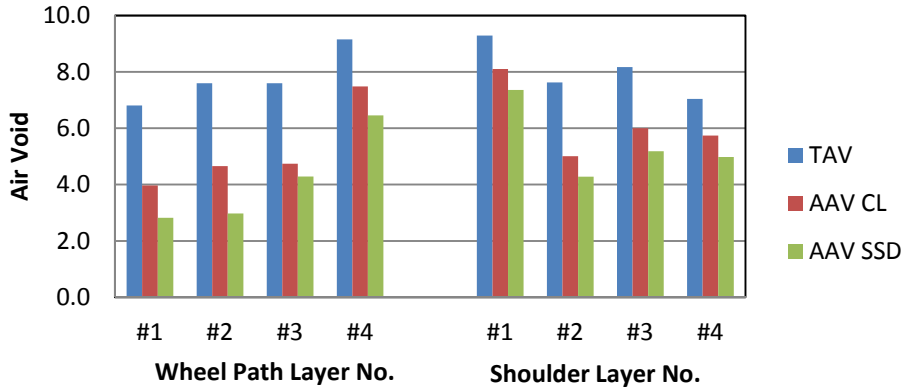
LRD US277
2nd Core (2009) Untreated

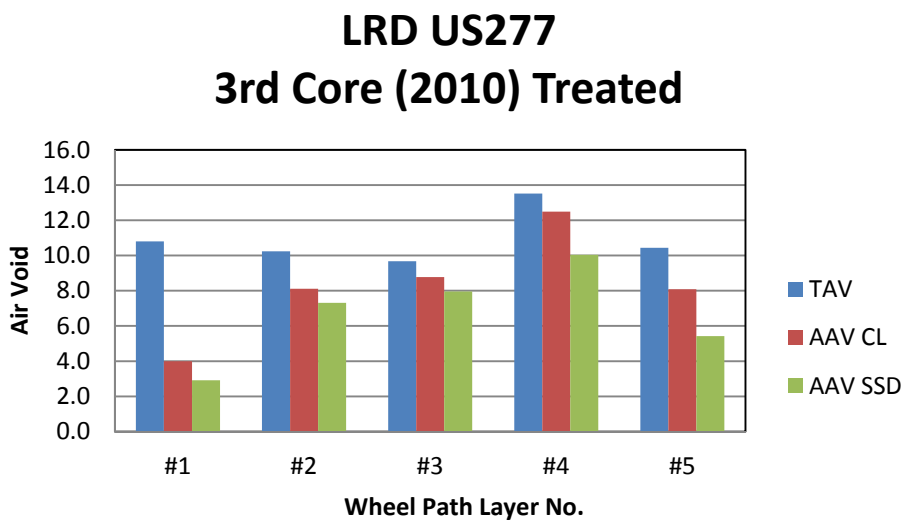


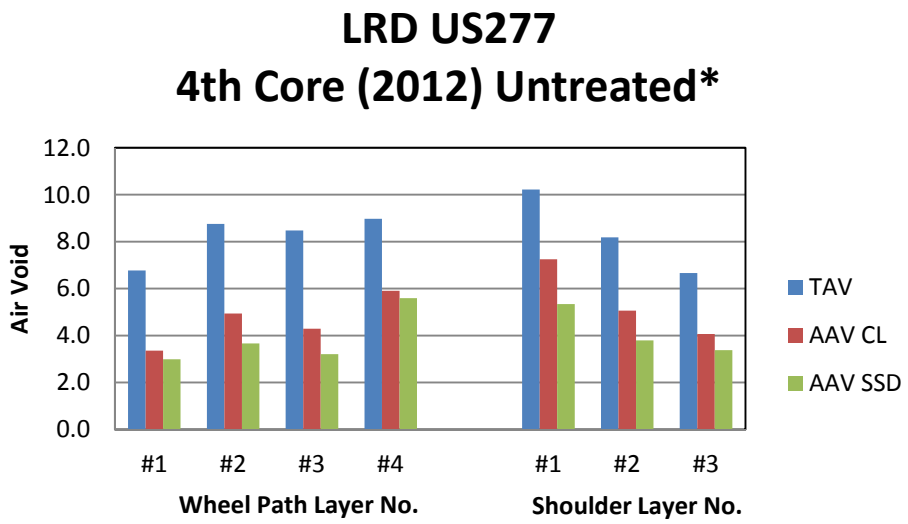
LRD US277
2nd Core (2009) Treated



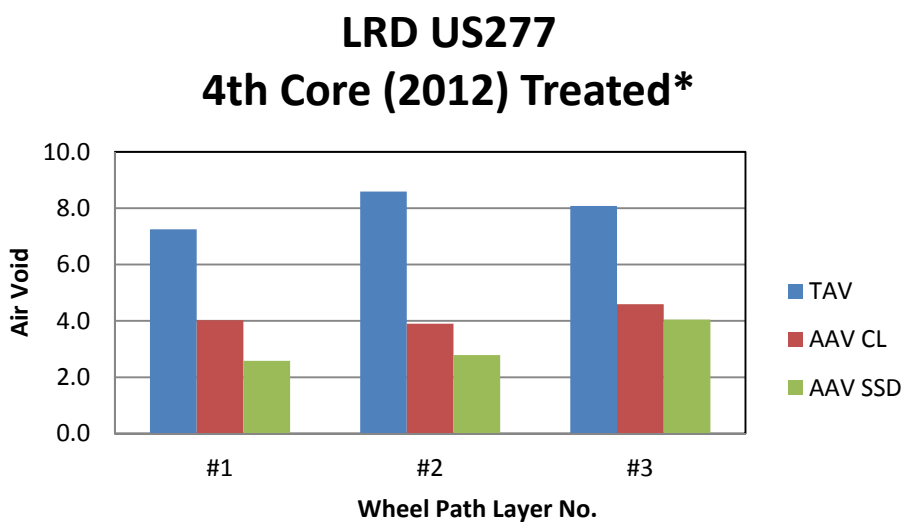
LRD US277
3rd Core (2010) Untreated







* Another Seal Coat layer was applied, and it was too thin to cut off.



* Another Seal Coat layer was applied, and it was too thin to cut off.

Table F23. MnRoad Field Core (Wheel Path)

Cons.: Unknown		Bulk S.G.	Maximum S.G.	Total Air Voids	Accessible A.V.		Binder Content
					Corelok	SSD	
1st Core (11/2008)	1st	2.27	2.47	7.97	6.69	2.98	4.0
	2nd	2.33	2.45	4.71	2.71	2.04	4.8
	3rd	2.33	2.44	4.45	2.77	2.01	4.8
	4th	2.30	2.45	6.39	4.56	3.44	4.4
	5th	2.29	2.42	5.35	4.64	3.62	4.0
	6th	2.26	2.44	7.46	6.11	4.04	4.4
	7th	2.30	2.47	6.88	6.43	5.37	4.0
	8th	2.28	2.47	7.59	6.94	6.11	4.0
	9th	2.24	2.47	9.53	9.45	6.51	4.3

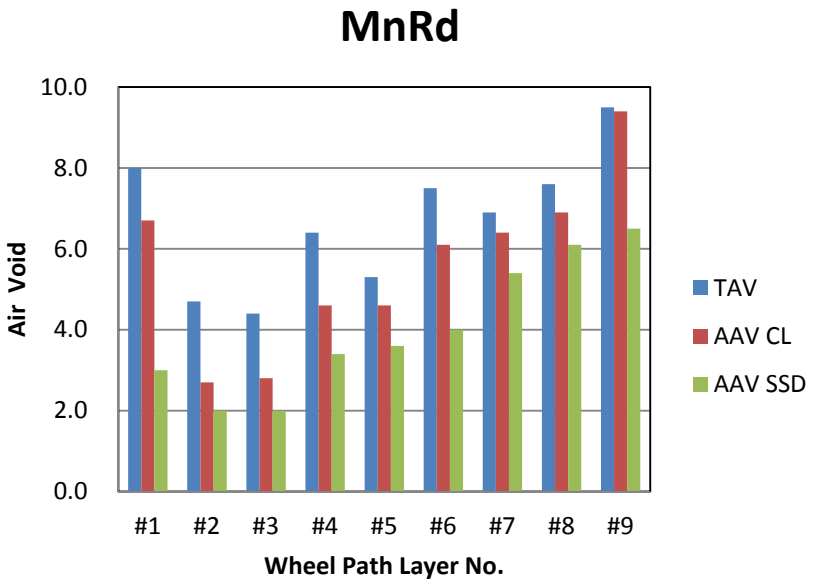


Table F24. FM1936 ODA Field Core (Wheel Path)

Cons.: 2002		Bulk S.G.	Maximum S.G.	Total Air Voids	Accessible A.V.		Binder Content
					Corelok	SSD	
1st Core (05/2008)	1st	2.16	2.33	7.19	5.56	1.99	2.4
	2nd	2.26	2.34	3.53	1.76	1.06	6.0
	3rd	2.26	2.34	3.19	2.11	1.35	5.6
	4th	2.26	2.32	2.45	1.69	1.12	6.0

Table F25. FM1936 ODA Field Core (Shoulder)

Cons.: 2002		Bulk S.G.	Maximum S.G.	Total Air Voids	Accessible A.V.		Binder Content
					Corelok	SSD	
1st Core (05/2008)	1st	2.09	2.38	12.47	10.81	5.83	5.2
	2nd	2.21	2.34	5.90	4.76	2.90	6.0
	3rd	2.25	2.34	3.96	2.63	1.53	6.0
	4th	2.23	2.35	4.90	3.39	2.70	5.6

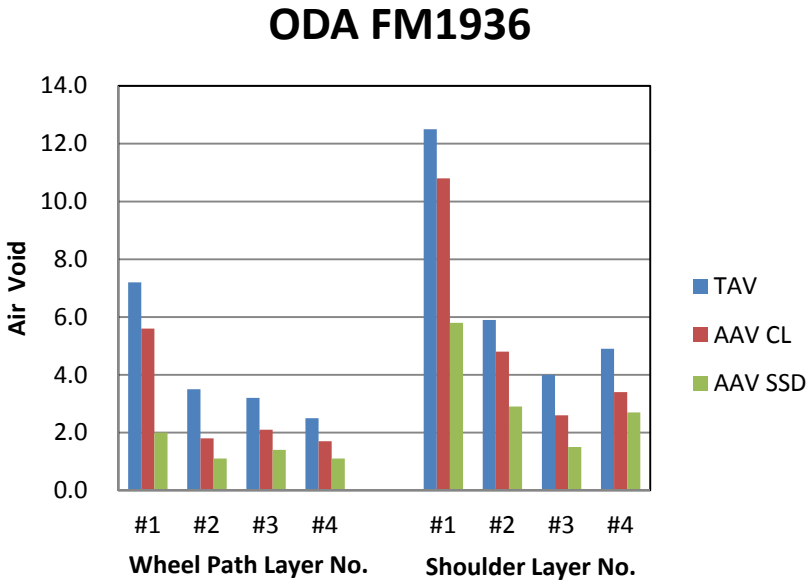


Table F26. FM2994 PHR Field Core (Wheel Path)

Cons.: 2002		Bulk S.G.	Maximum S.G.	Total Air Voids	Accessible A.V.		Binder Content
					Corelok	SSD	
1st Core (05/2008)	1st	2.12	2.44	13.13	11.47	4.37	3.2
	2nd	2.26	2.41	6.13	5.11	3.06	5.2
	3rd	2.23	2.40	6.96	6.33	3.89	4.8
	4th	2.22	2.44	8.89	7.86	4.42	4.8
	5th	2.23	2.40	7.01	6.86	4.49	4.8
	6th	2.21	2.37	6.49	5.49	2.25	4.0

Table F27. FM2994 PHR Field Core (Shoulder)

Cons.: 2002		Bulk S.G.	Maximum S.G.	Total Air Voids	Accessible A.V.		Binder Content
					Corelok	SSD	
1st Core (05/2008)	1st	2.09	2.46	14.84	14.16	8.33	4.4
	2nd	2.19	2.43	9.98	9.45	7.30	4.4
	3rd	2.19	2.45	10.47	10.21	7.34	4.0
	4th	2.13	2.43	12.53	11.93	8.14	4.4
	5th	2.15	2.42	11.11	10.99	7.35	4.4
	6th	2.15	2.41	10.86	11.99	7.38	4.0

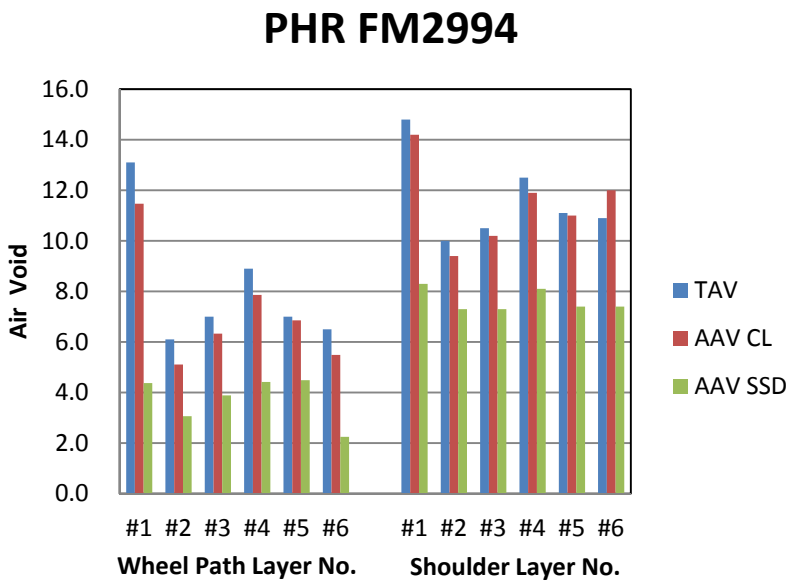


Table F28. US259 TYL Field Core (Wheel Path)

Cons.: 2007		Bulk S.G.	Maximum S.G.	Total Air Voids	Accessible A.V.		Binder Content
					Corelok	SSD	
1st Core (07/2008)	1st	2.34	2.51	6.79	5.89	4.67	Average 3.1
	2nd	2.31	2.51	7.93	7.33	6.78	
	3rd	2.06	2.38	13.10	7.75	6.91	
	4th	2.22	2.51	11.58	10.98	8.19	

Table F29. US259 TYL Field Core (Shoulder)

Cons.: 2007		Bulk S.G.	Maximum S.G.	Total Air Voids	Accessible A.V.		Binder Content
					Corelok	SSD	
1st Core (07/2008)	1st	2.26	2.51	9.82	9.66	7.36	-
	2nd	2.35	2.50	6.02	5.32	5.18	
	3rd	2.32	2.51	7.43	6.42	5.94	

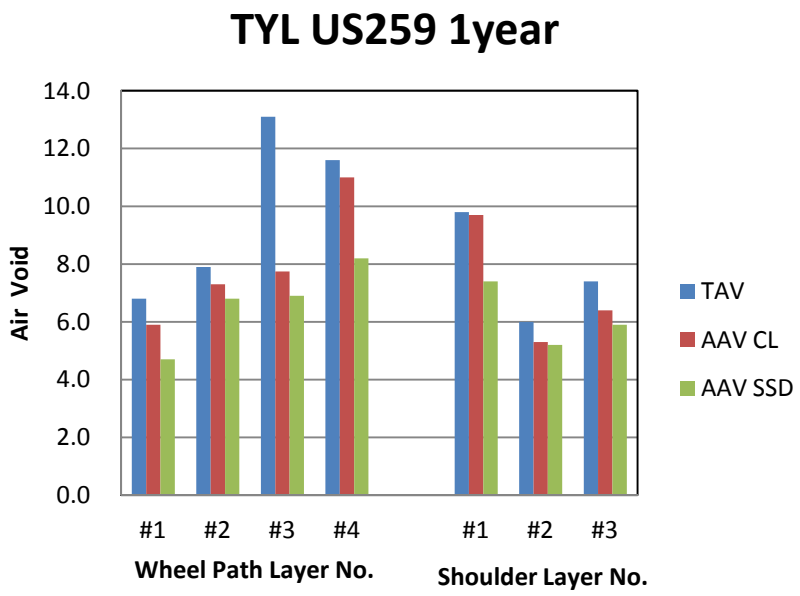


Table F30. IH35 WAC Field Core (Wheel Path)

Cons.: 2003		Bulk S.G.	Maximum S.G.	Total Air Voids	Accessible A.V.		Binder Content
					Corelok	SSD	
1st Core (08/2008)	1st	2.28	2.47	7.58	6.63	5.97	Average 4.4
	2nd	2.29	2.43	5.96	6.31	5.10	
	3rd	2.25	2.43	7.11	7.19	6.40	
	4th	2.28	2.44	6.61	6.08	5.50	
	5th	2.30	2.46	6.57	5.51	4.65	
	6th	2.29	2.44	6.19	5.99	4.98	

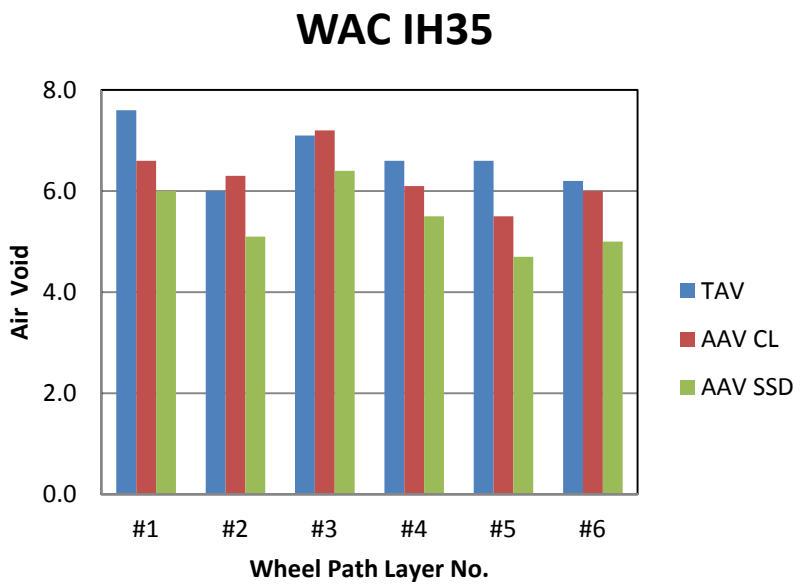


Table F31. US59 WFS Field Core (Wheel Path)

Cons.: 2007		Bulk S.G.	Maximum S.G.	Total Air Voids	Accessible A.V.		Binder Content
					Corelok	SSD	
1st Core (07/2008)	1st	2.23	2.52	11.52	10.46	7.61	Average 4.0
	2nd	2.30	2.51	8.35	7.65	7.15	
	3rd	2.32	2.49	6.91	6.76	6.32	
	4th	2.32	2.48	6.48	6.77	6.04	
	5th	2.24	2.51	10.62	8.75	5.30	

Table F32. US59 WFS Field Core (Shoulder)

Cons.: 2007		Bulk S.G.	Maximum S.G.	Total Air Voids	Accessible A.V.		Binder Content
					Corelok	SSD	
1st Core (07/2008)	1st	2.20	2.52	12.58	12.08	9.26	Average 3.6
	2nd	2.27	2.50	9.30	9.18	8.31	
	3rd	2.26	2.51	9.92	10.01	8.93	

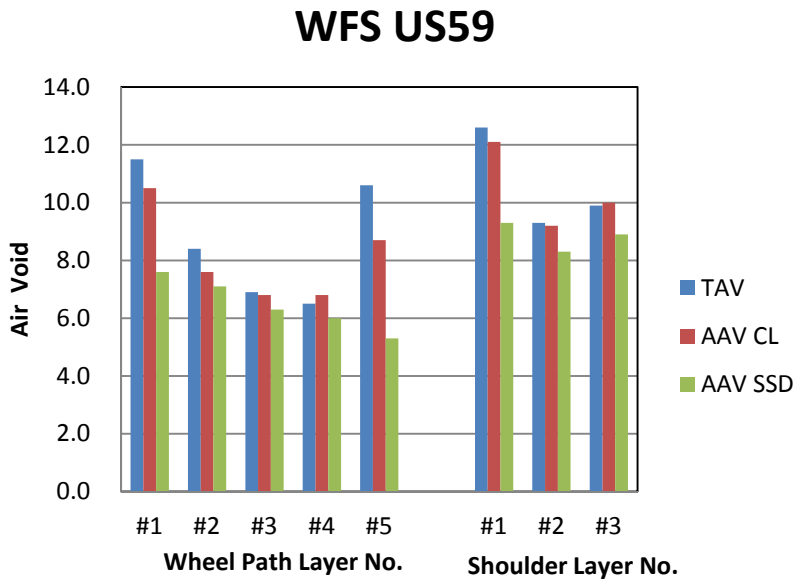
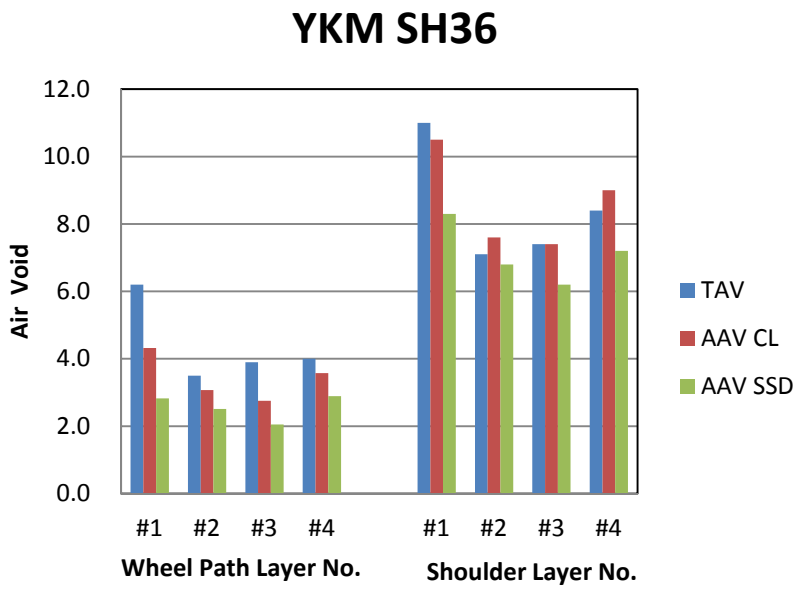


Table F33. SH36 YKM Field Core (Wheel Path)

Cons.: 2006		Bulk S.G.	Maximum S.G.	Total Air Voids	Accessible A.V.		Binder Content
					Corelok	SSD	
1st Core (06/2008)	1st	2.31	2.46	6.20	4.32	2.82	4.4
	2nd	2.35	2.44	3.54	3.07	2.51	4.0
	3rd	2.37	2.47	3.86	2.75	2.05	4.0
	4th	2.35	2.45	4.00	3.58	2.89	4.0

Table F34. SH36 YKM Field Core (Shoulder)

Cons.: 2006		Bulk S.G.	Maximum S.G.	Total Air Voids	Accessible A.V.		Binder Content
					Corelok	SSD	
1st Core (06/2008)	1st	2.19	2.46	10.99	10.48	8.27	4.4
	2nd	2.27	2.44	7.12	7.57	6.75	4.0
	3rd	2.27	2.45	7.35	7.40	6.20	4.0
	4th	2.23	2.44	8.44	9.02	7.21	4.8



APPENDIX G

TABLES OF HMAC LMLC MIXTURE PROPERTY DATA

Table G1. HMAC LMLC Mixture Property Data.

Type	Sample	SITE	Mix Type	Agg Material	Environmental Zone	Age	BINDER CONTENT	AV	FILM THICKNESS(microns)	DSR	CA	E_{ve}	N_f	C'	b	n	A
LMLC	1-1	Laredo	Type C	Limestone w/TR Screening	DW	0 months	4.0	3.8	5.1	2.34E-04	0.908	6138	6.24E+06	34.03117	0.034	0.71	9.28E-07
LMLC	1-2	Laredo	Type C	Limestone w/TR Screening	DW	0 months	4.0	3.2	5.1	2.34E-04	0.908	8698	6.10E+06	42.12133	0.035	0.54	1.41E-06
LMLC	2-1	Laredo	Type C	Limestone w/TR Screening	DW	0 months	4.0	9.4	5.1	5.12E-04	0.949	X					
LMLC	2-2	Laredo	Type C	Limestone w/TR Screening	DW	0 months	4.0	8.5	5.1	5.12E-04	0.949	5161	5.36E+06	33.62008	0.043	0.92	7.04E-07
LMLC	3-1	Laredo	Type C	Limestone w/TR Screening	DW	0 months	5.0	5.5	6.9	1.84E-04	0.940	4210	3.54E+08	21.52694	0.184	1.16	6.05E-09
LMLC	3-2	Laredo	Type C	Limestone w/TR Screening	DW	0 months	5.0	5.3	6.9	1.84E-04	0.940	4941	7.74E+06	34.38753	0.045	0.84	6.52E-07
LMLC	4-1	Laredo	Type C	Limestone w/TR Screening	DW	0 months	5.0	8.1	6.9	8.13E-05	0.862	4103	2.44E+06	39.79346	0.028	1.01	1.55E-06
LMLC	4-2	Laredo	Type C	Limestone w/TR Screening	DW	0 months	5.0	9.1	6.9	8.13E-05	0.862	3925	1.39E+07	31.01132	0.079	1.08	2.33E-07
LMLC	5-1	Laredo	Type C	Limestone w/TR Screening	DW	0 months	5.0	3.1	6.9	6.34E-05	0.826	6421	6.46E+05	45.43198	0.002	0.56	1.48E-05
LMLC	5-2	Laredo	Type C	Limestone w/TR Screening	DW	0 months	5.0	2.9	6.9	6.34E-05	0.826	6022	2.24E+07	35.89223	0.101	0.55	4.87E-07
LMLC	6-1	Laredo	Type C	Limestone w/TR Screening	DW	0 months	4.5	5.6	6.0	4.03E-04	0.916	4584	7.92E+05	43.85106	0.008	0.91	4.94E-06
LMLC	6-2	Laredo	Type C	Limestone w/TR Screening	DW	0 months	4.5	5.7	6.0	4.03E-04	0.916	4932	5.16E+06	33.38333	0.034	1.00	5.43E-07
LMLC	7-1	Laredo	Type C	Limestone w/TR Screening	DW	0 months	4.5	9.3	6.0	3.69E-04	0.877	3876	1.81E+06	53.62656	0.026	0.96	2.11E-06
LMLC	7-2	Laredo	Type C	Limestone w/TR Screening	DW	0 months	4.5	9.0	6.0	3.69E-04	0.877	3370	1.53E+07	46.11488	0.050	0.81	8.49E-07
LMLC	8-1	Laredo	Type C	Limestone w/TR Screening	DW	6 months	4.0	8.4	5.1	1.12E-03	1.202	6599	2.59E+06	42.16272	0.028	0.64	2.91E-06
LMLC	8-2	Laredo	Type C	Limestone w/TR Screening	DW	6 months	4.0	8.2	5.1	1.12E-03	1.202	5985	3.01E+06	40.21151	0.032	0.67	2.29E-06
LMLC	9-1	Laredo	Type C	Limestone w/TR Screening	DW	6 months	4.0	5.5	5.1	6.90E-04	1.244	7463	4.44E+06	43.14923	0.047	0.77	9.61E-07
LMLC	9-2	Laredo	Type C	Limestone w/TR Screening	DW	6 months	4.0	5.7	5.1	6.90E-04	1.244	4504	1.60E+06	53.61287	0.016	0.61	4.6E-06
LMLC	10-1	Laredo	Type C	Limestone w/TR Screening	DW	6 months	5.0	3.2	6.9	6.11E-04	1.088	6306	9.41E+06	40.303	0.063	0.65	7.73E-07
LMLC	10-2	Laredo	Type C	Limestone w/TR Screening	DW	6 months	5.0	3.0	6.9	6.11E-04	1.088	7651	3.72E+06	50.37186	0.031	0.61	2.01E-06
LMLC	11-1	Laredo	Type C	Limestone w/TR Screening	DW	6 months	5.0	5.7	6.9	5.78E-04	1.179	6122	3.54E+06	47.86218	0.043	0.80	1.23E-06
LMLC	11-2	Laredo	Type C	Limestone w/TR Screening	DW	6 months	5.0	5.4	6.9	5.78E-04	1.179	6966	2.57E+06	50.60675	0.033	0.57	3.46E-06
LMLC	12-1	Laredo	Type C	Limestone w/TR Screening	DW	6 months	4.5	8.4	6.0	1.01E-03	1.204	5666	3.59E+06	38.57665	0.046	0.86	1.14E-06
LMLC	12-2	Laredo	Type C	Limestone w/TR Screening	DW	6 months	4.5	8.7	6.0	1.01E-03	1.204	6114	3.86E+06	42.18757	0.056	0.79	1.23E-06
LMLC	13-1	Laredo	Type C	Limestone w/TR Screening	DW	6 months	4.5	2.5	6.0	5.75E-04	1.123	6917	6.42E+06	44.29374	0.041	0.82	5.95E-07
LMLC	13-2	Laredo	Type C	Limestone w/TR Screening	DW	6 months	4.5	2.8	6.0	5.75E-04	1.123	8416	1.90E+06	55.01065	0.029	0.93	1.16E-06
LMLC	14-1	Laredo	Type C	Limestone w/TR Screening	DW	6 months	4.5	5.6	6.0	1.05E-03	1.235	5990	5.25E+06	43.0896	0.040	0.80	8.92E-07
LMLC	14-2	Laredo	Type C	Limestone w/TR Screening	DW	6 months	4.5	5.7	6.0	1.05E-03	1.235	5258	5.14E+06	35.70198	0.036	0.69	1.44E-06
LMLC	15-1	Laredo	Type C	Limestone w/TR Screening	DW	6 months	4.0	8.3	5.1	1.20E-03	1.206	8443	3.93E+06	42.20805	0.053	0.70	1.29E-06
LMLC	15-2	Laredo	Type C	Limestone w/TR Screening	DW	6 months	4.0	8.5	5.1	1.20E-03	1.206	7942	2.58E+06	47.87023	0.031	0.51	3.98E-06
LMLC	16-1	Laredo	Type C	Limestone w/TR Screening	DW	6 months	4.0	5.5	5.1	1.44E-03	1.247	8214	7.52E+05	88.26263	0.040	0.57	9.71E-06
LMLC	16-2	Laredo	Type C	Limestone w/TR Screening	DW	6 months	4.0	5.8	5.1	1.44E-03	1.247	9353	X				
LMLC	17-1	Laredo	Type C	Limestone w/TR Screening	DW	6 months	5.0	6.2	6.9	1.34E-03	1.276	6860	3.68E+06	51.06867	0.065	0.73	1.48E-06
LMLC	17-2	Laredo	Type C	Limestone w/TR Screening	DW	6 months	5.0	6.1	6.9	1.34E-03	1.276	6978	4.93E+06	45.62419	0.070	0.60	1.61E-06
LMLC	18-1	Laredo	Type C	Limestone w/TR Screening	DW	9 months	5.0	2.6	6.9	9.87E-04	1.174	7821	3.82E+05	89.00025	0.018	0.54	2.38E-05
LMLC	18-2	Laredo	Type C	Limestone w/TR Screening	DW	9 months	5.0	2.8	6.9	9.87E-04	1.174	9111	6.92E+06	63.93874	0.052	0.35	2.51E-06
LMLC	19-1	Laredo	Type C	Limestone w/TR Screening	DW	9 months	5.0	8.7	6.9	9.19E-04	1.278	6869	2.45E+06	49.18996	0.053	0.71	2.28E-06

Type	Sample	SITE	Mix Type	Agg Material	Environmental Zone	Age	BINDER CONTENT	AV	FILM THICKNESS(microns)	DSR	CA	Eve	Nf	C'	b	n	A
LMLC	19-2	Laredo	Type C	Limestone w/TR Screening	DW	9 months	5.0	8.2	6.9	9.19E-04	1.278	6772	3.28E+06	44.68903	0.057	0.79	1.3E-06
LMLC	20-1	Laredo	Type C	Limestone w/TR Screening	DW	9 months	4.5	5.8	6.0	1.33E-03	1.256	8365	5.51E+06	46.52389	0.062	0.50	1.73E-06
LMLC	20-2	Laredo	Type C	Limestone w/TR Screening	DW	9 months	4.5	5.5	6.0	1.33E-03	1.256	7423	3.03E+06	49.43131	0.058	0.64	2.08E-06
LMLC	21-1	Laredo	Type C	Limestone w/TR Screening	DW	12 months	4.0	5.5	5.1	2.07E-03	1.379	10481	5.23E+05	87.43523	0.010	1.71	4.64E-06
LMLC	21-2	Laredo	Type C	Limestone w/TR Screening	DW	12 months	4.0	6.0	5.1	2.07E-03	1.379	10091	3.70E+05	97.8637	0.051	0.96	5.8E-06
LMLC	22-1	Laredo	Type C	Limestone w/TR Screening	DW	12 months	4.0	3.1	5.1	2.10E-03	1.289	9959	1.00E+07	49.3968	0.057	0.27	3.58E-06
LMLC	22-2	Laredo	Type C	Limestone w/TR Screening	DW	12 months	4.0	3.0	5.1	2.10E-03	1.289	11686	X				
LMLC	23-1	Laredo	Type C	Limestone w/TR Screening	DW	12 months	5.0	2.8	6.9	1.41E-03	1.270	9657	2.55E+06	60.90045	0.059	0.52	3.88E-06
LMLC	23-2	Laredo	Type C	Limestone w/TR Screening	DW	12 months	5.0	3.1	6.9	1.41E-03	1.270	9474	1.36E+06	66.06533	0.048	0.72	3.59E-06
LMLC	24-1	Laredo	Type C	Limestone w/TR Screening	DW	12 months	5.0	9.0	6.9	1.25E-03	1.343	7629	4.95E+06	44.42482	0.088	0.63	1.33E-06
LMLC	24-2	Laredo	Type C	Limestone w/TR Screening	DW	12 months	5.0	8.3	6.9	1.25E-03	1.343	7551	3.18E+06	53.29094	0.067	0.61	2.38E-06
LMLC	25-1	Laredo	Type C	Limestone w/TR Screening	DW	12 months	4.5	3.2	6.0	2.29E-03	1.278	10384	2.74E+06	58.26229	0.057	0.59	2.84E-06
LMLC	25-2	Laredo	Type C	Limestone w/TR Screening	DW	12 months	4.5	3.3	6.0	2.29E-03	1.278	10654	8.61E+06	48.01137	0.090	0.53	9.72E-07
LMLC	26-1	Laredo	Type C	Limestone w/TR Screening	DW	12 months	4.5	8.5	6.0	1.98E-03	1.311	7809	6.40E+06	42.81603	0.092	0.61	1.12E-06
LMLC	26-2	Laredo	Type C	Limestone w/TR Screening	DW	12 months	4.5	8.6	6.0	1.98E-03	1.311	7310	3.44E+06	42.9835	0.052	0.56	2.48E-06
LMLC	27-1	Laredo	Type C	Limestone w/TR Screening	DW	12 months	4.5	5.8	6.0	3.05E-03	1.351	8748	5.13E+06	41.62383	0.077	0.67	1.15E-06
LMLC	27-2	Laredo	Type C	Limestone w/TR Screening	DW	12 months	4.5	5.2	6.0	3.05E-03	1.351	9349	4.76E+06	52.84475	0.074	0.59	1.43E-06
LMLC	1-1	Childress	Type D	Granite	DC	0 months	4.8	2.7	8.8	8.36E-05	0.975	3466	3.53E+06	41.78276	0.022	0.79	1.83E-06
LMLC	1-2	Childress	Type D	Granite	DC	0 months	4.8	2.5	8.8	8.36E-05	0.975	4138	5.55E+06	43.27236	0.038	0.52	2.52E-06
LMLC	2-1	Childress	Type D	Granite	DC	0 months	4.8	9.5	8.8	1.06E-04	1.068	2133	X				
LMLC	2-2	Childress	Type D	Granite	DC	0 months	4.8	8.9	8.8	1.06E-04	1.068	1064	X				
LMLC	3-1	Childress	Type D	Granite	DC	0 months	5.8	5.9	10.7	8.26E-05	0.931	1933	2.05E+07	35.06102	0.054	1.53	1.39E-07
LMLC	3-2	Childress	Type D	Granite	DC	0 months	5.8	6.7	10.7	8.26E-05	0.931	1600	1.24E+07	33.36328	0.052	0.89	9.76E-07
LMLC	4-1	Childress	Type D	Granite	DC	0 months	5.8	9.8	10.7	7.54E-05	0.951	800	X				
LMLC	4-2	Childress	Type D	Granite	DC	0 months	5.8	9.2	10.7	7.54E-05	0.951	1323	4.49E+07	33.57845	0.047	2.11	5.65E-08
LMLC	5-1	Childress	Type D	Granite	DC	0 months	5.8	3.6	10.7	1.61E-04	0.931	2434	2.54E+06	36.52406	0.014	0.95	2.4E-06
LMLC	5-2	Childress	Type D	Granite	DC	0 months	5.8	3.5	10.7	1.61E-04	0.931	2292	8.25E+06	77.76292	0.047	1.43	1.62E-06
LMLC	6-1	Childress	Type D	Granite	DC	0 months	5.3	5.5	9.8	8.47E-05	0.952	914	X				
LMLC	6-2	Childress	Type D	Granite	DC	0 months	5.3	6.2	9.8	8.47E-05	0.952	1925	3.14E+07	37.00682	0.046	1.61	1.58E-07
LMLC	7-1	Childress	Type D	Granite	DC	0 months	5.3	9.4	9.8	1.12E-04	1.041	1755	X				
LMLC	7-2	Childress	Type D	Granite	DC	0 months	5.3	8.9	9.8	1.12E-04	1.041	1903	4.49E+07	35.68983	0.057	2.50	1.11E-08
LMLC	8-2	Childress	Type D	Granite	DC	6 months	4.8	9.4	8.8	3.14E-04	1.050	2917	4.81E+06	43.18342	0.067	0.90	1.33E-06
LMLC	8-4	Childress	Type D	Granite	DC	6 months	4.8	10.4	8.8	3.14E-04	1.050	3178	8.40E+05	48.09692	0.024	0.59	9.46E-06
LMLC	9-3	Childress	Type D	Granite	DC	6 months	4.8	6.1	8.8	3.52E-04	1.059	3362	1.55E+06	49.25861	0.047	0.36	1.18E-05
LMLC	9-4	Childress	Type D	Granite	DC	6 months	4.8	6.2	8.8	3.52E-04	1.059	4261	2.13E+06	49.40801	0.065	0.70	2.54E-06
LMLC	10-3	Childress	Type D	Granite	DC	6 months	5.8	3.3	10.7	1.96E-04	0.963	3418	9.28E+05	57.34431	0.034	0.46	1.36E-05
LMLC	10-4	Childress	Type D	Granite	DC	6 months	5.8	3.2	10.7	1.96E-04	0.963	2993	1.03E+06	49.36788	0.042	0.69	5.44E-06
LMLC	11-2	Childress	Type D	Granite	DC	6 months	5.8	6.5	10.7	2.66E-04	1.004	2770	3.36E+06	46.24532	0.050	0.52	4.8E-06
LMLC	11-4	Childress	Type D	Granite	DC	6 months	5.8	6.6	10.7	2.66E-04	1.004	2275	X				
LMLC	12-3	Childress	Type D	Granite	DC	6 months	5.3	11.6	9.8	2.27E-04	0.999	1976	3.12E+05	50.63069	0.039	1.41	1.8E-06
LMLC	12-4	Childress	Type D	Granite	DC	6 months	5.3	10.3	9.8	2.27E-04	0.999	2604	8.12E+05	43.52054	0.048	1.36	8.13E-07
LMLC	13-3	Childress	Type D	Granite	DC	6 months	5.3	3.3	9.8	2.97E-04	1.045	4694	1.30E+06	57.32339	0.012	0.30	1.71E-05
LMLC	13-4	Childress	Type D	Granite	DC	6 months	5.3	3.3	9.8	2.97E-04	1.045	3952	2.10E+06	46.2159	0.050	0.55	4.45E-06
LMLC	14-3	Childress	Type D	Granite	DC	6 months	5.3	6.0	9.8	1.82E-04	1.075	7551	3.12E+06	53.81675	0.067	0.60	2.47E-06

Type	Sample	SITE	Mix Type	Agg Material	Environmental Zone	Age	BINDER CONTENT	AV	FILM THICKNESS(microns)	DSR	CA	Eve	Nf	C'	b	n	A
LMLC	14-4	Childress	Type D	Granite	DC	6 months	5.3	5.7	9.8	1.82E-04	1.075	6772	X				
LMLC	15-1	Childress	Type D	Granite	DC	6 months	4.8	9.8	8.8	2.99E-04	1.177	4225	1.34E+06	46.88374	0.051	0.80	2.67E-06
LMLC	15-2	Childress	Type D	Granite	DC	6 months	4.8	9.1	8.8	2.99E-04	1.177	4335	9.79E+05	49.58525	0.043	0.82	3.44E-06
LMLC	16-1	Childress	Type D	Granite	DC	6 months	4.8	6.3	8.8	4.27E-04	1.191	5367	1.57E+06	51.38336	0.060	0.74	2.87E-06
LMLC	16-2	Childress	Type D	Granite	DC	6 months	4.8	6.0	8.8	4.27E-04	1.191	5753	3.13E+06	53.1364	0.073	0.49	3.43E-06
LMLC	17-1	Childress	Type D	Granite	DC	6 months	5.8	6.0	10.7	3.10E-04	1.092	3986	2.84E+06	48.15141	0.066	0.45	4.44E-06
LMLC	17-2	Childress	Type D	Granite	DC	6 months	5.8	6.2	10.7	3.10E-04	1.092	3864	1.89E+06	46.22996	0.065	0.69	2.83E-06
LMLC	18-1	Childress	Type D	Granite	DC	9 months	5.8	2.9	10.7	3.75E-04	1.055	5442	2.61E+06	51.21788	0.074	0.48	4.28E-06
LMLC	18-2	Childress	Type D	Granite	DC	9 months	5.8	3.4	10.7	3.75E-04	1.055	4950	5.49E+05	73.48294	0.024	0.67	1.04E-05
LMLC	19-1	Childress	Type D	Granite	DC	9 months	5.8	9.3	10.7	2.18E-04	1.085	2882	X				
LMLC	19-2	Childress	Type D	Granite	DC	9 months	5.8	8.7	10.7	2.18E-04	1.085	3182	6.55E+05	49.88993	0.051	1.03	2.53E-06
LMLC	20-1	Childress	Type D	Granite	DC	9 months	5.3	6.2	9.8	3.41E-04	1.049	4558	2.77E+06	47.61806	0.073	0.58	2.87E-06
LMLC	20-2	Childress	Type D	Granite	DC	9 months	5.3	6.1	9.8	3.41E-04	1.049	4354	2.18E+06	46.17195	0.050	0.51	4.57E-06
LMLC	21-1	Childress	Type D	Granite	DC	12 months	4.8	5.7	8.8	4.42E-04	1.146	6719	1.22E+06	69.40311	0.025	0.43	1.11E-05
LMLC	21-2	Childress	Type D	Granite	DC	12 months	4.8	6.2	8.8	4.42E-04	1.146	5965	1.49E+06	55.33776	0.046	0.55	5.84E-06
LMLC	22-1	Childress	Type D	Granite	DC	12 months	4.8	2.7	8.8	4.16E-04	1.183	7847	1.68E+06	61.88174	0.055	0.53	5.57E-06
LMLC	22-2	Childress	Type D	Granite	DC	12 months	4.8	2.8	8.8	4.16E-04	1.183	7173	7.18E+05	77.22677	0.015	0.44	1.81E-05
LMLC	23-1	Childress	Type D	Granite	DC	12 months	5.8	3.1	10.7	2.53E-04	1.042	5389	1.13E+06	54.86054	0.044	0.56	7.49E-06
LMLC	23-2	Childress	Type D	Granite	DC	12 months	5.8	2.9	10.7	2.53E-04	1.042	5266	9.12E+05	62.39656	0.023	0.45	1.35E-05
LMLC	24-1	Childress	Type D	Granite	DC	12 months	5.8	9.5	10.7	3.99E-04	1.129	3506	8.02E+05	52.83049	0.042	0.74	5.56E-06
LMLC	24-2	Childress	Type D	Granite	DC	12 months	5.8	9.6	10.7	3.99E-04	1.129	3375	1.40E+05	62.55021	0.006	0.67	4.02E-05
LMLC	25-1	Childress	Type D	Granite	DC	12 months	5.3	3.1	9.8	2.93E-04	1.038	5873	X				
LMLC	25-2	Childress	Type D	Granite	DC	12 months	5.3	2.6	9.8	2.93E-04	1.038	6408	3.64E+05	37.79129	0.010	0.87	7.71E-06
LMLC	26-1	Childress	Type D	Granite	DC	12 months	5.3	10.2	9.8	4.43E-04	1.154	2895	6.51E+05	47.58698	0.045	0.86	4.49E-06
LMLC	26-2	Childress	Type D	Granite	DC	12 months	5.3	10	9.8	4.43E-04	1.154	X					
LMLC	27-1	Childress	Type D	Granite	DC	12 months	5.3	5.8	9.8	4.21E-04	1.130	3614	2.11E+06	49.26609	0.061	0.54	4.23E-06
LMLC	27-2	Childress	Type D	Granite	DC	12 months	5.3	5.8	9.8	4.21E-04	1.130	3881	7.24E+05	43.78533	0.038	1.01	2.43E-06
LMLC	1-1	Paris	Type D	Sandstone	WC	0 months	4.9	3.7	6.6	2.47E-05	0.929	5069	1.12E+07	33.72654	0.088	0.82	2.51E-07
LMLC	1-2	Paris	Type D	Sandstone	WC	0 months	4.9	3.2	6.6	2.47E-05	0.929	5542	1.25E+07	35.93802	0.104	0.66	4.01E-07
LMLC	2-1	Paris	Type D	Sandstone	WC	0 months	4.9	9.8	6.6	6.04E-05	0.998	3059	3.39E+07	21.97238	0.138	0.80	9E-08
LMLC	2-2	Paris	Type D	Sandstone	WC	0 months	4.9	8.3	6.6	6.04E-05	0.998	2575	3.61E+07	22.04822	0.108	0.76	9.64E-08
LMLC	3-1	Paris	Type D	Sandstone	WC	0 months	5.9	6.7	8.2	3.63E-05	1.015	2979	1.25E+07	33.20636	0.080	1.17	6.43E-08
LMLC	3-2	Paris	Type D	Sandstone	WC	0 months	5.9	6.2	8.2	3.63E-05	1.015	3032	5.14E+07	27.01675	0.088	0.94	1.04E-07
LMLC	4-1	Paris	Type D	Sandstone	WC	0 months	5.9	9.3	8.2	5.44E-05	1.028	2111	2.13E+07	22.81119	0.065	1.06	5.54E-08
LMLC	4-2	Paris	Type D	Sandstone	WC	0 months	5.9	9.3	8.2	5.44E-05	1.028	2086	2.01E+07	21.96087	0.070	1.05	6.15E-08
LMLC	5-1	Paris	Type D	Sandstone	WC	0 months	5.9	3.3	8.2	2.58E-05	1.007	4131	2.39E+07	31.22665	0.112	1.19	3.16E-08
LMLC	5-2	Paris	Type D	Sandstone	WC	0 months	5.9	3.4	8.2	2.58E-05	1.007	3835	1.60E+07	31.34512	0.119	0.63	3.55E-07
LMLC	6-1	Paris	Type D	Sandstone	WC	0 months	5.4	6.3	7.4	3.84E-05	1.020	2647	1.09E+07	26.68883	0.065	0.96	1.55E-07
LMLC	6-2	Paris	Type D	Sandstone	WC	0 months	5.4	6.4	7.4	3.84E-05	1.020	3063	1.12E+07	34.86631	0.075	1.32	4.28E-08
LMLC	7-1	Paris	Type D	Sandstone	WC	0 months	5.4	10.0	7.4	3.41E-05	1.004	2267	3.11E+07	29.47267	0.084	1.64	5.51E-09
LMLC	7-2	Paris	Type D	Sandstone	WC	0 months	5.4	9.9	7.4	3.41E-05	1.004	2075	3.61E+08	26.77556	0.091	2.44	4.24E-11
LMLC	8-1	Paris	Type D	Sandstone	WC	6 months	4.9	10.7	6.6	4.95E-04	1.273	4993	2.39E+06	41.71475	0.063	0.87	1.19E-06
LMLC	8-2	Paris	Type D	Sandstone	WC	6 months	4.9	10.6	6.6	4.95E-04	1.273	4615	7.44E+05	46.73445	0.014	0.65	8.21E-06
LMLC	9-1	Paris	Type D	Sandstone	WC	6 months	4.9	6.9	6.6	6.46E-04	1.349	6190	7.49E+05	59.21312	0.048	1.02	2.33E-06

Type	Sample	SITE	Mix Type	Agg Material	Environmental Zone	Age	BINDER CONTENT	AV	FILM THICKNESS(microns)	DSR	CA	Eve	Nf	C'	b	n	A
LMLC	9-2	Paris	Type D	Sandstone	WC	6 months	4.9	7.4	6.6	6.46E-04	1.349	5740	1.22E+07	34.76021	0.135	0.96	1.7E-07
LMLC	10-1	Paris	Type D	Sandstone	WC	6 months	5.9	3.2	8.2	2.47E-04	1.129	6488	5.56E+06	43.88704	0.107	0.66	1.06E-06
LMLC	10-2	Paris	Type D	Sandstone	WC	6 months	5.9	3.5	8.2	2.47E-04	1.129	7337	2.71E+06	58.75023	0.072	0.47	4.26E-06
LMLC	11-1	Paris	Type D	Sandstone	WC	6 months	5.9	7.2	8.2	5.52E-04	x	4930	2.76E+06	45.19486	0.078	0.84	1.15E-06
LMLC	11-2	Paris	Type D	Sandstone	WC	6 months	5.9	7.0	8.2	5.52E-04	x	4639	2.64E+06	45.58513	0.078	0.81	1.33E-06
LMLC	12-1	Paris	Type D	Sandstone	WC	6 months	5.4	9.7	7.4	4.26E-04	1.238	4510	1.74E+06	42.20601	0.054	1.15	6.51E-07
LMLC	12-2	Paris	Type D	Sandstone	WC	6 months	5.4	9.8	7.4	4.26E-04	1.238	4076	6.48E+06	34.1768	0.099	0.72	7.26E-07
LMLC	13-1	Paris	Type D	Sandstone	WC	6 months	5.4	3.1	7.4	1.03E-03	1.199	6912	1.23E+06	55.64045	0.040	0.69	4.23E-06
LMLC	13-2	Paris	Type D	Sandstone	WC	6 months	5.4	3.3	7.4	1.03E-03	1.199	7412	3.90E+06	43.33617	0.082	0.66	1.51E-06
LMLC	14-1	Paris	Type D	Sandstone	WC	6 months	5.4	7.4	7.4	1.42E-03	1.206	6957	3.18E+06	48.14795	0.080	0.96	6.63E-07
LMLC	14-2	Paris	Type D	Sandstone	WC	6 months	5.4	7.6	7.4	1.42E-03	1.206	6482	8.29E+05	58.14189	0.036	0.77	4.84E-06
LMLC	15-1	Paris	Type D	Sandstone	WC	6 months	4.9	9.1	6.6	1.43E-03	1.428	5909	1.30E+06	61.89397	0.057	0.82	2.73E-06
LMLC	15-2	Paris	Type D	Sandstone	WC	6 months	4.9	10.4	6.6	1.43E-03	1.428	4824	2.85E+06	41.96111	0.070	0.90	9.24E-07
LMLC	16-1	Paris	Type D	Sandstone	WC	6 months	4.9	7.4	6.6	1.04E-03	1.454	6536	2.30E+06	48.3096	0.078	1.04	7.35E-07
LMLC	16-2	Paris	Type D	Sandstone	WC	6 months	4.9	7.3	6.6	1.04E-03	1.454	6105	3.10E+06	48.50694	0.075	1.02	5.79E-07
LMLC	17-1	Paris	Type D	Sandstone	WC	6 months	5.9	7.1	8.2	5.45E-04	1.371	5412	3.10E+06	50.14379	0.076	0.87	9.61E-07
LMLC	17-2	Paris	Type D	Sandstone	WC	6 months	5.9	7.0	8.2	5.45E-04	1.371	5722	4.55E+06	44.24976	0.093	0.72	1.09E-06
LMLC	18-1	Paris	Type D	Sandstone	WC	9 months	5.9	3.4	8.2	8.26E-04	1.485	8459	1.16E+06	75.75904	0.048	0.58	7E-06
LMLC	18-2	Paris	Type D	Sandstone	WC	9 months	5.9	3.8	8.2	8.26E-04	1.485	X					
LMLC	19-1	Paris	Type D	Sandstone	WC	9 months	5.9	10.2	8.2	6.98E-04	1.431	5342	5.86E+06	41.69641	0.109	0.65	1.07E-06
LMLC	19-2	Paris	Type D	Sandstone	WC	9 months	5.9	9.6	8.2	6.98E-04	1.431	5066	4.47E+06	42.63889	0.105	0.81	8.02E-07
LMLC	20-1	Paris	Type D	Sandstone	WC	9 months	5.4	8.5	7.4	5.67E-04	1.264	6430	3.45E+06	52.64324	0.059	0.58	2.02E-06
LMLC	20-2	Paris	Type D	Sandstone	WC	9 months	5.4	7.0	7.4	5.67E-04	1.264	5627	4.28E+06	41.52715	0.079	0.58	1.88E-06
LMLC	21-1	Paris	Type D	Sandstone	WC	12 months	4.9	6.8	6.6	4.56E-04	1.423	7239	7.21E+06	47.11647	0.088	0.64	7.64E-07
LMLC	21-2	Paris	Type D	Sandstone	WC	12 months	4.9	6.7	6.6	4.56E-04	1.423	7018	1.18E+07	43.84982	0.107	1.06	9.99E-08
LMLC	22-1	Paris	Type D	Sandstone	WC	12 months	4.9	3.4	8.2	8.29E-04	1.444	10023	3.66E+06	63.58981	0.066	0.60	1.75E-06
LMLC	22-2	Paris	Type D	Sandstone	WC	12 months	4.9	3.9	8.2	8.29E-04	1.444	9790	7.75E+06	54.60435	0.109	0.54	1.02E-06
LMLC	23-1	Paris	Type D	Sandstone	WC	12 months	5.9	2.9	8.2	3.39E-04	1.334	9020	5.03E+06	63.93066	0.101	0.77	6.59E-07
LMLC	23-2	Paris	Type D	Sandstone	WC	12 months	5.9	3.2	8.2	3.39E-04	1.334	8098	5.54E+06	58.46025	0.112	0.76	6.23E-07
LMLC	24-1	Paris	Type D	Sandstone	WC	12 months	5.9	10.5	8.2	9.74E-04	1.372	4693	5.03E+06	44.72942	0.084	0.73	7.62E-07
LMLC	24-2	Paris	Type D	Sandstone	WC	12 months	5.9	9.9	8.2	9.74E-04	1.372	4524	6.78E+06	45.32081	0.102	0.85	3.66E-07
LMLC	25-1	Paris	Type D	Sandstone	WC	12 months	5.4	3.9	7.4	9.18E-04	1.378	8897	2.79E+06	71.01786	0.082	1.24	2.28E-07
LMLC	25-2	Paris	Type D	Sandstone	WC	12 months	5.4	3.8	7.4	9.18E-04	1.378	9322	5.45E+06	52.69794	0.095	0.53	1.53E-06
LMLC	26-1	Paris	Type D	Sandstone	WC	12 months	5.4	10.8	7.4	8.42E-04	x	4634	3.42E+06	48.46652	0.069	1.22	1.98E-07
LMLC	26-2	Paris	Type D	Sandstone	WC	12 months	5.4	9.9	7.4	8.42E-04	x	4929	X				
LMLC	27-1	Paris	Type D	Sandstone	WC	12 months	5.4	7.5	7.4	9.20E-04	1.417	6717	7.90E+06	45.4426	0.103	0.67	6.07E-07
LMLC	27-2	Paris	Type D	Sandstone	WC	12 months	5.4	7.4	7.4	9.20E-04	1.417	5858	5.23E+06	46.72698	0.077	0.60	1.19E-06

APPENDIX H

TABLES OF HMAC FIELD SAMPLE MIXTURE PROPERTY DATA

Table H1. HMAC Field Sample Mixture Property Data.

ID	Sample	Construction Date	Mix Type	Agg Material	Environmental Zone	% Binder (Design)	%AV	E_{VE}	A	n	b	c_0	d (mm)	γ	N_f	c_{1000} (mm)
01A	US-290 RWP 1-1	2002	Type C	Limestone	M	4.40%	13.52	4131	3.59E-07	1.31	0.042	6.44E-04	51	1.98E-02	22,57	24.8
01B	US-290 RWP 1-2B	2002	Type C	Limestone	M	4.40%	13.56	4996	5.81E-06	0.73	0.0199	6.78E-04	51	1.98E-02	57,55	30.2
01C	US-290 RWP 1-5	2002	Type C	Limestone	M	4.40%	13.92	10409	Bad Data	Bad Data	Bad Data	Bad Data	51	1.98E-02	Bad Data	Bad Data
01A	US-290 RWP 3-1	2002	Type C	Limestone	M	4.40%	5.17	3881	7.47E-07	0.79	0.0531	6.29E-04	51	1.98E-02	369,63	24.7
01A	US-290 RWP 3-2	2002	Type C	Limestone	M	4.40%	6.81	5152	1.60E-07	1.03	0.0747	4.29E-04	51	1.98E-02	266,97	16.6
01D	US-290 WBS 1-1	2002	Type C	Limestone	M	4.40%	9.16	5550	1.95E-16	4.37	0.2793	3.95E-04	51	1.98E-02	95,86	16.4
01D	US-290 WBS 3-1	2002	Type C	Limestone	M	4.40%	9.28	4727	3.55E-07	0.7	0.1217	3.36E-04	51	1.98E-02	1,169,77	11.5
01D	US-290 WBS 3-3	2002	Type C	Limestone	M	4.40%	10.25	4597	2.15E-07	0.65	0.1339	2.63E-04	51	1.98E-02	2,557,97	7.2
02A	IH-20 RWP 1-1	2001	12.5 mm Sp	Sandstone	WC	4.40%	10.83	7560	Fail	Fail	Fail	Fail	64	1.47E-04	Fail	Fail
02B	IH-20 RWP 1-5	2001	12.5 mm Sp	Sandstone	WC	4.40%	9.60	6538	4.66E-06	0.15	0.1449	3.47E-04	64	1.47E-04	8,264,05	10.5
02C	IH-20 RWP 1-6	2001	12.5 mm Sp	Sandstone	WC	4.40%	8.75	7793	1.02E-06	0.61	0.0679	1.66E-04	64	1.47E-04	10,840,33	8.9
02D	IH-20 WBS 1-1	2001	12.5 mm Sp	Sandstone	WC	4.40%	12.38	3439	2.55E-07	1.04	0.0256	1.29E-04	64	1.47E-04	20,614,38	5.0
02E	IH-20 WBS 1-3	2001	12.5 mm Sp	Sandstone	WC	4.40%	10.07	6072	8.97E-07	0.74	0.0608	3.95E-04	64	1.47E-04	11,836,79	15.4
02F	IH-20 WBS 1-5	2001	12.5 mm Sp	Sandstone	WC	4.40%	11.12	6121	1.08E-06	0.73	0.0687	2.69E-04	64	1.47E-04	9,655,36	13.4
02E	IH-20 WBS 3-3	2001	12.5 mm Sp	Sandstone	WC	4.40%	12.51	9566	1.16E-07	1	0.1316	1.89E-04	64	1.47E-04	30,433,72	8.2
02E	IH-20 WBS 3-4	2001	12.5 mm Sp	Sandstone	WC	4.40%	10.34	9324	1.91E-06	0.41	0.1143	3.59E-04	64	1.47E-04	9,288,42	13.1
02E	IH-20 WBS 3-5	2001	12.5 mm Sp	Sandstone	WC	4.40%	13.86	7622	6.26E-07	0.74	0.1156	1.85E-04	64	1.47E-04	12,359,29	9.6
03A	IH-35 RWP 1-2	2003	19 mm SP	Igneous (granite?)/LS	M	5.30%	5.393	7329	9.81E-07	0.78	0.0722	3.32E-04	89	1.73E-05	69,850,21	16.8
03B	IH-35 RWP 1-3	2003	19 mm SP	Igneous (granite?)/LS	M	5.30%	3.526	4826	1.36E-06	0.72	0.0429	6.22E-04	89	1.73E-05	78,684,27	24.8
03A	IH-35 LWP 3-1	2003	19 mm SP	Igneous (granite?)/LS	M	5.30%	6.093	3771	1.66E-06	0.83	0.0448	6.09E-04	89	1.73E-05	85,437,82	26.2
03B	IH-35 LWP 3-2	2003	19 mm SP	Igneous (granite?)/LS	M	5.30%	9.553	4685	1.19E-06	0.99	0.0667	7.80E-04	89	1.73E-05	98,157,05	32.3
04A	SH-59 SBS 1-1	2007	Type D	Limestone	DC	4.90%	8.96	3864	5.90E-07	0.65	0.018	4.70E-04	57	2.19E-04	20,224,85	8.8
04B	SH-59 SBS 1-2	2007	Type D	Limestone	DC	4.90%	8.46	3760	1.68E-06	0.69	0.0117	2.41E-04	57	2.19E-04	6,827,68	9.3
04B	SH-59 SBS 1-3	2007	Type D	Limestone	DC	4.90%	8.4	5860	5.36E-07	0.72	0.0916	4.96E-04	57	2.19E-04	15,836,80	17.0
04A	SH-59 SBS 3-1	2007	Type D	Limestone	DC	4.90%	15.45	6791.76	1.67E-06	0.55	0.0911	3.06E-04	57	2.19E-04	6,395,23	13.0
04B	SH-59 SBS 3-3	2007	Type D	Limestone	DC	4.90%	9.03	6705.14	4.26E-06	0.69	0.0372	4.43E-04	57	2.19E-04	1,863,52	2.7
04C	SH-59 RWP 1-1	2007	Type D	Limestone	DC	4.90%	7.63	Fail	Fail	Fail	Fail	Fail	57	2.19E-04	Fail	Fail
04D	SH-59 RWP 1-3	2007	Type D	Limestone	DC	4.90%	8.59	Fail	Fail	Fail	Fail	Fail	57	2.19E-04	Fail	Fail
04C	SH-59 RWP 1-5	2007	Type D	Limestone	DC	4.90%	8.10	6451	1.74E-06	0.57	0.0735	2.69E-04	57	2.19E-04	6,523,15	12.3
04C	SH-59 RWP 1-6	2007	Type D	Limestone	DC	4.90%	7.84	6837	1.75E-06	0.77	0.0633	4.42E-04	57	2.19E-04	3,882,60	21.1
04E	SH-59 RWP 3-1	2007	Type D	Limestone	DC	4.90%	8.02	5477	2.63E-06	0.63	0.0524	3.96E-04	57	2.19E-04	3,929,15	18.5
04F	SH-59 RWP 3-3	2007	Type D	Limestone	DC	4.90%	7.79	7926	1.49E-06	0.65	0.0776	3.18E-04	57	2.19E-04	4,894,57	14.6
05B	IH-35 SBS 1-5 Layer 3	2007	25 mm SFHMAC	Taprock/River Gravel	DW	4.40%	3.27	3575	5.77E-07	0.85	0.0618	3.52E-04	152	5.06E-05	154,335,15	13.1
05A	IH-35 SBS 1-3 Layer 3	2007	25 mm SFHMAC	Taprock/River Gravel	DW	4.40%	3.62	4191	3.70E-07	1.06	0.0679	5.90E-04	152	5.06E-05	205,429,05	21.2
05A	IH-35 SBS 3-2 Layer 3	2007	25 mm SFHMAC	Taprock/River Gravel	DW	4.40%	3.16	3850	2.36E-07	0.78	0.1151	2.81E-04	152	5.06E-05	398,818,81	9.1
05A	IH-35 SBS 3-5 Layer 3	2007	25 mm SFHMAC	Taprock/River Gravel	DW	4.40%	3.32	3821	8.88E-06	0.58	0.0156	6.26E-04	152	5.06E-05	11,223,82	28.4
05A	IH-35 RWP 3-3 Layer 3	2007	25 mm SFHMAC	Taprock/River Gravel	DW	4.40%	7.00	4580	8.52E-06	0.74	0.0216	5.46E-04	152	5.06E-05	9,393,99	25.7
05A	IH-35 RWP 3-5 Layer 3	2007	25 mm SFHMAC	Taprock/River Gravel	DW	4.40%	7.05	4378	3.28E-06	0.69	0.0564	9.72E-04	152	5.06E-05	25,093,17	30.7
06A	IH-35 SBS 1-1 Layer 4	2007	12.5 mm Sp	River Gravel	DW	5.90%	3.55	2200	5.76E-07	0.37	0.1488	9.91E-04	64	1.16E-03	31,173,26	12.5
06B	IH-35 SBS 1-3 Layer 4	2007	12.5 mm Sp	River Gravel	DW	5.90%	2.52	1617	4.29E-07	0.19	0.3265	7.71E-04	64	1.16E-03	73,504,26	4.2
06A	IH-35 SBS 3-4 Layer 4	2007	12.5 mm Sp	River Gravel	DW	5.90%	4.00	1623	3.25E-08	1.68	0.0795	2.21E-03	64	1.16E-03	50,815,64	94.0
06A	IH-35 SBS 3-6 Layer 4	2007	12.5 mm Sp	River Gravel	DW	5.90%	1.56	1846	1.11E-08	1.82	0.0582	2.09E-03	64	1.16E-03	85,897,93	105.0
06A	IH-35 RWP 3-3 Layer 4	2007	12.5 mm Sp	River Gravel	DW	5.90%	4.64	1859	1.64E-08	1.76	0.1077	2.45E-03	64	1.16E-03	48,266,08	102.0
06A	IH-35 RWP 3-6 Layer 4	2007	12.5 mm Sp	River Gravel	DW	5.90%	4.98	1500	8.94E-08	1.09	0.0742	8.90E-04	64	1.16E-03	41,105,75	26.3
07A	US-69 SBS 3-1	2003	Type-C	River Gravel	WW	4.30%	14.53	6810	4.05E-06	0.71	0.049	4.99E-04	51	1.63E-04	1,889,76	27.0
07A	US-69 SBS 3-2	2003	Type-C	River Gravel	WW	4.30%	13.29	6553	2.90E-06	0.79	0.0314	5.17E-04	51	1.63E-04	2,295,51	23.7

ID	Sample	Construction Date	Mix Type	Agg Material	Environmental Zone	% Binder (Design)	%AV	E_{VE}	A	n	b	c_0	d (mm)	γ	N_f	c_{1000} (mm)
07A	US-69 RWP 1-1	2003	Type-C	River Gravel	WW	4.30%	9.08	Fail	Fail	Fail	Fail	Fail	51	1.63E-04	Fail	Fail
07B	US-69 RWP 1-3	2003	Type-C	River Gravel	WW	4.30%	8.65	6208	5.59E-06	0.19	0.034	1.05E-04	51	1.63E-04	4,784,34	8.5
07B	US-69 RWP 1-5	2003	Type-C	River Gravel	WW	4.30%	9.25	7308	1.64E-05	0.12	0.0151	9.56E-04	51	1.63E-04	1,939,16	25.4
07B	US-69 RWP 3-1	2003	Type-C	River Gravel	WW	4.30%	12.27	4454	7.65E-05	0.67	0.0142	1.26E-03	51	1.63E-04	142,68	114.0
07A	US-69 RWP 3-2	2003	Type-C	River Gravel	WW	4.30%	13.20	5564	Fail	Fail	Fail	Fail	51	1.63E-04	Fail	Fail
07A	US-69 RWP 3-3	2003	Type-C	River Gravel	WW	4.30%	12.53	4026	1.71E-05	1.04	0.1057	1.83E-03	51	1.63E-04	290,97	188.0
07B	US-69 RWP 3-6	2003	Type-C	River Gravel	WW	4.30%	14.49	2387	Bad Data	Bad Data	Bad Data	Bad Data	51	1.63E-04	Bad Data	Bad Data
08A	FM-649 RWP 1-3	2006	Type C	Limestone	DW	4.90%	10.84	7065	2.27E-06	0.42	0.0857	3.87E-04	51	1.69E-04	6,456,29	14.2

ID	Sample	Construction Date	Mix Type	Agg Material	Environmental Zone	% Binder (Design)	%AV	E_{VE}	A	n	b	c_0	d (mm)	γ	N_f	c_{1000} (mm)
08B	FM-649 RWP 1-4	2006	Type C	Limestone	DW	4.90%	11.06	7363	1.03E-05	0.39	0.0525	2.53E-04	51	1.69E-04	1,489,046	22.8
08B	FM-649 RWP 3-1	2006	Type C	Limestone	DW	4.90%	11.22	7142	Fail	Fail	Fail	Fail	51	1.69E-04	Fail	Fail
08B	FM-649 RWP 3-3	2006	Type C	Limestone	DW	4.90%	10.34	7121	Fail	Fail	Fail	Fail	51	1.69E-04	Fail	Fail
08B	FM-649 RWP 3-8T	2006	Type C	Limestone	DW	4.90%	12.07	7806	5.07E-06	0.8	0.0888	3.55E-04	51	1.69E-04	1,018,993	33.2
08B	FM-649 RWP 3-9T	2006	Type C	Limestone	DW	4.90%	12.42	6623	1.96E-06	0.64	0.0685	3.28E-04	51	1.69E-04	4,164,607	16.6
08C	FM-649 SBS 1-1	2006	Type C	Limestone	DW	4.90%	14.51	4340	2.44E-06	0.94	0.0922	8.57E-04	51	1.69E-04	2,183,519	32.2
08D	FM-649 SBS 1-3	2006	Type C	Limestone	DW	4.90%	14.05	4828	1.35E-06	2.48	0.0682	3.02E-04	51	1.69E-04	480,247	36.9
08D	FM-649 SBS 3-4	2006	Type C	Limestone	DW	4.90%	14.54	3698	Fail	Fail	Fail	Fail	51	1.69E-04	Fail	Fail
08D	FM-649 SBS 3-1	2006	Type C	Limestone	DW	4.90%	14.59	4550	1.29E-07	2.18	0.0135	4.66E-04	51	1.69E-04	6,662,116	16.1
08D	FM-649 SBS 3-6	2006	Type C	Limestone	DW	4.90%	14.61	4636	1.59E-05	0.14	0.0291	7.11E-04	51	1.69E-04	1,948,838	25.0
08D	FM-649 SBS 3-9T	2006	Type C	Limestone	DW	4.90%	16.02	5725	4.68E-06	0.72	0.033	5.43E-04	51	1.69E-04	1,766,075	26.6
08D	FM-649 SBS 3-10T	2006	Type C	Limestone	DW	4.90%	17.40	5645	1.86E-06	0.96	0.0469	5.67E-04	51	1.69E-04	2,341,580	26.2
09A	US-277 NBS 1-4	2008	Type C	Limestone w/TR Screenin	DW	4.50%	14.09	4407	Fail	Fail	Fail	Fail	76	2.62E-04	Fail	Fail
09B	US-277 NBS 1-5	2008	Type C	Limestone w/TR Screenin	DW	4.50%	7.39	4928	1.04E-06	0.89	0.0493	3.75E-04	76	2.62E-04	7,178,420	16.9
09C	US-277 NBS 1-6	2008	Type C	Limestone w/TR Screenin	DW	4.50%	9.45	4176	3.05E-06	0.89	0.0185	5.13E-04	76	2.62E-04	3,727,742	20.7
09D	US-277 NBS 2-1	2008	Type C	Limestone w/TR Screenin	DW	4.50%	8.50	4808	1.60E-06	0.74	0.0484	2.81E-04	76	2.62E-04	6,359,171	13.4
09E	US-277 NBS 2-3	2008	Type C	Limestone w/TR Screenin	DW	4.50%	6.93	6996	5.94E-08	1.63	0.0614	4.83E-04	76	2.62E-04	29,422,860	19.9
09F	US-277 NBS 3-1	2008	Type C	Limestone w/TR Screenin	DW	4.50%	7.65	6124	1.99E-06	0.7	0.0521	4.24E-04	76	2.62E-04	4,423,111	18.8
09G	US-277 NBS 3-3	2008	Type C	Limestone w/TR Screenin	DW	4.50%	7.54	4903	5.74E-06	0.66	0.0304	4.71E-04	76	2.62E-04	1,958,172	25.9
09H	US-277 NBS 4-2	2008	Type C	Limestone w/TR Screenin	DW	4.50%	7.33	5604	1.30E-06	0.34	0.2324	1.60E-04	76	2.62E-04	19,949,595	6.8
09I	US-277 NBS 4-3	2008	Type C	Limestone w/TR Screenin	DW	4.50%	6.74	5045	4.45E-06	0.85	0.0483	8.57E-04	76	2.62E-04	1,710,537	48.0
09J	US-277 NBS 4-4	2008	Type C	Limestone w/TR Screenin	DW	4.50%	8.18	4495	Fail	Fail	Fail	Fail	76	2.62E-04	Fail	Fail
09K	US-277 RWP 1-2	2008	Type C	Limestone w/TR Screenin	DW	4.50%	7.21	4459	3.58E-07	0.76	0.082	4.13E-04	76	2.62E-04	33,058,788	11.9
09L	US-277 RWP 1-5	2008	Type C	Limestone w/TR Screenin	DW	4.50%	7.17	4462	2.13E-07	0.88	0.1053	3.70E-04	76	2.62E-04	40,409,783	12.1
09M	US-277 RWP 2-1	2008	Type C	Limestone w/TR Screenin	DW	4.50%	8.50	6774	1.05E-06	0.86	0.0181	4.16E-04	76	2.62E-04	6,107,310	12.2
09N	US-277 RWP 2-3	2008	Type C	Limestone w/TR Screenin	DW	4.50%	7.34	4779	3.88E-06	0.64	0.0196	2.49E-04	76	2.62E-04	3,496,300	13.2
09O	US-277 RWP 2-1T	2008	Type C	Limestone w/TR Screenin	DW	4.50%	8.91	6959	6.83E-07	0.84	0.0757	4.51E-04	76	2.62E-04	11,510,043	16.7
09P	US-277 RWP 2-3T	2008	Type C	Limestone w/TR Screenin	DW	4.50%	7.89	5395	9.60E-07	0.86	0.0542	3.92E-04	76	2.62E-04	8,020,581	16.5
09Q	US-277 RWP 3-1	2008	Type C	Limestone w/TR Screenin	DW	4.50%	6.83	5469	2.23E-05	0.49	0.0022	4.71E-04	76	2.62E-04	835,637	22.6
09R	US-277 RWP 3-3	2008	Type C	Limestone w/TR Screenin	DW	4.50%	7.00	5540	1.68E-05	0.47	0.0046	4.71E-04	76	2.62E-04	1,111,482	23.2
09S	US-277 RWP 3-1T	2008	Type C	Limestone w/TR Screenin	DW	4.50%	9.29	4959	3.28E-06	0.73	0.0307	4.15E-04	76	2.62E-04	3,195,317	19.0
09T	US-277 RWP 3-2T	2008	Type C	Limestone w/TR Screenin	DW	4.50%	8.52	6840	1.14E-06	0.65	0.0583	4.12E-04	76	2.62E-04	9,695,098	13.7
09U	US-277 RWP 4-1	2008	Type C	Limestone w/TR Screenin	DW	4.50%	7.11	5065	3.86E-06	0.74	0.0294	7.05E-04	76	2.62E-04	2,739,725	30.1
09V	US-277 RWP 4-3	2008	Type C	Limestone w/TR Screenin	DW	4.50%	7.12	5686	9.13E-06	0.73	0.0415	5.62E-04	76	2.62E-04	1,012,094	40.9
09W	US-277 RWP 4-1T	2008	Type C	Limestone w/TR Screenin	DW	4.50%	8.75	5505	1.65E-06	0.98	0.0378	4.86E-04	76	2.62E-04	3,124,829	22.4
09F	US-277 RWP 4-4T	2008	Type C	Limestone w/TR Screenin	DW	4.50%	8.73	5022	1.20E-06	0.76	0.0639	5.57E-04	76	2.62E-04	8,101,370	20.1
10A	US-259 NBS 1-2(TYL)	2007	Type C	Sandstone/Limestone	WC	4.30%	5.86	4022	1.36E-07	1.97	0.0027	6.53E-04	51	2.43E-04	5,778,520	14.8
10B	US-259 NBS 3-1(TYL)	2007	Type C	Sandstone/Limestone	WC	4.30%	5.99	8163	1.16E-06	0.65	0.0744	4.06E-04	51	2.43E-04	6,254,499	19.0
10B	US-259 NBS 3-2(TYL)	2007	Type C	Sandstone/Limestone	WC	4.30%	5.92	6952	2.83E-07	0.88	0.0962	2.81E-04	51	2.43E-04	15,702,923	13.8
10C	US-259 NBS 3-6(TYL)	2007	Type C	Sandstone/Limestone	WC	4.30%	6.10	8268	1.16E-06	0.68	0.0793	4.53E-04	51	2.43E-04	5,139,303	21.7
10D	US-259 NBS 3-7T(TYL)	2007	Type C	Sandstone/Limestone	WC	4.30%	7.50	7302	5.74E-07	0.52	0.1411	2.03E-04	51	2.43E-04	18,269,304	8.0
10E	US-259 NBS 3-12T(TYL)	2007	Type C	Sandstone/Limestone	WC	4.30%	7.29	7509	1.90E-07	1	0.1081	2.91E-04	51	2.43E-04	18,946,121	14.3
10F	US-259 RWP 1-5(TYL)	2007	Type C	Sandstone/Limestone	WC	4.30%	6.47	7430	1.06E-06	0.22	0.1809	2.72E-04	51	2.43E-04	21,413,167	5.0
10G	US-259 RWP 1-6(TYL)	2007	Type C	Sandstone/Limestone	WC	4.30%	6.53	6430	3.77E-07	0.44	0.3777	7.03E-04	51	2.43E-04	37,100,239	12.3
10G	US-259 RWP 3-4(TYL)	2007	Type C	Sandstone/Limestone	WC	4.30%	7.59	10742	2.07E-05	0.47	0.0176	5.45E-04	51	2.43E-04	406,382	43.0
10G	US-259 RWP 3-5(TYL)	2007	Type C	Sandstone/Limestone	WC	4.30%	6.99	10149	Fail	Fail	Fail	Fail	51	2.43E-04	Fail	Fail
10B	US-259 RWP 3-6(TYL)	2007	Type C	Sandstone/Limestone	WC	4.30%	7.48	8537	6.04E-06	0.75	0.0146	5.25E-04	51	2.43E-04	789,896	29.0
10H	US-259 RWP 3-7T(TYL)	2007	Type C	Sandstone/Limestone	WC	4.30%	8.68	8258	5.72E-06	0.65	0.0209	5.20E-04	51	2.43E-04	1,157,493	27.4
10G	US-259 RWP 3-8T(TYL)	2007	Type C	Sandstone/Limestone	WC	4.30%	7.57	8580	Fail	Fail	Fail	Fail	51	2.43E-04	Fail	Fail
10B	US-259 RWP 3-9T(TYL)	2007	Type C	Sandstone/Limestone	WC	4.30%	6.95	8256	1.16E-05	0.29	0.0372	5.66E-04	51	2.43E-04	1,509,203	30.0
11A	US-82 EBS 1-1	2008	CMHB-F	Limestone	DC	6.20%	9.25	7349	2.55E-06	0.63	0.0621	1.86E-04	64	2.34E-04	3,448,108	14.1

ID	Sample	Construction Date	Mix Type	Agg Material	Environmental Zone	% Binder (Design)	%AV	E_{VE}	A	n	b	c_0	d (mm)	γ	N_f	c_{1000} (mm)
11B	US-82 EBS 1-5	2008	CMHB-F	Limestone	DC	6.20%	8.60	4826	1.31E-06	0.21	0.3713	6.76E-04	64	2.34E-04	24,736,308	8.0
11C	US-82 EBS 1-6	2008	CMHB-F	Limestone	DC	6.20%	10.08	6190	1.28E-05	0.71	0.0172	4.22E-04	64	2.34E-04	656,940	32.3
11D	US-82 EBS 2-4	2008	CMHB-F	Limestone	DC	6.20%	8.40	6530	1.41E-06	0.54	0.0885	2.65E-04	64	2.34E-04	9,317,740	12.8
11E	US-82 EBS 2-5	2008	CMHB-F	Limestone	DC	6.20%	7.32	6144	4.93E-06	0.37	0.0425	3.25E-04	64	2.34E-04	4,227,926	17.1
11F	US-82 EBS 2-1T	2008	CMHB-F	Limestone	DC	6.20%	11.16	2334	9.49E-07	0.93	0.0407	5.68E-04	64	2.34E-04	12,339,511	22.3
11G	US-82 EBS 2-4T	2008	CMHB-F	Limestone	DC	6.20%	7.98	5637	8.46E-07	0.60	0.0871	3.74E-04	64	2.34E-04	13,535,877	13.9
11H	US-82 EBS 3-4	2008	CMHB-F	Limestone	DC	6.20%	7.98	7625	6.29E-07	1.45	0.0825	3.58E-06	64	2.34E-04	1,678,192	26.8
11I	US-82 EBS 3-5	2008	CMHB-F	Limestone	DC	6.20%	6.31	7917	3.77E-06	0.48	0.0782	2.90E-04	64	2.34E-04	3,505,238	17.7
11J	US-82 EBS 3-5T	2008	CMHB-F	Limestone	DC	6.20%	7.35	6359	1.25E-06	0.62	0.0971	2.56E-04	64	2.34E-04	9,015,754	12.4
11K	US-82 EBS 3-6T	2008	CMHB-F	Limestone	DC	6.20%	7.18	5875	2.84E-06	0.62	0.1215	2.87E-04	64	2.34E-04	4,143,432	20.5
11L	US-82 EBS 4-1	2008	CMHB-F	Limestone	DC	6.20%	8.34	7133	1.73E-05	0.15	0.0483	3.11E-04	64	2.34E-04	2,064,751	25.3
11M	US-82 EBS 4-2	2008	CMHB-F	Limestone	DC	6.20%	7.99	7522	7.27E-06	0.44	0.0465	3.32E-04	64	2.34E-04	2,162,148	23.8
11N	US-82 EBS 4-6T	2008	CMHB-F	Limestone	DC	6.20%	7.39	6679	9.00E-06	0.73	0.0294	5.02E-04	64	2.34E-04	845,261	40.3
11O	US-82 EBS 4-7T	2008	CMHB-F	Limestone	DC	6.20%	8.48	6659	3.02E-06	1.06	0.0492	3.19E-04	64	2.34E-04	1,424,177	29.2
11P	US-82 RWP 1-1	2008	CMHB-F	Limestone	DC	6.20%	8.76	6900	2.17E-07	0.91	0.1241	6.53E-04	64	2.34E-04	24,481,434	21.9
11Q	US-82 RWP 1-2	2008	CMHB-F	Limestone	DC	6.20%	7.27	8170	7.62E-07	0.92	0.0567	3.60E-04	64	2.34E-04	5,126,332	19.3
11R	US-82 RWP 1-5	2008	CMHB-F	Limestone	DC	6.20%	7.56	6300	3.16E-06	1.1	0.0103	6.04E-04	64	2.34E-04	1,090,174	28.6
11S	US-82 RWP 1-6	2008	CMHB-F	Limestone	DC	6.20%	7.41	8274	1.84E-06	0.47	0.0802	2.01E-04	64	2.34E-04	7,455,448	11.2
11T	US-82 RWP 2-4	2008	CMHB-F	Limestone	DC	6.20%	8.28	6428	8.85E-07	0.55	0.1025	2.09E-04	64	2.34E-04	13,719,081	9.7
11U	US-82 RWP 2-6	2008	CMHB-F	Limestone	DC	6.20%	7.36	6870	2.06E-06	0.41	0.0787	1.91E-04	64	2.34E-04	8,273,400	10.3
11V	US-82 RWP 2-5T	2008	CMHB-F	Limestone	DC	6.20%	6.60	5238	1.31E-06	0.72	0.0665	5.41E-04	64	2.34E-04	7,944,728	25.0
11W	US-82 RWP 2-6T	2008	CMHB-F	Limestone	DC	6.20%	6.72	5411	1.15E-06	0.7	0.0585	3.73E-04	64	2.34E-04	8,411,574	17.6
11X	US-82 RWP 3-2	2008	CMHB-F	Limestone	DC	6.20%	6.93	7692	1.82E-06	0.58	0.0739	2.09E-04	64	2.34E-04	5,328,098	13.6
11Y	US-82 RWP 3-4	2008	CMHB-F	Limestone	DC	6.20%	8.24	7435	2.19E-06	0.7	0.0958	2.59E-04	64	2.34E-04	3,319,197	20.3
11Z	US-82 RWP 3-5T	2008	CMHB-F	Limestone	DC	6.20%	5.06	5986	4.32E-06	0.26	0.0449	9.66E-05	64	2.34E-04	6,542,829	79.3
11AA	US-82 RWP 3-6T	2008	CMHB-F	Limestone	DC	6.20%	5.79	6945	8.49E-07	0.67	0.1026	3.42E-04	64	2.34E-04	10,323,461	14.7
11AB	US-82 RWP 4-2	2008	CMHB-F	Limestone	DC	6.20%	6.94	7796	2.01E-05	0.26	0.0338	4.09E-04	64	2.34E-04	1,227,711	35.5
11AC	US-82 RWP 4-3	2008	CMHB-F	Limestone	DC	6.20%	7.78	7366	7.37E-05	0.12	0.0384	4.94E-04	64	2.34E-04	527,028	82.8
11AD	US-82 RWP 4-3T	2008	CMHB-F	Limestone	DC	6.20%	10.07	5712	1.45E-06	0.45	0.1436	1.09E-04	64	2.34E-04	11,895,202	66.2
11AE	US-82 RWP 4-6T	2008	CMHB-F	Limestone	DC	6.20%	5.77	6060	1.46E-06	0.59	0.091	5.39E-04	64	2.34E-04	8,773,079	23.5
11AF	US-82 RWP 4-7T	2008	CMHB-F	Limestone	DC	6.20%	7.00	4092	1.83E-05	0.35	0.0333	4.02E-04	64	2.34E-04	1,328,656	36.9
12A	US-84 EBS 1-1	2009	CHMB-C	River Gravel/Limestone	DC	4.80%	6.65	6998	1.65E-06	0.58	0.0922	5.03E-04	51	1.82E-04	6,280,827	19.4
12A	US-84 EBS 1-3	2009	CHMB-C	River Gravel/Limestone	DC	4.80%	5.02	5931	2.39E-06	0.39	0.0918	2.70E-04	51	1.82E-04	8,194,835	12.2
12A	US-84 EBS 2-3	2009	CHMB-C	River Gravel/Limestone	DC	4.80%	4.92	6201	1.02E-06	0.56	0.0778	4.34E-04	51	1.82E-04	12,773,552	16.6
12A	US-84 EBS 2-4	2009	CHMB-C	River Gravel/Limestone	DC	4.80%	13.32	3616	1.18E-07	1.68	0.1501	1.46E-03	51	1.82E-04	106,849,092	77.7
12A	US-84 EBS 2-5	2009	CHMB-C	River Gravel/Limestone	DC	4.80%	3.36	3379	2.96E-08	1.47	0.0935	1.34E-03	51	1.82E-04	394,959,291	47.0
12A	US-84 EBS 2-3T	2009	CHMB-C	River Gravel/Limestone	DC	4.80%	6.04	3727	5.37E-08	1.29	0.0871	8.50E-04	51	1.82E-04	218,032,806	30.7
12A	US-84 EBS 2-4T	2009	CHMB-C	River Gravel/Limestone	DC	4.80%	2.91	4898	6.07E-08	0.81	0.1568	3.72E-04	51	1.82E-04	186,241,197	11.8
12A	US-84 EBS 3-2	2009	CHMB-C	River Gravel/Limestone	DC	4.80%	5.79	4518	6.61E-07	1.22	0.0519	1.13E-03	51	1.82E-04	10,267,036	48.1
12A	US-84 EBS 3-5	2009	CHMB-C	River Gravel/Limestone	DC	4.80%	4.09	5422	2.82E-07	1.08	0.0921	7.11E-04	51	1.82E-04	19,082,712	31.7
12A	US-84 EBS 3-3T	2009	CHMB-C	River Gravel/Limestone	DC	4.80%	7.51	3634	3.59E-07	0.76	0.099	4.61E-04	51	1.82E-04	44,252,852	13.3
12A	US-84 EBS 3-4T	2009	CHMB-C	River Gravel/Limestone	DC	4.80%	6.19	5773	1.45E-06	0.45	0.1014	2.78E-04	51	1.82E-04	11,870,470	10.6
12A	US-84 RWP 1-1	2009	CHMB-C	River Gravel/Limestone	DC	4.80%	4.56	7285	1.90E-06	0.5	0.0572	3.64E-04	51	1.82E-04	7,175,694	16.9
12A	US-84 RWP 1-3	2009	CHMB-C	River Gravel/Limestone	DC	4.80%	2.86	5522	2.00E-06	0.47	0.0412	4.21E-04	51	1.82E-04	9,509,013	17.9
12A	US-84 RWP 1-6	2009	CHMB-C	River Gravel/Limestone	DC	4.80%	4.34	5983	9.18E-06	0.35	0.0211	5.22E-04	51	1.82E-04	2,314,349	27.8
12A	US-84 RWP 2-2	2009	CHMB-C	River Gravel/Limestone	DC	4.80%	3.31	7156	1.45E-06	0.41	0.0866	3.72E-04	51	1.82E-04	11,470,585	13.9
12A	US-84 RWP 2-3	2009	CHMB-C	River Gravel/Limestone	DC	4.80%	3.88	3663	1.47E-07	0.83	0.0742	5.41E-04	51	1.82E-04	136,330,943	16.0
12A	US-84 RWP 2-5	2009	CHMB-C	River Gravel/Limestone	DC	4.80%	5.74	8137	6.78E-07	0.89	0.0817	4.01E-04	51	1.82E-04	7,154,127	23.1
12A	US-84 RWP 2-1T	2009	CHMB-C	River Gravel/Limestone	DC	4.80%	3.93	6578	1.85E-07	0.85	0.0874	3.51E-04	51	1.82E-04	41,850,637	14.3
12A	US-84 RWP 2-4T	2009	CHMB-C	River Gravel/Limestone	DC	4.80%	2.91	5311	2.83E-07	0.79	0.0767	6.00E-04	51	1.82E-04	35,711,048	22.0

ID	Sample	Construction Date	Mix Type	Agg Material	Environmental Zone	% Binder (Design)	%AV	E_{VE}	A	n	b	c_0	d (mm)	γ	N_f	c_{1000} (mm)
12A	US-84 RWP 2-5T	2009	CHMB-C	River Gravel/Limestone	DC	4.80%	4.49	4652	9.02E-06	0.4	0.0164	8.73E-04	51	1.82E-04	2,469,985	35.4
12A	US-84 RWP 3-5	2009	CHMB-C	River Gravel/Limestone	DC	4.80%	4.76	8385	1.86E-06	0.44	0.0741	3.21E-04	51	1.82E-04	7,010,653	14.5
12A	US-84 RWP 3-6	2009	CHMB-C	River Gravel/Limestone	DC	4.80%	4.03	6609	4.57E-06	0.44	0.042	4.19E-04	51	1.82E-04	3,608,424	23.9
12A	US-84 RWP 3-2T	2009	CHMB-C	River Gravel/Limestone	DC	4.80%	2.11	4429	3.03E-07	0.72	0.0713	5.85E-04	51	1.82E-04	52,652,922	20.8
12A	US-84 RWP 3-3T	2009	CHMB-C	River Gravel/Limestone	DC	4.80%	1.95	4376	3.21E-07	0.74	0.0496	6.18E-04	51	1.82E-04	42,617,693	21.0
13A	US-83 RWP 1-1	2008	Type-D	Granite	DC	5.30%	5.80	3000	Bad Data	Bad Data	Bad Data	Bad Data	51	2.18E-04	Bad Data	Bad Data
13B	US-83 RWP 1-5	2008	Type-D	Granite	DC	5.30%	9.81	1800	4.66E-06	0.58	0.002	1.59E-03	51	2.18E-04	5,246,070	22.4
13C	US-83 RWP 1-6	2008	Type-D	Granite	DC	5.30%	7.40	2467	1.12E-06	1.41	0.0198	1.28E-03	51	2.18E-04	7,401,666	57.2
13D	US-83 RWP 2-1	2008	Type-D	Granite	DC	5.30%	5.39	3335	1.11E-06	0.75	0.0316	5.79E-04	51	2.18E-04	15,704,464	21.8
13D	US-83 RWP 2-2	2008	Type-D	Granite	DC	5.30%	5.89	4137	4.95E-07	0.82	0.0671	5.08E-04	51	2.18E-04	20,289,381	20.1
13E	US-83 RWP 2-5	2008	Type-D	Granite	DC	5.30%	5.73	3289	3.13E-07	0.8	0.0796	6.11E-04	51	2.18E-04	43,523,745	19.4
13F	US-83 RWP 2-9T	2008	Type-D	Granite	DC	5.30%	4.30	2651	1.08E-07	1.42	0.0284	8.64E-04	51	2.18E-04	87,265,648	32.8
13G	US-83 RWP 2-11T	2008	Type-D	Granite	DC	5.30%	4.16	2536	1.90E-07	0.83	0.0541	5.68E-04	51	2.18E-04	103,672,442	16.1
13H	US-83 RWP 3-1	2008	Type-D	Granite	DC	5.30%	5.22	3759	6.66E-09	2.24	0.0489	7.21E-04	51	2.18E-04	213,286,205	35.3
13I	US-83 RWP 3-4	2008	Type-D	Granite	DC	5.30%	6.16	3822	4.48E-07	0.75	0.0801	5.20E-04	51	2.18E-04	28,543,661	18.0

ID	Sample	Construction Date	Mix Type	Agg Material	Environmental Zone	% Binder (Design)	%AV	E_{VE}	A	n	b	c_0	d (mm)	γ	N_f	c_{1000} (mm)
16E	FM-1936 SBS 1-2	2002	CMHB-F	Rhyolite	DW	7.30%	4.96	5172	9.65E-07	0.91	0.0495	1.15E-03	76	2.94E-04	7,157,503	47.7
16F	FM-1936 SBS 1-5	2002	CMHB-F	Rhyolite	DW	7.30%	4.97	4882	2.54E-07	2.48	0.0018	8.37E-04	76	2.94E-04	2,578,006	22.0
16F	FM-1936 SBS 3-3	2002	CMHB-F	Rhyolite	DW	7.30%	5.51	6684	7.92E-08	1.11	0.1256	6.83E-04	76	2.94E-04	38,043,223	26.3
16A	FM-1936 SBS 3-4	2002	CMHB-F	Rhyolite	DW	7.30%	5.69	6275	8.73E-07	0.74	0.0717	6.25E-04	76	2.94E-04	11,147,167	25.4
16F	FM-1936 SBS 3-5	2002	CMHB-F	Rhyolite	DW	7.30%	6.35	6405	6.57E-08	1.69	0.1155	7.52E-04	76	2.94E-04	12,715,441	49.5
17A	FM-2994 RWP 1-4	2002	Type-D	River Gravel	DW	5.50%	6.60	5040	4.72E-08	1.71	0.0739	6.21E-04	76	2.43E-04	25,966,165	26.8
17B	FM-2994 RWP 1-6	2002	Type-D	River Gravel	DW	5.50%	5.61	5097	5.37E-07	0.91	0.0692	4.13E-04	76	2.43E-04	14,291,777	17.7
17A	FM-2994 RWP 3-2	2002	Type-D	River Gravel	DW	5.50%	6.23	6756	3.46E-06	0.7	0.0812	4.47E-04	76	2.43E-04	2,995,135	29.5
17B	FM-2994 RWP 3-6	2002	Type-D	River Gravel	DW	5.50%	5.99	5983	5.53E-06	0.53	0.0517	3.77E-04	76	2.43E-04	2,964,643	23.9
17C	FM-2994 WBS 1-3	2002	Type-D	River Gravel	DW	5.50%	8.30	4140	1.31E-06	0.80	0.0608	3.60E-04	76	2.43E-04	8,441,135	16.8
17D	FM-2994 WBS 1-6	2002	Type-D	River Gravel	DW	5.50%	8.10	4597	1.36E-06	0.70	0.0673	4.47E-04	76	2.43E-04	8,678,263	17.6
17D	FM-2994 WBS 3-2	2002	Type-D	River Gravel	DW	5.50%	9.48	5400	1.08E-05	0.68	0.0759	3.70E-04	76	2.43E-04	1,107,752	36.3
17D	FM-2994 WBS 3-3	2002	Type-D	River Gravel	DW	5.50%	9.92	5140	2.55E-05	0.41	0.0229	4.74E-04	76	2.43E-04	955,461	38.1
18A	US-54 RWP 1-3	1998	Type-D	River Gravel	DC	?	7.59	5035	Bad Data	Bad Data	Bad Data	Bad Data	51	1.74E-04	Bad Data	Bad Data
18B	US-54 RWP 1-5	1998	Type-D	River Gravel	DC	?	6.92	5621	Fail	Fail	Fail	Fail	51	1.74E-04	Fail	Fail
18C	US-54 RWP 1-6	1998	Type-D	River Gravel	DC	?	5.79	Bad Data	Fail	Fail	Fail	Fail	51	1.74E-04	Fail	Fail
18D	US-54 RWP 2-2	1998	Type-D	River Gravel	DC	?	10.11	5809	Bad Data	Bad Data	Bad Data	Bad Data	51	1.74E-04	Bad Data	Bad Data
18E	US-54 RWP 2-4	1998	Type-D	River Gravel	DC	?	8.36	6757	1.81E-08	2.57	0.0407	5.46E-04	51	1.74E-04	2,970,626	30.6
18F	US-54 EBS 1-1	1998	Type-D	River Gravel	DC	?	9.67	5352	5.60E-07	0.91	0.0739	3.93E-04	51	1.74E-04	9,678,397	18.7
18G	US-54 EBS 1-3	1998	Type-D	River Gravel	DC	?	15.15	5503	2.71E-06	0.52	0.0698	4.29E-04	51	1.74E-04	4,150,131	18.1
18H	US-54 EBS 2-2	1998	Type-D	River Gravel	DC	?	9.71	6656	4.57E-06	1.48	0.0167	4.20E-04	51	1.74E-04	239,547	31.4
18I	US-54 EBS 2-5	1998	Type-D	River Gravel	DC	?	19.72	3620	Fail	Fail	Fail	Fail	51	1.74E-04	Fail	Fail
19B	SH-19/24 NBS 1-1	2000	Type-D	?	WC	?	12.99	3615	6.92E-08	1.23	0.0753	5.33E-04	51	1.64E-04	83,780,279	18.2
19C	SH-19/24 NBS 1-5	2000	Type-D	?	WC	?	13.12	Fail	Fail	Fail	Fail	Fail	51	1.64E-04	Fail	Fail
19B	SH-19/24 NBS 1-6	2000	Type-D	?	WC	?	11.75	5436	1.47E-05	0.28	0.0524	7.04E-04	51	1.64E-04	1,610,068	37.0
19B	SH-19/24 NBS 3-1	2000	Type-D	?	WC	?	13.79	6655	1.65E-06	0.71	0.0723	2.64E-04	51	1.64E-04	4,929,647	14.7
19B	SH-19/24 NBS 3-4	2000	Type-D	?	WC	?	11.90	7026	2.98E-06	0.59	0.0501	2.49E-04	51	1.64E-04	3,446,883	14.9
19D	SH-19/24 RWP 1-1	2000	Type-D	?	WC	?	7.25	Fail	Fail	Fail	Fail	Fail	51	1.64E-04	Fail	Fail
19D	SH-19/24 RWP 1-2	2000	Type-D	?	WC	?	7.56	4885	1.46E-05	1.33	0.0283	1.69E-03	51	1.64E-04	251,596	166.0
19B	SH-19/24 RWP 1-6	2000	Type-D	?	WC	?	9.29	3105	Fail	Fail	Fail	Fail	51	1.64E-04	Fail	Fail
19B	SH-19/24 RWP 3-1	2000	Type-D	?	WC	?	8.39	5339	Fail	Fail	Fail	Fail	51	1.64E-04	Fail	Fail
19D	SH-19/24 RWP 3-4	2000	Type-D	?	WC	?	8.63	6706	1.02E-07	0.87	0.1571	1.33E-04	51	1.64E-04	51,349,975	6.1
21F	SH-19/24 RWP 3-5	2000	Type-D	?	WC	?	8.63	6717	Fail	Fail	Fail	Fail	51	1.64E-04	Fail	Fail
20A	US-259 RWP 1-6(ATL)	2005	Type-D	River Gravel	WC	5.60%	5.00	5124	1.09E-06	0.91	0.0458	4.10E-04	51	2.11E-04	5,207,983	20.6
20B	US-259 RWP 1-3(ATL)	2005	Type-D	River Gravel	WC	5.60%	6.37	6848	6.14E-06	0.31	0.0492	2.35E-04	51	2.11E-04	3,178,180	14.4
20B	US-259 RWP 3-2(ATL)	2005	Type-D	River Gravel	WC	5.60%	5.61	6694	2.32E-06	0.58	0.0675	4.54E-04	51	2.11E-04	4,339,431	20.5
20B	US-259 RWP 3-3(ATL)	2005	Type-D	River Gravel	WC	5.60%	5.61	8067	1.06E-07	2.33	0.1072	4.51E-04	51	2.11E-04	1,183,418	44.0
20B	US-259 RWP 3-2T(ATL)	2005	Type-D	River Gravel	WC	5.60%	9.22	6955	1.76E-05	1.15	0.0496	3.43E-04	51	2.11E-04	166,534	44.2
20D	US-259 RWP 3-5T(ATL)	2005	Type-D	River Gravel	WC	5.60%	7.60	5468	2.89E-06	0.68	0.0605	3.73E-04	51	2.11E-04	3,530,834	20.7
20C	US-259 NBS 1-1(ATL)	2005	Type-D	River Gravel	WC	5.60%	7.18	6199	1.35E-06	0.66	0.0935	2.73E-04	51	2.11E-04	6,991,002	14.1
20D	US-259 NBS 1-5(ATL)	2005	Type-D	River Gravel	WC	5.60%	7.20	6084	7.13E-07	0.99	0.0659	4.19E-04	51	2.11E-04	7,572,491	19.8
20D	US-259 NBS 3-3(ATL)	2005	Type-D	River Gravel	WC	5.60%	6.69	6534	1.03E-06	0.62	0.106	3.16E-04	51	2.11E-04	8,735,579	13.4
20D	US-259 NBS 3-6(ATL)	2005	Type-D	River Gravel	WC	5.60%	7.47	6291	3.79E-06	0.7	0.0941	4.36E-04	51	2.11E-04	2,208,402	29.8
20D	US-259 NBS 3-2T(ATL)	2005	Type-D	River Gravel	WC	5.60%	8.42	6935	4.32E-06	0.76	0.1375	2.95E-04	51	2.11E-04	1,698,599	28.8
20D	US-259 NBS 3-6T(ATL)	2005	Type-D	River Gravel	WC	5.60%	9.48	6111	2.00E-06	0.52	0.0766	3.99E-04	51	2.11E-04	6,123,226	14.6
21A	US-190 NBS 1-1	2008	Type-C	Limestone	M	4.50%	11.81	Fail	Fail	Fail	Fail	Fail	51	1.59E-04	Fail	Fail
21B	US-190 NBS 1-2	2008	Type-C	Limestone	M	4.50%	11.84		Fail	Fail	Fail	Fail	51	1.59E-04	Fail	Fail
21C	US-190 NBS 1-5	2008	Type-C	Limestone	M	4.50%	11.61	Fail	Fail	Fail	Fail	Fail	51	1.59E-04	Fail	Fail
21D	US-190 NBS 1-6	2008	Type-C	Limestone	M	4.50%	14.64		Fail	Fail	Fail	Fail	51	1.59E-04	Fail	Fail
21A	US-190 NBS 3-1	2008	Type-C	Limestone	M	4.50%	16.94	9964	1.05E-04	0.34	0.109	5.12E-04	51	1.59E-04	149,526	121.0

ID	Sample	Construction Date	Mix Type	Agg Material	Environmental Zone	% Binder (Design)	%AV	E_{VE}	A	n	b	c_0	d (mm)	γ	N_f	c_{1000} (mm)
21B	US-190 NBS 3-2	2008	Type-C	Limestone	M	4.50%	16.41	9137	2.41E-04	0.63	0.0416	5.32E-04	51	1.59E-04	31,440	144.0
21A	US-190 NBS 3-3	2008	Type-C	Limestone	M	4.50%	17.21	10064	Fail	Fail	Fail	Fail	51	1.59E-04	Fail	Fail
21B	US-190 NBS 3-6	2008	Type-C	Limestone	M	4.50%	15.20	9218	Fail	Fail	Fail	Fail	51	1.59E-04	Fail	Fail
21E	US-190 RWP 1-1	2008	Type-C	Limestone	M	4.50%	6.73	9581	Fail	Fail	Fail	Fail	51	1.59E-04	Fail	Fail
21F	US-190 RWP 1-5	2008	Type-C	Limestone	M	4.50%	6.24	11787	1.13E-05	0.26	0.0158	2.60E-04	51	1.59E-04	1,807,322	18.5
21D	US-190 RWP 1-6	2008	Type-C	Limestone	M	4.50%	6.50	9724	1.93E-06	0.23	0.2701	1.32E-04	51	1.59E-04	10,881,894	6.8
21F	US-190 RWP 3-1	2008	Type-C	Limestone	M	4.50%	7.41	Fail	Fail	Fail	Fail	Fail	51	1.59E-04	Fail	Fail
21F	US-190 RWP 3-4	2008	Type-C	Limestone	M	4.50%	6.88	Fail	Fail	Fail	Fail	Fail	51	1.59E-04	Fail	Fail